



Anamimoghadam, Ommid (2013) *9-C-substituted phenalenones as promising precursors for the synthesis of novel stable phenalenyl-type cations and radicals*. PhD thesis.

<http://theses.gla.ac.uk/4433/>

Copyright and moral rights for this thesis are retained by the author

A copy can be downloaded for personal non-commercial research or study, without prior permission or charge

This thesis cannot be reproduced or quoted extensively from without first obtaining permission in writing from the Author

The content must not be changed in any way or sold commercially in any format or medium without the formal permission of the Author

When referring to this work, full bibliographic details including the author, title, awarding institution and date of the thesis must be given

**9-C-Substituted Phenalenones as Promising
Precursors for the Synthesis of Novel Stable
Phenalenyl-Type Cations and Radicals**

Ommid Anamimoghadam

PhD Thesis

School of Chemistry
University of Glasgow

April 2013

Für meine Eltern

Preface

The written work is a result of synthetic approaches to new phenalenyl type species with yet unknown potential for modern applications. Phenalenyl represents the smallest open shell framework in graphene and has attracted growing attention within the last two decades due to its unprecedented physicochemical features revealed in a series of quite recent discoveries. The research on these types of molecules is still ongoing to fully understand their nature and to apply them for modern applications as for instance, organic radical batteries, sensing molecules or material with multiphysical channels.

The initial idea of this project was based on the discovery on a phenalenyl type radical formed upon a photochemical reaction which will be presented and also employed (*Chapter 2*). A long persistence in solution was observed and calculations predicted a high thermodynamic stability. Therefore, a practical preparation was required leading to a synthetic route providing a series of derivatives. It is noteworthy that surprising and unprecedented effects encountered with regards to the analytical results.

Throughout the three years, the decisions determining the research efforts were met with a view on understanding the fundamental properties of the new synthesised molecules. A large part of the presented target molecules are positively charged heteroaromatics and neutral open-shell species. Open-shell species are compounds with a singly occupied molecular orbital (SOMO), that is, a radical. Despite the fact that they are usually highly reactive and easily form a covalent bond, they are attractive synthetic targets for chemists.

But how important is this for our everyday lives? This work has approached open-shell species and introduces their interesting features in terms of fundamental sciences and new functional materials as such as organic electrodes, molecular spintronic devices or quantum information processing which could have a huge impact on our society with regards to technology. Hence, an electron in a singly occupied molecular orbital could be compared with a valuable pearl in the open shell.



As a physical organic chemist, the determination of parameters and the employment of suitable analytical instruments such as evaluation of aromaticity, optical spectroscopy, ESR spectroscopy and cyclic voltammetry are crucial to investigate their properties. Based on the obtained data and an evaluation of the electronic structures, the characterisation as phenalenyl compounds could be justified.

Starting with an introduction to the principles and history of radical chemistry, the importance of the bottom-up approach of graphene fragments and their properties with respect to the zig-zag (open-shell) motif will be described. The reader will be introduced to important discoveries about the properties of phenalenyl radicals, and strategies aiming at the stabilisation of the parent phenalenyl framework. The stabilisation via the incorporation of a heteroatom in the aromatic framework is the principal characteristic of the phenalenyl derivatives synthesised in this work. These are related to the result of a previously discovered photochemical reaction, thus a brief review on the photochemical properties of *1H*-phenalen-1-one and aryl substituted *1H*-phenalenones is included as well.

Chapters 7-10 comprise the own work beginning with brief introductions specific to the topics dealt with. Then the results will be presented and separately discussed, hence the reader will find a result and discussion chapter which is followed by a conclusion of the corresponding chapter.

In the introduction (*Chapter 1-5*), molecules in schemes and figures are assigned to italics numbers in brackets. *Chapters 5* and *6* represent the aims and applied methods. The numbering of the molecules in *Chapter 7-10* then begins from 1 as bold figures and are only used for synthesised products, intermediates and species which are discussed in the text. Some target molecules are assigned to abbreviations containing letters. In the case of cationic species a “+”-sign is attached.

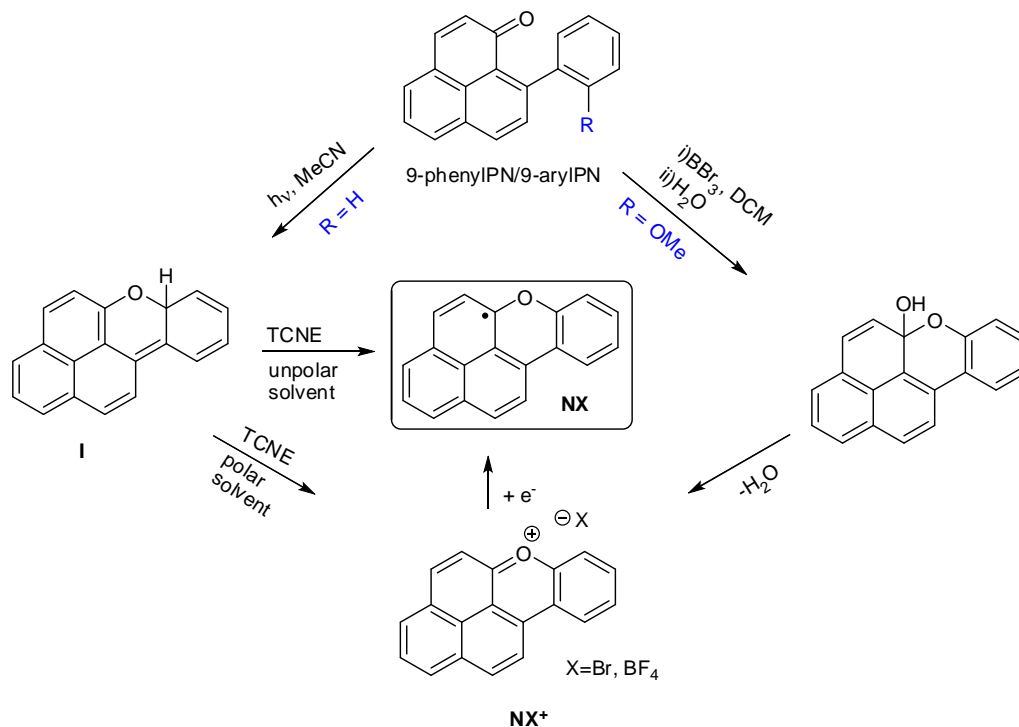
The appendix can be found at the end of the thesis containing all NMR spectra and X-ray data. Moreover, data from calculations and other analytical results (CV, ESR) which are linked in the thesis are attached.

The cyclic voltammograms, X-ray diffractions and some ESR spectra were kindly measured by *Dr Mark D. Symes, Dr Deliang Long (Cronin group, University of Glasgow, UK)* and *Daniel Sells (EPSRC EPR Centre, Manchester, UK)*, respectively.

The achievements of this work received great interest by the scientific community. For instance, Dr *Chris Kay* (*University College London, UK*) wishes to work on the potential of some of our prepared molecules with regards to modern applications as such as site-directed spin labeling of proteins using the phenalenyl radicals as spin probes as well as quantum information processing. Prof *Krishna Ganesh* (*ISER, Pune, India*) is interested in the potential of our phenalenyl cations undergoing (photo)oxidative reactions with DNA. For that reason, this project offers a great potential to extend its possibilities advancing different areas of modern physical organic chemistry.

Abstract

Previous research in the *Bucher* group led to the generation of a novel phenalenyl derived radical, naphtho[2,1,8-*mna*]xanthenyl (NX). Through the photolysis of 9-phenyl-1*H*-phenalenen-1-one (9-phenyl-PN), a transient 5*H*-naphtho[2,1,8-*mna*]xanthenone **I** with a very weak C(sp³)-H bond was formed and could undergo hydrogen abstraction in the presence of an electron acceptor such as tetracyanoethylene (TCNE) or benzoquinone (BQ).¹¹⁸ As a result, NX was formed which exhibited a long persistence based on electronic stabilisation (*Scheme A*). This thesis deals with the practical preparation of potential precursors of NX type radicals involving new naphtho[2,1,8-*mna*]xanthenium (NX⁺) salts synthesised from 9-aryl-1*H*-phenalenen-1-ones (9-aryl-PNs). 9-aryl-PNs will be prepared by a *Michael*-type *Grignard* addition which was introduced by *C.F. Koelsch* and *J.A. Anthes*.¹²² The key-step to the organic salts is the demethylation of the methoxy group at the *o*-position of the pendant 9-C aryl substituent of 9-aryl-PNs. Subsequently a reactive hemi-ketal will be formed which undergoes hydrolysis resulting in NX⁺. Based on the organic salts, electrochemical studies including the generation of the target radicals and characterisation via electron spin resonance spectroscopy were conducted.



Scheme A Synthetic pathways to the naphthoxanthenyl cation and radical starting with 9-phenyl-1*H*-phenalenen-1-one or 9-aryl-1*H*-phenalenen-1-one.

Similar to NX, 9-phenyl-PN derivatives with functional groups were prepared (*Figure A*). *S*-4-(1-oxo-1*H*-phenalen-9-yl)benzyl methanesulfonothioate **II** shall serve as a precursor for a paramagnetic sensing molecule. This could involve applications in biochemistry as such as site-directed spin labeling of proteins (SDSL).²²⁵ 9-(4-((TEMPO)methyl)phenyl)-1*H*-phenalen-1-one **III** was prepared including ESR experiments to observe the reversible β -phenyl quenching process through changes of parameters in the ESR spectrum. The photolysis of **III** in presence of TCNE was also carried out resulting in the biradical NXTEMPO consisting of one π -delocalised and one localised unpaired electron.

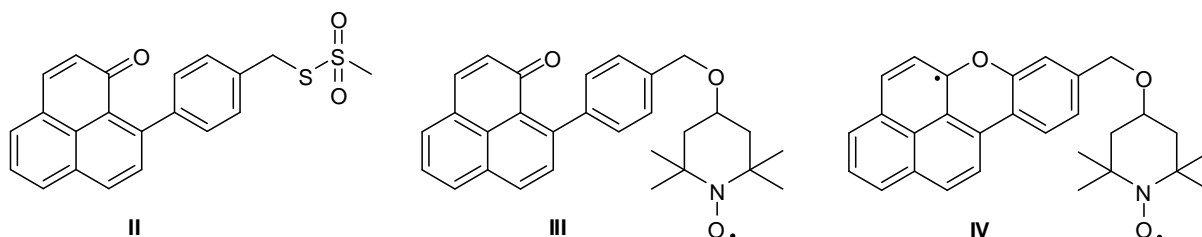
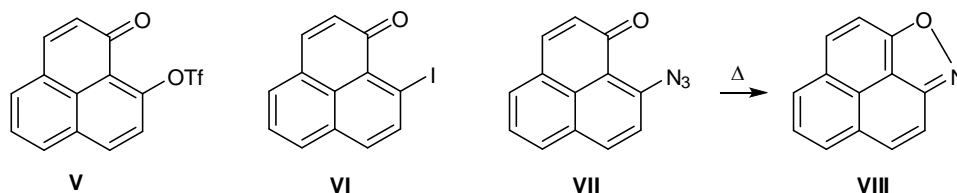


Figure A Molecular structures of *S*-4-(1-oxo-1*H*-phenalen-9-yl)benzyl methanesulfonothioate **II**, 9-(4-((TEMPO)methyl)phenyl)-1*H*-phenalen-1-one **III** and biradical (NXTEMPO).

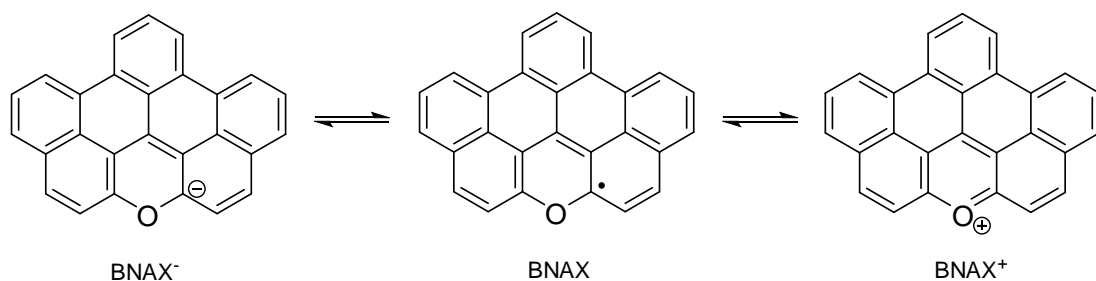
An additional achievement is the synthesis of 1-oxo-1*H*-phenalen-9-yl trifluoromethanesulfonate **V**, 9-iodo-1*H*-phenalen-1-one **VI** and phenaleno[1,9-*cd*]isoxazole **VIII** (*Scheme B*). The latter species resulted from thermal cyclisation of 9-azido-1*H*-phenalen-1-one **VII** similarly to 2-acyl-1-azido-3-phenalenones to phenaleno[1,2-*c*]isoxazol-7-one according to the literature.²⁵² Compounds **V** and **VI** are suggested as precursors for palladium catalysed coupling reactions^{256,257} which may serve as promising alternatives to the *Grignard* addition.



Scheme B Molecular structures of 1-oxo-1*H*-phenalen-9-yl trifluoromethanesulfonate **V**, 9-iodo-1*H*-phenalen-1-one **VI** and 9-azido-1*H*-phenalen-1-one **VII** resulting in phenaleno[1,9-*cd*]isoxazole **VIII**.

Benzo[5,6]naphthaceno[1,12,11,10-*ijklmna*]xanthylum (BNAX⁺), a polyaromatic hydrocarbon containing an oxygen atom in the aromatic framework, was prepared and modified by

substitution by alkyl chains by *K. Müllen* with the aim of generating discotic self-assembling aggregates. This research focused on their promising advances in the development of novel photovoltaic materials.²⁰ As a side project, the parent BNAX⁺ molecule was prepared to obtain crystals of sufficient quality to carry out X-ray structure analysis. With the obtained data, HOMA indices were derived to evaluate the aromaticity of the species. In addition, electrochemical studies (*Scheme C*) were carried out. It is noteworthy that BNAX⁺ represents the largest known PAH incorporating a pyrylium ring.



Scheme C Amphoteric species of benzo[5,6]naphthaceno[1,12,11,10-*jklmna*]xanthyl.

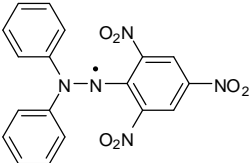
Statement of sources

I hereby certify that this material, which I now submit for assessment on the programme of study leading to Doctor of Philosophy degree in Chemistry is entirely my own work, that I have exercised reasonable care to ensure that the work is original, and does not to the best of my knowledge breach any law of copyright, and has not been taken from the work of others save and to the extent that such work has been cited and acknowledged within the text of my work.

Ommid Anamimoghadam

Signed: _____ Date: _____

Abbreviations

AcOH	Acetic acid
APT	Atomic polar tensor
B[a]NX	Benzo[a]naphtho[8,1,2- <i>jkl</i>]xanthenyl
B[i]NX	Benzo[i]naphtho[2,1,8- <i>mna</i>]xanthenyl
BNAX	Benzo[5,6]naphthaceno[1,12,11,10- <i>jklmna</i>]xanthylium
Bn	Benzene
BPQ	β -phenyl-quenching
COSY	Correlation spectroscopy
CT	Charge transfer
CW-ESR	Continuous wave-electron spin resonance
DCM	Dichloromethane
DDQ	2,3-Dichloro-5,6-dicyano-1,4-benzoquinone
DFT	Density functional theory
DIBAL-H	Diisobutylaluminium hydride
DMF	Dimethylformamide
DMSO	Dimethyl sulfoxide
DPPH	 2,2-diphenyl-1-picrylhydrazyl
DTPLY	1,9-Dithiophenalenyl
EtOAc	Ethyl acetate
EtOH	Ethanol
hfc	Hyperfine coupling constant
HOMA	Harmonic oscillating
HOMO	Highest occupied molecular orbital
IC	Internal conversion
ISC	Intersystem crossing

LUMO	Lowest unoccupied molecular orbital
MeCN	Acetonitrile
MeOH	Methanol
NaMTS	Sodium methanesulfonothioate
NBS	<i>N</i> -Bromosuccinimide
NICS	Nucleus independent chemical shift
NOESY	Nuclear <i>Overhauser</i> effect spectroscopy
NX	Naphtho[1,2,8- <i>mna</i>]xanthenyl
NXMTS	S-4-(1-oxo-1 <i>H</i> -phenalen-9-yl)benzyl methanesulfonothioate
NXTEMPO	8-((TEMPO)methoxy)naphtho[2,1,8- <i>mna</i>]xanthenyl
OAH	Odd alternant hydrocarbon
PAH	Polyaromatic hydrocarbon
PLY	Phenalenyl
PN	1 <i>H</i> -phenalen-1-one
SCE	Saturated calomel electrode
SDSL	Site-directed spin labeling
SOMO	Singly occupied molecular orbital
TB6OPO	Tri- <i>tert</i> -butyl-6-oxophenalenoxyl
TBPLY	2,5,8-tri- <i>tert</i> -butylphenyl
TCNE	Tetracyanoethylene
TFA	Trifluoroacetic acid
TEMPO	(2,2,6,6-Tetramethylpiperidin-1-yl)oxyl
Tf ₂ O	Triflic anhydride
THF	Tetrahydrofuran
TLC	Thin layer chromatography
TOTA	Trioxatriangulenium
TTPLY	1,6,7,9-Tetrathiophenalenyl

Table of Contents

1. Introduction to carbocations and carbon centred radicals.....	1
2. Principles.....	7
2.1. Electron spin resonance (ESR) spectroscopy.....	7
2.2. Cyclic voltammetry.....	10
2.3. Energy state diagram (<i>Jablonski</i> diagram).....	12
3. Review of closed shell polyaromatics and open shell polyaromatics according to phenalenyl.....	14
4. The photochemistry of phenalenones and the naphtho[2,1,8- <i>mna</i>]xanthenyl skeleton.....	37
5. Aims.....	47
6. Applied methods.....	48
6.1. Solvents and reagents.....	48
6.2. Spectroscopic methods.....	48
6.3. Chromatographic methods.....	48
6.4. Analytical methods.....	49
7. Approaches to new phenalenyl based naphthoxanthenyl cations and radicals.....	49
7.1. Introduction.....	49
7.2. Results.....	52
7.2.1. Initial attempt to synthesise the naphtho[2,1,8- <i>mna</i>]xanthenium cation.....	52
7.2.2. Synthesis of 9-aryl-1 <i>H</i> -phenalen-1-ones.....	54
7.2.3. ¹ H-NMR spectroscopy of 9-aryl-1 <i>H</i> -phenalen-1-ones.....	56
7.2.4. UV/Vis & mass spectrometry of 9-aryl-1 <i>H</i> -phenalen-1-ones.....	61

7.2.5	Synthesis of naphthoxanthenyl cations.....	62
7.2.6.	¹ H-NMR spectroscopy of naphthoxanthenyl cations.....	63
7.2.7.	UV/Vis, fluorescence & mass spectroscopy of naphthoxanthenyl cations.....	67
7.2.8.	X-ray structure analysis of naphthoxanthenyl cations.....	69
7.2.9.	Cyclic voltammetry results of naphthoxanthenyl cations.....	74
7.2.10.	Generation of naphthoxanthenyl radicals.....	76
7.3.	Discussion.....	79
7.3.1.	Initial attempt to synthesise the naphtho[2,1,8- <i>mna</i>]xanthenium cation.....	79
7.3.2.	Synthesis of 9-aryl-1 <i>H</i> -phenalen-1-ones.....	86
7.3.3.	Synthesis of naphthoaxnathenyl cations and radicals.....	92
7.3.4.	X-ray structure analysis, spectral effects and HOMA evaluation.....	101
7.3.5.	Cyclic voltammetry studies of naphthoxanthenyl cations.....	114
7.3.6.	Electron spin resonance spectroscopy.....	115
7.4.	Conclusions.....	118
8.	Synthesis of a potential probe for SDSL studies and an ESR responsively switchable molecule controlled via irradiation.....	120
8.1.	Introduction.....	120
8.2.	Results.....	122
8.2.1.	Synthesis of 9-(4-(TEMPO-methyl)phenyl)-1 <i>H</i> -phenalen-1-one.....	122
8.2.2.	¹ H-NMR spectroscopy.....	123
8.2.3.	UV/Vis and mass spectroscopy.....	126
8.2.4.	X-ray structure analysis.....	127

8.2.5. ESR spectroscopy.....	128
8.3. Discussion.....	131
8.3.1. Synthesis.....	131
8.3.2. ESR photoexperiment.....	133
8.4. Conclusions.....	135
9. Functionalisation and structures of novel phenalenones and the first closed-shell phenalenyl involving an isoxazol group.....	135
9.1. Introduction.....	135
9.2. Results.....	138
9.2.1. Synthesis.....	138
9.2.2. ¹ H-NMR spectroscopy.....	139
9.2.3. UV/Vis spectroscopy.....	143
9.2.4. X-ray structure analysis.....	144
9.3. Discussion.....	149
9.3.1. Synthesis.....	149
9.3.3. X-ray structure analysis.....	152
9.4. Conclusions.....	153
10. HOMA evaluation and cyclic voltammetry results of BNAX ⁺	153
10.1. Introduction.....	153
10.2. Results.....	154
10.2.1. Synthesis.....	154
10.2.2. X-ray structure analysis.....	155

10.2.3. Cyclic voltammetry.....	156
10.3. Discussion.....	157
10.3.1. Synthesis.....	157
10.3.2. HOMA evaluation and computational results.....	159
10.3.3 Electrochemical properties.....	161
10.4. Conclusions.....	163
11. Experimental section.....	164
12. Appendix.....	187
13. References.....	251

1. Introduction to carbocations and carbon centred radicals

Physical organic chemistry deals with the structure and reactivity of molecules. This has involved exploring mechanisms by detection of reaction intermediates, excited, charged and subvalent entities. Thus, the utilisation of advanced analytical methods has been indispensable to access insight into the behaviour and structure of those species or to explain the stability of unexpectedly stable molecules and their features. In this thesis, the two most important species, carbocation and radical, will be introduced.

Carbocation:

A carbocation generally exhibits sp^2 geometry with an empty π -orbital (*Figure 1.1*). Hence, the carbon atom accommodates six valence electrons and exhibits a planar structure which makes it electrophilic. As carbocations have not been analytically identified for a long period of time, their existence had been called into question.

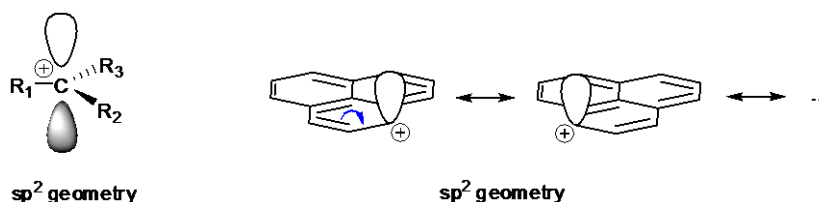
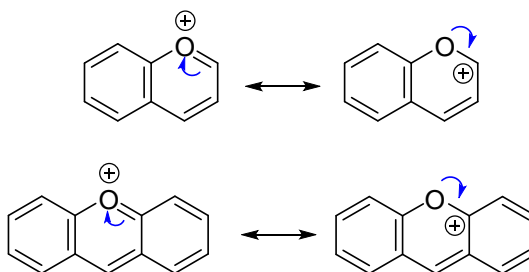


Figure 1.1 Planar carbocations; Left: localised positive charge; Right: π -delocalised phenalenyl cation.

When *F.C. Whitmore* generalised the concept of carbocations, the notation R_3C^+ still had not been asserted in any of his publications.¹ Eventually, well-respected scientists, worth mentioning *G.A. Olah* (Nobel prize in 1994), helped to get the idea of carbocations enforced by elaborated kinetic and stereochemical studies and analysis of reaction products.^{2,3} In the 1920s, *C. K. Ingold* and *E.H. Hughes* investigated nucleophilic substitution (S_N1) and elimination reactions (E1). This revealed the importance of carbocation intermediates as the basis for this type of reactions. Nucleophilic attack can occur orthogonal to the three sp^2 orbitals from i.e. above and below the plane.

The stabilisation of carbocations can be promoted either by steric effects, electron-donating groups or delocalisation of the empty π -orbital. As a good example, benzopyrylium- and xanthylium cations are stabilised through π -conjugation with contribution from the concomitant electron donating ability of the ether oxygen in its resonance structure (*Scheme 1.1*). The characterisation had been argued by *A. Werner* and *A. Baeyer* if they are oxonium or carbenium salts.^{4,5} Today both perspectives are considered as correct.



Scheme 1.1 Resonance structures between carbenium and oxonium ions of benzopyrylium and xanthylium cations.

In nature, stable carbocations play a crucial role in many ways. Among them are flavylium cations, also known as anthocyanins. Besides their antioxidant properties, they are responsible for the protection from intense sunlight in plant tissues including leaves, stems, fruits, roots and flowers. Due to the chromane ring, flavylium cations fluoresce cyanic colors ranging from salmon pink through red and violet to dark blue (*Figure 1.2*).⁶

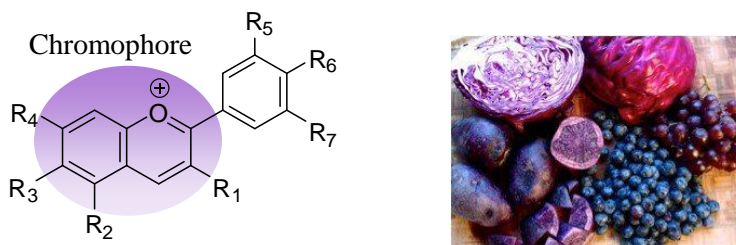


Figure 1.2 Structure of flavylium cations.

A further cation composed of a xanthylium and a phenalenyl unit has been detected via mass spectroscopy as a $(M-1)^+$ peak of 9-aryl substituted phenalenones (*Figure 1.3*).⁷ Phenalenones are fungicides classified as phytoanticipins or phytoalexins in plant tissues.⁸ Phytoalexins are characteristic for their subsequent production in plants after a microbial attack. Those are able

to undergo photochemical reactions often involving the generation of singlet oxygen.⁹ Despite extensive studies on phenalenones, the cyclised cation has only been detected via mass spectroscopy, hence more detailed structural characterisation or properties are necessary.

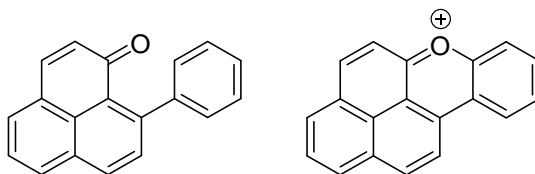


Figure 1.3 Structure of 9-(phenyl)-1H-phenalen-1-one and the naphtho[2,1,8-mna]xanthenium cation.

Carbon centred radicals:

Carbon centred radicals are molecules with an open shell configuration. They can be neutral or charged and accommodate one unpaired electron in the valence orbital. Hence, they are subvalent species with a high propensity to undergo dimerisation, disproportionation, electron transfer or H-abstraction. *Figure 1.4* depicts a neutral carbon centred radical which exhibits either 1) a quasi-trigonal sp_2 (e.g. methyl radical) or pyramidal geometry (e.g. trifluoromethyl) or 2) an sp^2 geometry in a conjugated π -electron system.

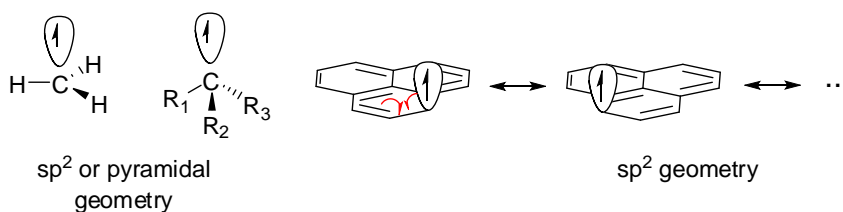


Figure 1.4 Neutral carbon centred radicals.

Carbon centred radicals can be stabilised by steric effects, adjacent electron-withdrawing groups, electron-donating groups and π -conjugation. They can be electrophilic or nucleophilic depending on the energy of the singly occupied molecular orbital (SOMO) (*Figure 1.5*). Thus a high-energy SOMO and a low-energy SOMO tend to exhibit a nucleophilic and an electrophilic character, respectively. Considering the energy level diagram, a SOMO is located between the highest occupied molecular orbital (HOMO) and the lowest unoccupied molecular orbital (LUMO). A decrease of the energy of the SOMO can occur by influence of

π -conjugation, adjacent electron-withdrawing groups and steric relief. In case of an electron donating group such as ether oxygen, the energy of the SOMO is increased through the interaction between SOMO and the non-bonding orbital of oxygen. The resulting reactivity of a high-energy SOMO and a low-energy SOMO (towards electron rich and electron poor alkenes, for instance) can be illustrated by the energy level diagram, as depicted in *Figure 1.5*.

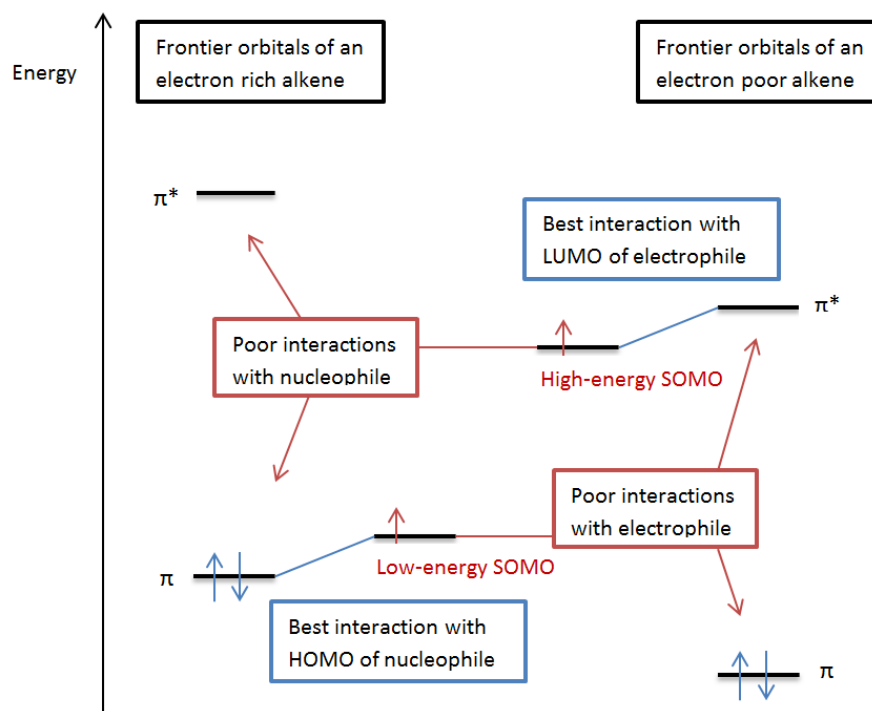


Figure 1.5 Energy level diagram illustrating SOMOs of electrophilic and nucleophilic radicals interacting with nucleophiles and electrophiles, respectively.

In the history of organic chemistry, the term “radical” was introduced by *A.L. Lavoisier* in 1789¹⁰ and initiated the development of the radical theory. Before 1900, a radical was generally described as a part of a molecule which does not change its atomic connectivity after a chemical transformation. *Figure 1.6* illustrates this concept of radicals with the example of benzoyl. Various scientists supported this core idea among them *J.F. Liebig* and *F. Wöhler* who suggested the benzoyl radical in 1832.¹¹ Benzoyl represented an immutable substructure through a series of conversions of benzaldehyde, benzoic acid, benzoyl chloride, benzoic amide and benzoyl cyanide.¹² *J.J. Berzelius*, a father of modern organic chemistry, considered the radical theory as a breakthrough in organic chemistry and had the idea of isolating radicals in an unbound state.¹³

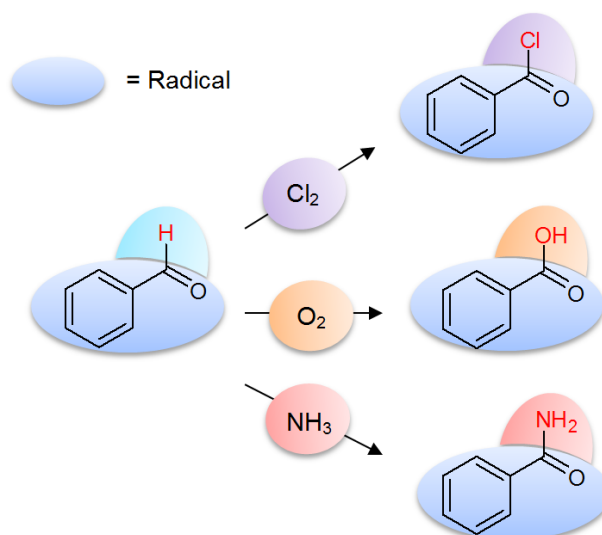
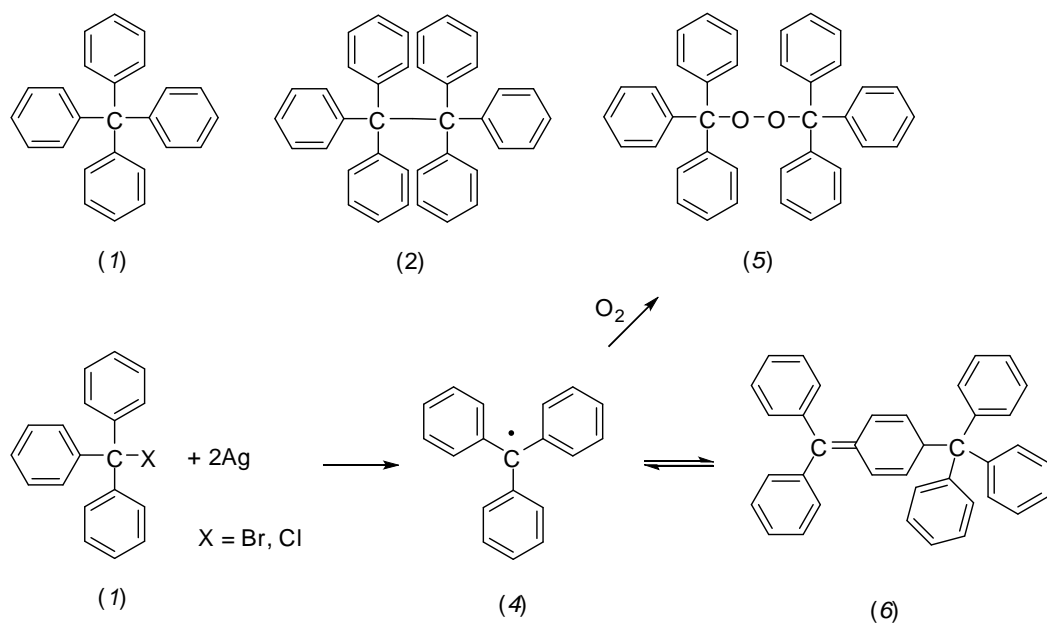


Figure 1.6 Idea of the benzoyl radical according to the radical theory. Benzoyl as an immutable fragment is considered a radical.

However, the truth about radicals remained unexplained during the 19th century. In particular the atomic structure of carbon still had to be clarified. *F.A. Kekulé* had to deal with the structural theory of the tetra-valent carbon atom which already gave rise to the benzene problem.¹⁴ Thus the isolation of a trivalent carbon became doubtful at this time. Eventually, in 1900 the questioning of the radical theory declined thanks to *M.J. Gomberg*'s discovery of the triphenylmethyl radical which established the paradigm of today.¹⁵

For the first time, *M.J. Gomberg* was able to show evidence of a free carbon centred radical, the propeller-like triphenylmethyl (4) (*Scheme 1.2*). First, the synthesis of hexaphenylethane (2) was attempted to compare its reactivity with tetraphenylmethane (1). After heating of halogenated triphenylmethane (3) in the presence of silver, a new colourless and crystalline compound precipitated, suggesting an oxygen containing compound according to the elemental analysis. *M.J. Gomberg* assumed that the reaction resulted in white crystalline triphenylmethylperoxide (5) by airborne oxygen. Subsequently the experiment was conducted under a CO₂-atmosphere. This resulted in a clear solution which became reversibly discoloured upon heating. Again in the atmosphere of oxygen, (5) was rapidly formed. With regards to those observations, he concluded the generation of coloured (4) which was in equilibrium with its dimer (6). Remarkably, these experiments clarified the paradigm of

radicals and revealed three typical radical reactions, thermolytic cleavage, dimerisation and reaction with oxygen.



Scheme 1.2 Generation of the triphenylmethyl radical by *M.J. Gomberg*.

Since *Gomberg*'s pioneering work, radical chemistry occupied one of the central positions in physical organic chemistry. This involved the studies of electronic and geometric structures of new species as well as the observation of short-lived reactive intermediates via spectroscopic methods.

Significant advances in radical chemistry were triggered by electron spin resonance spectroscopy (ESR).¹⁶ ESR spectroscopy is based on the detection of paramagnetic molecules absorbing microwave radiation in a strong magnetic field. The magnetic momentum can only align in defined direction whereas the transition occurs by absorption of a quantum of energy. An ESR spectrum reveals information of spin orbit interactions (via *g*-factor which varies from the value of a free electron ($g_{\text{electron}} = 2.0023$) and spin densities correlating with hyperfine coupling constants (*hfc*). Empirical and *ab initio* methods of quantum chemistry have been developed to the extent that theoretical interpretations of complex spectra can explain the relationship between the geometry and electronic structure.

Today a physical organic chemist bears the challenge to design and develop modern functional devices and materials. To comply with the needs of society, scientific communities in photochemistry, green chemistry, material sciences, scientific computing, analytical chemistry and organic synthesis involve the research and achievements of newly advanced technology with respect to miniaturisation and more environmental friendly and powerful devices. Stabilisation of excited, charged or subvalent entities have led to great advances in the development of organic based magnets¹⁷, conductive, semi-conductive and photovoltaic materials^{18,19,20}, organic-based catalysts²¹, reagents²², analytical methodology,²³ switchable devices^{19,24}, new computational architecture (quantum computing)^{25,26} and other subjects of modern chemistry.

2. Principles

2.1. Electron spin resonance (ESR) spectroscopy

Electron spin resonance spectroscopy (ESR) is a selective analytical method which detects species containing an unpaired electron. A signal will be observed when a required amount of energy is absorbed resulting in a change of the electron spin. This is achieved by sweeping a magnetic field under a microwave radiation of constant energy.

An unpaired electron in a magnetic field generates a magnetic moment μ_E^z along the z-axis (direction of the applied magnetic field) where only two values are allowed. This stands in relation to the electron spin quantum number $\pm 1/2$ associated with the spin angular momentum. Thus the magnetic moment μ_E^z of an electron can be described as:

$$\mu_E^z = -S_z \cdot g \cdot \mu_B$$

where g represents the g -factor ($g = 2.00323$ for a free electron) and μ_B is the *Bohr* magneton ($9.274 \cdot 10^{-28} \text{ J}\cdot\text{G}^{-1}$). If a magnetic field is applied, the z -component of the spin angular momentum operator S_z has a parallel or antiparallel orientation. This splits into two different energy terms, known as the *Zeeman-effect* (*Figure 2.1.1*). The phenomenon can be expressed with the help of the Hamiltonian H involving the applied magnetic field B .

$$H = -\mu_E^z \cdot B = S_z \cdot g \cdot \mu_B \cdot B$$

The difference of energy between both energy terms E_a and E_b can be determined by

$$\Delta E = E_a - E_b = +1/2 \cdot g \cdot \mu_B \cdot B - (-1/2) \cdot g \cdot \mu_B \cdot B = g \cdot \mu_B \cdot B = h \cdot \nu$$

and can be viewed as the energy required (e.g. from a photon) to make a transition feasible. In ESR spectroscopy, this transition will be realised by microwave energy which is perpendicular to the magnetic field B . This transition involves a flip of the spin. The gyromagnetic ratio γ_E , a ratio of the magnetic dipole moment of the electron to its angular momentum, indicates by the term

$$\gamma_E = \nu/B = (g \cdot \mu_B)/h$$

that the requirement for a resonance can be achieved by variation of the frequency or the field strength. It is common that an ESR spectrometer is equipped with an X-Band source emitting a frequency of ~ 10 GHz where a free electron can be found at 3390 Gauss.

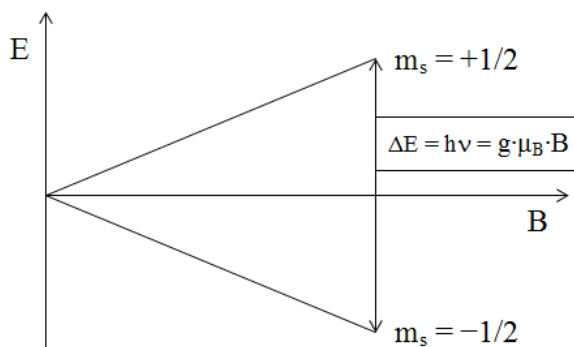


Figure 2.1.1 Illustration of *Zeeman-effect*.

Considering a free electron, the resonance spectrum only reveals an integrated intensity proportional to the radical concentration. This does not appear to lead to detailed analytical information. However, unpaired electrons interact with their environment and can be observed in ESR spectra indicating information of the structure of a radical or dynamics in radical reactions.

An electron experiences interactions with the nuclear magnetic moments, the so-called nuclear hyperfine interactions. A nucleus of spin I is able to split the electron spin levels into $(2 \cdot M \cdot I + 1)$ sublevels. M represents the number of equal nuclei. The splitting pattern will be reflected in

the spectrum and assigned to hyperfine coupling constants (hfc). As an example, the ESR spectrum of the symmetric phenalenyl is depicted in *Figure 2.1.2* to illustrate a multi-lined pattern caused by nuclear hyperfine interactions.²⁷ Considering the two groups of equal nuclei of the protons at the α - and β -positions, one may calculate the number of lines to be expected. There are $M_\alpha = 6$ equal nuclei at the α -positions and $M_\beta = 3$ equal nuclei at the β -positions. Therefore $(2 \cdot 6 \cdot 1/2 + 1) \cdot (2 \cdot 3 \cdot 1/2 + 1) = 7 \cdot 4 = 28$ sublevels should be generated which are confirmed with the number of lines in the ESR spectrum. According to the line intensities, the distribution follows the *Pascal's* triangle. Thus the α -protons and β -protons cause a split into 1:6:15:20:15:6:1 (assigned to black numbers in *Figure 2.1.2*) and 1:3:3:1 (assigned to red numbers), respectively, representing a septet of quartets.

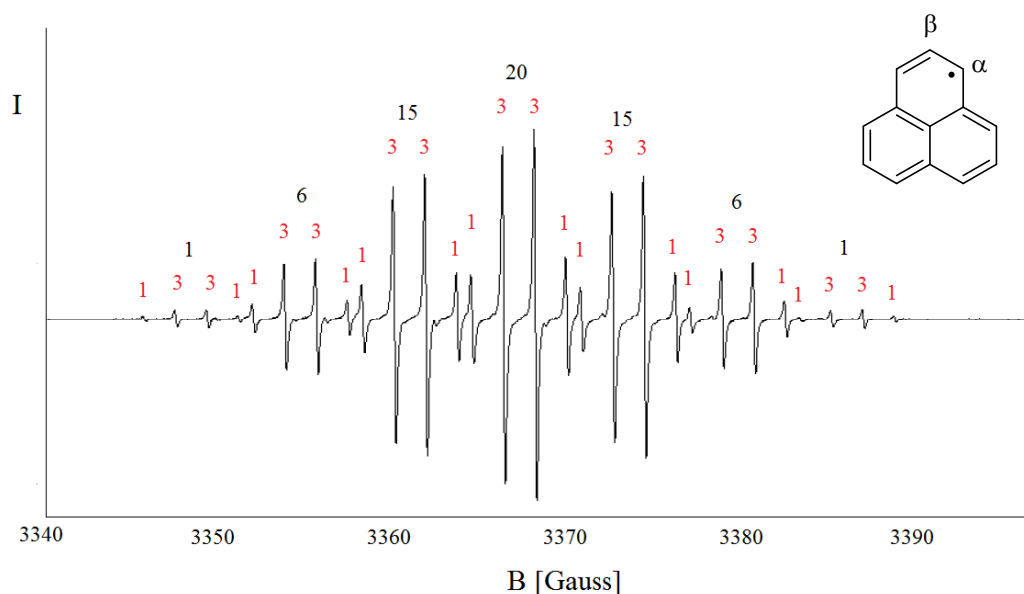


Figure 2.1.2 X-Band ESR spectrum of phenalenyl.²⁷

The hyperfine coupling constants are proportional to the spin densities in a radical molecule. Thus a fully electronic structure can be interpreted and used to predict, for instance, the most reactive positions in a carbon-centred molecule. Prevalently the support of spectra simulations is necessary due to the complexity of the splitting pattern especially in π -conjugated species.

ESR spectroscopy is a highly sensitive technique which is able to detect a radical with a concentration of only 10^{-9} mol/l at room temperature. Due to a timescale of 10-100 ns,

diffusion controlled processes can be recorded and used to interpret mechanisms of rapid reactions.

2.2. Cyclic Voltammetry

Cyclic voltammetry has developed as a useful technique to investigate electrochemical oxidation and reduction reactions. Considering the unit volt (Joule/Coulomb), it appears intuitive that voltage describes the amount of energy which is required to move a charge. Based on this key concept, an electron transfer can be induced by an applied voltage allowing the redox potential, kinetic parameters as well as diffusion constants to be determined. The simplest instrumental set-up (*Figure 2.2.1*) requires a reference electrode, a working electrode and a counter electrode dipped in an electrolyte solution. A controlled potential between the working electrode and reference electrode is provided by a potentiostat. The potential at the working electrode can be varied by a voltage scan generator. At the same time a recording device captures the resulting current-voltage curve, the so-called cyclic voltammogram which can be processed via a computer.

An electrochemical process is in great part governed by the *Nernst* equation which involves the relationship between the electrode and the concentrations of the oxidised (O) and reduced (R) species.



$$\text{Nernst equation: } E = E^{\text{Ox/Red}} + [R \cdot T / (z \cdot F)] \cdot \ln(c_{\text{O}} / c_{\text{R}})$$

$E^{\text{Ox/Red}}$ represents the potential where the electron transfer between O and R is in equilibrium, F is the *Faraday* constant ($96.485 \text{ C} \cdot \text{mol}^{-1}$) and c_{O} and c_{R} are the concentrations of O and R, respectively. If a potential is applied, then the concentrations c_{O} and c_{R} on the electrode surface will vary from those in the bulk solution. The redox process on the electrode surface will increase the current which is reflected in the cyclic voltammogram on the y-axis. If the electron transfer occurs very rapidly the process is mostly diffusion controlled. This can be expressed by *Fick's* first law describing the mass transfer from an area of high concentration to an area of low concentration.

$$\text{Fick's law: } J = dn / A \cdot dt = -D \cdot (\delta c / \delta x)_{x=0}$$

J represents the flux of moles of material n diffusing per unit area A per unit time t , D is the diffusion constant and $(\delta c/\delta x)_{x=0}$ is the partial derivative of the concentration with respect to distance. If the species reaches the electrode surface then the distance x will be taken as 0.

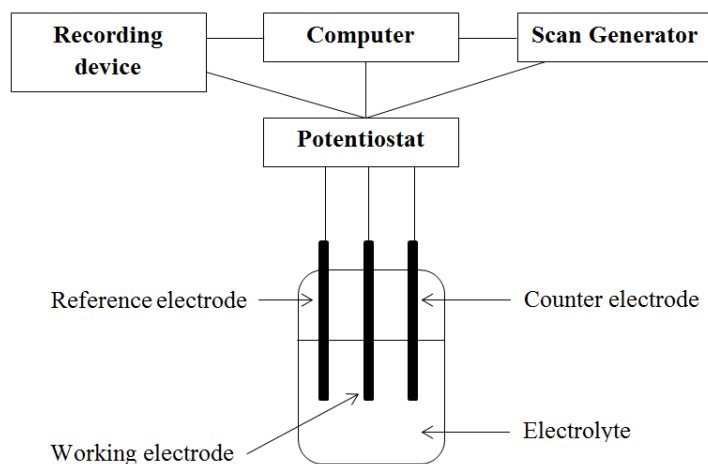


Figure 2.2.1 Instrumental set-up for a cyclic voltammetry measurement.

Invoking *Faraday's* law, the flux and the charge passed for an oxidation or reduction can be expressed in a relationship, so that a current is given by

$$\begin{aligned} \text{Faraday's law: } Q &= z \cdot n \cdot F & \Leftrightarrow & \quad Q = \int_0^t I dt \\ \Leftrightarrow \quad I &= dQ/dt = -z \cdot F \cdot dn/dt = -z \cdot F \cdot A \cdot J = z \cdot F \cdot A \cdot D \cdot (\delta c/\delta x)_{x=0} \end{aligned}$$

where z represents the valence number of ions and I is the current. This is the fundamental equation which is used to calculate the current in an amperometric experiment.

A cyclic voltammogram generally reflects the current passing over a range of chosen voltage. The quantification of the potential derives from a chosen constant sweep rate (volts per second) and a switching potential where the sweeping will be reversed. Since the sweep rate, the initial potential and the switching potential are known, current versus applied potential can be recorded in the form of a cyclic course, hence the term cyclic voltammetry. The sweeping rate called v is involved in the equation for the peak current and is expressed as follows:

$$I_p = (2.69 \cdot 10^5) \cdot n^{3/2} \cdot A \cdot D^{1/2} \cdot v^{1/2} \cdot c$$

The variable c is the concentration in the bulk solution (typically in mol cm^{-3}).

According to the above-described fundamentals of cyclic voltammetry, the below-depicted scheme may illustrate single electron transfers of an electrochemically reversible molecule such as the stable phenalenyl radical 2,5,8-tri-*tert*-butylphenalenyl (Figure 2.2.2).

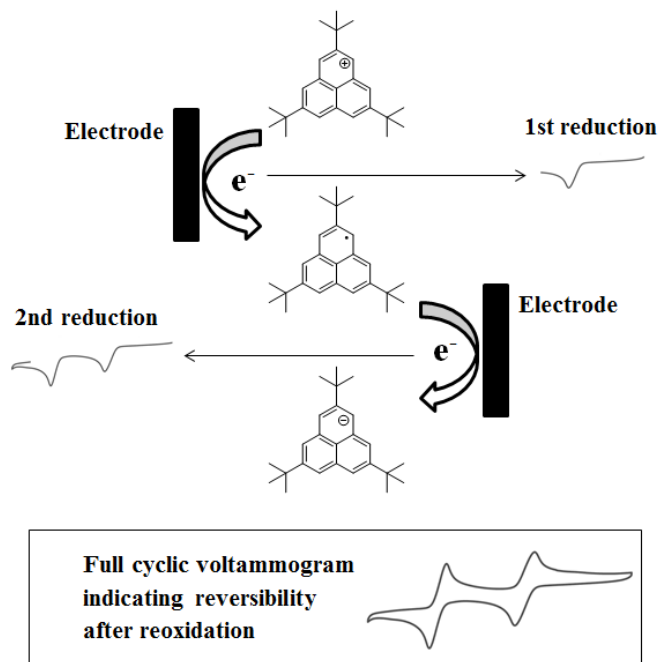


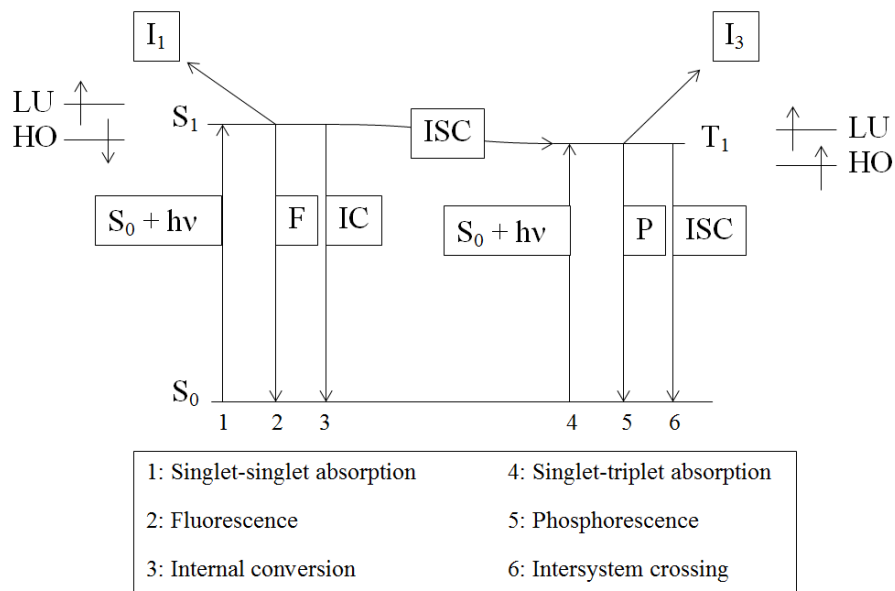
Figure 2.2.2 Illustration of redox processes of a stable phenalenyl radical. The graphic depicts the progress of a cyclic voltammogram indicating two reduction steps starting from the cation. After the switching potential, the sweep direction will be reversed and the anion will be oxidised twice resulting in the cation again.

Based on an electron transfer in organic molecules diverse type of scenarios can occur. Among them are protonation or deprotonation, bond formation or bond cleavage, nucleophilic or electrophilic attack, polymerization, isomerization or conformational change or the formation of multi-redox species which can reversibly donate or accept an electron. This thesis will mainly deal with multi-redox based species exhibiting full reversibility.

2.3. Energy state diagram (*Jablonski diagram*)

A state energy diagram illustrates the relative positions of the electronic and vibrational levels of a molecule in its excited state(s). The photochemical processes interconnect spin states of

different energies, these are the ground state (S_0), the first singlet state (S_1) and the first triplet state (T_1). Further excited singlet states S_n ($n = 2, 3, \dots$) are existent but usually highly destabilised and generally undergo very fast non radiative deactivation, known as internal conversion (IC), to the lowest excited singlet state. Radiative relaxation therefore occurs from the lowest excited states in accordance with *Kasha's rule*.²⁸ IC is of vibrational nature and thus transfers heat to the surrounding environment. In a similar way, triplet states of higher energy than T_1 may occur but due to simplification those states are neglected to demonstrate the fate and characteristics of excited states in a *Jablonski diagram*. *Scheme 2.3.1* shows potential photochemical pathways by means of an energy state diagram (*Jablonski-diagram*).



Scheme 2.3.1 Illustration of an energy state diagram (*Jablonski-diagram*).

A singlet-singlet absorption of photons generates the lowest excited state S_1 . From the excited singlet state, there are four types of transformations: fluorescence (F), IC, a reaction to give an intermediate with the singlet state (I_1) and intersystem crossing (ISC).

A common decay pathway is the singlet-singlet emission of photons, called fluorescence. In that case the singlet spin configuration falls back to the ground-state orbital configuration retaining its multiplicity. The radiative lifetime (τ_0) is typically 10^{-10} to 10^{-6} seconds.

IC can also appear between the energy levels of S_1 and the ground-state S_0 . This transition is a type of radiationless transition and also occurs without change in multiplicity.

A transition from S_1 to intermediate I_1 (subscript labels the multiplicity) is related to primarily photochemical processes. In this way, the emerging intermediate can undergo a secondary thermal reaction resulting in a product.

By intersystem crossing (ISC) the spin configuration of the excited singlet state is able to switch to the triplet spin configuration. Thus this transition generates a change in multiplicity from one to three. The lifetime can range from microseconds to seconds. As the spins of the electrons do not cancel each other out, a magnetic repulsion is generated which forces the electrons apart. This reduces electronic repulsion and sets the energy level for a triplet state below the singlet state from which the transition proceeds. The transition is considered a forbidden transition and is governed by quantum mechanics which takes place by overlap of the vibrational levels of both singlet and triplet state.

Once the triplet spin configuration is formed, there are three pathways depicted that show how this excited state will proceed further: phosphorescence P, ISC and a reaction to an intermediate with a triplet state (I_3). In case of P, T_1 emits light and falls to the ground state changing the multiplicity back to the singlet state. Likewise ISC can occur by transition from T_1 to S_0 which results in change of multiplicity plus release of energy as heat. A primary photoreaction from T_1 may produce a reactive intermediate I_3 which is triplet spin configured and can proceed further via secondary thermal reactions.

Henceforth, it poses a challenge to determine which of the pathways are the most probable in a species under examination. This has to be determined via experiments and can be supported by quantum chemical calculations which are beyond the scope of this thesis.

3. Review of closed shell polyaromatics and open shell polyaromatics according to phenalenyl

Since the isolation of graphene in 2004²⁹ (*Figure 3.1*), the two-dimensional layer of carbon atoms has been in the spotlight in material sciences. Although the thermodynamical stability of graphene was questioned more than 70 years ago³⁰, *A.K. Geim* and *K.S. Novoselov* demonstrated a simple method by pressing graphite on an adhesive tape, sticking the tape against itself and peeling away. By repeating this procedure, eventually a single atom thick

carbon layer could be obtained. The follow-up experiments revealed remarkable results which led to the discoverers winning the *Nobel* prize in 2010. Graphene now represents an exceptional substance with extraordinary qualities in fundamental physics suggesting a future with numerous applications.

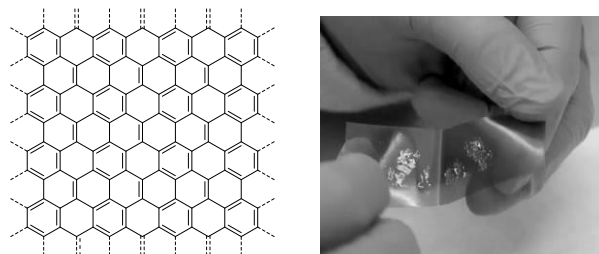
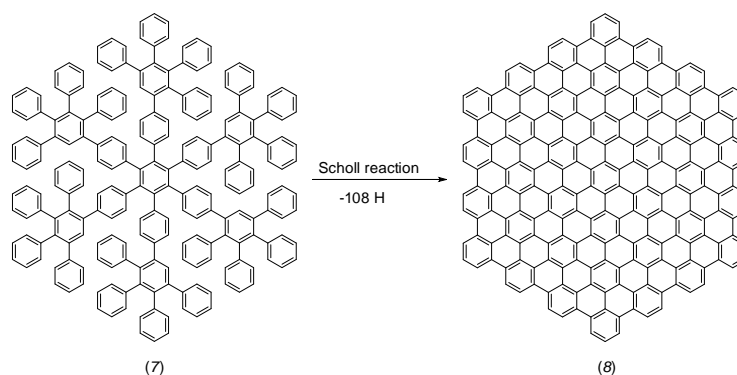


Figure 3.1 Left) Framework of graphene; right) Graphite/graphene flakes on tape.

In organic chemistry interest in sp^2 hybridised molecules was especially attributed to *A. Kekule* (resonance structure of benzene)³¹, *E. Hückel* (HMO-theory, $4n+2$ rule)³², *E. Clar* (*Clar's* sextet theory)³³, and *K. Müllen* (studies of large PAHs)³⁴ along with the understanding and syntheses of polycyclic aromatic hydrocarbons (PAHs)³⁵. PAHs often occur in oil, coal and tar deposits and are of lipophilic character.³⁶ The larger PAHs are the more challenging their synthesis becomes due to their solvophobic nature.

The largest synthesised PAH (**8**) (*Scheme 3.1*) consists of 222 carbon atoms and was prepared by oxidative cyclodehydrogenation of large dendritic oligophenylene (**7**) by *K. Müllen et al.*³⁷ The precursor (**7**) was prepared from suitable building blocks by *Diels-Alder* reactions or cyclotrimerisation. *K. Müllen et al.* also focused on the design of PAHs with improved solubility by introducing alkyl substituents.



Scheme 3.1 Key step for the synthesis of largest synthetic PAH produced in a laboratory.³⁷

One breakthrough was the synthesis of a structurally perfect and soluble nanoribbon (**9**) with lengths of 12 nm (*Figure 3.2*).³⁸ The key step is again provided by the *Scholl* reaction (dehydrogenation) and gives the synthetic approach an advantage compared with physical exfoliation and lithography methods.

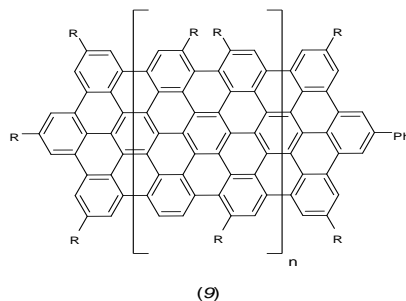


Figure 3.2 Soluble nanoribbon.³⁸

The reactivity, stability and aromatic character of polyaromatic hydrocarbons can be clarified by *Clar's sextet theory*.³⁹ *E. Clar* proposed to consider an aromatic sextet as a unit and depicted this by a closed ring as suggested by *R. Robinson*.⁴⁰ This empirical method permits us to present possible resonance structures in an annulated PAH framework. Considering the free movement of electrons in aromatic systems, a delocalisation of π -electrons is symbolised by an arrow pointing towards the displacement of an aromatic sextet. Hence, the most stable aromatics consist of aromatic sextets only, as per the examples presented in *Figure 3.3*.

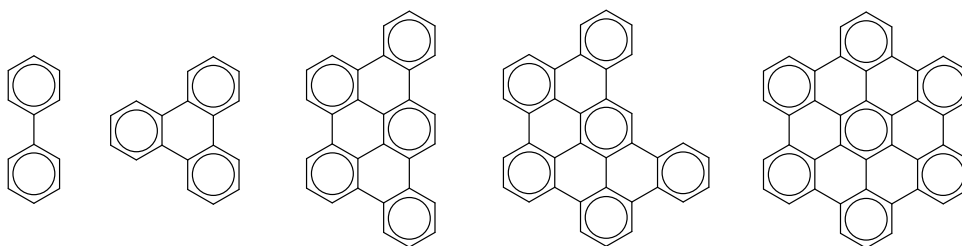


Figure 3.3 Aromatic compounds exhibiting highly thermodynamic stability.

In case of acenes, the stability decreases with the number of annulated benzene rings (*Figure 3.4*). This can be illustrated by *Clar's sextet theory* indicating only one aromatic sextet distributed over the whole molecule. The resulting reduced aromaticity involves a decrease of thermodynamic stability which explains the challenges of the isolation of large acenes.^{41,42}

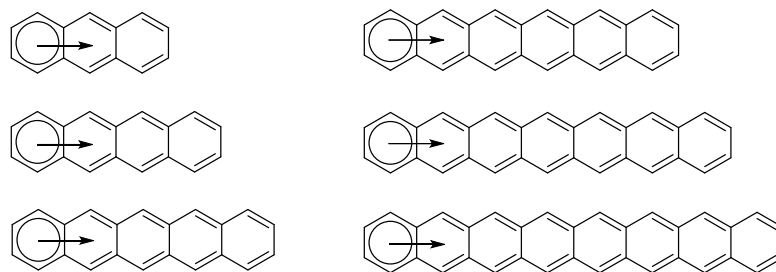
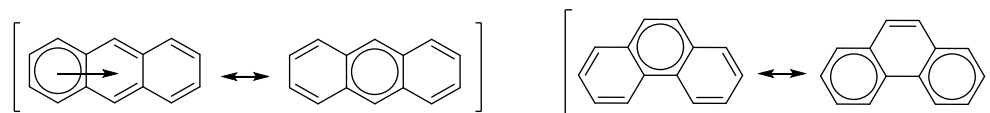


Figure 3.4 Delocalisation in acenes.

Comparing the isomers phenanthrene and anthracene (*Scheme 3.2*), the resonance structure of phenanthrene may hold two sextets for one of the two *Clar* structures in contrary to anthracene which exhibits only one sextet in each *Clar* structure. Thus, phenanthrene has a higher degree of aromaticity inducing a larger HOMO-LUMO gap which can be observed in the UV spectrum. Because higher energy is required to excite phenanthrene, an absorbance can be found at 293 nm.⁴³ Anthracene absorbs at 363 nm instead.⁴⁴



Scheme 3.2 Resonance structures of anthracene and phenanthrene according to *Clar's* rule.

However, the characterisation criteria for aromaticity are more complicated than counting the number of *Clar* sextets. A plethora of experimental measurements and computational methods are in use to solve possible controversies regarding the evaluation of aromaticity.⁴⁵ This has involved the determination of thermodynamic stability via thermolytic studies⁴⁶, geometry with respect to bond length alternation (eg. HOMA)^{47,48,49} and three-dimensional shape (e.g. helicenes)⁵⁰, as well as investigations of magnetic properties (diamagnetic susceptibility exaltation⁵¹, nucleus-independent chemical shifts (NICS)⁵² etc.).

In the case of heteroaromatics, the incorporation of a heteroatom can distort an aromatic cloud as a result of the electronegative effect.⁵³ Considering nitrogen and the elements in the 16th group of the periodic table, the influence of heteroatoms can exhibit a π -excessive or a π -deficient character in monocyclic aromatic rings depending on the topology of the aromatic

ring (*Figure 3.5*). Oxygen and sulfur have a similar influence on the aromatic ring. However, due to the lower electronegativity of sulfur, sulfur-containing aromatics are generally more delocalised to some extent. Regarding nitrogen, in the six-membered pyridine ring, the aromatic cloud will be more electron poor giving a π -deficient character. In a five membered ring, π -excessive effects are common which also counts for oxygen and sulfur. In the cases of selenium and tellurium, the covalent radius is extensively larger, diminishing π -orbital overlap. This results in a destabilising effect with high propensity toward oxidation.

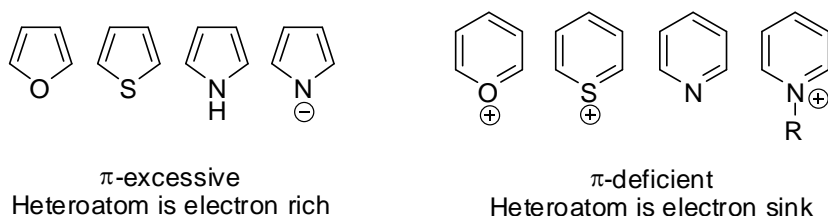


Figure 3.5 π -excessive and π -deficient heteroaromatics.⁵³

The effect of heteroatoms in a monocyclic aromatic ring was quantified by *A.T. Balaban*.⁵⁴ The interactions between the heteroatom and the aromatic cloud are ascribed to the aromaticity constant k derived from calculations involving the effective potential in the π -system (calculated after a modified *Slater* formula)⁵⁵, the number of π -electrons and the effective charge. For benzene, $k = 0$ was set as default. Analog to this, sodium cyclopentadienide and tropylium perchlorate were assigned to $k = -100$ and $k = +100$, respectively (*Figure 3.6*). The atoms are classified regarding the number of electrons which they can contribute to the aromatic system. Thus a tripartite grouping of X (two π -electrons), Y (one π -electron) and Z (zero π -electrons) type atoms was established. This allows a relative quantification of aromaticity in heteroaromatics with respect to purely carbon based π -electron systems. Hence, an evaluation of the nucleophilic or electrophilic character can be estimated. *Table 3.1* represents some k values of monocyclic aromatic compounds incorporating nitrogen and oxygen atoms.^{53,54}

Type	X	Y	Z
	#	 +50	 -50
	 -100	 0	 +100
	 -97	 +23	 +123
	 -26	 +74	#
	 -3	 +97	#

Table 3.1 k values for heteroatoms in monocyclic aromatic rings of different topology.^{53,54}

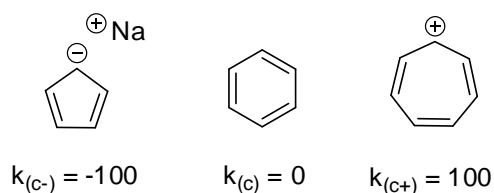
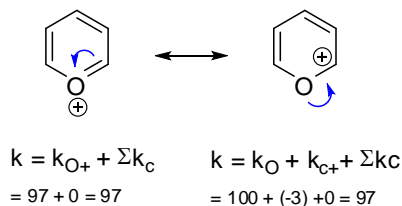


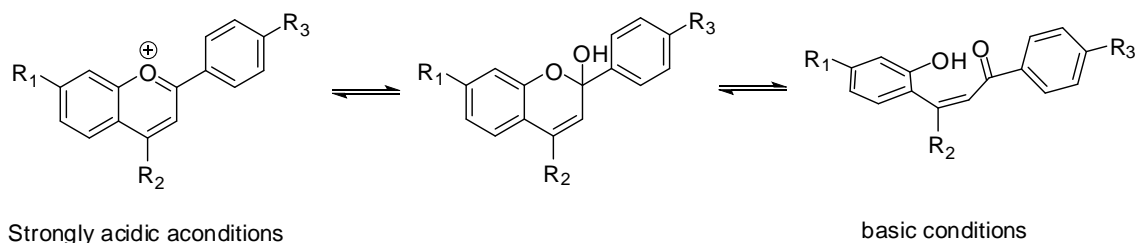
Figure 3.6 Aromaticity constants assigned to sodium cyclopentadienide, benzene and tropylium perchlorate according to *A.T. Balaban*.⁵³

It appears intuitive that the k value for the ether oxygen can be used to derive the quantity of k for the positively charged counterparts. This relationship can be illustrated considering the resonance structure of the pyrylium cation (*Scheme 3.3*). The assessment of aromaticity by these “aromaticity constants”, however, lacks generalisation particularly in case of benzannulation or in PAHs.⁵³ Nevertheless, this method has been introduced in four books on aromaticity.^{53,56}



Scheme 3.3 Resonance structure of the pyrylium cation.

The large value of $k = 97$ indicates a highly electrophilic character. Although the single pyrylium cation can be isolated having perchlorate as counterion, it easily reacts with water at the 2-position. Similarly, the benzannulated chromenyl cation tends to be attacked by a nucleophile.⁵⁷ With flavylium cations a pH dependent equilibrium between cation, hemi-ketal and ring opening can be observed (*Scheme 3.4*).⁵⁸ To decrease the electrophilic character which is largely localised at the 2-position of the chromenyl cation, further 2,3-benzannulation may decrease the reactivity towards nucleophiles. The resulting xanthenyl cation is more stabilised by participation of the introduced aromatic ring.⁵⁹



Scheme 3.4 pH dependent equilibrium between cation, hemi-ketal and ring opening of a flavylium cation.⁵⁸

With respect to PAHs, the incorporation of heteroatoms can distinctly modulate the electronic structure and reveals promising strategies for developing functional materials. For instance, large positively charged PAHs incorporating heteroatoms (*Figure 3.7*; DBNT: dibenzo[*jk,mn*]naphtha[2,1,8-*fgh*]thebenidinium, BNAX: benzo[5,6]naphthaceno[1,12,11,10-*ijklmna*]xanthylium, BNATX: benzo[5,6]naphthaceno[1,12,11,10-*ijklmna*]thioxanthylium) exhibit high stability and profound changes in their optoelectronic properties which were demonstrated by *K. Müllen et al.*²⁰

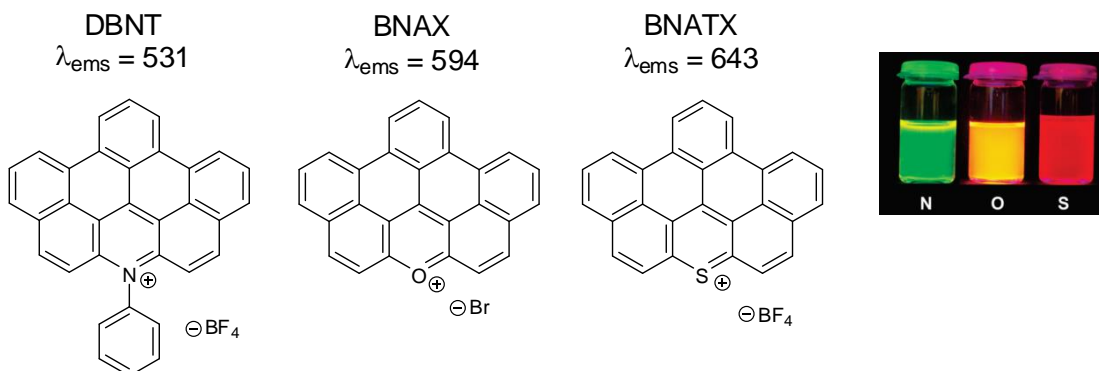


Figure 3.7 Molecular structures of DBNT, BNAX and BNATX including fluorescence emission values.²⁰

In terms of intermolecular interactions between two aromatic layers, π -conjugated molecules are mostly related with the terms “ π -stack” or “ π - π interaction”. Aromaticity usually involves an electrostatic quadrupole, which leads to different types of interactions to consider: face-centred, off-centred and edge-to-face-centred (*Figure 3.8*).^{60,61} The driving force for the attraction between two aromatic systems is generally described by the solvent, electrostatic and structural parameters of the molecule. Solvophobic effects and *van der Waal's* forces usually induce π - π interactions in a face-centred manner. This also adds to polarisation effects which can influence the electrostatic interactions by a decrease of π - π repulsion. In addition, the planar rigid shape of its aromatic framework gives rise to a lower preorganisation energy which may lead to a greater *London*-dispersion-force-induced stabilisation. However, according to a conclusion from calculations, in fact, the polarisability and rigid structure of benzene, for instance, are not the dominant factors for a π - π interaction. Because of the high electron density in the core, π - π -repulsion occurs and forces edge-to-face-centred or off-centred parallel interactions.⁶² Electron-withdrawing substituents can change this setting by inducing a deficiency of electron density. *Grimme* pointed out that π - π interactions of aromatic hydrocarbons should be taken into account for systems with about ten or more carbon atoms.⁶³ For this reason, it is rather appropriate to refer to π - π interactions in smaller aromatic compounds when they are substituted, for instance in biology (e.g. DNA, proteins).⁶⁴

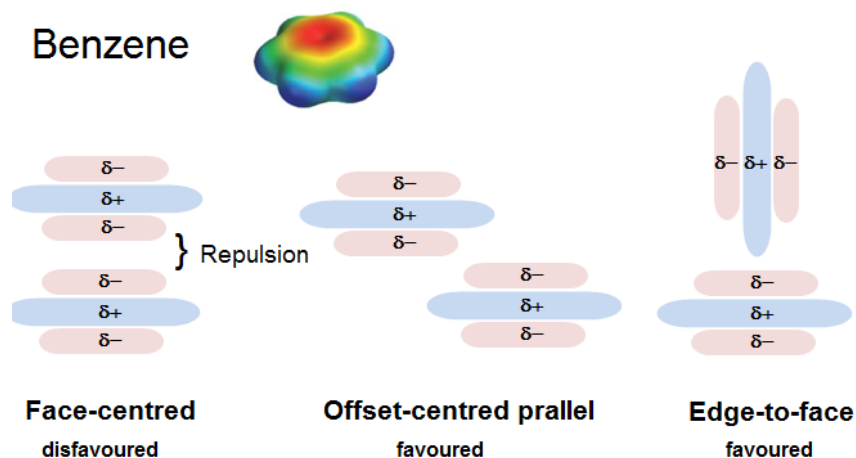


Figure 3.8 Types of π -interactions of benzene.⁶⁰

The studies on closed shell PAHs by organic chemists can be viewed as a top-down approach of graphene fragments. In graphene chemistry, two types of fragments can be classified in

their simplest form based on the geometry of their edges (*Figure 3.9*). Arm-chaired graphene fragments exhibit a closed shell nature. Their counterparts, zigzag graphene fragments represent open shell PAHs (odd alternant hydrocarbons: OAHs) in a logical consequence. The smallest and most fundamental species is phenalenyl, a π -conjugated radical composed on 13 carbon atoms.

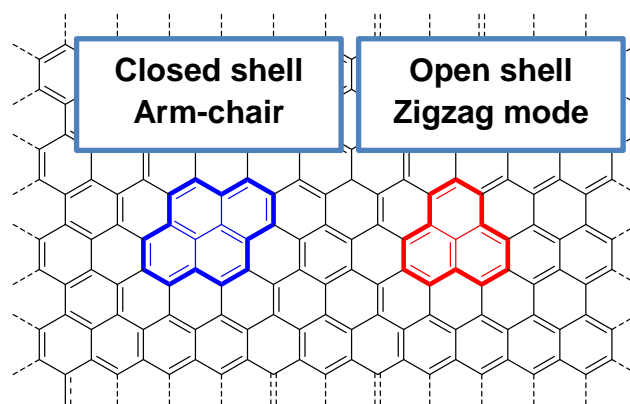
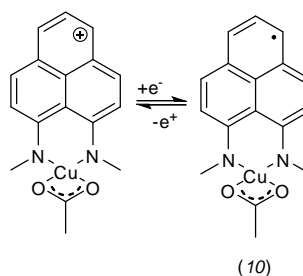


Figure 3.9 Arm-chair and zigzag mode of graphene fragments.

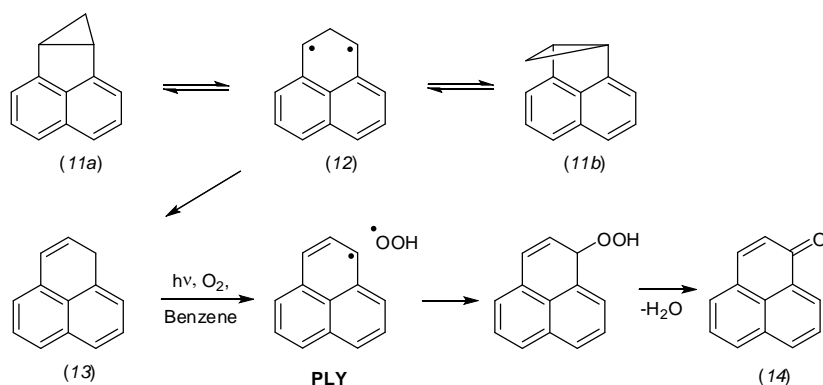
Due to their unique electronic and magnetic features, PLY based materials enabled new areas of physical organic chemistry such as “*spintronics*” and “*synthetic organic spin chemistry*”.⁶⁵ It is noteworthy that in 1975 this was already pointed out by *Haddon* in reference to the multistage redox properties of open shell polyaromatic hydrocarbons linked to conductive properties.⁶⁶ Therefore PLY has been accepted as a fundamental species which introduced new possibilities in the research on intriguing new molecules with yet unknown qualities.

In organometallic chemistry, PLY has been considered as a potential ligand in organometallic catalysts. This is attributed to its property to undergo reversible redox reactions resulting in symmetric species with invariant bond orders.^{67,68} For example, in terms of transition metal catalysts, complex (*10*) is able to perform a *Henry* reaction (*Scheme 3.5*).²¹



Scheme 3.5 Transition metal catalyst based on PLY.²¹

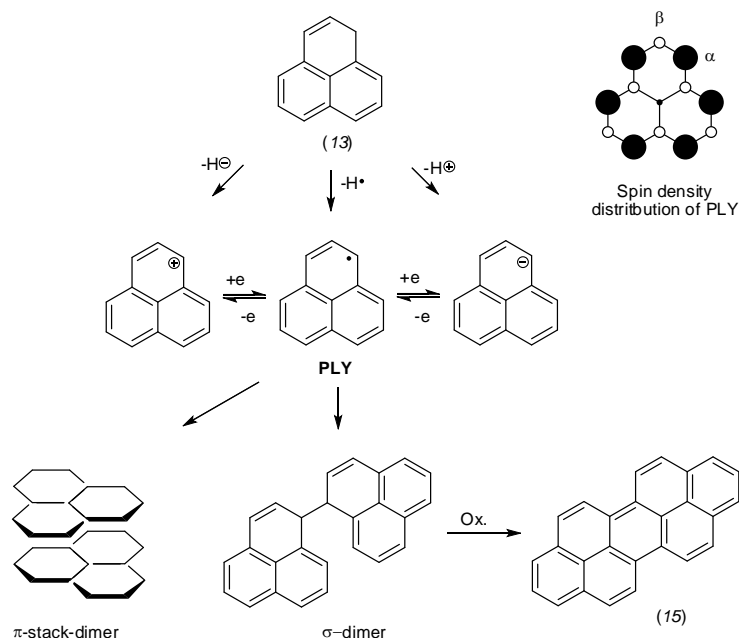
To review the properties of phenalenyl, it is reasonable to illustrate its relationship with phenalenes. With respect to studies of short-lived species, the fate of *2H*-phenalene (*12*) has been reported by *Pagni et al.* Compound (*12*) could be generated upon irradiation or thermolysis of naphthocyclopropane (*11*).⁶⁹ Subsequently, participation in either epimerisation or isomerisation resulted in (*11a*), (*11b*) or (*13*), respectively (*Scheme 3.6*). Calculated electronic energies at the B3LYP/6-31G(d) level of theory for the ground states of (*12*) and (*13*) showed that singlet (*13*) ranks as a more stabilised species than (*12*) in its triplet state.⁷⁰ A more elaborate study and discussion on the complex behaviour of (*12*) is found in the literature.^{69,71,72,73,74,75}



Scheme 3.6 Reaction pathway of *2H*-phenalene generated from naphthocyclopropane.⁶⁹

The isolation of (*13*) was first achieved in low yield by *Lock and Gergely* in 1944 and consequently improved by *Boekelheide and Larrabee*.^{76,77} However, (*13*) tends to undergo hydrogen abstraction. The reaction with oxygen under irradiation yields *1H*-phenalen-1-one (*14*) by recombination with a generated hydroperoxy radical and subsequent dehydration.

The reactivity of (13) is characterised by its low C-H bond dissociation energy ($\Delta H_{\text{Diss}} = 65.3$ kcal/mol)⁷⁸ and pronounced carbon acidity⁷⁹. Therefore (13) was considered a potential precursor for generating a stable 12 π -anion, 13 π -radical or 14 π -cation via deprotonation, hydrogen abstraction or hydride cleavage, respectively (Scheme 3.7).⁸⁰



Scheme 3.7 Generation of 12 π , 13 π and 14 π -electron systems of phenalenyl from 1*H*-phenalene and π - and σ -dimerisation of the phenalenyl radical.

The stability of each amphoteric species is provided by conjugation of the π -orbitals. In the case of the 12 π -cation, the stability can be traced to the basic nature of 1-*H*-phenalen-1-one (14).⁸¹ The enhanced polarisation of the carbonyl group gave reason to assume that the PLY nucleus exhibits stability by delocalising the partial positive charge.

The simple PLY represents a persistent species in radical chemistry, that is, its isolation has not been achieved in the solid state but it can be stored indefinitely in solution.⁸⁰ This is due to its sensitivity to oxygen as well as its propensity to undergo σ -dimerisation and subsequent formation of peropyrene (15) by oxidative cyclisation. The C-C bond between the monomers occurs at the α -carbons exhibiting the highest spin densities as a consequence of the spin polarisation effect. Alternatively, PLY can dimerise in an interesting paramagnetic π -dimer (Scheme 3.7).⁸⁰

Therefore significant research has been undertaken to shift the equilibrium in favour of the π -dimer. The 2,5,8-tri-*tert*-butylphenyl radical (TBPLY) represents the prototype in this approach.⁸² For the first time, a phenalenyl radical could be studied in detail in its solid state. The design of TBPLY was modeled on the cyclopentadienyl radical (*16*), the first neutral hydrocarbon radical (*Figure 3.10*). TBPLY was stabilised through sterically hindering groups, and rendering X-ray crystal structure analysis possible.⁸³

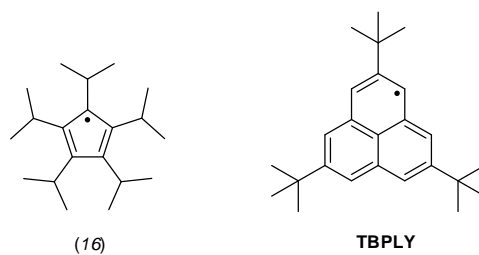


Figure 3.10 Molecular structure of cyclopentadienyl and TBPLY.

In this way, three tertiary butyl groups were introduced at the β -positions of PLY, preventing the σ -dimerisation by steric repulsion effects. The PLY skeleton exhibits a nearly planar geometry with an interplanar distance between 3.201-3.323 Å. At this distance a maximum overlap of the SOMOs is expected, showing a large antiferromagnetic intermolecular exchange interaction ($2J/k_B = -2000$ K) with a ground state spin singlet in the π -dimer. This intermolecular transition could be also confirmed in electronic spectra observed at 510-700 nm.

By the means of temperature-dependent electronic spectra, thermochromism of TBPLY in a hexane solution was monitored in the range of 200-300 K at 530-670 nm (*Figure 3.11*). This phenomenon was also visible with the naked eye where the red purple colour at room temperature gradually changed to blue at about 200 K.⁸⁴

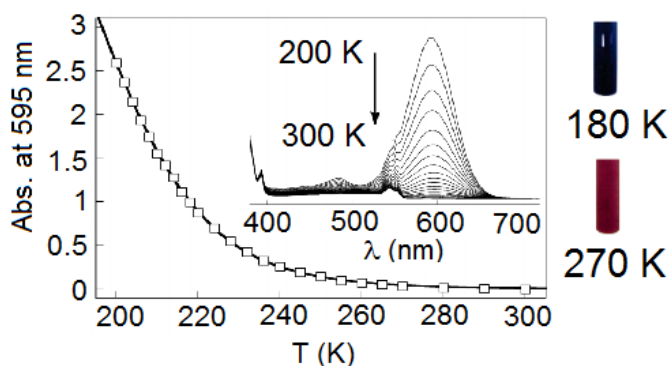


Figure 3.11 Observable thermochromism of TBPLY in temperature-dependent electronic spectra.⁸⁴

In addition, using cold-spray ionization mass spectrometry (CSI-MS), the π -dimer could be detected at low temperature. This revealed the first detection of the molecular weight ($m/z = 666.5$) of open shell molecule aggregates in solution.⁸⁴

Pioneering insights were obtained by ^1H - and ^{13}C -NMR measurements and the determination of NICS values of the π -dimer.⁸⁴ The formation of a π -dimer could be observed in NMR spectra at low temperature below 190 K. According to ^1H -NMR spectra, the appearance of two signals at 6.47 ppm and 1.48 ppm were assigned to the α -protons and the *tert*-butyl groups, respectively (*Figure 3.12*). This appearance of the signals is described as a quenching effect of the paramagnetic electrons which were originally delocalised in the planar PLY skeleton. In fact, the dimerisation is based on the polarisation of the electron density in the center of the π -dimer. Via quantum chemical calculations, NICS values of the monomer and π -dimer were determined indicating a strong aromaticity between the pancake bonded dimer (B; -7.1 ppm) compared to the monomer (A; -3.8 ppm).

According to cyclic voltammetry experiments, TBPLY in acetonitrile shows two totally reversible redox waves, +0.27 V and -1.26 V (vs. SCE) corresponding to reduction from cation to radical and radical to anion, respectively. An estimate of the amphotericity can be obtained by summing up the potential values. This gives a value of $E_{\text{sum}} = E_{\text{Ox}} + (-E_{\text{red}}) = 1.53$ V and is close to the value of the parent PLY (1.6 V).⁸⁵ The evaluation is similar to that of a HOMO-LUMO gap for closed-shell species. For open-shell species, E_{sum} represents the coulombic repulsion between the electron in the former SOMO and a transferred electron occupying the same orbital to form the anion.

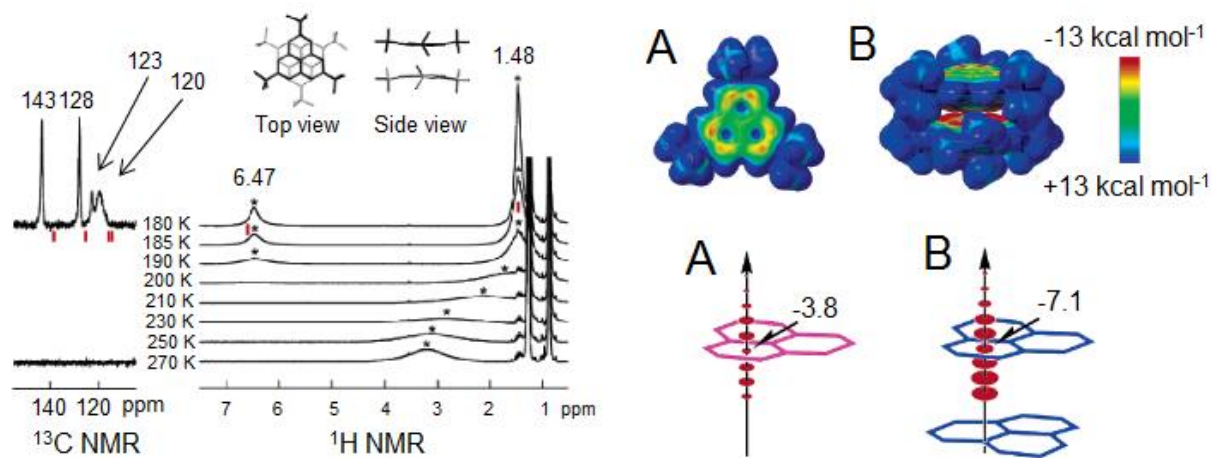
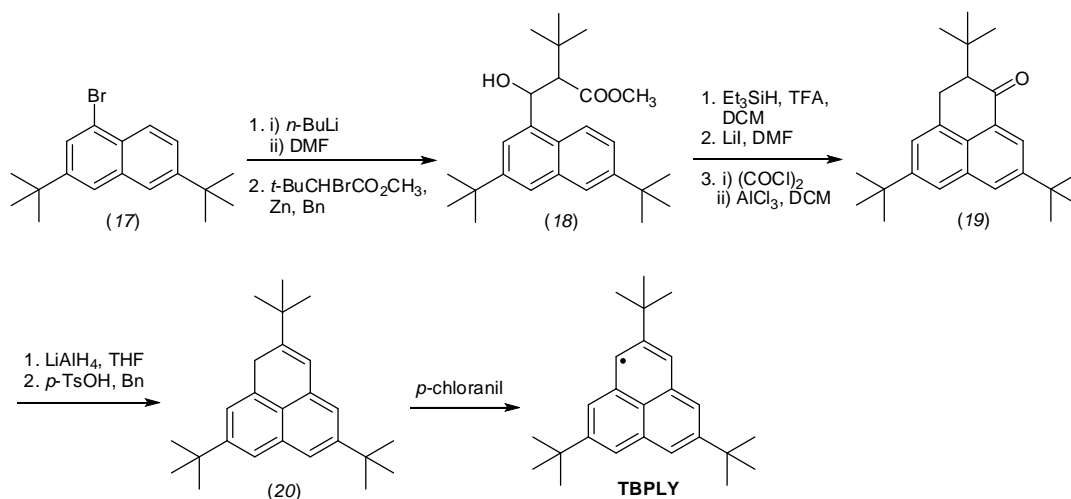


Figure 3.12 Left) Observable π -quenching effect by temperature-dependent ^1H and ^{13}C NMR spectra of TBPLY; Right) Calculated NICS values for TBPLY indicating aromaticity generation between the layers in a π -dimer.⁸⁴

Looking at the electron paramagnetic resonance (ESR) spectrum of TBPLY in toluene, the g -factor lies at 2.0028 being close to that of PLY (2.0027).⁸⁶ Six protons with hyperfine coupling constants of -0.620 mT can be assigned to the α -positions of the symmetric skeleton. Due to the fact, that the *tert*-butyl groups have a small electronic effect and are located at the β -positions exhibiting the lowest spin densities anyway, the stability is mainly associated with steric repulsion effects by the substituents and the “aromaticity generation” in the interior of the π -dimer. In conclusion, TBPLY can be regarded as the most electronically fundamental PLY radical that can be crystallised.

The synthesis of TBPLY is depicted in *Scheme 3.8* according to the literature.⁸² Lithiation of the brominated 2,7-di-*tert*-butylnaphthalene (17) followed by a *Reformatsky* reaction results in the ester (18). Conducting a reduction using triethylsilane and subsequent cleavage of a C-O bond of the ester group with lithium iodide gives a carboxyl derivative. Performing a *Friedel-Crafts* cyclisation yields the phenalnone derivative (19). Using lithium aluminum hydride and dehydration, phenalene derivative (20) can be prepared and then oxidized by *p*-chloranil in degassed toluene to obtain TBPLY as blue crystals. TBPLY can be stored under air for one week until formation of *tert*-butyl substituted phenalene.

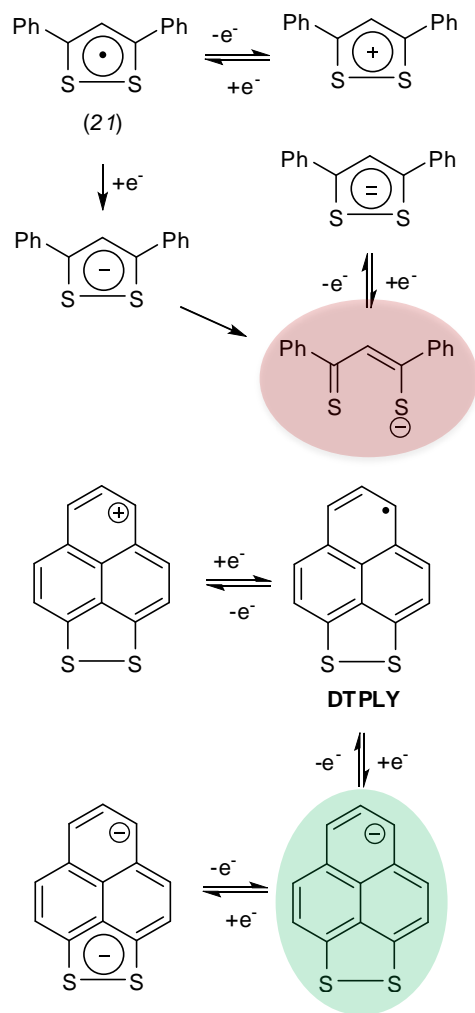


Scheme 3.8 Synthesis of TBPLY.⁸²

The first PLY-type radical stabilised by electronic effects instead of sterically hindering groups was published by *Haddon et al.* in 1978.⁸⁷ 1,9-Dithiophenalenyl (DTPLY) was generated from the stable hexafluorophosphate (PF_6^-) salt by reducing reagents and electrochemical methods. Motivated by the redox ability of the 1,2-dithioly system (21), the introduction of a disulfide bridge in the PLY structure was expected to increase the thermodynamic stability. In fact, cyclic voltammetry studies for DTPLY showed three reversible redox waves indicating no decomposition at -0.22 V, -0.77 V and -1.53 V (volts vs. SCE) corresponding to the reduction from the cation to the radical, from the radical to the anion and from the anion to the dianion, respectively (*Scheme 3.9, Figure 3.13*). This contrasts with (21) as its reduced species, the anion, rapidly undergoes sulfur-sulfur bond scission confirmed by comparison of the UV spectrum with those of nickel and zinc chelates.⁸⁸

After 30 years, the first X-ray structure analysis of DTPLY was reported using the triflate salt as precursor.⁸⁹ The interplanar distance of DTPLY is in a range of 3.13-3.22 Å and hence shorter than that of TBPLY (*Figure 3.14*). Similar to TBPLY the π -dimer is arranged face to face where one molecule is rotated 180° with respect to the other. This ensures a maximum SOMO-SOMO overlap providing an optimal stabilisation. In addition, intermolecular S-S contacts (3.56 Å) are proposed to be a further driving force for the mode of crystallisation. Although the distance is smaller than a typical *van der Waals* interaction (3.6 Å), the π -dimers trap the electrons indicating no considerable interaction with neighbouring dimers. This

assumption is supported by conductivity measurements where DTPLY is insulating at room temperature, with $\sigma_{RT} < 10^{-6} \text{ S cm}^{-1}$.



Scheme 3.9 Electrochemistry of 1,2-dithiolyl and DTPLY.^{88,89}

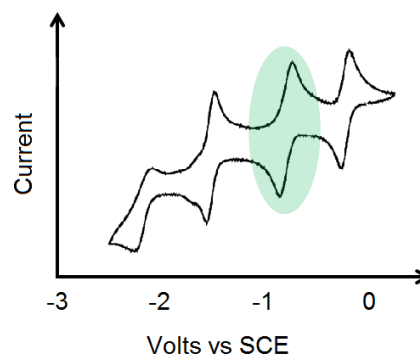
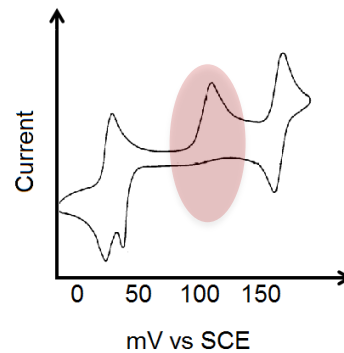


Figure 3.13 CV diagrams of 1,2-dithiolyl system (21) and DTPLY. The coloured redox waves indicate the irreversible (red) and reversible (blue) addition of an electron to the radical of (21) and DTPLY, respectively.^{88,89}

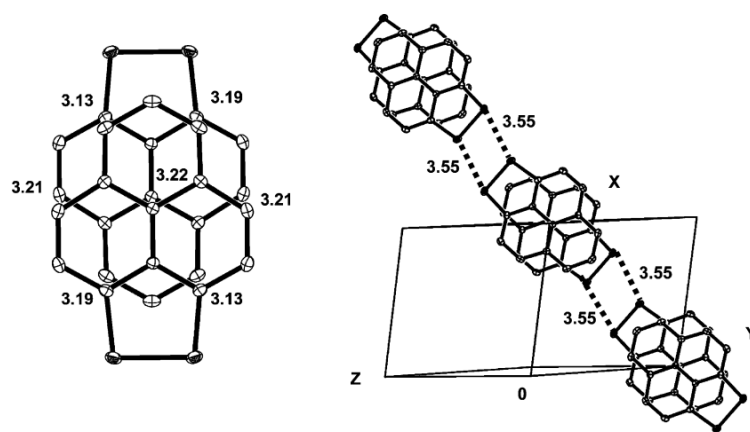


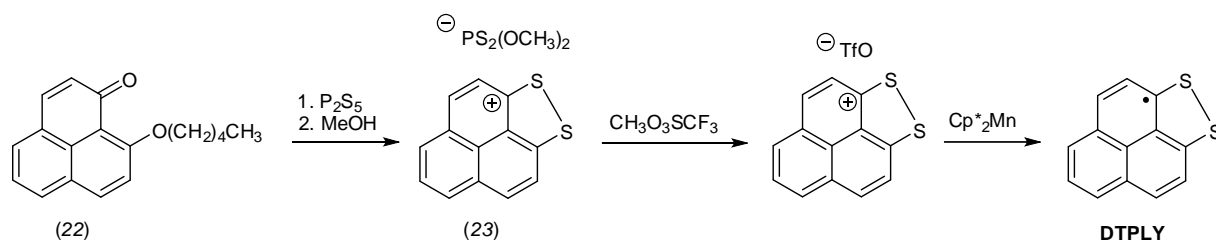
Figure 3.14 X-ray structure of DTPLY: Left) Top view of DTPLY π -dimer; Right) Intermolecular S-S interactions.⁸⁹

ESR measurements and electrochemical data were reported revealing a considerable removal of spin density from the PLY skeleton on both sulfur atoms.⁸⁹ The hyperfine coupling constants are significantly decreased by 0.09-0.123 mT at the α -positions in comparison with the pristine PLY (Table 3.2). The g-value is 2.042 for DTPLY in dichloromethane exhibiting a discrepancy of 0.015 ($g(\text{PLY}) = 2.027$).

Position	PLY	TBPLY	DTPLY
1, 9	0.630	0.620	-
2, 8	0.182	-	0.151
3, 7	0.630	0.620	0.507
4, 6	0.630	0.620	0.540
5	0.182	-	0.156

Table 3.2 Hyperfine coupling constants (in mT) of PLY, TBPLY and DTPLY obtained from ESR spectra.^{82,89}

The synthesis of DTPLY is depicted in *Scheme 3.10*. Pentyloxyphenalenone (22) was treated with an excess of phosphorus pentasulfide in toluene and subsequently refluxed in methanol yielding the cation (23). Then, counter-anion exchange using methyl trifluoromethanesulfonate and subsequent reduction with decamethylmanganocene results in DTPLY as black microcrystalline solid. The crystals can be stored for up to 24 hours but in solution the compound decomposes readily even under an inert atmosphere.



Scheme 3.10 Synthesis of DTPLY.⁸⁷

More recently, the synthesis of further PLY based radicals was attempted by *Hou et. al.* incorporating verdazyl units (24) into the PLY framework (*Figure 3.15*).⁹⁰ Cyclic voltammetry studies conducted using the PF_6^- salts revealed two redox waves for each indicating a thermodynamic stability of those radicals. The amphotericity, the sum of the oxidation and reduction potentials, could be evaluated for each resulting in $E_{\text{sum}} = 1.05$ V, 1.09 V and 0.98 V for (25), (26) and (27), respectively. These values represent the coulombic repulsion between the electron in the former SOMO and a transferred electron occupying the same orbital to form the anion. However, only radical (26) could be identified via ESR spectroscopy. The reasons why the detection of (25) and (27) was in vain were attributed to possible σ -dimerisation at the α -positions. According to DFT calculations, their spin densities were distinctly higher than those of (26).

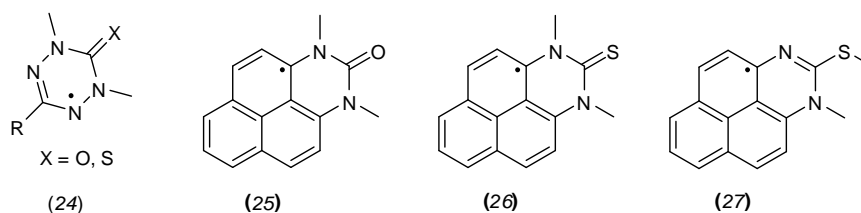
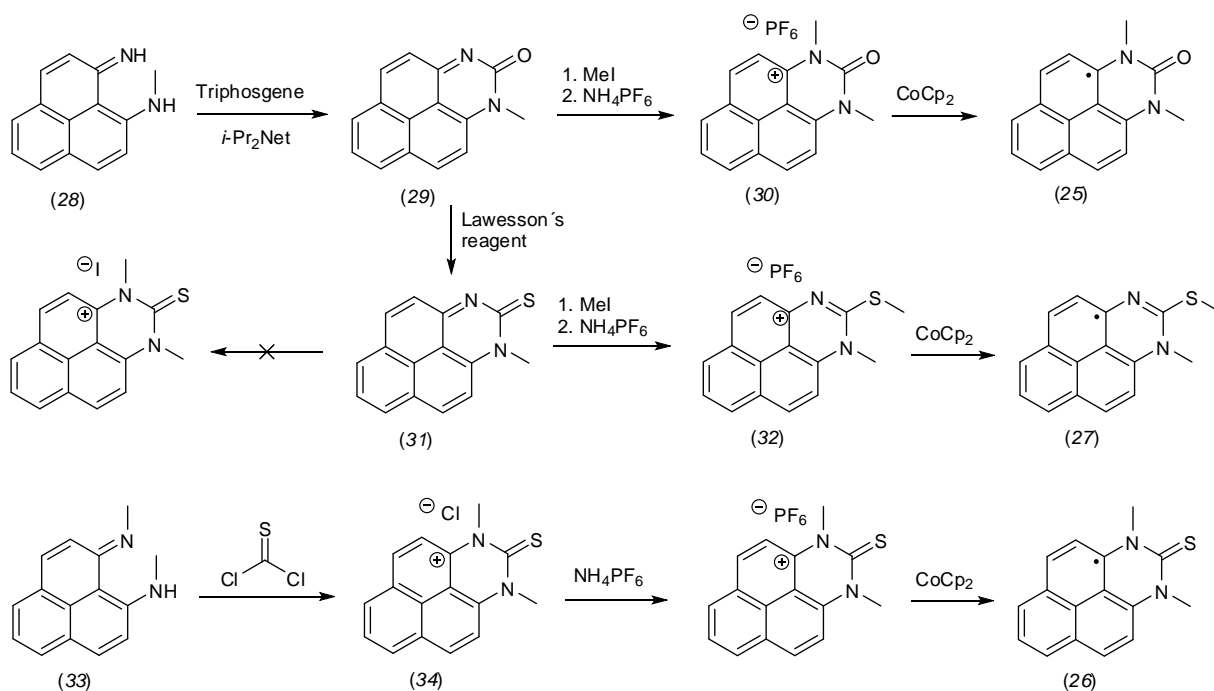


Figure 3.15 Molecular structure of verdazyl and further radicals based on PLY and verdazyl units.⁹⁰

Nevertheless, the cationic precursors for the target molecules (26) and (27) could be crystallised to carry out X-ray structure analysis. This indicated π - π stacking arrangements with a distance of 3.45 Å and 3.43 Å for (26) and (27), respectively.

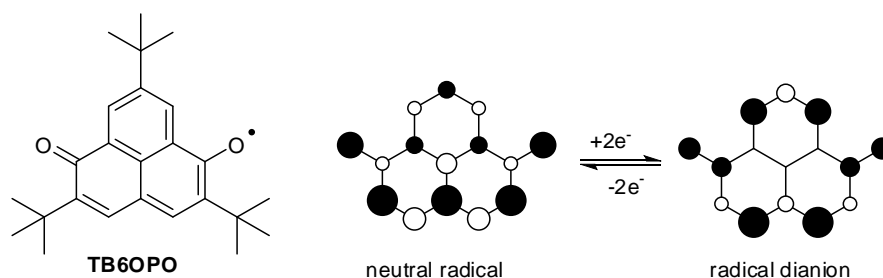
The synthetic pathways towards (25)-(27) are depicted in *Scheme 3.11*. Initially, only the synthesis of (25) and (26) was attempted. Starting from 1-imino-*N*-methyl-1*H*-phenalen-9-amine (28), 1-methylbenzo[*gh*]perimidin-2(1*H*)-one (29) was formed using triphosgene. Then methylation via methyl iodide resulted in the cationic species. Subsequent counter-anion exchange yielded the PF₆⁻ salt (30) and could be reduced by decamethylcobaltocene to the target radical (25). This approach failed in case of (26). After transformation of (29) to the thiocarbonyl (31) by means of Lawesson's reagent, a following methylation instead preferred to occur on the sulfur atom resulting in (32). This was then treated in a uniform manner as for (25) and resulted in radical (27). Radical (26) could be prepared reacting (33) with thiophosgene resulting in the chloride salt (34). Counter-anion exchange followed by reduction gave target radical (26).



Scheme 3.11 Synthesis of radicals based on PLY and verdazyl units.⁹⁰

It is noteworthy that tri-*tert*-butyl-6-oxophenalenoxyl (TB6OPO) is an exceptionally stable PLY radical compared to the above described PLY species. TB6OPO exhibits redox based

spin diversity.⁹¹ This means that a paramagnetically amphoteric species shows a changed electronic spin structure (*Scheme 3.12*) upon a single electron transfer by reduction or oxidation. According to cyclic voltammetry measurements, TB6OPO has two-stage one-electron redox waves involving the reduction from the radical to the anion and from the anion to the radical dianion. The radical dianion can also be generated chemically from the neutral radical using alkali metals and can be stored under an inert atmosphere at room temperature. ESR studies revealed the altered electronic spin structure indicated by a decrease in the *g*-value (from 2.0049 for the neutral radical to 2.0037 for the radical dianion), a broadening of the spectral width and varied hyperfine coupling constants for the radical dianion versus the neutral radical. The highest spin densities for the radical dianion are located at the α -positions similar to the parent PLY, TBPLY, DTPLY and verdazyl derived PLY radicals. However, the highest spin densities in the PLY framework of the neutral radical are at the β -positions which are also confirmed by DFT calculations. This demonstrates a topological symmetry control by the introduction of two oxygen atoms at the α -positions.



Scheme 3.12 TB6OPO and redox based spin diversity.⁹¹

To provide sufficient stability, three *tert*-butyl groups at the beta-positions were introduced analogous to TBPLY. Isomers of TB6OPO were considered including other oxygen substituted phenalenyl systems at α,α -, α,β - and β,β -positions (*Figure 3.16*).⁹² The latter isomer is subjected to instability as it has two unpaired electrons in the naphthoxyl structure. On the other hand, α,α - and α,β -substituted isomers constitute monoradical structures.

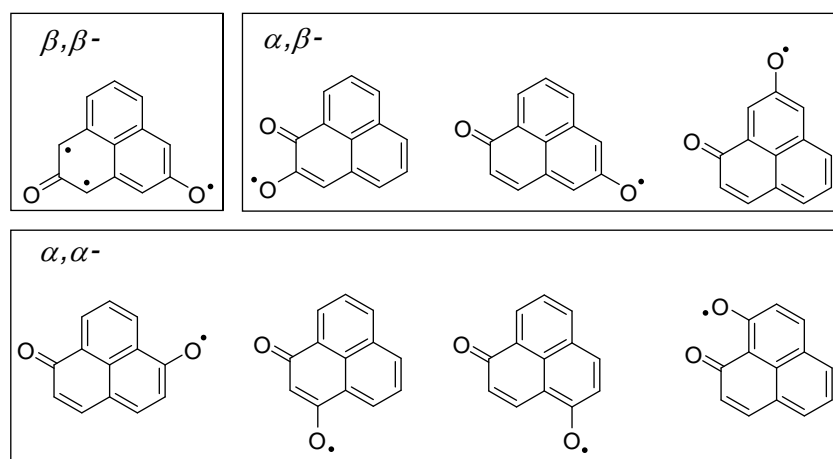
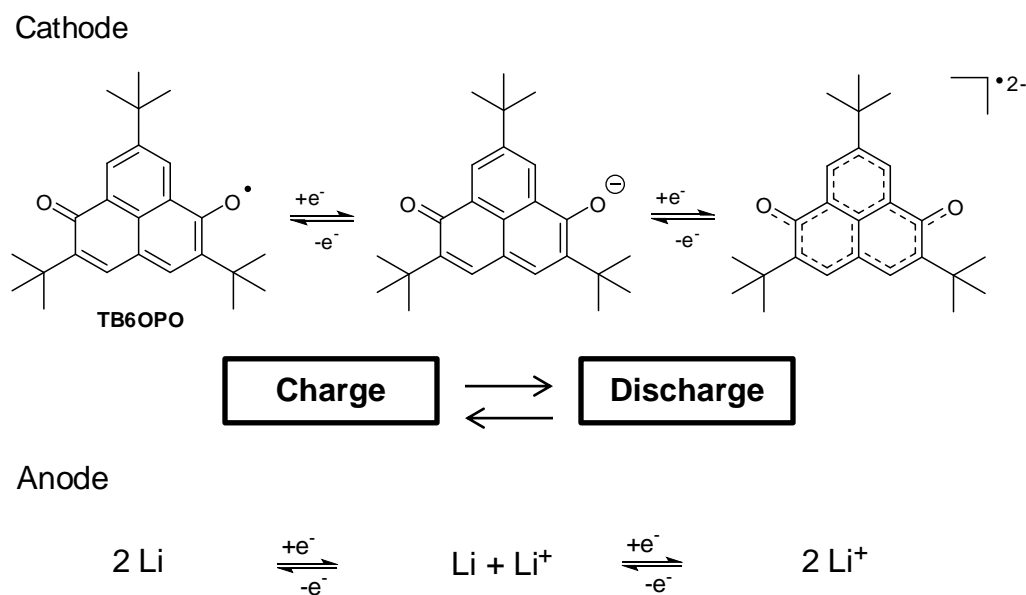


Figure 3.16 Possible isomers of oxophenoxy radicals.⁹²

Morita et al. mainly focused on the ability of α,α -substituted oxophenoxy radicals to facilitate an efficient stabilisation by steric hindering groups at the β -positions which led to an application-oriented breakthrough in developing a molecular crystalline secondary battery (*Figure 3.17* & *Scheme 3.13*).⁹³ Due to its multistage redox ability a large number of electrons can be accommodated in the molecule and this enables its utilization as an electrode active material. The battery exhibits a comparable performance in discharge capacity (182 Ah/kg) to lithium ion secondary batteries (150~170 Ah/kg). It is noteworthy that this value was improved based on the concept of degenerate molecular orbitals. The same authors demonstrated the promising multistage redox properties of trioxotriangulene derivatives, distinctly exceeding the discharge capacity of Li-ion batteries with 300 Ah/kg.⁹⁴ From the economical and environmental point of view, this has the advantage that no precious metals are required. A more detailed understanding of the redox processes is still ongoing in order to apply the degeneracy of SOMOs to the design of more powerful electrodes.

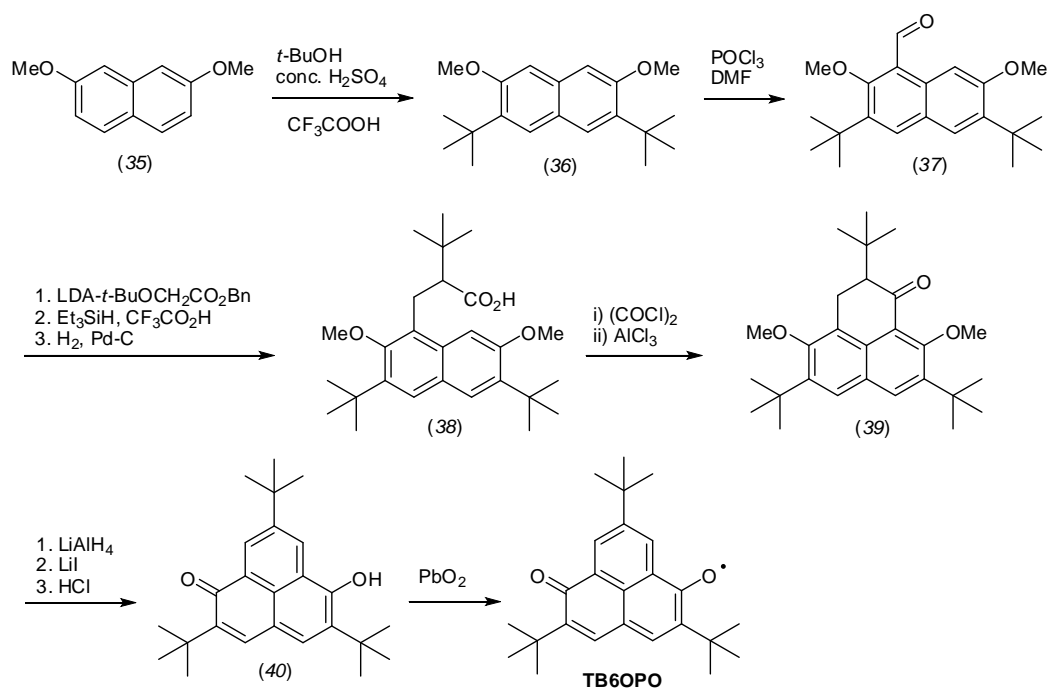


Figure 3.17 Molecular crystalline secondary battery based on TB6OPO.⁶⁵



Scheme 3.13 Redox process in molecular crystalline battery based on electro active TB6OPO cathode.^{65,94}

TB6OPO was prepared by *Morita et. al* and is shown in *Scheme 3.14*.⁹⁵ The use of *tert*-butanol and trifluoroacetic acid rendered possible a *Friedel-Crafts* reaction with 2,7-dimethoxynaphthalene (35) yielding 2,7-di-*tert*-butyl-3,6-dimethoxynaphthalene (36). After a *Vilsmeier-Hack* reaction resulting in (37), benzyl-*tert*-butylacetate with lithium diisopropylamide was used to obtain isomers of the aldol product which were subsequently converted to the carboxylic acid derivative (38) by elimination and deesterification. Followed by chlorination and *Friedel-Crafts* cyclisation, phenalanone derivative (39) was obtained. Reduction of the carbonyl group was achieved with lithium aluminum hydride. This was followed by demethylation using lithium iodide leading to a triol which was treated with HCl to yield phenalanol derivative (40). The final step to TB6OPO proceeds via the use of a large excess of active lead oxide in benzene at room temperature.



Scheme 3.14 Synthesis of TB6OPO.⁹⁵

In conclusion, the selection of the TBPLY, DTPLY, VPLY and TB6OPO justified prototypes illustrates design strategies to access stabilised radicals and obtain insights into the nature of the PLY framework. These are realised through steric hindering groups and electronic effects. In case of TB6OPO, the hybridization of phenalenyl and phenoxy reveals an alteration of the electronic spin structure and gives rise to redox spin diversity. By introducing steric hindering groups in a similar way to TBPLY, TB6OPO can be handled at room temperature and utilised as an electro active material. DTPLY and VPLY exemplify the realisation of PLY radicals with less steric protection. The isolation of such PLY radicals is rarely present in literature. In fact, DTPLY is the only stable PLY radical, stabilised through electronic effects, which was analysed by X-ray diffraction.

4. The photochemistry of phenalenones and the naphthoxanthenyl skeleton

“I shall have to show that constitutional peculiarities of the strangest kind, entailing liability to the action of certain poisons, are correlated with the colour of the skin. I will here give a single case, on the high authority of Professor Wyman; he informs me that, being surprised at all the pigs in a part of Virginia being black, he made inquiries, and ascertained that these animals feed on the roots of the *Lachnanthes tinctoria*, which colours their bones pink, and, excepting in the case of the black varieties, causes the hoofs to drop off.” (Charles Darwin)

In Charles Darwin’s treatise “on the origin of the species” the first observation of a photodynamic toxicity originating from plants was described based on the ingestion of *Lachnanthes tinctoria* by pigs (Figure 4.1).⁹⁶ The recognition that black pigs did not suffer from the toxic effects indicated the activity of the extracts being dependent on illumination. The molecule *lachnanthocarphone* **1** was isolated and identified as the major extract from the seeds of this plant and its toxicity was investigated using *Staphylococcus epidermis* as test organisms.⁹⁷ Upon exposure of *lachnanthocarphone* to light, crude extracts of seed pods and root aglycones of *Lachnanthes tinctoria* revealed a correlation between cell death and irradiation which were, however, less distinctive for the isolated *lachnanthocarphone*.

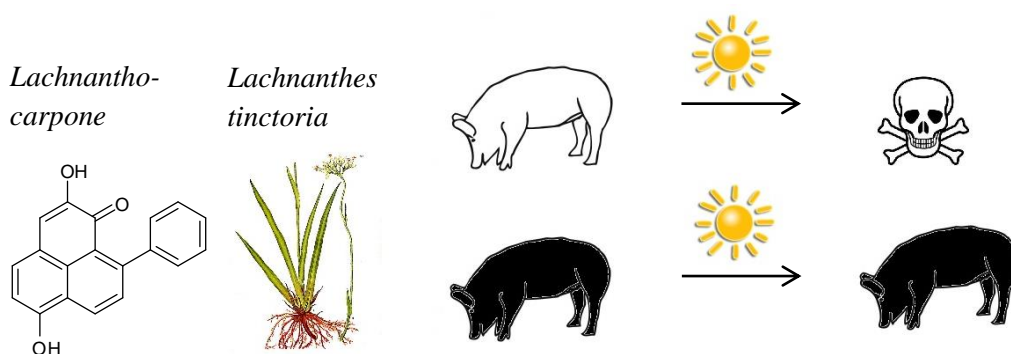


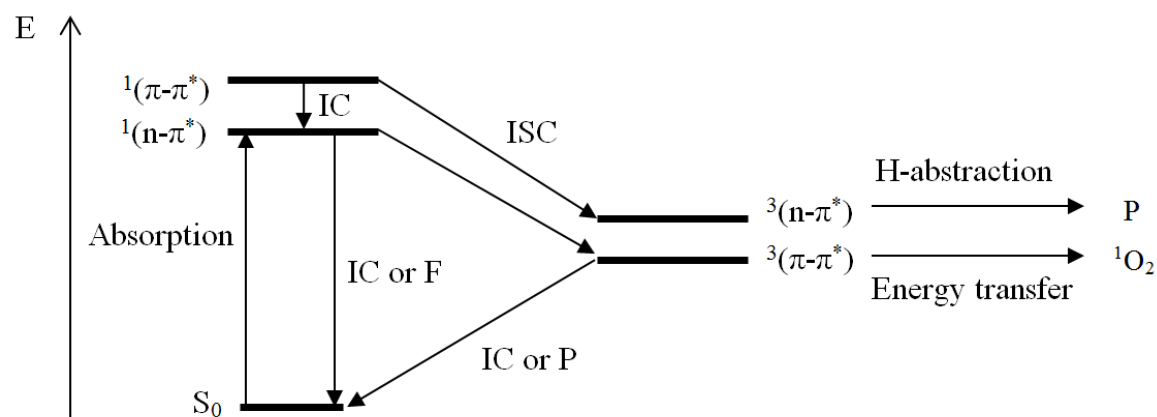
Figure 4.1 Ingestion of *Lachnanthes tinctoria* by white and black pigs. Upon sun exposure white pigs suffer from the photodynamic toxicity of the plant extracts. *Lachnanthocarphone* is the major substance which has been isolated from *Lachnanthes tinctoria*.

A variety of 1*H*-phenalen-1-one (PN) based compounds have been extracted from plants and fungi showing phototoxic properties of different strengths and are classified as phytoanticipins and phytoalexins.⁹⁸ A large series has been isolated and studied especially in banana plants

(*Musaceae*)^{99,100,101,102} and plants of the genus *Haemodracea*^{103,104}. Phytoalexins are characterised as secondary metabolites which can be accumulated upon microbial attack. On the other hand, phytoanticipins are already present in the plant and will be released upon mechanical exposure. *Lachnanthocarpon* is classified as phytoanticipin. As their protective functionality is certainly based on the absorption of light, PN and its derivatives have become of photochemical importance. They were identified as potential singlet oxygen (¹O₂) sensitisers. Singlet oxygen is highly reactive and able to react with many organic molecules.

Photochemical studies on the unsubstituted PN showed photostability, with a quantum yield of intersystem crossing (ISC) and ¹O₂ production close to unity in polar as well as non-polar solvents.¹⁰⁵ PN is therefore ideal as a reference sensitiser for the quantum yield determination of ¹O₂.

Upon irradiation, PN will be excited from the singlet ground state S₀ to its singlet states S₁ and S₂ in an n-π* and π-π* electronic configuration, respectively (*Scheme 4.1*). The depopulation of a singlet state occurs via internal conversion (IC), fluorescence (F) or singlet-triplet transition by ISC. The latter process is most likely due to the large energy gap (2.64 eV)¹⁰⁶ between the ground state and the excited singlet state. Additionally, due to the rigidity of PN, a vibrational relaxation in the form of IC is disfavoured. Thus ISC proceeds efficiently with a quantum yield close to one resulting in a triplet manifold.



Scheme 4.1 Jablonski diagram depicting the photochemical pathway of PN.

According to the rules of *El-Sayed*, large spin-orbit coupling elements are proposed to exist between 1(n-π*) and 3(π-π*) (superscripts 1 and 3 are assigned to the singlet state and the

triplet state, respectively).¹⁰⁷ On the contrary, coupling elements between $^1(\pi-\pi^*)$ and $^3(\pi-\pi^*)$ are insignificant. Competing IC from $^1(\pi-\pi^*)$ to $^1(n-\pi^*)$ proceeds more rapidly than ISC from $^1(\pi-\pi^*)$ to a triplet state. Therefore, it is generally accepted that PN most likely generates a triplet manifold from the $^1(n-\pi^*)$ state.

According to DFT calculations¹⁰⁸, the ground state and $^n(\pi-\pi^*)$ states ($n = 1, 3$) exhibit large dipole moments with a negative charge accumulation at the carbonyl group. In contrast to this, very small dipole moments are assigned to $^n(n-\pi^*)$ states ($n = 1, 3$). For that reason, polar solvents should lower the energy of $^n(\pi-\pi^*)$ states ($n = 1, 3$). Consequently, $^1(\pi-\pi^*)$ is affected by solvent polarity as expected. This results in a smaller energy gap between both singlet states. The $^3(\pi-\pi^*)$ state remains stable or shows tendency to lower the energy under polar conditions. However, the $^3(n-\pi^*)$ state can be destabilised being above the $^1(\pi-\pi^*)$ state which may impede ISC between these states making H-abstraction more unlikely. Generally H-abstraction is considered to proceed from the $^3(n-\pi^*)$ state. Based on this hypothesis, C. Flors and S. Nonell determined the energy gap between the $^3(\pi-\pi^*)$ and the $^3(n-\pi^*)$ in benzene in presence of an H-donor (Bu₃SiH) via laser flash photolysis.¹⁰⁹ Both triplet states $^3(\pi-\pi^*)$ and $^3(n-\pi^*)$ are separated by an energy gap of 9 kJ/mol. Noteworthy, they exhibit close proximity and could also afford partial mixing to facilitate an H-abstraction reaction.¹¹⁰

In most cases, solvent effects on PN are not expected to have a crucial impact and display only a small effect on H-abstraction. This can be seen in several studies on the quantum yield determination of $^1\text{O}_2$ production. Minor changes between polar and non-polar solvents were observed, for instance, in methanol ($\Phi\Delta = 0.97 \pm 0.03$) and in benzene $\Phi\Delta = 0.93 \pm 0.04$.¹¹⁰ The lowest yet-measured $\Phi\Delta$ value was obtained in *N,N'*-dimethylacetamide being 0.87 ± 0.05 .¹¹¹ In conclusion, due to an ISC close to one and a build-up of the $^3(\pi-\pi^*)$ state, the major photochemical outcome of PN leads to an energy transfer process on triplet oxygen ($^3\text{O}_2$) resulting in an efficient $^1\text{O}_2$ production.

With the above-described fate of excited PN, one may conclude that phototoxins incorporating a PN unit realise plant or fungi protection by highly reactive $^1\text{O}_2$. However, in case of *lachnanthocarpon*, it still poses the question why this molecule itself does not work as efficiently as the crude extracts of *lachnanthes tinctoria*.

Considering 3-, 4- and 9-aryl substituted PN derivatives in benzene (Table 4.1), a distinctly lower value for a quantum yield of $^1\text{O}_2$ production was obtained in case of 9-aryl-PN.⁹ 3-aryl-

PNs and 4-aryl-PNs exhibit considerably higher values ($\Phi_{\Delta} = 0.94$ and $\Phi_{\Delta} = 0.72$, respectively) compared to 9-aryl-PNs ($\Phi_{\Delta} \leq 0.08$). However, the introduction of a hydroxyl group at the 2-position of 3-aryl-PNs induces a decrease of the Φ_{Δ} value which could be due to tautomeric effects between the carbonyl and the hydroxyl group.⁷ 9-aryl-PNs show a considerably higher quantum yield ($\Phi_{\Delta} = 0.51$) if a nitro group is introduced at the *o*-position of the pendant phenyl group. This could be attributed to steric or electronic effects influencing a quenching effect which will be described in the next paragraph.¹¹² Interestingly, 3- and 4-aryl-PNs are usually found in plants after infection which characterises them as phytoalexins. Accordingly, this could be related to a strategic use of aryl-PNs by plants and fungi to prevent an excess of potential sensitisers which could result in possible damage to the plant itself.

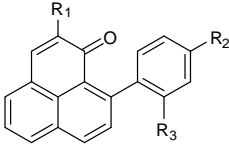
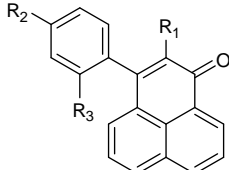
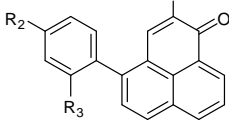
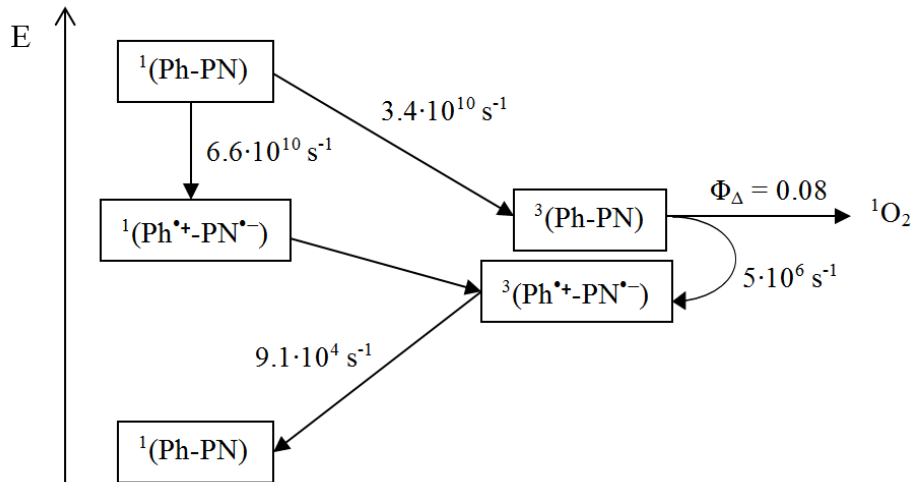
Molecule	R ₁	R ₂	R ₃	Φ_{Δ}
 9-Aryl-PN	H	OMe	H	0.002
	OH	OH	H	0.01
	H	OMe	H	0.01
	OH	H	H	0.03
	OMe	H	H	0.08
	H	H	H	0.08
	H	H	NO ₂	0.51
 3-Aryl-PN	H	OMe	H	0.94
 4-Aryl-PN	OH	OMe	H	0.12
	OMe	H	H	0.72

Table 4.1 Calculated quantum yields of ¹O₂ production in benzene of 9-, 3- and 4-aryl-1*H*-phenalen-1-ones.⁹

C. Flors and *S. Nonell* investigated the photochemical pathway of 9-phenyl-PN via time-resolved spectroscopic methods.¹¹² The experiments indicated a decrease of ¹O₂ production by an intramolecular charge-transfer (CT) complex. The proposed outcome of irradiation of 9-phenyl-PN is depicted in *Scheme 4.2*. The stated kinetic constants are based on experimental results. From the singlet excited state, 9-phenyl-PN is able to generate either the triplet state or the CT complex. The triplet state, generated at a rate of $3.4 \cdot 10^{10} \text{ s}^{-1}$, may perform ¹O₂

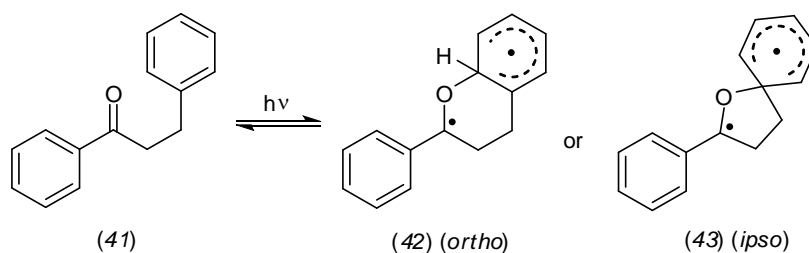
production with a quantum yield of $\Phi_{\Delta} = 0.08$. At a rate of $5 \cdot 10^6 \text{ s}^{-1}$, the CT complex will be formed and decays to the ground state at a rate of $9.1 \cdot 10^4 \text{ s}^{-1}$. This represents a plausible explanation for the significant decrease of efficiency in accordance with $^1\text{O}_2$ production by 9-aryl-PNs.



Scheme 4.2 Energy diagram depicting the photochemical pathway of 9-PhPN assigned as Ph-PN.¹¹²

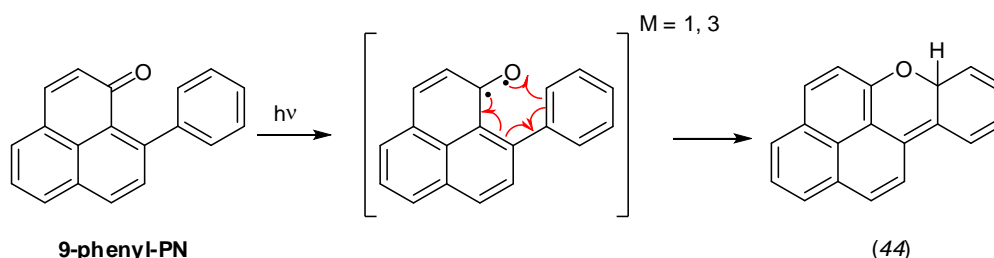
The CT complex formation was attributed to a deactivation of triplet aromatic ketones by a so-called β -phenyl quenching (BPQ) which usually proceeds from $^3(n-\pi^*)$ states.¹¹³ BPQ is based on the interaction between the keto group of the $^3(n-\pi^*)$ state and the π -system of the phenyl group which are gauche ($\theta = 60^\circ$) to each other.¹¹⁴ In the case of 9-phenyl-PN a gauche relationship is also expected⁹⁹ fulfilling a requirement to induce a charge transfer from the phenyl group to the PN moiety. This can proceed via the triplet state and the singlet state as can be taken from *Scheme 4.2*. Substitution at the phenyl group plays a crucial role in influencing the π -system and consequently the interaction with the oxygen atom of the carbonyl.¹¹⁵

In a mechanistic scenario, the photocyclisation of aromatic ketones such as β -phenylpropiophenone (41) by BPQ was suggested to lead to a short-lived biradical (42) or (43) decaying very fast to its singlet ground state (*Scheme 4.3*).¹¹⁶ In fact, calculations predict an addition of the carbonyl oxygen to the *ipso* or *ortho* position of the phenyl ring where the latter position is less favoured.¹¹⁷



Scheme 4.3 BPQ of β -phenylpropiophenone leading to diradical transients.^{116,117}

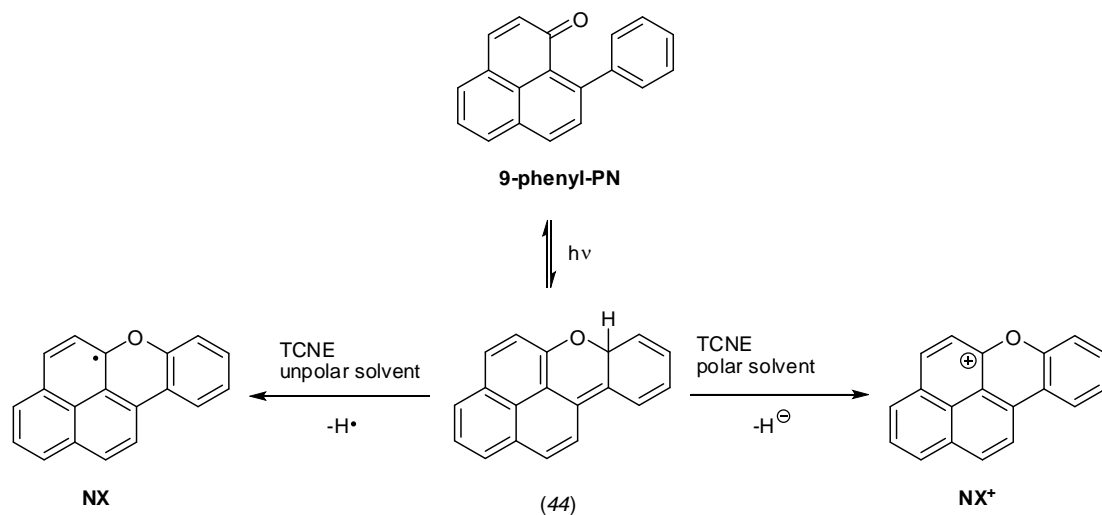
If one may now compare (42) with 9-phenyl-PN, a photocyclization of 9-phenyl-PN at the *o*-position would lead to a closed shell species (*Scheme 4.4*). This is because the carbonyl group and the phenyl group are incorporated in one conjugated system. By delocalisation of the unpaired electron from the phenyl group to the phenalenyl (PLY) system, both unpaired electrons will be recombined to give 1*H*-2-oxa-benzpyrene (44).



Scheme 4.4 Photolysis of 9-phenyl-PN.

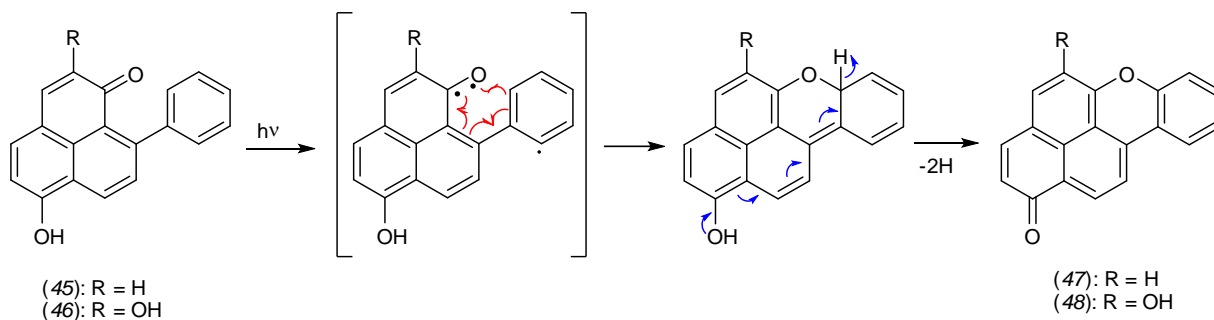
On going studies on the photolysis of 9-phenyl-PN led to the discovery of the formation of a short lived species (44) which undergoes rapid electrocyclic ring opening (*Scheme 4.5*).¹¹⁸ According to DFT calculations, *G. Bucher & S. Nonell* proposed that the cyclisation is favoured at the *o*-position of the phenyl group. Due to a very weak C-H bond ($BDE_{\text{calc}} = 37.4 \text{ kcal mol}^{-1}$) in (44), the use of tetracyanoethylene (TCNE) in non-polar solvents renders possible the generation of a stable PLY type radical naphtho[2,1,8-*mna*]xanthenyl (NX) with remarkable persistence.¹¹⁸ In case of polar solvents, hydride cleavage is predicted and gives the corresponding naphtho[2,1,8-*mna*]xanthenium cation (NX^+). Both the radical and cation were identified via calculated and experimental UV/Vis spectra. NX was also detected via ESR spectroscopy giving a highly complicated spectrum. Nevertheless these results are based

on a photochemical approach yielding low amount of material. Therefore a practical preparation of NX and NX⁺ is necessary.



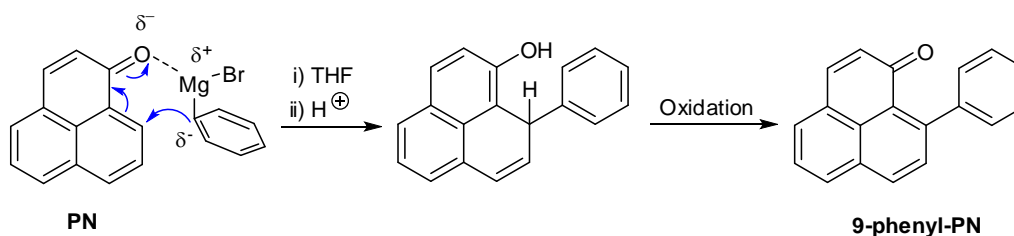
Scheme 4.5 Photolysis of 9-phenyl-PN leading to radical or cation species in presence of TCNE.¹¹⁸

It is noteworthy that the photoinduced cyclisation of *lachnanthocarpone* was previously reported by *J.M Edwards* and *U. Weiss*.⁷ Under oxidative conditions the photolysis of *lachnanthocarpone* (46) resulted in the naphthoxanthenone (48) (Scheme 4.6). The first attempts to cyclise a 9-phenyl-PN without a hydroxyl group at the 2-position was not successful. A tautomeric *o*-quinone structure was assumed to be necessary. Nevertheless, *R.G. Cooke* and *I.J. Dagley* demonstrated the feasibility of the photochemical oxidative cyclisation of 6-hydroxy-9-phenylphenalenone (45) yielding the unsubstituted naphtho[2,1,8-*mna*]xanthenone (47).¹¹⁹ This may proceed in a manner similar to 9-phenyl-PN, though involving the donation of an electron pair by the hydroxyl group at the 6-position which forms the ketone and presumably induces a hydride cleavage. Thus, ruling out the hydroxyl group at the 6-position of the PN unit may result in a short lived closed shell species. In analogy to phenalene (see Chapter 3), this represent a key step for the formation of a PLY type radical or charged species.



Scheme 4.6 Proposed mechanism of the photolysis of 6-hydroxy-9-phenyl-PN resulting in naphtho[2,1,8-*mma*]xanthenones.

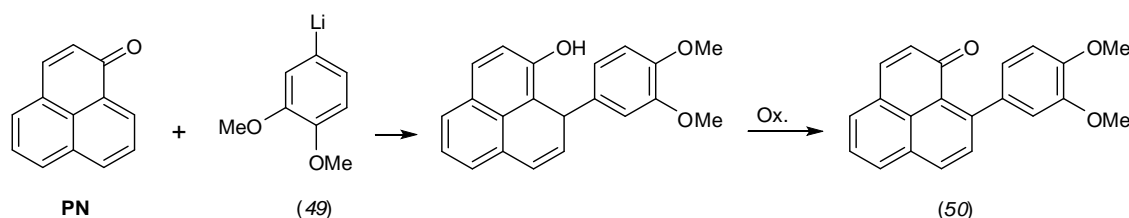
A plethora of derivatives of aryl-PNs and naphthoxanthenones have been synthesised and investigated in terms of their phototoxicity and their structural characterization by NMR spectroscopy.^{120,121} *C.F. Koelsch* and *J.A. Anthes* demonstrated access to 9-phenyl-PN through a *Michael-type Grignard* addition using phenylmagnesium bromide and PN followed by oxidation.¹²² The reaction became well-established and has been employed in the production of a large series of 9-aryl-PNs. Due to the symmetry of the PLY nucleus, the selectivity of the *Grignard* addition is largely affected by the keto group bringing forward the substitution at the *peri* position. This proceeds by the directing effect of the oxygen with the magnesium atom of the *Grignard* reagent resulting in a 6-membered ring constellation (*Scheme 4.7*).



Scheme 4.7 Synthesis of 9-phenyl-PN via a *Michael-type Grignard* addition reaction.¹²²

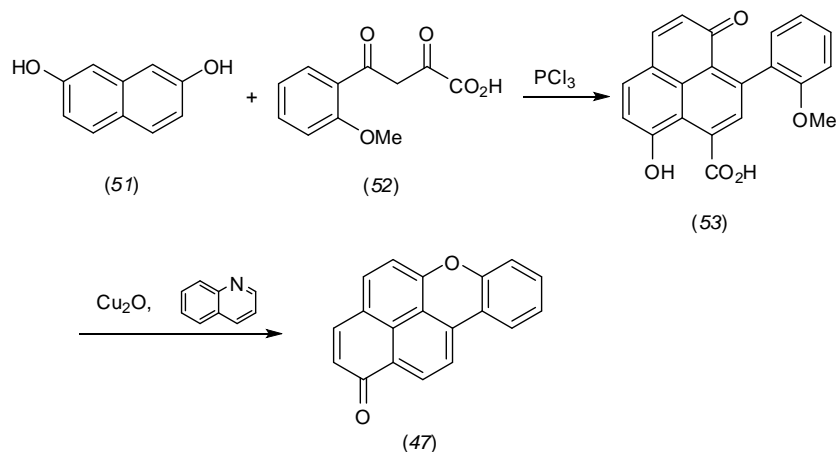
Alternatively, *G.I. Feutrill* and *M.L. Whitelaw* demonstrated the synthesis of 9-aryl-PN using aryllithium reagents.¹²³ In case of 9-phenyl-PN a moderate yield of 60% could be obtained. Conducting a *Grignard* reaction, 9-phenyl-PN could be produced in an improved yield of 85%. The lack of efficiency of aryllithium reagents can be assigned to their tendency to undergo 1,2-addition to the carbonyl group. The generation of a *Grignard* reagent based on 4-bromo-1,2-dimethoxybenzene was unsuccessful but 3,4-dimethoxyphenyllithium (49) could

be realised instead and employed for synthesizing (50) at $-60\text{ }^{\circ}\text{C}$ in a moderate yield of 47% (Scheme 4.8). Despite the generally lower selectivity of aryllithium reagents for the substitution of PN at the 9-position, the synthesis can represent an alternative if certain molecules cannot be used as *Grignard* reagents. In the case of 4-bromo-1,2-dimethoxybenzene, metallation to the methoxy groups may compete with the metal-halogen exchange, which appears to be less pronounced for the lithiation process.



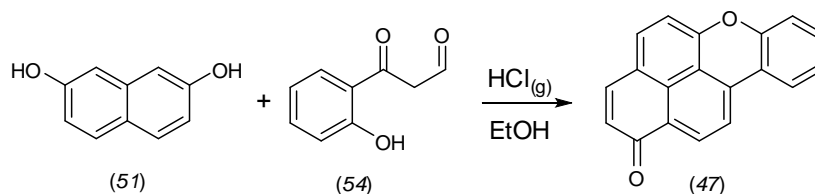
Scheme 4.8 9-C addition on 1*H*-phenalen-1-one (PN) using an aryllithium reagent.¹²³

The thermal synthesis via condensation of compound (47) was reported by *R.G. Cooke* and *I.J. Dagley* (Scheme 4.9).^{124,125} Naphthalene-2,7-diol (51), 4-(2-methoxyphenyl)-2,4-dioxobutanoic acid (52) and phosphoryl chloride were reacted by refluxing in sodium carbonate solution followed by filtration and subsequent acidification of the filtrate yielding 6-methoxy-9-(2-methoxyphenyl)-1-oxophenalenone-carboxylic acid (53) (only the methylated species was isolated and characterised).¹²⁵ Compound (53) was then heated with cuprous oxide and quinoline and worked up with acid resulting in (47). Considering the crude yield of (53) (claimed to be 64%), the overall yield of (47) would be 36%. In a previous report by the same authors, (47) was prepared in a 4-step synthesis adding up to a total yield of 9%.¹²⁴



Scheme 4.9 Acid-catalytic synthesis of naphtha[2,1,8-*mna*]xanthenone.¹²⁵

An alternative method to prepare (47) was reported by *Thomson et al.* involving bubbling a stream of HCl gas through a solution of 2,7-dihydroxy-naphthaldehyde (51) and 2-hydroxyacetophenone (54) in ethanol (*Scheme 4.10*).¹²⁶ Hence, an acid-catalysed cyclization will be expected analogous to the reported synthesis by *Cooke et al.*¹²⁵ This method was claimed to be a more rapid way to prepare (47) in a higher overall yield of 32%.



Scheme 4.10 Acid-catalytic synthesis of naphtha[2,1,8-*mna*]xanthenone **6** via HCl gas.¹²⁶

In conclusion, studies on the photochemistry of PN and its derivatives revealed insights into the mechanism of singlet oxygen production and BPQ by 9-aryl substituted PNs. The photoinduced cyclisation of 6-hydroxy-9-aryl-PN results in naphtho[2,1,8-*mna*]xanthenone. 9-phenyl-PN instead generates a short lived intermediate (44) with a considerably weaker C-H bond than that of phenalene. Although PN derivatives have generally been attractive to phytochemists and photochemists, their use as potential precursors for stable PLY type radicals could be considered in terms of fundamentally important open shell species. Interestingly, mass spectra of 9-aryl-PNs show dominant (M-1)⁺ peaks which are characteristic of naphtho[2,1,8-*mna*]xanthenium cations.^{7,127} However, besides the syntheses of various 9-aryl-PN and naphtho[2,1,8-*mna*]xanthenones, the isolation of pristine or substituted naphtho[2,1,8-*mna*]xanthenium cationic species NX⁺ or the naphtho[2,1,8-*mna*]xanthenyl radical NX have not yet-been reported.

5. Aims

The main focus of this research includes the synthetic methodology giving access to a series of new phenalenyl type cations and radicals incorporating a pyryl ring. The research work was performed considering the below-mentioned facts to investigate the resulting products and to discuss the scope and limitations of the made advances.

I) The base structure naphtho[2,1,8-*mna*]xanthenyl and benzannulated derivatives were prepared using the same synthetic approach to demonstrate the use of the procedure for the synthesis of interesting phenalenyl-type cations or radicals incorporating a pyryl ring.

II) The new cationic species was investigated via UV/Vis spectroscopy and fluorescence spectroscopy.

III) The aromaticity of the cations was evaluated using HOMA indices and subsequently discussed in terms of *Clar's* sextets theory.

IV) The cations were investigated via cyclic voltammetry and their corresponding radicals were analysed via ESR spectroscopy.

V) Functionalised 9-phenyl-PN were prepared and suggested as potential precursors for NX radicals with regards to modern applications.

VII) The functionalisation of phenalenone at the 9-C position was carried out to present new promising precursors. These can be regarded as useful for the substitution of 1*H*-phenalenone at the 9-C-position which are not accessible with the previously known procedures in the literature.

VIII) The largest known polyaromatic hydrocarbon incorporating a pyrylium ring, benzo[5,6]naphthaceno[1,12,11,10-*jklmna*]xanthyl cation, was prepared and investigated analogous to the naphtho[2,1,8-*mna*]xanthenyl cations involving X-ray structure analysis, HOMA evaluation and cyclic voltammetry.

6. Applied methods

6.1. Solvents and reagents

All used solvents and starting materials are commercially available (*Fisher Scientific & Sigma-Aldrich*) and were adopted without purification.

6.2. Spectroscopic methods

NMR-spectroscopy: ^1H -NMR spectra were recorded on a *Bruker400 UltrashieldTM* using *MestReNova* software. The corresponding peaks of the used solvents served as internal standards. CDCl_3 (7.26/77.36 ppm); $\text{DMSO-}d_6$ (2.50/39.5 ppm); D_2O (4.79 ppm); acetone- d_6 (2.05/ 29.84 & 206.16 ppm).

EPR-spectroscopy: *Bruker ESR Elexsys 500 X-Band*; cylindric SHQE cavity (T101 Modus), Software: *Xepr View*.

IR-spectroscopy: Infrared spectra were recorded on *FT-IR – 8400S Shimadzu* spectrometer using *Shimadzu IR-Solution 1.30* Software.

UV-spectroscopy: UV spectra were recorded on *UV-3600 Shimadzu* spectrophotometer. The samples were analyzed in quartz cuvettes.

Fluorescence

spectroscopy: RF-5301PC *Shimadzu*.

6.3. Chromatographic methods

Column

Chromatography: Column chromatography was carried out using silica gel 60 (particle size 0.06-0.2 nm) 70-230 mesh ASTM.

Thin Layer

Chromatography: Thin layer chromatography was carried out using *Merck* silica gel 60 F₂₅₄.

6.4. Analytical methods

Melting points: Melting points were determined using a *Griffin* melting point apparatus.

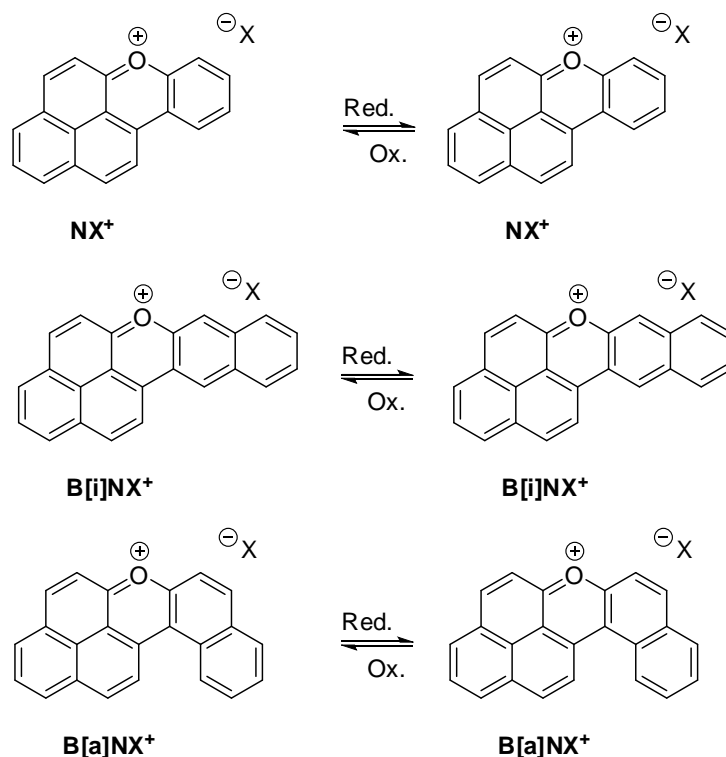
7. Approaches to new phenalenyl based naphthoxanthenyl cations and radicals

7.1. Introduction

π -conjugated radicals based on phenalenyl (PLY), the smallest open-shell graphene-fragments, have played a fundamental role arising in a new research field called “spintronics” or “synthetic organic spin chemistry”.^{65,128,129,130} TBPLY, a sterically protected π radical, introduced insights into unprecedented intermolecular interactions providing additional stabilisation by an aromaticity generation between a pair of phenalenyl layers in the solid state.^{82,84,131} With this π -orbital overlap, the paramagnetic character is maintained and is considered being in equilibrium with a diamagnetic σ -dimer.¹³²

Moreover, phenalenyl is described as an amphoteric species exhibiting reversible electron transfer abilities to form radical, cation or anion with invariant bond orders.⁶⁶ Advances have been made with regards to stabilisation of the open-shell fragment by functionalisation^{85,133} or incorporation of heteroatoms^{87,89}, topological effects on the spin density distribution^{92,95,134,135}, extension to larger Non-*Kekulé* frameworks yielding enhanced amphotericity^{136,137,138}, coordination with metal atoms^{21,139,140,141} and incorporation of heteroatoms in the phenalenyl unit itself^{134,142}. This eventually opened the door to a plethora of new catalytic reagents and molecular-based functional materials. In particular modern applications in terms of organic conductive and semi-conductive materials^{143,144,145}, organic radical batteries⁹⁴, thermochromic crystals¹⁴², switchable or sensing molecules¹⁴⁶ through to species with multiple physical channels¹⁴⁷ intriguingly motivated the research on phenalenyl-based compounds.

In most cases the approach to phenalenyl radicals has been realised from phenalenes which tend to abstract hydrogen, or to cleave a hydride or to undergo deprotonation.^{80,134} Alternatively, the reduction of the corresponding cations proved to be successful.^{82,148,149,150} Based on the latter concept, a universal methodology to prepare new planar and non-planar carbenium ions involving a pyryl ring, from yet-unpublished precursors 9-(2-methoxyaryl)-1*H*-phenalen-1-ones will be introduced via only four reaction steps. Subsequently the radicals will be generated electrochemically. The characterisation is carried out via electron spin resonance spectroscopy supported by calculations of the Mulliken spin densities based on the M05-2X level of theory using the basis set 6-31G**. Starting with the parent naphthoxanthenyl (NX), the two benzannulated isomers, benzonaphtho[*i*]xanthenyl (B[*i*]NX) and benzonaphtho[*a*]xanthenyl (B[*a*]NX), could be formed upon reduction from their corresponding cations (*Scheme 7.1.1*)



Scheme 7.1.1 Reversible reduction of NX^+ , $\text{B}[i]\text{NX}^+$ and $\text{B}[a]\text{NX}^+$ forming their corresponding PLY-based neutral radicals.

The characterised radicals are stabilised by electronic effects which are rarely present in the literature. To our knowledge, only 1,9-dithiophenalenyl (DTPLY) and 1,6,7,9-tetrathiophenalenyl (TTPLY) can be found as electronically stabilised radicals based on

heteroatoms incorporated in the conjugated spin system of a carbon-based phenalenyl unit with regards to achievements by Haddon et. al. (*Figure 7.1.1*)^{87,89,151} Hence the stabilisation effect of phenalenyl by introduction of a chromenyl unit is unknown.

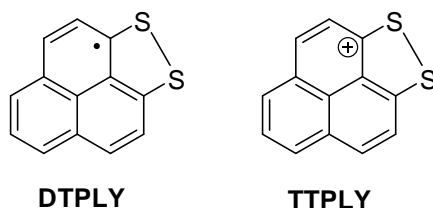
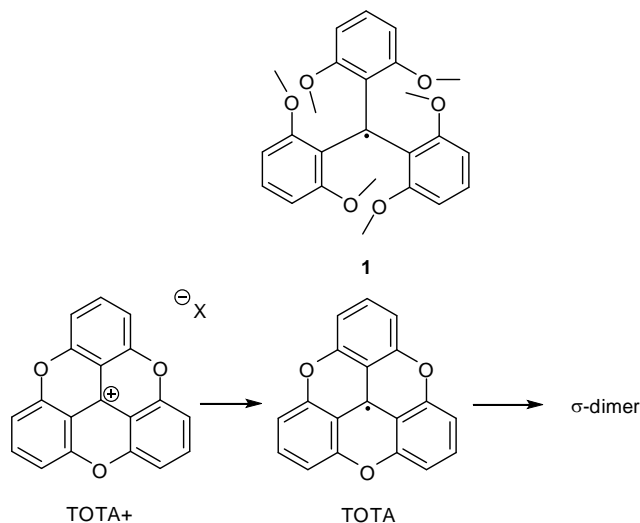


Figure 7.1.1 Molecular structures of 1,9-dithiophenalenyl and 1,6,7,9-tetrathiophenalenyl synthesised by Haddon et. al.^{87,89,151}

It is important to mention that the conveniently prepared carbenium ions represent a class of substances which have only been observed in mass spectra. Dominant $(M-1)^+$ peaks indicated NX cations from cyclisation of 9-aryl 1*H*-phenalen-1-ones in various literature reports.^{7,127} Since there is no explicit characterisation available, the preparation of the carbenium cations may reveal an interesting novel chromophore.

A fundamental carbenium ion involving pyryl rings is trioxatriangulenium ($TOTA^+$).¹⁵² Theoretical aspects have been investigated with regards to its stabilisation effects and stacking arrangements involving carbenium-oxonium equilibria including a pronounced resonance stabilisation with the aid of X-ray structure analysis.¹⁵³ Certainly studies were carried out according to its electrophilic character relative to OH^- expressed by pK_R values showing high stability.¹⁵⁴ Further explorations by introduction of electron-withdrawing substituents led to the modulation of the spacer group in the solid state with the view of pyroelectric materials.¹⁵⁵ Additionally, $TOTA^+$ derived species have been considered as commercially attractive dyes giving rise to various applications.^{156,157} For instance, TOTA based cations showed their propensity to intercalate with DNA and undergo photoinduced charge transport processes resulting in cleavage of guanin bases which are of use in mutation research.^{158,159} However, $TOTA^+$ is merely based on xanthenyl units and does not give rise to a highly stable neutral radical upon reduction.¹⁶⁰ With respect to *Gomberg's* trityl radical, the studies on stabilisation effects by resonance and steric hindrance, 2,6,2',6',2'',6''-hexamethoxytriphenylmethyl (*Scheme 7.1.2*) showed a persistence of few hours in solution and could be kept under oxygen

free conditions for three weeks.¹⁶¹ In the contrary, the planar TOTA radical immediately undergoes σ -dimerisation which is due to its extreme decrease of steric protection.



Scheme 7.1.2 Molecular structure of 2,6,2',6',2'',6''-hexamethoxytriphenylmethyl and TOTA⁺ reduced to its corresponding neutral radical which rapidly undergoes σ -dimerisation.¹⁶¹

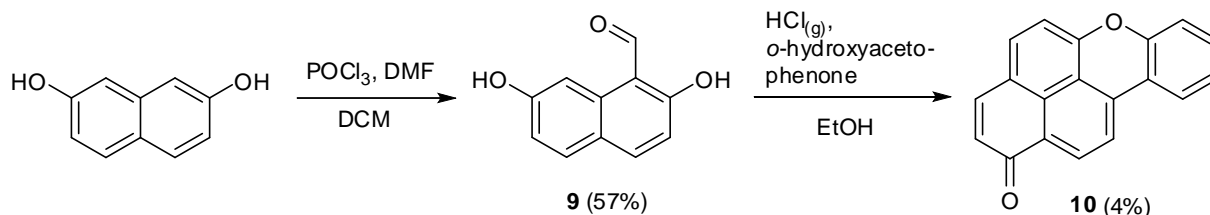
Therefore, naphthoxanthenyl ions and radicals may unify the features of phenalenyl and pyryl derived species. It can be expected that the presented cations reveal photochemical properties based on the extreme perturbation by the incorporated oxygen atom and also amphoteric properties largely provided by the phenalenyl unit including increased stabilisation through possible paramagnetic π -dimerisation as a neutral radical. As a side note, naphthoxanthenyl exhibit the molecular framework of the mutagen benzpyrene.¹⁶² In the case of B[a]NX the mutagenic property is possibly enhanced through its helical geometry.^{163,164} Therefore the species could also be of particular interest for biochemical studies.

7.2. Results

7.2.1. Initial attempt to synthesise the naphthoxanthenyl cation

Initially, the naphtho[2,1,8-*mna*]xanthenyl cation (NX⁺) was approached by reduction of 1*H*-naphtho[2,1,8-*mna*]xanthen-1-one **10**. The synthesis of **10** was conducted by an acid catalysed reaction using 2,7-dihydroxy-1-naphthaldehyde **9** and 2-hydroxyacetophenone according to the literature (*Scheme 7.2.1.1*).¹²⁶ The starting material was prepared by a *Vilsmeier-Haack*¹⁶⁵

reaction on naphthalene-2,7-diol. Naphthalene-2,7-diol was dissolved in DCM and DMF and added carefully to the *Vilsmeier* reagent generated from POCl₃ with DMF. The desired product **9** was obtained in a yield of 57% (see *Appendix 1 & 2* for full ¹H- and ¹³C-spectra).



Scheme 7.2.1.1 Synthesis towards 1*H*-naphtho[2,1,8-*mna*]xanthen-1-one.¹²⁶

The acidic component for the preparation of **10** was provided by the use of HCl gas generated from concentrated HCl solution and CaCl₂. The CaCl₂ is able to remove H₂O from the concentrated HCl solution. This provides sufficient gas-volume for the reaction by one set-up (*Figure 7.2.1.2*). The HCl gas was passed off through a plastic hose to purge through a gently stirring ethanol solution containing **9** and 2-hydroxyacetophenone. After reflux with Na₂CO₃ in H₂O/EtOH and subsequent workup, the desired compound was obtained as a red powder in 4% yield (see *Appendix 3 & 4* for full ¹H- and ¹³C-spectra).

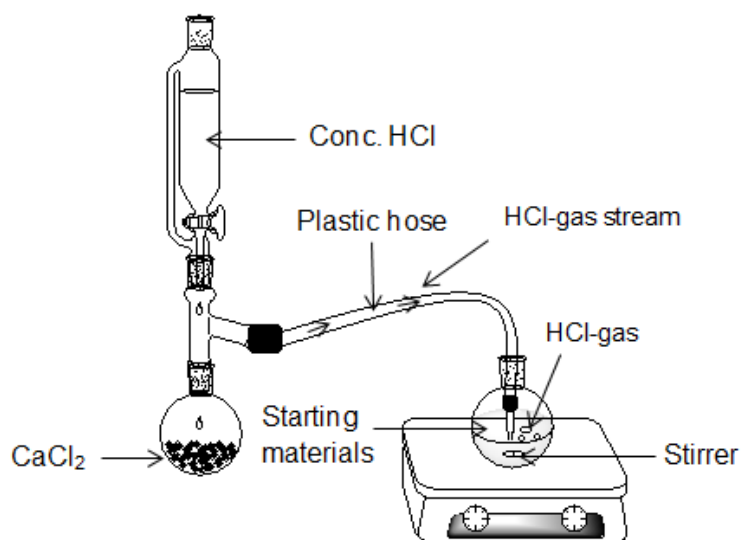
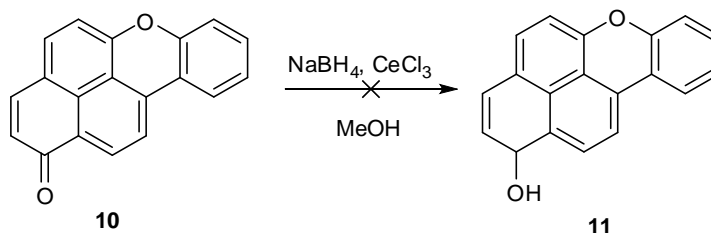


Figure 7.2.1.2 Set-up of HCl gas generation from concentrated HCl solution with CaCl₂.

By means of the *Luche*¹⁶⁶ reduction using NaBH₄ and CeCl₃ the transformation of **10** to 1*H*-naphtho[2,1,8-*mna*]xanthen-1-ol **11** was attempted (Scheme 7.2.1.2). However, the experiments resulted in an inseparable mixture which appeared to decompose or undergo reactions while column chromatography was carried out. Hydroxide cleavage of **11** resulting in the NX⁺ would have been the final step according to this synthetic method. However, due to the difficulties of the reduction reaction and inefficiency of the preparation of **10**, this approach was not taken further.

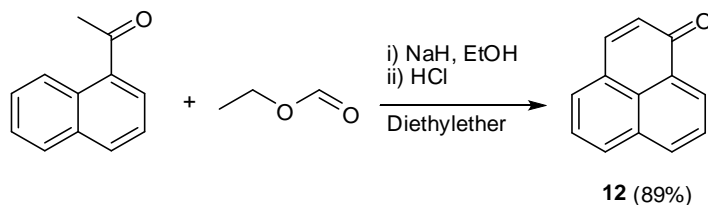


Scheme 7.2.1.2 Attempted reduction of 1*H*-naphtho[2,1,8-*mna*]xanthen-1-one to 1*H*-naphtho[2,1,8-*mna*]xanthen-1-ol.

7.2.2. Synthesis of 9-aryl-1*H*-phenalen-1-ones

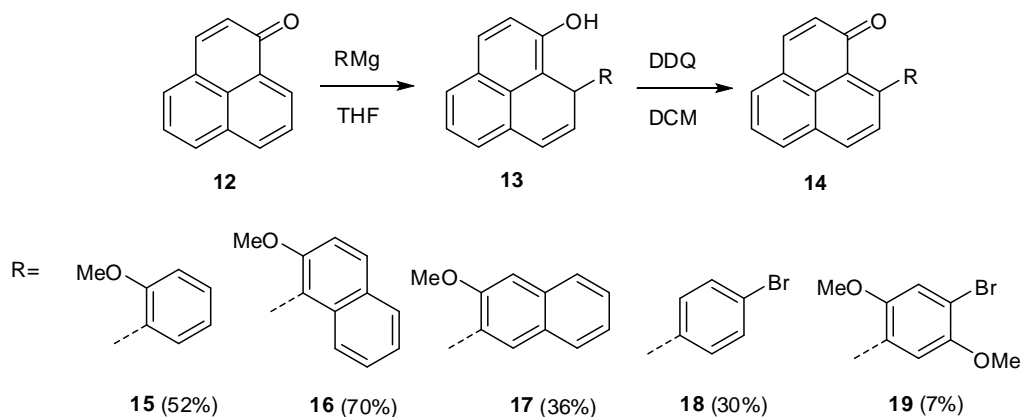
According to the reported procedure by *Koelsch* and *Anthes*¹²², the synthesis of 9-aryl-1*H*-phenalen-1-ones was achieved conducting well-established *Michael*-type *Grignard* addition reactions of *o*-methoxyaryl magnesium bromides with 1*H*-phenalen-1-one **12** and subsequent oxidation using DDQ.

12 is commercially available, but expensive (10g: ~170 £). In a large scale, **12** was prepared by *Claisen*¹⁶⁷ condensation using methyl 1-naphthyl ketone with ethyl formate in the presence of NaH in accordance with the literature (Scheme 7.2.2.1).⁶⁹ A yield of 89% was achieved.



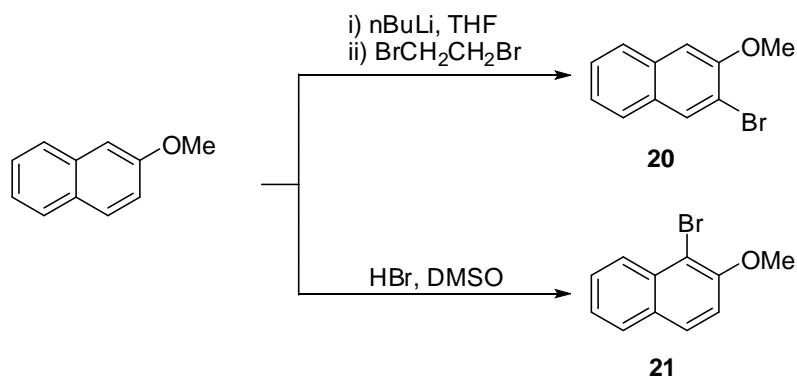
Scheme 7.2.2.1 Synthesis of 1*H*-phenalen-1-one via *Claisen* condensation.

The *Michael-type Grignard* addition was carried out using aryl magnesium bromide in THF under reflux yielding crude 1-aryl-1*H*-phenalen-9-ol **13**. Subsequent reflux with DDQ in DCM resulted in the desired products **14**, 9-(2-methoxyphenyl)-1*H*-phenalen-1-one **15**, 9-(2-methoxynaphthalen-1-yl)-1*H*-phenalen-1-one **16** and 9-(3-methoxynaphthalen-2-yl)-1*H*-phenalen-1-one **17** in yields of 36-70% (*Scheme 7.2.2.2*). The *Grignard* reagents were generated using magnesium with the corresponding brominated aromatic compounds in THF. Analogous to the above described synthesis, 9-(4-bromophenyl)-1*H*-phenalen-1-one **18** and 9-(4-bromo-2,5-dimethoxyphenyl)-1*H*-phenalen-1-one **19** were synthesised in yields of 30% and 7%, respectively. In case of **19**, the isolated solid had a pale orange appearance. However, after recrystallisation from acetone, red crystals were obtained.



Scheme 7.2.2.2 Synthesis of 9-aryl-1*H*-phenalen-1-ones.

The starting materials 2-bromo-3-methoxynaphthalene **20** and 1-bromo-2-methoxynaphthalene **21** were not commercially available and thus prepared according to the literature.^{168,169} 1-Bromo-2-methoxynaphthalene was synthesised by bromination of 2-methoxynaphthalene using HBr in DMSO under reflux giving the product in 91% yield (*Scheme 7.2.2.3*). 2-bromo-3-methoxynaphthalene was obtained in 98% through lithiation at the 3-position and subsequent halogenation with 1,2-dibromoethane in THF at -78 °C.



Scheme 7.2.2.3 Synthesis of 2-bromo-4-methoxynaphthalene and 1-bromo-2-methoxynaphthalene.^{168,169}

7.2.3. ¹H-NMR spectroscopy of 9-aryl-1H-phenalen-1-ones

The ¹H-NMR spectrum of **15** is shown in *Figure 7.2.3.1* (see *Appendix 13 & 14* for full ¹H- and ¹³C-spectra). Eleven proton signals in the aromatic area can be found which can be assigned to seven protons of the phenalenone skeleton and four protons of the phenyl group. The methoxy group is detected as a singlet peak at 3.73 ppm with an integration of three indicating three equivalent protons in relation to a proton signal in the aromatic area. The doublet with a shift of 6.60 ppm has a coupling constant of $J = 9.7$ Hz which is identical with the doublet at 7.67 ppm. This is in agreement with the roof effect suggesting that the signals at 6.60 ppm and 7.67 ppm are assigned to the protons at the 2- and 3-positions, respectively. Considering the COSY spectrum, the multiplet between 7.40-7.46 ppm and the observed triplet of doublets at 7.12 ppm ($J = 7.4, 0.8$ Hz) represent the protons at the 4'- and 5'-positions of the phenyl ring. The doublet of doublets and the doublet signal at 7.03 ppm ($J = 8.2$ Hz) and 7.22 ppm ($J = 7.4, 1.7$ Hz) are detected as the protons at the 3'- and 6'-positions. An expected ABX spin system¹⁷⁰ corresponding to the proton at the 5-position of the phenalenone skeleton is overlapped by a doublet at 7.61-7.49 ppm. The overlapped doublet of doublets signal at 7.57 ppm couples with the doublets at 7.73 ppm ($J = 6.6$ Hz) and 8.01 ppm ($J = 8.2$ Hz) which represent the 4- and 6-positions of the phenalenone skeleton, respectively. The doublet at low field with a chemical shift of 8.18 ppm ($J = 8.3$ Hz) is characteristic for the 7-position in 9-aryl-1H-phenalen-1-ones according to the literature.¹⁷⁰ This couples with the doublet at 7.60 ppm ($J = 8.3$ Hz) which represents the proton at the 8-position.

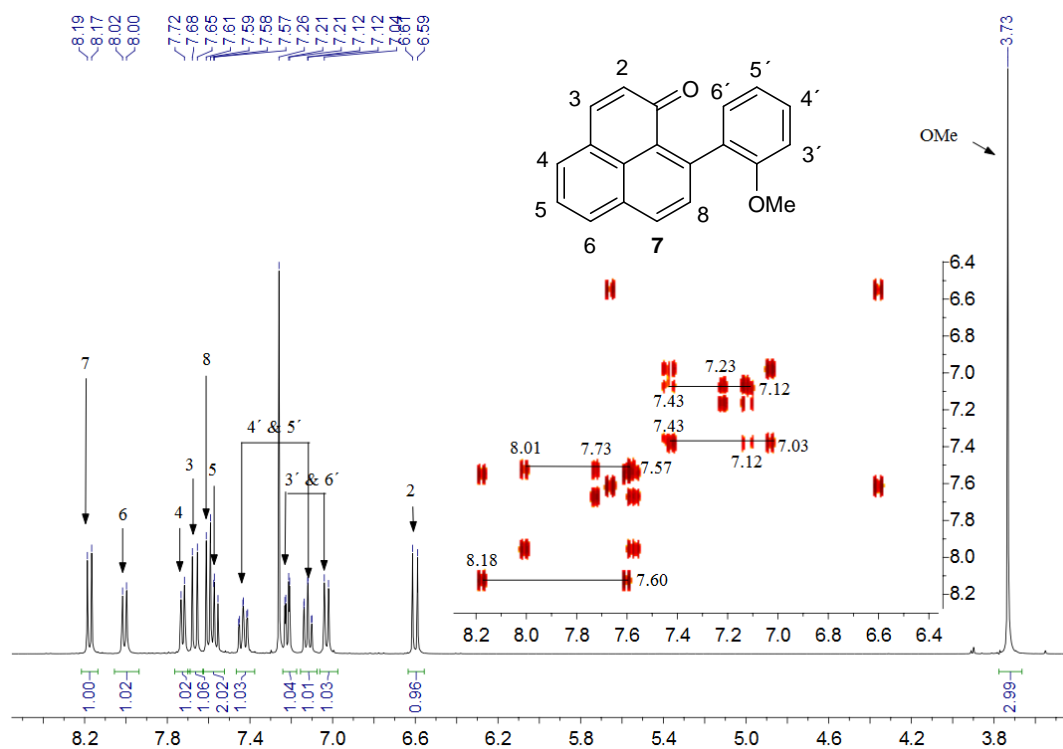


Figure 7.2.3.1 ¹H-NMR spectrum including COSY of 9-(2-methoxyphenyl)-1H-phenalen-1-one **15**. Measured at room temperature (400 MHz; CDCl₃).

The ¹H-NMR spectrum of **16** shows 13 proton signals in the aromatic area and one singlet signal at 3.79 ppm indicating the methoxy group of the naphthalenyl substituent (*Figure 7.2.3.2*; see *Appendix 17 & 18* for full ¹H- and ¹³C-spectra). The doublet at 6.50 ppm ($J = 9.7$ Hz) is assigned to the 2-position analogous to compound **15**. Thus the doublet at 7.70 ppm ($J = 9.7$ Hz) represents the proton at the 3-position. The ABX spin system based on the 5-position is detected at 7.66 ppm indicating a characteristic doublet of doublets ($J = 8.2, 7.1$ Hz).¹⁷⁰ According to the COSY spectrum, this signal couples with two doublets at 7.80 ppm ($J = 6.3$ Hz) and 8.10 ppm ($J = 8.2$ Hz) representing the adjacent 4- and 6-positions, respectively. Two doublets of doublets of doublets at 7.20 ppm ($J = 8.1, 6.7, 1.3$ Hz) and 7.30 ppm ($J = 8.1, 6.7, 1.2$ Hz) are assigned to the protons at the 6'- and 7'-positions of the naphthalenyl moiety. The 5'- and 8'-positions can be found as the two doublets at 7.10 ppm ($J = 8.5$ Hz) and 7.85 ppm ($J = 8.1$ Hz). Two doublets at 7.42 ppm and 7.94 ppm exhibit an identical coupling constant of $J = 9.0$ Hz and can be assigned to the 3'- and 4'-positions. The two remaining

protons, at the 7- and 8-positions are detected as two doublets at 8.27 ppm and 7.59 ppm with equal coupling constants of $J = 8.3$ Hz, respectively.

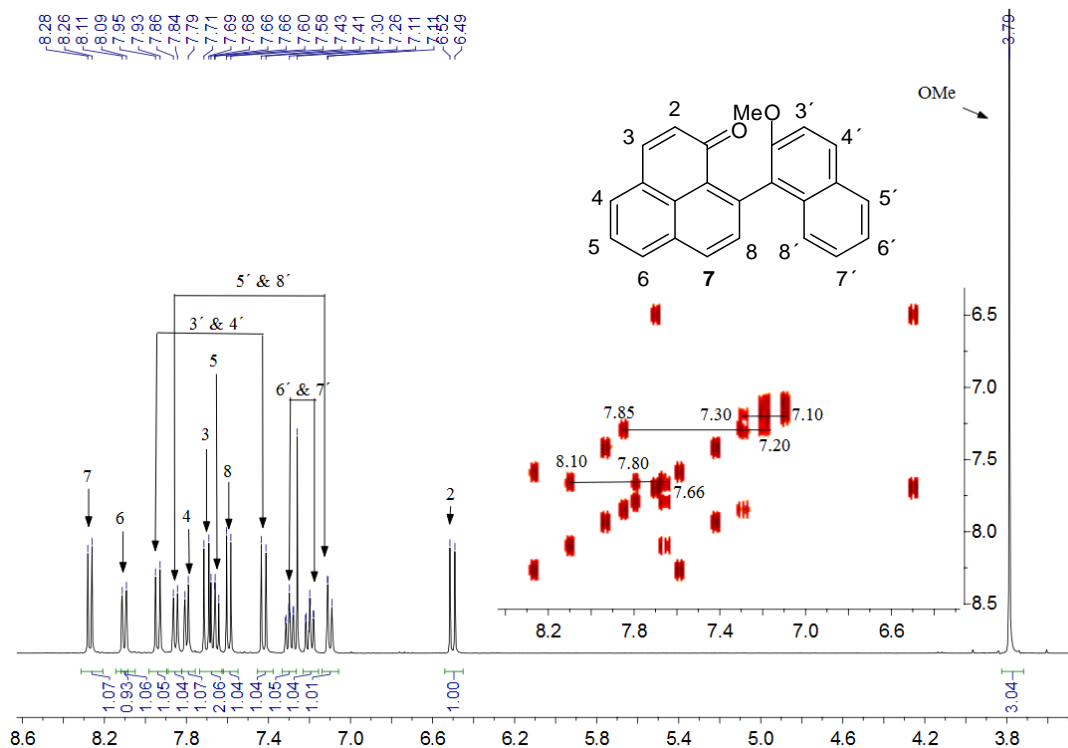


Figure 7.2.3.2 ^1H -NMR spectrum including COSY of 9-(2-methoxynaphthalen-1-yl)-1H-phenalen-1-one **16**. Measured at room temperature (400 MHz; CDCl_3).

The ^1H -NMR spectrum of **17** shows 13 aromatic peaks and a singlet at 3.79 ppm indicating the methoxy group of the naphthalenyl group (Figure 7.2.3.3; see Appendix 15 & 16 for full ^1H and ^{13}C -spectra). Two singlets at 7.22 ppm and 7.62 ppm are assigned to the 3'- and the 8'-positions of the naphthalenyl group, respectively. The doublet 6.58 ppm ($J = 9.7$ Hz) represents the proton at the 2-position coupling with the proton at the 3-position at 7.69 ppm. Two doublets of doublets of doublets are given at 7.33 ppm ($J = 8.1, 6.9, 1.2$ Hz) and 7.44 ppm ($J = 8.2, 6.9, 1.3$ Hz) which can be assigned to the 5' and 6'-positions. The doublet of doublets indicating the 5-position is overlapped by a singlet signal at 7.62 ppm, however, the characteristic coupling constants can still be determined as being $J = 8.2, 7.0$ Hz. At low field, the doublet at 8.22 ppm ($J = 8.3$ Hz) is assigned to the 7-position coupling with the 8-position detected as a doublet at 7.66 ppm ($J = 8.3$ Hz). The four remaining protons at the 4-, 6-, 4' and

7' positions can be assigned to the signals at 8.06 ppm ($J = 8.2, 1.0$ Hz) and overlapped signals between 7.75-7.81 ppm.

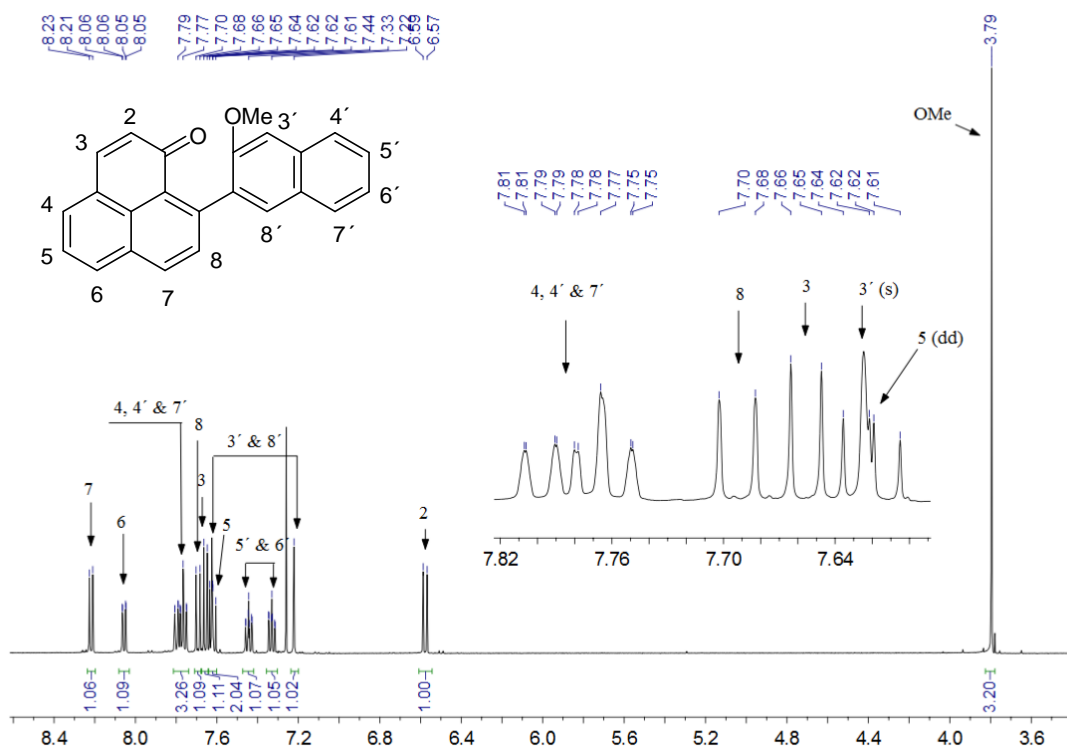


Figure 7.2.3.3 ¹H-NMR spectrum of 9-(3-methoxynaphthalen-2-yl)-1H-phenalen-1-one **17**. Measured at room temperature (400 MHz; CDCl₃).

For compound **18**, 11 protons in the aromatic area could be found in the ¹H-NMR spectrum (Figure 7.2.3.4; see Appendix 19 & 20 for ¹H- and ¹³C-spectra). The four protons of the *p*-bromophenyl group can be assigned at 7.25 ppm ($J = 9.4$ Hz) and 7.58 ppm ($J = 8.4$ Hz) representing 2 protons for each singlet. At 6.59 ppm ($J = 9.7$ Hz), the characteristic doublet represents the 2-position of the phenalenone skeleton which couples with the 3-position at 7.70 ppm ($J = 9.7$ Hz). The doublet of doublets at 7.63 ppm exhibits typical coupling constants of $J = 8.2, 7.1$ Hz which can be assigned to the 5-position. The two doublets at 8.18 ppm and 7.54 ppm have identical coupling constants of 8.3 Hz. Those are assigned to the 7- and 8-positions, respectively. The two remaining proton signals at 7.79 ppm ($J = 6.8, 0.6$ Hz) and 8.05 ppm ($J = 8.2, 0.8$ Hz) thus represent the protons at the 4- and 6-positions.

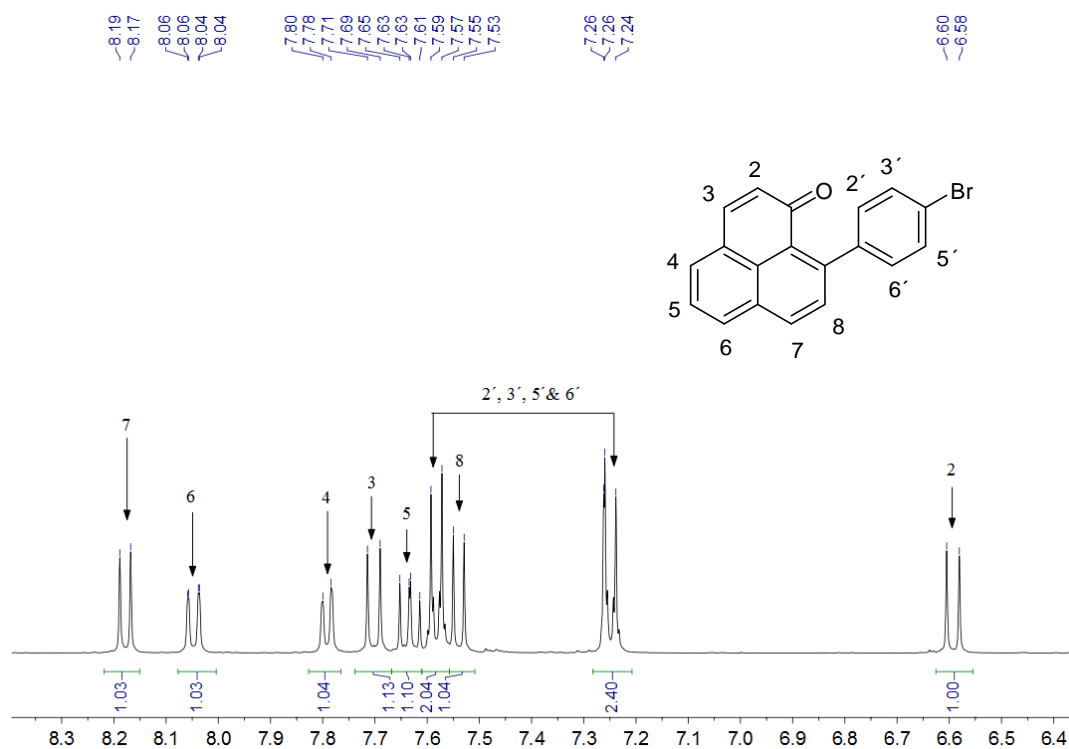


Figure 7.2.3.4 $^1\text{H-NMR}$ spectrum of 9-(4-bromophenyl)-1*H*-phenalen-1-one **18**. Measured at room temperature (400 MHz; CDCl_3).

The $^1\text{H-NMR}$ spectrum of **19** shows 9 proton signals in the aromatic area and two singlets at 3.65 ppm and 3.84 ppm representing the two methoxy groups of the phenyl group (Figure 7.2.3.5; see Appendix 23 & 24 for full $^1\text{H-}$ and $^{13}\text{C-}$ spectra) Two singlets at 6.78 ppm and 7.18 ppm indicate the 3'- and 6'- positions of the benzene ring, respectively. The doublet at 6.58 ppm ($J = 9.7$ Hz) is assigned to the proton at the 2-position coupling with the proton at the 3-position which can be found at 7.69 ppm ($J = 9.7$ Hz). The multiplet at 7.61 ppm can be assigned to the 5-position. At 8.19 ppm and 7.54 ppm, two doublets exhibit identical coupling constants of $J = 8.3$ Hz. Those can be assigned to the 7- and 8-positions, respectively. The two remaining doublets at 7.77 ppm ($J = 7.0$ Hz) and 8.04 ppm ($J = 8.2$ Hz) represent the protons in the 4- and 6-positions, respectively.

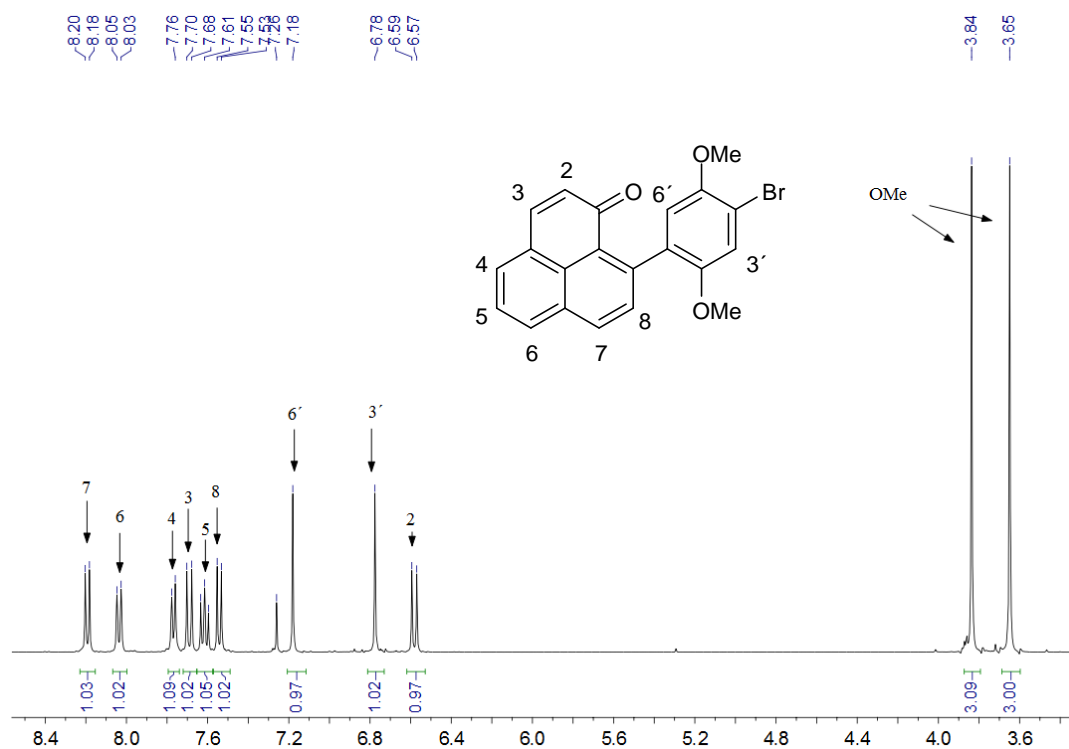


Figure 7.2.3.5 ¹H-NMR spectrum of 9-(4-bromophenyl)-1H-phenalen-1-one **19**. Measured at room temperature (400 MHz; CDCl₃).

7.2.4. UV/Vis & mass spectrometry of 9-aryl-1H-phenalen-1-ones

Normalised UV/Vis spectra of **15-19** are given in (Figure 7.2.4.1). All the 9-aryl-1H-phenalen-1-ones indicate a maximum absorption peak at 360 nm in MeCN. In the cases of **16** and **19** the peaks are broader compared to **15**, **17** and **18**. For the naphthalenyl substituted compounds moderate absorption can be observed at 338 nm and 316 nm for **16** and **17**, respectively, indicating the expected absorption for the 2-methoxynaphthalenyl group.¹⁷¹ The data are in agreement with the literature for 9-aryl-1H-phenalen-1-ones.¹⁷²

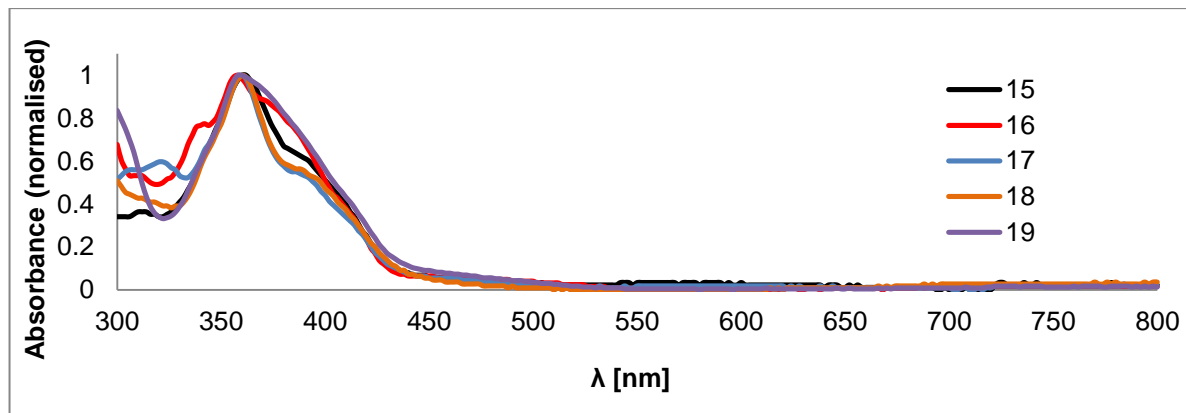
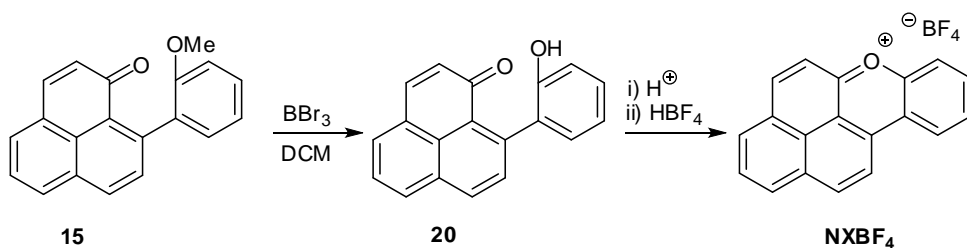


Figure 7.2.4.1 Normalised UV/Vis spectra of 9-aryl-1*H*-phenalen-1-ones **15-19**.

Regarding the mass spectra, **15-17** were confirmed with dominant $(M-31)^+$ peaks which can be ascribed to the corresponding naphthoxanthenyl cations. In the case of **18**, dominant $(M-1)^+$ peaks were detected for both isotopes of bromide, $C_{19}H_{10}^{81}BrO$ and $C_{19}H_{10}^{79}BrO$, indicating the presence of the corresponding naphthoxanthenyl cations. Additionally, high resolution mass spectroscopy confirmed the presence of **15-19**.

7.2.5 Synthesis of naphthoxanthenyl cations

The synthesis of naphtho[2,1,8-*mna*]xanthenium (NX) salts was achieved by *McOmie* demethylation¹⁷³ and subsequent cyclisation of 9-(2-methoxyaryl)-1*H*-phenalen-1-ones. The reaction proceeded predominantly via S_N2 substitution, forming the alcohol after quenching with H_2O . 9-(2-hydroxyaryl)-1*H*-phenalen-1-one undergoes intramolecular cyclisation to give the reactive hemi-ketal which subsequently hydrolysed and resulted in the stable NX cation with bromide as counterion. The cations with bromide as counterion were well soluble in H_2O which made the extraction by distilled H_2O feasible. *Scheme 7.2.5.1* depicts this approach using **15** as an example. The isolation was conveniently carried out by counter ion exchange using HBF_4 . This rapidly decreased the solubility and the precipitate was separated via filtration giving $NXBF_4$ in yields of 63-67%.



Scheme 7.2.5.1 Preparation of naphtho[2,1,8-*mna*]xanthenium tetrafluoroborate.

Analogous to this, benzo[*i*]naphtho[2,1,8-*mna*]xanthenium tetrafluoroborate (B[*i*]NXBF₄) and benzo[*a*]naphtho[8,1,2-*jkl*]xanthenium tetrafluoroborate (B[*a*]NXBF₄) were also prepared in yields of 64 and 67%, respectively.

Demethylation of **19** was found to be difficult which is related to the second methoxy group. Only crude material of the corresponding salt could be made, and so, no full characterisation is available.

7.2.6. ¹H-NMR spectroscopy of naphthoxanthenyl cations

The ¹H-NMR spectrum of NXBF₄ shows 11 proton signals between 8.18 ppm and 9.54 ppm indicating a lowfield shift based on the positive charge of the compound (*Figure 7.2.6.1*; see *Appendix 25 & 26* for full ¹H- and ¹³C-spectra). The two protons at the 8- and 9-positions are assigned to the two doublets of doublets of doublets at 8.15 ppm and 8.38 ppm with calculated coupling constants of $J = 8.3, 7.0, 1.3$ Hz and $J = 8.6, 7.0, 1.5$ Hz, respectively. Confirmed by COSY, those protons coupling with the protons at the 7- and 10-positions can be found as a doublet and a doublet of doublets at 8.44 ppm ($J = 8.4$ Hz) and 9.17 ppm ($J = 8.3, 1.4$ Hz), respectively. At 8.61 ppm ($J = 7.8$ Hz) a triplet represents the 2-position. According to the COSY spectrum, two overlapped signals at 9.22 ppm couple with this triplet. Thus those signals are assigned to the 3- and 1-positions. Four remaining doublets represent the protons at the 4-, 5-, 11- and 12-positions. As the proton at the 5-position is in the vicinity of the electronegative oxygen atom, the chemical shift is expected to be downfield. Thus the doublet at 9.51 ppm ($J = 8.8$ Hz) indicates this proton and couples with the proton at the 4-position detected as a doublet at 9.32 ppm ($J = 8.8$ Hz). The two doublets at 8.59 ppm ($J = 9.2$ Hz) and 9.44 ppm ($J = 9.2$ Hz) are therefore assigned to the 11- and 12-positions. It is noteworthy that

the chemical shifts may vary due to π -stacking interactions correlating with the concentration.¹⁷⁴

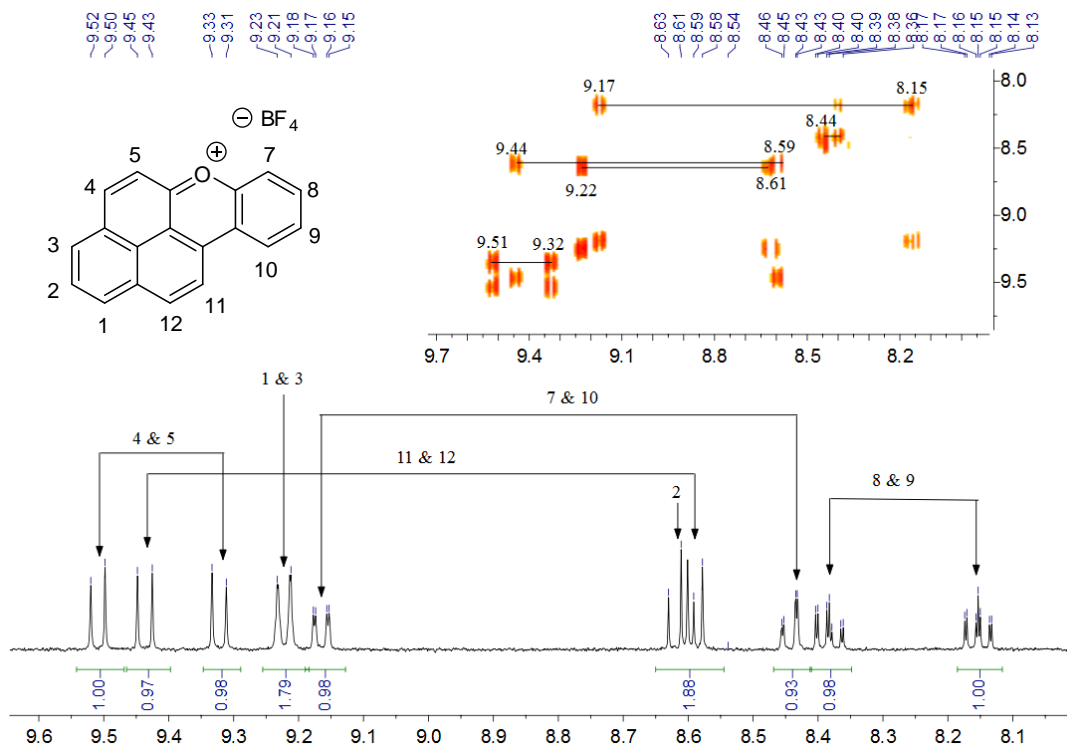


Figure 7.2.6.1 ^1H -NMR spectrum including COSY of naphtho[2,1,8-*mna*]xanthenium tetrafluoroborate (NXBF_4). Measured at room temperature (400 Hz, CD_3CN).

As expected, the ^1H -NMR spectrum of $\text{B}[i]\text{NXBF}_4$ shows 13 proton signals between 7.71 ppm and 9.49 ppm in the aromatic area (Figure 7.2.6.2; see Appendix 27 & 28 for full ^1H - and ^{13}C -spectra). Two singlets at 8.61 ppm and 9.49 ppm are assigned to the protons at the 7- and 12-positions. Two triplets at 7.71 ppm ($J = 7.5$ Hz) and 7.79 ppm ($J = 7.1$ Hz) represent the protons at the 9- and 10-positions. As two doublets at 8.15 ppm ($J = 8.4$ Hz) and 8.25 ppm ($J = 8.5$ Hz) show a roof effect in the direction of the two triplets, they are assigned to the protons at the 8- and 11-positions. The 4- and 5- positions are assigned to two doublets at 9.20 ppm and 9.36 ppm with an identical coupling constant of $J = 8.7$ Hz. The doublet at 9.29 ppm ($J = 9.1$ Hz) couples with the doublet at 8.39 ppm ($J = 9.1$ Hz) indicating the 13- and 14-positions. Two overlapped signals at 9.05 ppm therefore represent the 1- and 3-positions coupling with the triplet at 8.43 ppm ($J = 7.7$ Hz) representing the 2-position.

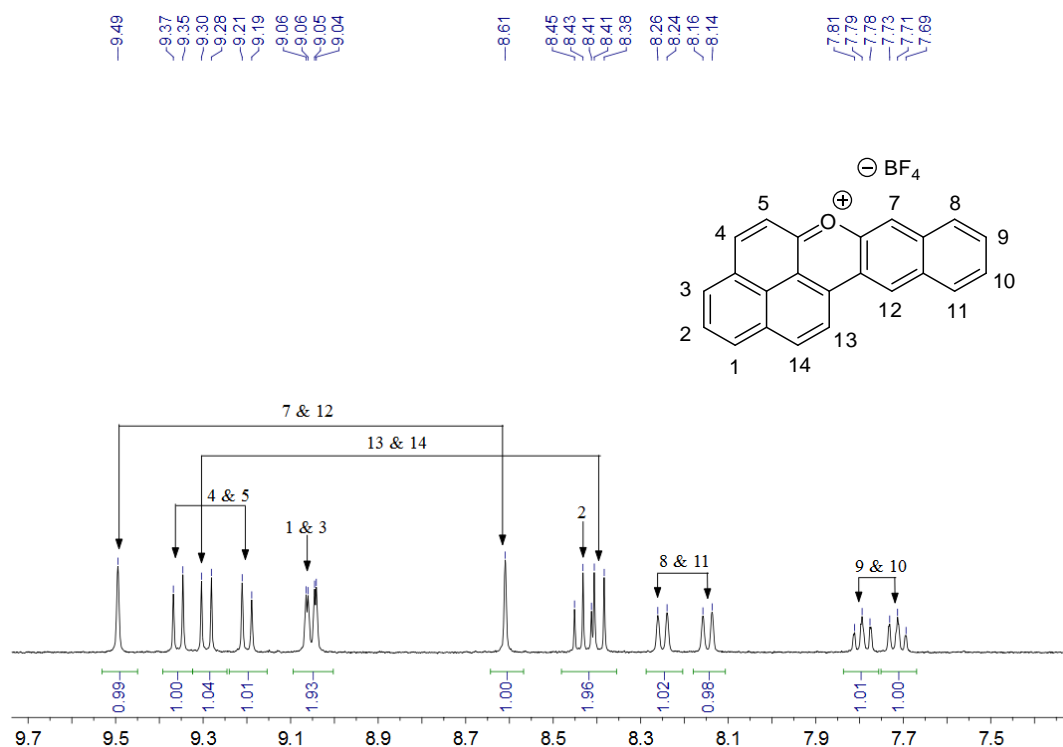


Figure 7.2.6.2 ^1H -NMR spectrum of benzo[*i*]naphtho[2,1,8-*mna*]xanthenium tetrafluoroborate ($\text{B}[i]\text{NXBF}_4$). Measured at room temperature (400 Hz, CD_3CN).

A ^1H -NMR spectrum of $\text{B}[a]\text{NXBF}_4$ is depicted in *Figure 7.2.6.3* below (see *Appendix 29 & 30* for full ^1H - and ^{13}C -spectra). Between 7.95 ppm and 9.61 ppm, 13 aromatic proton signals are given showing a lowfield effect caused by the positive charge of the species. Two doublets of doublets of doublets at 7.95 ppm ($J = 8.0, 7.1, 1.0$ Hz) and 8.07 ppm ($J = 8.5, 7.1, 1.4$ Hz) represent the protons at the 10- and 11-positions. With the aid of a COSY spectrum, the protons at the 9- and 12-positions are shown to be at 8.33 ppm ($J = 8.0, 1.2$ Hz) and 9.28 ppm ($J = 8.5$ Hz) detected as a doublet of doublets and a doublet, respectively. The triplet at 8.58 ppm ($J = 7.7$ Hz) is assigned to the proton at the 2-position. According to the COSY spectrum, the two overlapped doublets at 9.15 ppm indicate the protons at the 1- and 3-positions. The two doublets at 9.61 ppm and 9.39 ppm with an identical coupling constant of $J = 9.1$ Hz exhibit a roof effect in the direction of each other. Thus they are assigned to the protons at the 4- and 5-positions in analogy to NXBF_4 .

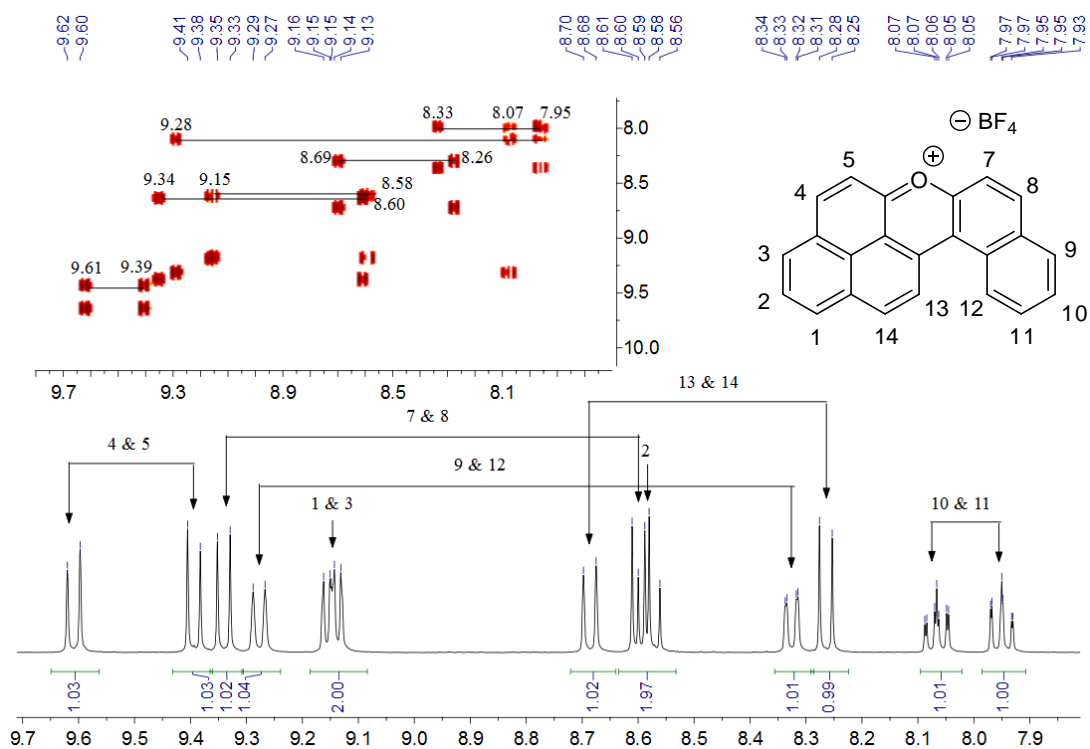


Figure 7.2.6.3 $^1\text{H-NMR}$ spectrum including COSY of benzo[*a*]naphtho[8,1,2-*ijkl*]xanthenium tetrafluoroborate ($\text{B}[a]\text{NXBF}_4$). Measured at room temperature (400 Hz, CD_3CN).

Four remaining doublets, with an identical coupling constant of $J = 9.1$ Hz, are grouped in two pairs representing the protons at the 7- and 8-positions and the 13- and 14-positions assigned with the aid of the COSY spectrum. According to a NOESY spectrum (Figure 7.2.6.4), the doublet at 8.69 ppm shows a cross peak with the proton at the 12-position which has a chemical shift of 8.33 ppm. Therefore it is assumed that this doublet signal represents the proton at the 13-position due to the fjord region. Using the COSY, the proton at the 14-position can then be found at 8.69 ppm. Due to the low quality of the NOESY, a more indicative point is the downfield shift of the doublet at 9.34 ppm which can be ascribed to the positive charge (presumably enhanced close to the oxygen). This phenomenon is comparable with NXBF_4 and $\text{B}[i]\text{NXBF}_4$. Therefore this doublet is considered to be assigned to the 7-position. Subsequently, the 7- and 8-positions can be assigned to 8.61 ppm and 9.34 ppm using the COSY spectrum.

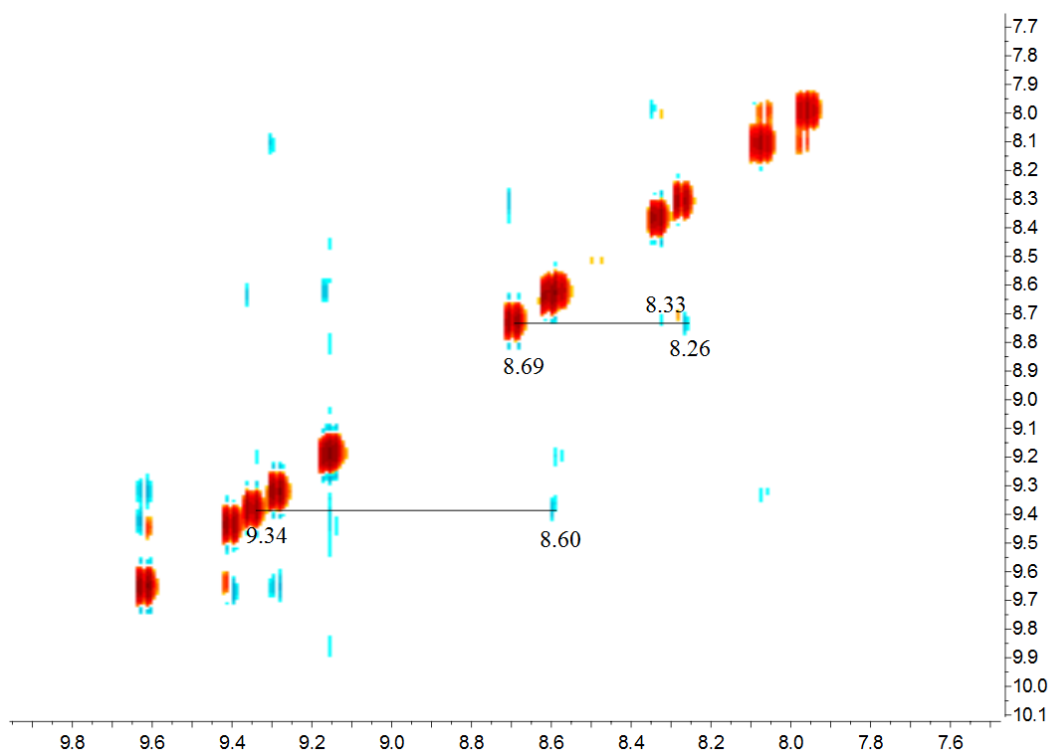


Figure 7.2.6.4 NOESY of benzo[*a*]naphtho[8,1,2-*jkl*]xanthenium tetrafluoroborate B[*a*]NXBF₄.

7.2.7. UV/Vis, fluorescence & mass spectroscopy of naphthoxanthenyl cations

Normalised UV/Vis spectra of NXBF₄, B[*i*]NXBF₄ and B[*a*]NXBF₄ in MeCN show absorption maxima at 456 nm, 469 nm and 505 nm, respectively (*Figure 7.2.7.1*). BNX[*i*]BF₄ exhibits a bathochromic shift of 13 nm compared to NXBF₄. A distinct discrepancy can be observed between the two isomers BNX[*i*]BF₄ and BNX[*a*]BF₄. The latter compound shows a broader absorption with a maximum at 505 nm which gives a bathochromic shift of 36 nm compared to BNX[*i*]BF₄. Further moderate absorption can be observed between 300-340 nm for both compounds which can be ascribed to the naphthalenyl unit.

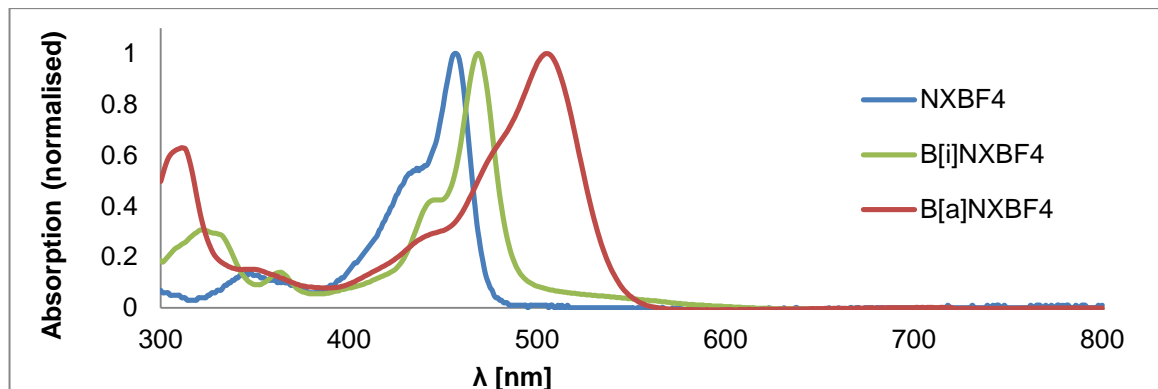


Figure 7.2.7.1 Normalised UV/Vis spectra of NXBF₄, B[i]NXBF₄ and B[a]NXBF₄ in MeCN.

The different intensities of fluorescence emission of NXBF₄, B[i]NXBF₄ and B[a]NXBF₄ could be observed with the naked eye (see photo in *Figure 7.2.7.2*). Fluorescence spectra show the fluorescence emission of NXBF₄ (2.8×10^{-5} mol/l), B[i]NXBF₄ (1×10^{-5} mol/l) and B[a]NXBF₄ (3.1×10^{-6} mol/l) upon excitation at 435 nm, 465 nm and 505 nm, respectively. NXBF₄ emits between 450 and 600 nm with a maximum at 471 nm giving a Stokes shift of 15 nm. B[i]NXBF₄ also indicates an emission up to 600 nm, however, with a considerably lower intensity. The maximum peak lies at 516 nm which corresponds to a Stokes shift of 47 nm. A broad absorption between 510 nm and 690 nm can be observed for B[a]NXBF₄ showing a bathochromic shift and a higher intensity with a maximum peak at 562 nm. The Stokes shift is comparable with B[i]NXBF₄. The spectra were recorded choosing an excitation slit width of 1.5 nm and an emission slit width of 3 nm, however, in case of B[i]NXBF₄ the fluorescence emission was negligibly weak so that the spectrum of this salt was measured at an excitation slit width of 3 nm and an emission slit width of 5 nm. This resulted in a recognizable emission peak which is still considerably low compared to NXBF₄ and B[a]NXBF₄.

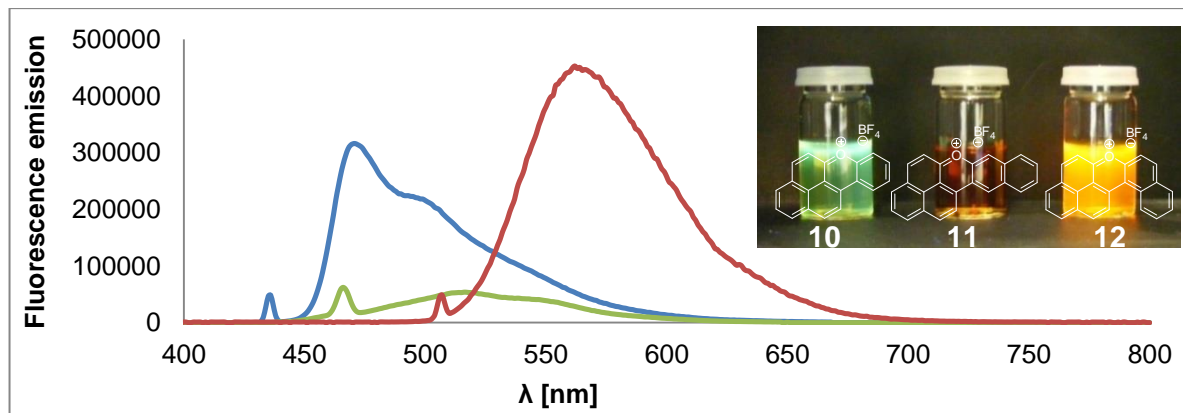


Figure 7.2.7.2 Fluorescence spectra of NXBF_4 ($2.8 \cdot 10^{-5}$ mol/l), $\text{B}[i]\text{NXBF}_4$ ($1 \cdot 10^{-5}$ mol/l) and $\text{B}[a]\text{NXBF}_4$ ($3.1 \cdot 10^{-6}$ mol/l) recorded in MeCN. Photo shows the salts dissolved in MeCN in presence of UV irradiation.

According to mass spectra, M^+ peaks of $m/z = 205$ for NXBF_4 and $m/z = 305$ for $\text{B}[a]\text{NXBF}_4$ and $\text{B}[i]\text{NXBF}_4$ were detected. Additionally, the structure was confirmed by high resolution mass spectroscopy and X-ray structure analysis.

7.2.8. X-ray structure analysis of naphthoxanthenyl cations

The crystals of the salts crystallised from acetone were of sufficient quality to carry out X-ray structure analyses. The X-ray resolutions show the three salts being packed in triclinic space groups. NXBF_4 was crystallised from acetone resulting in antiparallel π -stacking arrangements with distances between 3.294-3.372 Å ($\text{C}_\pi\text{-C}_\pi$) (Table 7.2.8.1 & Figure 7.2.8.1; see also Appendix 57 & 58).

Interacting atoms	Distance [Å]
C1-C5b	3.344
C3-C9	3.294
C3b-C9b	3.372
C5a-C11	3.343
C9a-C10	3.370
C9-C9b	3.325
C7-C11	3.363

Table 7.2.8.1 Atoms of NX^+ involved in π -stacking interactions.

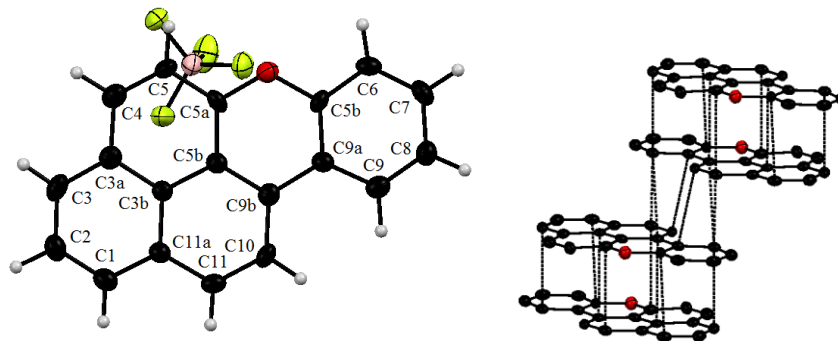


Figure 7.2.8.1 Left: X-ray crystal structure of NXBF_4 . Right: $\text{C}_\pi\text{-C}_\pi$ contacts; hydrogens and counterions are omitted for clarity.

The bond lengths of the cation are depicted in *Figure 7.2.8.2*. The shortest bond length is 1.338 Å and lies between the oxygen and the C5a atom indicating a strong bonding. Considering the bay region, the bond angles are 123.9° (C9a-C9b-C10) and 124.4° (C9-C9a-C9b) exhibiting a torsion angle of 0.2°.

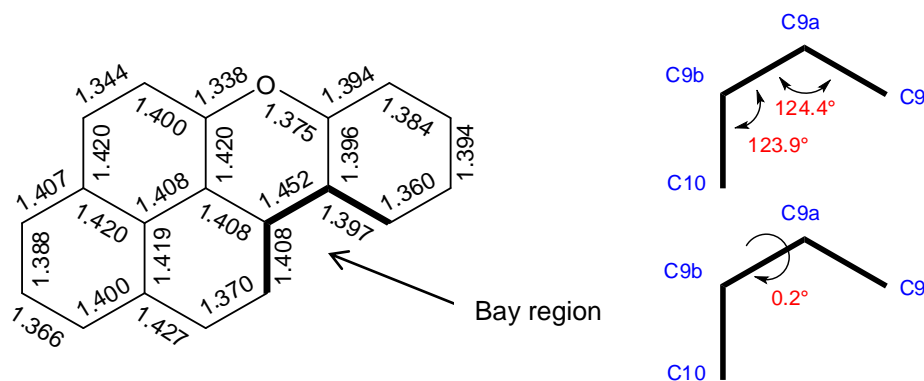


Figure 7.2.8.2 Bond lengths of NX^+ including bond and torsion angles according to X-ray structure analysis.

According to the crystal packing structure, short intermolecular contacts of 2.663 Å between the oxygen and the hydrogen atoms at the 5-position can be observed. All intermolecular contacts below 3.139 Å involving the counterion and NX^+ can be found in *Table 7.2.8.2* and are depicted in *Figure 7.2.8.3*.

Contact between two atoms	Distance [Å]
O-H5	2.663
B-H2	2.977
B-H10	2.881
B-H12	3.026
F1-O	2.937
F1-H1	2.478
F1-H2	2.360
F2-C5a	3.139
F2-H5	2.421
F2-H10	2.528
F2-H11	2.381
F3-H2	2.568
F3-H10	2.381
F3-C10	3.120
F4-H4	2.316
F4-H8	2.652
F4-H12	2.637

Table 7.2.8.2 Contact distances of NXBF_4 .

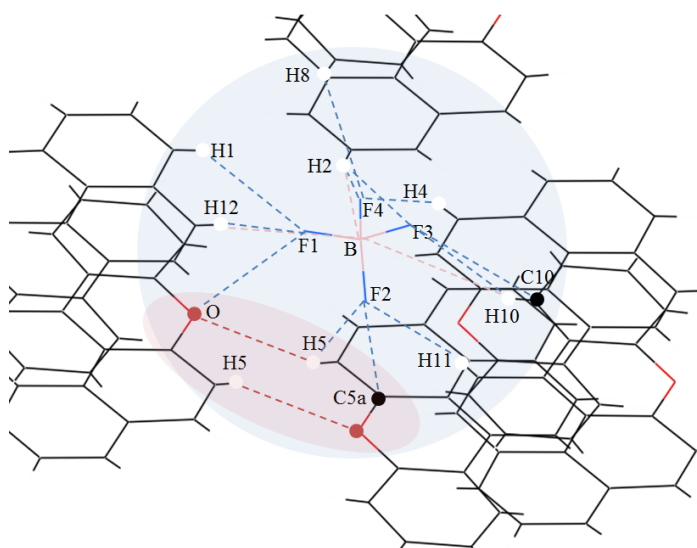


Figure 7.2.8.3 Section of the packing structure of NXBF_4 indicating intermolecular distances.

In the case of $B[i]NXBF_4$, the X-ray structure analysis indicates an arrangement similar to $NXBF_4$ showing antiparallel π - π overlap with a slightly lower separation of 3.286-3.389 Å (C_π - C_π) overall (Table 7.2.8.3 & Figure 7.2.8.4; see also Appendix 61 & 62).

Interacting atoms	Distance [Å]
C5a-C13	3.354
C3-C11	3.313
C5b-C1	3.383
C1-C8	3.318
C6a-C13	3.286
C3b-C11b	3.355
C11-C11b	3.389

Table 7.2.8.3 Atoms of $B[i]NX^+$ involved in π -stacking interactions.

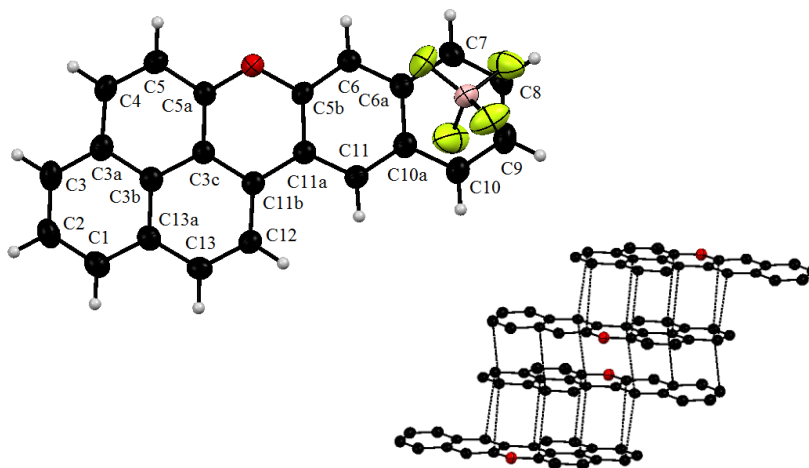
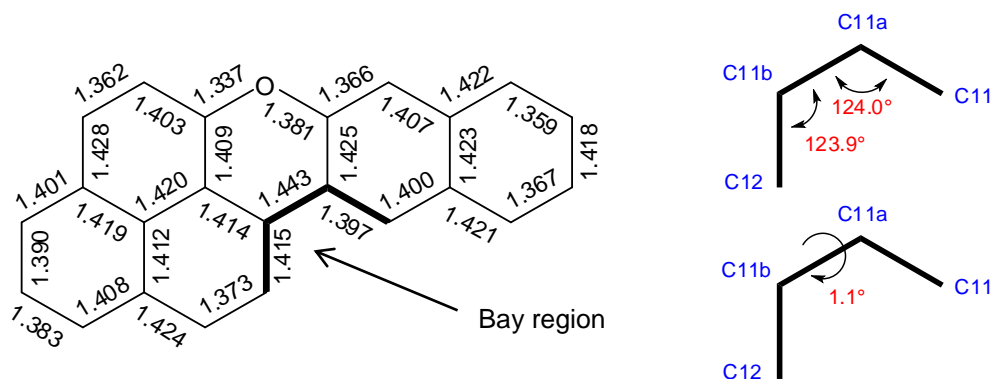


Figure 7.2.8.4 Left: X-ray crystal structure of $B[i]NXBF_4$. Right: C_π - C_π contacts; hydrogens and counterions are omitted for clarity.

Considering the bond lengths of $B[i]NXBF_4$, the bond between the oxygen and C5a atom exhibits the shortest bond length in the molecule which is almost identical to $NXBF_4$ (Figure 7.2.8.5). With regards to the bay region, the C11a-C11b bond length is decreased by 0.009 Å compared to that of $NXBF_4$. Furthermore, a slight reduction of the bond angle between C11-C11a-C11b can be observed. This is concomitant with a twist of 1.1° indicating a difference of 0.9° compared to $NXBF_4$.



There are no considerable contacts between the oxygen and the proton at the 5-position as in NXBF₄. All contacts between the anion and the cation below 3.162 Å can be found in *Table 7.2.8.4* and *Figure 7.2.8.6*.

Contact between two atoms	Distance [Å]
O-F2	2.937
B-H12	3.056
B-H14	3.065
F1-H4	2.611
F1-H14	2.436
F2-C5a	2.972
F2-H12	2.376
F2-H13	2.421
F3-H2	2.509
F3-H11	2.667
F3-C2	3.162
F4-H1	2.454
F4-H9	2.471

Table 7.2.8.4 Contact distances of B[*i*]NXBF₄.

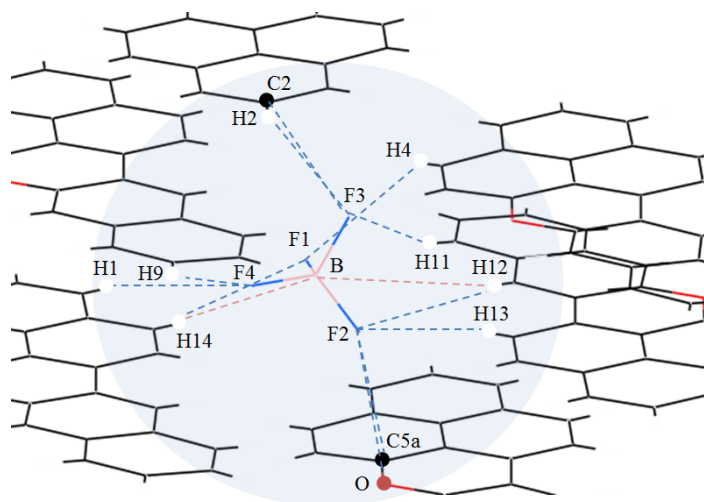


Figure 7.2.8.6 Section of packing structure of B[*i*]NXBF₄ indicating intermolecular distances.

The X-ray structure analysis of B[*a*]NXBF₄ also reveals antiparallel π - π overlapping, however, to a lesser extent than for NXBF₄ or B[*a*]NXBF₄ with a separation of 3.288-3.388 Å (C_{π} - C_{π}) (*Table 7.2.8.5* & *Figure 7.2.8.7*; see also *Appendix 63* & *64*).

Interacting atoms	Distance [Å]
C3-C11c	3.288
C3b-C3b	3.373
C1-C13b	3.388
C3-C13	3.292

Table 7.2.8.5 Atoms of B[*a*]NX⁺ involved in π -stacking interactions.

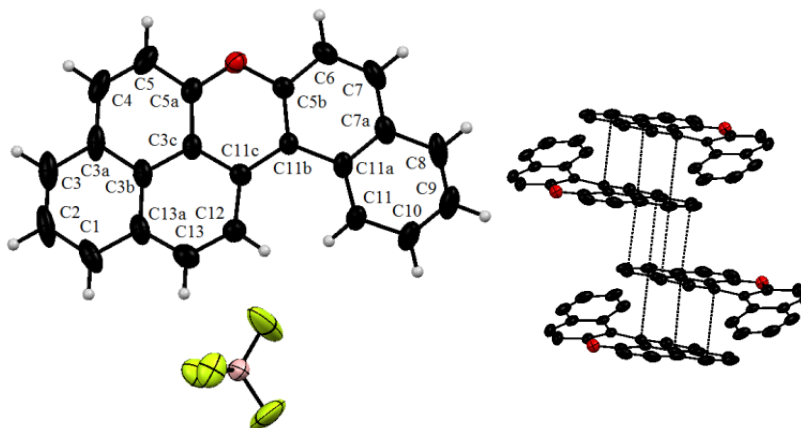


Figure 7.2.8.7 Left: X-ray crystal structure of B[*a*]NXBF₄. Right: C_{π} - C_{π} contacts; hydrogens and counterions are omitted for clarity.

In comparison with NXBF₄, distinct decreases of the bond lengths between the oxygen and C5a atom (1.332 Å) and the C11b and C11c atoms (1.430 Å) in the fjord region can be shown

(Figure 7.2.8.8). Considering the fjord region, the bond angles are 127.1° (C11b-C11c-C12) and 125.8° (C11-C11a-C11b) with a concomitant twist of 17.3° based on the C11b-C11c bond. Hence, the naphthalenyl moiety clearly shows a helical orientation.

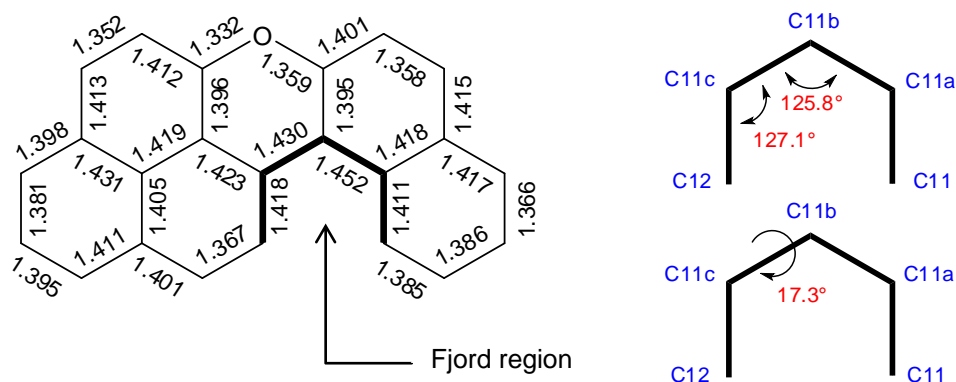


Figure 7.2.8.8 Bond lengths of B[a]NX⁺ including bond and torsion angles according to X-ray structure analysis.

Regarding intermolecular contacts, no considerable contacts between the oxygen atom and the C5a-carbon can be observed similar to B[i]NXBF₄. Table 7.2.8.6 shows all distances between the cation and the BF₄ counterion below 3.185 Å which are depicted in Figure 7.2.8.9.

Contact between two atoms	Distance [Å]
B-H1	3.185
B-H4	3.012
F1-C5	3.038
F1-C5a	3.155
F1-H1	2.414
F1-H4	2.600
F1-H14	2.405
F2-C13	3.161
F2-H8	2.422
F2-H9	2.542
F2-H13	2.493
F3-C10	3.109
F3-H2	2.523
F3-H10	2.279
F4-H4	2.384

Table 7.2.8.6 Contact distances of B[a]NXBF₄.

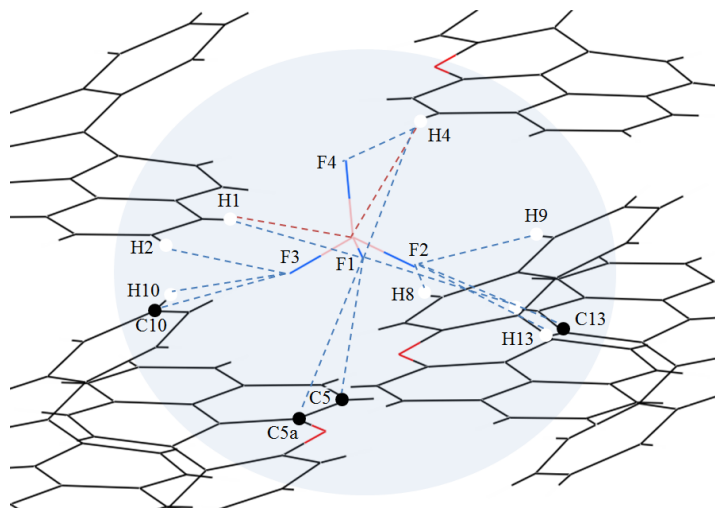


Figure 7.2.8.9 Section of packing structure of B[a]NXBF₄ indicating intermolecular distances.

7.2.9. Cyclic voltammetry results of naphthoxanthenyl cations

The studies of NXBF₄ using cyclic voltammetry under an argon atmosphere revealed two reversible redox waves (*Figure 7.2.9.1*). The potential for the reduction of the cation resulting in the radical is $E_{1/2} (1) = -0.52$ V and for the formation of the anion resulting from the reduction of the radical is $E_{1/2} (2) = -1.66$ V (all potentials vs. the ferrocene/ferrocenium couple). In contrast to the HOMO-LUMO gap evaluation for closed-shell species, the sum of the oxidation and reduction potentials (termed the “amphotericity”¹⁷⁵) represents the coulombic repulsion between the electron in the former SOMO and a transferred electron occupying the same orbital to form the anion. This value amounts to $E_{\text{sum}} = E_{\text{ox}} + (-E_{\text{red}}) = 1.14$ V in this case and is in a range typical for phenalenyl-type radicals.¹⁷⁶ If the cyclic voltammogram is recorded under an atmosphere of air, the redox wave centred around -0.52 V remains unchanged, but the second reduction at -1.66 V becomes irreversible, and multiple new peaks appear below -1 V vs. ferrocene/ferrocenium (see *Appendix 54*).

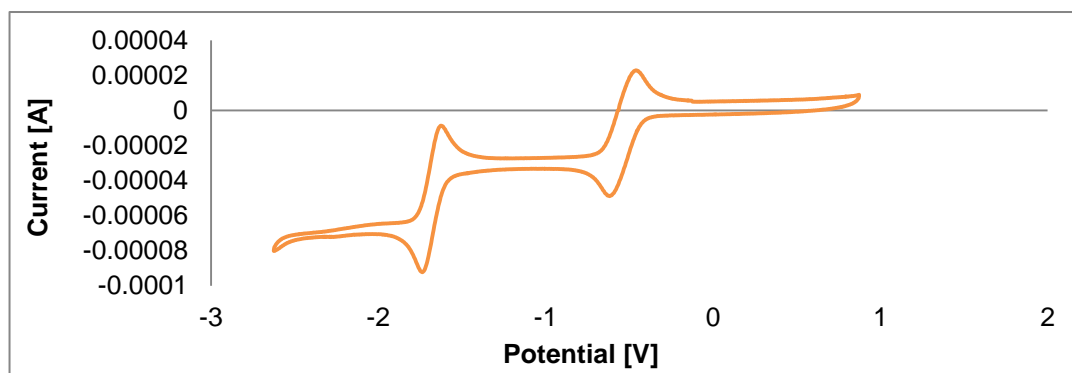


Figure 7.2.9.1 Cyclic voltammogram of NXBF₄ at room temperature obtained at a scan rate of 20 mV s⁻¹ on a glassy carbon working electrode of area 0.071 cm². A Pt mesh counter electrode was used and the reference electrode was Ag/AgNO₃. The electrolyte (0.1 M NBu₄-BF₄ in MeCN) was degassed thoroughly with argon before spectrum acquisition. Peaks are referenced to the Fc/Fc⁺ couple (wave not shown).

In the case of B[*i*]NXBF₄, two reversible redox waves are given at -0.43 V and -1.53 V for the reduction from the cation to the radical and from the radical to the anion, respectively (*Figure 7.2.9.2*). In comparison to NXBF₄, the potential values are less negative indicating a shift of 0.09 V and 0.13 V for the generation of the radical and the anion, respectively. Hence, the amphotericity is $E_{\text{sum}} = 1.10$ V which is slightly lower than that of NXBF₄.

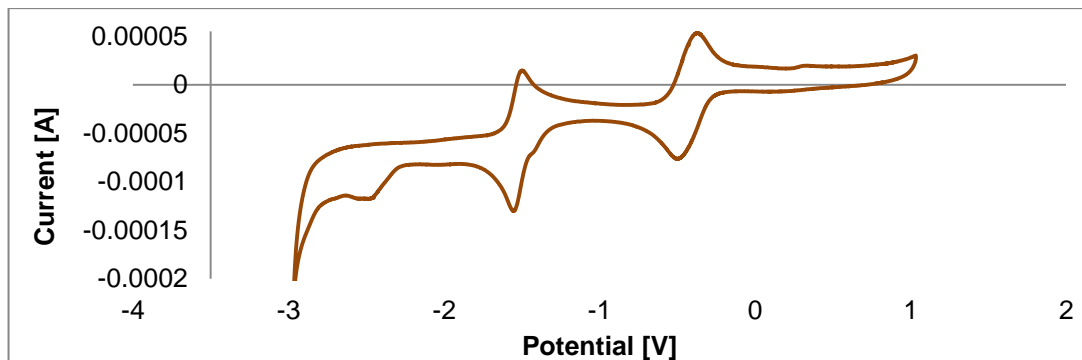


Figure 7.2.9.2 Cyclic voltammogram of B[i]NXBF₄ at room temperature obtained at a scan rate of 100 mV s⁻¹ on a glassy carbon working electrode of area 0.071 cm². A Pt mesh counter electrode was used and the reference electrode was Ag/AgNO₃. The electrolyte (0.1 M NBu₄-BF₄ in MeCN) was degassed thoroughly with argon before spectrum acquisition. Peaks are referenced to the Fc/Fc⁺ couple (wave not shown).

On the contrary, B[a]NXBF₄ exhibits reversible redox waves at more negative potential values at -0.59 V and -1.67 V for reduction from the cation to the radical and from the radical to the anion, respectively (*Figure 7.2.9.3*). This gives a potential shift of 0.07 V and 0.01 V compared to NXBF₄ with an amphotericity of E_{sum} = 1.08.

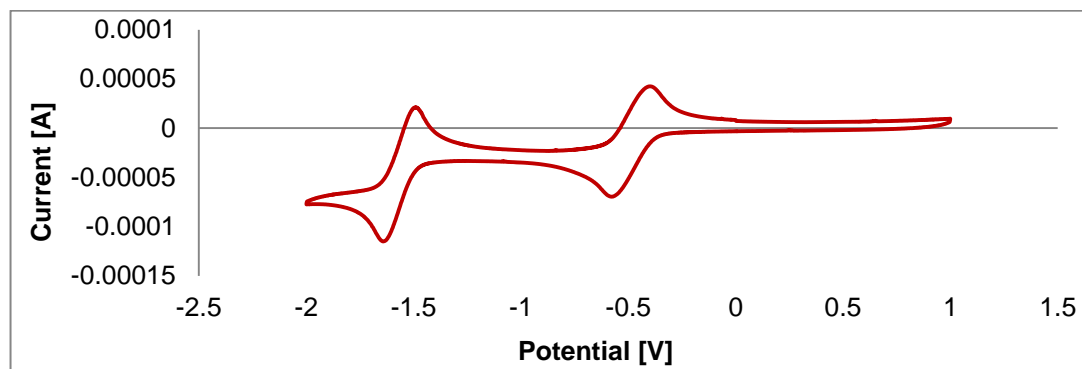


Figure 7.2.9.3 Cyclic voltammogram of B[a]NXBF₄ at room temperature obtained at a scan rate of 100 mV s⁻¹ on a glassy carbon working electrode of area 0.071 cm². A Pt mesh counter electrode was used and the reference electrode was Ag/AgNO₃. The electrolyte (0.1 M NBu₄-BF₄ in MeCN) was degassed thoroughly with argon before spectrum acquisition. Peaks are referenced to the Fc/Fc⁺ couple (wave not shown).

7.2.10. Generation of naphthoxanthenyl radicals

The radicals, NX, B[*i*]NX and B[*a*]NX were formed using NaI in MeCN resulting in brownish solids containing the corresponding radicals. The purification of the radicals via recrystallisation in solvents such as MeCN, acetone, DCM, EtOAc, cyclohexane, benzene, toluene or diethylether was unsuccessful. A sublimation of NX was attempted at about 200 °C under vacuum which gave a reddish deposition on the glass surface but no useful crystals were obtained for X-ray structure analysis. Well-resolved ESR spectra were obtained in DMSO. The crude products showed intense paramagnetic signals with g-values close to that of a free electron ($g = 2.002319$). The ESR spectrometer was calibrated according to perylene. *Figure 7.2.10.1* shows a complicated spectrum of NX indicating a g-value of 2.003 and a linewidth of 32 gauss. The complicated line pattern derives from eleven unequal protons resulting in $(2 * 1 * \frac{1}{2} + 1)^{11} = 2048$ ($(2 * M * \frac{1}{2} + 1)^n$) lines. The simulation spectra were made by *Dr. Dirk Grote (Ruhr-Universität Bochum)* using a dataset of four hyperfine coupling constants with values of 5.9, 2.3, 1.9 and 1.5 Gauss and *Dr. Victor Chechik (University of York)* who used a dataset of 2 x 5.33, 2 x 4.47, 1 x 3.83, 2 x 1.38 and 2 x 1.29 Gauss. *Figure 7.2.10.1* depicts both the simulation and the measured signals of NX. The radical exhibited high persistence and the sample exhibited the same paramagnetic ESR response after more than 2 years.

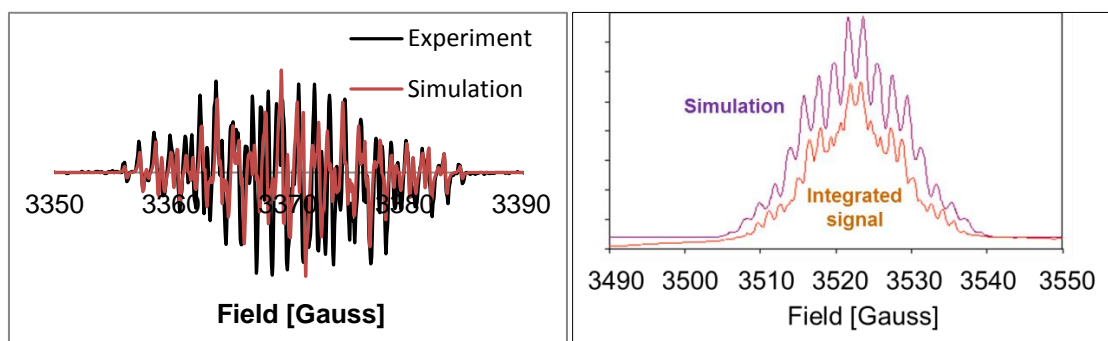


Figure 7.2.10.1 Left: CW-ESR spectrum (1st derivative) of NX in DMSO after 35 scans at room temperature including simulation spectrum by *Dr. Victor Chechik* (modulation amplitude: 0.2 Gauss; conversion time: 20.48 ms; sweep time: 20.97 s; time constant: 5.12 ms). Right: Integration of measured signal including simulation by *Dr. Dirk Grote (Ruhr-Universität Bochum)*.

In the case of B[*i*]NX, a highly complicated spectrum results from 13 unequal protons ($(2 * 1 * \frac{1}{2} + 1)^{13} = 8192$ lines). A less-resolved ESR spectrum was obtained indicating a g-value of 2.008 and a linewidth of 36 Gauss (*Figure 7.2.10.2*).

The simulation was carried out with the support of the *EPSRC ESR Center* in Manchester using a data set of 4 x 5.30, 4 x 1.74 and 5 x 0.45 Gauss. *Figure 7.2.10.2* and *Figure 7.2.10.3* show the first and second derivatives of the measured absorbance and the corresponding simulation, respectively.

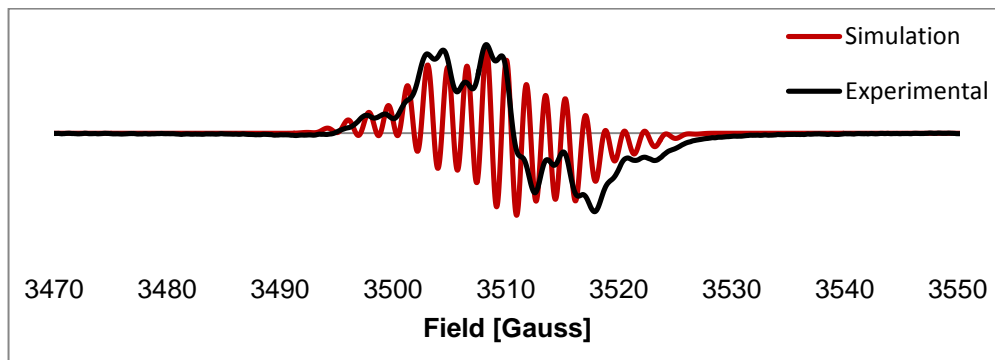


Figure 7.2.10.2 Measured CW-ESR spectrum (1st derivative) of B[i]NX in DMSO (black) after 250 scans at room temperature (modulation amplitude: 0.1 Gauss; conversion time: 1.59 ms; sweep time: 12.40 s; time constant: 20.48 ms. Simulation spectrum (red) is superimposed on the experimental spectrum.

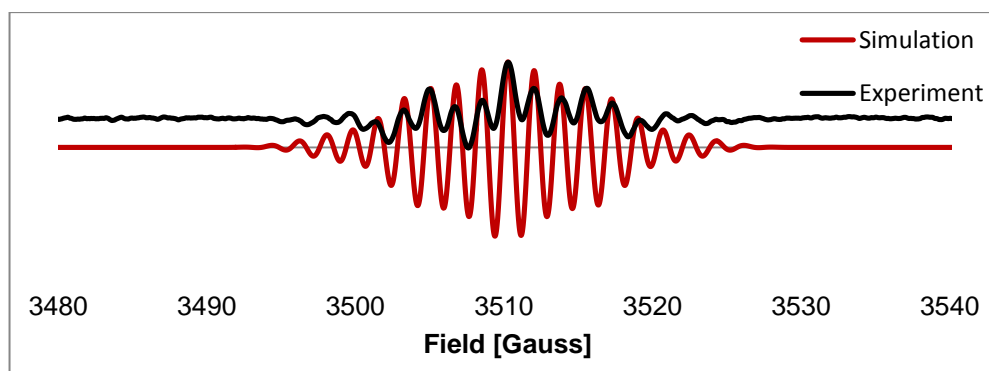


Figure 7.2.10.3 Measured CW-ESR spectrum (2nd derivative) of B[i]NX (black) superimposed on the simulation (red).

The ESR spectrum of B[a]NX shows a highly complicated pattern similar to B[i]NX. The simulation of a reasonable approximate spectrum was without success. The *g* factor is 2.008 with a linewidth of 26 Gauss. Since no simulation is available, it is presumed that the first and second derivative of the ESR signal depicted in *Figure 7.2.10.4* and *7.2.10.5*, respectively, represent the neutral radical B[a]NX.

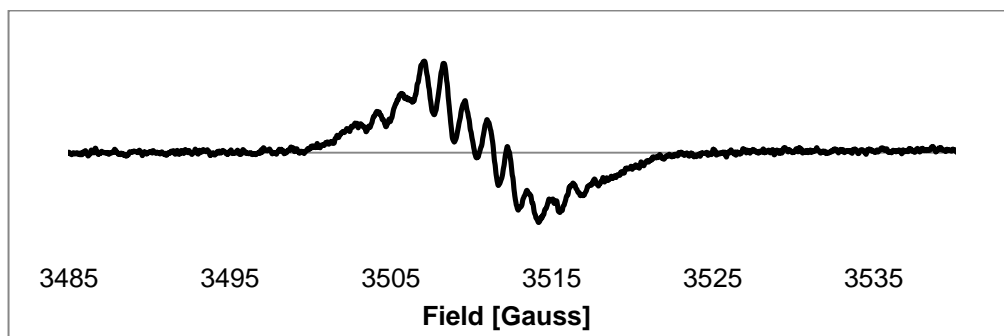


Figure 7.2.10.4 Measured CW-ESR spectrum (1st derivative) of B[a]NX in DMSO after 205 scans at room temperature (modulation amplitude: 0.25 Gauss; conversion time: 3.98 ms; sweep time: 12.42 s; time constant: 20.48 ms).

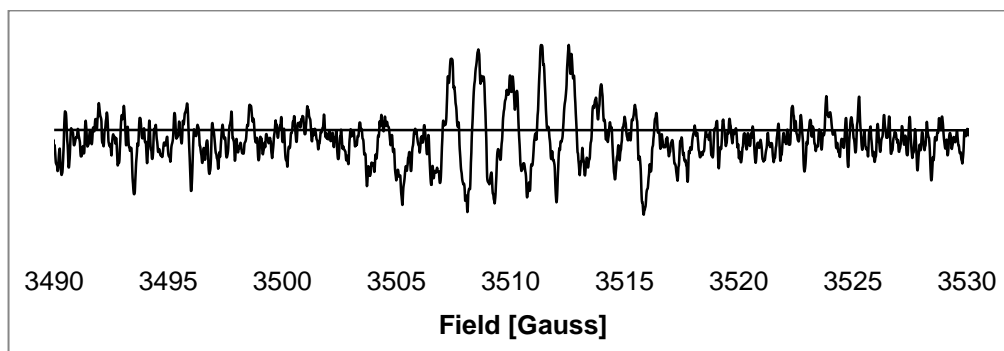


Figure 7.2.10.5 Measured CW-ESR spectrum (2nd derivative) of B[a]NX.

NXBF₄ was also reduced using NaI in DMSO and a sample with a concentration of 5.9×10^{-6} mol/l was prepared for UV/Vis spectroscopy. The spectrum shows peaks at 372 nm, 395 nm and 412 nm and broad absorptions at 460 nm and 492 nm (*Figure 7.2.10.1*). Hence, the presence of the cation is largely depleted resulting in the corresponding radical and could be confirmed via ESR spectroscopy.

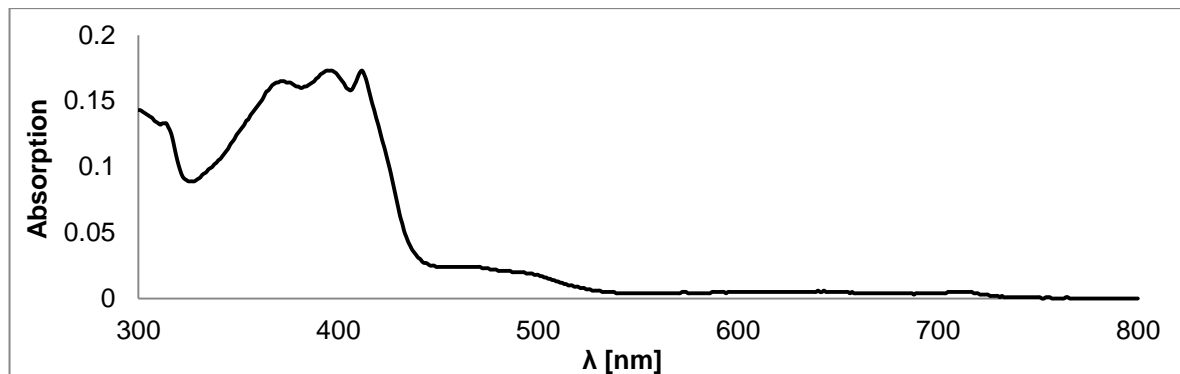
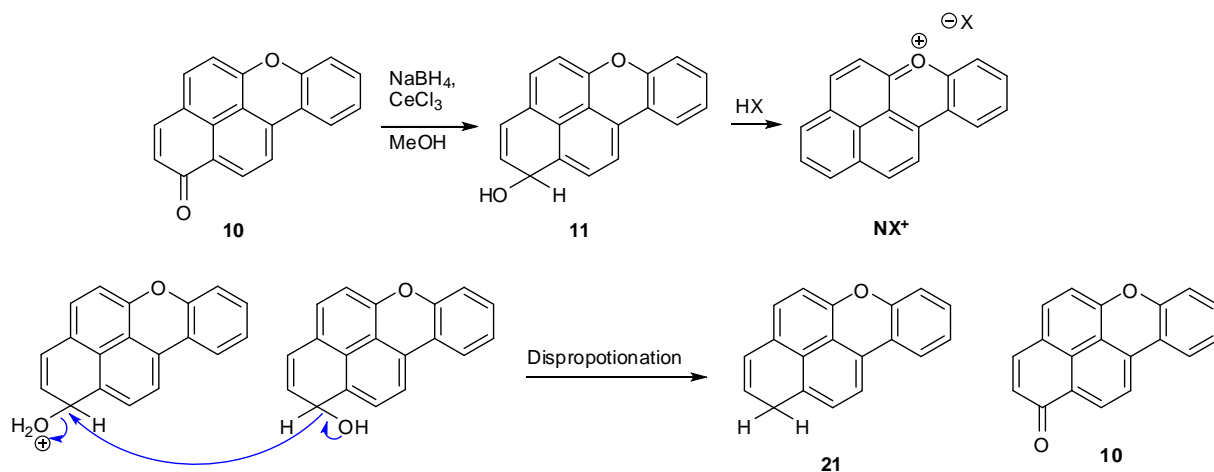


Figure 7.2.10.1 UV/Vis spectrum of NX (5.9×10^{-6} mol/l) in DMSO.

7.3. Discussion

7.3.1. Initial attempt to synthesise the naphtho[2,1,8-*mna*]xanthenium cation

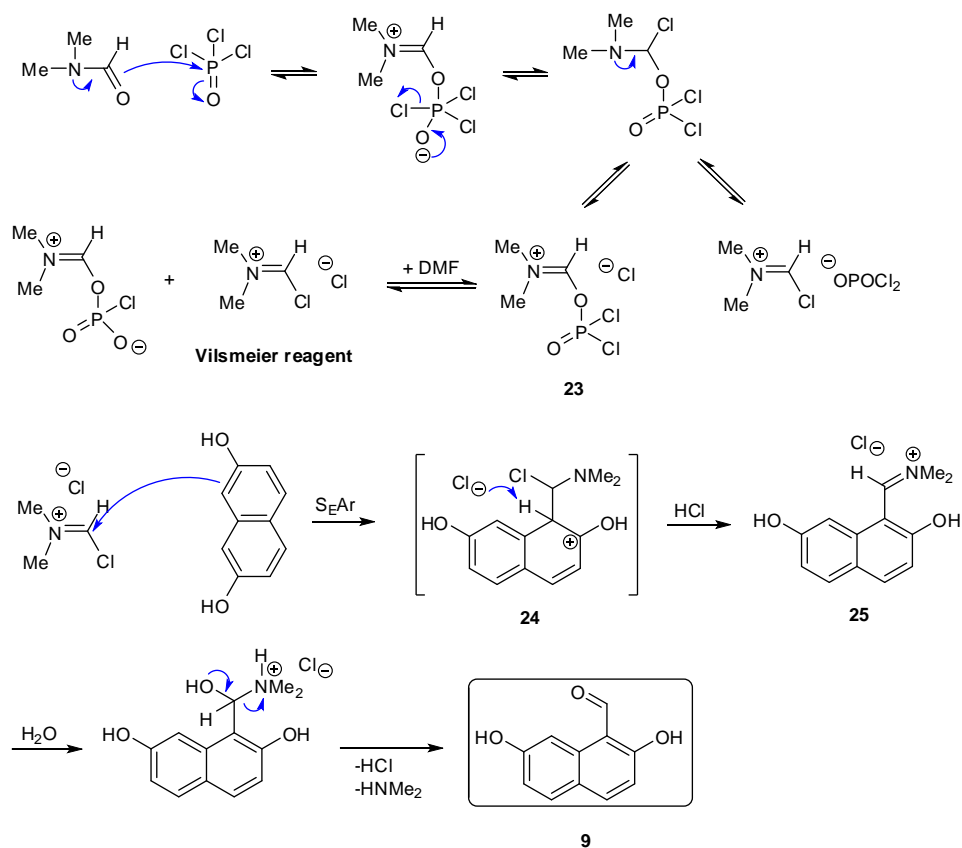
The synthesis of NX^+ and the corresponding radical was attempted by subjecting **10** to a *Luche* reduction. The reaction was proposed to yield the alcohol **11** which would have been intended to be transformed to NX^+ by an acid providing a counterion such as HBr or HBF_4 (*Scheme 7.3.1.1*). However, the *Luche* reduction resulted in an inseparable mixture including starting material after column chromatography. It is possible that a disproportionation of **11** resulted in the formation of 1*H*-naphtho[2,1,8-*mna*]xanthene **21** and **10**. This behavior has been reported for 1*H*-phenalen-1-one (PN) and larger PAHs in the literature.^{177,178} Once **21** is formed, hydrogen transfer or reaction with oxygen may result in the radical or ketone analogous to 1*H*-phenalene. A promising agent to form 1*H*-phenalene is diisobutylaluminum hydride (DIBAL-H) which gives 1*H*-phenalene in net yield of 85% resulting from PN.¹⁷⁹ However, the approach to **21** was not intended and is suggested for future studies.



Scheme 7.3.1.1 Illustration of the proposed synthesis of naphtho[2,1,8-*mna*]xanthenium **10** via *Luche* reduction and an assumed disproportionation of naphtho[2,1,8-*mna*]xanthenol **11**.

The synthesis of naphtho[2,1,8-*mna*]xanthenone had been continuously improved since 1978.^{123,126,119,124,180,181} The preparation of **10** was conducted under acidic conditions according to the most recent paper.¹²⁶ In this synthesis, 2,7-dihydroxynaphthalene-1-carbaldehyde **9** was used as starting material which is, however, not commercially available. Therefore **9** was prepared via a *Vilsmeier-Haack* formylation. Initially, the reaction of 1 eq 2,7-dihydroxynaphthalene with 1.2 eq POCl₃ and 12.2 eq DMF was carried out resulting in a yield of 14% after purification by column chromatography. Addition of DCM to 3.7 eq DMF had a profound effect on the yield with a result of up to 57%. Possible reasons for the improvement are the decrease of viscosity in the reaction and the decreased polarity effect of the DMF/DCM mixture. Since DCM exhibits a lower dipole moment than DMF, the reactivity of the *Vilsmeier* reagent is increased which improves the conditions for the electrophilic aromatic substitution.¹⁸²

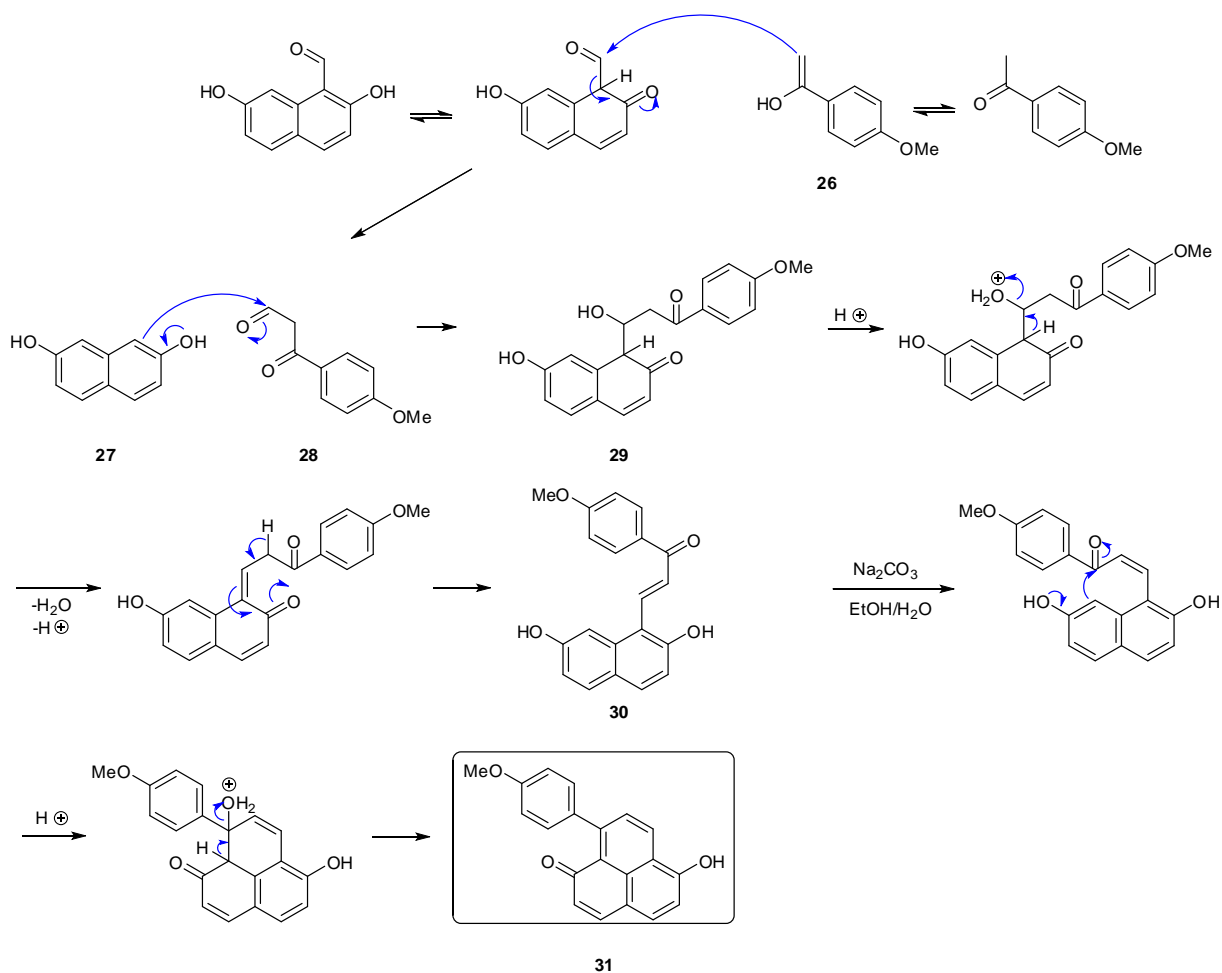
The mechanism of the *Vilsmeier-Haack* reaction is depicted in *Scheme 7.3.1.2* showing the formation of the *Vilsmeier* reagent which is in equilibrium with the iminium salt **23**. Subsequent electrophilic substitution on the naphthalene skeleton results in **25**. After hydration, deprotonation and cleavage of dimethylamine proceeds yielding the desired product **9**.



Scheme 7.3.1.2 Mechanistic scenario of the generation of the *Vilsmeier* reagent and subsequent formylation of 2,7-dihydroxynaphthalene **9**.

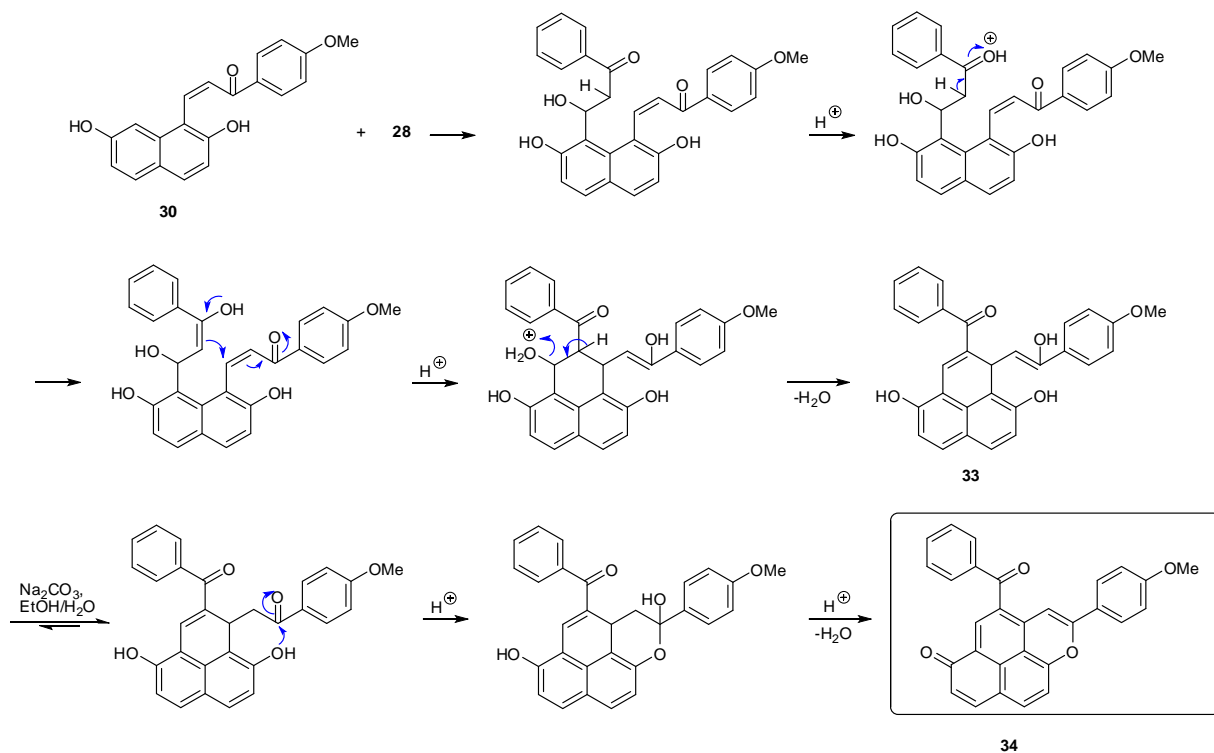
According to *R.H. Thomson et al.*, the reaction of **9** with *o*-hydroxyacetophenone resulted in **10** under acidic conditions and subsequent basification in a yield of 32%.¹²⁶ In our laboratory, **10** could be isolated in a yield of 4% only (see *Appendix 3 & 4* for full ¹H- and ¹³C-spectra). This was a further justification for ending this approach as low amounts of **10** were available to carry out representative experiments in the final reduction step (see *Figure 7.3.1.1*). Employing similar conditions, the reaction of **9** (1 eq) with 4-methoxyacetophenone **26** (0.5 eq) yielding compound **30** was discussed by the same authors (*Scheme 7.3.1.3*). It is appropriate to elucidate the proposed routes based on **9** with **26** in order to understand the formation of **10** and to indicate the reason for a lower yield in comparison to **30**. Starting with **9**, under acidic conditions the enol tautomer of acetophenone **26** attacks the carbonyl group forming compound **29** or undergoes deformylation of **9** resulting in 2,7-dihydroxynaphthalene **27** and benzoylacetaldehyde **28**. **27** then undergoes an electrophilic aromatic substitution reaction with **28** giving compound **29**. Then dehydration and subsequent deprotonation forms

30. Afterwards, by treatment of **30** with a base in an EtOH/H₂O solution, *peri*-cyclisation and again dehydration yields **31**.



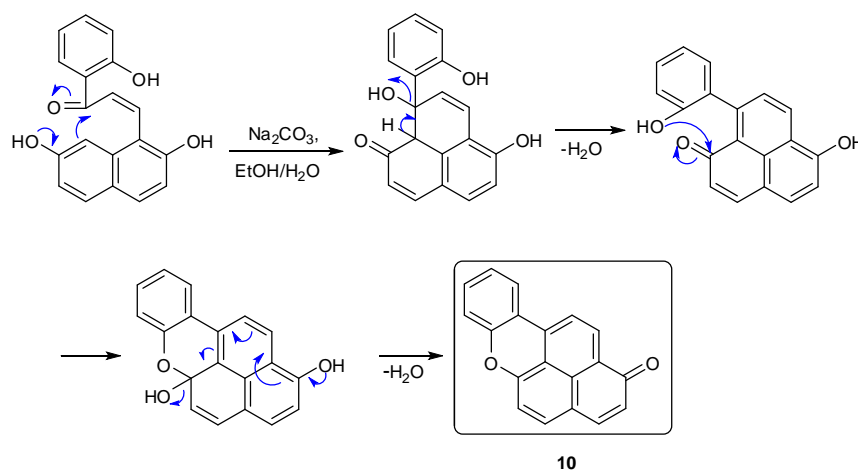
Scheme 7.3.1.3 Mechanistic scenario of the acid-catalysed synthesis of 6-hydroxy-9-(4-methoxyphenyl)-1H-phenalen-1-one **31** proposed by *R.H. Thomson et al.*¹²⁶

Additionally, **30** may undergo an electrophilic aromatic substitution reaction at the 8-position with a second molecule of **28** (*Scheme 7.3.1.4*). Cyclisation and a further dehydration step proceeds resulting in the ethenol **33**. Under basic conditions the equilibrium is on the side of the ketone-tautomer which undergoes a nucleophilic attack from the *peri*-hydroxy group on the ketone. Subsequent dehydration then gives **34**.



Scheme 7.3.1.4 Mechanistic scenario of the acid-catalysed synthesis of pyranophenalenone **34** proposed by *R.H. Thomson et al.*¹²⁶

Both compounds **31** and **34** were isolated in yields of 53% and 33%, respectively. Now analogous to the mechanism forming **29**, using **9** with 2-hydroxyacetophenone instead of **26**, subsequently *peri*-cyclisation and dehydration appears to be a reasonable route to obtain **10** (*Scheme 7.3.1.5*).

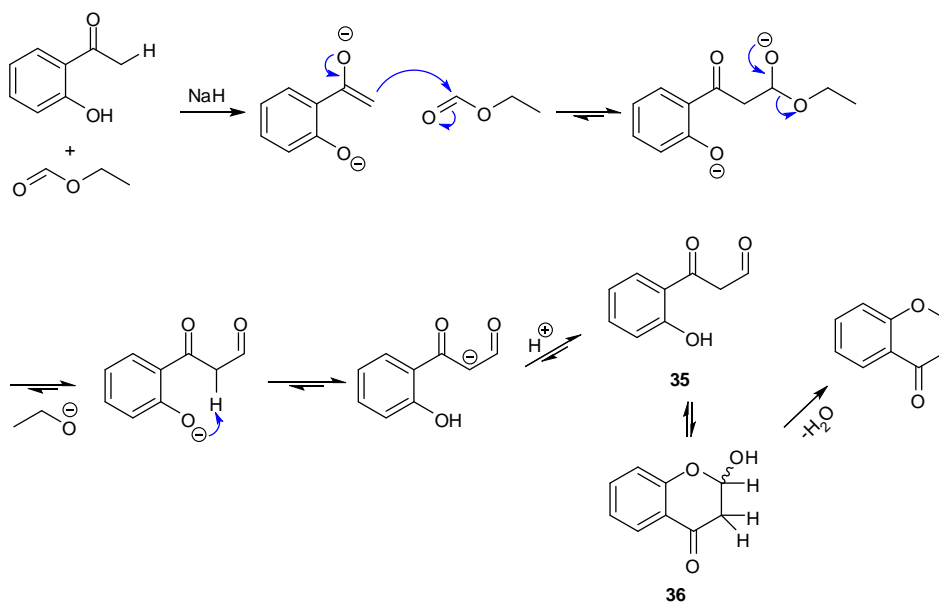


Scheme 7.3.1.5 Mechanistic scenario towards 1*H*-naphtho[2,1,8-*mna*]xanthen-1-one **10**.

Considering a supplemental experiment conducted by *Thomson et al.*, **27** reacts with **28** forming **34** in a yield of 28%. This may support the assumption that **28** is involved in the above-described mechanistic scenario. With regards to this, the formation of **34** requires **28** to be formed in any case so that a second electrophilic aromatic substitution can proceed. According to their results, compound **31** was obtained in a low yield of 5% assumingly due to the excessive amount of **27** (10 eq) used compared to **28**.

However, according to the synthesis of **10**, the existence of 3-(2-hydroxyphenyl)-3-oxopropanal **35** after deformylation may contradict the proposed mechanism. Since the formation of **35** is known to rapidly undergo intramolecular cyclisation yielding 4*H*-chromen-4-one under acidic conditions.¹⁸³

Therefore the preparation of **35** was attempted to carry out a reaction with **27** in acidic ethanol to give evidence if the formation of **10** based on **35** is feasible. According to the literature¹⁸⁴, **35** can be prepared via a *Claisen*¹⁶⁷ condensation reaction. An excess of sodium hydride removes the α -proton of the acetyl group of *o*-hydroxyacetophenone resulting in an enolate anion which subsequently undergoes nucleophilic attack on the carbonyl group of ethylformate. Subsequently an ethoxide anion is generated which removes an α -proton forming a water-soluble and highly resonance-stabilised enolate anion. After adding an acid, compound **35** should be obtained. However, the recorded ¹H-NMR spectrum of the crystals, obtained in a yield of 28%, showed the cyclic structure of 2-hydroxychroman-4-one (*Figure 7.3.1.1*; see *Appendix 5 & 6* for full ¹H- and ¹³C-spectra) which matches with the published spectrum in the literature.¹⁸⁵



Scheme 7.3.1.6 Synthesis of 3-(2-hydroxyphenyl)-3-oxopropanal **35** via *Claisen* condensation and subsequent cyclisation and dehydration leading to 2-hydroxychroman-4-one **36** and 4*H*-chromen-4-one, respectively.¹⁸⁴

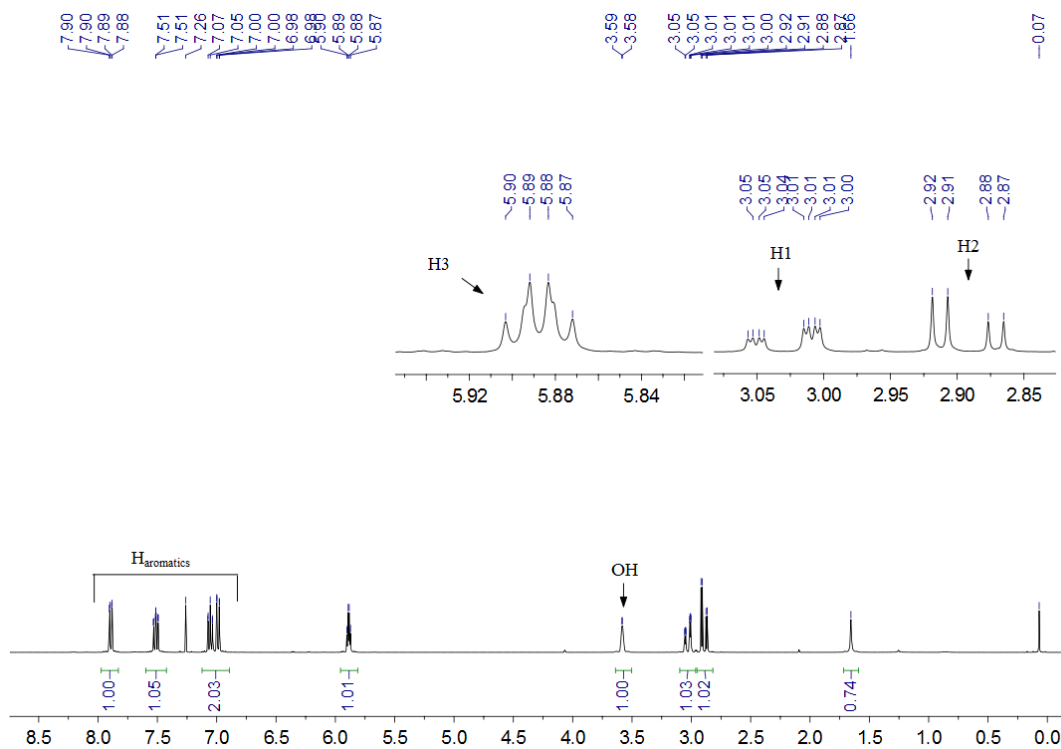
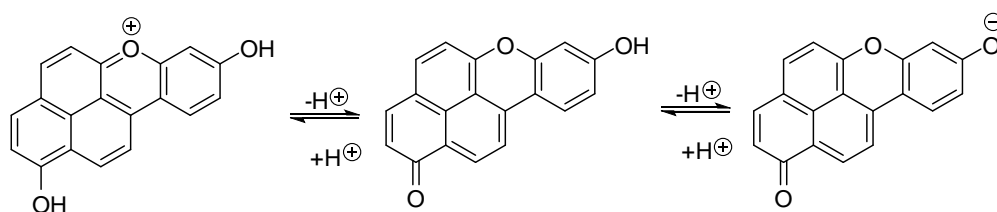


Figure 7.3.1.1 ¹H-NMR spectrum (400 MHz; CDCl₃) of 2-hydroxychroman-4-one.

Presumably the cyclisation already proceeded through the excess of acid which was used to quench the *Claisen* condensation reaction. This result shows that **35** is very instable under acidic conditions and tends to cyclise which can further be dehydrated yielding 4*H*-chromen-4-one. Thus the presence of **35** appears to be unlikely as the cyclisation step would rapidly impede the electrophilic aromatic substitution with **27**.

Moreover, traces of water during column chromatography could affect the elution which explains why dry conditions were suggested in the literature.¹²⁶ It is assumed that **10** could alternate its polarity under protic conditions or could even be protonated as it may exhibit a basic character similar to 1-*H*-phenalen-1-one. This may influence the retention factor distinctly and result in difficulties to elute and separate **10** from crude material. With regards to this, it is noteworthy that *Cooke et al.* described acid-base equilibria based on 8-hydroxy-1*H*-naphtho[2,1,8-*mna*]xanthen-1-one involving the change of colour (Scheme 7.3.1.8).¹²⁷



Scheme 7.3.1.8 Acid-base equilibria of 8-hydroxy-1*H*-naphtho[2,1,8-*mna*]xanthen-1-one described by *Cooke et al.*¹²⁷

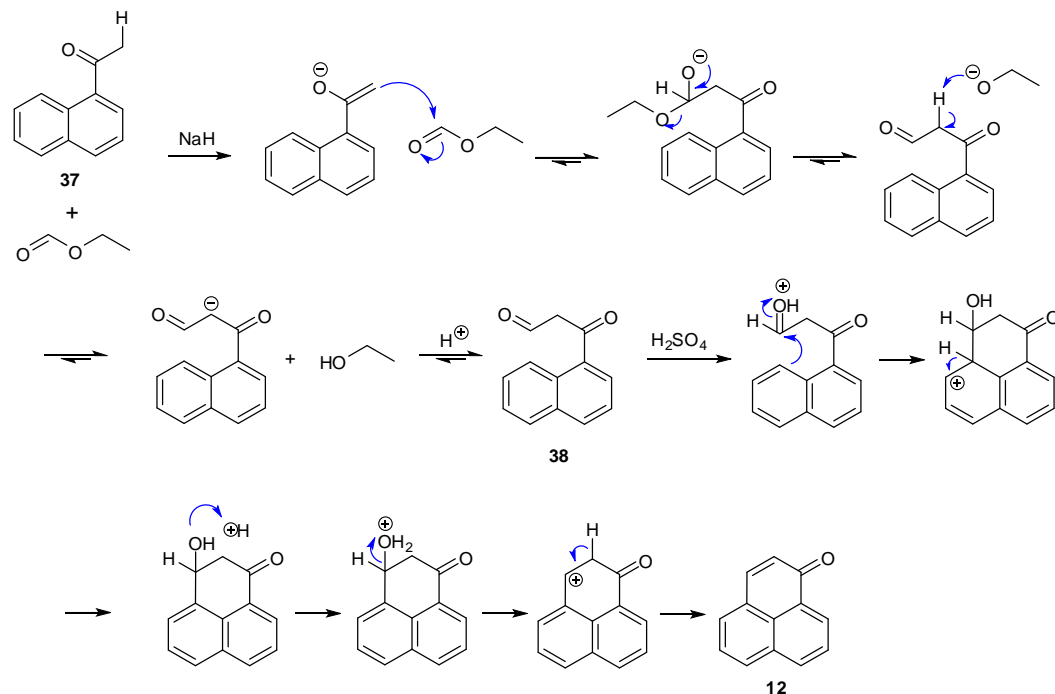
As the attempted preparation including the isolation of **10** appeared to be tedious despite the short synthetic route, the approach to NX^+ using **10** was not taken further. Instead we focused on the alternative pathway via 9-(2-methoxyaryl)-1*H*-phenalen-1-ones.

7.3.2. Synthesis of 9-aryl-1*H*-phenalen-1-ones

9-Aryl-1*H*-phenalen-1-ones are related to photodynamic toxins biosynthesized in numerous plants and fungi for their protection against microbial attack or mechanical exposure. Parent 1*H*-phenalen-1-ones as well as C-3 or C-4 substituted aryl-1*H*-phenalen-1-ones exhibit high quantum yields of singlet oxygen production. In comparison to those, numerous studies showed a distinct decrease of quantum yields for various 9-aryl-1*H*-phenalen-1-ones. In this

work, the research was mainly focused on their use as precursors to provide a convenient preparation of novel stabilised organic cations and radicals without steric hindering groups.

The synthesis of 1*H*-phenalen-1-one **12** has been continuously improved since 1934.^{69,186,187,188,189,190} In this project the preparation of **12** was conducted according to the reported procedure by *R. M. Pagni et al* giving a yield of 89% (lit. 78%; 97% based on the used technical grade starting material).⁶⁹ The reaction is based on a *Claisen*¹⁶⁷ condensation (*Scheme 7.3.2.1*). Starting with deprotonation of 1-(naphthalen-1-yl)ethanone **37** by sodium hydride, nucleophilic attack by the enolate on the partially positively charged carbon of the ethyl formate results in 3-(naphthalen-1-yl)-3-oxopropanal **38** upon cleavage of an ethanolate molecule. Subsequent acidification results in a cascade reaction initiated by cyclisation of **38**. This is followed by deprotonation and elimination yielding the target compound **12**.



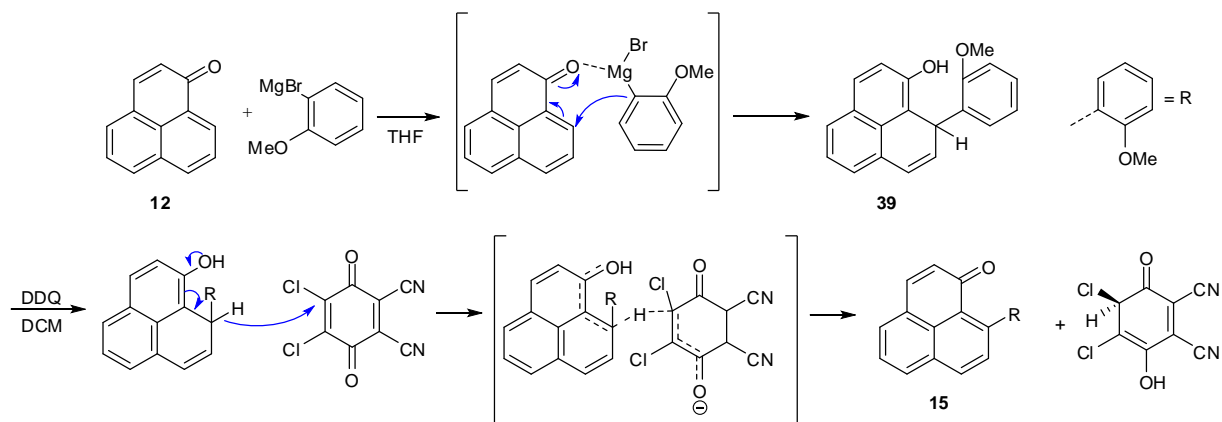
Scheme 7.3.2.1 Mechanism towards 1-*H*-phenalen-1-one according to the literature.⁶⁹

The synthesis of 9-aryl-1*H*-phenalen-1-ones successfully resulted in a series of new products. According to the literature, usual eluents for chromatographic purification are mixtures of ether, hexane and ethyl acetate. In our laboratories, it turned out that the isolation using only DCM as eluent in about 150-200 ml of silica (scaled with scale used in described procedure)

revealed very good results although large retention factors without reasonable separation were observed according to the TLC plates. A maximum conversion of the starting material **12** was important to avoid an overlap with the desired product in the column.

The well-established *Michael-type Grignard* addition on the 9-C position is based on the interaction between the oxygen of the keto group and the magnesium of the *Grignard* reagent (*Scheme 7.3.2.2*). The directing effect provides a 6-centre transition state in which the anionic carbon attacks the 9-C position of **12** yielding 1-aryl-phenalen-9-ols such as **39**. Generally, the reaction was carried out under reflux between 50-60 °C in THF. In THF, corresponding *Grignard* reagents of arylhalides are reported as monomeric for aryl bromides particularly.¹⁹¹ Moreover, THF allows the reaction to be carried out at higher temperature. This is of importance as a high activation barrier is expected for breaking the aromaticity of the phenalenone.

The oxidation step using DDQ may proceed via hydrogen transfer from **39** to the DDQ molecule. The resulting partial positive charge at the 9-C carbon of the phenalen-9-ol will be compensated by deprotonation and delocalisation yielding the target molecule **15**.

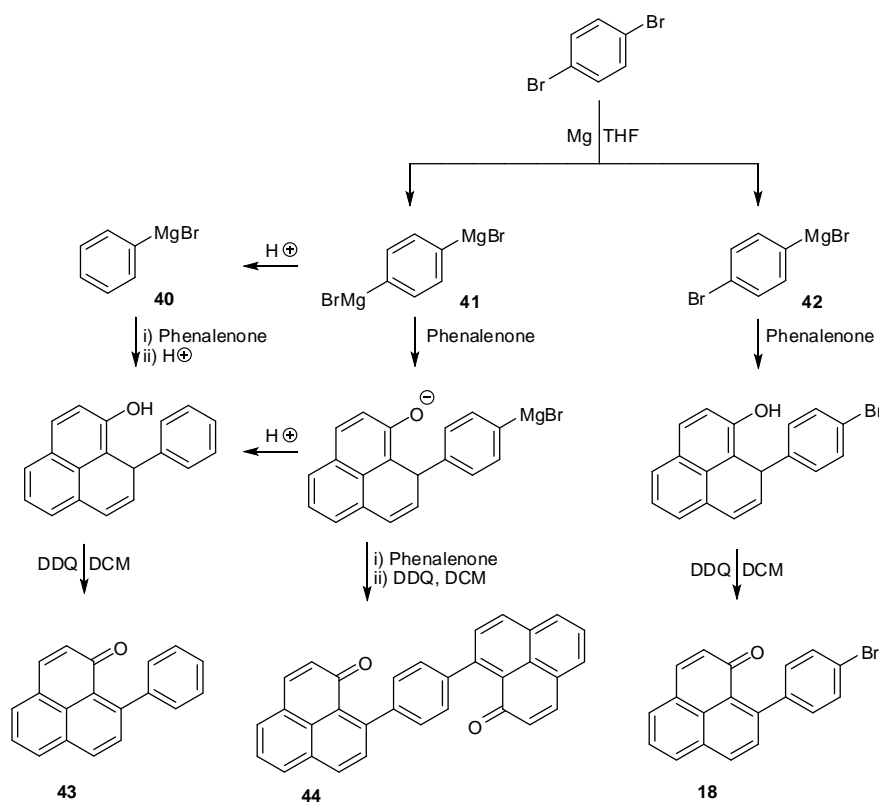


Scheme 7.3.2.2 *Michael-type Grignard* addition on 1H-phenalen-1-one **12** and subsequent oxidation via DDQ resulting in 9-(2-methoxyphenyl)-1H-phenalen-1-one **15**.

Although the preparation of 9-aryl-1H-phenalen-1-ones was described as difficult due to the steric hindrance by the *o*-methoxy substituent of the *Grignard* reagent, good yields between 36-70% for 9-(2-methoxyaryl)-1H-phenalen-1-ones were obtained over two steps.¹⁸¹

9-(4-Bromophenyl)-1*H*-phenalen-1-one **18** was isolated in 30% yield. The low yield is probably attributed to the formation of di-*Grignard* products. The formation of **44** requires a sufficient excess of magnesium and absolute dry conditions for apparatus, solvent, and starting materials used (*Scheme 7.3.2.3*). Di-*Grignard* reactions are generally feasible, however, difficult to achieve particularly when the two halogen atoms are not far away from each other.¹⁹² Initially, the synthesis of di-*Grignard* product **44** was attempted, however, no promising results were obtained.

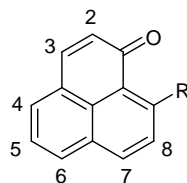
Using similar reaction conditions as for **15-17**, the mono-*Grignard* product **18** was isolated and characterised. **18** can be used for catalytic coupling reactions. Therefore **44** could be approached using **18** with 1*H*-phenalen-1-one having a suitable functional group at the 9-position. As a byproduct, 9-(phenyl)-1-*H*-phenalen-1-one **43** was isolated in a yield of 13% (see Appendix **21** & **22** for full ¹H- and ¹³C-spectra). This probably resulted from a mono-*Grignard* reagent **40** which was generated by protonation of a di-*Grignard* reagent **41** through traces of water. Alternatively, **41** reacted with **12** and subsequently underwent protonation yielding **18**.



Scheme 7.3.2.3 Synthetic routes of Grignard reactions starting with 1,4-dibromobenzene with 1*H*-phenalen-1-one **12**.

9-(4-Bromo-2,5-dimethoxyphenyl)-1*H*-phenalen-1-one **19** resulted in a low yield of 7% which can be explained by similar criteria as for **18** including the effect of steric hindrance in the *Grignard* reagent.

According to the NMR spectra of the obtained 9-aryl-1*H*-phenalen-1-ones, the expected doublets of doublets for the ABX spin system at the 5-position could be found by analogy to the literature.¹⁹³ The considerable upfield signal representing the 2-position was also present indicating no *Michael*-type addition on the 3-position. *Table 7.3.2.1* shows an overview of the chemical shifts and coupling constants of the protons of the phenalenone skeleton of **15-19**. These data show that no considerable variation of chemical shifts including coupling constants are observed, so that the ¹H-NMR characterisation of further analogs can be referred to these data.



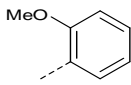
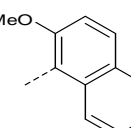
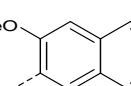
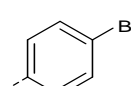
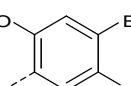
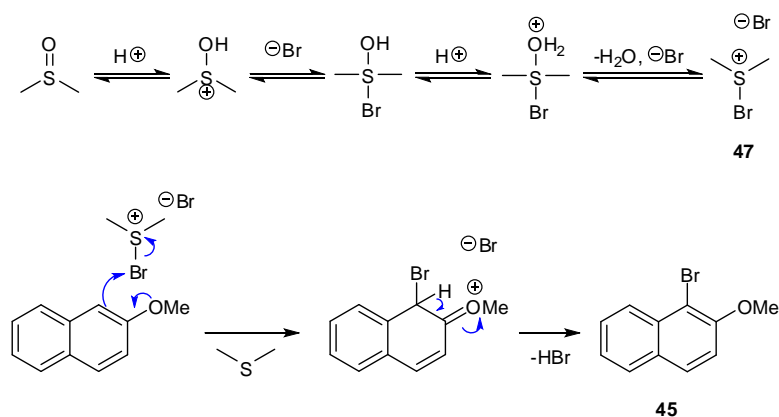
R	H2	H3	H4	H5	H6	H7	H8
	δ (6.60 ppm) $J = 9.7$ Hz	δ (7.67 ppm) $J = 9.7$ Hz	δ (7.57 ppm) $J = 6.6$ Hz	δ (7.57 ppm) overlapped	δ (8.01 ppm) $J = 8.2$ Hz	δ (8.18 ppm) $J = 8.3$ Hz	δ (7.60 ppm) $J = 8.3$ Hz
	δ (6.50 ppm) $J = 9.7$ Hz	δ (7.70 ppm) $J = 9.7$ Hz	δ (7.80 ppm) $J = 6.3$ Hz	δ (7.66 ppm) $J = 8.2, 7.1$ Hz	δ (8.10 ppm) $J = 8.2$ Hz	δ (8.27 ppm) $J = 8.3$ Hz	δ (7.59 ppm) $J = 8.3$ Hz
	δ (6.58 ppm) $J = 9.7$ Hz	δ (7.69 ppm) $J = 9.7$ Hz	δ (7.78 ppm) overlapped	δ (7.62 ppm) $J = 8.2, 7.0$ Hz	δ (8.06 ppm) $J = 8.2, 1.0$ Hz	δ (8.22 ppm) $J = 8.3$ Hz	δ (7.66 ppm) $J = 8.3$ Hz
	δ (6.59 ppm) $J = 9.7$ Hz	δ (7.70 ppm) $J = 9.7$ Hz	δ (7.79 ppm) $J = 6.8, 0.6$ Hz	δ (7.63 ppm) $J = 8.2, 7.1$ Hz	δ (8.05 ppm) $J = 8.2, 0.8$ Hz	δ (8.18 ppm) $J = 8.3$ Hz	δ (7.54 ppm) $J = 8.3$ Hz
	δ (6.58 ppm) $J = 9.7$ Hz	δ (7.69 ppm) $J = 9.7$ Hz	δ (7.77 ppm) $J = 7.0$ Hz	δ (7.61 ppm) multiplet*	δ (8.04 ppm) $J = 8.2$ Hz	δ (8.19 ppm) $J = 8.3$ Hz	δ (7.54 ppm) $J = 8.3$ Hz

Table 7.3.2.1 Chemical shifts and coupling constants of 9-aryl-1*H*-phenalen-1-ones **15-19**. *Coupling constants could not be determined due to resolution issues.

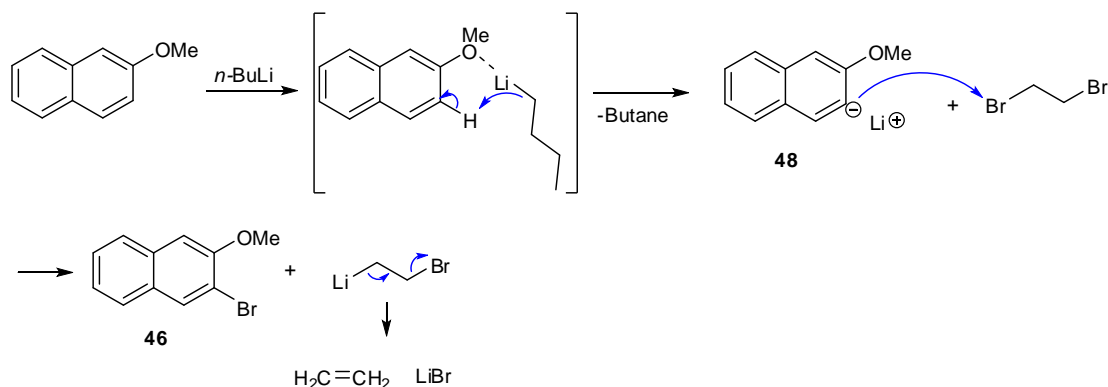
Additional evidences for the correct structure are (M-31)⁺ peaks in the mass spectra and the results from high resolution mass spectroscopy analysis which are in agreement with the calculated m/z . Ultimately, the X-ray data obtained for **15** (*Appendix 55 & 56*) gives evidence for the selective addition at the 9-position of the phenalenone skeleton.

For the synthesis of **16** and **17**, 1-bromo-2-methoxynaphthalene **45** and 2-bromo-3-methoxynaphthalene **46** needed to be prepared. The synthesis of **45** was carried out by electrophilic aromatic substitution at the α -position of the more activated ring (*Scheme 7.3.2.4*). This was performed by bromination via in situ generated bromodimethylsulfonium bromide **47** from DMSO and HBr (48%) according to the literature.¹⁶⁸ **45** was obtained in a yield of 91%.



Scheme 7.3.2.4 Synthesis of 1-bromo-2-methoxynaphthalene **45** via in situ generated bromodimethylsulfonium bromide **47**.

To prepare **46**, first the 3-position was lithiated using *n*-BuLi then brominated by 1,2-dibromoethane (*Scheme 7.3.2.5*). The metalation occurs via a fast intermediate state initiated by coordination of the lithium atom with a non-bonding orbital of the methoxy group of 2-methoxynaphthalene.¹⁹⁴ This is followed by intermediate removal of the *o*-hydrogen by the *n*-butyl anion resulting in butane and reagent **48**. Afterwards, using 1,2-dibromoethane, **48** will be brominated through metal and halogen exchange yielding product **46** and 1-bromoethyl lithium which reacts further forming ethylene and lithium bromide. According to this procedure, a very good yield of 98% could be obtained.



Scheme 7.3.2.5 Synthesis of 2-bromo-3-methoxynaphthalene **46** via lithiation and subsequent bromination.

7.3.3. Synthesis of naphthoxanthenyl cations and radicals

The practical preparation of a naphthoxanthenium (NX) cation to generate the corresponding radical represents the main focus of this project. Using 9-(2-methoxyphenyl)-1*H*-phenalen-1-one **15** as a precursor proved to be a considerable advantage compared to 1*H*-naphtho[2,1,8-*mna*]xanthen-1-one **10**. This is attributed to their differences in solubility and their preparation enabling access to derivatives. Since no literature about the properties and stability of NX^+ is present, the biggest challenge was to manage the isolation of the salts which required mild and convenient conditions. Upon deprotection of the methoxy group, 9-(2-hydroxyphenyl)-1*H*-phenalen-1-one may cyclise to form an hemi-ketal which undergoes hydroxide cleavage or hydrolysis yielding NX^+ . A similar reaction step results in **10** considering the mechanistic scenario illustrated in *Scheme 7.3.1.5*.¹²⁶ Now ruling out the formation of a keto-group at the 6-position, NX^+ can be obtained instead.

On a small scale, D_2O was used to extract and analyse via $^1\text{H-NMR}$ spectroscopy to see if NXBr was formed (*Appendix 52*). 11 Proton signals in the aromatic area were found with a strong downfield shift indicating a delocalised positive charge. According to a second sample from another batch, significant alternations of the chemical shift were also observed. This is attributed to $\pi\text{-}\pi$ stacking interactions correlating with the concentration of the sample.¹⁹⁵

It is important to point out the solubility of the salt in water making a convenient isolation feasible. In the history, the isolation of pyrylium had been in vain due to its unexpectedly high solubility in water. Therefore the compound had been un-isolated for decades.¹⁹⁶ Similarly, the cations with bromide as counterions were not expected to be water soluble due to their large

size if one compares them to the unsubstituted pyrylium cation benzo[5,6]naphthaceno[1,12,11,10-*ijklmna*]xanthylum (BNAX⁺) prepared by *Müllen et. al.*²⁰ This particularly stands for the isomers B[*i*]NXBr and B[*a*]NXBr exhibiting a polyaromatic system consisting of six rings involving 23 carbon atoms. The actual high solubility may be ascribed to the asymmetric structure and the polarising effect of the phenalenyl unit. Due to its high propensity to stabilize a positive charge⁸¹, a more pronounced resonance structure between an oxonium and carbenium ion is postulated on the side of the phenalenyl unit.

Although the extraction of the target compounds with water appears to be convenient, the eventual removal of boric acid and water needed to be considered. To remove boric acid, methanol was added and the solution was heated at 75°C. Boric acid and excess of methanol react to give the boric ester having a boiling point at 68°C.¹⁹⁷ An azeotropic mixture with methanol decreases the boiling point thus the temperature should be sufficiently high to separate the impurity. However, after removal of water via rotary evaporation under vacuum, a dark solid was obtained showing broadening effects in the ¹H-NMR spectrum. Apparently, at high temperature unknown solvent effects or reactions occur which could be due to impurities undergoing side reactions including decomposition. For that reason, counter ion exchange using such as HBF₄ was found to be the most suitable procedure to isolate NX⁺. In this way, the precipitation of naphtho[2,1,8-*mna*]xanthenium tetrafluoroborate (NXBF₄) was induced in the aqueous solution. Eventually, the target compound could be separated by vacuum filtration yielding 63%.

The deprotected 9-(2-hydroxyaryl)-1*H*-phenalen-1-ones appeared to be very unstable in water and immediately cyclised yielding the cations. Only 9-(2-hydroxynaphthalenyl)-1*H*-phenalen-1-one could be identified via ¹H NMR spectroscopy (*Figure 7.3.3.1*; see *Appendix 32* for full ¹H-spectrum) which was found as a weakly soluble precipitate in water as well as in DCM after quenching the demethylation reaction. Thus the extraction with water did not easily proceed at room temperature as in the cases of NX⁺ and B[*i*]NX⁺. Possibly a higher kinetic stability is given based on the intramolecular overcrowding preventing the nucleophilic attack from the hydroxyl group on the ketone. This could be overcome by stirring the solution with an excess of water at 35-40 °C for 1 hour. The obtained red aqueous solution could then be separated and treated with HBF₄ to give the target salt analogous to NXBF₄ and its isomer B[*i*]NXBF₄.

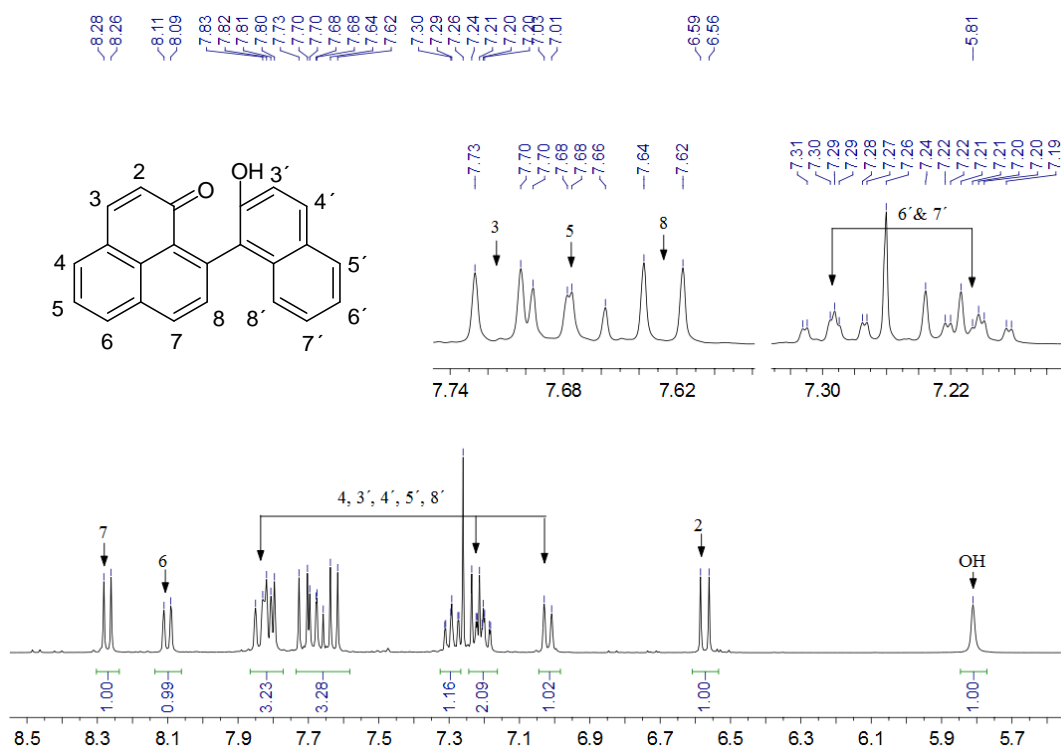
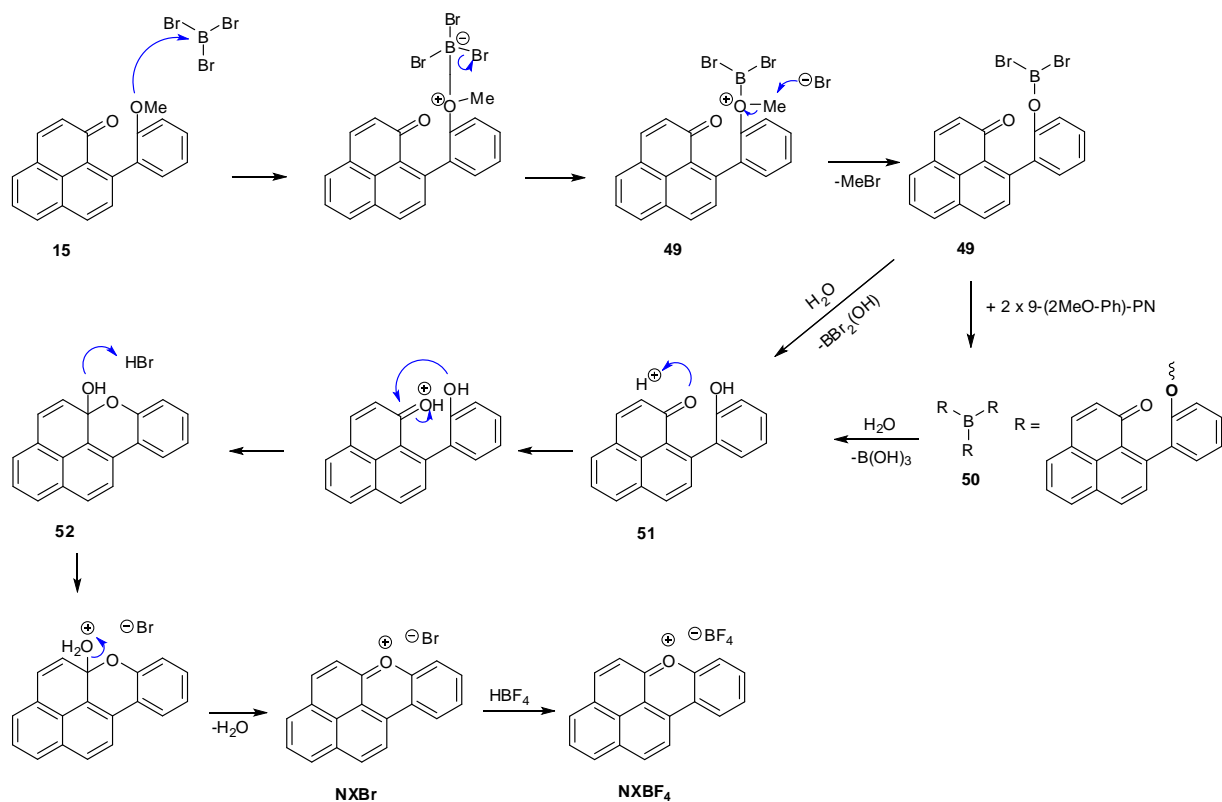


Figure 7.3.3.1 ¹H-NMR spectrum of 9-(2-hydroxy)-1H-phenalen-1-one. Measured at room temperature (400 MHz; CDCl₃).

Scheme 7.3.3.1 depicts the mechanistic scenario of the *McOmie* demethylation.¹⁷³ Based on an S_N2 substitution reaction, initial coordination of BBr₃ with the methoxy group is followed by removal of methylbromide forming **49**. Those steps can be repeated forming boron-tri-9-(2-methoxy)-1H-phenalen-1-one **50**. By treatment of **49** or **50** with water, boric acid and 9-(2-hydroxy)-1H-phenalen-1-one **51** will be formed which rapidly undergoes cyclisation to give hemi-ketal **52**. Subsequent elimination yields NXBr. By the mean of counterion exchange using HBF₄, NXBF₄ precipitates.



Scheme 7.3.3.1. Mechanism of *McOmie* demethylation of 9-(2-methoxyphenyl)-1*H*-phenalen-1-one **15** resulting in naphtho[2,1,8-*mna*]xanthenium bromide (NXBr) and subsequent counter ion exchange.

According to the $^1\text{H-NMR}$ spectrum, NXBF_4 could be confirmed, however, often broadening effects or only two sharp signals, a triplet and a doublet at the aromatic area, were observed. The results from the elemental analysis of the organic salt indicated the correct composition for NXBF_4 so that a reaction process was presumed to proceed in solution. This result was comparable with the isolated NXBr after removal of boric acid and water. The broadening effects lead to the assumption that the presence of the NX radical may be responsible for electron exchange with the cationic species.

Similar effects were observed for NX^+ with perchlorate (X-ray structure in *Appendix 59 & 60*) and hexafluorophosphate as counterions isolated using HClO_4 and NaPF_6 , respectively. Additionally, NX tetraphenylborate was attempted to isolate which appeared to decompose in its solid state under an atmosphere of air. The storage of NXBF_4 dissolved in water lead to milky glass surfaces after a few weeks indicating HF resulting from the decomposition of BF_4 . The possible hydrolysis of BF_4 and PF_6 in ionic liquids is known in the literature.¹⁹⁸ Due to the

complexity regarding the stability of the cation, the investigations were mainly focused on NXBF₄ in MeCN. Although the X-ray structure of NXClO₄ was obtained, further work with this salt was minimised due to its potentially explosive character.¹⁹⁹

According to UV/Vis spectra in MeCN, a decomposition of NXBF₄ could be observed. Within 90 minutes, 7 spectra were recorded (*Figure 7.3.3.2*) at room temperature. A decrease of absorption peaks at 455 nm and increases at 385 and 535 nm results in an isosbestic point at 412 nm indicating that the concentration of the cation is diminished concomitant with the generation of a new species.

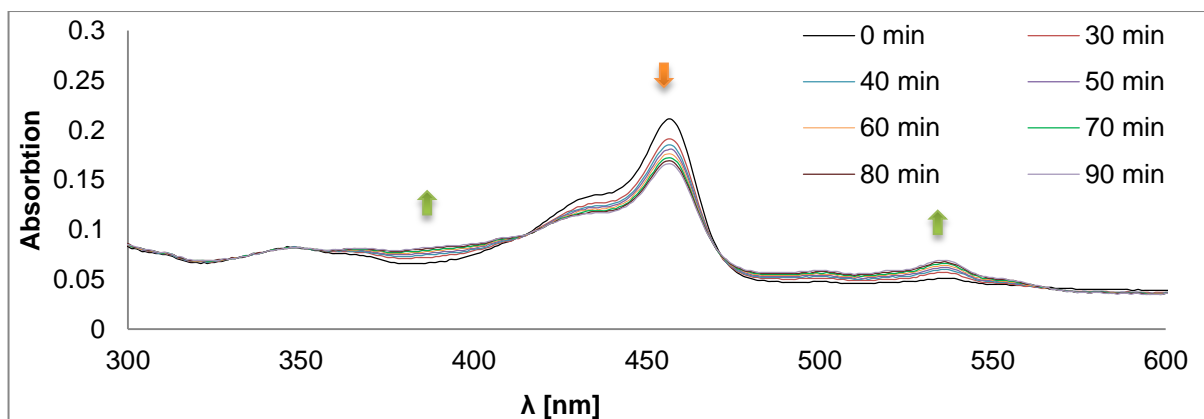
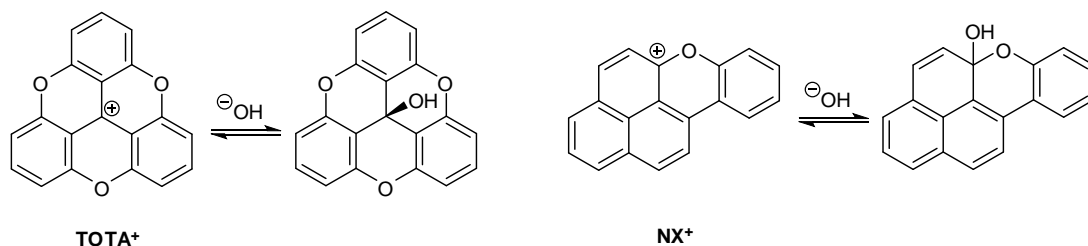


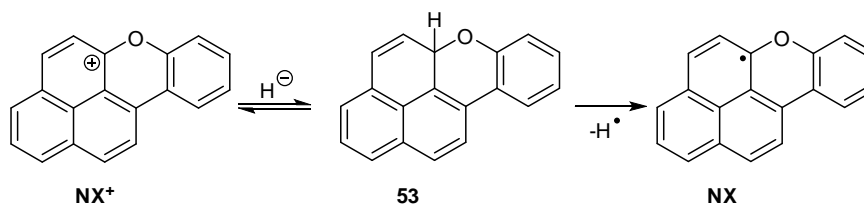
Figure 7.3.3.2 Time-dependent UV/Vis spectra of NXBF₄ in MeCN at room temperature.

Due to these observations, the thermodynamic stability of NX⁺ was first called into question. The reactivity of polyaromatic carbenium ions toward nucleophiles has been described for the stable trioxatriangulenylium cation (TOTA⁺) and derived helicenes.^{154,200} This involved alkylation using alkyllithium reagents¹⁵⁴, leuco ethers in alcohol solvents²⁰¹, cyanocarbon substitution in MeCN with NaH, and reduction by hydride transfer using NaBH₄.²⁰² The stability of TOTA⁺ was expressed by a pK_R⁺ value representing the equilibrium between the carbenium ion and the corresponding carbinol (*Scheme 7.3.3.2*). The equilibrium was reported to be predominantly on the side of the carbenium ion in water. Considering the electronic structure of NX⁺, it can be assumed that the positive charge is pronounced at the C5a-carbon adjacent to the electronegative oxygen. Hence, the equilibrium represents the reversibility of NX⁺ and the hemi-ketal which is predominantly on the side of NX⁺ in water. This is confirmed with the dissolution of NXBr as the hemi-ketal would precipitate in the contrary.



Scheme 7.3.3.2 Trioxatriangulenylium cation (TOTA⁺) versus naphtho[2,1,8-*mna*]xanthen-5a-ylum cation (NX⁺).

In accordance with the electrophilic character of heteroaromatic cations, it is assumed that an impurity of an unknown reducing reagent or a hydride source may have reacted with NX⁺ predominantly at the 5a-position. Unfortunately, the attempt to characterise a responsible reducing agent was unsuccessful. It is noteworthy that reduction by a hydride source, via NaBH₄, has been demonstrated with cationic helicenes in the literature.²⁰² In the case of a hydride attack, 5a*H*-naphtho[2,1,8-*mna*]xanthene **53** would be formed which was investigated as a short-lived intermediate.¹¹⁸ This could undergo hydrogen abstraction in an aprotic solvent yielding the radical (Scheme 7.3.3.3).



Scheme 7.3.3.3 Hydride transfer on NX⁺ and subsequent hydrogen abstraction forming NX.

Initially, the crystallisation of NXBF₄ could not be achieved in solvents such as acetonitrile and acetone. This was due to the above described phenomenon which resulted in a mixture of cation, radical and unknown polyaromatic byproducts (see Appendix 31 for full ¹H-spectrum). The appearance of the resulting residue was black with a green lustre. According to X-ray capillary diffraction the black greenish substance indicates an almost identical crystalline arrangement to NXBF₄ (Figure 7.3.3.3). Therefore it can be assumed that the strong colour change is derived from traces of impurities in the crystals.

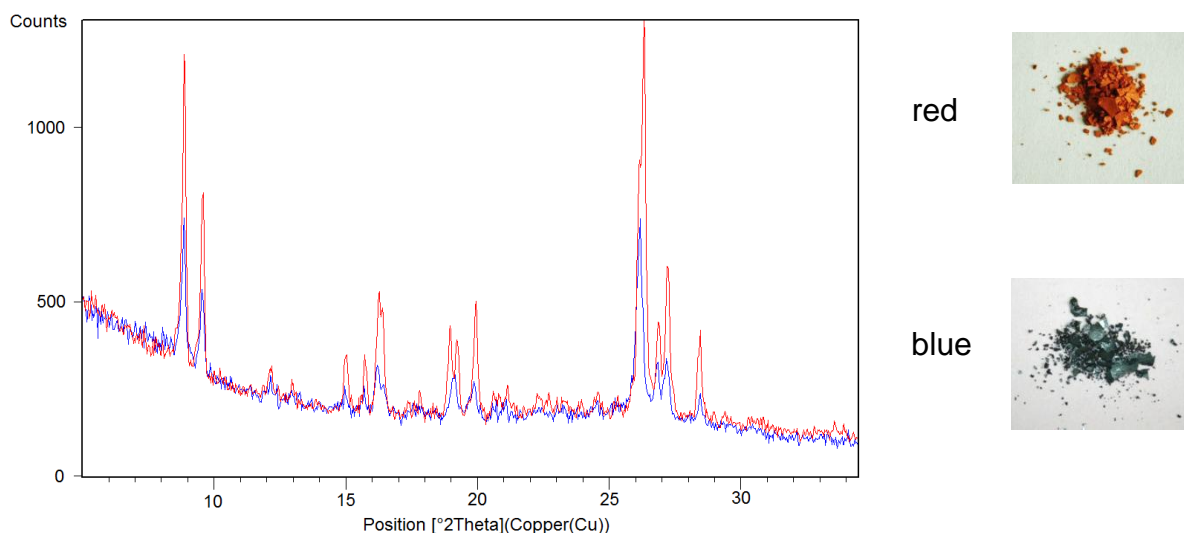


Figure 7.3.3.3 X-ray powder diffraction via capillary of NXBF_4 before and after dissolution in acetone. Similar appearance of black solid with a green lustre was obtained from MeCN.

Remarkably, the crude radical was stored under air and could still be detected after 2 years. Solid state ESR measurements of the crude dark material supported by the *EPSRC ESR* center in Manchester revealed a paramagnetic signal in the ESR spectrum even at temperatures above the melting point (422 K). Additionally, an increase of the paramagnetic intensity was observed.

It is assumed that possible σ -dimers could be homolytically dissociated giving in return a higher concentration of the radical. However, this would also mean that the dimerisation of two radicals to diamagnetic products should induce depletion unless the dimers caused an electron transfer reaction with NX^+ . Alternatively, charge transfer complexes between the radical or resulting products from the radical and the cation can be presumed which may dissociate upon dissolution in DMSO. In DMSO well resolved spectra indicating the target radical species were obtained. It is noteworthy that a change of colour from green to brown was observed after a couple of seconds when the dark material was dissolved in DMSO in an ESR sample tube.

To rule out oxygen and photochemical processes in the decomposition process, argon was purged through the solution for several minutes and the solution left overnight protected from light. This resulted in the crude cation-radical mixture at a higher rate (*Figure 7.3.3.4*). As

TOTA⁺ was reported as an oxidiser upon photo-activation as demonstrated by reports on its damaging effects on DNA²⁰³, photochemical processes were considered which may induce disruption of this decomposing process.



Figure 7.3.3.4 NXBF₄ dissolved in MeCN under an argon atmosphere protected from light over night. Left: Immediately after dissolution. Right: 1 Day later.

Thus ¹H-NMR spectra of a UV (360 ± 40 nm) irradiated sample in MeCN were taken at intervals of 20 minutes (*Figure 7.3.3.5*). Interestingly, a consistent attenuation of the broadening effect could be observed. After sufficient irradiation eleven protons indicating NX⁺ could be detected and assigned via COSY. The broadening effects show a clear correlation with the calculated *Mulliken* spin densities and hyperfine coupling constants (hfc) from the simulated ESR spectrum for NX (*Table 7.3.3.1*).²⁰⁴ The reason for the broadening effect is due to electron hopping from the radical to the cation.

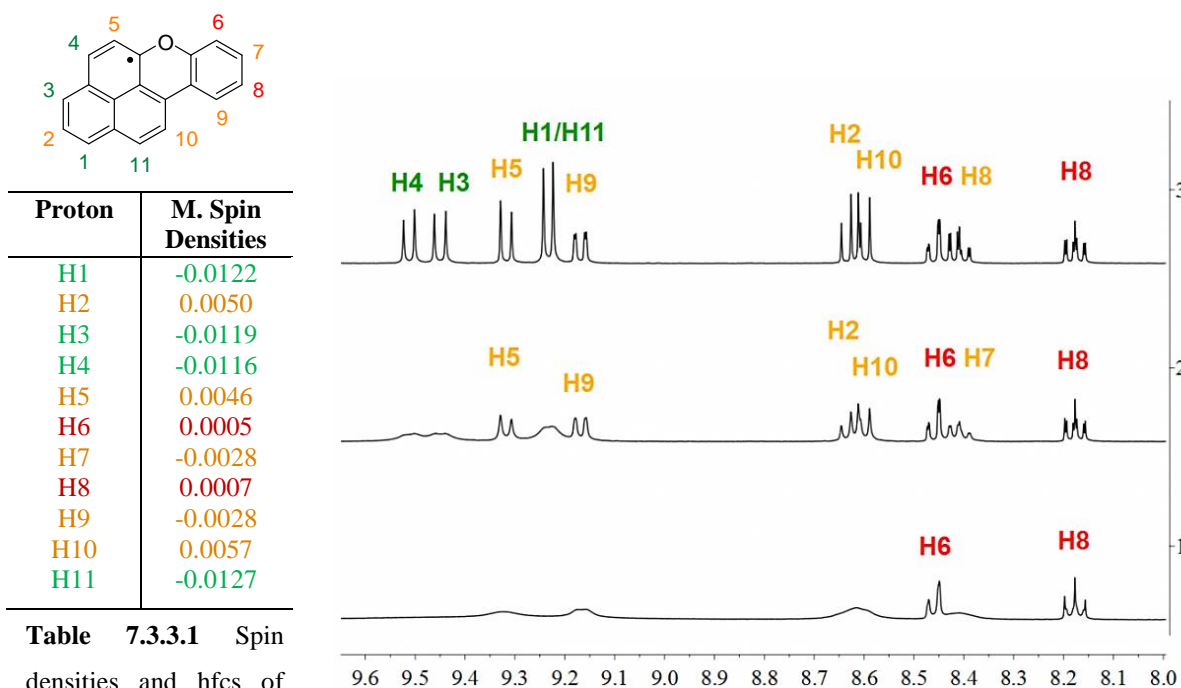


Table 7.3.3.1 Spin densities and hfc of NX calculated by Gaussian03 at M05-2X/6-31G** level of theory.²⁰⁴

Figure 7.3.3.5 ¹H-NMR spectra of NXBF₄ in MeCN representing depletion of a paramagnetic species, presumably NX. Spectra were taken in intervals of 20 min.

It was assumed that NXBF₄ gave rise to charge transfer complexes involving NX. According to the literature, 6,12-dioxanthrene, a closed shell heteroaromatic molecule consisting of two fused xanthene units showed a strong propensity to form charge transfer complexes incorporating I₃, 2,4,6-trinitrophenol or maleonitriledithiolate.²⁰⁵ Since the change of the appearance of NXBF₄ including the unprecedented ¹H-NMR effects were unknown, electrorecrystallisation was attempted to afford a crystalline material conductive to X-ray structure analysis.²⁰⁶

The set-up of this electrorecrystallisation experiment was based on a glass cell filled with an electrolyte containing *tetra*-butylammonium tetrafluoroborate and NXBF₄ in oxygen free and dry acetonitrile (*Figure 7.3.3.6*). Two platinum electrodes connected to an electrical source were dipped in the electrolyte. A glass filter prevented the dispersion of a precipitated product throughout the whole cell. Generally, the relationship for the recrystallisation on the surface of an electrode can be expressed by

$$I = c \cdot t^2 \sim I/S = \text{constant}$$

where I is the applied current, t is the time, S is the surface of the electrode and c represents the constant determined by the ratio of current and surface.

In case of NXBF₄ the formation of a microcrystalline dark-greenish material was obtained on the electrode surface. However, the crystal quality was not sufficient for X-ray resolutions. All attempts to achieve large crystals to confirm a charge-transfer complex consisting of NX⁺ and NX were unsuccessful.

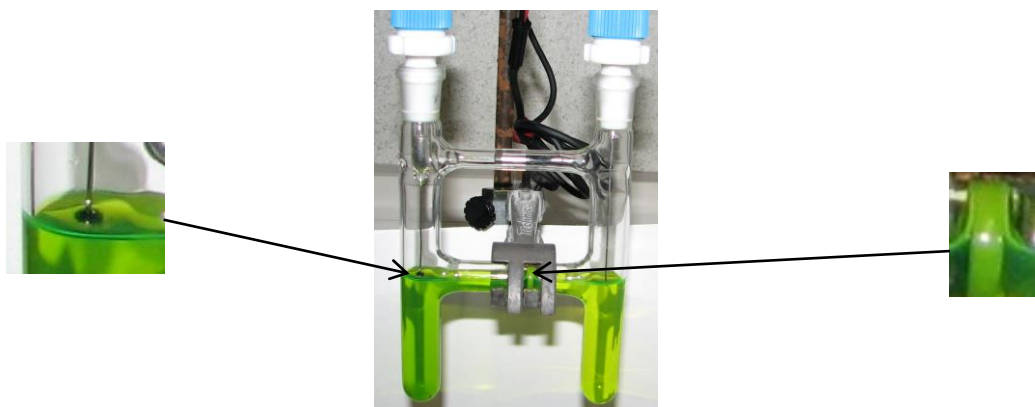


Figure 7.3.3.6 Set-up of an electrorecrystallisation cell containing NXBF₄ and N(butyl)₄BF₄ dissolved in oxygen free MeCN.

Significantly, there was no reversibility of the radical generation observed after irradiation. In addition, this phenomenon could not be reproduced with samples which were exposed to air for over one year. Hence, impurities must have triggered those effects and it is concluded that NX^+ is a highly stable carbenium-oxonium cation which does not decompose over a long period of time under open atmosphere (2 years aged samples). It is noteworthy that fresh samples isolated from the reaction did not show these effects in a different laboratory. The encountered phenomenon, however, raised questions. Future studies are necessary to prove if NX^+ gives rise to charge transfer complexes.

Similar results as described above were obtained in case of benzo[*i*]naphtho[2,1,8-*mna*]xanthenium (B[*i*]NX) and benzo[*a*]naphtho[8,1,2-*jkl*]xanthenium (B[*a*]NX). This included the broadening effects in the $^1\text{H-NMR}$ spectra which could be impeded by irradiation (see *Appendix 53* for B[*a*]NXBF₄). Also electrorecrystallisation was conducted in the case of B[*a*]NX showing an accumulation of presumably conductive material of low crystal quality on one electrode. The microcrystalline material of B[*a*]NX exhibited a red-brown colour.

7.3.4 X-ray structure analysis, spectral effects and HOMA evaluation

The recrystallisation of NXBF₄ was achieved from acetone. This resulted in orange needles with sufficient crystal quality to carry out X-ray structure analysis. The driving force behind the crystallisation can be partly explained with respect to the distances between the counter ion and the cation (see Results: *Table 7.2.3.2, 7.2.3.4 & 7.2.3.6 & Figures 7.2.3.9, 7.2.3.12 and 7.2.3.15*).²⁰⁷ In case of NXBF₄, the proximity between the proton at the 5 position and the oxygen of the opponent cation indicates a short bond of 2.663 Å, which would be in the range of hydrogen bond interactions. This probably explains the fast crystallisation of larger crystals of NXBF₄ within hours compared to B[*i*]NXBF₄ and B[*a*]NXBF₄ which took a couple of days.

The synthesised salts are good examples of steric overcrowding. Thus they were investigated regarding their geometry based on their bay- and fjord regions. The general concept of steric compensation in bay regions can occur either (1) by in-plane distortion which involves the increase of bond angles or (2) by out-of plane distortion resulting in increase of torsion angles.¹⁶³ Regarding fjord regions, steric compensation is generally exhibited through the latter type. The bond angles of NX^+ are 123.9° (C9a-C9b-C10) and 124.4° (C9-C9a-C9b) in

the bay region with a torsion angle of 0.2° . $B[i]NX^+$ shows a slight abbreviation regarding the bond angle between C11-C11a-C11c with 124.0° . This slight decrease of 0.4° is compensated by a twist of 1.1° , a discrepancy of 0.9° compared to NX^+ . In case of $B[a]NX^+$, clearly the naphthalenyl moiety is out-of-plane in comparison to NX^+ and $B[i]NX^+$. Due to the proximity of the two hydrogens at the 11- and 12-positions (1.964 \AA) the steric strain is relieved by twisting the C11b-C11c bond by an angle of 17.3° and exhibits a bond length of 1.430 \AA . As a side note, due to the resulting helical orientation, $B[a]NX^+$ represents a chiral molecule, hence this synthetic approach may be of high interest to develop amphoteric heterohelicenes with regards to new asymmetric catalysts.²⁰⁸ The obtained crystals consist of a racemic mixture (1:1) of the P- and M-enantiomers (*Figure 7.3.4.1*).

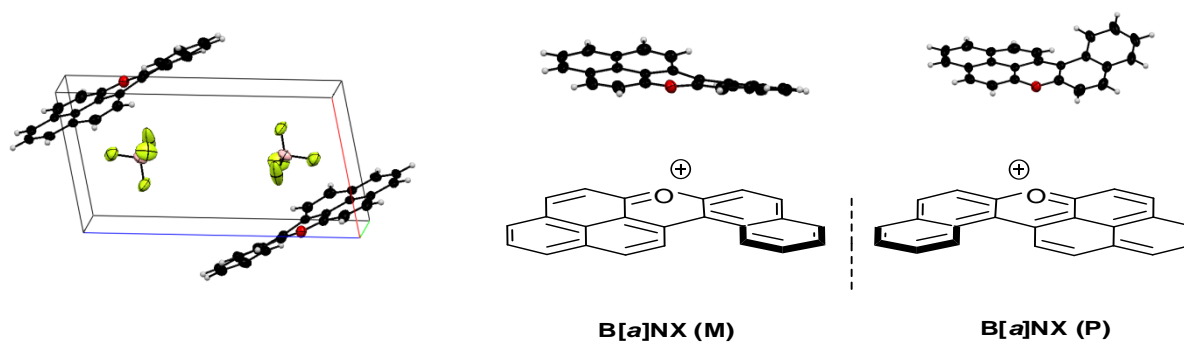


Figure 7.3.4.1 Crystal cell of $B[a]NX^+$ showing a racemic mixture.

According to the UV/Vis spectra (*Results: Figure 7.2.7.1*), $NXBF_4$, $B[i]NXBF_4$ and $B[a]NX_4$ exhibited differences in their absorption wavelengths. In agreement with *Clar's rule*³⁹, a bathochromic shift from 456 nm to 469 nm could be observed for $B[i]NXBF_4$ compared to $NXBF_4$. This is due to the extension of the polyaromatic framework from 19 to 23 carbon atoms whereas the number of *Clar* sextets remains unchanged.²⁰⁹ However, the two isomers $B[i]NXBF_4$ and $B[a]NX_4$ showed absorption peaks at 469 nm and 505 nm, respectively. This means that the latter species is bathochromically shifted by 36 nm.

The spectroscopic divergence between $B[i]NX^+$ and $B[a]NX^+$ cannot be explained by the assessment of the aromaticity via *Clar's* sextet theory only. If one ignores the presence of the heteroatom and charge, the mesomeric *Clar* structures of $B[i]NX^+$ versus $B[a]NX^+$ would indicate a decrease of aromaticity for $B[i]NX^+$ compared to $B[a]NX^+$ considering the number of *Clar* sextets. In addition, helicenes usually exhibit larger HOMO-LUMO gaps compared to

acenes.²¹⁰ This would imply a lower HOMO-LUMO gap for B[*i*]NX⁺ which is not represented in the spectra. According to geometric bond length equalisation,²¹¹ the maximum bond length alternation for the whole aromatic framework gives $\Delta r_{CC}^{NX^+} = 0.114 \text{ \AA}$, $\Delta r_{CC}^{B[i]NX^+} = 0.106 \text{ \AA}$, $\Delta r_{CC}^{B[a]NX^+} = 0.120 \text{ \AA}$ for NX⁺, B[*i*]NX⁺ and B[*a*]NX⁺, respectively. This would mean that B[*a*]NX⁺ is less aromatic which is conclusive in accordance with the spectral change. However, NX⁺ would be less aromatic than B[*i*]NX⁺ which shows that this simple evaluation exhibit a lack of generalisability.

An evaluation of the aromaticity may help to conclude the spectral effects, however, this appears to be non-trivial due to the involvement of heteroatom perturbation, charge delocalisation and atomic overcrowding (in case of B[*a*]NX⁺). Commonly, the variation of bond lengths can be used to deduce the degree of aromaticity which would be provided by the datasets from the X-ray structure analysis.^{212,213} *Julg* and *François* introduced this idea with the first aromaticity index A_j , a normalised function, which is entirely based on the bond length alternation.²¹⁴ This method is limited in cases of heterocycles as distinct perturbations by e.g. heteroatoms are not considered. Based on the same idea, *Bird* suggested replacing the bond lengths by *Gordy's* bond orders which took the bonds of C-X (X = e.g. heteroatom) into consideration.²¹⁵

However, mere bond length variations are not considered to be an ultimate criterion for the characterisation of aromaticity.²¹⁶ For instance, *Julg's* and *Bird's* formulas can give misleading index values indicating high aromaticity for inner rings in polyaromatic molecules which are not even closely in agreement with other methods such as calculated NICS values²¹⁷ or HOMA (harmonic oscillation model of aromaticity) values.²¹⁶ In fact, aromaticity is still not fully understood and this has led to the development of a plethora of methods (e.g. diamagnetic susceptibility exaltation²¹¹, para delocalisation index (PDI)²¹⁸, nucleus independent shift (NICS) etc.). In terms of bond length alternation the most encouraging procedure is considered to be HOMA which can also take bonds involving heteroatoms into account and is often in agreement with NICS values.²¹⁹

In this thesis, the spectroscopic results will be discussed using calculated HOMA indices for single 6-membered rings derived from bond lengths obtained from the X-ray structure analysis. Additionally, the sextet theory will be employed to suggest the most reasonable *Clar* structures. In case of NX⁺ calculated APT atomic charges²²⁰ and bond lengths will be

presented and compared with the experimental results. Due to the extreme distortion in the pyryl ring, this ring will not be displayed with a *Robinson* circle.

By means of calculations conducted by *G. Bucher*, the positive charge distribution in the electronic system was assessed. Using the m052x 6-31G** level of theory, calculated atomic polar tensor (APT) charges show pronounced positive charges of 0.855 and 0.813 at the C5a- and C9b-carbons, respectively (*Table 7.3.4.1*). Hence, the two favoured resonance structures are proposed as depicted in *Scheme 7.3.4.1*. According to the X-ray data the C5a-O bond has the shortest bond length of 1.338 Å. This argues in favour of the resonance structure NX⁺₍₂₎ representing the oxonium and carbenium ions. Thus the experimental result may indicate a larger positive charge pronounced at the C5a than at the C5b-carbon. This can be attributed to the propensity of the phenalenyl unit which can accommodate the positive charge to a higher extent than the benzyl ring.⁸¹

Atom	APT charge	Atom	APT charge
O	-0.662	C5b	0.373
C1	0.302	C6	-0.104
C2	-0.192	C7	0.046
C3	0.187	C8	-0.157
C3a	-0.282	C9	0.119
C3b	-0.071	C9a	-0.461
C3c	-0.300	C9b	0.813
C4	0.416	C10	-0.525
C5	0.460	C11	0.524
C5a	0.855	C11a	-0.388

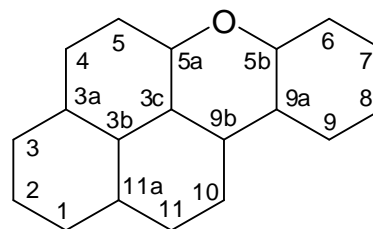
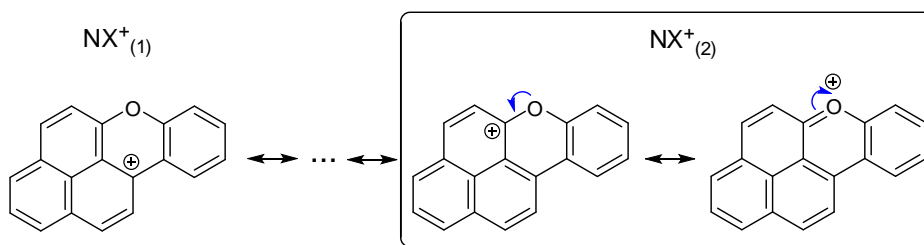
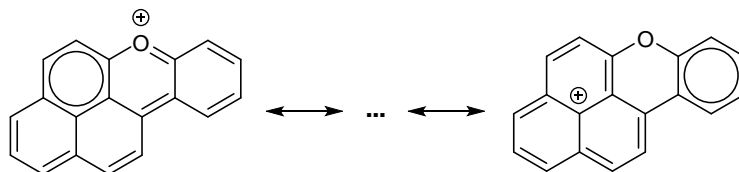


Table 7.3.4.1 APT atomic charges obtained using m052x 6-31g** level of theory.



Scheme 7.3.4.1 Pronounced mesomeric structures of NX⁺ deduced from APT atomic charges obtained using the m052x 6-31g** level of theory.

At the C3b-position the positive charge is negligible with a value of -0.071. This is reasonable, as the corresponding mesomeric structure would exhibit an antiaromatic structure in the phenalenyl unit. This can also be illustrated by the loss of a *Clar* sextet (*Scheme 7.3.4.2*).



Scheme 7.3.4.2 Mesomeric structures of NX^+ indicating loss of an aromatic *Clar* sextet in the phenalenyl unit in the case of the positive charge being localised in the centre.

The HOMA index considers additional reference bond lengths R_{opt} which are assumed to be optimal for the corresponding type of bond. $R(CC)_{opt}$ represents C-C bonds in conjugated systems with 1.388 Å. For the C5a-O bonds in NX^+ , $B[i]NX^+$ and $B[a]NX^+$, $R(CO)_{opt}$ was chosen with 1.265 Å.²¹⁵ The formula is defined as follows

$$HOMA = 1 - \frac{1}{n} \left\{ \sum \alpha(CC) [(R(CC)_{opt} - R_i)] + \alpha(CO) [(R(CO)_{opt} - R_i)] \right\}$$

where n is the number bonds, α is a normalisation constant (257.7 and 157.38 for C-C bonds and C-O bonds, respectively), and R_i is the given individual bond length. An ideally aromatic molecule such as benzene exhibits a maximum HOMA index of 1.

The HOMA indices for the pyryl ring (P) and the four benzene (A, B, C, D) rings are shown in *Table 7.3.4.2*. Considering ring A and ring C with $HOMA_A = 0.8723$ and $HOMA_C = 0.8279$, respectively, a relatively higher degree of delocalisation can be proposed in those rings compared to ring B with $HOMA_B = 0.7615$. Thus the conjugation of a π -electron towards ring C (green arrow) is more pronounced than towards ring B (red arrow) (*Figure 7.3.3.11*). That is, ring A and ring C establish a delocalising naphthalenyl unit to a higher extent compared to the ring A and ring B or ring B and ring C. The role of naphthalenyl and its aromatic behaviour has been described by *E. Clar* as a separable aromatic unit in a series of PAHs.³⁹ Expectedly, the pyryl ring P exhibits the lowest index of $HOMA_P = 0.3030$ which is ascribed to the immediate distortion of the aromatic cloud by the heteroatom. Ring D indicates the highest degree of aromaticity with $HOMA = 0.9563$ which points out the polarising effect of

the phenalenyl nucleus, which enhances the positive charge at the C5a carbon instead of the C5b carbon (see *Table 7.3.4.1*). In the case of a positive charge at the C5b or C9a, the aromaticity of ring D would break which is not favoured and in agreement with the calculated APT atomic charges (0.373 and -0.461, respectively). This can also be illustrated by the *Clar* structure in *Figure 7.3.4.2* showing only one possible sextet for the molecule. Due to the loss of the aromaticity of ring D, this charge distribution appears to be distinctly less favoured.

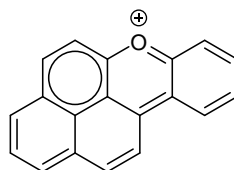
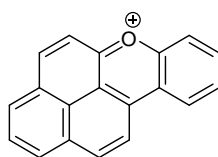
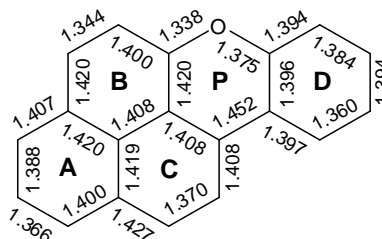


Figure 7.3.4.2 *Clar* structure of NX^+ with a *Robinson* circle in ring B.

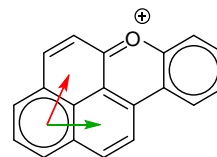
Hence, it is reasonable to suggest the following *Kekulé* and *Clar* structures for NX^+ as depicted in *Figure 7.3.4.3*.

Ring	HOMA
A	0.8723
B	0.7615
C	0.8279
D	0.9563
P	0.3030

Table 7.3.4.2 HOMA indices of assigned rings in NX^+ .



Kekulé structure



Clar structure

Figure 7.3.4.3 *Kekulé* and *Clar* structures of NX^+ and bond lengths of NX^+ according to X-ray structure analysis with assignment of the rings.

Considering the calculations based on the m052x 6-31g** level of theory, the bond lengths vary to a certain extent compared to the experimental data. As a consequence, ring A and ring B are determined to be the more aromatic naphthalenyl unit than ring A and ring C as shown by the HOMA indices ($\text{HOMA}_A = 0.7033$; $\text{HOMA}_B = 0.7162$; $\text{HOMA}_C = 0.6396$; *Table*

7.3.4.3). That is, the mobility of a π -electron from ring A to ring B is slightly more pronounced than the mobility from ring A to ring C. Moreover, the aromaticity is generally underestimated for the whole molecule. The HOMA index for the pyryl ring even gives a value below zero. Consider the following data of the APT atomic charges based on the m052x 6-31g** level of theory. This shows a high APT charge of 0.813 at the C9b carbon atom which is close to the charge of 0.855 at the C5a carbon. Now looking at the *Clar* structures sketched in *Figure 7.3.4.4*, it appears to be reasonable that ring B and C show similar HOMA indices with respect to the computed bond lengths.

Ring	HOMA
A	0.7033
B	0.7162
C	0.6396
D	0.8986
P	-0.0172

Table 7.3.4.3 HOMA indices for NX^+ derived from calculated bond lengths based on the m052x 6-31g** level of theory.

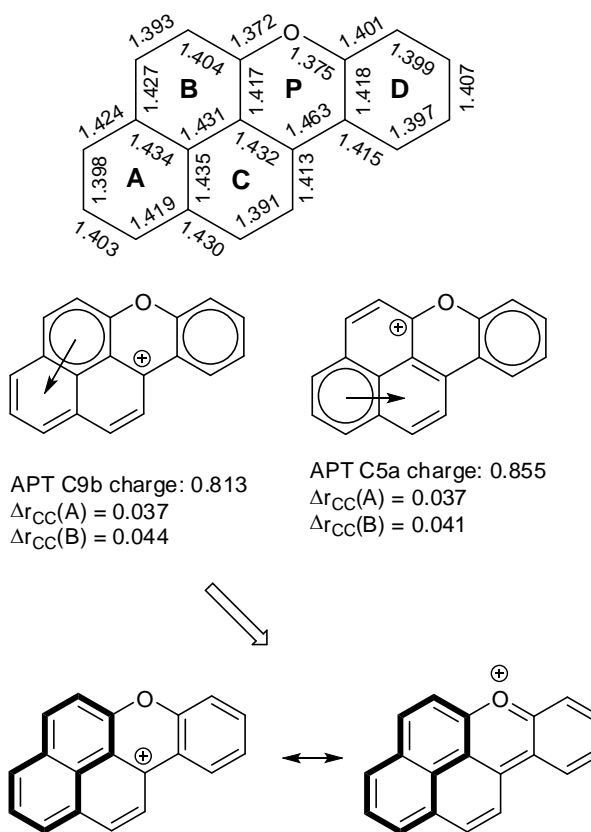


Figure 7.3.4.4 *Clar* structures of NX^+ considering positive charges at the C5a and C9b position and computed bond lengths of NX^+ with assignment of the rings. The calculations suggest more pronounced resonance structures maintaining a naphthalenyl unit in the phenalenyl framework as depicted

Considering the delocalisation of a π -electron from the possible adjacent atoms to the C9b carbon, C3c and C11 are incorporated in the phenalenyl unit, however, C9a is part of the higher aromaticity ring D. The calculations appear to suggest more pronounced resonance structures involving the maintenance of a naphthalenyl unit consisting of ring A and B in the phenalenyl framework (*Figure 7.3.4.4*). This is concomitant with the decrease of aromaticity in ring D and a more pronounced oxonium-carbenium resonance structure on the side of the benzene ring D.

According to the literature, the stability of the pyrylium cation is largely achieved by having the positive charge on the two carbon atoms adjacent to the oxygen.²²¹ Since the C5a-O bond exhibits a distinctly shorter bond of 1.344 Å compared to the C5b-O bond in accordance with X-ray data, a more pronounced oxonium-carbenium resonance structure is postulated on the side of the phenalenyl unit. This is concomitant with the high HOMA index for ring D. Therefore, it is suggested that the positive charge at the C9b is overestimated by the computational method and is instead more pronounced at the C5a carbon. This is justified considering the distinctly stronger bond with 1.344 Å between the C4 and C5 carbons, showing a discrepancy of 0.049 Å compared to the computed value.

HOMA indices for the separated 6-membered rings resulted in reasonable conclusions with regards to *Clar's* characteristics. Thus HOMA will also be employed for B[*i*]NX⁺ and B[*a*]NX⁺ which may lead to a possible explanation for the unexpected spectral effects. In the case of B[*i*]NX⁺, ring A and ring C exhibit a slightly higher degree of aromaticity compared to the corresponding rings in NX⁺ (*Table 7.3.4.2*). Due to the benzannulation at ring D forming a naphthalenyl unit attached to the pyryl ring P, the mobility of a π -electron from ring D to ring E is increased. According to the literature, a higher aromaticity of acenes has been found to be in the inner rings by means of NICS studies.²²² However, due to the presence of a pyryl ring, the nature of the delocalisation (HOMA_P = 0.2734) is more complex. Considering the shortened C11a-C11b bond length, and elongated C5b-O bond length, a possible *Clar-Kekulé* structure would present the equilibrium between the donation of an electron from the non-bonding orbital of the oxygen, a π -electron from the C11a-C5b bond and the C11b-C12 bond (*Figure 7.3.4.5*). The movement of the π -electron from the C11a-C11b bond would result in a favoured aromatic ring D leaving the positive charge at the C11b carbon. The donation from the heteroatom would give an oxonium ion resulting in an aromatic sextet in ring B. It is assumed that there is a more complex and distributed charge between the C11a, C11b and C5b

carbons compared to NX^+ (corresponding to the C9a, C9b and C5b carbons). This interdependency between breaking the aromaticity of the naphthalenyl unit consisting of ring D and ring E and the positive charge at the C11b carbon may lead to an enhanced perturbation in the pyryl ring. This may affect the rings in the phenalenyl unit to some extent. Ring B exhibits an elongation of the C4-C5 bond with 1.362 Å (C4-C5 bond in NX^+ : 1.344 Å) and enhanced degree of aromaticity ($\text{HOMA}_B = 0.7884$) if one compares that to ring B of NX^+ .

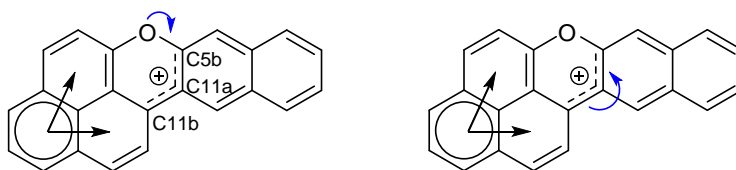


Figure 7.3.4.5 Putative *Clar-Kekulé* resonance structures for $\text{B}[i]\text{NX}^+$

It is very hard to understand this aromatic system if only HOMA indices are available. Taking a more simplified view, one can say that the benzannulation extends the conjugated system with four additional π -electrons leading to the smaller HOMO-LUMO gap which explains the bathochromic shift compared to NX^+ . Considering the values in *Table 7.3.4.4*, the most stable *Clar* and *Kekulé* structures are suggested as depicted in *Figure 7.3.4.6*.

Ring	HOMA
A	0.9083
B	0.7884
C	0.8056
D	0.8426
E	0.7572
P	0.2734

Table 7.3.4.4

HOMA indices of assigned rings in $\text{B}[i]\text{NX}^+$

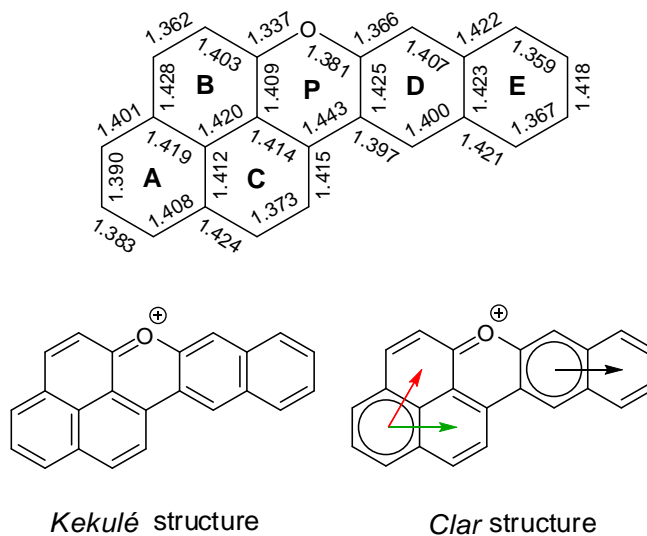


Figure 7.3.4.6 *Kekulé* and *Clar* structures of $\text{B}[i]\text{NX}^+$ and bond lengths of $\text{B}[i]\text{NX}^+$ according to X-ray structure analysis with assignment of the rings.

In $B[a]NX^+$, the HOMA index for the pyryl ring P is clearly increased with $HOMA_P = 0.5159$ compared to NX^+ and its isomer (Table 7.3.4.5). Taking the HOMA values of phenanthrene²²³, the outer rings exhibit the highest degree of aromaticity which is in agreement with the most thermodynamically stable *Clar* structure with two *Clar* sextets (Figure 7.3.4.7). Hence the increase of the HOMA index in the pyryl ring P can be ascribed to the polarisation effect ascribed to the topology of the aromatic framework.

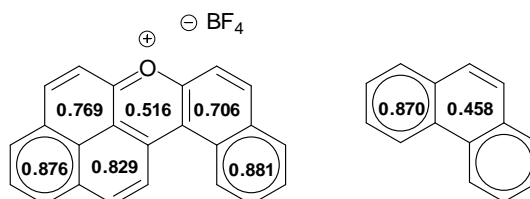


Figure 7.3.4.7 *Clar* structures of $B[a]NX^+$ and phenanthrene showing HOMA for single rings (HOMA indices for phenanthrene are taken from the literature).²²³

$B[a]NX^+$ is distorted sterically through intramolecular overcrowding. In an overcrowded fjord region, the compensation by a bond twist is often accompanied by the alternation of bond lengths. In this case, there is a significant reduction to 1.430 Å in comparison to NX^+ (1.452 Å) and its isomer (1.443 Å). This appears to be accompanied with a shorter bond length of 1.359 Å for the O-C5b bond. It is possible that this bond would be even shorter if atomic overcrowding would not take place. That is, $B[a]NX^+$ has probably a higher propensity to be in the resonance structure $B[a]NX^+_{(M1)}$ (Figure 7.3.4.8). Considering this resonance structure a conclusion for the bathochromic shift for $B[a]NX^+$ compared to its isomer will be suggested.

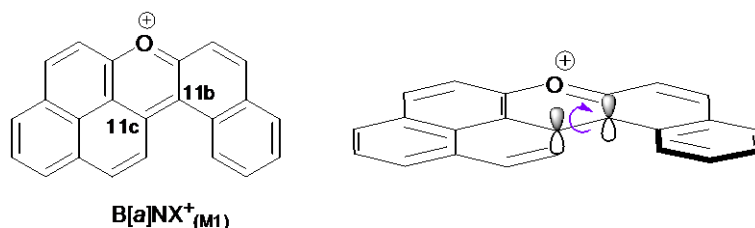


Figure 7.3.4.8 Possible resonance structure of $B[a]NX^+$ which could give rise for no-nodal plane at the twisting bond.

According to *R. I. T. Cromartie* and *J. N. Murrell*, it was proposed that a bathochromic shift resulting from the torsion of a bond in a π -electron system requires an orbital that has no node through this bond.⁵⁰ Otherwise a hypsochromic shift would result from twisting a bond where an occupied orbital has a node through that bond. Following this proposal, it is required that an occupied orbital exhibits no node through the C11b-C11c bond which is represented with a double bond in *Figure 7.3.4.8*. As the nodal plane is now affected by the twist, energy increase is induced which may result in a decrease of the HOMO-LUMO gap. This could explain the spectral differences between $B[i]NX^+$ and $B[a]NX^+$. *Figure 7.3.4.9* depicts the suggested *Clar* and *Kekulé* structures for $B[a]NX^+$

Ring	HOMA
A	0.8769
B	0.7693
C	0.8288
D	0.7061
E	0.8812
P	0.5159

Table 7.3.4.5 HOMA indices of assigned rings in $B[a]NX^+$.

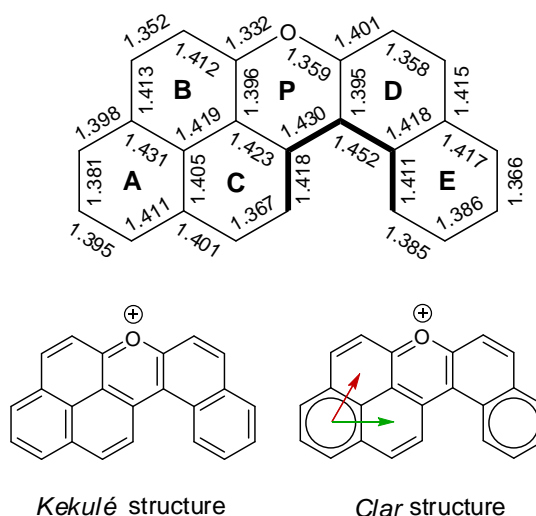


Figure 7.3.4.9 *Kekulé* and *Clar* structures of $B[a]NX^+$ and bond lengths of $B[a]NX^+$ according to X-ray structure analysis with assignment of the rings.

Additionally, computational methods were employed to calculate the HOMO-LUMO gap of NX^+ , $B[i]NX^+$ and $B[a]NX^+$ (*Figure 7.3.4.10*). The obtained approximations are based on the B3LYP-6-31G** level of theory (using *Spartan*). The bathochromic shift for $B[a]NX^+$ compared with NX^+ is reasonable due to the extension of a benzene ring. This appears to be consistent with the calculations with 7.02 eV and 7.72 eV, respectively. However, based on this basis set, the HOMO-LUMO gap for $B[i]NX^+$ is distinctly lower than that of $B[a]NX^+$ with 6.74 eV which would represent the intuitive assumption due to the acene-like framework.

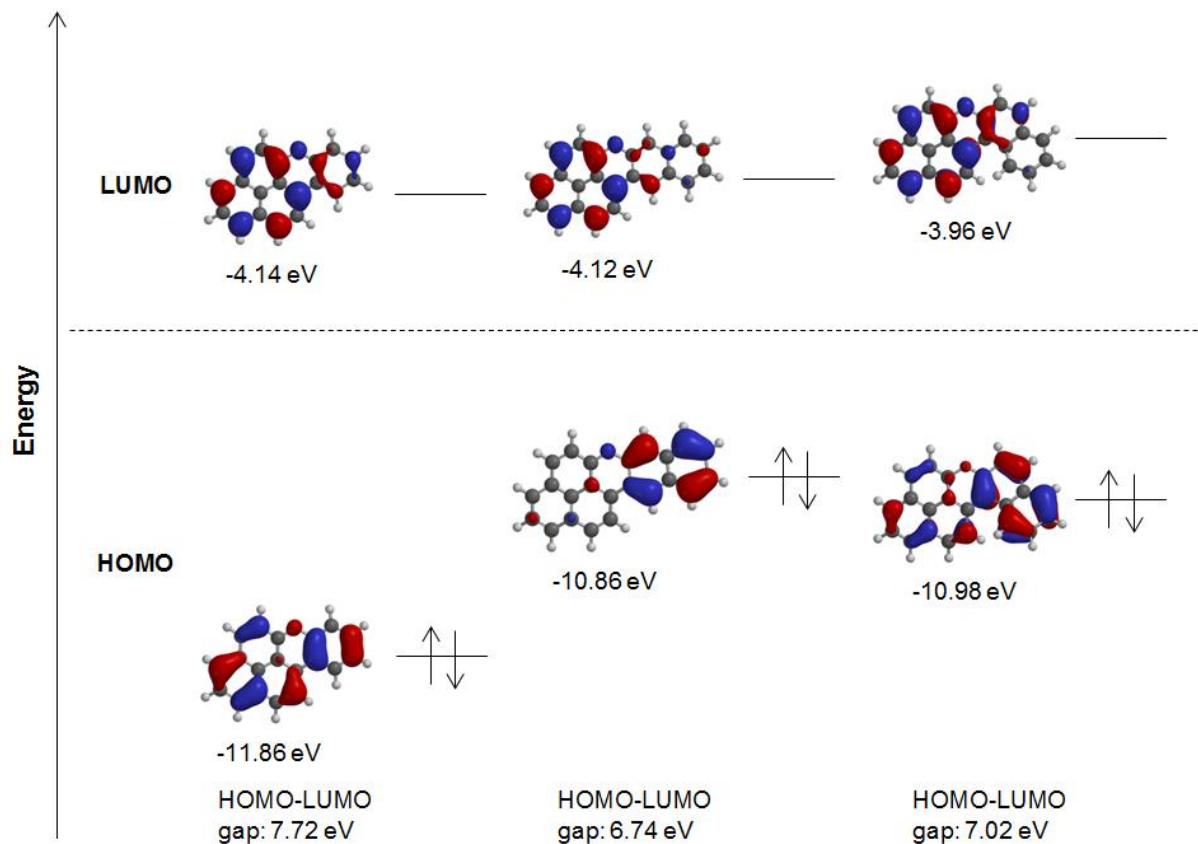


Figure 7.3.4.10 Calculated HOMO and LUMO energies of NX^+ , $\text{B}[i]\text{NX}^+$ and $\text{B}[a]\text{NX}^+$ based on the B3LYP-6-31G** level of theory.

Looking at the experimental UV/Vis-spectra, it is presumed that the HOMO-LUMO transition of $\text{B}[i]\text{NX}^+$ lies between 500 nm and 600 nm with a distinctly low intensity (*Figure 7.3.4.11*).

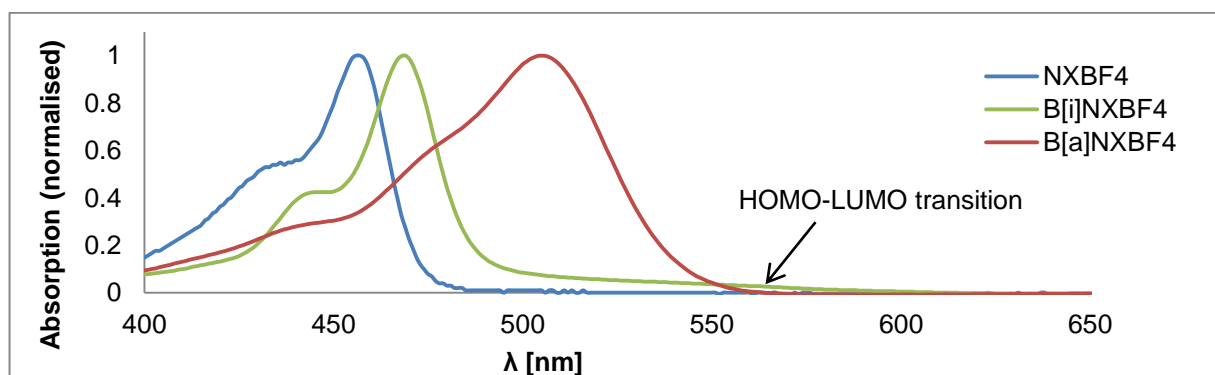


Figure 7.3.4.11 UV/Vis spectra of NX^+ , $\text{B}[i]\text{NX}^+$, $\text{B}[a]\text{NX}^+$. The presumed HOMO-LUMO transition for $\text{B}[i]\text{NX}^+$ is indicated between 500 nm and 600 nm.

However, the calculated spectra using the same basis set shows no absorption between 500-600 nm. Instead this absorption is calculated to be from 600 nm. Hence, the calculations presumably underestimated this transition (*Figure 7.3.4.12*) and thus a higher HOMO-LUMO gap for $B[i]NX^+$ is assumed regarding the experimental results. It is noteworthy that these calculations were carried out implying vacuum conditions.

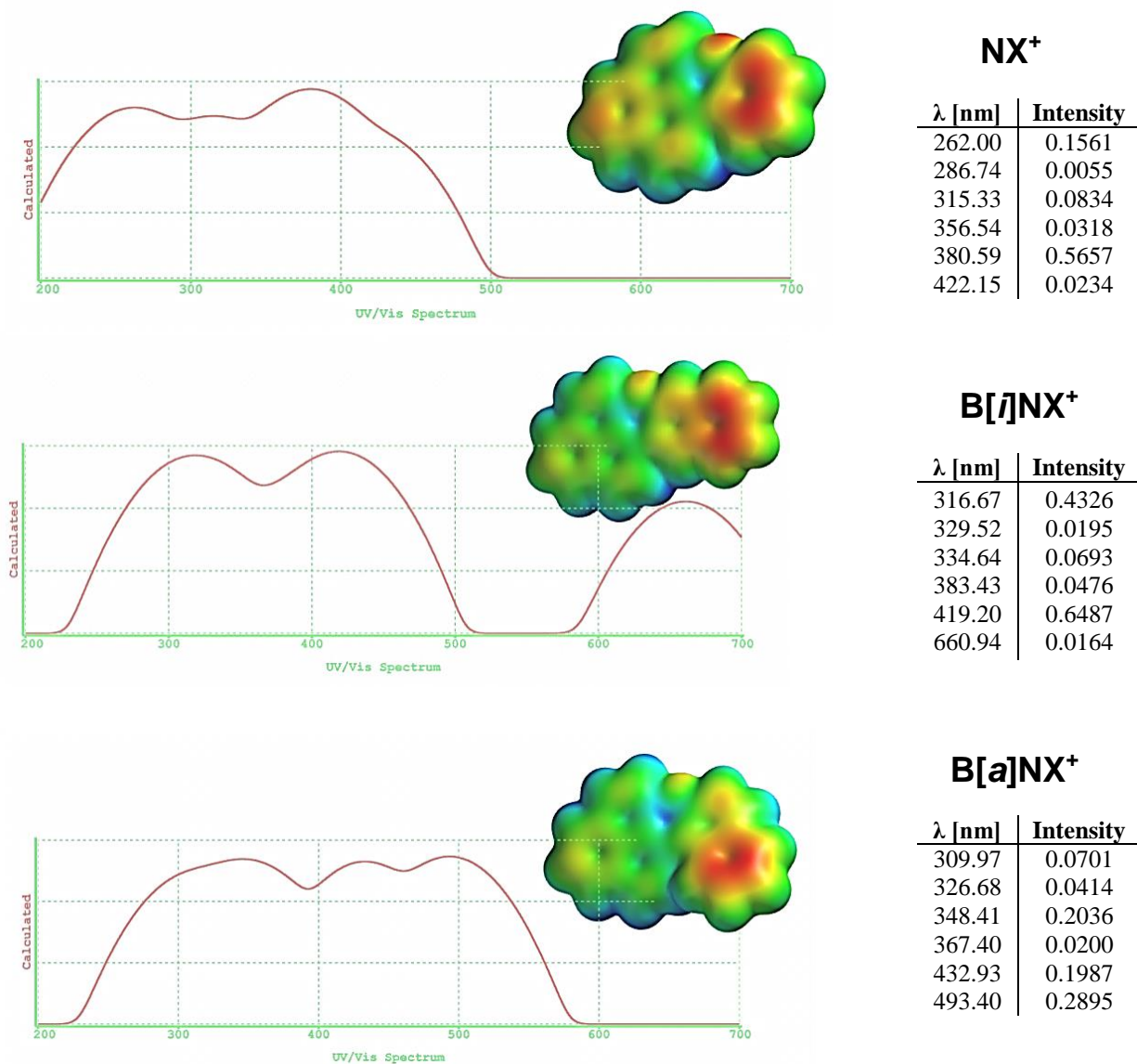


Figure 7.3.4.12 Calculated UV/Vis spectra of NX^+ , $B[i]NX^+$ and $B[a]NX^+$ based on the B3LYP-6-31G** level of theory (using *Spartan*).

For NX^+ the maximum peak was calculated to be at 381 nm which is by far an underestimated wavelength as the maximum peak is at 456 nm according to the experimental result. A weaker absorption is predicted to be at 422 nm still showing a strong variation from the experimental spectrum. In the case of $\text{B}[a]\text{NX}^+$, the obtained absorption wavelengths are more promising and in agreement with the recorded data. The calculated maximum peak at 493 nm can be assigned to the detected peak at 505 nm with a reasonable abbreviation of 13 nm.

In terms of fluorescence emission, $\text{B}[i]\text{NX}^+$ revealed a relatively low intensity compared to NX^+ and $\text{B}[a]\text{NX}^+$. This can be attributed to collisional quenching by π - π stacking interactions. Considering $\text{B}[a]\text{NX}^+$, the helical structure results in the minimisation of π - π interactions.²²⁴ Consequently, the fluorescence intensity is distinctly enhanced compared to $\text{B}[i]\text{NX}^+$.

The bathochromic shift of $\text{B}[a]\text{NX}^+$ with 46 nm compared to $\text{B}[i]\text{NX}^+$ was expected considering the results from the absorption spectroscopy. Fluorescence emission characteristically exhibits a Stokes shift, that is, the emission peaks generally occur at higher wavelength than the peaks in the absorption spectrum. This is due to loss of energy by other possible photochemical or thermal relaxation processes from the excited state.

7.3.5. Cyclic voltammetry studies of naphthoxanthenyl cations

According to cyclic voltammetry studies, all the three species show two reversible redox waves representing the reduction from the cation to the radical and the reduction from the radical to the anion under argon atmosphere. The reversibility illustrates the amphoteric character supported by the incorporated phenalenyl unit. The derived values representing the amphotericity are between the parent phenalenyl ($E_{\text{sum}} = 1.6 \text{ V}$) and DTPLY ($E_{\text{sum}} = 0.57 \text{ V}$) and exhibit slight abbreviations between 0.04-0.06 V.⁸⁹ Therefore all three species can be considered as having similar electrochemical properties. This is largely attributed to the phenalenyl nucleus.

Based on the first reduction step forming the radical from the cation, the energy levels of the LUMOs between the investigated species can be discussed. This is due to relationship between the applied potential and an electron transfer. The more voltage is required to induce an electron transfer a lower electron donating ability is suggested, hence, the LUMO is located at

a higher energy level if voltage E is more negative. Consider the calculated LUMO energy of NX^+ , $B[i]NX^+$ and $B[a]NX^+$ based on the B3LYP-6-31G** level of theory depicted in (*Figure 7.3.4.10*). Comparing the potential values of the first reduction steps of all three species, -0.52 V, -0.43 V and -0.59 V for NX^+ , $B[i]NX^+$ and $B[a]NX^+$, respectively, $B[a]NX^+$ would have the highest LUMO energy. This is in agreement with the calculations predicting -3.96 eV. However, the hypothesis would then also suggest that the LUMO energy of NX^+ is higher than that of $B[i]NX^+$ which is not the case with -4.14 eV and -4.12 eV for NX^+ and $B[i]NX^+$, respectively. It is therefore possible that a more appropriate basis set needs to be employed, in particular for $B[i]NX^+$, since contradictions could be found in the simulated UV/Vis spectrum (*Figure 7.3.4.12*).

The electrochemical results are important as they demonstrate the thermodynamic stability of the corresponding radicals. Since no steric hindering groups are involved, NX , $B[i]NX$ and $B[a]NX$ are remarkable molecules. They represent the first neutral phenalenyl based radicals incorporating a chromenyl or benzochromenyl unit to perturb and stabilise the electronic system. X-ray structure analysis of the radicals would be desirable for investigations on the π -stacking arrangement. This would give access to details to understand the role of the heteroatom which may provide further stabilisation through intermolecular interactions in the solid state.

7.3.6. Electron spin resonance spectroscopy

Due to the high number of inequivalent protons, the spectra obtained are hard to assign the corresponding hyperfine coupling constants. Therefore a simulation is required to confirm the structure of the neutral radicals. With the aid of the calculated *Mulliken* spin densities, a good approximation can be obtained to deduce an appropriate data set of hfcs for the simulation (see *Appendix 77-79*).

Using a data set of 4 x 5.30, 4 x 1.74 and 5 x 0.45 Gauss, this was successful for $B[i]NX$. The simulated spectrum matched the experimental spectrum sufficiently. For all species the highest spin densities, hence the largest hfcs, are assigned at the α -positions of the phenalenyl unit which points to its structure as a typical phenalenyl radical. Regarding the NMR effects, these data correlate well with the observed broadening effects which gives further indications for the

correctly predicted spin densities. According to the data set used, the electronic stabilisation can be shown by the reduction of the spin densities in the phenalenyl unit and the almost negligibly low spin densities in the annulated benzene and naphthalene units in NX, B[*i*]NX and B[*a*]NX (Figure 7.3.6.1, B[*i*]NX (Figure 7.3.6.2) and B[*a*]NX (Figure 7.3.6.3), respectively).

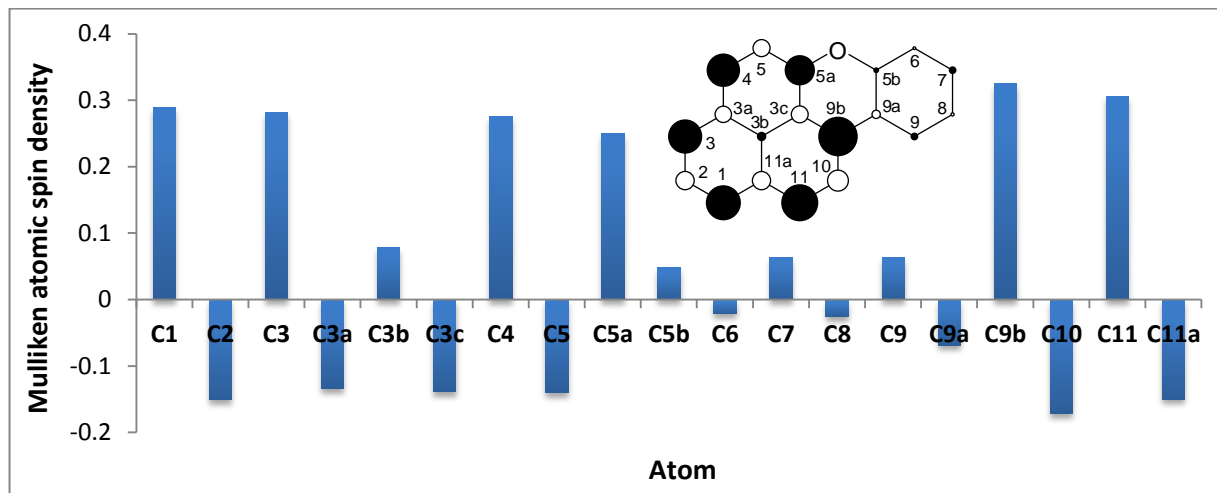


Figure 7.3.6.1 Illustration of *Mulliken* spin densities of NX.

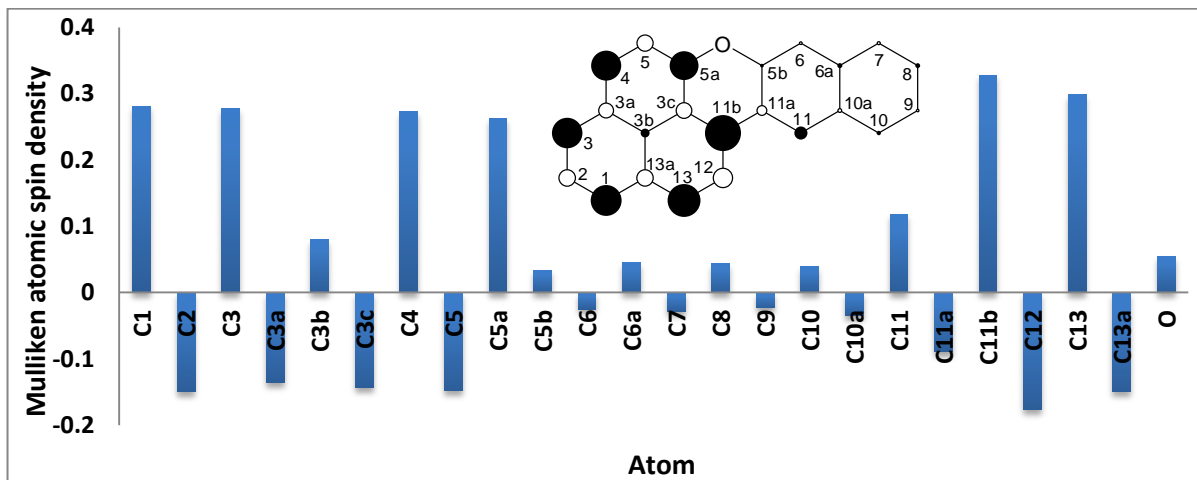


Figure 7.3.6.2 Illustration of *Mulliken* spin densities of B[*i*]NX.

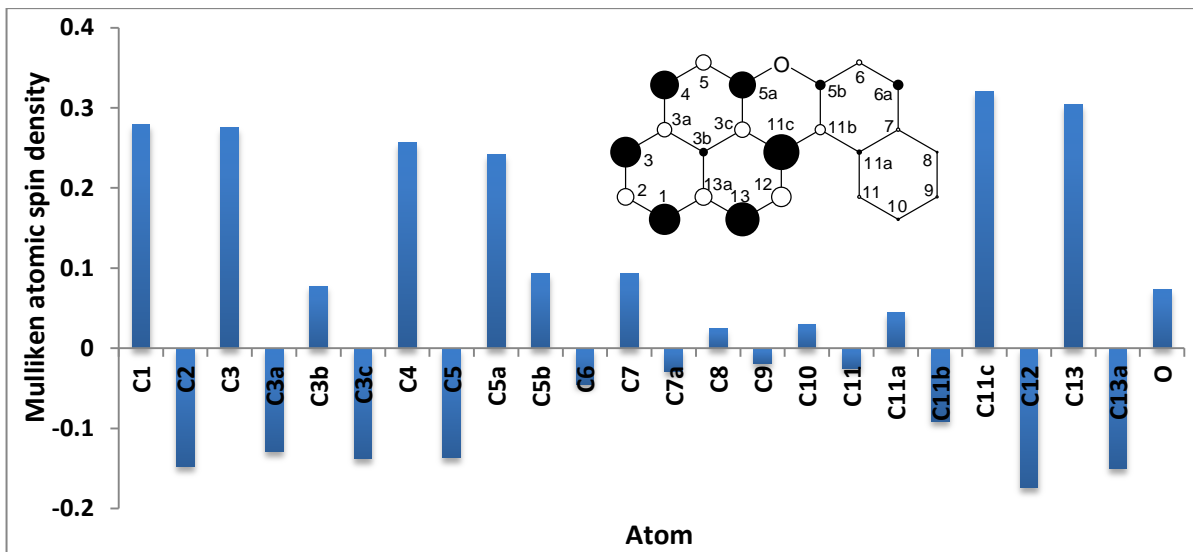


Figure 7.3.6.3 Illustration of *Mulliken* spin densities of B[a]NX.

It is therefore of interest to know if the chromenyl or benzchromenyl units play an important role in the solid state. However, no crystals of sufficient quality could be obtained although a high stability was proposed due to the spectra obtained of aged crude solids containing the radicals. This does not exclude the possibility of obtaining crystals of sufficient quality. It is assumed that the asymmetric structure may not allow a sufficient driving force for one possible π -dimer. Considering the X-ray results of DTPLY and TBPLY according to the literature,⁸² two radicals are arranged so that the positions with the highest spin densities can overlap. Possibly this gives rise to the generation of the intermolecular aromaticity generation. Hence, in the cases of NX, B[i]NX and B[a]NX, the following dimer interactions presumably occur as depicted in *Figure 7.3.6.4*. The question is therefore if the α -positions have been sufficiently perturbed so that different forms of π -dimerisation may not proceed.

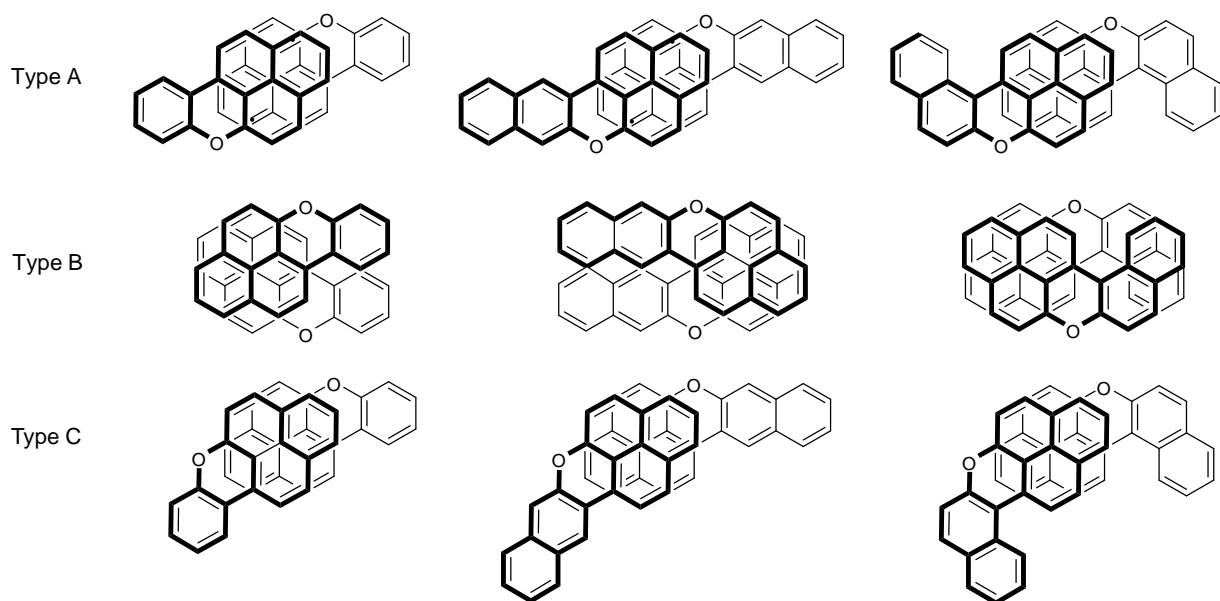


Figure 7.3.6.4 Proposed types of π -dimerisation based on the assumption that the radicals tend to interact intermolecularly between the positions with the highest spin densities.

This also raises the question as to whether the arrangement between these three forms of π -dimers are competitive and may impede a good driving force for the crystallisation. Alternatively, more than one form of A, B or C exist in the solid state resulting in a mixture of crystals. Both would make the isolation of crystals difficult for X-ray structure analysis. A further pathway is σ -dimerisation at the α -positions which could result in a large closed shell PAH through a follow-up oxidative cyclisation. The reaction with oxygen is also possible resulting in a ketone analogous to the parent PLY radical. These processes represent the reactions conventionally competitive to the π -dimerisation.

7.4. Conclusions

The synthesis of new phenalenyl based cations was successfully achieved based on a convenient synthetic procedure using 9-(2-methoxyaryl)-1*H*-phenalen-1-ones. Subsequent reduction to their corresponding neutral radicals revealed remarkably long persistence under air. However, the solids obtained are crude and possibly mixtures of radical, cation, and possible σ -dimers of the radical which could have cyclised to large closed shell PAHs. Generally, it has been difficult to find out the encountered effects such as paramagnetic

broadening effects in the NMR spectra including the progressive formation of an unknown black substance with a green lustre. The studies showed that the prepared species exhibit typical electronic structures according to the parent phenalenyl, hence they can be characterised as phenalenyl-type radicals. The extension of the framework by chromenyl or benzchromenyl decreased the spin densities in the phenalenyl unit to a certain extent. The spin densities in the chromenyl and benzchromenyl substructures are distinctly smaller or even negligible. However, as long as no solid state properties can be deduced via X-ray structure analysis, the truth about the π -dimerisation including the role of the chromenyl or benzchromenyl groups remains uncertain.

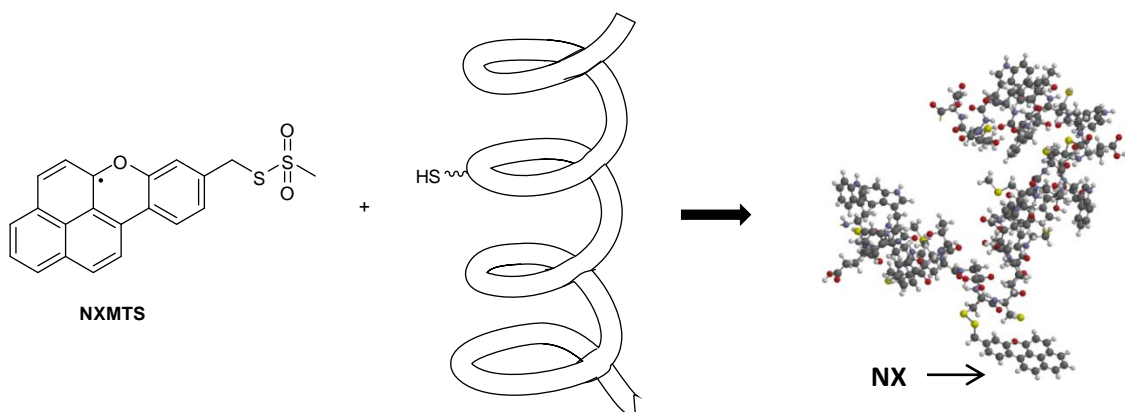
The cations showed interesting photochemical properties, in particular, in the cases of the two isomers $B[i]NX^+$ and $B[a]NX^+$. These compounds showed unexpected differences in their absorption wavelengths. X-ray structure analysis and the evaluation of aromaticity with the aid of HOMA indices could illustrate their divergence of delocalisation based on the position of the benzannulation. The presence of the fjord region in the case of $B[a]NX^+$ appeared to influence the HOMO-LUMO gap dramatically. Using computational methods based on the B3LYP-6-31G** level of theory resulted in controversies in the case of $B[i]NX^+$ with regards to the UV spectra and the HOMO-LUMO gaps if one compares those with the derived results from the experimental UV/Vis spectrum and data from the cyclic voltammetry, respectively.

According to the X-ray resolution a distinctly shorter C5b-O bond could be observed indicating a high bond order. This is consistent with a lower order of the C11a-C11b bond compared to its isomer and NX^+ . The influence of atomic overcrowding in $B[a]NX^+$ may have also induced an elongation of the twisting bond. It is noteworthy that this bond is part of a π -deficient pyryl ring. Therefore the synthetic procedure gives access to heteroaromatic compounds where the overcrowded regions could be modified in order to reveal new photochemical properties. To our knowledge the modification of helicenes involving the twist of bonds in a pyryl ring has not been well-investigated in the literature. Hence NX , $B[i]NX$ and $B[a]NX$ represent a new class of dyes with a promising perspective due to the convenient and universal synthetic methodology.

8. Synthesis of a potential probe for SDSL studies and an ESR responsively switchable molecule controlled via irradiation

8.1. Introduction

In the previous chapter, the thermodynamic stability of the naphthoxanthenyl radical (NX) was demonstrated by reversible redox waves according to cyclic voltammetry results. Despite the lack of structural information on NX in the solid state, the persistence under air appears to be very long. For that reason, we wished to take the next step and approached functionalised NX radicals which might be of use in terms of applications. Therefore two 9-aryl-1*H*-phenalen-1-ones were prepared which are substituted with selected functional groups. Those could serve as precursors for new sensing open-shell species regarding site directed spin labeling (SDSL)²²⁵ of supramolecular biomolecules (proteins, DNA, RNA) or quantum information processing.²²⁶ SDSL represents a powerful method to investigate structure and motion of large biomolecules monitored by ESR spectroscopy. This is realised by labeling the target protein, DNA or RNA by a radical such as TEMPO.²²⁷ Based on the molecular environment of the spin label, tumbling effects can vary related to the motion of the biomolecule. This allows access to a series of information such as solvent accessibility, local geometry, flexibility and structural changes upon chemical or physical events.²²⁸

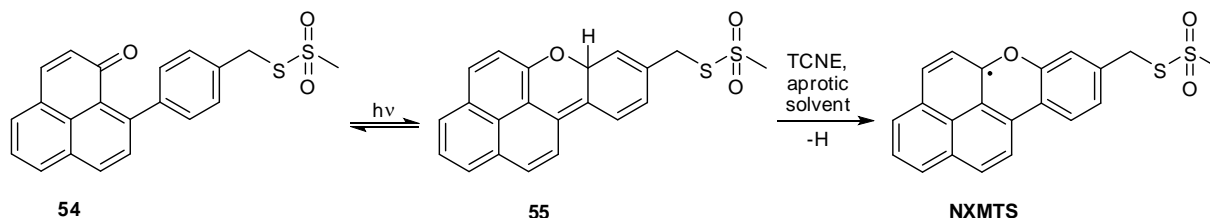


Scheme 8.1.1 An example of SDSL using NXMTS.

The tumbling phenomenon is quantified by the rotational correlation time τ which can vary depending on the degree of mobility of the spin label. If the mobility is decreased due to the environmental modification, the lineshape of the ESR signal will be influenced involving

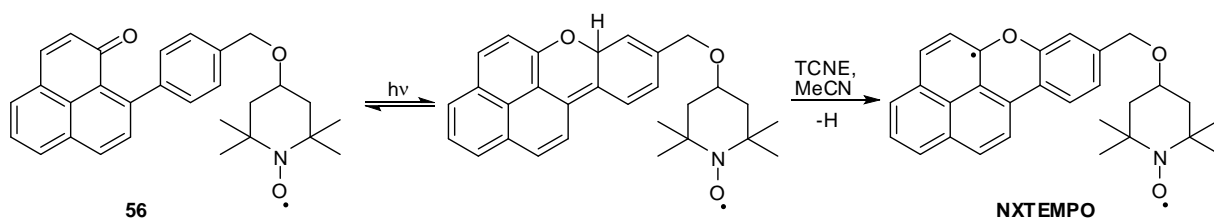
broadening effects and change of the amplitude.²²⁸ If one considers the TEMPO radical in solution, where a very short rotational correlation time is given, an isotropic spectrum with three equally intense hyperfine lines will be observed in the ESR spectrum. These represent the detection of three allowed transitions of equal probability based on the coupling between the unpaired electron residing in one orbital and the three quantum states of the ¹⁴N nuclei ($M_I = -1, 0, 1$). Once this mobility is restricted the unpaired electron exhibits a more pronounced orientation along the N-O bond. This leads to an orientation-depending hyperfine coupling between the unpaired electron and the ¹⁴N nuclei. As a result, the ESR spectrum shows an anisotropic spectrum with broadening effects. Eventually this sensing property was useful to develop SDSL which was well-employed in studies on a series of biomolecules.^{229,230,231} Furthermore distances between two spin labels can be predicted in high precision based on the interaction of electronic magnetic moments, so-called dipole dipole interaction.^{232,233,234} This requires two spin labels which are in a distance range below 25 Å. This allows the analysis of protein-RNA interactions, for instance. A good example represents the investigated interaction between the HIV Rev peptide and the Rev response element (RRE) RNA.²³⁵ With the aid of the spin labeled RNA and the spin labeled peptide, the distances between them could be measured using the dipolar EPR method.

With respect to this method, the NX radical is considered a potential spin label. A common linker group is methanethiosulfonate (MTS) which is widely used to attach an ESR responsive probe (e.g. TEMPO) to cysteine in a protein.²²⁸ Therefore S-4-(1-oxo-1*H*-phenalen-9-yl)benzyl methanethiosulfonate **54** was synthesised (see *Scheme 8.1.1*). The key step for the formation of the NX radical is the photocyclisation proceeding via β -phenyl quenching generating **55** (*Scheme 8.1.2*).²³⁶ This can subsequently undergo hydrogen abstraction in presence of e.g. TCNE to yield the NX-type radical.



Scheme 8.1.2 Photolysis of S-4-(1-oxo-1*H*-phenalen-9-yl)benzyl methanethiosulfonate **54**.

A further synthetic target was 9-(4-(TEMPO-methyl)phenyl)-1*H*-phenalen-1-one **56**. **56** shall represent an ESR switchable molecule and is supposed to encode a potential qubit in terms of quantum computing. In quantum information processing, several challenges are encountered such as short decoherence times and difficulties to develop suitable algorithms. Quantum computing is still in its infancy, but it can be realised.^{117,226} Organic radicals recently received growing attention triggered by advances in this new field using biradicals as an effective two spin quantum bit.²³⁷ 9-(4-(TEMPO-methyl)phenyl)-1*H*-phenalen-1-one **56** is considered a potential one quantum bit system and will be investigated in near future by our collaborators. Furthermore, **56** could be investigated with regard to photocyclisation yielding a very short lived intermediate. The cyclised form may reveal alternation of the lineshape in the ESR spectrum. Those studies will be carried out in the future using matrix isolation spectroscopy. Additionally, the photolysis of **56** was conducted forming NXTEMPO, a phenalenyl based species accommodating one delocalised (NX) electron plus one localised (TEMPO) unpaired electron (*Scheme 8.1.3*).



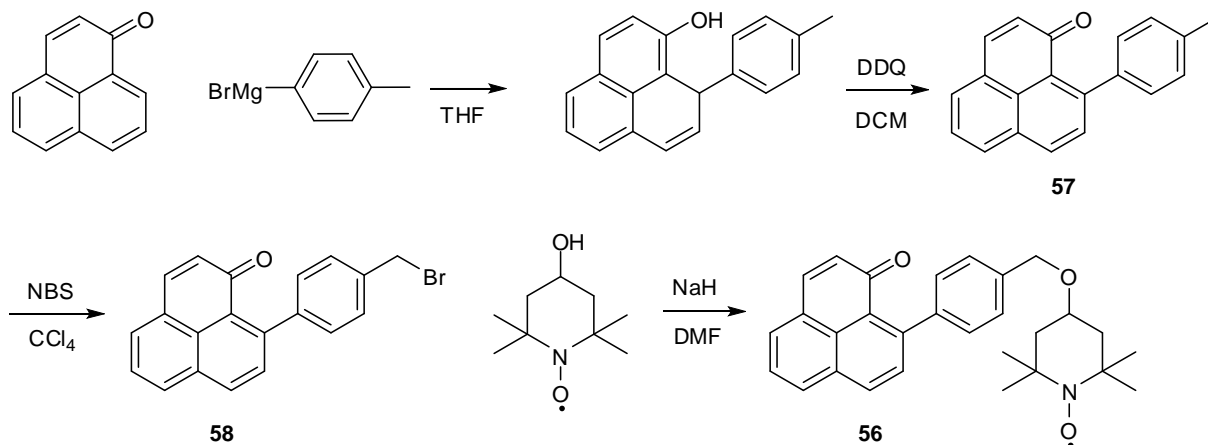
Scheme 8.1.3 Reversible β -phenyl quenching upon irradiation and formation of NXTEMPO via TCNE.

8.2. Results

8.2.1. Synthesis of 9-(4-(TEMPO-methyl)phenyl)-1*H*-phenalen-1-one

Conducting the well-established *Michael-type Grignard* addition to the 9-position of 1*H*-phenalen-1-one and subsequent oxidation using DDQ, 9-*p*-tolyl-1*H*-phenalen-1-one **57** was prepared in a yield of 60% (*Scheme 8.2.1*). Afterwards, bromination of the methyl group was carried out using NBS in CCl₄ resulting in 9-(4-(bromomethyl)phenyl)-1*H*-phenalen-1-one **58** in a very good yield of 96%.²³⁸ According to the literature²³⁹, nucleophilic substitution of **58** with 4-hydroxy-TEMPO proceeded in presence of NaH in DMF. This gave the target compound 9-(4-(TEMPO-methyl)phenyl)-1*H*-phenalen-1-one **56** in a yield of 44% after

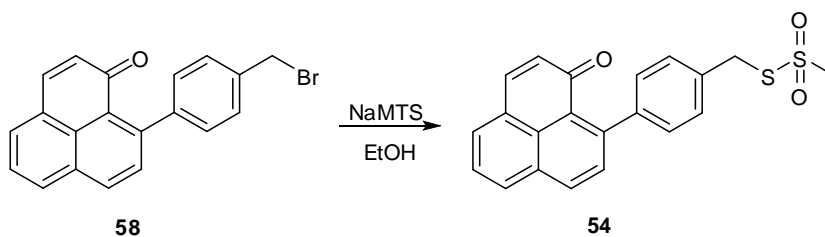
column chromatography. Starting with 1*H*-phenalen-1-one, the total yield of **56** is 26% over 4 steps.



Scheme 8.2.1 Synthetic route towards 9-(4-(TEMPO-methyl)phenyl)-1*H*-phenalen-1-one **56**.

The photolysis of **56** in the presence of TCNE in MeCN gave a brown crude material. It is presumed that NXTEMPO is formed with regards to the obtained ESR spectrum which is shown in the ESR spectroscopy section.

Compound **58** also served as a precursor to carry out a nucleophilic substitution using sodium methanesulfonate (NaMTS) in ethanol.²⁴⁰ This resulted in the desired compound **54** in a good yield of 84% after column chromatography.



Scheme 8.2.2 Synthesis of S-4-(1-oxo-1*H*-phenalen-9-yl)benzyl methanesulfonate **54**.

8.2.2. ¹H-NMR spectroscopy

Considering the collected data in *Chapter 7 (Table 7.3.2.1)* the assignment of all 9-C substituted phenalenones can be made with confidence. As expected, the ¹H-NMR spectrum of

57 shows 11 aromatic protons between 6.60-8.15 ppm of which four are overlapped at 7.30 ppm (*Figure 8.2.2.1*, see *Appendix 33 & 34* for full ^1H - and ^{13}C -spectra). The methyl group is detected as a singlet at 2.46 ppm. The proton at the 2-position can be found at 6.60 ppm ($J = 9.7$ Hz).¹²⁰ This couples with the doublet at 7.67 ppm ($J = 9.7$ Hz) representing the proton at the 3-position. The proton at the 5-position is assigned to the doublet of doublets at 7.60 ppm ($J = 8.2, 7.1$ Hz). The doublet at lowfield with a chemical shift of 8.14 ppm ($J = 8.3$ Hz) represents the proton at the 7-position. This allows the assignment of the proton at the 8-position to the doublet at 7.59 ppm ($J = 8.3$ Hz). The two remaining signals at 7.75 ppm ($J = 7.1, 1.0$ Hz) and 8.02 ppm ($J = 8.2, 1.0$ Hz) can be assigned to the protons at the 4- and 6-positions, respectively.

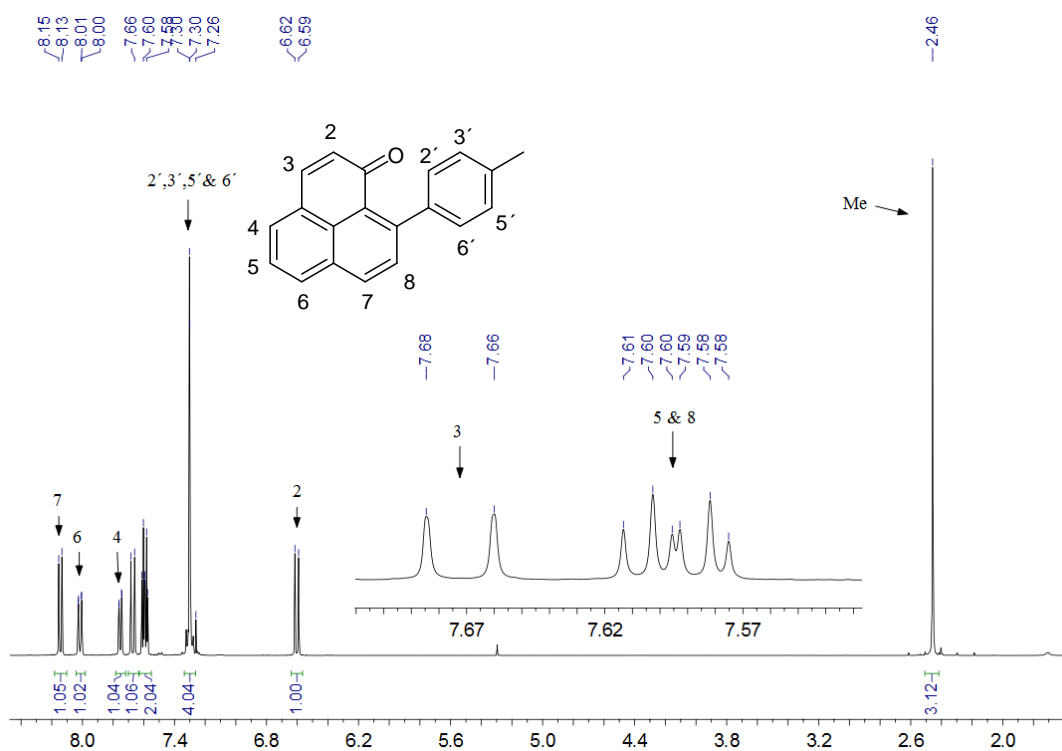


Figure 8.2.2.1 ^1H -NMR spectrum of 9-p-tolyl-1H-phenalen-1-one **57** measured at room temperature (400 MHz; CDCl_3).

According to **58**, again 11 proton signals at the aromatic area were detected between 6.58-8.17 ppm including the methylene group at 4.60 ppm (*Figure 8.2.2.2*; see *Appendix 35 & 36* for full ^1H - and ^{13}C -spectra). The protons at the 2', 3', 5' and 6'-positions are assigned at 7.35 ppm and 7.48 ppm each representing 2 protons of the benzyl group. The proton at the 2-position is

assigned at 6.58 ppm ($J = 9.7$ Hz) coupling with the proton at the 3-position at 7.69 ppm ($J = 9.7$ Hz). The typical ABX spin system for the 5-position can be found at 7.62 ppm ($J = 8.2$, 7.1 Hz). The lowfield signal at 8.17 ppm ($J = 8.3$ Hz) is assigned to the proton at the 7-position which couples with the proton at the 8-position at 7.58 ppm ($J = 8.3$ Hz). The two remaining proton signals at 7.78 ppm ($J = 6.5$ Hz) and 8.04 ppm ($J = 7.6$ Hz) are assigned to the protons at the 4- and 6-positions, respectively.

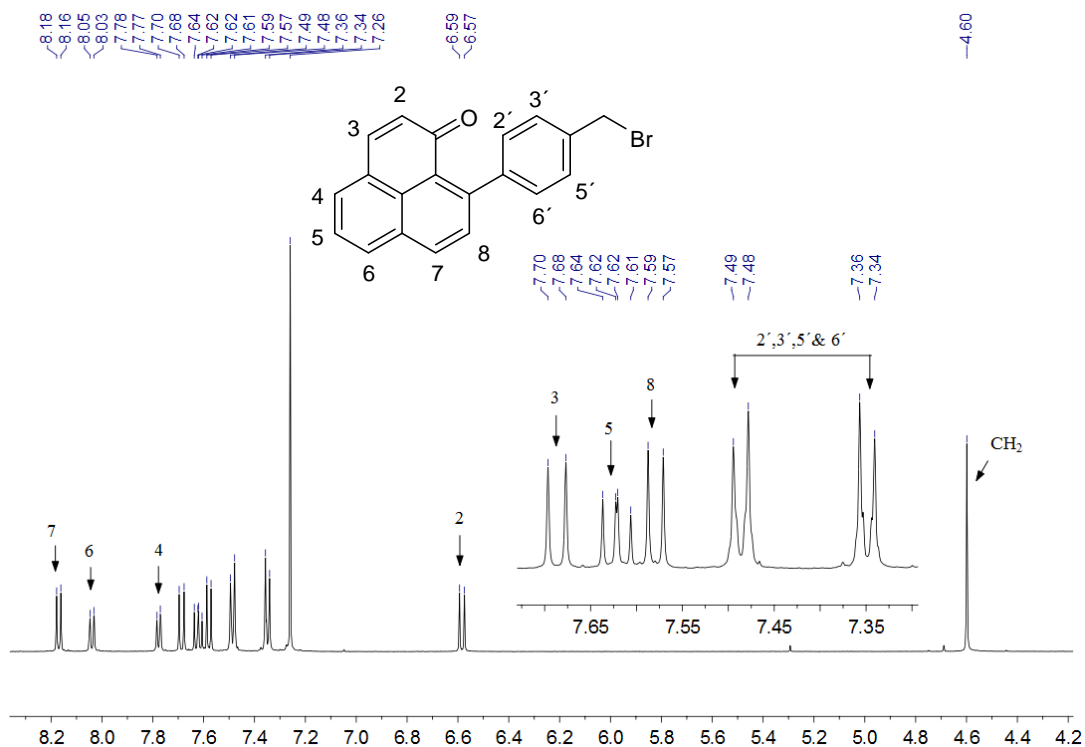


Figure 8.2.2.2 ^1H -NMR spectrum of 9-(4-(bromomethyl)phenyl)-1*H*-phenalen-1-one **58** measured at room temperature (500 MHz; CDCl_3).

The ^1H -NMR spectrum of **59** shows 11 proton signals in the aromatic area and two singlet signals at 4.45 and 3.05 ppm which are assigned to the methylene and methyl group, respectively (Figure 8.2.2.3; see Appendix 37 & 38 for full ^1H - and ^{13}C -spectra). The two signals at 7.37 ppm and 7.51 ppm represents the 4 protons of the substituted aryl ring. The proton at the 2-position can be found as a doublet at 6.56 ppm ($J = 9.7$ Hz), coupling with the proton at the 3-position, detected as a doublet at 7.70 ppm ($J = 9.7$ Hz). The two doublet signals at 7.55 ppm ($J = 8.3$ Hz) and 8.19 ppm ($J = 8.3$ Hz) are assigned to the protons at the

8- and 7-positions, respectively. The ABX spin system for the proton at the 5-position can be found at 7.62 ppm ($J = 8.2, 7.1$ Hz). The two remaining groups at the 4- and 6- positions are represented as two doublets at 7.80 ppm ($J = 6.3$ Hz) and 8.05 ppm ($J = 8.2$ Hz), respectively.

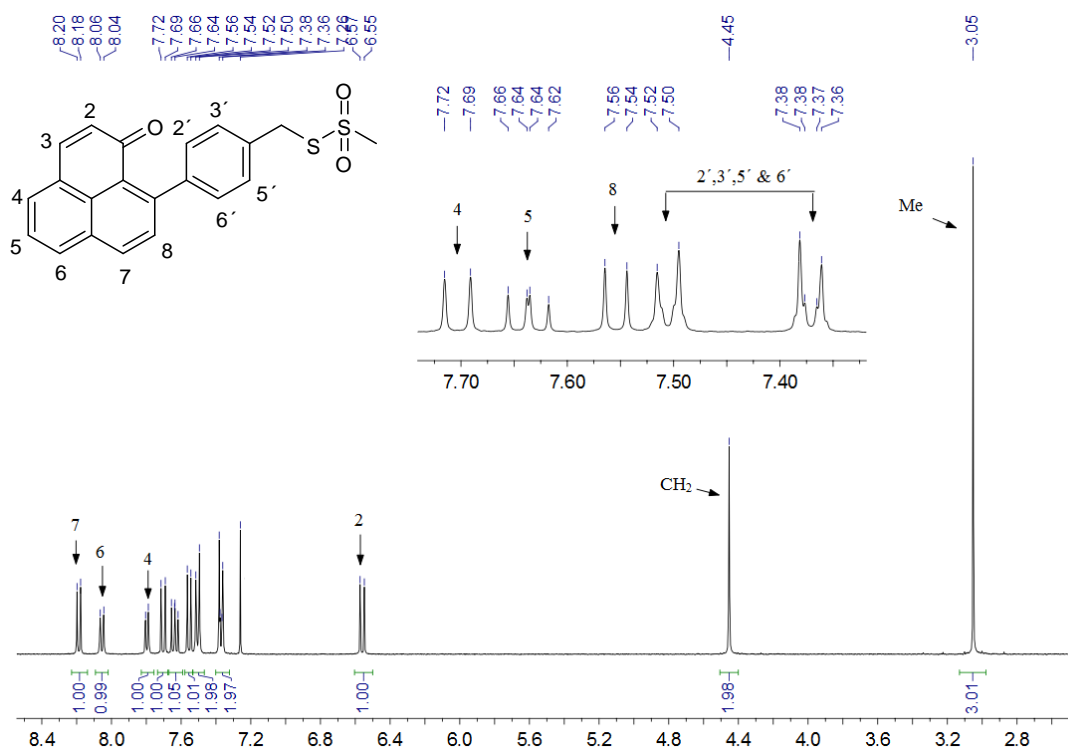


Figure 8.2.2.3 $^1\text{H-NMR}$ spectrum of S-4-(1-oxo-1H-phenalen-9-yl)benzyl methanesulfonate **54** measured at room temperature (400 MHz; CDCl_3).

8.2.3. UV/Vis and mass spectroscopy

All the four compounds only absorb between 330-500 nm with a maximum peak at 360 nm which is characteristic for 9-aryl-1H-phenalen-1-ones (*Figure 8.2.3.1*).

According to the mass spectra (isobutane CI^+), a $(\text{M}+\text{H})^+$ peak could be observed for **57**, however, there was no dominant $(\text{M}-1)^+$ or $(\text{M}-16)^+$ peak (16 represents the mass of methyl group plus the mass of the proton at the *o*-position of the aryl ring) which would indicate a cyclised naphthoxanthenyl cation. Similarly, **58** and **59** did not show a dominant peak for the corresponding NX cation. In the case of **56**, the mass spectroscopic method using electron ionization gave a peak at 255 m/z indicating the parent NX cation. The four new compounds could additionally be confirmed via high resolution mass spectroscopy.

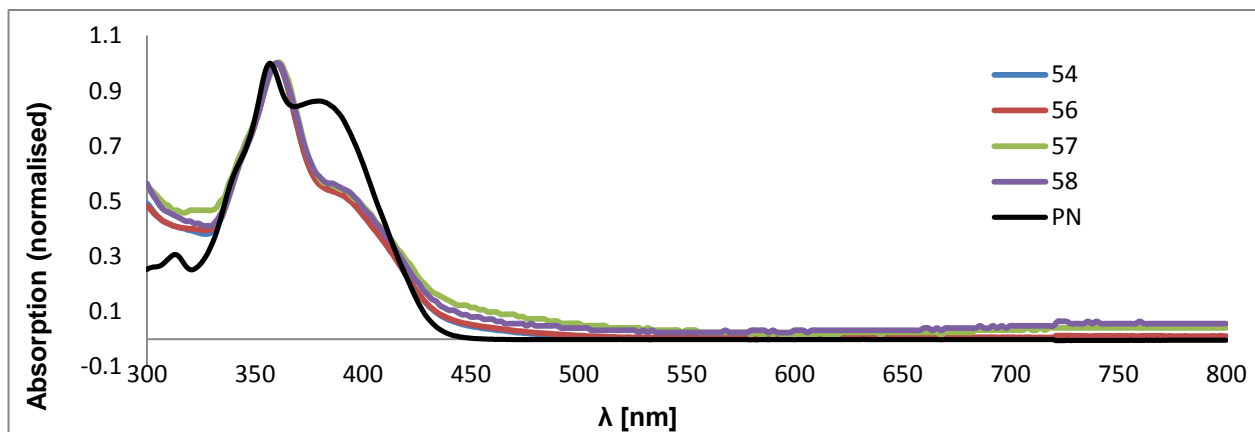


Figure 8.2.3.1 Normalised UV/Vis spectra of S-4-(1-oxo-1*H*-phenalen-9-yl)benzyl methanesulfonate **54**, 9-(4-(TEMPO-methyl)phenyl)-1*H*-phenalen-1-one **56**, 9-*p*-tolyl-1*H*-phenalen-1-one **57**, 9-(4-(bromomethyl)phenyl)-1*H*-phenalen-1-one **58** and 1*H*-phenalen-1-one (PN).

8.2.4. X-ray structure analysis

Compound **56** could be recrystallised from acetone giving orange crystals with sufficient quality to carry out X-ray structure analysis. As the TEMPO substituent exhibits an unpaired electron resulting in broadening effects in NMR spectra, X-ray data can ultimately confirm the right structure. **56** crystallises in a monoclinic space group (*Figure 8.2.4.1*).

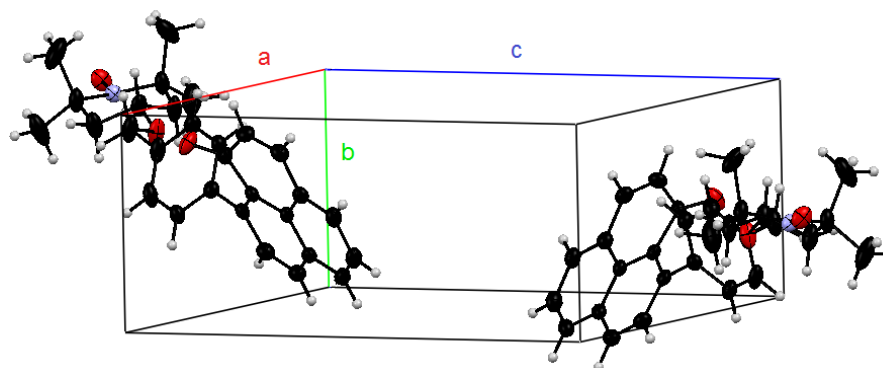


Figure 8.2.4.1 Monoclinic space group involving two molecules of 9-(4-(TEMPO-methyl)phenyl)-1*H*-phenalen-1-one **56**.

The distances between the oxygen attached to the nitrogen in TEMPO group and 9-phenylphenalenone unit ranges between 7.780 Å and 16.644 Å (*Figure 8.2.4.2*). All remaining X-ray data obtained can be found in *Appendix 65 & 66*.

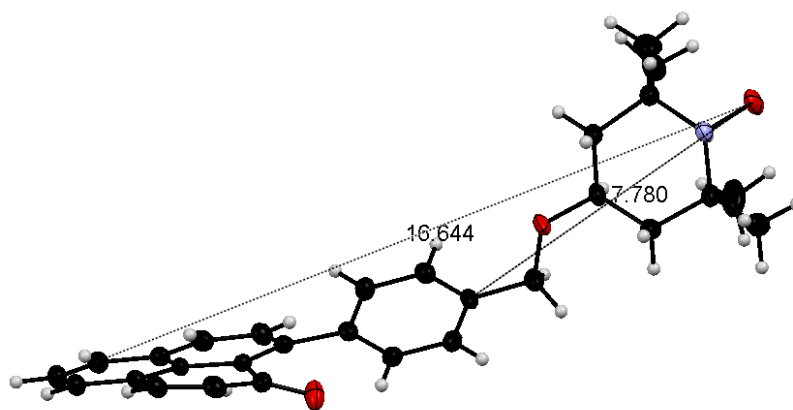


Figure 8.2.4.2 Shortest and longest distances between the oxygen of the TEMPO substituent and the 9-phenyl-1*H*-phenalen-1-one unit.

8.2.5. ESR spectroscopy

Figure 8.2.5.1 shows the ESR spectrum of **56** in EtOH/MeCN (5:1) at room temperature showing a signal at 3506 gauss with an almost isotropic lineshape with a linewidth of 33 gauss representing the three hyperfine splittings for a typical TEMPO radical. The *g*-factor is 2.0075 (standard: DPPH; see *Appendix 81*). The experiments were carried out at the *EPSRC ESR centre* in Manchester. **56** was frozen in EtOH/MeCN (5:1) and measured via ESR spectroscopy. The resulting spectrum gave a signal at 3369 gauss with an asymmetrical lineshape due to the strongly decreased mobility in the EtOH/MeCN frozen glass (*Figure 8.2.5.2*). The linewidth and *g*-factor are 71 gauss and 2.085, respectively.

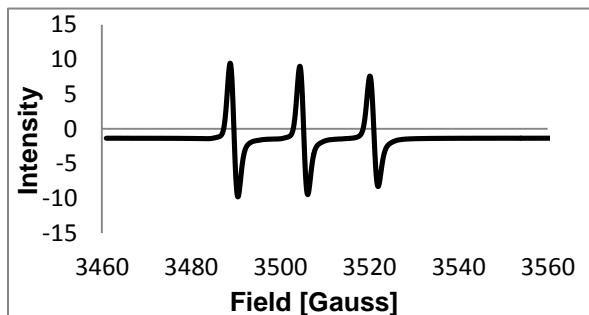


Figure 8.2.5.1 CW-ESR spectrum (1st derivative) of **54** in EtOH/MeCN (5:1) at room temperature (modulation amplitude: 0.7 Gauss; conversion time: 7 ms; sweep time: 10 s; time constant: 40.96 ms).

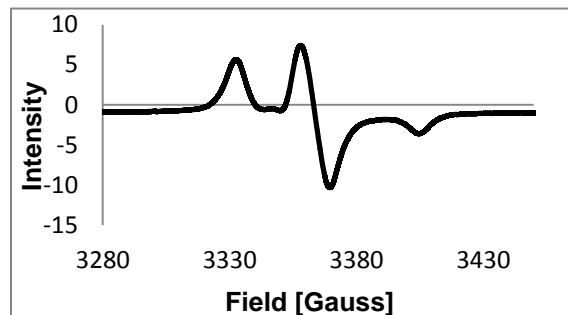


Figure 8.2.5.2 CW-ESR spectrum (1st derivative) of **54** in EtOH/MeCN (5:1) at 100K (modulation amplitude: 0.1 Gauss; conversion time: 0.32 ms; sweep time: 10.24 s; time constant: 20.48 ms).

According to the photolysis of **54**, an ESR signal at 3509 gauss was detected indicating the proposed biradical NXTEMPO. The sample could be stored for weeks without depletion of the signal. The linewidth and g-factor are 27 gauss and 2.0024, respectively. The spectra of **54** and NXTEMPO are overlapped in *Figure 8.2.5.3* in order to assign residual starting material. Generally the result indicates a stable paramagnetic species involving a π -conjugated unpaired electron which is proposed to be NXTEMPO.

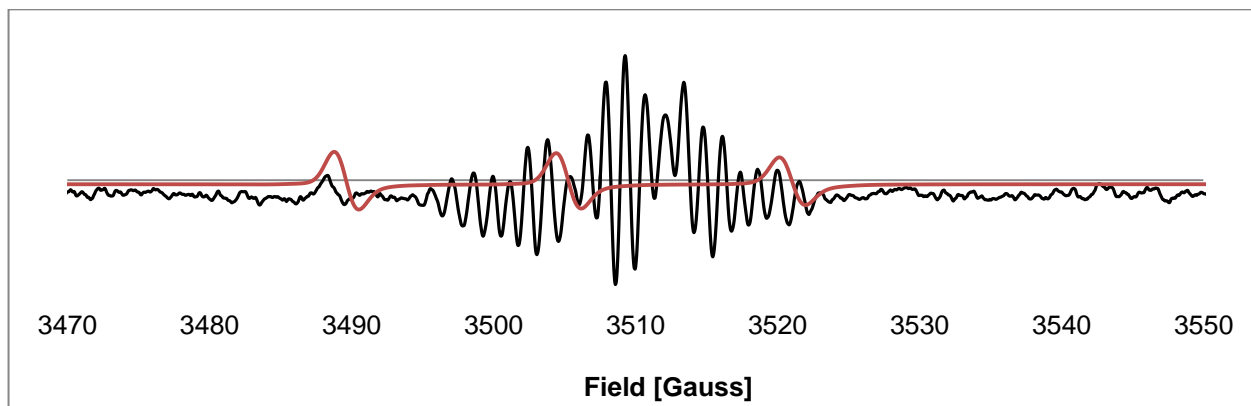


Figure 8.2.5.3 CW-ESR spectrum (1st derivative) of **54** in MeCN at room temperature (modulation amplitude: 0.7 gauss; conversion time: 7 ms; sweep time: 10 s; time constant: 40.96 ms). ESR signal of compound **56** is overlaid (red); see *Figure 8.2.5.1* for applied instrumental parameters.

In addition the brown solid containing the biradical was dissolved in MeCN and a UV/Vis spectrum was recorded showing peaks at 367 nm, 397 nm and 410 nm plus broad absorptions

between 445 nm and 650 nm. Compare the spectrum of NXTEMPO with the spectrum of NX. Both species consists of the same chromophore, thus a very strong similarity can be seen as depicted in (Figure 8.2.5.4).

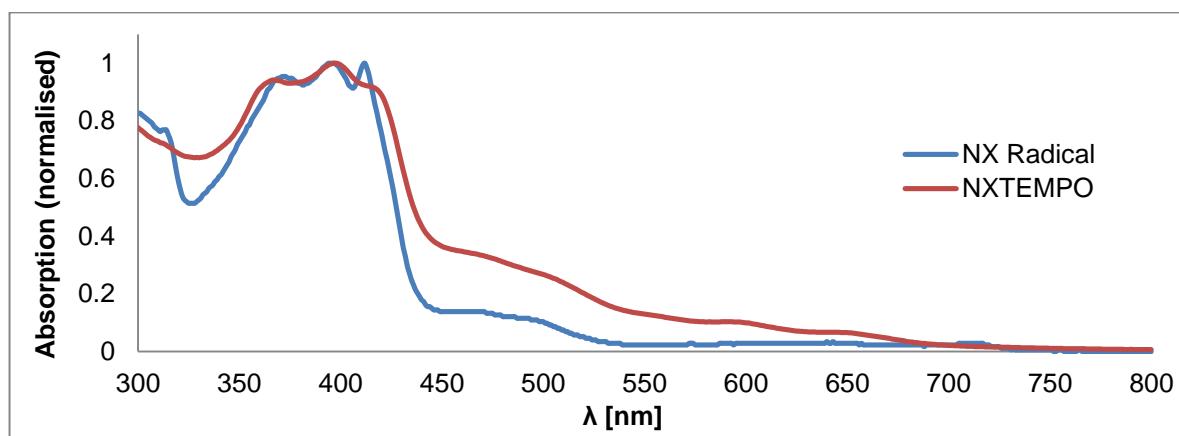


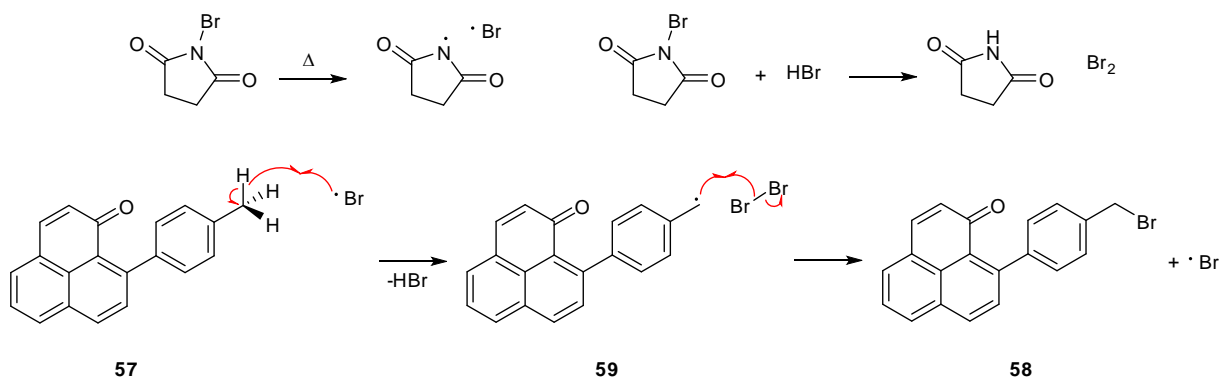
Figure 8.2.5.4 Normalised UV/Vis spectra of NXTEMPO (in MeCN) and NX (in DMSO).

8.3. Discussion

8.3.1. Synthesis

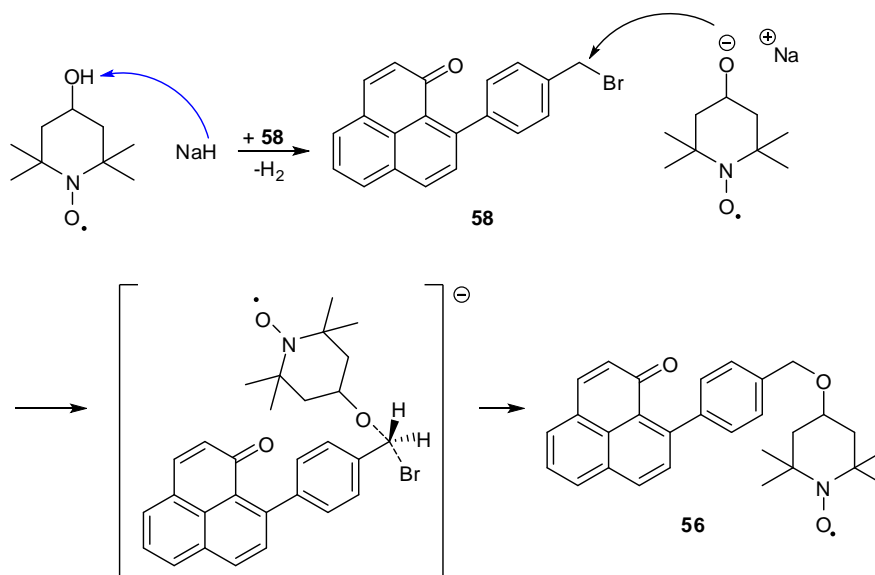
Based on the *Michael-Type Grignard* addition the synthesis of the precursor **57** could be achieved over two steps. The bromination using NBS proved to be an appropriate procedure to obtain **58** in a very good yield. Subsequently **58** could be successfully employed as precursor for both target compounds **54** and **56**. The two compounds have been submitted to our collaborator *Dr. Chris Kay (University College London)* for SDSL studies and advancing studies in terms of quantum information processing.

The bromination step proceeds through a typical radical chain reaction initiated by the homolytic cleavage of NBS into a succinimidyl and a bromine radical (*Scheme 8.3.1.1*). The bromine radical reacts with the substrate **57** at the methyl substituent generating the radical **59** and HBr. HBr reacts with NBS and forms bromine which in return can undergo a radical reaction with **59** yielding the desired compound **58**.



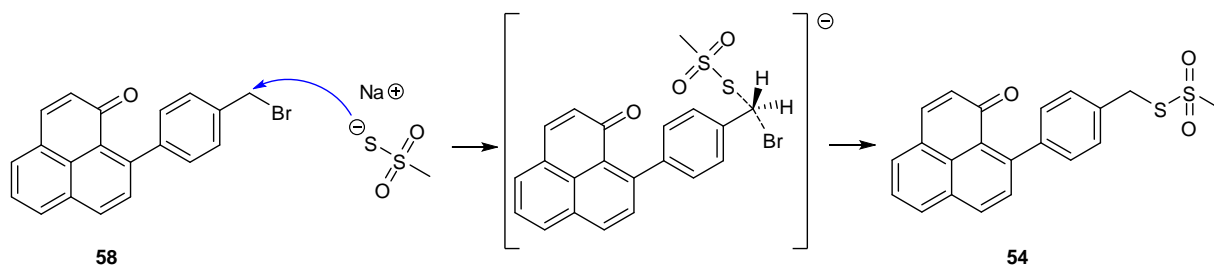
Scheme 8.3.1.1 Mechanism for the bromination of 9-(4-tolyl)-1*H*-phenalen-1-one **57** with NBS yielding 9-(4-(bromomethyl)phenyl)-1*H*-phenalen-1-one **58**.

The mechanism for **56** starts with the deprotonation of 2,2,6,6-tetramethylpiperidine-1,4-diol and subsequently undergoes nucleophilic substitution of S_N2 type at the brominated carbon (Scheme 8.3.1.2).



Scheme 8.3.1.2 Mechanism for the synthesis of 9-(4-(TEMPO-methyl)phenyl)-1*H*-phenalen-1-one **56** proceeding via S_N2 nucleophilic substitution.

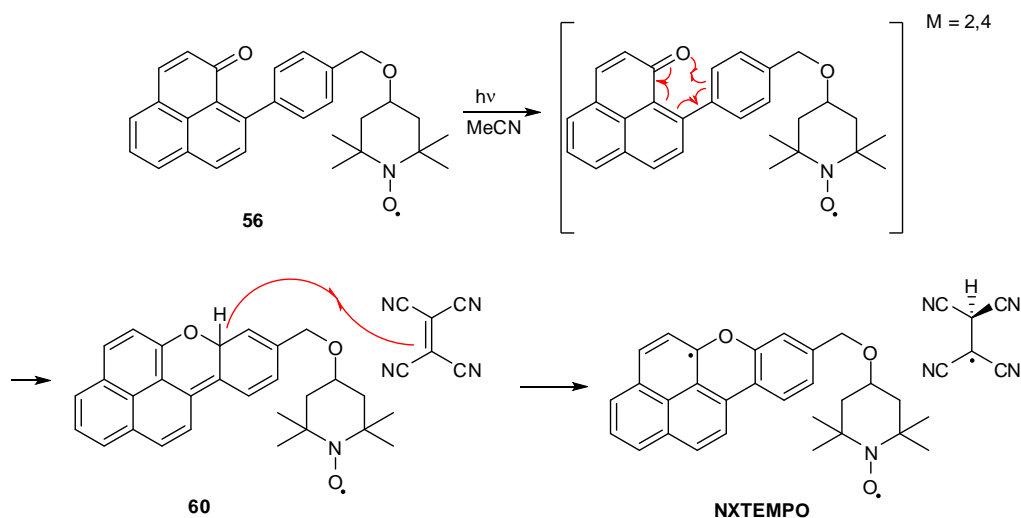
Similarly, compound **54** was prepared via a S_N2 nucleophilic substitution using NaMTS with **58** (Scheme 8.3.1.3).



Scheme 8.3.1.3 Mechanism for the synthesis of *S*-4-(1-oxo-1*H*-phenalen-9-yl)benzyl methanethiosulfonate **54** proceeding via S_N2 nucleophilic substitution.

8.3.2. Photolysis

The photolysis of **56** appeared to yield the desired conjugated radical substituted with a TEMPO group. *Scheme 8.3.2.5* depicts the proposed mechanism for the photolysis initiated by the excitation of **56** allowing β -phenyl quenching from either the doublet or quartet state.¹¹² In the presence of TCNE, hydrogen abstraction occurs yielding the target biradical NXTEMPO and 1,1,2,2-tetracyanoethyl radical.



Scheme 8.3.2.5 Proposed mechanism for the photolysis of 9-(4-(TEMPO-methyl)phenyl)-1*H*-phenalen-1-one **56**.

In the case of NXTEMPO, an ESR spectrum was obtained with a complicated hyperfine splitting at 3509 gauss. Unfortunately, a corresponding simulation of the spectrum could not be achieved. It is difficult to assign the spike at 3488 gauss. Either it is ascribed to the unconverted starting material **56** or the produced splitting of the TEMPO moiety of

NXTEMPO. According to the X-ray structure analysis of **56**, the determined distances of 7.780 -16.644 Å (hence below 25 Å) between the TEMPO-oxygen and the carbons of the 9-phenyl-1*H*-phenalen-1-one are indicative for intramolecular dipole-dipole interactions in NXTEMPO. Therefore, the lineshape for both units might be influenced so that attempts to simulate a corresponding spectrum were additionally difficult.

8.4. Conclusions

The syntheses of the target compounds **54** and **56** were accomplished via convenient procedures. In the case of **54**, SDSL studies will be performed to determine information of structural geometry of proteins employing the effect of dipole-dipole interactions. The photolysis of **56** appeared to be conducted successfully giving a persistent organic radical. However, the structural confirmation via simulation could not be carried out due to the complexity based on the asymmetry plus dipole-dipole interactions based on the TEMPO unit and the π -conjugated NX unit. The investigations of **56** for quantum information processing will be carried out through our collaborators in the future.

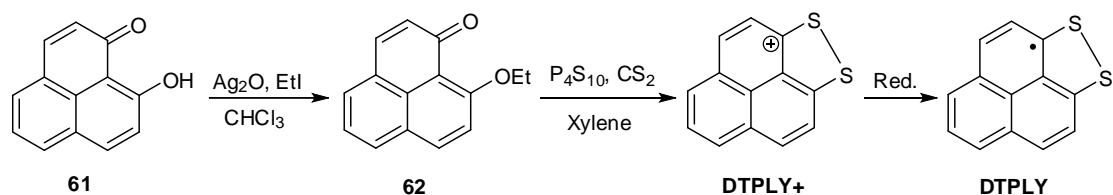
9. Functionalisation and structures of novel phenalenones and the first closed-shell phenalenyl involving an isoxazol group

9.1 Introduction

The substitution at the 9-C position of 1*H*-phenalen-1-one has been of permanent importance in synthetic chemistry regarding the production of new phototoxins through to phenalenyl based functional materials.

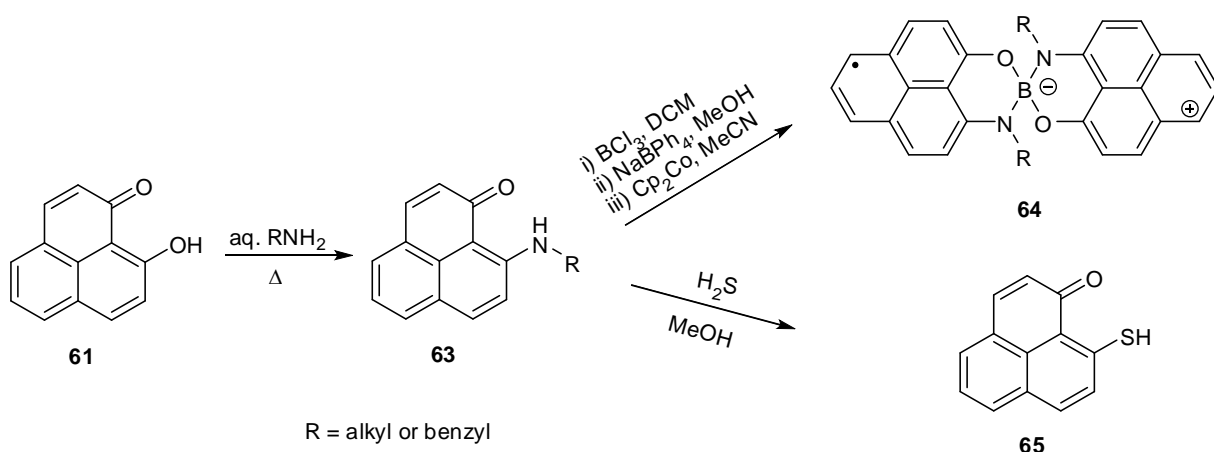
9-Aryl-1*H*-phenalen-1-ones are of fundamental interest according to intramolecular photochemical pathways competing with phototoxic properties involving singlet oxygen production.^{9,172,112} Since *Koelsch* and *Anthes* introduced the *Michael*-Type *Grignard* addition on 1*H*-phenalen-1-one at the 9-C position, a large series of 9-aryl-1*H*-phenalen-1-ones has subsequently been synthesized.^{122,127} However, the synthesis encountered difficulties when the desired *Grignard* reagent could not be generated due to sterical hinderance, for instance.^{181,241}

In terms of novel molecule-based functional materials, the functionalisation of the parent phenalenone is very useful to synthesise new phenalenyl based open-shell species.¹³³ For instance, for the synthesis of *Haddon's* prototype of an electronically stabilised phenalenyl radical, 1,9-dithiophenalenyl (DTPLY), 9-hydroxy-1*H*-phenalen-1-one needed to be transformed to 9-ethoxy-1*H*-phenalen-1-one to disrupt the strong intramolecular hydrogen bond between the two oxygens in the *peri* position.⁸⁷ This was achieved by introduction of an alkoxy group giving **62** so that subsequent replacement using phosphorus pentasulfide could be achieved yielding DTPLY⁺ which could then be reduced to DTPLY (*Scheme 9.1.1*).



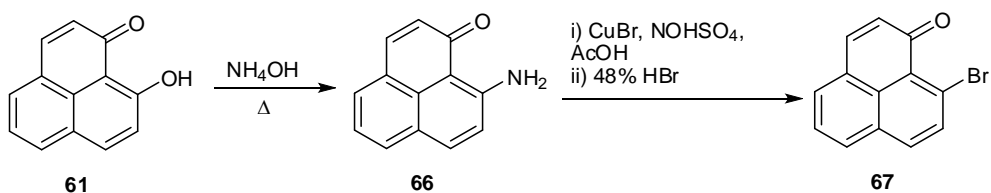
Scheme 9.1.1 Disruption of the intramolecular hydrogen bond in 9-hydroxy-1*H*-phenalen-1-one by introduction of an alkoxy group. Subsequently the formation of 1,9-dithiophenalenyl (DTPLY) could be achieved.

Further advances were made by introducing alkyl and benzylamines **63** which was crucial in allowing access to intriguing phenalenyl based radicals advancing novel types of molecule-based functional materials as such **64** (*Scheme 9.1.2*).^{143,147,242,243} As a side note, a sulfur derivative **65** was achieved by bubbling H₂S gas a MeOH solution containing **63**.²⁴⁴



Scheme 9.1.2 Introduction of alkyl and benzylamines. Resulting compounds **63** were subsequently employed for the preparation of a sulfur derivative **65** or a phenalenyl based radicals such as **64**.

The halogenation at the 9-C position can be found in only one publication. 9-Bromo-1*H*-phenalen-1-one **67** was prepared involving a multistep reaction using 9-amino-1*H*-phenalenone **66** with copper(I) bromide and nitrosyl sulfuric acid followed by treatment with 48% HBr.²⁴⁵ **66** can be prepared by direct amination of **61** using ammonium hydroxide at 125 °C (Scheme 9.1.3).²⁴²



Scheme 9.1.3 Preparation of 9-bromo-1*H*-phenalen-1-one **67** from 9-amino-1*H*-phenalen-1-one **66**. **66** can be prepared by direct amination using NH₄OH.

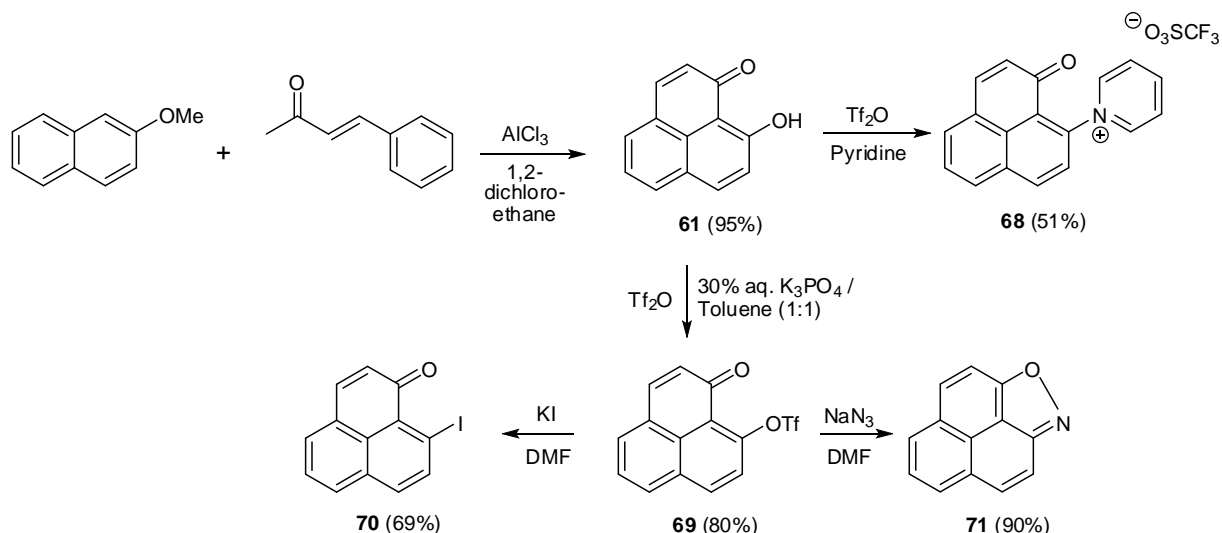
Considering these previous approaches, the substitution at the 9-C position of 1*H*-phenalen-1-ones has often attracted attention due to their required availability for substitution to form compounds of fundamental interest.^{122,123,246} As effective functional groups mainly alkoxy and amine groups are reported. Our group is particularly interested in an alternative synthesis of new 9-C substituted species which may be not accessible via previous conditions involving the *Michael*-type *Grignard* addition. Hence, the availability of a potential leaving group is desired.

In this chapter 1-oxo-1*H*-phenalen-9-yl triflate **69** may represent a useful substrate for an alternative synthesis towards new phenalenones and phenalenyl type species. The initial attempts to synthesize **69** from **61** with triflic anhydride in pyridine did not result in the desired compound. Surprisingly the salt 1-(1-oxo-1*H*-phenalen-9-yl)pyridinium triflate **68** was obtained instead. The synthesis of **68** was finally achieved using K₃PO₄ as a base. **68** subsequently gave access to 9-iodo-1*H*-phenalen-1-one **70** which should represent a better leaving group than 9-bromo-1*H*-phenalen-1-one **67**. Additionally, the closed shell phenalenyl molecule, phenaleno[1,9-*cd*]isoxazole **71** was synthesized. The substrates **69** and **70** are suggested for organometallic catalysis reactions for the future (e.g. *Stille*-, *Suzuki*-, *Negishi*-coupling).^{247,248,249}

9.2. Results

9.2.1. Synthesis

The synthesis of **61** was conducted according to the literature.²⁵⁰ This was achieved via a *Friedel-Crafts* acylation by portion-wise addition of AlCl_3 to a mixture of 2-methoxynaphthalene and cinnamoylchloride in 1,2-dichloroethane (*Scheme 9.2.1.1*). Subsequently the reaction was acidified in ice-water containing HCl. The desired compound was obtained in a yield of 95% (lit.: 54.4% after sublimation) without any further purification (see *Appendix 39* & **40** for full ^1H - and ^{13}C -spectra).



Scheme 9.2.1.1 Synthetic routes to 1-oxo-1H-phenalen-9-yl triflate **69**, 1-(1-oxo-1H-phenalen-9-yl)pyridinium triflate **68**, 9-iodo-1H-phenalen-1-one **70** and phenaleno[1,9-cd]isoxazole **71**.

The synthesis of **69** was conducted by adding Tf_2O gradually to a stirred bilayer of toluene dissolving **61** and a 30% aqueous K_3PO_4 solution.²⁵¹ The organic layer was separated and evaporated to dryness. Further purification was carried out via column chromatography to give a pale yellow powder in a yield of 80%. **69** appeared to be very stable and could be stored under air without decomposition.

When pyridine was used as a base, only traces of the desired compound including starting material were obtained. It was noticed that a large amount of material was dissolved in the aqueous pyridine solution. This could not be extracted using organic solvents such as ethyl acetate or diethylether. The aqueous layer was left overnight in the fumehood until dark brown

needles were formed. Those were separated by filtration and revealed to be **68** obtained in a yield of 51%.

9-Iodo-phenalenone **70** could be conveniently synthesised by nucleophilic substitution using **69** as a precursor. This resulted in the desired compound in a yield of 69% after column chromatography.

71 was synthesised by treatment of **69** with sodium azide in DMF at room temperature. The azide substituted phenalenone appeared to be very unstable at room temperature and underwent thermolytic cyclisation giving the isoxazole in a yield of 90%.²⁵² Phenalenyl itself represents the smallest open-shell graphene fragment which is in the case of **71** transformed to a closed shell by incorporation of two different heteroatoms. That is, compound **71** may represent an interesting molecule from the fundamental point of view.

9.2.2 ¹H-NMR spectroscopy

The assignment of the signals in the ¹H-NMR spectra could be largely made with the aid of the collected data in *Table 7.2.3.1* (*Chapter 7*; Discussion). In the case of **68** the proton at the 2-position was assigned to the doublet at 6.53 ppm with $J = 9.8$ Hz (*Figure 9.2.2.1*; see *Appendix 41 & 42* for full ¹H- and ¹³C-spectra). This couples with the doublet at 7.96 ppm. The doublet at 8.65 ppm exhibits a coupling constant of $J = 8.6$ Hz which couples with the doublet at 7.90 ppm ($J = 8.5$ Hz). Those are assigned to the 7- and 8- position, respectively. The latter signal is overlapped by a signal representing the 5-position. A multiplet at 8.24 ppm represents two protons which are interpreted as the 3'- and 5'-position of the pyridinium ring. Due to the roof effects regarding the two doublets at 8.10 ppm ($J = 7.0$ Hz) and 8.33 ppm ($J = 8.4$ Hz), these peaks are assigned to the 4- and 6-position coupling with the signal representing the 5-position. The two detected signals at lowfield, a multiplet representing two protons and a triplet of triplet, are found to be the protons at the 2'- and 6'-position and the 4'-position respectively. The chemical shift at lowfield is ascribed to the positive charge of the pyridinium ring.

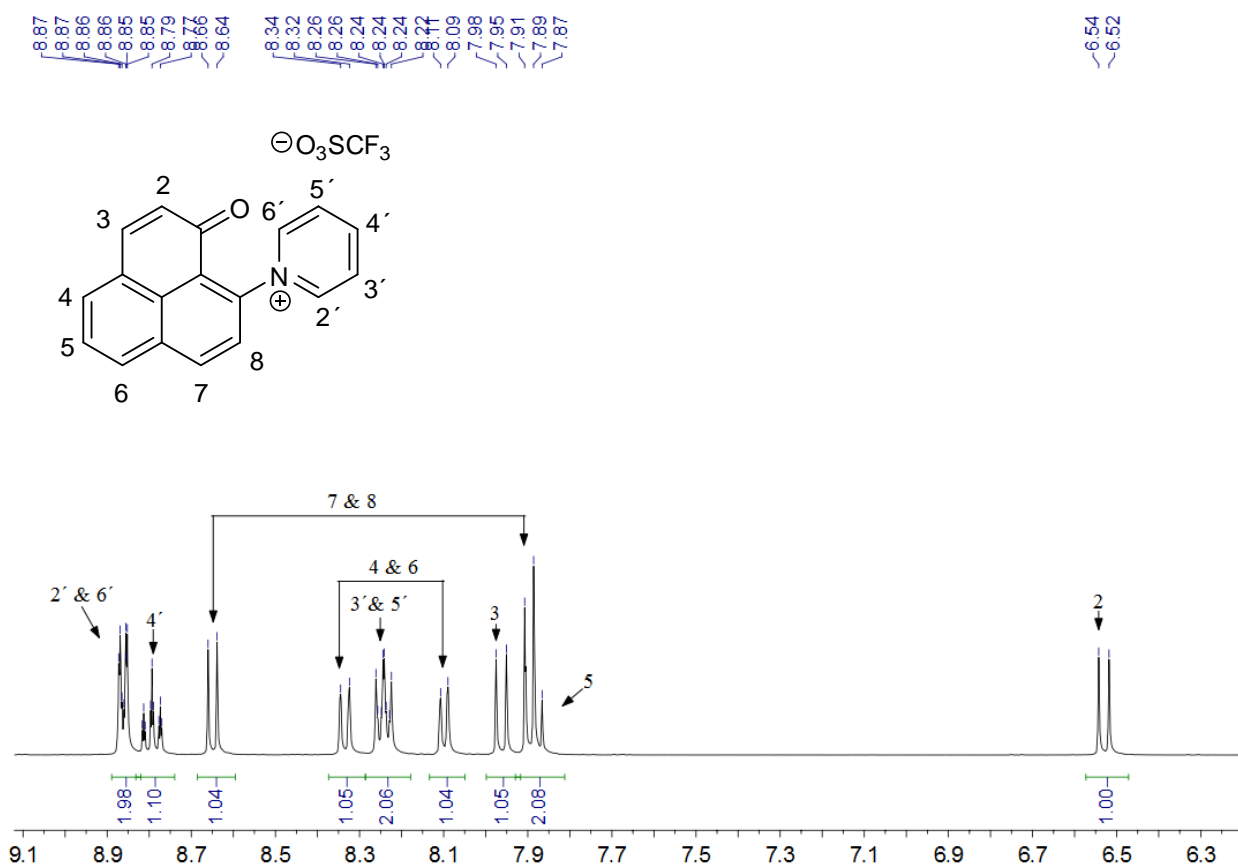


Figure 9.2.2.1 ^1H -NMR spectrum of 1-(1-oxo-1*H*-phenalen-9-yl)pyridinium triflate **68** measured at room temperature (400 MHz; CD_3CN).

In the case of **69**, the detected signals are similar to the obtained chemical shifts and coupling constants from previously synthesised arylphenalenones. At 6.65 ppm ($J = 9.8$ Hz), the doublet is found to be the proton at the 2-position which couples with the doublet at 7.67 ppm (*Figure 9.2.2.2*; see *Appendix 43 & 44* for full ^1H - and ^{13}C -spectra). The characteristic ABX spin system is assigned to the doublet of doublets at 7.62 ppm ($J = 8.3, 7.1$ Hz). This couples with the protons at the 6- and 4-position at 7.98 ppm ($J = 8.3, 0.8$ Hz; observed as doublet of doublets) and 7.77 ppm ($J = 6.6$ Hz), respectively. The protons at the 7- and 8-positions are then be found at 8.22 ppm ($J = 8.9$ Hz) and 7.52 ppm ($J = 8.8$ Hz).

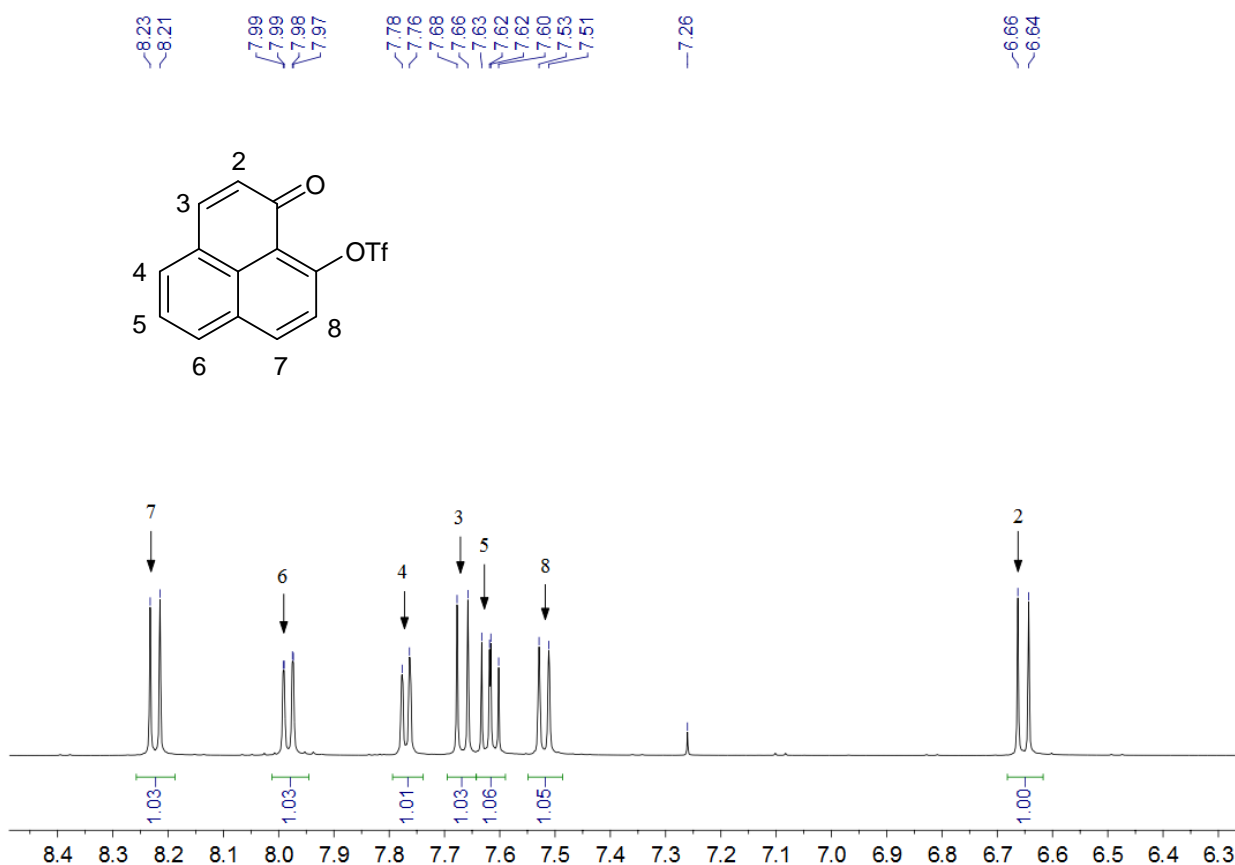


Figure 9.2.2.2 ^1H -NMR spectrum of 1-oxo-1*H*-phenalen-9-yl trifluoromethanesulfonate **69** measured at room temperature (400 MHz; CD_3CN).

The ^1H -NMR spectrum of **70** shows the signals for the protons at the 2- and 3- positions at 6.79 ppm and 7.66 ppm with a coupling constant of $J = 9.7$ Hz, respectively (*Figure 9.2.2.3*; see *Appendix 45 & 46* for full ^1H - and ^{13}C -spectra). The protons at the 7- and 8-positions are found at the 8.37 ppm ($J = 8.5$ Hz) and 7.70 ppm, respectively. The latter signal is overlapped by a doublet representing the 4-position. The proton at the 5-position is detected as a doublet of doublets at 7.61 ppm ($J = 8.1, 7.1$ Hz). The proton at the 6-position is represented by a doublet of doublets at 7.97 ppm ($J = 8.2, 0.9$ Hz).

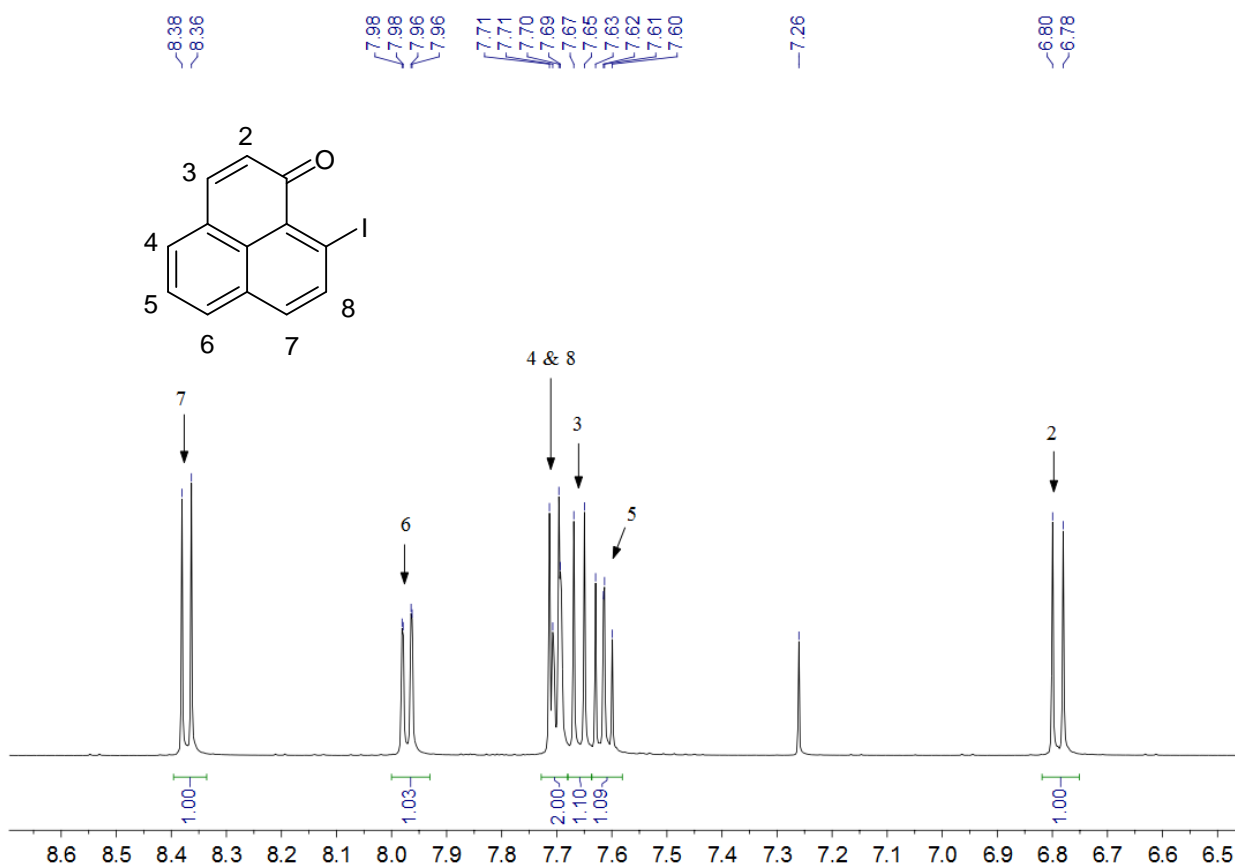


Figure 9.2.2.3 ^1H -NMR spectrum of 9-iodo-1*H*-phenalen-1-one **70** measured at room temperature (500 MHz; CDCl_3).

In the case of **71**, the chemical shifts show a distinct divergence compared to the previously prepared 9-C substituted phenalenones. The chemical shift for the proton at the 2-positions is found more lowfield at 7.73 ppm with a coupling constant of $J = 9.4$ Hz (Figure 9.2.2.4; see Appendix 47 & 48 for full ^1H - and ^{13}C -spectra). The proton at the 3-position can be assigned to the doublet at 7.99 ppm exhibiting an identical coupling constant of $J = 9.4$ Hz. A typical ABX spin system can be found at 7.90 ppm ($J = 8.1, 7.4$ Hz). Hence, the corresponding peaks for the protons at the 4- and 6-positions can be assigned to the two doublets at 8.27 ppm ($J = 8.1$ Hz) and 8.13 ppm ($J = 7.4$ Hz), respectively. The two protons at the 7- and 8-positions are then assigned to the two doublets at 8.24 ppm and 7.95 ppm ($J = 9.0$ Hz), respectively.

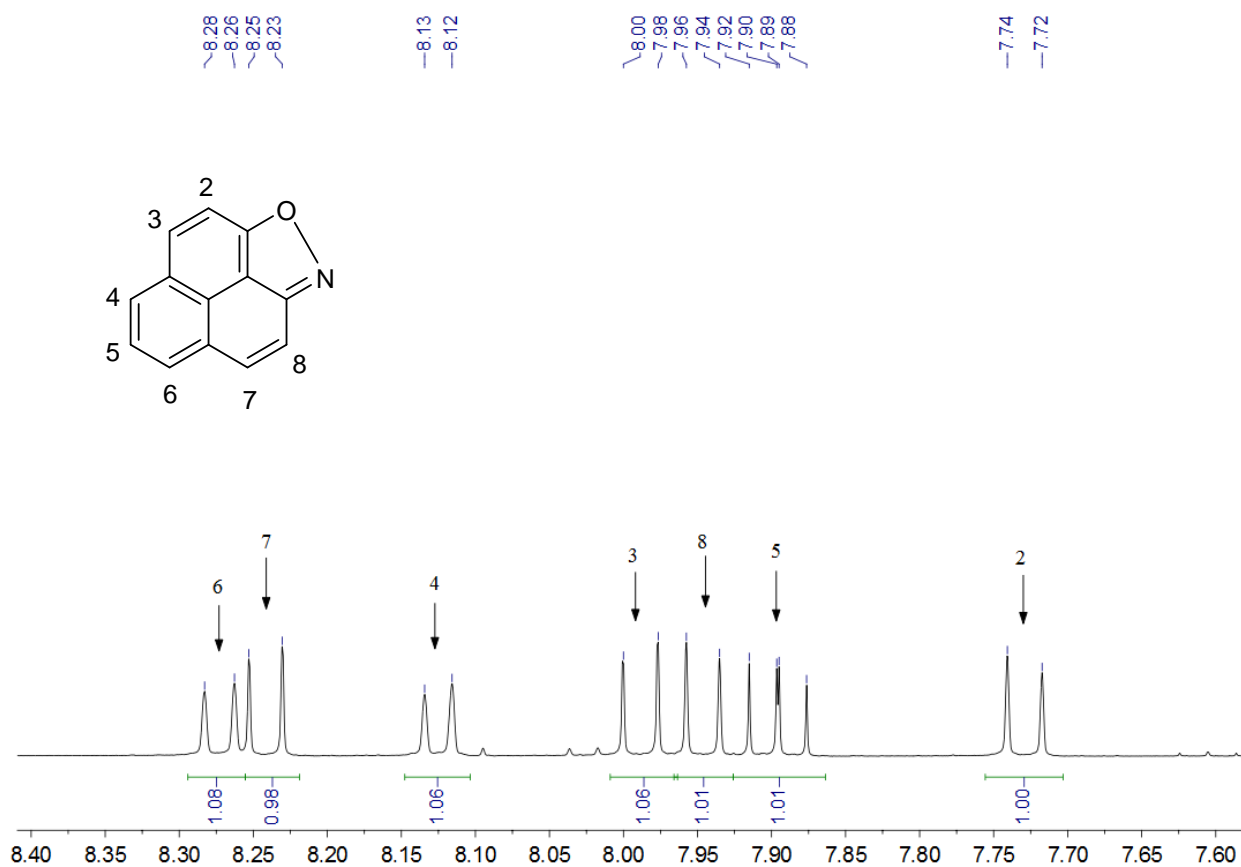


Figure 9.2.2.4 $^1\text{H-NMR}$ spectrum of phenaleno[1,9-*cd*]isoxazole **71** measured at room temperature (400 MHz; CDCl_3).

9.2.3. UV/Vis spectroscopy

Figure 9.2.3.1 shows the normalised UV/Vis spectra of **68-71** between 300-800 nm. For comparison purposes the absorption spectrum of the parent 1*H*-phenalen-1-one (PN) with a maximum absorption peak at 354 nm and a broader peak at 376 nm is also presented. Comparing the spectra of **68** and **69** with the spectrum of PN, similarities can be observed with maximum absorption peaks at 354 nm and 358 nm and broad absorption at 383 nm and 389 nm, respectively. For **68** the broad absorption exhibits a higher intensity with a slight bathochromic shift compared to **69**. In the case of **70**, a maximum absorption peak at 358 nm and a distinctly lower absorption from 380 nm until 420 nm can be observed. The phenalenyl-based isoxazol compound **71** exhibits a hypsochromical shift for the maximum absorption with 328 nm compared to PN (UV/Vis spectrum from 200 nm can be found in *Appendix 80*). Furthermore, moderate absorption peaks occur at 314 nm (sharp) and 340-360 nm (broad).

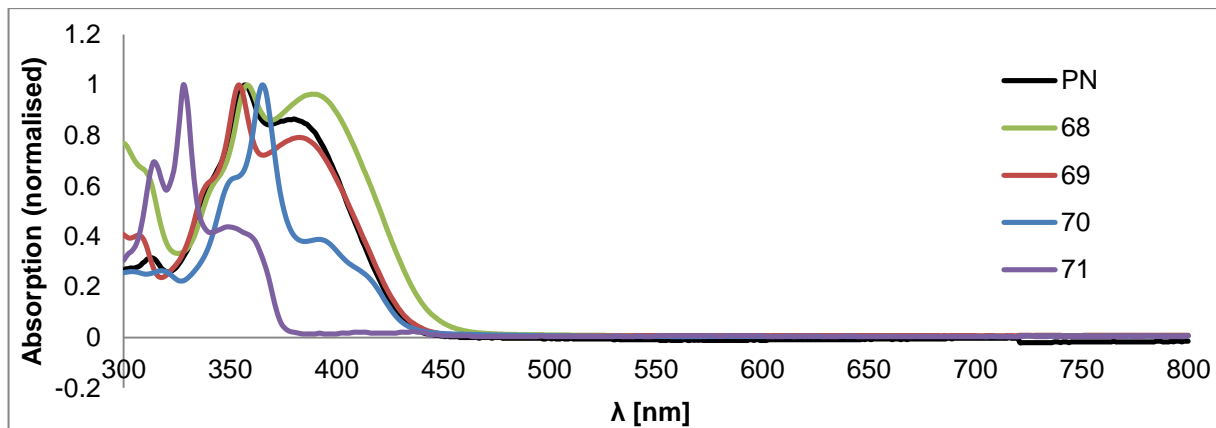


Figure 9.2.3.1 Normalised UV/Vis spectra of 1*H*-phenalen-1-one (PN), 1-(1-oxo-1*H*-phenalen-9-yl)pyridinium triflate **68**, 1-oxo-1*H*-phenalen-9-yl trifluoromethanesulfonate **69**, 9-iodo-1*H*-phenalen-1-one **70** and phenaleno[1,9-*cd*]isoxazole **71**.

9.2.4 X-ray structure analysis

Yellow Crystals of **68** were obtained from acetone. The X-ray structure analysis shows a large orthorhombic space group incorporating acetone molecules in a ratio 1:2 (*Figure 9.2.4.1*; see also *Appendix 67 & 68*). The intermolecular contacts between acetone and pyridinium molecules ranging a distance between 3.124 Å and 3.691 Å can be found in *Table 9.2.4.1* and are sketched in *Figure 9.2.4.2*). There are no indications for considerable π -stacking interactions representing the driving force for the crystal packing.

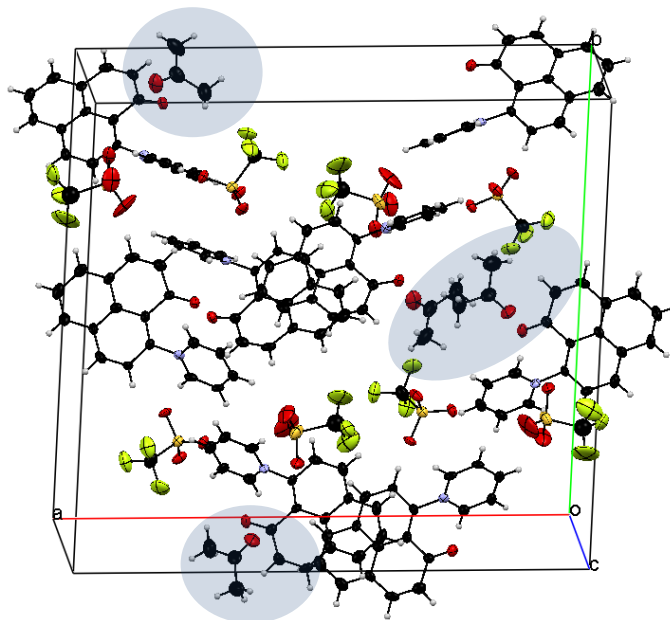


Figure 9.2.4.1 Orthorhombic space group of 1-(1-oxo-1*H*-phenalen-9-yl)pyridinium triflate **68**.

Contacts	Distance
a	3.315
b	3.456
c	3.691
d	3.362
e	3.162
f	3.379
g	3.554
h	3.124
i	3.554

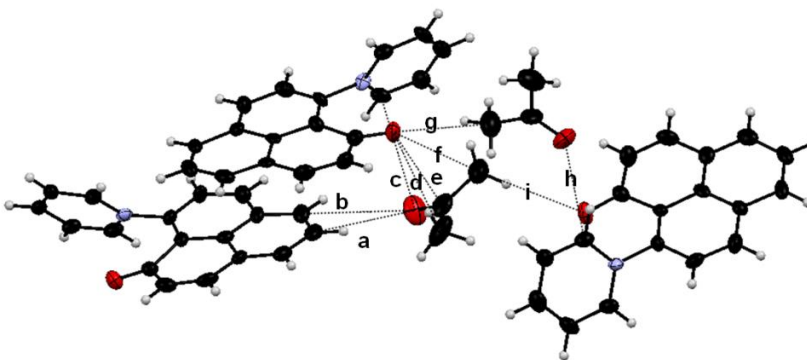


Table 9.2.4.1 Distances between acetone and 1-(1-oxo-1*H*-phenalen-9-yl)pyridinium molecules **68**.

Figure 9.2.4.2 Intermolecular contacts between acetone and 1-(1-oxo-1*H*-phenalen-9-yl)pyridinium**68** molecules in the crystal structure.

X-ray diffraction of **69** shows a monoclinic space group involving 12 molecules (*Appendix 69 & 70*). These are separated by π -stacking interactions to a moderate extent. The shortest interplanar separations observed are 3.366 Å and 3.396 Å (*Figure 9.2.4.4*). The triflate groups are able to rotate in solution. In the crystal, different conformations are given which appear to tilt the stacking arrangement (*Figure 9.2.4.3*).

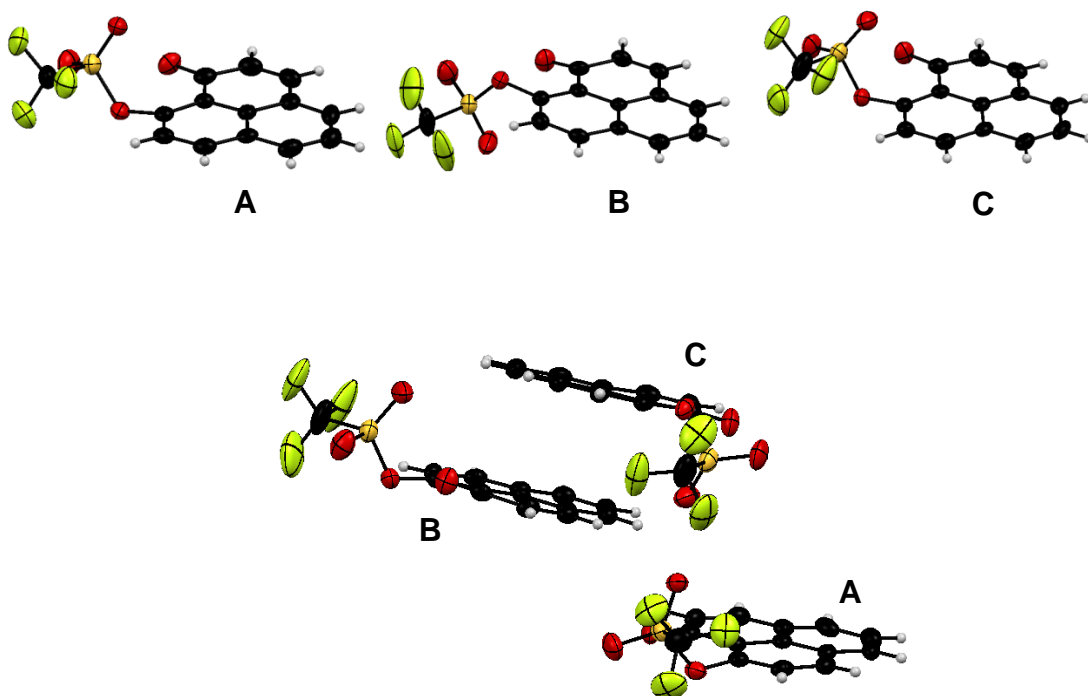


Figure 9.2.4.3 Conformations of 1-oxo-1*H*-phenalen-9-yl triflate **69** in the crystal structure.

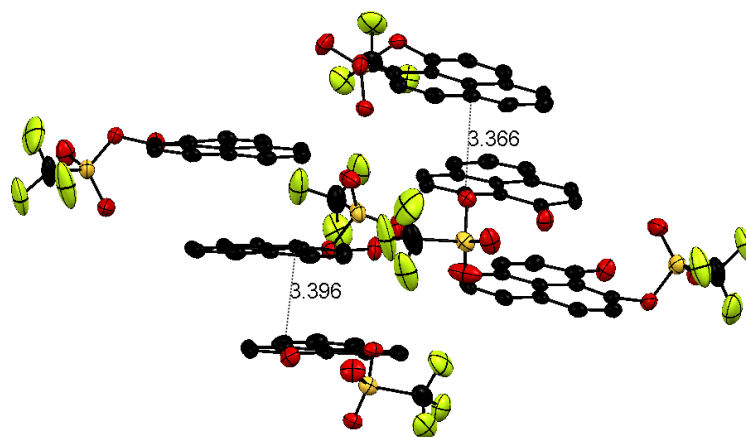


Figure 9.2.4.4 Shortest interplanar distances observed in the crystal structure of 1-oxo-1*H*-phenalen-9-yl triflate **69**. Above the conformational isomers related to the depicted stacking arrangement.

In the case of **70**, 8 molecules are arranged in a monoclinic space group. π -stacking interactions can be observed with lengths of 3.417 Å, 3.374 Å and 3.589 Å (Figure 9.2.4.5; Table 9.2.4.2; see also Appendix 71 & 72). Intermolecular iodine-iodine contacts are separated by 3.811 Å.

Contacts	Distance
A	3.417
B	3.374
C	3.589
d	3.811

Table 9.2.4.2 Distance between iodine atoms and interplanar distances between pairs of 9-iodo-1*H*-phenalen-1-one **64**.

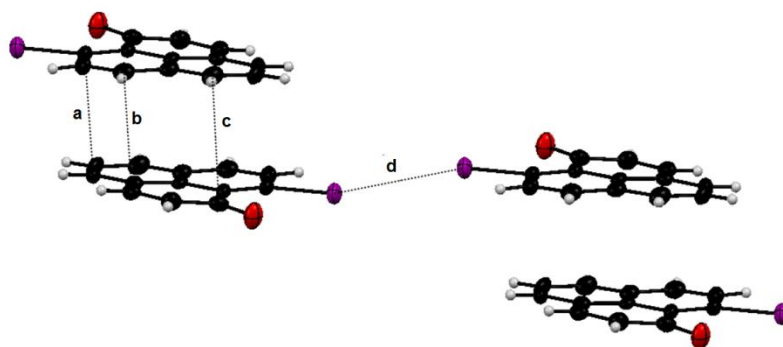


Figure 9.2.4.5 Stacking arrangement of 9-iodo-1*H*-phenalen-1-one **70** in the crystal structure.

Compound **71** does not exhibit π -stacking interactions between the phenalenyl framework (see also *Appendix 73 & 74*). Instead, the molecules are aligned in a parallel manner. Those are in return arranged perpendicular to the neighbouring aligned molecules (*Figure 9.2.4.6*). It is noteworthy, that two disorderd parts are shown at two positions with 50% occupancy, thus **71** is shown as a molecule incorporating two isoxazole groups (*Figure 9.2.4.7*). The extremely short intermolecular separations of 2.321 Å between the nitrogen and oxygen atoms are outside the typical distance, in fact such short contact distances have not been observed.²⁵³ Hence this part can be considered as an artifact due to above mentioned disorder in the crystal structure. This result is not based on the quality of the crystals but the nature of the crystal structure of **71**. Thus improved crystal quality would give the same result. Reasonable contact distances involving the heteroatoms can be assigned to the separation between the oxygen and two hydrogen atoms with 2.536 Å and 2.601 Å, respectively (*Figure 9.2.4.8*). In addition, N-H interactions of 2.572 Å can be observed along the aligned molecules (*Figure 9.2.4.7*).

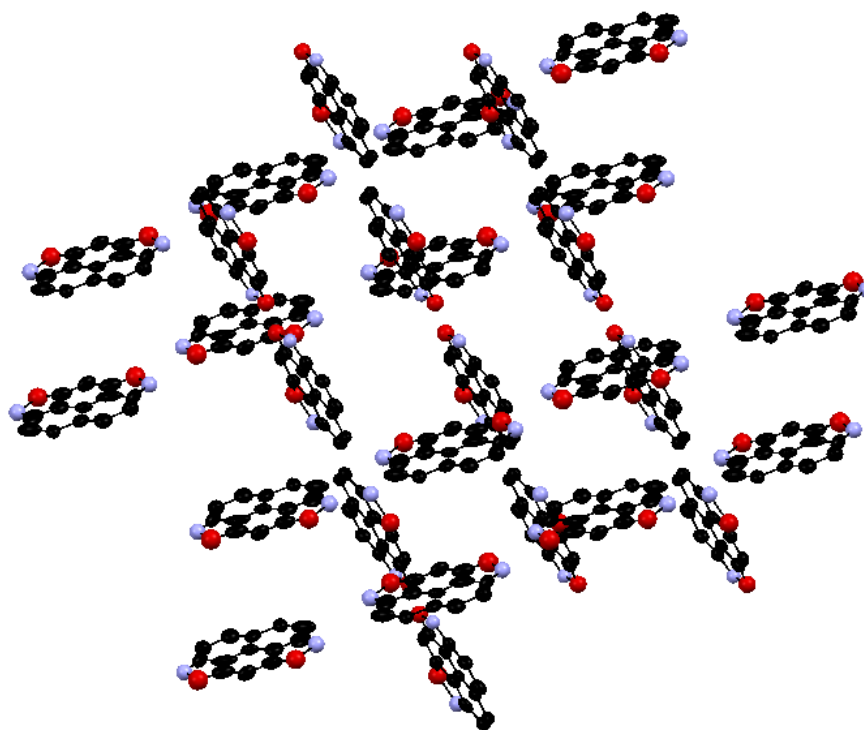


Figure 9.2.4.6 Intermolecular arrangement of phenaleno[1,9-*cd*]isoxazole **71** in the crystal structure.

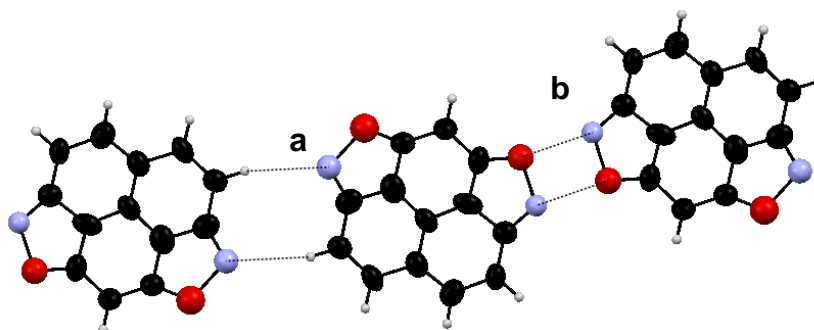


Figure 9.2.4.7 Intermolecular interactions between phenaleno[1,9-*cd*]isoxazole **71** molecules along the aligned arrangement ($a = 2.572 \text{ \AA}$; $b = 2.321 \text{ \AA}$).

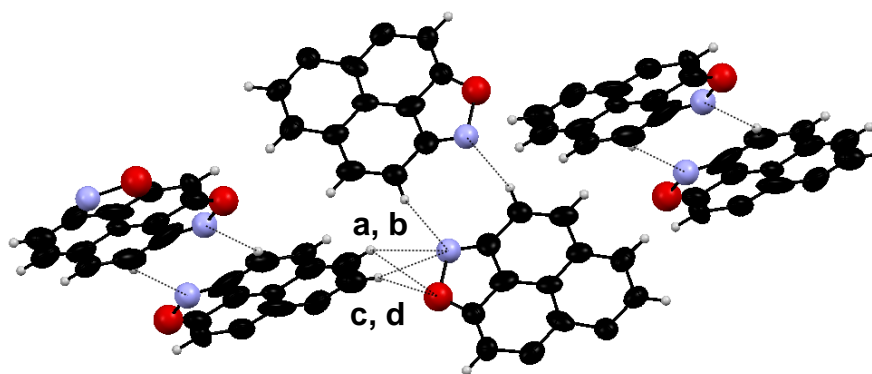
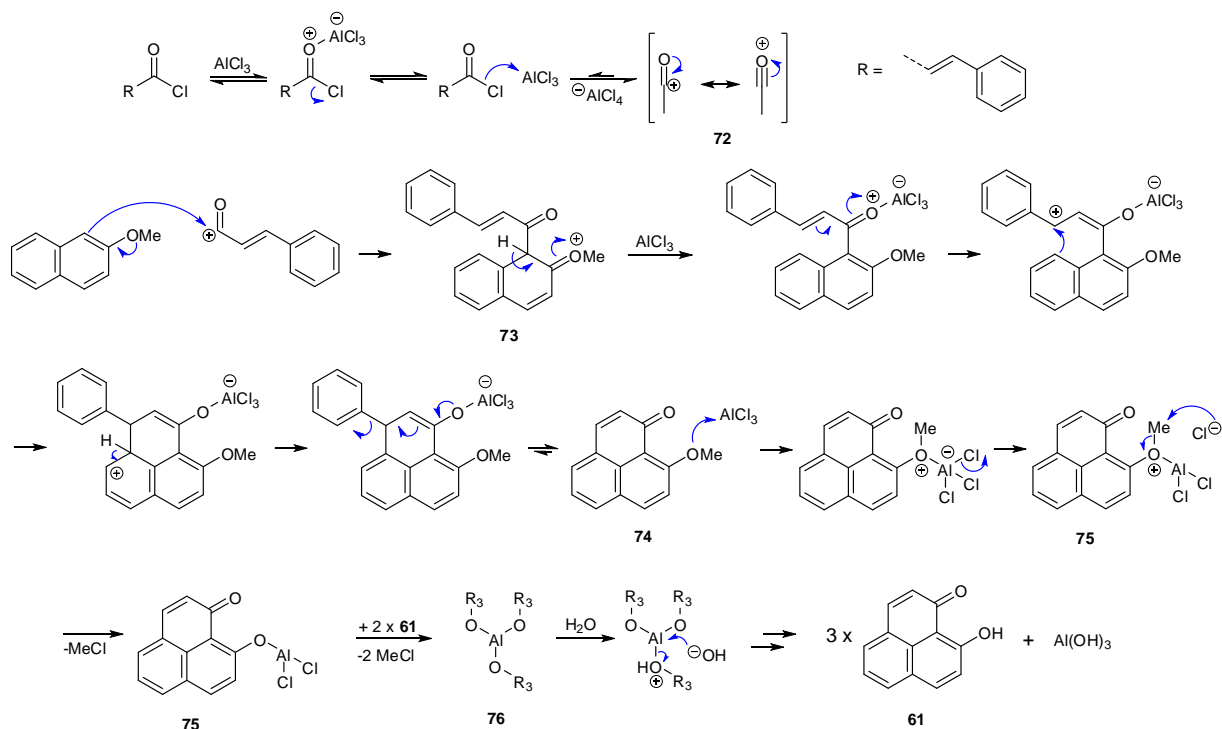


Figure 9.2.4.8 Intermolecular interactions between phenaleno[1,9-*cd*]isoxazole **71** molecules involving oxygen and hydrogen atoms (a, b (N-H contacts) = 2.657 Å, 2.494 Å; c, d (O-H contacts) = 2.536 Å, 2.601 Å). Isoxazol groups presumed as an artifact are hidden.

9.3. Discussion

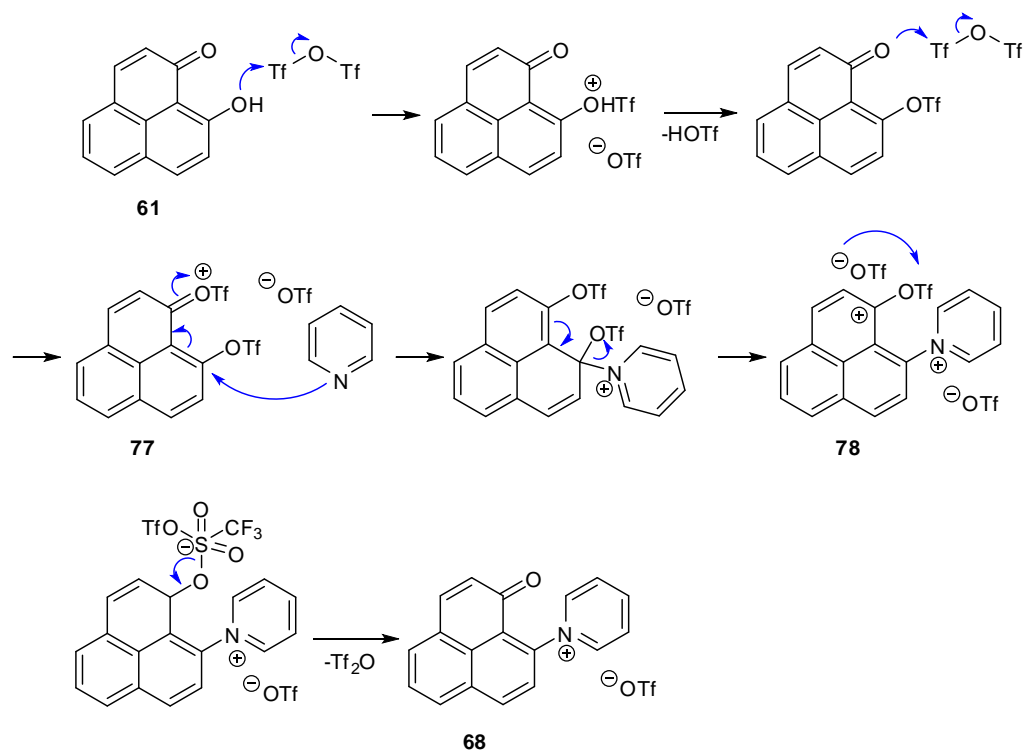
9.3.1. Synthesis

The synthesis of the starting material **61** was achieved via a *Friedel-Crafts* acylation. Starting with the coordination of AlCl_3 with cinnamoylchloride, the subsequent removal of chloride gives the resonance stabilised cation **72** (*Scheme 9.3.1.1*). Alternatively the removal of chloride can occur directly with the same result. At the 1-position of the naphthalene, electrophilic aromatic substitution yields intermediate **73** undergoing deprotonation to reestablish the aromaticity. The resulting α,β -unsaturated carbonyl compound then undergoes an anomalous elimination of the phenyl group resulting **74**. *R.C. Fuson* described the loss of benzene referring to the reversibility of the *Friedel-Crafts* condensation.²⁵⁴ According to this, α,β -unsaturated carbonyl compounds which are substituted at the β -carbon tend to rather undergo hydrogenation than condensation with benzene in presence of AlCl_3 . Since the solvent used is 1,2-dichloroethane, the loss of the phenyl group is expected yielding **74**. The residual methoxy group is demethylated as AlCl_3 also works as a potential deprotection reagent. The mechanistic scenario for the deprotection initially proceeds with a coordination of the oxygen with the metal atom. Subsequently $\text{S}_{\text{N}}2$ nucleophilic substitution leads to the formation of methylchloride and alkoxyaluminum **75**. This process can be repeated through to the formation of trialkoxy aluminum **76**. By treatment with water aluminum hydroxide and product **61** will be obtained.



Scheme 9.3.1.1 Mechanism for the synthesis of 9-hydroxy-1H-phenalen-1-one **61** involving a *Friedel-Crafts* acylation and demethylation.

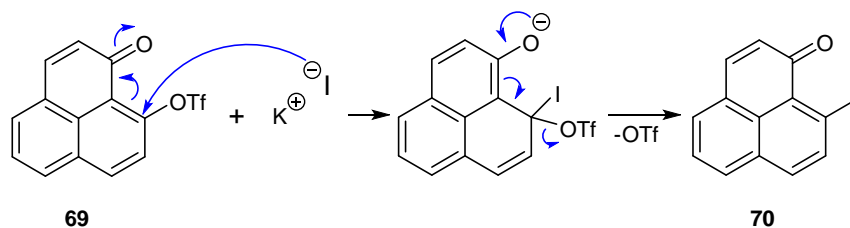
The result of **68** from **61** with Tf₂O in pyridine was surprising. Initially it was assumed that **69** was generated and subsequently substituted by pyridine. Therefore, compound **69** was stirred in pyridine to observe if **69** is readily reactive with the used base. However, only starting material could be isolated. Hence, an excess of Tf₂O appeared to be required. Subsequently **69**, dissolved in pyridine, was treated with 1 eq of Tf₂O. As a result, **68** was obtained in a moderate yield of 36%. Hence, a possible mechanism is based on a second nucleophilic attack from the remaining ketone on Tf₂O (*Scheme 9.3.1.2*). It is assumed that **77** will be subsequently attacked by a pyridine molecule. Then cleavage of one triflate group results in a dicationic intermediate **78**. Subsequently a triflate anion may attack the sulfur atom of the triflate group and generates **68** and trifluoromethanesulfonic anhydride. Hence, this reaction is proposed to proceed catalytically.



Scheme 9.3.1.2 Proposed mechanism towards 1-(1-oxo-1*H*-phenalen-9-yl)pyridinium triflate **68**.

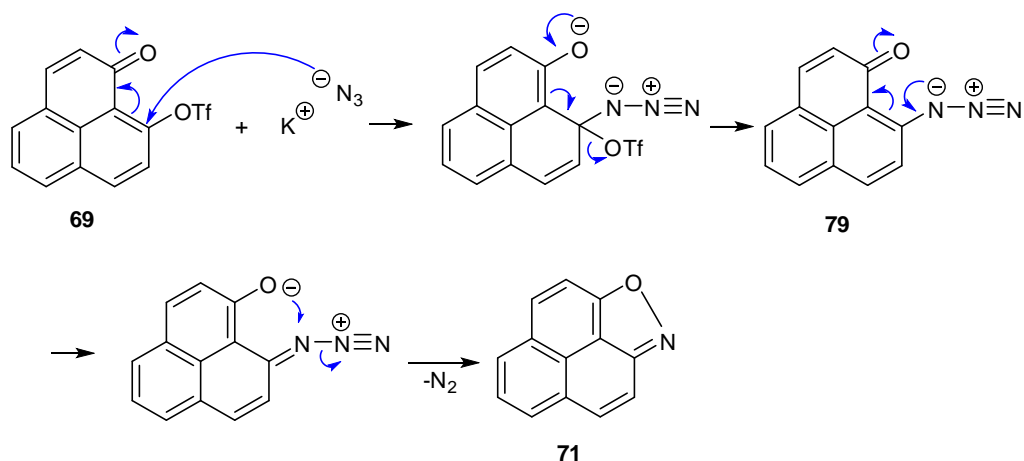
Eventually, the synthesis of **69** could be achieved using aqueous K_3PO_4 (30%) in a bilayer mixture with toluene. Again a doubly substituted triflate cation **77** is postulated which will be rapidly attacked by water. As a triflate group is considered as a better leaving group than hydroxide, the ketone will be formed resulting in the desired compound **69**.

The syntheses of **70** and **71** are based on nucleophilic substitution reactions ($\text{S}_{\text{N}}\text{Ar}$). In the case of **70**, iodide attacks the partially positively charged carbon involving a delocalisation of a negative charge on the oxygen of the former ketone (*Scheme 9.3.1.3*). Subsequently the ketone will be formed again involving the cleavage of a trifluoromethanesulfonate giving the desired product.



Scheme 9.3.1.3 Mechanism towards 9-iodo-1*H*-phenalen-1-one **70** via nucleophilic substitution.

Similarly **71** was formed involving an unstable azide **79** which could not be isolated at room temperature as a rapid isoxazole formation proceeded with release of nitrogen yielding **71** (Scheme 9.3.2.4).²⁵² Ideally, this reaction is carried out with a full conversion of starting material as **71** appears to decompose while column chromatography is carried out. Therefore, the experiment was conducted under mild conditions and the product was recrystallised from ether extracts.



Scheme 9.3.2.4 Mechanism towards phenaleno[1,9-*cd*]isoxazole **71** via nucleophilic substitution involving thermolytic cleavage of nitrogen.

9.3.3. X-ray structure analysis

According to the X-ray structure analysis for **68-71**, only general interpretations were considered in this thesis. In **65**, intermolecular contact distances between nitrogen and oxygen atoms of 2.321 Å are shown, which must be an artifact with regards to reported histograms of intermolecular N-O separations.²⁵³

As far as **68**, **69** and **71** are concerned, it can be summarized that there are no indications for a considerate driving force for crystallisation based on π - π stacking interactions. This is due to the disruptive effects of the large substituents. The pyridinium salt **68** also incorporates acetone in its crystal lattice which additionally influences the arrangement and may even enhance the driving force for the crystallisation process. The release of acetone under vacuum and heat supply was not attempted to see if the crystal structure would suffer from the disruption by the exclusion of acetone. In the case of **70**, expectedly intermolecular contacts

between iodine atoms are observed. Among the presented species, **70** exhibited the highest degree of π - π stacking interactions.

9.4. Conclusions

The compounds **69** and **70** are valuable to achieve or improve the synthesis of new 9-C substituted phenalenones which are difficult to access or may not be even possible with the previously used synthetic methods. As an example, the employment of organometallic catalysts could be considered to provide advances in the synthesis of novel molecules based on phenalenyl.^{255,256} Isoxazole is interesting in its own right as it represents the first closed shell phenalenyl species realised by incorporation of an isoxazole group. Future work could involve investigations on the physical properties as well as their application in alternative synthetic routes to novel 9-C substituted phenalenones or phenalenyl based functional materials.

10. HOMA evaluation and cyclic voltammetry results of BNAX⁺

10.1 Introduction

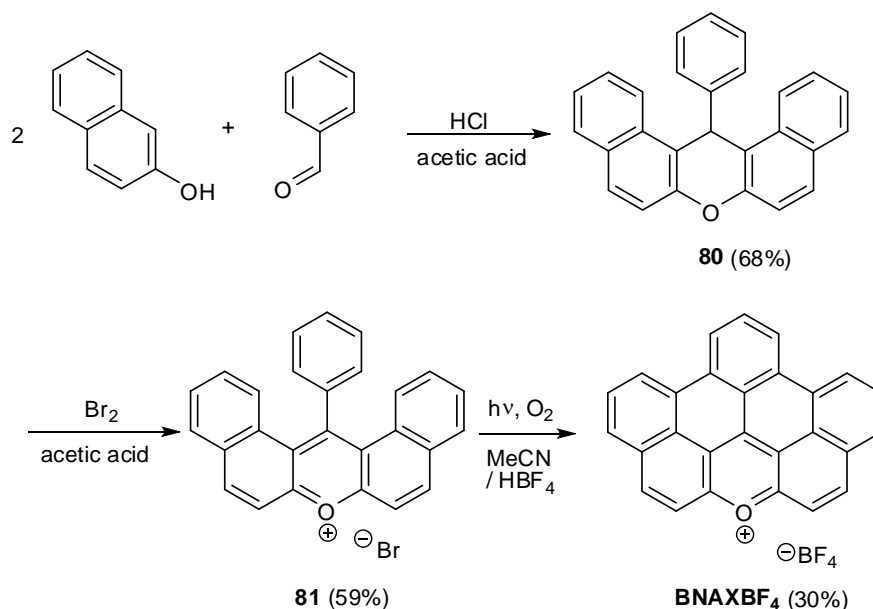
The research on heteroatom containing PAHs has been widely developed in terms of functional materials based on optoelectronic and electronic properties.^{257,258,259} Among them, large PAHs incorporating a pyrylium ring are rarely present in the literature due to the difficulty of their synthesis.^{260,261} Müllen *et. al.* introduced the largest synthesised pyrylium type PAH, the Benzo[5,6]naphthaceno[1,12,11,10-*ijklmna*]xanthyl cation (BNAXBF₄) to the area of supramolecular chemistry, for the first time.^{20,262} They were particularly interested in their discotic self-assembling structures provided by the substitution of alkyl chains leading to liquid crystalline materials with semiconducting properties. In contrast to that, this chapter deals with the evaluation of the aromaticity of BNAX⁺, using HOMA. The X-ray structure analysis of BNAX⁺ in its solid crystal structure is achieved so that HOMA indices in the PAH framework of BNAX⁺ can be determined using the obtained bond lengths data. In addition, cyclovoltammetry studies were carried out to measure the corresponding radical and to determine the amphotericity value analogous to previously described naphthoxanthenium cations in *Chapter 7*. Hence, with the perspective on heterocyclic π -radicals, BNAX⁺ was also considered a precursor for a stable open shell species.

10.2 Results

10.2.1. Synthesis

The synthesis of BNAX^+ was achieved in three steps following the reported procedure.²⁰ The last step, involving the photooxidation reaction, was carried out using MeCN instead of acetic acid.

The preparation of 14-phenyl-14*H*-dibenzo[*a,j*]xanthenes **80** proceeds conveniently in a yield of 68% (lit.: 60 %).²⁰ Two equivalents of 2-naphthol react with 1 eq of benzaldehyde yielding **80**, in presence of a catalytic amount of concentrated HCl, in acetic acid under reflux (*Scheme 10.2.1.1*).



Scheme 10.2.1.1 Synthesis towards Benzo[5,6]naphthaceno[1,12,11,10-*ijklmna*]xanthylium tetrafluoroborate BNAXBF_4 .

The next step involved the dehydrogenation of **80** resulting in 14-phenyldibenzo[*a,j*]xanthenium bromide **81**. This was achieved in a yield of 59%, obtained as red crystals with a golden lustre (lit.: 83%).²⁰

In contrast to the described procedure from the literature, the amount of **81** used in acetic acid did not totally dissolve to carry out the photocyclisation. Therefore, MeCN was used instead of acetic acid. Additionally 5 ml of HBF_4 (48% wt. in H_2O) was added, resulting in the

corresponding BNAXBF₄. A *Luzchem* photoreactor was employed to irradiate **81** at 360 ± 40 nm for 2 hours. The solution changed from red to purple and large black needles indicating BNAXBF₄ were obtained in a yield of 30% (lit.: 96% for BNAXBr).²⁰ The crystals were of good quality to carry out X-ray structure analysis.

10.2.2. X-ray structure analysis

According to the X-ray structure analysis, BNAXBF₄ is arranged in a triclinic space group (*Appendix 75 & 76*). As expected, a high degree of π -stacking interactions can be observed, however, these are not arranged in a discotic-like manner. That is, aliphatic substituents with sufficient length are necessary to allow a linear stacking structure with face to face planarity with a discotic-like arrangement.²⁵⁷ In the solid state, BNAXBF₄ exhibits, similarly to NXBF₄, B[*i*]NXBF₄ and B[*a*]NXBF₄ (see *Chapter 7*), antiplanar π -stacking interactions, however, these arrangements establish two angular columns which are parallel to each other (*Figure 10.2.2.1, 10.2.2.2*). Between these columns π - π interacting pairs of BNAX⁺ are located exhibiting a planar separation of 3.367-3.393 Å. BF₄ counterions can be found between the differently angular stacking structures (*Figure 10.2.2.2*). All bond lengths of BNAX⁺ are depicted in *Figure 10.2.2.3* showing very similar bond lengths for both C-O bonds (1.362 Å and 1.368 Å).

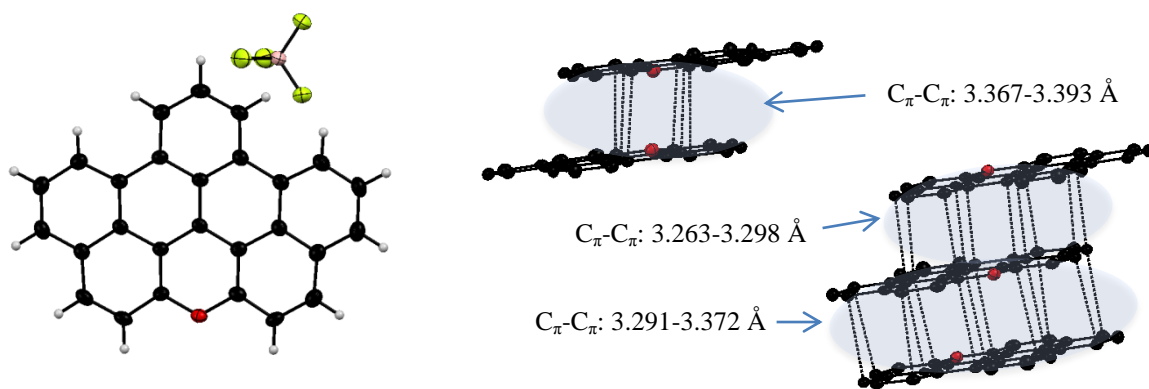


Figure 10.2.2.1 X-ray diffraction of BNAXBF₄ and π -stacking separation between BNAX molecules.

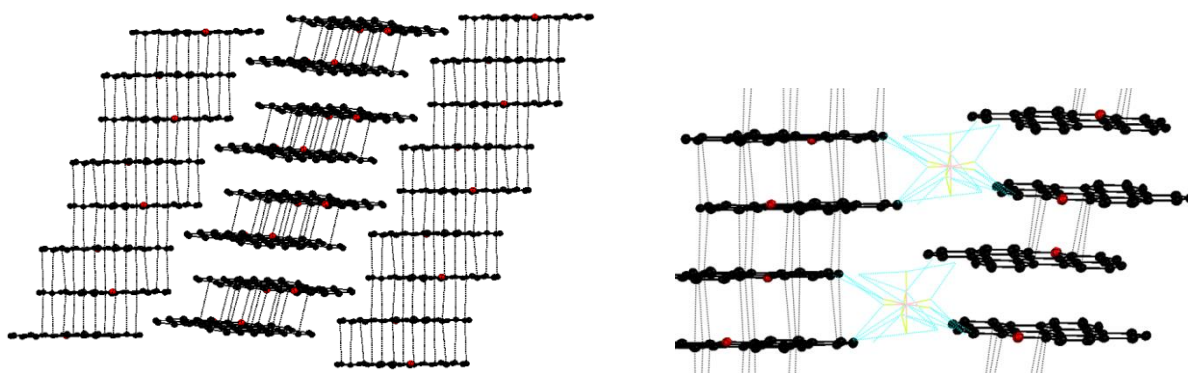


Figure 10.2.2.2 Left: Crystal order of BNAX units showing pronounced π -stacking interactions. Right: Separations between counterion and BNAX cation.

10.2.3. Cyclic voltammetry

Since BNAX tends to precipitate, only a low concentration could diffuse towards the electrode to give rise to possible redox waves. In DMF, two redox waves are shown presumably representing reduction from the cation to the radical and from the radical to the anion (*Figure 10.2.3.1*). The reduction from the cation resulting in the radical occurs at $E_{\text{red}} = -0.91$ V and the reduction from the radical resulting in the anion can be found at $E_{\text{ox}} = -1.82$ V. Hence, the amphotericity can be quantified with $E_{\text{sum}} = E_{\text{ox}} - (-E_{\text{red}}) = -0.91$ V.

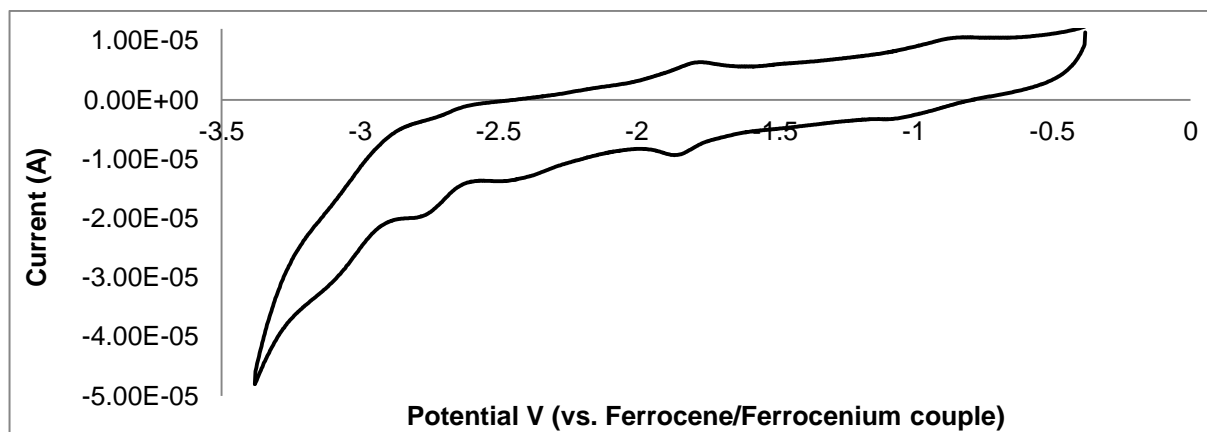
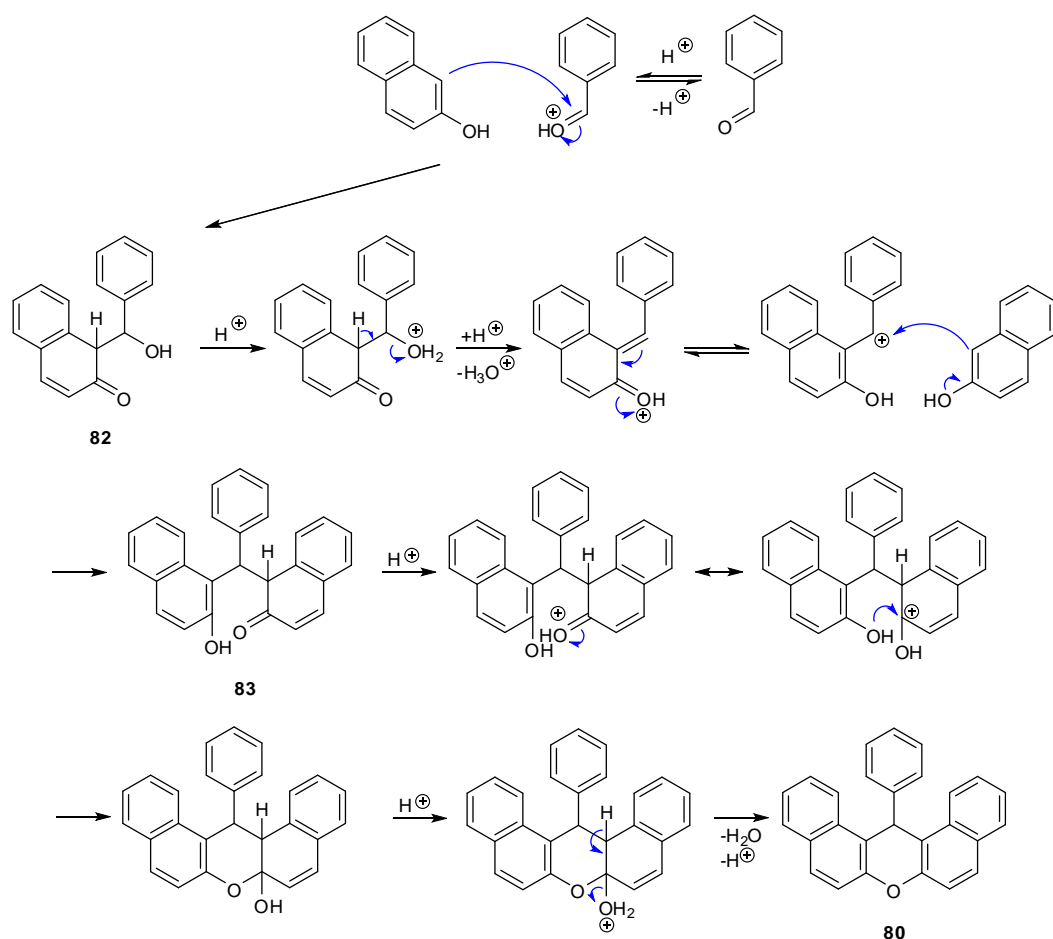


Figure 10.2.3.1 Cyclic voltammogram of BNAXBF₄ in DMF.

10.3. Discussion

10.3.1. Synthesis

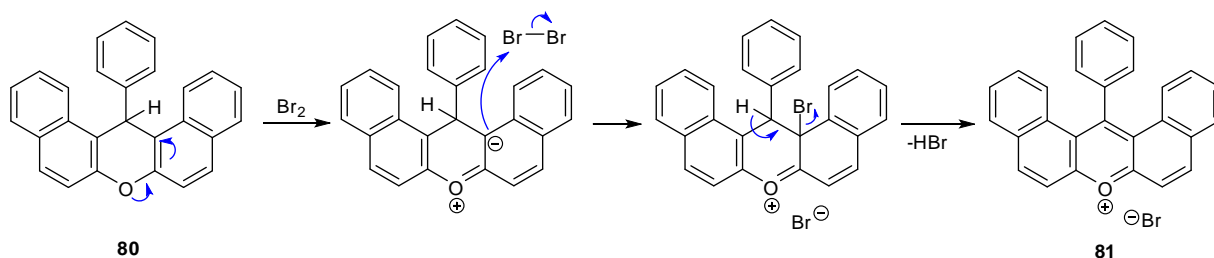
According to the synthesis of **80**, the mechanistic scenario is depicted in *Scheme 10.3.1.1*. The reaction is initiated by the nucleophilic attack from the ketone tautomer of 2-hydroxynaphthalene from the 1-position at the positively charged carbon of the benzaldehyde. Subsequently dehydration proceeds, yielding 1-benzylidenenaphthalen-2(1*H*)-one **82**. Then protonation of the keto group results in the hydroxyl group, concomitant with the formation of a carbocation. This undergoes electrophilic aromatic substitution with a second 2-hydroxynaphthalene molecule at the 1-position. As a result, compound **83** is obtained, which subsequently undergoes hemi-ketal formation and dehydration yielding the desired product **80**.



Scheme 10.3.1.1 Mechanistic scenario for the formation of 14-phenyl-14H-dibenzo[*a,j*]xanthenes **80**.

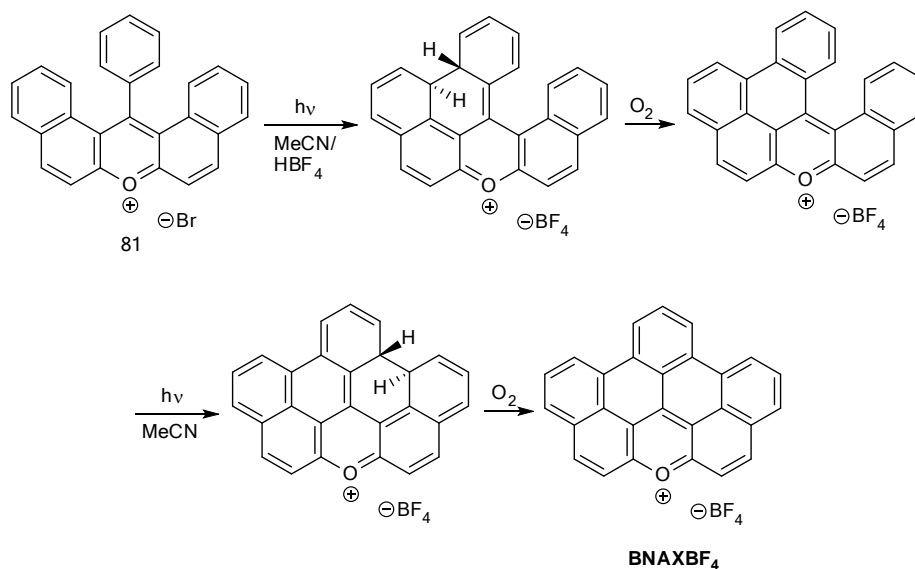
The dehydrogenation of **80** is performed by bromination at the negatively charged carbon due to a possible oxonium resonance structure. Subsequently, elimination proceeds giving HBr

and the desired salt **81**. The remaining negatively charged bromide takes the role of the counterion (*Scheme 10.3.1.2*).



Scheme 10.3.1.2 Dehydrogenation of 14-phenyl-14H-dibenzo[*a,j*]xanthenes **80** resulting in 14-phenyldibenzo[*a,j*]xanthenium bromide **81**.

The photocyclisation of heteroatom containing aromatics can be referred to a series of references which successfully resulted in the planarisation of larger conjugated PAHs.^{263,264,265} For the synthesis of the BNAX⁺, MeCN was used as a better solubility was expected for the product to allow a slower crystallisation process. This is important to obtain crystals of sufficient quality for X-ray structure analysis.²⁶⁶ Presumably the reaction proceeds stepwise by formation of dihydro derivatives resulting from the photoinduced cyclisation and subsequent oxidation via oxygen (*Scheme 10.3.1.3*). Due to the lack of solubility or possibly strong intermolecular interactions, leading to aggregation, the structure of the compound could not be interpreted via NMR spectroscopy.



Scheme 10.3.1.3 Photocyclisation 14-phenyldibenzo[*a,j*]xanthenium bromide **81** resulting in BNAXBF₄.

10.3.2 HOMA evaluation and computational results

Analogous to the pyrylium cations (NX^+ , $\text{B}[i]\text{NX}^+$ and $\text{B}[a]\text{NX}^+$) in *Chapter 7*, the evaluation of the aromaticity of BNAX^+ was conducted using the HOMA formula.²¹⁵

$$\text{HOMA} = 1 - \frac{1}{n} \left\{ \sum \alpha(\text{CC})[(R(\text{CC})_{\text{opt}} - R_i)] + \alpha(\text{CO})[(R(\text{CO})_{\text{opt}} - R_i)] \right\}$$

where n is the number of bonds, α is a normalisation constant (257.7 and 157.38 for C-C bonds and C-O bonds, respectively), and R_i is the given individual bond length. $R(\text{CC})_{\text{opt}}$ represents C-C bonds in conjugated systems with 1.388 Å. In the case of the oxonium-carbenium bond, $R(\text{CO})_{\text{opt}}$ was chosen with 1.265 Å according to the literature.²¹⁵ An ideally aromatic molecule such as benzene exhibits a maximum HOMA index of 1.

Ring	HOMA
A	0.8255
B	0.9111
C	0.5192
D	0.8421
E	0.9080
F	0.5102
G	0.8587
P	0.4210

Table 10.3.2.1
HOMA indices of assigned rings in BNAX^+ .

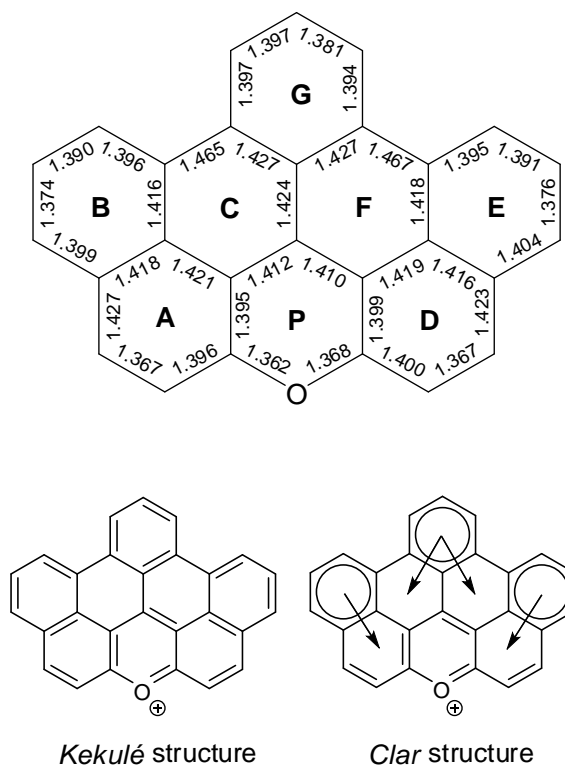


Figure 10.3.2.1 *Kekulé* and *Clar* structures of BNAX^+ and bond lengths of BNAX^+ according to X-ray structure analysis with assignment of the rings.

As expected, the pyrylium ring P exhibits the lowest HOMA value with $\text{HOMA}_P = 0.4210$ (*Table 10.3.2.1*) due to the perturbation caused by the oxygen atom. The degrees of aromaticity for the inner rings C and F are distinctly lower compared to the outer ones. Ring B

and ring E exhibit the highest degrees of aromaticity. Since the inner rings are less aromatic than ring A and ring D, the mobility of a π -electron is pronounced from ring B and ring E to ring A and to ring D, respectively. The HOMA index for ring G is in the range between ring A and D. As the benzannulated rings C and F are less aromatic than ring G, an aromatic sextet can be assigned to ring G whereas a π -electron can only move to its adjacent rings C or F. Using the calculated HOMA values for all rings, a reasonable *Clar* structure or *Kekulé* structure can be sketched as shown in *Figure 10.3.2.1*.

Furthermore the potential surface of BNAX^+ was calculated based on the B3LYP level of theory (using *Spartan*) using a basis set of 6-31G**. The highest negative character is predicted to be in the rings B, G and E (*Figure 10.3.2.2*). The highest positive character is in the π -deficient pyryl ring as expected.

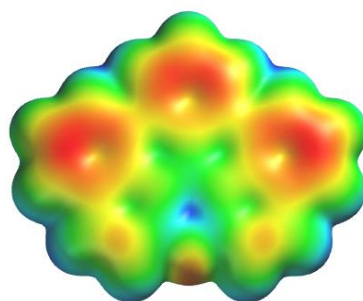


Figure 10.3.2.2 Potential surface of BNAX^+ calculated based on the B3LYP level of theory using a basis set of 6-31G**.

As the inner rings in BNAX^+ are distinctly less aromatic than the outer rings, the electronic structure is fundamentally different from the previously described and evaluated naphthoxanthenyl cations. BNAX^+ does not represent a phenalenyl type cation in contrast to NX^+ , $\text{B}[i]\text{NX}^+$ and $\text{B}[a]\text{NX}^+$ (*Figure 10.3.2.3*). Instead two outer naphthalenyl units exhibit a pronounced aromaticity. Hence, the electronic structure and features of the corresponding BNAX radical can be expected to be different as well.

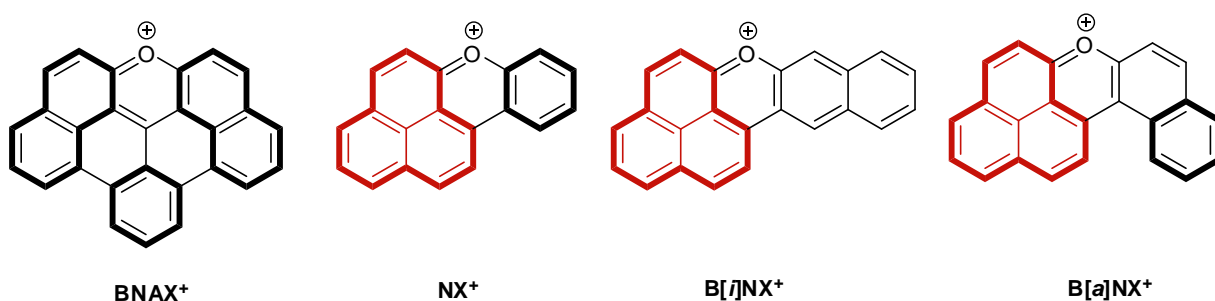


Figure 10.3.2.3 Illustration of potential phenalenyl units in pyrylium cations. BNAX^+ does not exhibit the electronic structure to be classified as phenalenyl type cations.

10.3.3 Electrochemical properties

The poor solubility of BNAX^+ eases the preparation by precipitation, however, this also makes it difficult to carry out cyclic voltammetry experiments. The intensity of the redox waves are low compared with the redox waves resulting from NX^+ , $\text{B}[i]\text{NX}^+$ and $\text{B}[a]\text{NX}^+$. However, the redox process can be assigned and the difference of the redox potentials gave a value of $E_{\text{sum}} = 0.91 \text{ V}$ which is below the ones of naphthoxanthenyl cations. This indicates lower repulsion energy between two electrons in the same orbital. Additionally the first reduction step occurs at a more negative potential (-0.91 V) with a difference of 0.39 V compared with NX^+ ($E_{\text{red}} = -0.52 \text{ V}$; see *Figure 7.2.9.1* in *Chapter 7*). Therefore, a higher energy for the LUMO of BNAX^+ can be postulated since more potential is required to transfer a charge to the empty orbital. This is well in agreement with conducted computational calculations.

The HUMO-LUMO gap was calculated based on the basis set of B3LYP-6-31G** showing energy levels of -3.77 eV and -10.44 eV for the LUMO and HOMO, respectively (*Figure 10.3.3.1*). The energy for the LUMO is higher compared with the naphthoxanthenyl cations (NX^+ : -4.14 eV ; $\text{B}[i]\text{NX}^+$: -4.12 eV ; $\text{B}[a]\text{NX}^+$: -3.96 eV). The HOMO-LUMO gap is the lowest with 6.67 eV among this series (NX^+ : 7.72 eV ; $\text{B}[i]\text{NX}^+$: 6.74 eV ; $\text{B}[a]\text{NX}^+$: 7.02 eV). Considering these data, the calculation for the LUMO of BNAX^+ appears to be reasonable comparing with those of $\text{B}[a]\text{NX}^+$ due to the extension of the polyaromatic framework with two further benzene rings. As a reminder the obtained calculations for NX^+ and $\text{B}[i]\text{NX}^+$ revealed some controversies with regards to the experimental results from the cyclic voltammetry and UV/Vis spectra. It can be presumed that the first observed redox wave

represents the reduction to the neutral radical supported by the higher LUMO energy calculated.

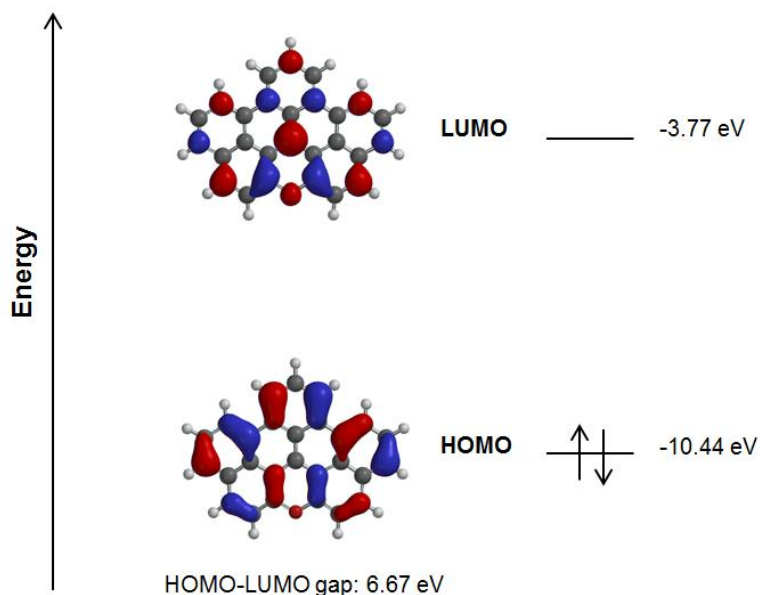


Figure 10.3.3.1 Calculated HOMO and LUMO energies of BNAX^+ based on the B3LYP level of theory using a basis set of 6-31G**.

BNAX^+ in solution gave an intense paramagnetic signal with a g-factor of 2.003 and a linewidth of 6 gauss (ESR spectroscopy instrument is calibrated with DPPH). Hence, the presence of a paramagnetic species presumed to be the corresponding neutral radical was detected. As no hyperfine coupling constants could be found, an assignment of the spin densities is not feasible to discuss the electronic distribution.

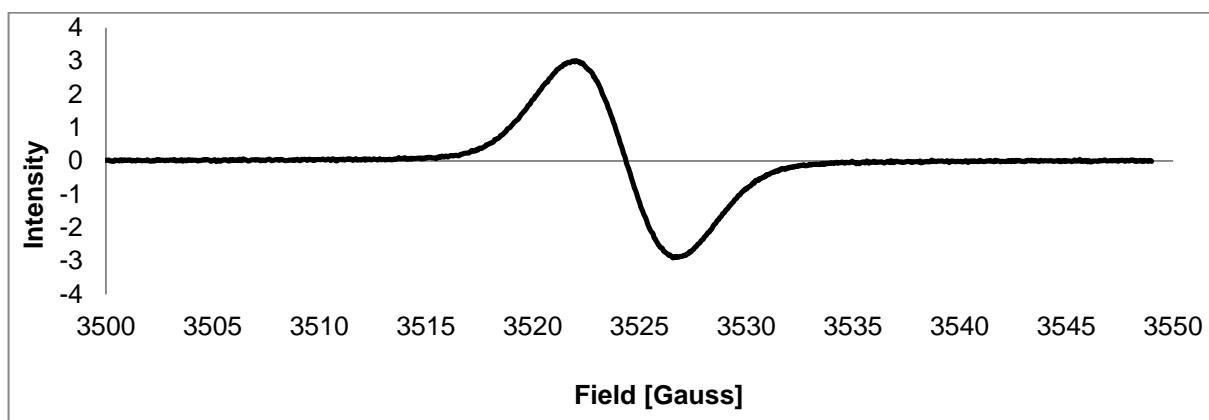


Figure 10.5.3 Measured CW-ESR spectrum (1^{st} derivative) of BNAXBF_4 containing a radical in DMSO 1 scan at room temperature (modulation amplitude: 1.0 Gauss; conversion time: 81.92 ms; sweep time: 83.89 s; time constant: 20.48 ms).

10.4. Conclusions

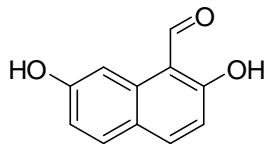
The synthesis and X-ray structure analysis of BNAXBF₄ was accomplished following the reported procedure. Based on the data obtained by X-ray structure analysis HOMA evaluation with respect to *Clar's* rule could be carried out and compared with the previously synthesised naphthoxanthenyl cations. In fact, BNAX shows no similarity to phenalenyl type cations and gave distinct differences in electrochemical properties. A distinct decrease of the amphotericity could be derived from the cyclic voltammetry experiments and confirmed using computational methods which indicates a higher LUMO energy and a smaller HOMO-LUMO gap. The discrepancies in their physicochemical properties illustrate that the way a polyaromatic species is condensed plays a crucial role in the electronic structure. In BNAX⁺, two phenalenyl skeletons can fit in, however, the highest degree of aromaticity is rather pronounced at the outer rings resulting in two naphthalenyl units and one aromatic sextet, hence, the inner rings are distinctly less aromatic. BNAX⁺ is already a known compound, however, the presented results in this chapter have not been considered and represent more detailed investigations on its aromaticity and its electrochemical properties. This includes also the existence of a stable corresponding neutral radical detected by ESR spectroscopy. It is desired to isolate the neutral radical, however, solubility issues of BNAX⁺ made this difficult. It is noteworthy to point out that BNAX⁺ is by far more difficult to handle in solution and not soluble in water in contrast with the naphthoxanthenyl cations. With this come restrictions in its use for applications such as site-directed spin labeling, for instance.

11. Experimental section

2,7-Dihydroxy-1-naphthaldehyde (9)

A three-neck round bottom flask containing 5 ml (65 mmol; 1 eq) of DMF was placed in an NaCl/ice-bath. Under nitrogen atmosphere, 6.5 ml (71 mmol; 1.1 eq) of POCl₃ were added slowly from a separation funnel while the temperature was controlled and kept under 30 °C. After 1 hour stirring, 10.00 g (62 mmol; 1 eq) of 2,7-dihydroxynaphthalene, dissolved in 10 ml DMF and 20 ml DCM, were added carefully to the *Vilsmeier* reagent using a dropping funnel. The temperature was kept between 20-35 °C. After 1 hour the ice bath was removed and the mixture was stirred for 6 h. The reaction was carefully quenched with 40 ml H₂O

while the flask was cooled by an ice bath so that the temperature was kept under 55 °C. The yellow solution was then stirred overnight. The next day a yellow precipitate was obtained and separated by vacuum filtration. The product was recrystallized from isopropanol/H₂O and gave the product as fine yellow needles in a yield of 57 % (6.7 g; 0.36 mmol).

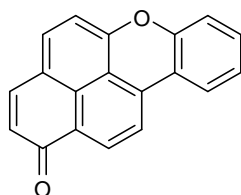


Chemical Formula: C₁₁H₈O₃
Molecular Weight: 188.18

¹H-NMR (400 MHz; DMSO-*d*₆) δ 6.94 (dd, *J* = 8.7, 2.4 Hz, 1H), 6.95 (d, *J* = 8.9 Hz, 1H), 7.70 (d, *J* = 8.8 Hz, 1H), 7.96 (d, *J* = 8.9 Hz, 1H), 8.34 (d, *J* = 2.3 Hz, 1H), 10.03 (s, OH), 10.69 (s, CHO), 11.71 (s, OH). ¹³C-NMR (100 MHz; DMSO-*d*₆) δ 105.20 (CH), 111.61 (Cq), 114.60 (CH), 115.74 (CH), 122.14 (Cq), 130.55 (CH), 133.70(Cq), 138.25(CH), 158.92 (C-OH), 164.61 (C-OH), 191.87 (C=O). MS (EI+) *m/z* (rel. intensity): 188 (M⁺, 100), 187 (99), 171 (13), 160 (100), 159 (88), 132 (88), 115 (31), 103 (100), 102 (71), 78 (73), 77 (100), 63 (100), 51 (65), 26 (45). HRMS calcd for C₁₁H₈O₃: 188.0473, found: 188.0472. Elemental analysis: Theory: C, 70.21; H, 4.29; C, Result: 70.01; H, 4.26. Melting point: 141 °C; crystals obtained from isopropanol/H₂O (lit.: 163-164 °C; crystals from CHCl₃)²⁶⁷.

1*H*-naphtho[2,1,8-*mna*]xanthen-1-one (10)

2,7-Dihydroxy-1-naphthaldehyde (2.0 g; 10.63 mmol; 1 eq) and 1.5 ml (12.46 mmol; 1.2 eq) of *o*-hydroxyacetophenone were dissolved in 50 ml EtOH in a round bottom flask. A stream of gaseous HCl generated from conc. HCl-solution and CaCl₂ was purged through the slowly stirring solution for 4 hours. The colour changed from yellow to purple through to red-orange. The solvent was then evaporated off using a rotary evaporater. Afterwards, 2.6 g of Na₂CO₃ in a mixture of 25 ml H₂O and 25 ml EtOH were added and refluxed for 1 hour. A dark red solid precipitated. The dark purple mixture was diluted with H₂O (400 ml) and the precipitate was separated by vacuum filtration. By column chromatography (chloroform-ethyl acetate/9:1) the red-orange fraction was collected giving a yield of 4% (112 mg; 0.4 mmol; lit.: 32%)¹¹⁹.

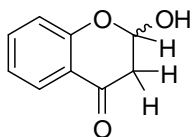


Chemical Formula: C₁₉H₁₀O₂
Molecular Weight: 270.28

¹H-NMR (400 MHz; CDCl₃) δ 6.86 (d, *J* = 9.6 Hz, 1H), 7.31 (d, *J* = 8.1 Hz, 1H), 7.42 – 7.37 (m, 1H), 7.46 (dd, *J* = 8.3, 1.1 Hz, 1H), 7.58 (ddd, *J* = 8.5, 7.3, 1.5 Hz, 1H), 7.87 (d, *J* = 9.6 Hz, 1H), 7.92 (d, *J* = 8.1 Hz, 1H), 8.17 (d, *J* = 8.0 Hz, 1H), 8.21 (dd, *J* = 8.0, 1.3 Hz, 1H), 8.87 (d, *J* = 8.0 Hz, 1H). ¹³C-NMR (400 MHz; CDCl₃) δ 109.08 (CH), 115.91 (CH), 118.00 (CH), 119.14 (Cq), 120.42 (Cq), 123.79 (CH), 124.70 (CH), 127.31 (CH), 131.87 (CH), 133.07 (CH), 133.83 (CH), 140.46 (CH), 184.20 (C=O). MS (EI+) *m/z* (rel. intensity): 270 (M⁺, 10), 242 (5), 231 (3), 213 (3), 160 (3), 146 (3), 129 (4), 105 (6), 87 (10), 85 (63), 83 (100), 57 (6), 47 (14), 44 (19). Melting Point: 176 °C; crystals obtained from chloroform-ethyl acetate (226 °C; crystals from methanol)¹¹⁹.

2-Hydroxychroman-4-one (35)

Sodium hydride (2.3 g as a mixture of 60% in mineral oil (w/w); 58 mmol; 8 eq) was suspended in diethylether (35 ml) in a two-neck round bottom flask. The apparatus was kept under nitrogen atmosphere. While stirring, ethylformate (5.4 ml; 67 mmol; 9 eq) was gradually added to the suspension. The flask was placed in a NaCl/ice bath when *o*-hydroxyacetophenone (0.92 ml; 7.6 mmol; 1 eq) was slowly added. After 15 minutes, the mixture was refluxed for 10 minutes and subsequently cooled down to room temperature. Then 25 ml of diethylether were added and the mixture was stirred overnight. The next day the yellow suspension formed was poured in 50 ml ice/water. The solution was left for two hours in an ice bath until the product precipitated as colourless needles. The mineral oil was separated by the means of a pipette from the aqueous mixture and the product was isolated by vacuum filtration giving a yield of 28 % (354 mg; 2.1 mmol)²⁶⁸.

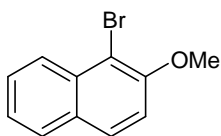


Chemical Formula: C₉H₈O₃
Molecular Weight: 164.16

$^1\text{H-NMR}$ (400 MHz; CDCl_3) δ 2.89 (dd, $J = 16.8, 4.6$ Hz, 1H), 3.03 (ddd, $J = 16.7, 3.4, 1.5$ Hz, 1H), 3.59 (s, OH), 5.89 (dd, $J = 7.9, 4.5$ Hz, 1H), 6.99 (dd, $J = 8.3, 0.7$ Hz, 1H), 7.08 – 7.03 (m, 1H), 7.51 (ddd, $J = 8.4, 7.2, 1.8$ Hz, 1H), 7.89 (dd, $J = 7.8, 1.7$ Hz, 1H). $^{13}\text{C-NMR}$ (100 MHz; CDCl_3) δ 43.92 (CH₂), 95.18 (CH), 118.43 (CH), 122.08 (CH), 126.69 (CH), 136.51 (CH), 158.00 (Cq), 190.76 (Cq), 204.53 (C=O). MS (Isobutane C+) m/z (rel. intensity): 165 ((M + H)⁺, 100), 147 (20), 121 (5), 85 (3), 69 (6). Melting point: 79 °C; crystals obtained from H₂O (lit.: 88°C; crystals from benzene/diethylether).²⁶⁹

1-Bromo-2-methoxynaphthalene (45)

The synthesis was carried out according to the literature¹⁶⁸ using 1.00 g (6.3 mmol; 1 eq) of 2-methoxynaphthalene dissolved in 40 ml DMSO. When the starting material was totally dissolved, 15 ml of HBr solution (48% in aqueous solution; 133 mmol; 21 eq) were added gradually. The reaction was kept at 40°C and stirred for 2 days. The desired product precipitated and was isolated via vacuum filtration, washed with H₂O and dried under vacuum giving a yield of 91% (1.36 g; 5.8 mmol; lit.: 96%)¹⁶⁸.

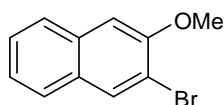


Chemical Formula: C₁₁H₉BrO
Molecular Weight: 237.09

$^1\text{H-NMR}$ (400 MHz; acetone- d_6) δ 3.99 (s, OMe), 7.44 (ddd, $J = 8.0, 6.9, 1.1$ Hz, 1H), 7.52 (d, $J = 9.0$ Hz, 1H), 7.62 (ddd, $J = 8.4, 6.8, 1.3$ Hz, 1H), 7.93 (d, $J = 8.2$ Hz, 1H), 8.00 (d, $J = 9.0$ Hz, 1H), 8.07 (d, $J = 8.6$ Hz, 1H). $^{13}\text{C-NMR}$ (100 MHz; acetone- d_6) δ 56.85 (OMe), 106.89 (Cq), 114.25 (CH), 124.25 (CH), 125.09 (CH), 128.07 (CH), 128.31 (CH), 129.32 (Cq), 129.34 (CH), 132.23 (Cq), 153.60 (Cq). MS (EI+) m/z (rel. intensity): 238 (M⁺; C₁₁H₉O⁸¹Br, 28), 236 (M⁺; C₁₁H₉O⁷⁹Br, 29), 223 (4), 221 (4), 195 (24), 193 (24), 127 (10), 114 (20), 85 (62), 83 (100), 78 (33), 63 (45), 47 (20), 44 (10). Melting point: 83-84 °C; crystals from DMSO (lit.: 82 °C; crystals from hexane)²⁷⁰.

2-Bromo-3-methoxynaphthalene (46)

The synthesis was carried out according to the literature¹⁶⁹ using 14.00 g (88 mmol, 1 eq) of 2-methoxynaphthalene dissolved in 60 ml of dry THF. To the stirring solution 40 ml n-butyllithium (2.5 M in hexane; 100 mmol; 1.1 eq) was added dropwise under argon atmosphere at room temperature. After stirring for 2.5 h at room temperature, 11.5 ml of (133 mmol; 1.5 eq) 1,2-dibromoethane were added dropwise at -78 °C and the reaction mixture was allowed to warm up to room temperature. Then 50 ml of aqueous NaOH (1 M) were added and the reaction was refluxed for 1 h. THF was removed under reduced pressure and subsequently extraction with CH₂Cl₂ was carried out. The organic extracts were washed with H₂O and brine, dried over MgSO₄ and evaporated until dryness. The product was recrystallized from hexane in the fridge to obtain white crystals in a yield of 73 % (15.33 g; 65 mmol; lit.: 75%)¹⁶⁹.



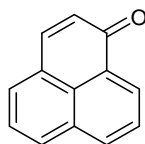
Chemical Formula: C₁₁H₉BrO
Molecular Weight: 237.09

¹H-NMR (400 MHz; CDCl₃) δ 4.01 (s, OMe), 7.16 (s, 1H), 7.36 (ddd, *J* = 8.1, 6.9, 1.2 Hz, 1H), 7.45 (ddd, *J* = 8.2, 6.9, 1.2 Hz, 1H), 7.69 (d, *J* = 8.2 Hz, 1H), 7.72 (d, *J* = 8.6 Hz, 1H), 8.06 (s, 1H). ¹³C-NMR (100 MHz; CDCl₃) δ 56.42 (OMe), 107.00 (CH), 113.68 (Cq), 124.67 (CH), 126.78 (CH), 126.85 (CH), 126.90 (CH), 129.76 (Cq), 132.51 (CH), 133.82 (Cq), 153.92 (Cq). MS (EI+) *m/z* (rel. intensity): 238 (M⁺; C₁₁H₉O⁸¹Br, 99), 236 (M⁺; C₁₁H₉O⁷⁹Br, 100), 223 (9), 221 (10), 195 (55), 193(57), 127(22), 114 (30), 84 (32), 49 (35). HRMS calcd for C₁₁H₉O⁷⁹Br: 235.9837, found: 235.9843. Melting point: 66-67 °C; crystals from hexane (lit.: 66-68 °C, crystals from hexane)¹⁶⁹.

1*H*-phenalen-1-one (12)

To 1 l of diethylether were added 30 g of NaH/oil dispersion (60% hydride (w/w); 0.75 mol; 2.2 eq), 1 ml EtOH, 57 g (0.34 mol; 1 eq) 1-acetonaphthone, and 50 g (0.68 mol; 2 eq) ethyl formate. With vigorous stirring the mixture was brought to reflux at 40 °C. When the temperature increased sharply, heating was discontinued. After 90 minutes, most of the ether boiled out and a whitish precipitate occurred. Then 500 ml of H₂O were added to dissolve the

solid. The aqueous solution was washed with diethylether (3 x 150 ml) and acidified with 70 ml conc. HCl. This caused the precipitation of a white solid which was extracted with diethylether (3 x 150 ml) and dried over MgSO₄. After removing the solvent, a yellow oily residue was obtained. The residue was diluted with 350 ml of DCM and added dropwise to 350 ml of vigorously stirred 80% H₂SO₄ solution, cooled in an ice-water bath. Afterwards the aliquot diluted with 500 ml of H₂O was extracted with DCM (5 x 200 ml). The organic fractions were dried over MgSO₄ and the solvent was removed via rotary evaporation. The product was recrystallised in hexane/diethylether as yellow crystals in a yield of 90 % (54 g; 0.30 mol; lit.: 78 % (97%))⁶⁹.



Chemical Formula: C₁₃H₈O
Molecular Weight: 180.20

¹H-NMR (400 MHz; CDCl₃) δ 6.72 (d, *J* = 9.8 Hz, 1H), 7.58 (dd, *J* = 8.2, 7.1 Hz, 1H), 7.81 – 7.67 (m, 3H), 8.01 (d, *J* = 8.5 Hz, 1H), 8.19 (dd, *J* = 8.1, 0.9 Hz, 1H), 8.62 (dd, *J* = 7.4, 1.1 Hz, 1H). ¹³C-NMR (100 MHz; CDCl₃) δ 126.76 (CH), 127.25 (CH), 127.69 (Cq), 127.99 (Cq), 129.39 (CH), 129.62 (Cq), 130.47 (CH), 131.46 (CH), 132.04 (CH), 132.30 (Cq), 135.00 (CH), 141.87 (CH), 185.77 (C=O). IR (ATIR) ν_{max} 1636 (C=O), 1618, 1586, 1574, 1564, 1508, 1462, 1435, 1393, 1356, 1285, 1236, 1182, 1148, 1121, 1099, 1072, 1032, 986, 972, 957, 937, 924, 827, 810, 772, 731, 702, 642, 627, 613. MS (Isobutane CI+) *m/z* (rel. intensity): 181 (M + H)⁺, 70, 173 (9), 137 (7), 128 (12), 113 (13), 85 (64), 71 (100). Melting Point: 149-150° C; crystals from hexane/diethylether (lit. 156-156.5; crystals from methanol)¹⁸⁸.

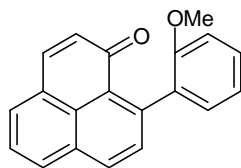
General procedure for 9-(2-methoxyphenyl)-1*H*-phenalen-1-one, 9-(2-methoxynaphthalenyl)-1*H*-phenalen-1-one and 9-(3-methoxynaphthalenyl)-1*H*-phenalen-1-one

In a two-neck round bottom flask, Mg in 5 ml of THF was activated by 0.1 ml 1,2-dibromoethane under argon atmosphere. Then the brominated aryl compound mixed with dry THF was added dropwise by means of a syringe. By slow stirring and heating up, the *Grignard*-reagent began to form. After 45 min, 1.00 g (5.5 mmol, 1 eq) of phenalenone

dissolved in 10 ml dry THF, was gradually added to the grey solution. The mixture was then refluxed for 4 h. After cooling down to room temperature, the reaction was quenched with 5 ml sat. NH₄Cl-solution. Then 20 ml H₂O was added and the product was extracted with EtOAc (3 x 30 ml) and washed with 20 ml brine and dried over MgSO₄. When the solvent was evaporated to dryness, the crude product and 1.30 g DDQ (5.6 mmol; 1 eq) were mixed in DCM and refluxed over night at 55-60 °C. The next day, the solvent was evaporated by rotary evaporator within the fumehood. By flash column chromatography using silica and DCM as eluent, the desired product was obtained.

9-(2-methoxyphenyl)-1*H*-phenalen-1-one (15)

Following the general procedure, the *Grignard* reagent was generated from 0.34 g (14 mmol; 2.5 eq) Mg and 1.4 ml (11 mmol; 2 eq) *o*-bromoanisol mixed with 2 ml THF at 30-40 °C. After reflux with phenalenone (1 eq) at 55-60 °C and subsequent oxidation with DDQ 9-(2-methoxyphenyl)-phenalenone was obtained as orange powder in a yield of 52% (0.83 g; 2.9 mmol).



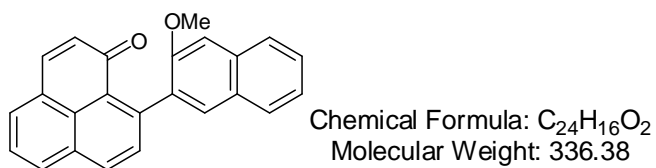
Chemical Formula: C₂₀H₁₄O₂
Molecular Weight: 286.32

¹H-NMR (400 Hz; CDCl₃) δ 3.73 (s, OMe), 6.60 (d, *J* = 9.7 Hz, 1H), 7.03 (d, *J* = 8.2 Hz, 1H), 7.12 (td, *J* = 7.4, 0.8 Hz, 1H), 7.22 (dd, *J* = 7.4, 1.7 Hz, 1H), 7.40-7.46 (m, 1H), 7.55-7.61 (m, 2H), 7.67 (d, *J* = 9.7 Hz, 1H), 7.73 (d, *J* = 6.6 Hz, 1H), 8.01 (d, *J* = 8.2 Hz, 1H), 8.18 (d, *J* = 8.3 Hz, 1H). ¹³C-NMR (100 Hz; CDCl₃) δ 55.63 (OMe), 77.36 (Cq), 110.71 (CH), 120.95 (CH), 126.24 (CH), 126.90 (Cq), 128.15 (Cq), 128.42 (Cq), 128.71 (CH), 128.74 (CH), 130.16 (CH), 131.17 (CH), 131.66 (2CH), 131.82 (Cq), 132.22 (Cq), 133.85 (CH), 140.31 (CH), 143.67 (Cq), 156.41 (Cq), 185.64 (C=O). UV (in MeCN) – λ_{max} [nm] (log ε): 310 (3.58), 361 (4.01), 384 (3.83). IR (ATIR) ν_{max} [cm⁻¹] 3022- 2825 (CH_{aromatic}, weak), 1634 (C=O, sharp & intense), 1624, 1579, 1553, 1488, 1459, 1431, 1397, 1385, 1354, 1285, 1267, 1234 (C-O, sharp & intense), 1176, 1120, 1106, 1082, 1055, 1025. MS (EI+) *m/z* (rel. intensity): 286 (M⁺, 12), 255 (100), 271 (7), 226 (10) 213 (10), 187 (5), 163 (3), 143 (3), 113 (5), 85 (39), 83 (59), 69 (4), 47 (10). HRMS calcd for C₂₀H₁₄O₂: 286.0994, found: 286.0993. Elemental analysis:

Theory: C, 83.90; H, 4.93; Result: C, 83.55; H, 4.97. Melting Point: 121-124 °C; crystals from CH₂Cl₂.

9-(3-methoxynaphthalenyl)-1*H*-phenalen-1-one (17)

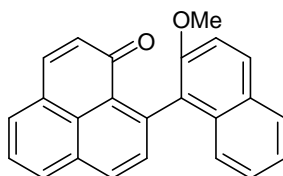
Following the general procedure, the *Grignard* reagent was generated from 0.23 g (9.4 mmol; 1.7 eq) Mg and 1.97 g (8.32 mmol; 1.5 eq) 2-bromo-3-methoxynaphthalene dissolved in 5 ml THF at 40-50 °C. After reflux with phenalenone (1 eq) and subsequent oxidation with DDQ, 9-(3-methoxynaphthalenyl)-phenalenone was obtained as yellow powder in a yield of 36% (0.68 g; 2 mmol).



¹H-NMR (400 MHz; CDCl₃) δ 3.79 (s, OMe), 6.58 (d, *J* = 9.7 Hz, 1H), 7.22 (s, 1H), 7.33 (ddd, *J* = 8.1, 6.9, 1.2 Hz, 1H), 7.44 (ddd, *J* = 8.2, 6.9, 1.3 Hz, 1H), 7.64 – 7.60 (m, 2H), 7.66 (d, *J* = 8.2 Hz, 1H), 7.69 (d, *J* = 9.8 Hz, 1H), 7.77 (t, *J* = 7.6 Hz, 1H), 7.80 (dd, *J* = 8.2, 0.5 Hz, 1H), 8.06 (dd, *J* = 8.2, 1.0 Hz, 1H), 8.22 (d, *J* = 8.3 Hz, 1H). ¹³C-NMR (100 MHz; CDCl₃) δ 55.78 (OMe), 105.49 (Cq), 123.73 (CH), 126.28 (CH), 126.24 (CH), 126.84 (CH), 127.47 (CH), 127.87 (2CH), 128.36 (Cq), 128.86 (Cq), 129.54 (Cq), 130.35 (CH), 131.20 (2CH), 131.73 (CH), 131.84 (CH), 132.28 (Cq), 133.94 (CH), 134.64 (Cq), 134.85 (Cq), 140.35 (Cq), 155.79 (Cq), 185.49 (C=O). UV (in MeCN) – λ_{max} [nm] (log ε): 305 (3.73), 320 (3.75), 360 (3.97). IR (ATIR) ν_{max} [cm⁻¹] 3010-2827 (CH_{aromatic}, weak), 1636 (C=O, sharp & intense), 1622, 1598, 1579, 1555, 1503, 1497, 1476, 1458, 1427, 1390, 1385, 1352, 1327, 1248, 1244, 1241 (C-O, sharp), 1198, 1171, 1123, 1107, 1076, 1040. MS (EI+) *m/z* (rel. intensity): 336 (M⁺, 23), 320 (7), 306 (80), 305 (100), 292 (14), 276 (27), 263 (30), 237 (7), 160 (18), 153 (23), 146 (15), 132 (11), 86 (12), 84 (18), 49 (12), 44 (8). HRMS calcd for C₂₄H₁₆O: 336.1150, found: 336.1146. Melting point: 194-196 °C; crystals from CH₂Cl₂.

9-(2-methoxynaphthalenyl)-1*H*-phenalen-1-one (16)

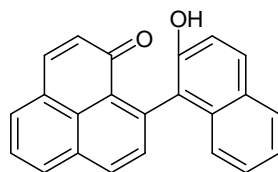
Following the general procedure, the *Grignard* reagent was generated from 0.23 g (9.4 mmol; 1.7 eq) Mg and 1.97 g (8.32 mmol; 1.5 eq) 1-bromo-2-methoxynaphthalene dissolved in 5 ml THF at 40-50 °C. After reflux with phenalenone (1 eq) and subsequent oxidation with DDQ 9-(2-methoxynaphthalenyl)phenalenone was obtained as orange powder in a yield of 70% (1.30 g; 3.86 mmol).



Chemical Formula: C₂₄H₁₆O₂
Molecular Weight: 336.38

¹H-NMR (400 MHz; CDCl₃) δ 3.79 (s, OMe), 6.50 (d, *J* = 9.7 Hz, 1H), 7.10 (d, *J* = 8.5 Hz, 1H), 7.20 (ddd, *J* = 8.1, 6.7, 1.3 Hz, 1H), 7.30 (ddd, *J* = 8.1, 6.7, 1.2 Hz, 1H), 7.42 (d, *J* = 9.0 Hz, 1H), 7.59 (d, *J* = 8.3 Hz, 1H), 7.66 (dd, *J* = 8.2, 7.1 Hz, 1H), 7.70 (d, *J* = 9.7 Hz, 1H), 7.80 (d, *J* = 6.3 Hz, 1H), 7.85 (d, *J* = 8.1 Hz, 1H), 7.94 (d, *J* = 9.0 Hz, 1H), 8.10 (d, *J* = 8.2 Hz, 1H), 8.27 (d, *J* = 8.3 Hz, 1H). ¹³C-NMR (100 MHz; CDCl₃) δ 56.85 (OMe), 113.95 (CH), 123.58 (CH), 124.16 (CH), 126.23 (Cq), 126.35 (CH), 126.54 (CH), 127.97 (Cq), 128.29 (CH), 128.66 (Cq), 128.70 (Cq), 128.94 (CH), 129.44 (Cq), 130.33 (CH), 131.15 (CH), 131.84 (CH), 132.20 (Cq), 132.56 (2CH), 134.21 (CH), 153.06 (Cq), 185.39 (C=O). UV (in MeCN) – λ_{max} [nm] (log ε): 312 (3.75), 341 (3.91), 358 (4.03). IR (ATIR) ν_{max} [cm⁻¹] 3032-2830 (CH_{aromatic}, weak), 1630 (C=O, sharp & intense), 1609, 1591, 1545, 1510, 1447, 1380, 1384, 1329, 1253 (C-O, sharp & intense), 1236, 1183, 1176, 1145, 1120, 1084, 1065, 1064. MS (EI+) *m/z* (rel. intensity): 336 (M⁺, 9), 305 (93), 263 (7), 153 (8), 86 (65), 84 (100), 51 (22), 49 (68), 47 (18). HRMS calcd for C₂₄H₁₆O: 336.1150, found: 336.1145. Melting point: 203-205 °C; crystals from CH₂Cl₂.

By-product: 9-(2-hydroxyphenyl)-1*H*-phenalen-1-one

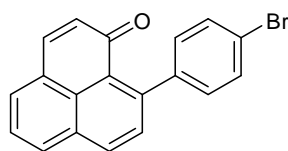


Chemical Formula: C₂₃H₁₄O₂
Molecular Weight: 322.36

$^1\text{H-NMR}$ (400 MHz; CDCl_3) δ 5.81 (s), 6.57 (d, $J = 9.7$ Hz, 1H), 7.02 (d, $J = 8.5$ Hz, 1H), 7.20 (ddd, $J = 8.2, 6.8, 1.3$ Hz, 1H), 7.22 (d, $J = 8.8$ Hz, 1H), 7.29 (ddd, $J = 8.1, 6.9, 1.1$ Hz, 1H), 7.63 (d, $J = 8.3$ Hz, 1H), 7.68 (dd, $J = 8.1, 7.2$ Hz, 1H), 7.71 (d, $J = 9.7$ Hz, 1H), 7.89 – 7.77 (m, 3H), 8.10 (d, $J = 7.6$ Hz, 1H), 8.27 (d, $J = 8.3$ Hz, 1H).

9-(4-bromophenyl)-1*H*-phenalen-1-one (18)

Following the general procedure, the Grignard reagent was generated from 0.23 g (9.4 mmol; 1.7 eq) Mg and 1.96 g (8.32 mmol; 1.5 eq) 1,4-dibromobenzene dissolved in 5 ml THF at 40–50 °C. After reflux with phenalenone and subsequent oxidation with DDQ, 9-(4-bromophenyl)-1*H*-phenalen-1-one was isolated by column chromatography using diethylether/DCM (3:2) as orange crystals in a yield of 30 % (0.56 g; 1.67 mmol).

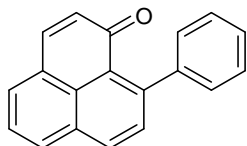


Chemical Formula: $\text{C}_{19}\text{H}_{11}\text{BrO}$
Molecular Weight: 335.19

$^1\text{H-NMR}$ (400 MHz; CDCl_3) δ 6.59 (d, $J = 9.7$ Hz, 1H), 7.25 (d, $J = 9.4$ Hz, 2H), 7.54 (d, $J = 8.3$ Hz, 1H), 7.58 (d, $J = 8.4$ Hz, 2H), 7.63 (dd, $J = 8.2, 7.1$ Hz, 1H), 7.70 (d, $J = 9.7$ Hz, 1H), 7.79 (dd, $J = 6.8, 0.6$ Hz, 1H), 8.05 (dd, $J = 8.2, 0.8$ Hz, 1H), 8.18 (d, $J = 8.3$ Hz, 1H). $^{13}\text{C-NMR}$ (100 MHz; CDCl_3) δ 121.56 (Cq), 126.17 (Cq), 126.75 (CH), 128.47 (Cq), 128.63 (Cq), 129.79 (2CH), 130.55 (CH), 131.36 (CH), 131.57 (2CH), 131.78 (CH), 131.95 (CH), 132.07 (Cq), 134.06 (CH), 140.73 (CH), 141.96 (Cq), 146.34 (Cq), 185.84 (C=O). UV (in MeCN) – λ_{max} [nm] (log ϵ): 360 (4.10). IR (ATIR) ν_{max} [cm^{-1}] 3027 ($\text{CH}_{\text{aromatic}}$, weak), 1636, 1630, 1622 (C=O, sharp & intense), 1567, 1550, 1485, 1450, 1438, 1394, 1348, 1277, 1242, 1215, 1180, 1125, 1069, 1009. MS (EI+) m/z (rel. intensity): 336 (M^+ , $\text{C}_{19}\text{H}_{11}^{81}\text{BrO}$, 32), 335 (($\text{M}-1$) $^+$, $\text{C}_{19}\text{H}_{10}^{81}\text{BrO}$, 67), 334 (M^+ , $\text{C}_{19}\text{H}_{11}^{79}\text{BrO}$, 33), 333 (($\text{M}-1$) $^+$, $\text{C}_{19}\text{H}_{10}^{79}\text{BrO}$, 63), 255 (87), 226 (31), 200 (10), 199 (5), 150 (8), 113 (30), 86 (65), 84 (100), 49 (69), 44 (18). HRMS calcd for $\text{C}_{19}\text{H}_{10}^{79}\text{BrO}$: 332.9915, found: 332.9920. Elemental analysis: Theory: C, 68.08; H, 3.31; Result: C, 68.04; H, 3.16. Melting point: 184–185 °C; crystals from CH_2Cl_2 .

Side product: **9-phenyl-1*H*-phenalen-1-one**

9-phenyl-1*H*-phenalen-1-one was isolated as orange crystals in a yield of 13 % (180 mg; 0.70 mmol).

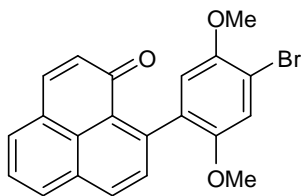


Chemical Formula: C₁₉H₁₂O
Molecular Weight: 256.30

¹H-NMR (400 MHz; CDCl₃) δ 6.60 (d, *J* = 9.7 Hz, 1H), 7.52 – 7.35 (m, 5H), 7.60 (d, *J* = 8.3 Hz, 1H), 7.62 (dd, *J* = 8.2, 7.1 Hz, 1H), 7.69 (dd, *J* = 9.7, 0.4 Hz, 1H), 7.78 (dd, *J* = 7.1, 1.2 Hz, 1H), 8.04 (dd, *J* = 8.2, 1.2 Hz, 1H), 8.17 (d, *J* = 8.3 Hz, 1H). ¹³C-NMR (100 MHz; CDCl₃) δ 126.18 (Cq), 126.50 (CH), 127.28 (CH), 127.97 (2CH), 128.40 (2CH), 128.49 (Cq), 128.63 (Cq), 130.65 (CH), 131.52 (CH), 131.72 (CH), 131.85 (CH), 131.88 (Cq), 133.84 (CH), 140.50 (Cq), 143.03 (CH), 147.77 (Cq), 185.88 (C=O). MS (EI+) *m/z* (rel. intensity): 255 ((M-1)⁺, 100), 226 (15), 224 (5), 136 (3), 121 (7), 83 (88), 47 (27). Melting point: 132-134 °C; crystals from acetone (lit. 150-152°C; recrystallised twice from acetic acid)¹²².

9-(4-bromo-2,5-dimethoxyphenyl)-1*H*-phenalen-1-one (19)

Following the general procedure, the *Grignard* reagent was generated from 0.30 g Mg (12.5 mmol; 2.3 eq) Mg and 2.48 g (8.37 mmol; 1.5 eq) 1,4-dibromo-2,5-dimethoxybenzene dissolved in 5 ml THF at 50 °C. After reflux with phenalenone and subsequent oxidation with DDQ, 9-(4-bromo-2,5-dimethoxyphenyl)-1*H*-phenalen-1-one was purified twice using column chromatography (first light petroleum / EtOAc (8:2); then DCM) resulting as orange-red powder in a yield of 3% (0.13 g; 0.14 mmol). The desired compound recrystallised in acetone as dark red crystals.



Chemical Formula: C₂₁H₁₅BrO₃
Molecular Weight: 395.25

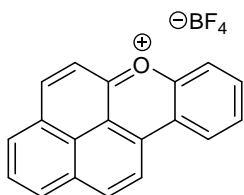
¹H-NMR (400 MHz; CDCl₃): δ 3.65 (s, OMe), 3.84 (s, OMe), 6.58 (d, *J* = 9.7 Hz, 1H), 6.78 (s, 1H), 7.18 (s, 1H), 7.54 (d, *J* = 8.3 Hz, 1H), 7.66 – 7.58 (m, 1H), 7.69 (d, *J* = 9.7 Hz, 1H),

7.77 (d, $J = 7.0$ Hz, 1H), 8.04 (d, $J = 8.2$ Hz, 1H), 8.19 (d, $J = 8.3$ Hz, 1H). ^{13}C -NMR (100 MHz; CDCl_3) δ 56.62 (MeO), 57.03 (MeO), 110.60 (Cq), 113.26 (CH), 116.62 (CH), 126.62 (CH), 127.05 (Cq), 128.27 (Cq), 128.61 (Cq), 130.20 (CH), 131.39 (CH), 131.46 (CH), 131.80 (CH), 132.14 (Cq), 132.27 (Cq), 134.03 (CH), 140.53 (CH), 142.42 (Cq), 150.58 (Cq), 150.91 (Cq), 185.56 (C=O). UV (in MeCN) – λ_{max} [nm] (log ϵ): 360 (4.06). IR (ATIR) ν_{max} [cm^{-1}] 3034-2832 ($\text{CH}_{\text{aromatic}}$, weak), 1634 (C=O, sharp & intense), 1622, 1579, 1553, 1488, 1460, 1451, 1431, 1397, 1385, 1354, 1298, 1267, 1233 (C-O, sharp & intense), 1176, 1127, 1120, 1102, 1082, 1053, 1023. MS (EI+) m/z (rel. intensity): 396 (M^+ , $\text{C}_{21}\text{H}_{15}^{81}\text{BrO}_3$, 18), 335 ($(\text{M})^+$, $\text{C}_{21}\text{H}_{15}^{79}\text{BrO}_3$, 17), 365 ($(\text{M}-31)^+$ $\text{C}_{20}\text{H}_{12}^{81}\text{BrO}_2$, 66), 363 ($(\text{M}-31)^+$ $\text{C}_{20}\text{H}_{12}^{79}\text{BrO}_2$, 100), 350 (5), 348 (4), 322 (12), 320 (11), 300 (7), 285 (8), 269 (10), 200 (9), 176 (8), 158 (6), 91 (4). HRMS calcd for $\text{C}_{21}\text{H}_{15}^{79}\text{BrO}_3$: 394.0205, found: 394.0209. Melting point: 95 °C; orange powder from H_2O), 135 °C; red crystals from acetone.

General procedure for naphtho[2,1,8-*mna*]xanthenium tetrafluoroborate (NXBF₄), benzo[*i*]naphtho[2,1,8-*mna*]xanthenium tetrafluoroborate (B[*i*]NXBF₄) and benzo[*a*]naphtho[8,1,2-*jkl*]xanthenium tetrafluoroborate B[*a*]NXF₄

0.100 g 9-(2-Methoxyphenyl)-1*H*-phenalen-1-one (0.35 mmol) was dissolved in 40 ml DCM in a round bottom flask placed in a NaCl/ice bath. Argon was purged through for 5 minutes and the flask was sealed with a septum and supplied with an argon-filled balloon. While stirring, 1.2 ml BBr_3 in heptane (1 M) was slowly added by syringe. The colour of the solution changed from orange to dark brown. After 10 minutes, the NaCl/ice-bath was removed and the solution was stirred for 4 hours. The solution became red-orange and a precipitation occurred. Adding 30 ml of H_2O quenched the reaction and dissolved the precipitate giving an orange solution. The aqueous layer was separated. The organic salt was extracted with distilled H_2O from DCM. When the aqueous layers were combined and filtered, 5 ml HBF_4 -solution were added, giving a yellow precipitate which was separated by vacuum filtration.

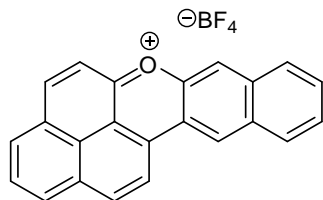
Following the general procedure naphtho[2,1,8-*mna*]xanthenium tetrafluoroborate (NXBF₄) was obtained as a yellow powder in a yield of 36%.



Chemical Formula: $C_{19}H_{11}BF_4O$
Molecular Weight: 342.09

1H -NMR (400 MHz; CD_3CN): 8.14 (ddd, $J = 8.3, 6.9, 1.4$ Hz, 1H), 8.37 (ddd, $J = 8.6, 6.9, 1.4$ Hz, 1H), 8.45 – 8.40 (m, 1H), 8.63 – 8.52 (m, 2H), 8.56 (d, $J = 9.1$ Hz, 1H), 8.59 (t, $J = 7.8$ Hz, 1H), 9.13 (dd, $J = 8.3, 1.4$ Hz, 1H), 9.19 (d, $J = 7.8$ Hz, 2H), 9.28 (d, $J = 8.8$, 1H), 9.41 (d, $J = 9.2$ Hz, 1H) 9.47 (d, $J = 8.8$ Hz, 1H). ^{13}C -NMR (100 Hz; CD_3CN): 116.08 (Cq), 120.38 (Cq), 120.63 (2CH), 121.88 (Cq), 123.03 (CH), 126.76 (CH), 128.77 (Cq), 129.81 (CH), 131.08 (Cq), 131.53 (CH), 138.09 (CH), 140.84 (CH), 141.59 (CH), 145.30 (Cq), 147.96 (CH), 149.03 (CH), 153.69 (Cq), 164.44 (C=O⁺). UV (in MeCN) – λ_{max} [nm] (log ϵ): 347 (3.30), 363 (3.20), 435(3.89), 457 (4.16). IR (ATIR) ν_{max} [cm^{-1}] 3093 (CH_{aromatic}, weak), 1632 (C=O⁺, sharp & intense), 1621, 1610, 1603, 1583, 1567, 1551, 1507, 1454, 1412, 1355, 1330, 1284, 1245, 1228, 1198, 1145, 1138, 1088, 1047, 1032 (B-F, sharp & intense), 988, 866. MS (FAB+) m/z (rel. intensity): 255 (42), 232 (22), 214 (5), 179 (5), 157 (38), 154 (22), 137 (25), 136 (18), , 107 (7), 101 (8), 80 (100), 79 (7), 64 (4), 40 (4). HRMS calcd for $C_{19}H_{11}O$: 305.0966, found: 305.0967. Elemental analysis: Theory: C, 66.66; H, 3.22; Result: C, 66.76; H, 3.11. Melting point: 215-217°C; crystals from acetone.

Following the general procedure, benzo[*i*]naphtho[2,1,8-*mna*]xanthenium tetrafluoroborate B[*i*]NXBF₄ was obtained as a brown powder in a yield of 64%.

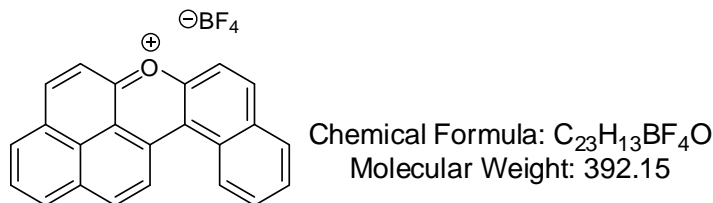


Chemical Formula: $C_{23}H_{13}BF_4O$
Molecular Weight: 392.15

1H -NMR (400 MHz; CD_3CN) δ 7.71 (t, $J = 7.5$ Hz, 1H), 7.79 (t, $J = 7.1$ Hz, 1H), 8.15 (d, $J = 8.4$ Hz, 1H), 8.25 (d, $J = 8.5$ Hz, 1H), 8.39 (d, $J = 9.1$ Hz, 1H), 8.43 (t, $J = 7.7$ Hz, 1H), 8.61 (s, 1H), 9.05 (m, 2H), 9.20 (d, $J = 8.7$ Hz, 1H), 9.29 (d, $J = 9.1$ Hz, 1H), 9.36 (d, $J = 8.7$ Hz, 1H), 9.49 (s, 1H). ^{13}C -NMR (100 MHz; CD_3CN) δ 115.63 (Cq), 116.82 (CH), 118.66 (Cq), 120.92 (CH), 122.33 (Cq), 123.45 (CH), 128.40 (CH), 128.48 (CH), 128.63 (Cq), 128.96

(CH), 130.21 (CH), 131.20 (Cq), 131.45 (CH), 131.86 (CH), 132.33 (Cq), 137.30 (Cq), 141.83 (CH), 142.75 (CH), 145.96 (Cq), 148.40 (CH), 149.11 (Cq), 150.36 (CH), 166.07 (C=O⁺). UV (in MeCN) – λ_{max} [nm] (log ϵ): 322 (4.15), 363 (3.82), 469 (4.68). IR (ATIR) ν_{max} [cm⁻¹] 3074 (CH_{aromatic}, weak), 1603, 1597, 1591, 1566 (C=O⁺, sharp & intense), 1507, 1472, 1445, 1421, 1360, 1334, 1288, 1239, 1211, 1199, 1163, 1144, 1136, 1027 (B-F, sharp & intense). MS(EI+) *m/z* (rel. intensity): 305 (100), 276 (21), 274 (9), 231 (5), 219 (5), 187 (8), 181 (7), 169 (8), 153 (13), 131 (10), 119 (8), 85 (6), 69 (16), 44 (83), 40 (15), 36 (22). HRMS calcd for C₂₃H₁₃O⁺: 305.0966, found: 336.0967. Melting point: 276-280 °C, crystals from acetone.

Following the general procedure, benzo[*a*]naphtho[8,1,2-*ijkl*]xanthenium tetrafluoroborate B[*a*]NXBF₄ was obtained as a brown powder in a yield of 67%.



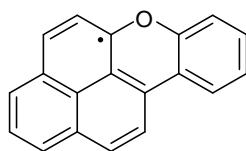
¹H-NMR (400 MHz; CD₃CN) δ 7.95 (ddd, *J* = 8.0, 7.1, 1.0 Hz, 1H), 8.07 (ddd, *J* = 8.5, 7.1, 1.4 Hz, 1H), 8.26 (d, *J* = 9.1 Hz, 1H), 8.33 (dd, *J* = 8.0, 1.2 Hz, 1H), 8.58 (t, *J* = 7.7 Hz, 1H), 8.60 (d, *J* = 9.1 Hz, 1H), 8.69 (d, *J* = 9.1 Hz, 1H), 9.18 – 9.10 (m, 2H), 9.28 (d, *J* = 8.5 Hz, 1H), 9.34 (d, *J* = 9.1 Hz, 1H), 9.39 (d, *J* = 9.1 Hz, 1H), 9.61 (d, *J* = 9.1 Hz, 1H). ¹³C-NMR (100 MHz; CD₃CN) δ 117.00 (Cq), 117.64 (Cq), 118.65 (CH), 120.11 (CH), 121.84 (Cq), 126.27 (CH), 128.26 (CH), 129.20 (Cq), 129.24 (Cq), 129.97 (CH), 130.57 (Cq), 131.39 (CH), 131.43 (CH), 131.45 (CH), 133.17 (Cq), 139.27 (CH), 140.42 (CH), 140.95 (CH), 144.32 (Cq), 146.73 (CH), 146.88 (CH), 155.76 (Cq), 161.38 (C=O⁺). UV (in MeCN) – λ_{max} [nm] (log ϵ): 311 (4.91), 505 (5.12). IR (ATIR) ν_{max} [cm⁻¹] 3061, 1617, 1602, 1577, 1564, 1545, 1518, 1495, 1472, 1431, 1412, 1382, 1350, 1324, 1279, 1246, 1236, 1224, 1192, 1176, 1147, 1137, 1115, 1091, 1032, 983. MS(EI+) *m/z* (rel. intensity): 305 (100), 276 (28), 274 (10), 153 (9), 152 (8), 137 (7), 69 (3), 44 (4), 40 (3). HRMS calcd for C₂₃H₁₃O⁺: 305.0966, found: 305.0972. Melting point: 273-275 °C; crystals from acetone.

Naphtho[1,2,8-*mna*]xanthenyl (NX)

0.05 g (0.1 mmol) naphthoxanthenium tetrafluoroborate and 0.05 g (0.1 mmol) of tetrabutylammonium iodide were dissolved in 5 ml dry acetonitrile. Under argon, the solution was stirred at room temperature for 1 h. After evaporation via rotary evaporator, 5 ml distilled H₂O was added. A yellow solution with a brown precipitate was obtained. The material containing **1** was separated through filtration and washed with 5 ml distilled H₂O. 0.03 g precipitate containing **1** was isolated.

Procedure to obtain UV sample:

In 7 ml of nitrogen saturated DMSO (technical grade), 14 mg (1 eq; 0.04 mmol) of naphtho[1,2,8-*mna*]xanthenium tetrafluoroborate were dissolved and added via a syringe to 74 mg of NaI (12 eq; 0.49 mmol) in a dry flask flushed with nitrogen. The mixture was heated up at 40 °C and stirred for 2 h. The colour became dark orange and a sample was taken using a syringe for UV/Vis and ESR spectroscopy measurements.

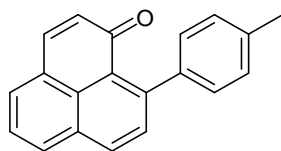


Chemical Formula: C₁₉H₁₁O^{•+}
Molecular Weight: 255.29

UV (in DMSO) – λ_{max} [nm] (log ϵ): 372 (4.45), 395 (4.47), 412 (4.47), 460 (3.61), 492 (3.53).

9-*p*-Tolyl-1*H*-phenalen-1-one (57)

Following the general procedure, the *Grignard* reagent was generated from 0.23 g (9.6 mmol; 2.5 eq) Mg and 1.42 g (8.3 mmol; 2 eq) 1-bromo-4-methylbenzene mixed with 3 ml THF at 30-40 °C. After reflux with phenalenone (1 eq) at 55-60 °C and subsequent oxidation with DDQ 9-*p*-tolyl-1*H*-phenalen-1-one was obtained as orange powder in a yield of 60% (0.90 g; 3.3 mmol).

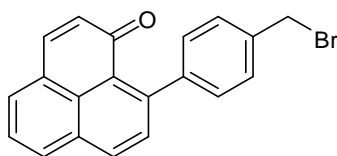


Chemical Formula: C₂₀H₁₄O
Molecular Weight: 270.32

¹H-NMR (400 Hz; CDCl₃) δ 2.45 (s, Me), 6.60 (d, *J* = 9.7 Hz, 1H), 7.34 – 7.27 (m, 4H), 7.59 (d, *J* = 8.3 Hz, 1H), 7.60 (dd, *J* = 8.2, 7.1 Hz, 2H), 7.67 (d, *J* = 9.7 Hz, 1H), 7.76 (d, *J* = 7.0 Hz, 1H), 8.02 (dd, *J* = 8.2, 1.0 Hz, 1H), 8.15 (d, *J* = 8.3 Hz, 1H). ¹³C-NMR: (100 Hz; CDCl₃) δ 21.46 (CH₃), 126.16 (Cq), 126.35 (CH), 127.96 (2CH), 128.49 (Cq), 128.52 (Cq), 129.15 (2CH), 130.66 (CH), 131.44 (CH), 131.72 (Cq), 131.80 (CH), 131.84 (CH), 133.79 (CH), 136.98 (Cq), 139.97 (Cq), 140.38 (CH), 147.88 (Cq), 185.91 (C=O). UV (in MeCN) – λ_{max} [nm] (log ε): 360 (4.14). IR (ATIR) ν_{max} [cm⁻¹] 3010 (CH_{aromatic}, weak), 1635, 1627, 1619 (C=O, sharp & intense), 1580, 1553, 1518, 1494, 1453, 1437, 1397, 1383, 1351, 1279, 1254, 1243, 1218, 1181, 1155, 1126, 1108, 1038, 1017. MS (Isobutane CI+) *m/z* (rel. intensity): 271 ((M+H)⁺, 17), 137 (12), 113 (31), 85 (45), 73 (100), 71 (57). HRMS calcd for C₂₀H₁₅O: 271.1123, found: 271.1119. Melting point: 138-140 °C; crystals from CH₂Cl₂.

9-(4-(Bromomethyl)phenyl)-1H-phenalen-1-one (58)

In a 2-neck round bottom flask flushed with argon, 300 mg of 9-*p*-tolyl-1H-phenalen-1-one, 198 mg of *N*-bromosuccinimide were mixed with 30 ml of CCl₄. The flask was connected to a reflux apparatus flushed with argon and then 30 mg of benzoylperoxide were added. The mixture was refluxed for 5 h. After cooling down the mixture, filtration was carried out. The filtrate was separated via rotary evaporation within the fumehood. An orange crude solid was obtained and purified via recrystallisation using diethylether/hexane yielding 92%.



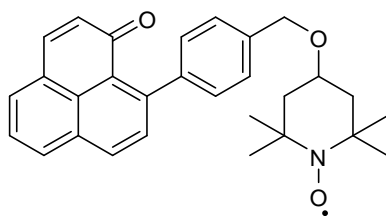
Chemical Formula: C₂₀H₁₃BrO
Molecular Weight: 349.22

¹H-NMR (500 Hz; CDCl₃) δ 4.60 (s, CH₂), 6.58 (d, *J* = 9.7 Hz, 1H), 7.35 (d, *J* = 8.2 Hz, 2H), 7.49 (d, *J* = 8.1 Hz, 2H), 7.58 (d, *J* = 8.3 Hz, 1H), 7.62 (dd, *J* = 8.2, 7.1 Hz, 1H), 7.69 (d, *J* = 9.7 Hz, 1H), 7.78 (d, *J* = 6.5 Hz, 1H), 8.04 (d, *J* = 7.6 Hz, 1H), 8.17 (d, *J* = 8.3 Hz, 1H). ¹³C-NMR (125 MHz; CDCl₃) δ 33.73 (CH₂), 126.42 (Cq), 126.67 (CH), 128.61 (2CH), 128.85

(Cq), 128.82 (Cq), 129.18 (2CH), 130.70 (CH), 131.57 (CH), 131.59 (CH), 131.89 (CH), 132.15 (Cq), 133.91 (CH), 136.78 (Cq), 140.58 (CH), 143.38 (Cq), 147.11 (Cq), 185.81 (C=O). UV (in MeCN) – λ_{max} [nm] (log ϵ): 360 (4.09). IR (ATIR) ν_{max} [cm^{-1}] 3011 ($\text{CH}_{\text{aromatic}}$, weak), 1631 (C=O, sharp & intense), 1622, 1580, 1549, 1491, 1437, 1410, 1398, 1383, 1349, 1277, 1249, 1231, 1208, 1175, 1149, 1134, 1127, 1108, 1081, 1041, 1018. MS (Isobutane CI+) m/z (rel. intensity): 351 ($\text{C}_{20}\text{H}_{14}\text{O}^{81}\text{Br}+\text{H}$), 100), 349 ($\text{C}_{20}\text{H}_{14}\text{O}^{79}\text{Br}+\text{H}$), 99), 305 (26), 271 (63), 262 (9), 95 (3), 69 (12). HRMS calcd for $\text{C}_{20}\text{H}_{14}\text{OBr}$: 349.0228, found: 349.0231. Melting point: 197-199 °C; crystals from diethylether/hexane.

9-(4-((TEMPO)methoxy)phenyl)-1*H*-phenalen-1-one (56)

In 3 ml of DMF, 110 mg of 4-hydroxy-TEMPO were dissolved and treated with 38 mg (pure after separation of oil with hexane) of NaH. The reaction flask was placed in an ice-bath and the mixture was stirred for 1 hour. Afterwards 200 mg of 9-(4-tolyl)-1*H*-phenalen-1-one in 8 ml of DMF were added gradually and the ice-bath was removed. After stirring overnight at room temperature, the reaction was quenched with 30 ml of H_2O and the product was extracted using EtOAc (3 x 30ml) and the organic phase was subsequently washed with saturated NaCl solution (2 x 20 ml). The crude product was purified via column chromatography on silica using DCM as an eluent giving 44 % yield (88 mg; 0.2 mmol).

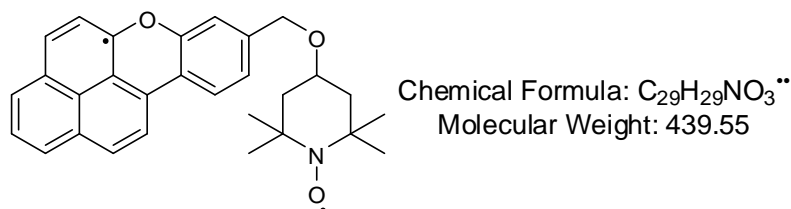


Chemical Formula: $\text{C}_{29}\text{H}_{30}\text{NO}_3^{\bullet}$
Molecular Weight: 440.55

UV (in MeCN) – λ_{max} [nm] (log ϵ): 360 (4.00). IR (ATIR) ν_{max} [cm^{-1}] 3058, 2991, 2967, 2953, 2928, 2855, 1636, 1576, 1553, 1492, 1464, 1452, 1439, 1377, 1363, 1350 (N-O \cdot , sharp & intense)²⁷¹, 1320, 1287, 1241, 1217, 1175, 1125, 1080, 1003. MS (EI+) m/z (rel. intensity): 440 (15), 410 (62), 408 (3), 285 (15), 269 (100), 255 (21), 239 (18), 208 (5), 124 (33), 98 (4), 91 (3), 58 (4), 41 (3). HRMS calcd for $\text{C}_{29}\text{H}_{30}\text{O}_3\text{N}$: 440.2226, found: 440.2223. Melting point: 134-136 °C; crystals from CH_2Cl_2 .

8-((TEMPO)methoxy)naphtho[2,1,8-*mna*]xanthenyl (NXTEMPO)

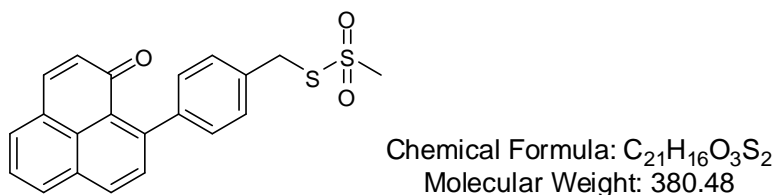
In 5 ml of MeCN, 10 mg of 9-(4-((TEMPO)methoxy)phenyl)-1*H*-phenalen-1-one and 3 mg of TCNE were dissolved. The yellow solution was purged through with Argon for 10 minutes and then irradiated at a wavelength of 360 ± 40 nm for 1 hour. Then the solvent was separated via rotary evaporation and the brown solid containing the biradical was used for ESR and UV measurements indicating the proposed target species.



UV (in MeCN) – λ_{max} [nm]: 367, 397, 410, *broad absorptions between 445-650 nm*.

S-4-(1-oxo-1*H*-phenalen-9-yl)benzyl methanesulfonothioate (54)

100 mg of 9-(4-(bromomethyl)phenyl)-1*H*-phenalen-1-one and 39 mg of sodium methanethiosulfonate were dissolved in 10 ml of ethanol. The mixture was then refluxed for 3 h. Afterwards 100 ml of H_2O were added and the product was extracted using CH_2Cl_2 (3 x 30 ml). By means of column chromatography on silica using CH_2Cl_2 as an eluent, the desired compound was obtained in a yield of 84% (124 mg; 0.3 mmol).

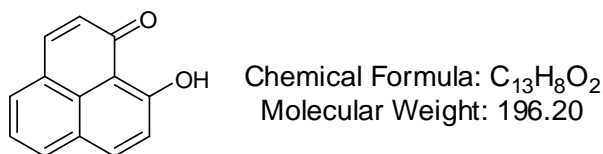


1H -NMR (400 Hz; $CDCl_3$) δ 3.05 (s, Me), 4.45 (s, CH_2), 6.56 (d, $J = 9.7$ Hz, 1H), 7.37 (d, $J = 8.2$ Hz, 2H), 7.51 (d, $J = 8.2$ Hz, 2H), 7.55 (d, $J = 8.3$ Hz, 1H), 7.64 (dd, $J = 8.2, 7.1$ Hz, 1H), 7.70 (d, $J = 9.7$ Hz, 1H), 7.80 (d, $J = 6.3$ Hz, 1H), 8.05 (d, $J = 8.2$ Hz, 1H), 8.19 (d, $J = 8.3$ Hz, 1H). ^{13}C -NMR: (100 Hz; $CDCl_3$) δ 41.00 (CH_2), 51.72 (CH_3), 126.45 (Cq), 126.74 (CH), 128.63 (Cq), 128.78 (Cq), 128.80 (2CH), 129.33 (2CH), 130.60 (CH), 131.35 (CH), 131.68 (CH), 131.92 (CH), 132.19 (Cq), 133.95 (CH), 134.13 (Cq), 140.64 (CH), 143.40 (Cq), 146.78

(Cq), 185.76 (C=O). UV (in MeCN) – λ_{max} [nm] (log ϵ): 360 (3.99). IR (ATIR) ν_{max} [cm^{-1}] 3063, 3029, 2929, 1631, 1622, 1580, 1553, 1494, 1402, 1385, 1354, 1312, 1258, 1243, 1216, 1179, 1128 (S=O, sharp & intense), 1017. MS (Isobutane CI+) m/z (rel. intensity): 381 (13), 357 (3), 335 (14), 303 (6), 285 (49), 271 (35), 245 (8), 153 (5), 137 (18), 113 (10), 81 (100), 59 (47). HRMS calcd for $\text{C}_{21}\text{H}_{17}\text{O}_3\text{S}_2$: 381.0619, found: 381.0617. Melting Point: 172-174 °C crystals from CH_2Cl_2 .

9-Hydroxy-1*H*-phenalen-1-one (61)

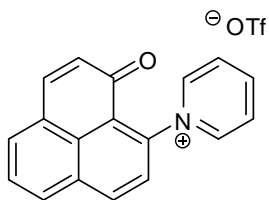
In 200 ml of 1,2-dichloroethane, 19.8 g (119 mmol; 1 eq) of cinnamoyl chloride and 22.0 g (139 mmol; 1.2 eq) of 2-methoxynaphthalene were dissolved. The solution was cooled in a NaCl/ice bath. Then 18 g (135 mmol; 1.1 eq) of AlCl_3 were slowly added while stirring within 5 minutes. After 1 h of stirring, the reaction was cooled again and further 18 g of AlCl_3 were added. The reaction was stirred at room temperature over night. The next day, the mixture was refluxed for 3 hours. After that, a mixture of 150 g of ice and 80 ml of conc. HCl were added to the reaction mixture. The result was a yellow-brown solid which was extracted using DCM (4 x 300 ml). After filtration and rotary evaporation, the product was obtained in a yield of 95% (22.15 g, 113 mmol; lit.: 54% after sublimation).²⁵⁰



$^1\text{H-NMR}$ (400 MHz; CDCl_3) δ 7.17 (d, $J = 9.3$ Hz, 2H), 7.60 (t, $J = 7.6$ Hz, 1H), 8.01 (d, $J = 7.7$ Hz, 2H), 8.09 (d, $J = 9.3$ Hz, 2H), 16.04 (s, 1OH). $^{13}\text{C-NMR}$ (100 MHz; CDCl_3) δ 111.23 (Cq), 123.86 (2CH), 124.18 (CH), 125.71 (2Cq), 127.01 (Cq), 133.02 (2CH), 141.21 (2CH), 179.32 (2CO). MS (EI+) m/z (rel. intensity): 196 (100), 168 (45), 154 (3), 139 (36), 113 (4), 98 (4), 84 (8), 70 (25), 44 (17). Melting point: 165-166 °C; crystals from CH_2Cl_2 (lit.: 201-202 °C)²⁵⁰.

1-(1-Oxo-1*H*-phenalen-9-yl)pyridinium triflate (68)

To a cooled solution of 100 mg (0.5 mmol; 1 eq) of 9-hydroxy-1*H*-phenalen-1-one in 5 ml of pyridine, 0.1 ml (0.6 mmol; 1.2 eq) of triflic anhydride was added dropwise while stirring under argon atmosphere. After 5 minutes the ice bath was removed and the reaction was stirred for 4 h. Then 10 ml of H₂O was added and extraction using diethylether (3 x 15 ml) was carried out. The brown aqueous layer was left in a beaker in the fumehood over night. The next day the brown solid was washed with 50 ml of H₂O giving the product in a yield of 51% (106 mg, 0.3 mmol).



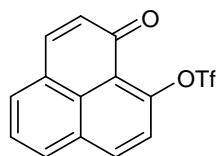
Chemical Formula: C₁₈H₁₂NO⁺
Molecular Weight: 258.29

¹H-NMR (400 MHz; CD₃CN) δ 6.53 (d, *J* = 9.8 Hz, 1H), 7.89 (t, *J* = 8.3 Hz, 2H), 7.96 (d, *J* = 9.8 Hz, 1H), 8.27 – 8.20 (m, 2H), 8.33 (d, *J* = 8.4 Hz, 1H), 6.53 (d, *J* = 9.8 Hz, 1H), 8.79 (tt, *J* = 7.9, 1.4 Hz, 1H), 6.53 (d, *J* = 9.8 Hz, 2H). ¹³C-NMR (100 MHz; CD₃CN) δ 120.51 & 123.70 (*J*_{C,F} = 320 Hz), 122.81 (C_q), 126.61 (CH), 128.31 (C_q), 129.30 (2CH), 129.84 (CH), 130.29 (CH), 133.57 (CH), 134.79 (CH), 135.45 (CH), 138.04 (CH), 142.59 (C_q), 143.41 (CH), 146.17 (CH), 148.53 (CH), 184.66 (C=O) (*two quaternary carbons could not be observed, possibly due to signal overlap*). UV (in MeCN) – λ_{max} [nm] (log ε): 300 (3.84), 358 (3.95), 388 (3.94). IR (ATIR) ν_{max} [cm⁻¹] 3124-3065 (CH_{aromatics}, weak), 1640, 1628 (C=O, sharp & intense), 1579, 1559, 1474, 1346 (S=O, slightly broad & intense), 1256, 1239, 1224, 1156 (S=O, slightly broad & intense), 1131, 1118, 1028 (CF₃, sharp & intense), 963. MS (FAB+) *m/z* (rel. intensity): 259 (36), 258 (100), 180 (27), 154 (13), 138 (5), 40 (25). HRMS calcd for C₁₈H₁₂ON: 258.0919, found: 258.0916. Melting point: 172-173 °C; crystals from pyridine/H₂O.

1-Oxo-1*H*-phenalen-9-yl trifluoromethanesulfonate (69)

In a round bottom flask, 500 mg (2.5 mmol; 1 eq) of 9-hydroxy-1*H*-phenalen-1-one were dissolved in 50 ml of toluene. Then 50 ml of an aqueous K₃PO₄ solution (30% (w/w)) was added and the flask was placed in a NaCl/ice bath. While stirring, 0.52 ml (3.1 mmol; 1.2 eq)

of triflic anhydride was added dropwise to the mixed bilayer. After 5 minutes the ice bath was removed and the reaction was stirred for 1 h. The organic layer was separated via separation funnel. Using 20ml of toluene the aqueous layer was extracted once and combined with the organic layer. After rotary evaporation under vacuum pressure the product was obtained as pale yellow crystals in a yield of 80% (710 mg; 2.2 mmol).

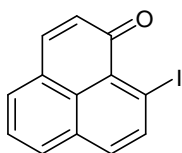


Chemical Formula: C₁₄H₇F₃O₄S
Molecular Weight: 328.26

¹H-NMR (400 MHz; CDCl₃) δ 6.72 (d, *J* = 9.8 Hz, 1H), 7.57 (d, *J* = 8.8 Hz, 1H), 7.69 (dd, *J* = 8.2, 7.1 Hz, 1H), 7.73 (d, *J* = 9.8 Hz, 1H), 7.84 (d, *J* = 6.9 Hz, 1H), 8.05 (d, *J* = 8.2 Hz, 1H), 8.27 (d, *J* = 8.9 Hz, 1H). ¹³C-NMR (100 MHz; CDCl₃) δ 115.21-122.89 (quartet, *J*_{C,F} = 317 Hz, CF₃), 120.77 (Cq), 122.18 (CH), 127.77 (CH), 128.26 (Cq), 128.37 (Cq), 129.80 (CH), 131.65 (Cq), 131.81 (CH), 132.87 (CH), 136.90 (CH), 140.96 (CH), 149.46 (Cq), 183.35 (C=O). ¹⁹F NMR (CDCl₃) δ -73.79 (s). UV (in MeCN) – λ_{max} [nm] (log ε): 307 (3.57), 354 (3.96), 382 (3.86). IR (ATIR) [cm⁻¹] ν_{max} 3058 (CH_{aromatic}, weak), 1636 (C=O, sharp & intense), 1588, 1577, 1569, 1506, 1422, 1401, 1364, 1348, 1243, 1219, 1199, 1180, 1168, 1139, 1123, 1102, 1070. MS (EI+) *m/z* (rel. intensity): 378 (90), 264 (12), 236 (41), 195 (38), 167 (34), 139 (100), 69 (10), 44 (4). HRMS calcd for C₁₄H₇F₃O₄S: 328.0017, found: 328.0013. Melting point: 107-108 °C; crystals from acetone.

9-Iodo-1*H*-phenalen-1-one (70)

In a round bottom flask, 300 mg (0.9 mmol; 1 eq) of 1-oxo-1*H*-phenalen-9-yl trifluoromethanesulfonate and 758 mg (4.6 mmol; 5 eq) of KI were combined in 5 ml of dry DMF. The mixture was heated at 80 °C under argon atmosphere over night. The next day, the reaction was diluted with 100 ml of H₂O. The product was extracted with diethylether (4 x 50 ml), washed with H₂O (4 x 50 ml) and 30 ml of saturated NaCl solution. Afterwards, the ether solution was dried over Na₂SO₄ and evaporated via rotary evaporation. A column chromatography was carried out using DCM as eluent yielding the desired product as orange crystals in a yield of 69% (193 mg; 0.6 mmol).

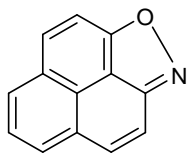


Chemical Formula: C₁₃H₇IO
Molecular Weight: 306.10

¹H-NMR (500 MHz; CDCl₃) δ 6.79 (d, *J* = 9.7 Hz, 1H), 7.61 (dd, *J* = 8.1, 7.1 Hz, 1H), 7.66 (d, *J* = 9.7 Hz, 1H), 7.70 (d, *J* = 8.6 Hz, 1H), 7.70 (d, *J* = 6.9 Hz, 1H), 7.97 (dd, *J* = 8.2, 0.9 Hz, 1H), 8.37 (d, *J* = 8.5 Hz, 1H). ¹³C-NMR (125 MHz; CDCl₃) δ 100.25 (Cq), 126.94 (CH), 127.23 (Cq), 128.49 (Cq), 128.71 (Cq), 129.28 (CH), 131.54 (CH), 131.98 (CH), 132.42 (Cq), 133.97 (CH), 140.01 (CH), 142.24 (CH), 183.49 (C=O). UV (in MeCN) – λ_{max} [nm] (log ε): 307 (3.74), 365 (4.33), 384 (3.91). IR (ATIR) ν_{max} [cm⁻¹] 3033 (CH_{aromatic}, weak), 1623 (C=O, sharp & intense), 1572, 1548, 1487, 1427, 1401, 1353, 1331, 1256, 1243, 1182, 1126, 1090, 1046, 1000. MS (EI+) *m/z* (rel. intensity): 306 (100), 278 (16), 151 (73), 150 (29), 84 (14), 75 (6), 49 (13). HRMS calcd for C₁₃H₇IO: 305.9542, found: 305.9546. Melting point: 121-122 °C; crystals from acetone.

Phenaleno[1,9-*cd*]isoxazole (71)

In a round bottom flask, 100 mg (0.3 mmol; 1 eq) of 1-oxo-1*H*-phenaleno-9-yl trifluoromethanesulfonate and 100 mg (1.5 mmol; 5 eq) of NaN₃ were mixed in 10 ml of DMF. Under argon atmosphere, the reaction was stirred at room temperature for 72 h. The solution was diluted with 100 ml of H₂O and subsequently extracted with diethylether (4 x 30 ml). After washing with H₂O (3 x 50 ml) and 30 ml of saturated NaCl solution, the ether solution was dried over Na₂SO₄. The solvent was removed via rotary evaporation yielding the desired product as yellow crystals in a yield of 90% (53 mg; 0.3 mmol).



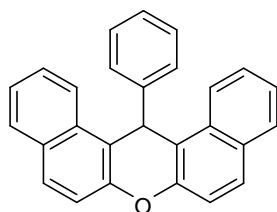
Chemical Formula: C₁₃H₇NO
Molecular Weight: 193.20

¹H-NMR (400 MHz; CDCl₃) δ 7.73 (d, *J* = 9.4 Hz, 1H), 7.90 (dd, *J* = 8.1, 7.4 Hz, 1H), 7.95 (d, *J* = 9.0 Hz, 1H), 7.99 (d, *J* = 9.4 Hz, 1H), 8.13 (d, *J* = 7.4 Hz, 1H), 8.24 (d, *J* = 9.0 Hz, 1H), 8.27 (d, *J* = 8.1 Hz, 1H). ¹³C-NMR (100 MHz; CDCl₃) δ 111.89 (CH), 115.42 (CH), 117.45 (Cq), 122.90 (Cq), 126.57 (CH), 127.31 (CH), 127.67 (CH), 128.09 (Cq), 128.17 (Cq), 130.30

(CH), 134.43 (CH), 153.59 (Cq), 161.21 (Cq). UV (in MeCN) – λ_{max} [nm] (log ϵ): 314 (4.08), 328 (4.24), 338 (3.88). IR (ATIR) ν_{max} [cm^{-1}] 3035 ($\text{CH}_{\text{aromatic}}$, weak), 1695, 1633, 1617, 1577, 1550, 1495, 1475, 1458, 1412, 1344, 1317, 1237, 1219, 1181, 1142, 1115, 1001. . MS (EI+) m/z (rel. intensity): 193 (100), 164 (31), 138 (18), 137 (8), 111 (3), 87 (4), 83 (5), 63 (3), 40 (3). HRMS calcd for $\text{C}_{13}\text{H}_7\text{NO}$: 193.0528, found: 193.0527. Melting point: 176 °C; crystals from acetone.

14-phenyl-14H-dibenzo[*a,j*]xanthene (85)

1 ml of HCl were added to a solution of 40 ml of glacial acetic acid containing 5.1 ml (50 mmol; 1 eq) of benzaldehyde and 14.43 g (100 mmol; 2 eq) of 2-naphthol. The solution was refluxed at 100 °C under argon atmosphere for 4 h. After cooling down, white crystals were separated by filtration yielding the pure product in a yield of 79% (14.1 g; 39 mmol; lit.: 60%).²⁰



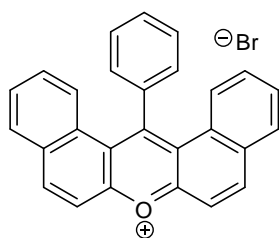
Chemical Formula: $\text{C}_{27}\text{H}_{18}\text{O}$
Molecular Weight: 358.43

$^1\text{H-NMR}$ (400 Hz; CDCl_3) δ 6.49 (s, 1H), 6.99 (t, $J = 7.4$ Hz, 1H), 7.14 (t, $J = 7.7$ Hz, 2H), 7.41 (t, $J = 7.4$ Hz, 2H), 7.49 (d, $J = 8.9$ Hz, 2H), 7.53 (d, $J = 7.3$ Hz, 2H), 7.60 – 7.54 (m, 2H), 7.79 (d, $J = 8.9$ Hz, 2H), 7.83 (d, $J = 8.1$ Hz, 2H), 8.40 (d, $J = 8.5$ Hz, 2H). $^{13}\text{C-NMR}$ (100 Hz, CDCl_3) δ 38.16 (CH), 117.46 (Cq), 118.14 (CH), 122.81 (CH), 124.36 (CH), 126.50 (Cq), 126.91 (CH), 128.38 (CH), 128.60 (CH), 128.92 (CH), 128.97 (CH), 131.19 (Cq), 131.59 (Cq), 145.11 (Cq), 148.89 (Cq). (*The literature reports only 11 peaks, therefore the literature report is incomplete.*) MS (Isobutane CI+) m/z (rel. intensity): 359 (100), 281 (25), 85 (35), 73 (68). Melting Point: 180-181 °C; crystals from acetic acid (lit.: 181°C; crystals from ethanol/ H_2O)²⁷².

Benzo[5,6]naphthaceno[1,12,11,10-*jklmna*]xanthylium tetrafluoroborate (BNAXBF₄)

In a two-neck round bottom flask, 300 mg (0.8 mmol; 1 eq) of 14-phenyl-14*H*-dibenzo[*a,j*]xanthene were dissolved in 25 ml of glacial acetic acid under reflux at 100 °C. Then 0.05 ml (1 mmol; 1.2 eq) of Br₂ mixed with 5 ml acetic acid were added dropwise to the solution and the reaction was refluxed for 30 minutes. After cooling down the red solution, the precipitate was separated by vacuum filtration. The crude product was recrystallised from acetic acid resulting in red-orange crystals with a golden lustre in a yield of 59% (216 mg; 0.5 mmol; lit.: 83%). Without further purification, the batch of 14-phenyldibenzo[*a,j*]xanthenium bromide **86** were dissolved in 60 ml of MeCN and 5 ml of HBF₄ (48% (w/w)) solution. After UV irradiation over night, black needles indicating benzo[5,6]naphthaceno[1,12,11,10-*jklmna*]xanthylium tetrafluoroborate were obtained in a yield of 30% over two steps (112 mg; 0.3 mmol).

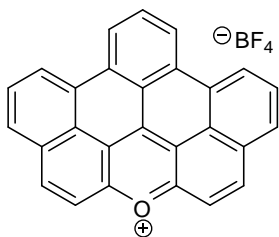
14-phenyldibenzo[*a,j*]xanthenium bromide



Chemical Formula: C₂₇H₁₇BrO
Molecular Weight: 437.33

¹H-NMR (400 Hz, MeCN) δ 7.22 (d, *J* = 8.8 Hz, 2H), 7.47 (ddd, *J* = 8.7, 7.2, 1.5 Hz, 2H), 7.60-7.53 (m, 2H), 7.82 (ddd, *J* = 8.0, 7.2, 1.0 Hz, 2H), 7.95-7.89 (m, 2H), 8.00 (ddd, *J* = 6.7, 3.9, 1.3 Hz, 1H), 8.29 (d, *J* = 9.1 Hz, 4H), 8.90 (d, *J* = 9.1 Hz, 2H). MS (FAB+) *m/z* (rel. intensity): 437 (M⁺; C₂₇H₁₇O⁸¹Br, 5), 435 (M⁺; C₂₇H₁₇O⁷⁹Br, 5), 357 (17), 329 (4), 307 (7), 176 (43), 154 (100), 136 (48), 84 (18), 24 (33). Melting Point: 210-212 °C; crystals from acetic acid. *Due to impurities a ¹³C NMR spectrum could not be interpreted.*

Benzo[5,6]naphthaceno[1,12,11,10-*jklmna*]xanthylium tetrafluoroborate (BNAXBF₄)

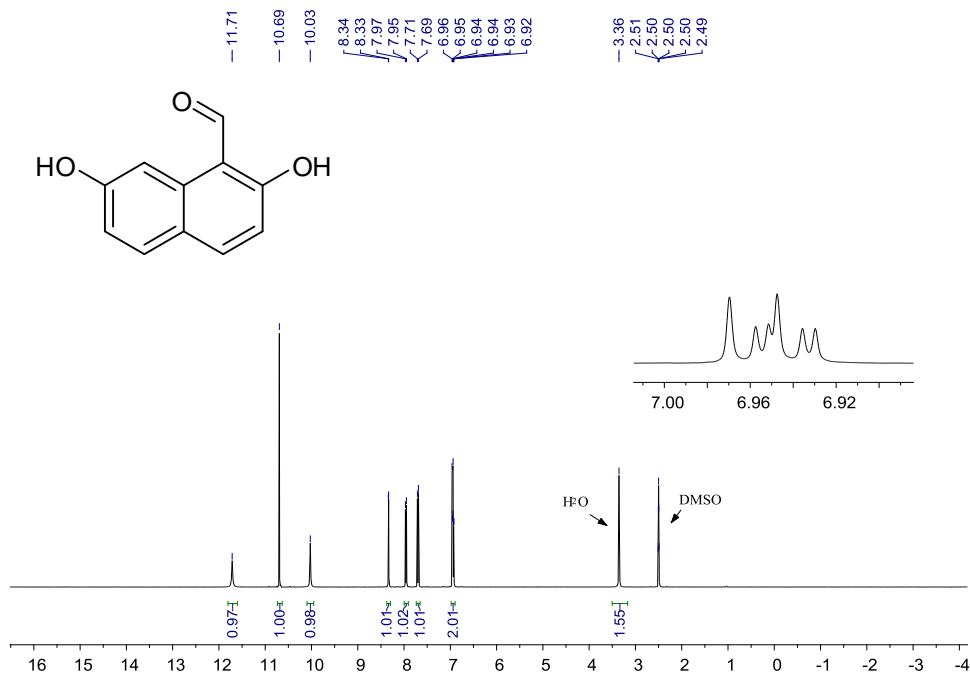


Chemical Formula: C₂₇H₁₃BF₄O
Molecular Weight: 440.20

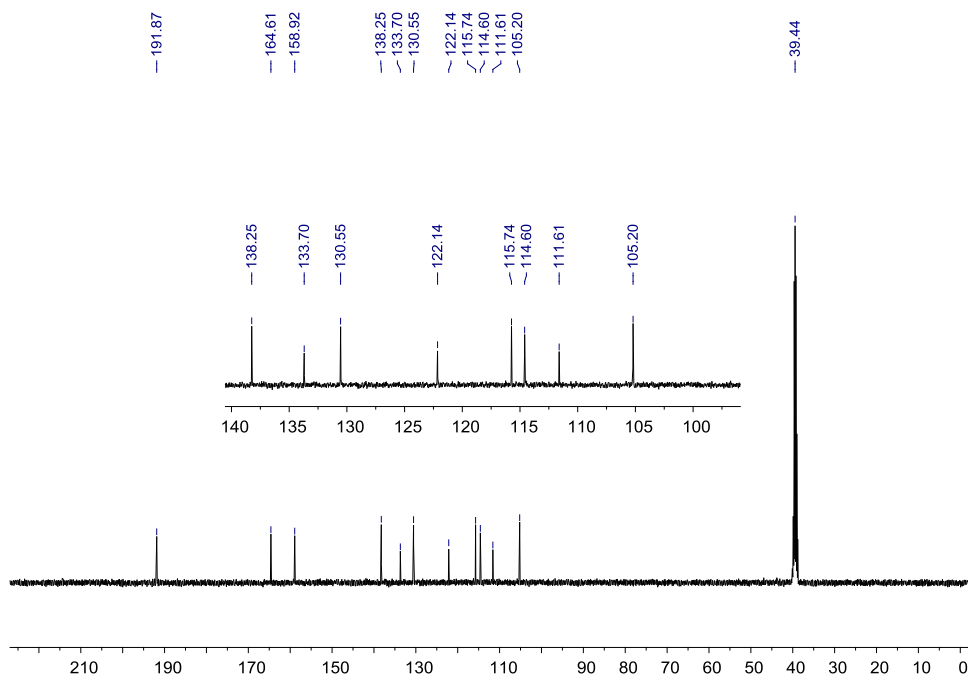
IR (ATIR) ν_{\max} [cm^{-1}] 3055 ($\text{CH}_{\text{aromatics}}$, weak), 1617, 1605, 1582 ($\text{C}=\text{O}^+$, intense), 1464, 1431, 1395, 1353, 1335, 1314, 1264, 1251, 1241, 1210, 1199, 1144, 1077, 1022 (B-F, intense). MS (FAB+) m/z (rel. intensity): 353 (36), 121 (30), 91 (10), 77 (10), 44 (100). . Melting Point: > 360 °C; crystals from acetonitrile. HRMS calcd for $\text{C}_{27}\text{H}_{13}\text{O}$: 353.0966, found: 353.0968. *NMR spectra could not be carried out due to poor solubility.*

12. Appendix

2,7-Dihydroxy-1-naphthaldehyde

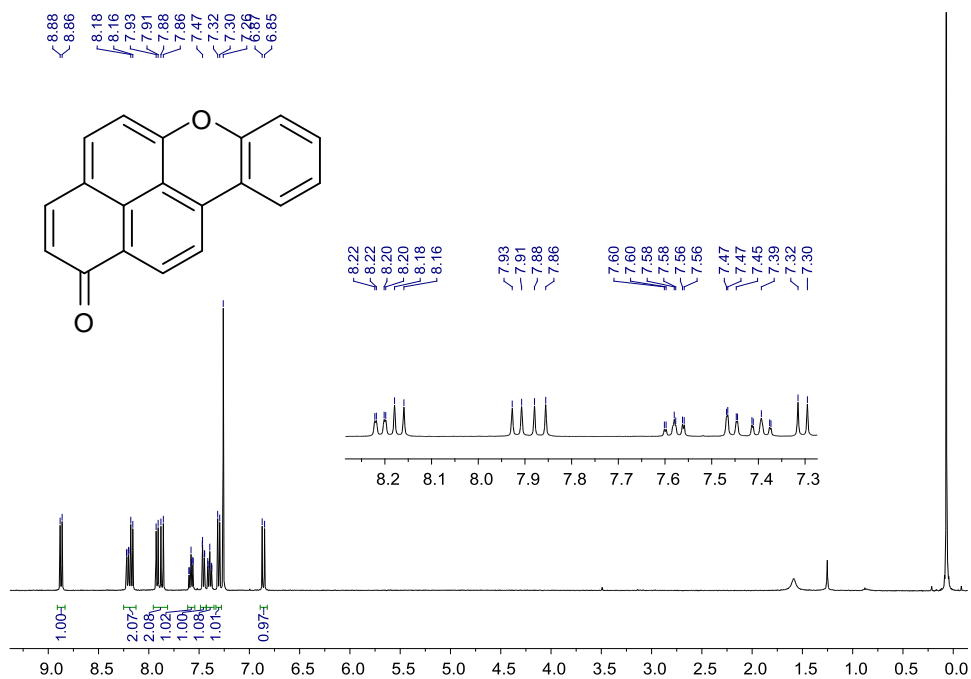


Appendix 1 $^1\text{H-NMR}$ spectrum (400 MHz; $\text{DMSO-}d_6$) of 2,7-dihydroxy-1-naphthaldehyde.

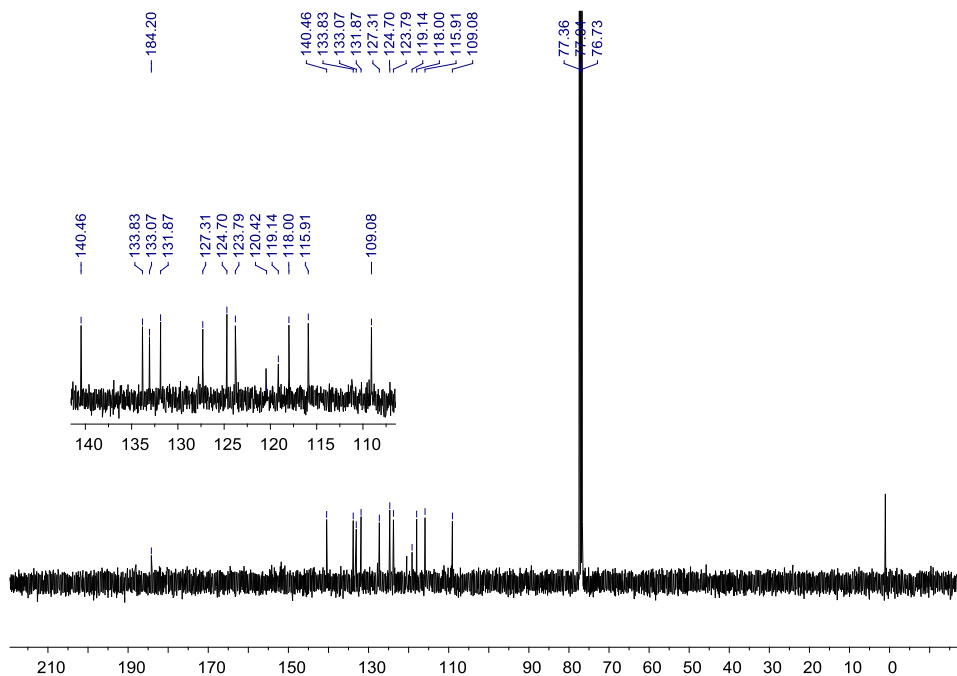


Appendix 2 $^{13}\text{C-NMR}$ spectrum (100 MHz; $\text{DMSO-}d_6$) of 2,7-dihydroxy-1-naphthaldehyde.

1*H*-naphtho[2,1,8-*mna*]xanthen-1-one

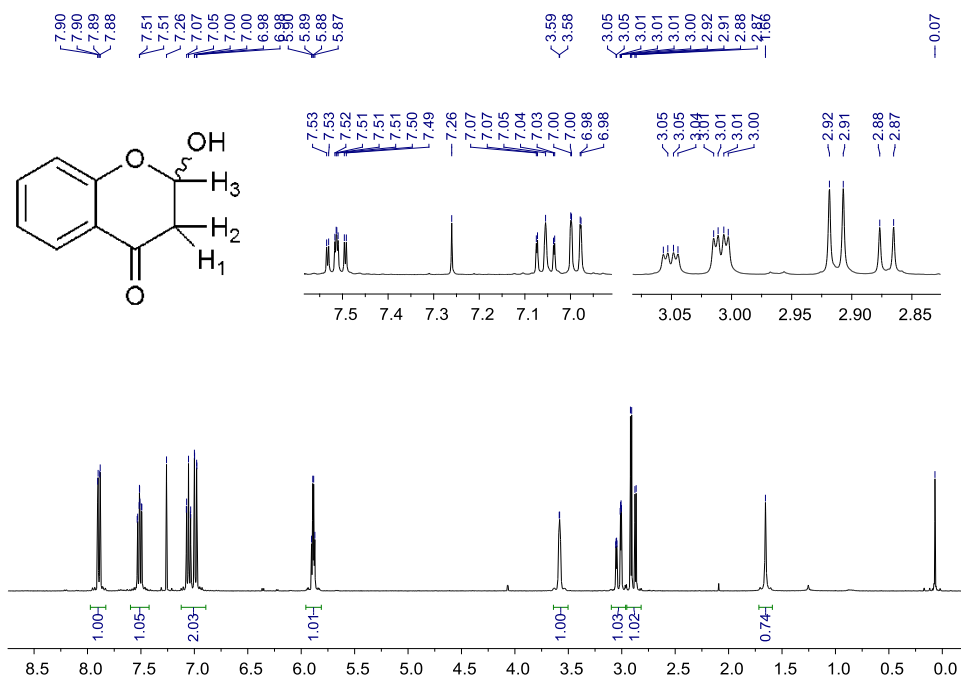


Appendix 3 ^1H -NMR spectrum (400 MHz; CDCl_3) of 1*H*-naphtho[2,1,8-*mna*]xanthen-1-one

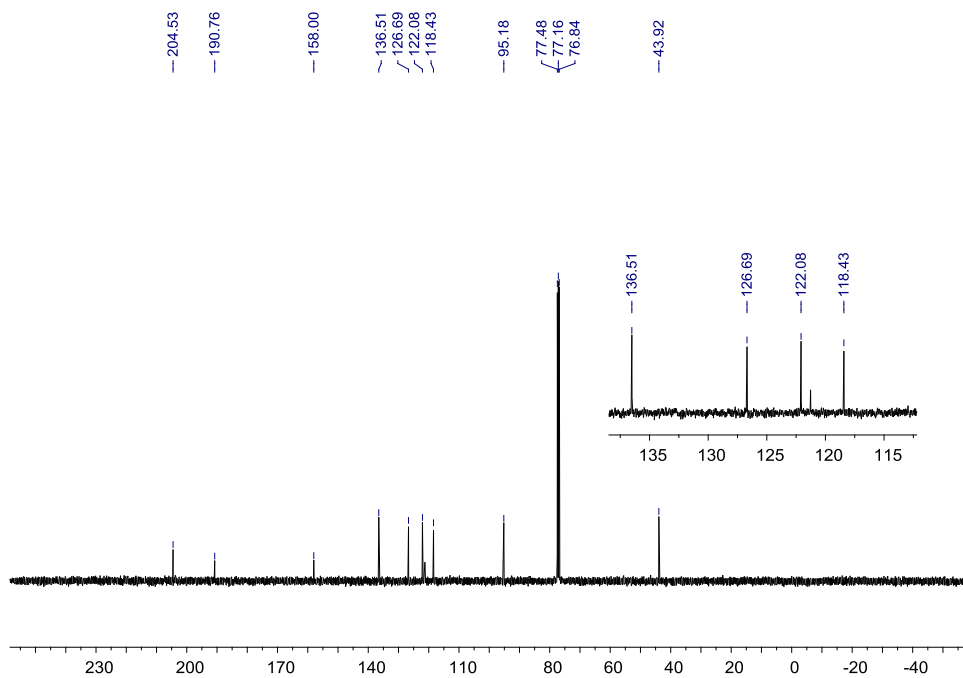


Appendix 4 ^{13}C -NMR spectrum (100 MHz; CDCl_3) of 1*H*-naphtho[2,1,8-*mna*]xanthen-1-one

2-hydroxychroman-4-one

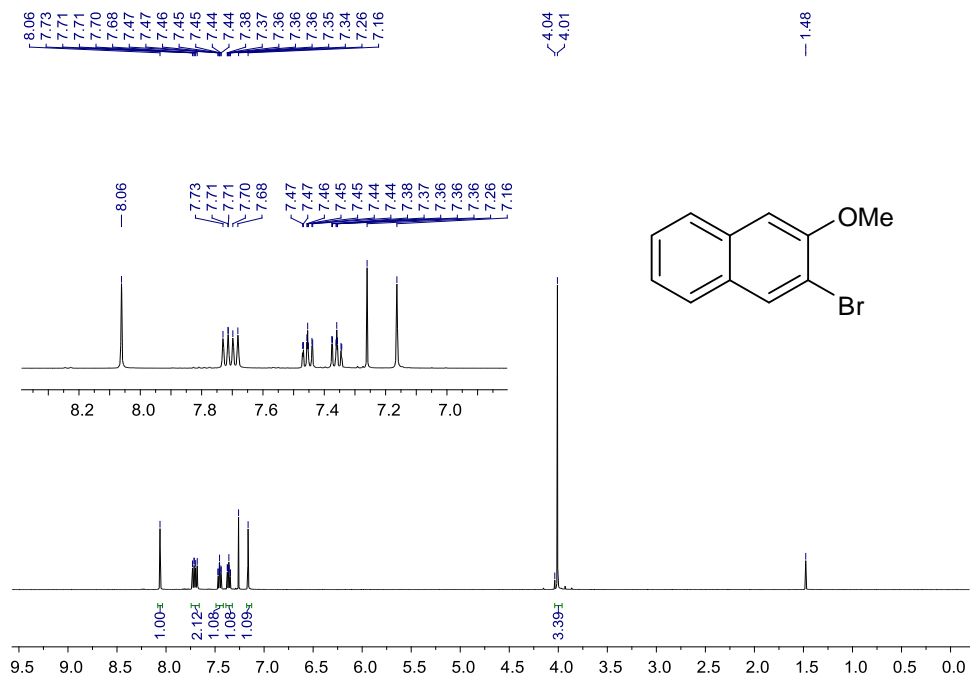


Appendix 5 ¹H-NMR spectrum (400 MHz; CDCl₃) of (R)-2-hydroxychroman-4-one.

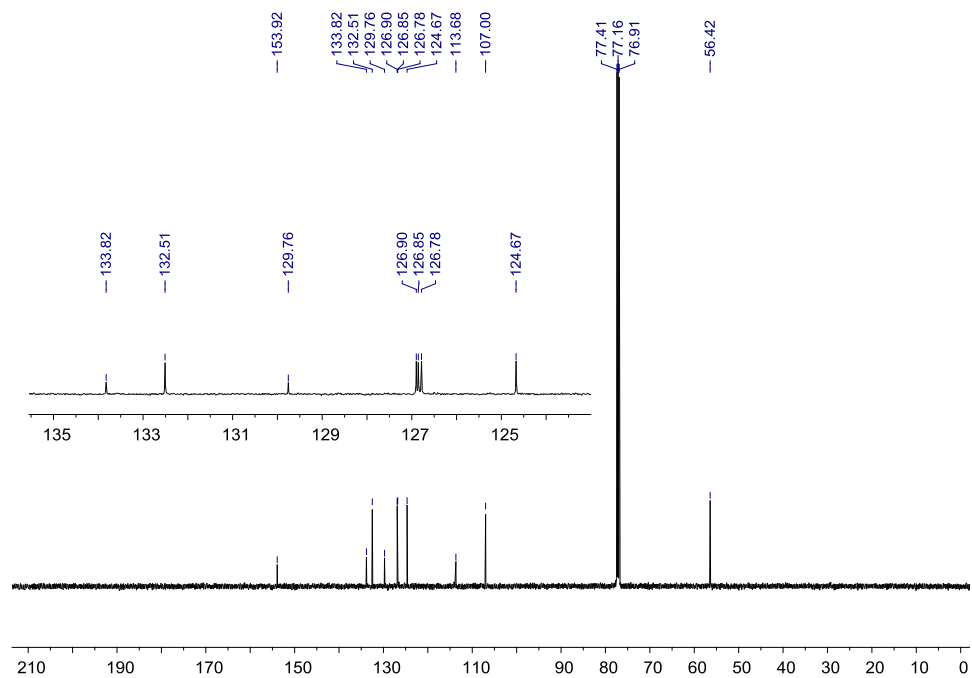


Appendix 6 ¹³C-NMR spectrum (100 MHz; CDCl₃) of (R)-2-hydroxychroman-4-one.

2-Bromo-3-methoxynaphthalene

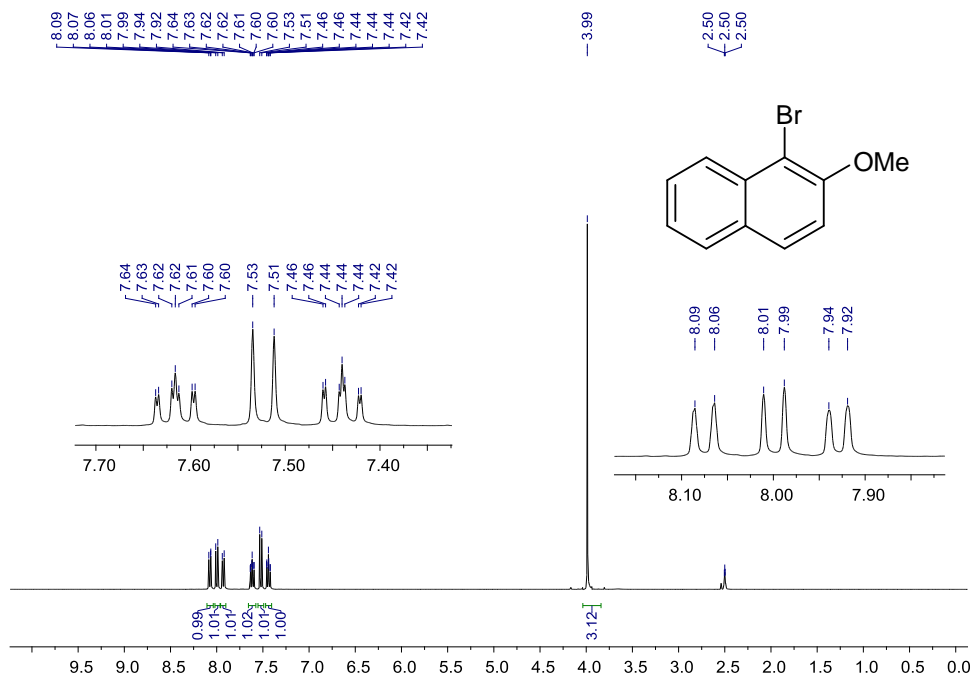


Appendix 7 ¹H-NMR spectrum (400 MHz; CDCl₃) of 2-bromo-3-methoxynaphthalene.

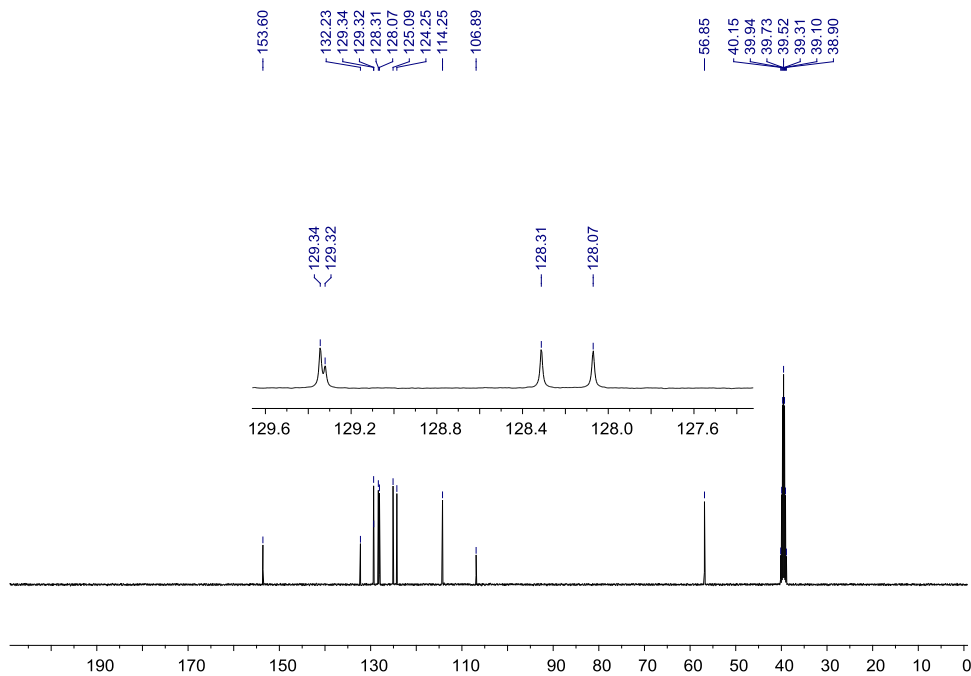


Appendix 8 ¹³C-NMR spectrum (100 MHz; CDCl₃) of 2-bromo-3-methoxynaphthalene.

1-Bromo-2-methoxynaphthalene

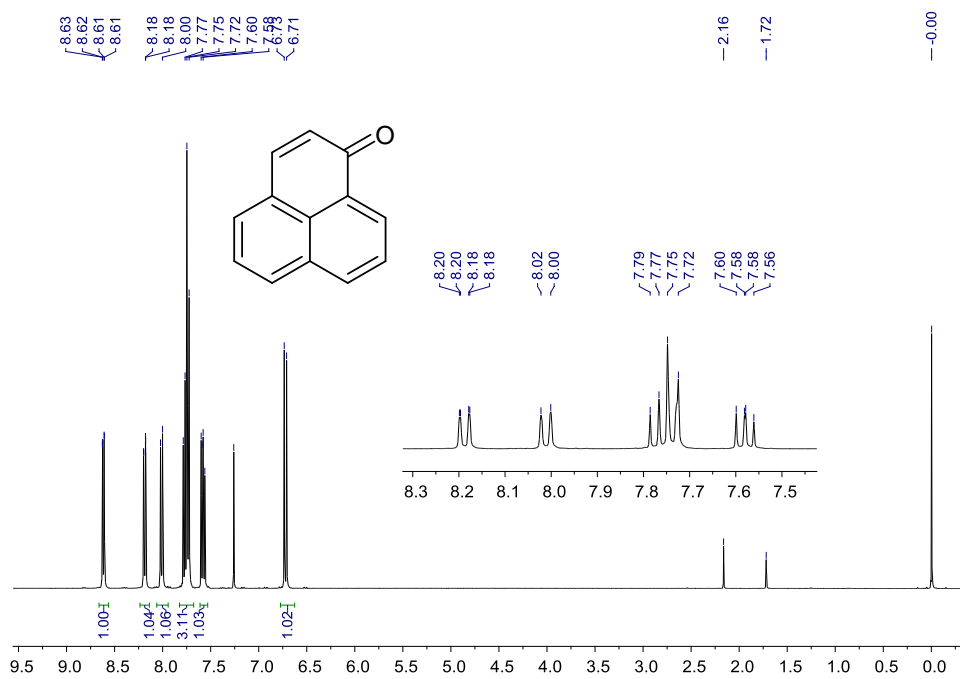


Appendix 9 ¹H-NMR spectrum (400 MHz; acetone-*d*₆) of 1-bromo-2-methoxynaphthalene.

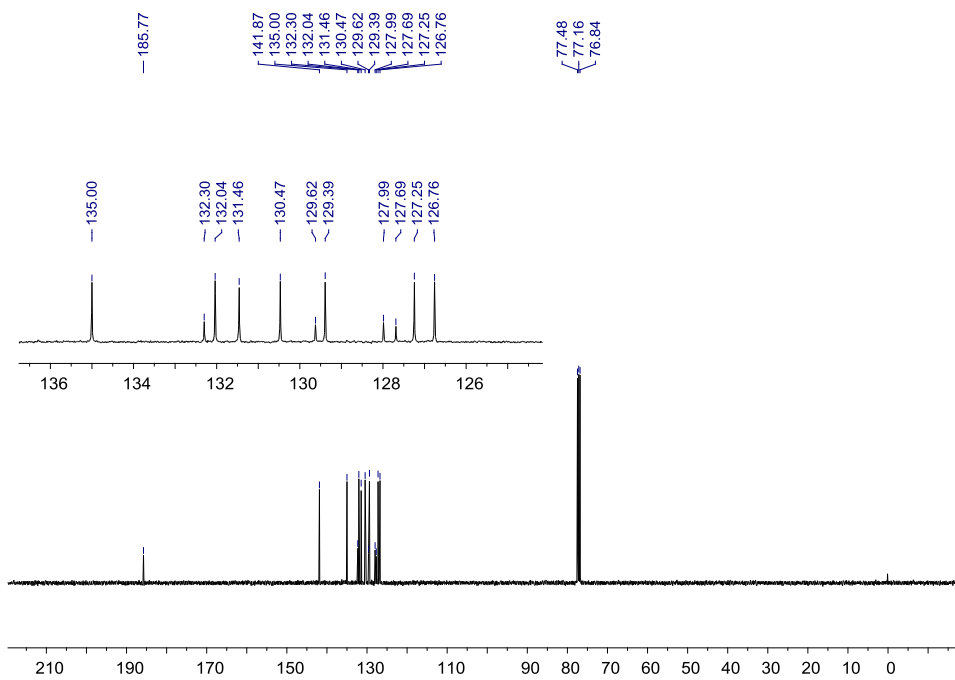


Appendix 10 ¹³C-NMR spectrum (100 MHz; acetone-*d*₆) of 1-bromo-2-methoxynaphthalene

1*H*-phenalen-1-one

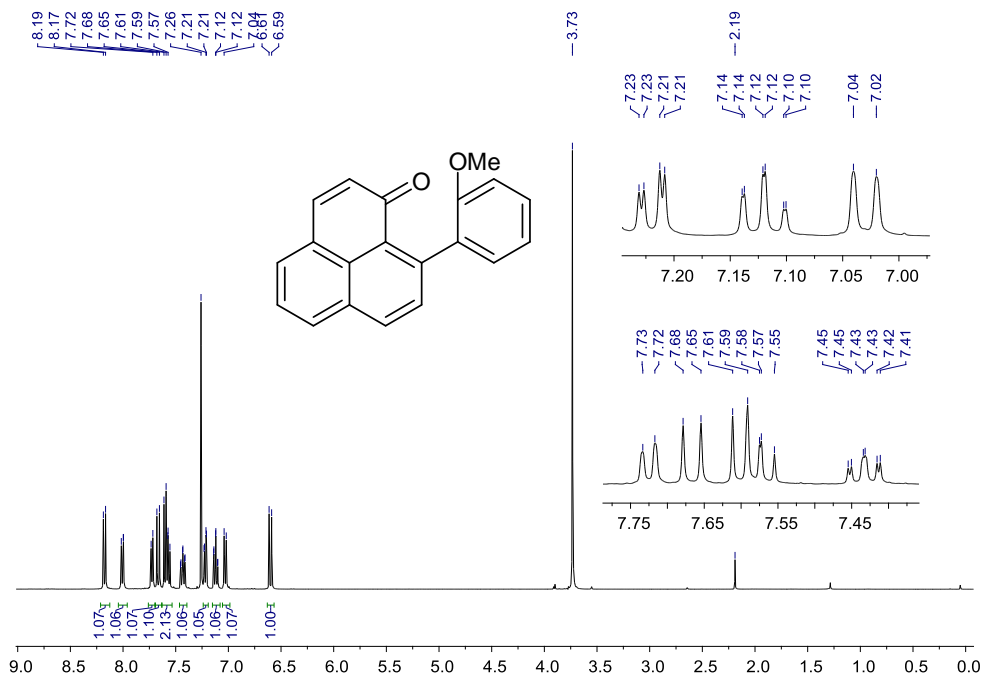


Appendix 11 ^1H -NMR spectrum (400 MHz; CDCl_3) of 1*H*-phenalen-1-one.

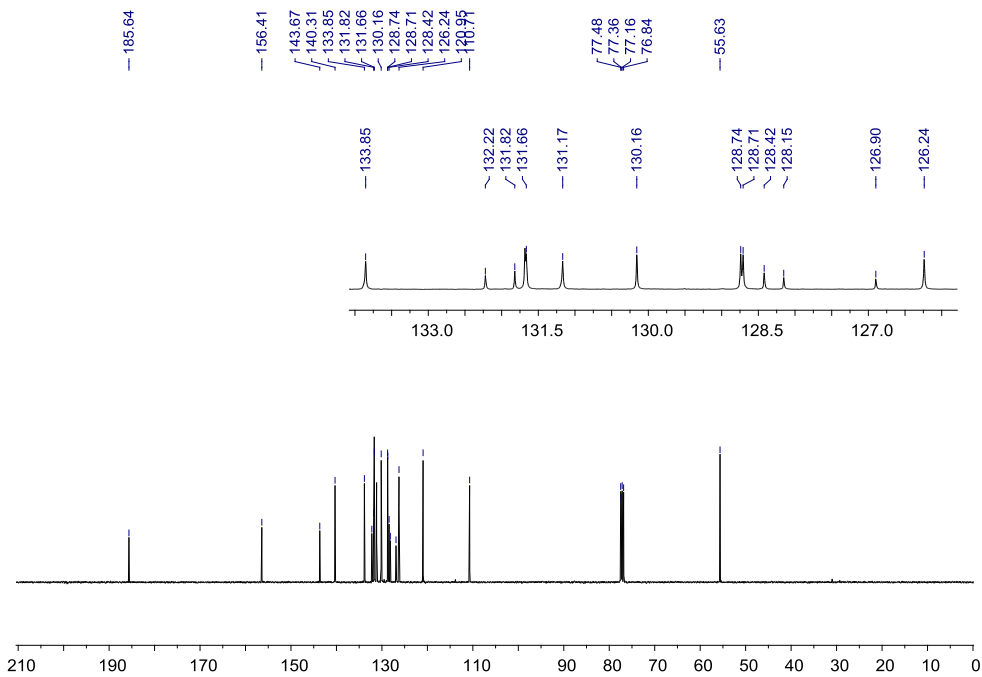


Appendix 12 ^{13}C -NMR spectrum (100 MHz; CDCl_3) of 1*H*-phenalen-1-one.

9-(2-Methoxyphenyl)-1*H*-phenalen-1-one

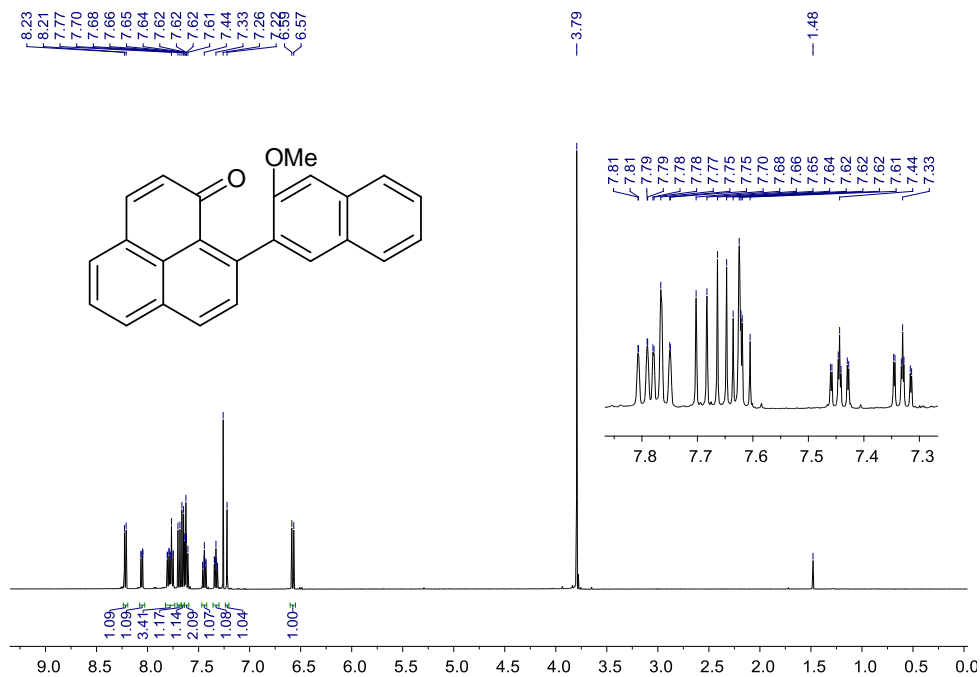


Appendix 13 ¹H-NMR spectrum (400 Hz; CDCl₃) of 9-(2-methoxyphenyl)-1*H*-phenalen-1-one.

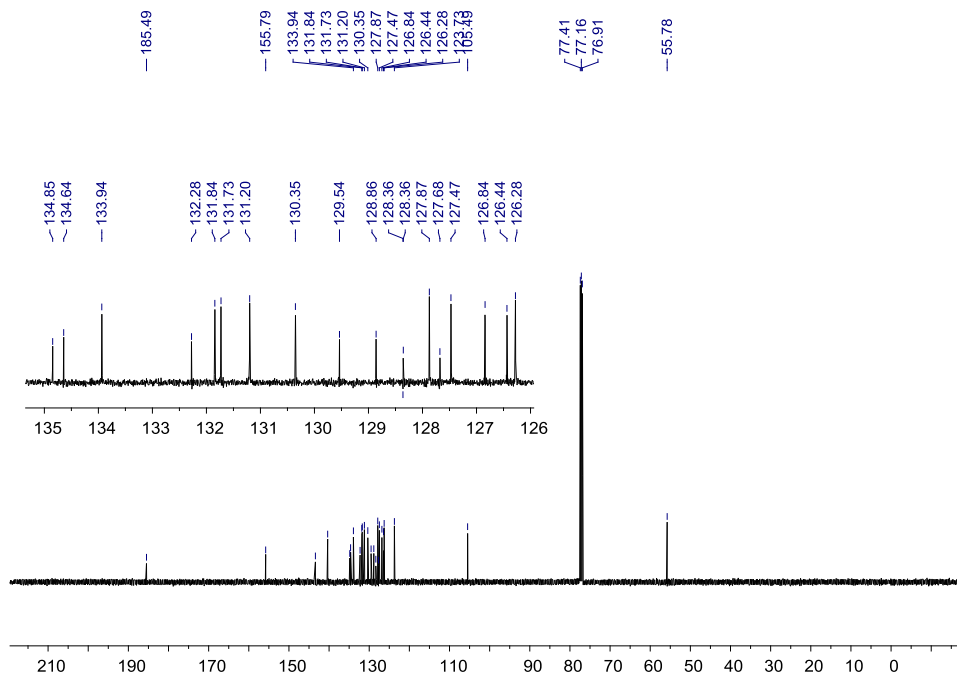


Appendix 14 ¹³C-NMR spectrum (100 Hz; CDCl₃) of 9-(2-methoxyphenyl)-1*H*-phenalen-1-one

9-(3-Methoxynaphthalenyl)-1*H*-phenalen-1-one

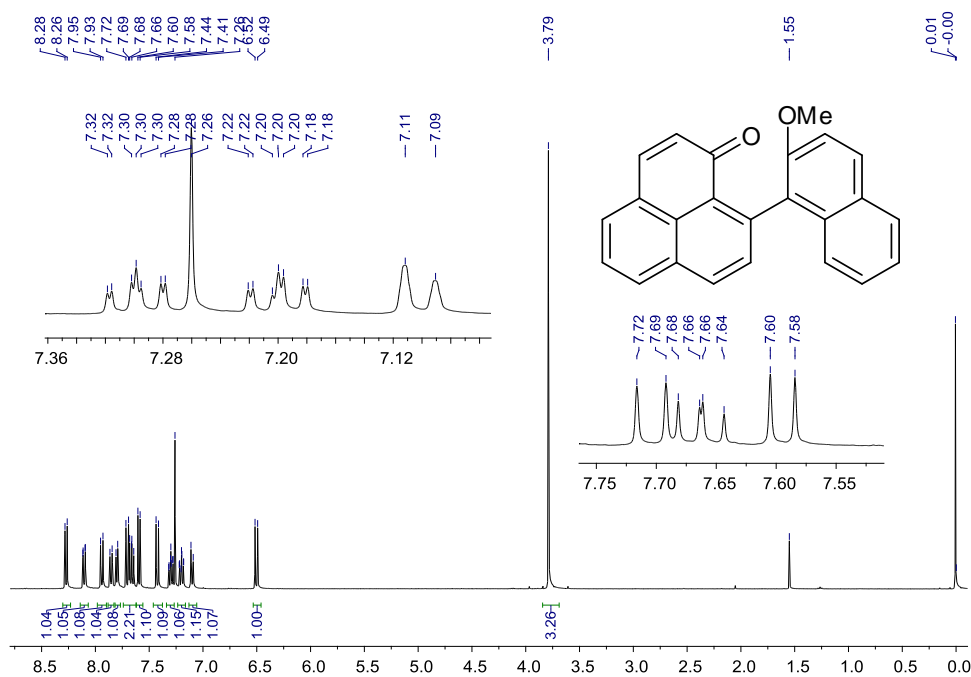


Appendix 15 ¹H-NMR spectrum (400 MHz; CDCl₃) of 9-(3-methoxynaphthalenyl)-1*H*-phenalen-1-one.

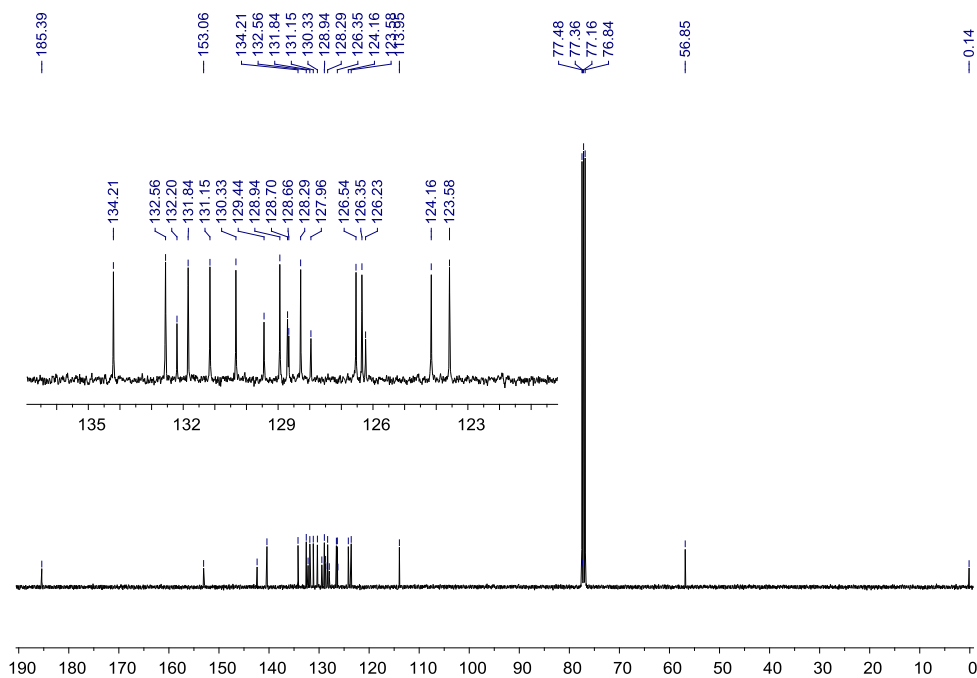


Appendix 16 ¹³C-NMR spectrum (100 MHz; CDCl₃) of 9-(3-methoxynaphthalenyl)-1*H*-phenalen-1-one.

9-(2-Methoxynaphthalenyl)-1*H*-phenalen-1-one

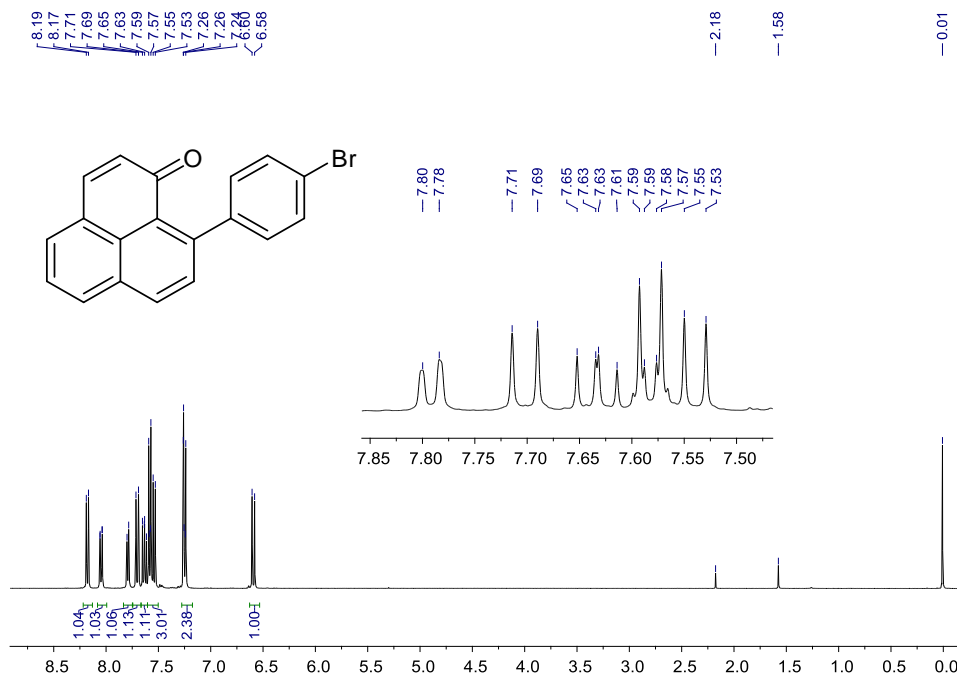


Appendix 17 ¹H-NMR spectrum (400 MHz; CDCl₃) of 9-(2-methoxynaphthalenyl)-1*H*-phenalen-1-one.

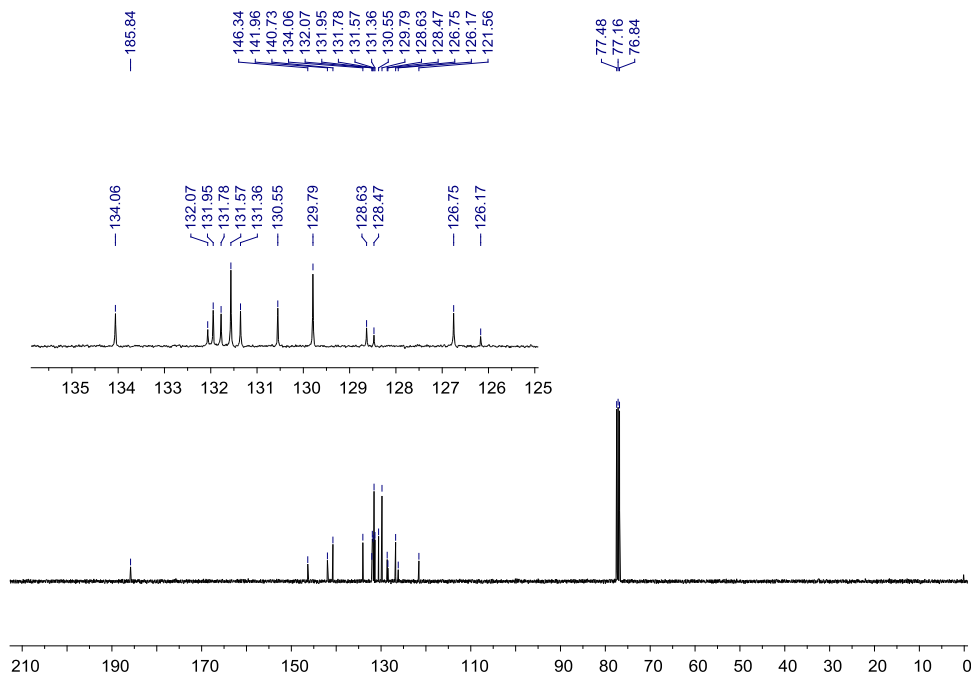


Appendix 18 ¹³C-NMR spectrum (100 MHz; CDCl₃) of 9-(2-methoxynaphthalenyl)-1*H*-phenalen-1-one.

9-(4-Bromophenyl)-1H-phenalen-1-one

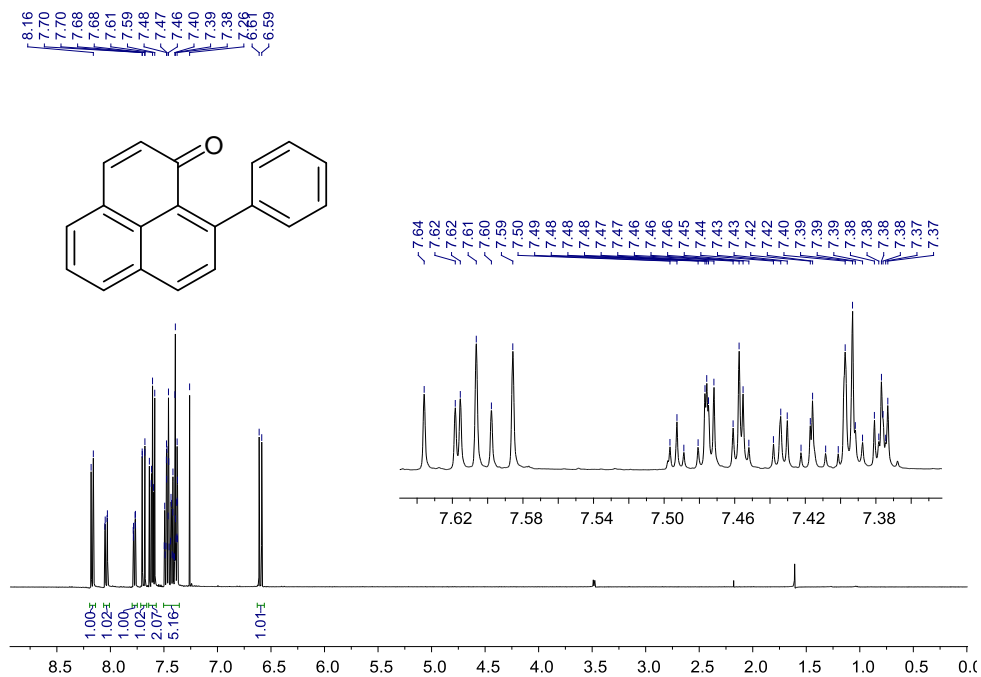


Appendix 19 ¹H-NMR spectrum (400 MHz; CDCl₃) of 9-(4-bromophenyl)-1H-phenalen-1-one.

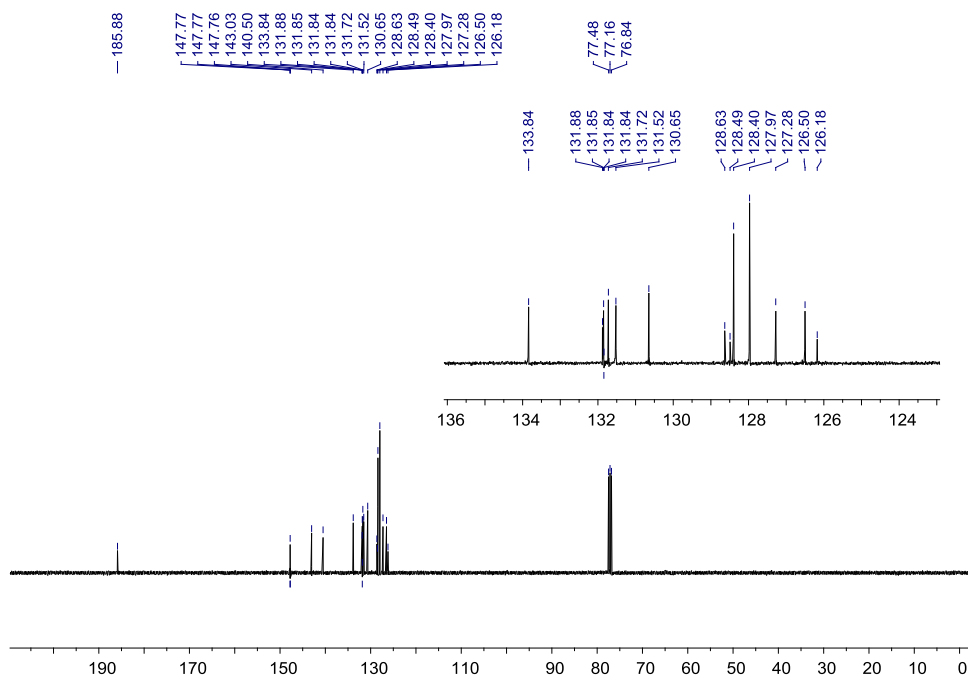


Appendix 20 ¹³C-NMR spectrum (100 MHz; CDCl₃) of 9-(4-bromophenyl)-1H-phenalen-1-one.

9-Phenyl-1*H*-phenalen-1-one

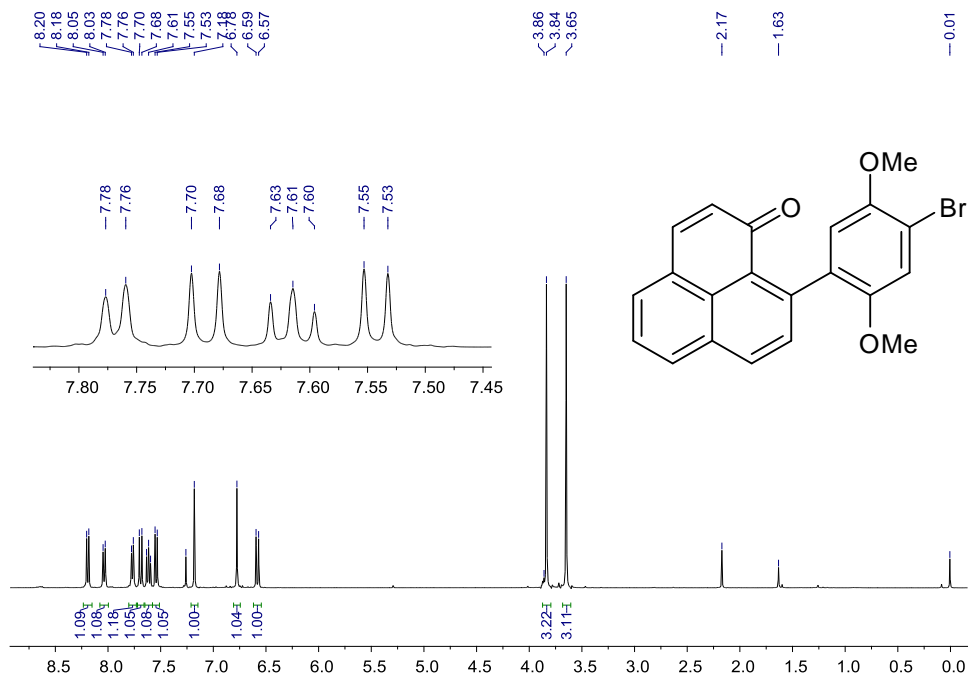


Appendix 21 ¹H-NMR spectrum (400 MHz; CDCl₃) of 9-phenyl-1*H*-phenalen-1-one.

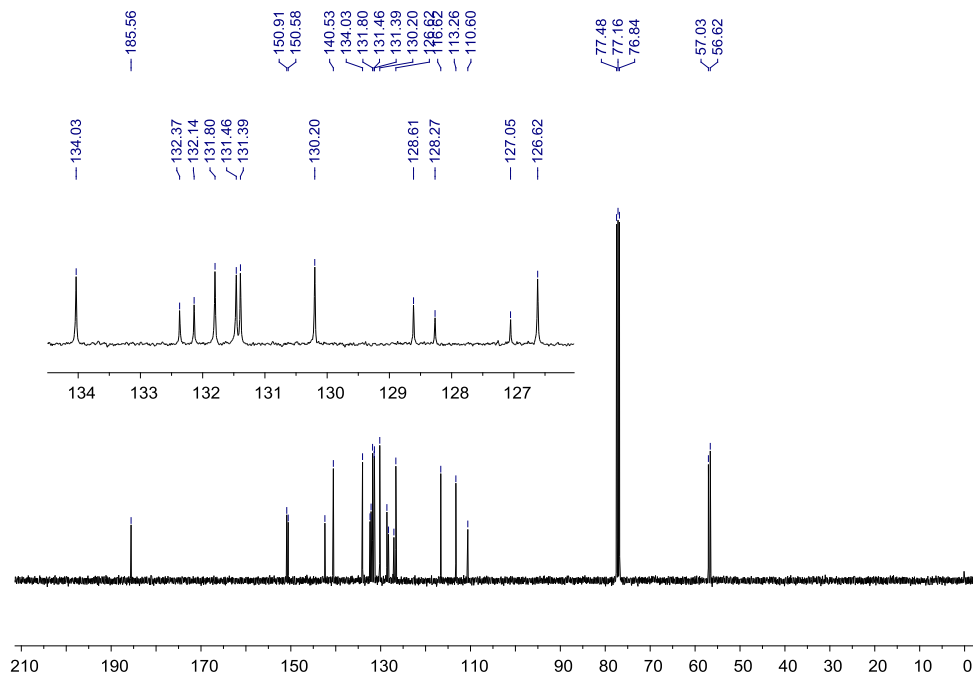


Appendix 22 ¹³C-NMR spectrum (100 MHz; CDCl₃) of 9-phenyl-1*H*-phenalen-1-one.

9-(4-Bromo-2,5-dimethoxyphenyl)-1*H*-phenalen-1-one

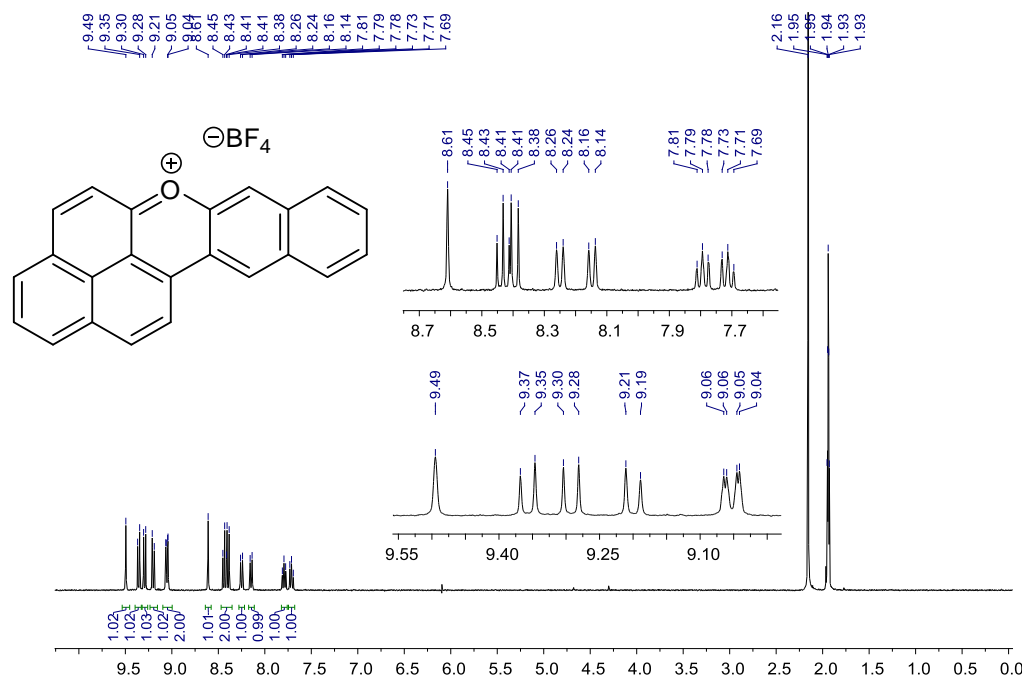


Appendix 23 ¹H-NMR spectrum (400 MHz; CDCl₃) of 9-(4-bromo-2,5-dimethoxyphenyl)-1*H*-phenalen-1-one.

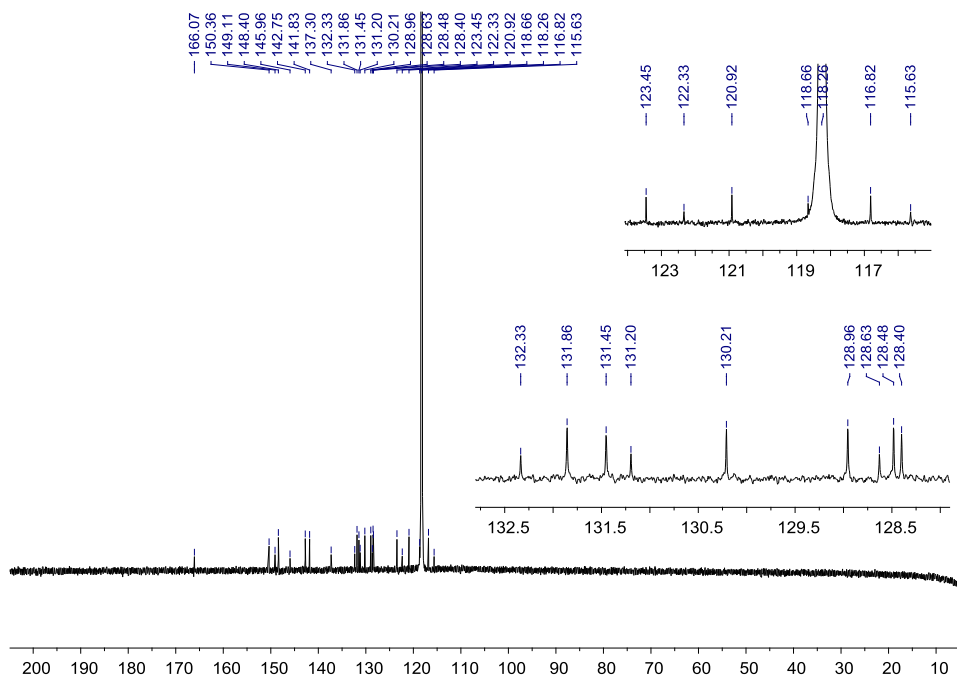


Appendix 24 ¹³C-NMR spectrum (100 MHz; CDCl₃) of 9-(4-bromo-2,5-dimethoxyphenyl)-1*H*-phenalen-1-one.

Benzo[*i*]naphtho[2,1,8-*mna*]xanthenium tetrafluoroborate

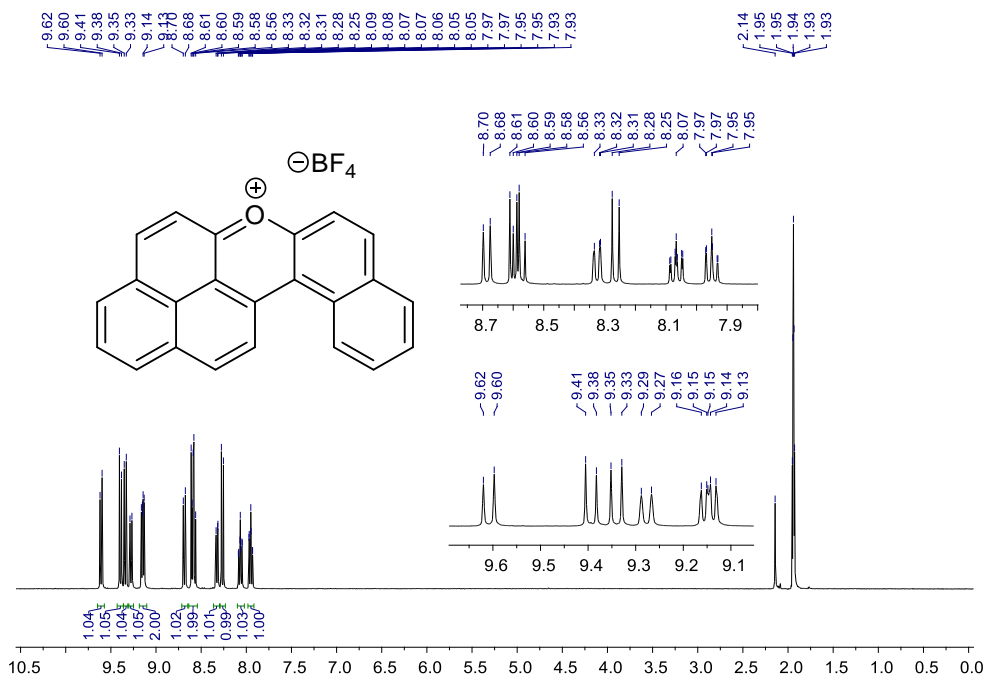


Appendix 27 ¹H-NMR spectrum (400 MHz; CD₃CN) of benzo[*i*]naphtho[2,1,8-*mna*]xanthenium tetrafluoroborate.

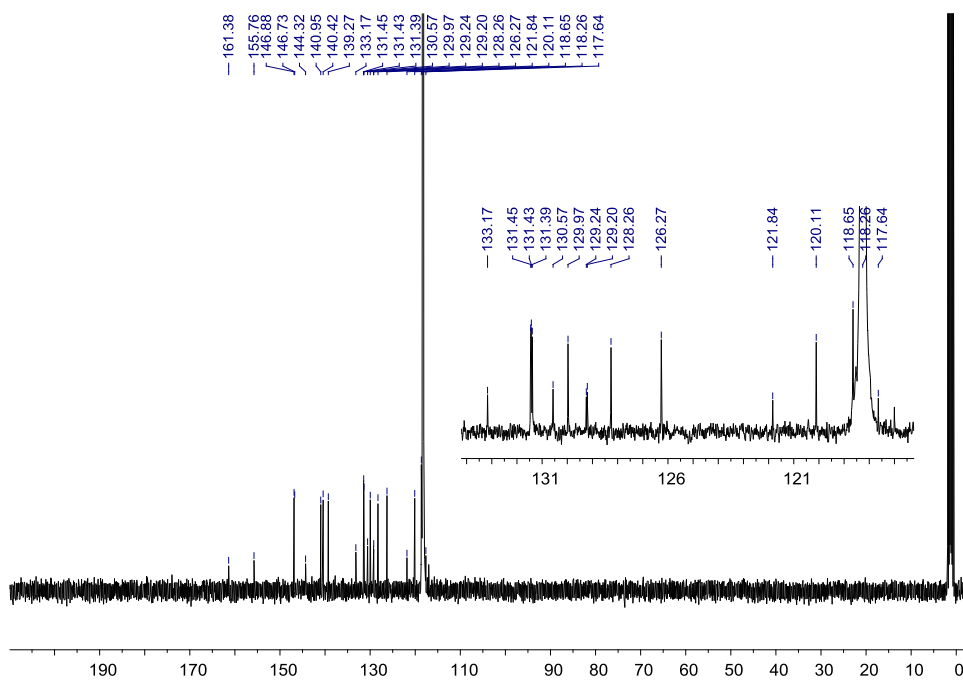


Appendix 28 ¹³C-NMR spectrum (100 MHz; CD₃CN) of benzo[*i*]naphtho[2,1,8-*mna*]xanthenium tetrafluoroborate.

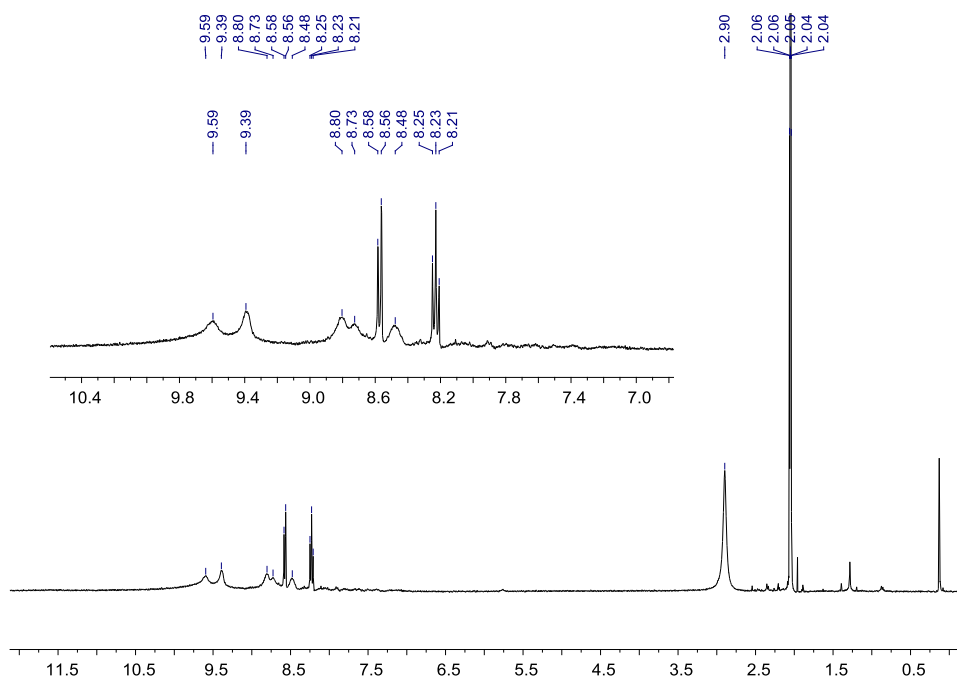
Benzo[*a*]naphtho[8,1,2-*ijkl*]xanthenium tetrafluoroborate



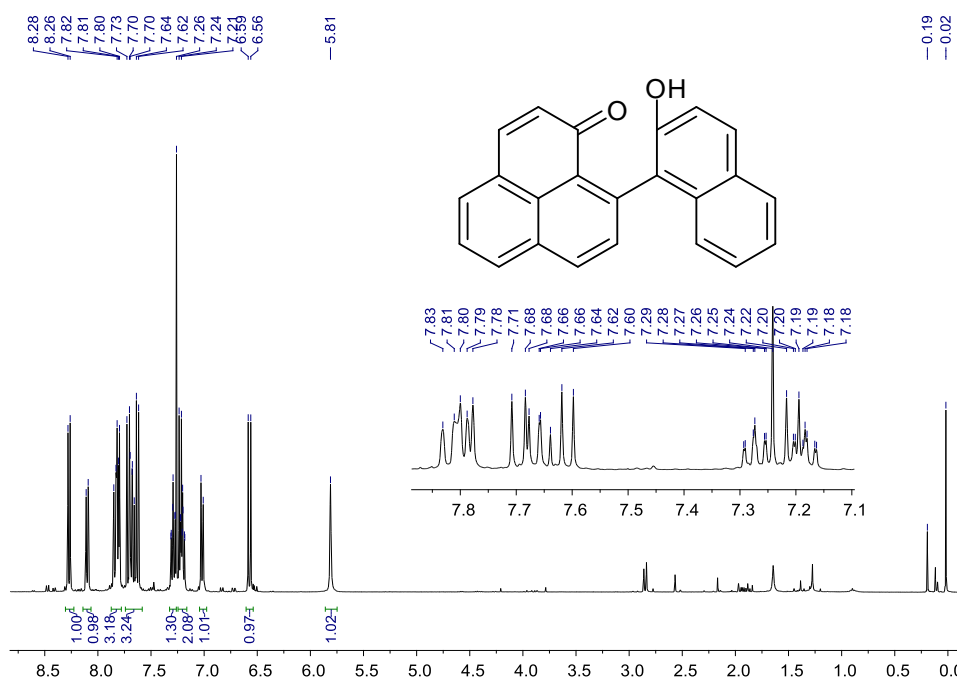
Appendix 29 $^1\text{H-NMR}$ spectrum (400 MHz; CD_3CN) of benzo[*a*]naphtho[8,1,2-*ijkl*]xanthenium tetrafluoroborate.



Appendix 30 $^{13}\text{C-NMR}$ spectrum (100 MHz; CD_3CN) of benzo[*a*]naphtho[8,1,2-*ijkl*]xanthenium tetrafluoroborate.

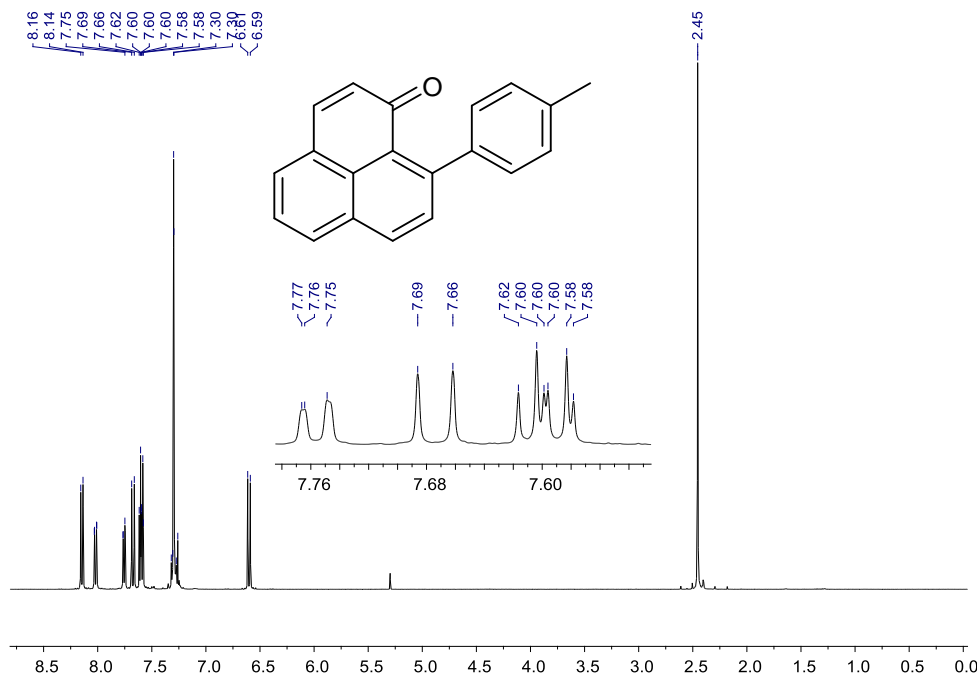


Appendix 31 $^1\text{H-NMR}$ spectrum (400 MHz; CD_3CN) of black material with green lustre obtained from acetone. Broadening effects indicate presence of radical NX.

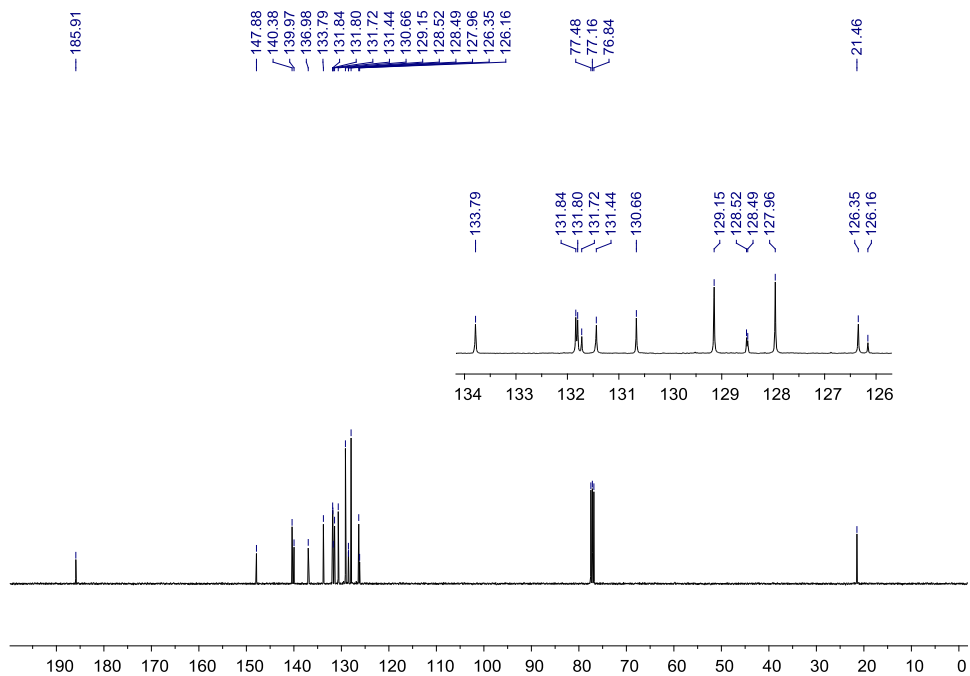


Appendix 32 $^1\text{H-NMR}$ spectrum (400 MHz; CDCl_3) of 9-(2-hydroxynaphthalenyl)-1H-phenalen-1-one

9-*p*-Tolyl-1*H*-phenalen-1-one

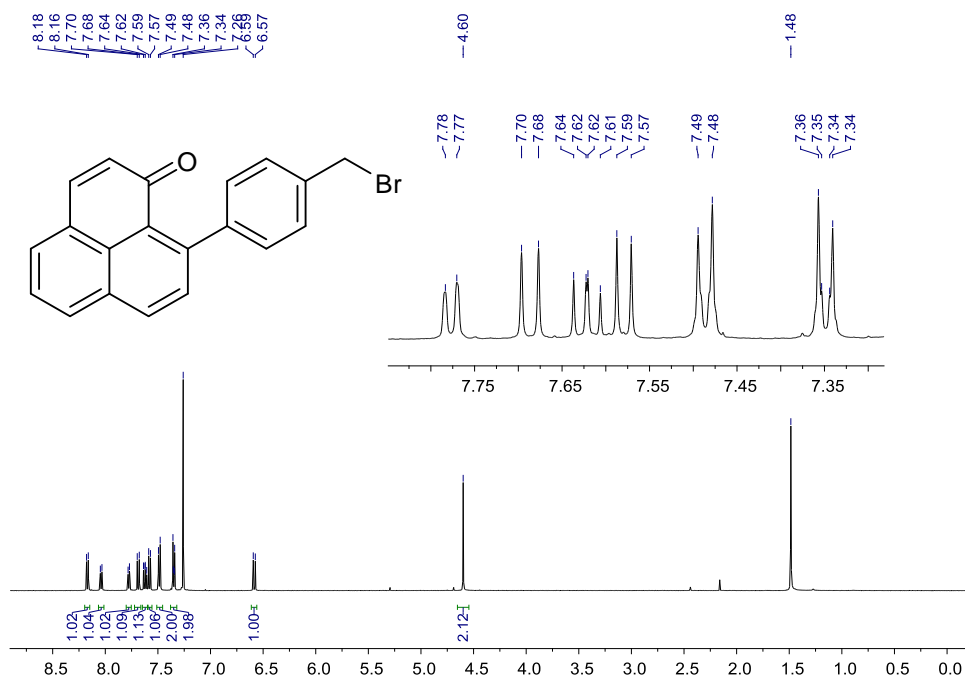


Appendix 33 ¹H-NMR spectrum (400 Hz; CDCl₃) of 9-*p*-tolyl-1*H*-phenalen-1-one.

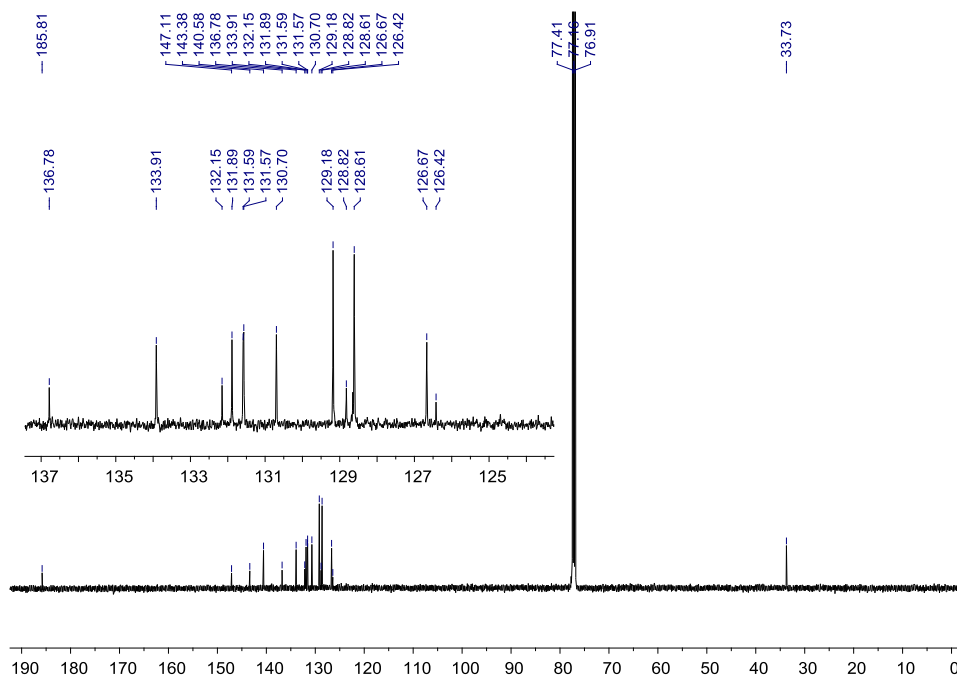


Appendix 34 ¹³C-NMR spectrum (100 Hz; CDCl₃) of 9-*p*-tolyl-1*H*-phenalen-1-one.

9-(4-(Bromomethyl)phenyl)-1*H*-phenalen-1-one

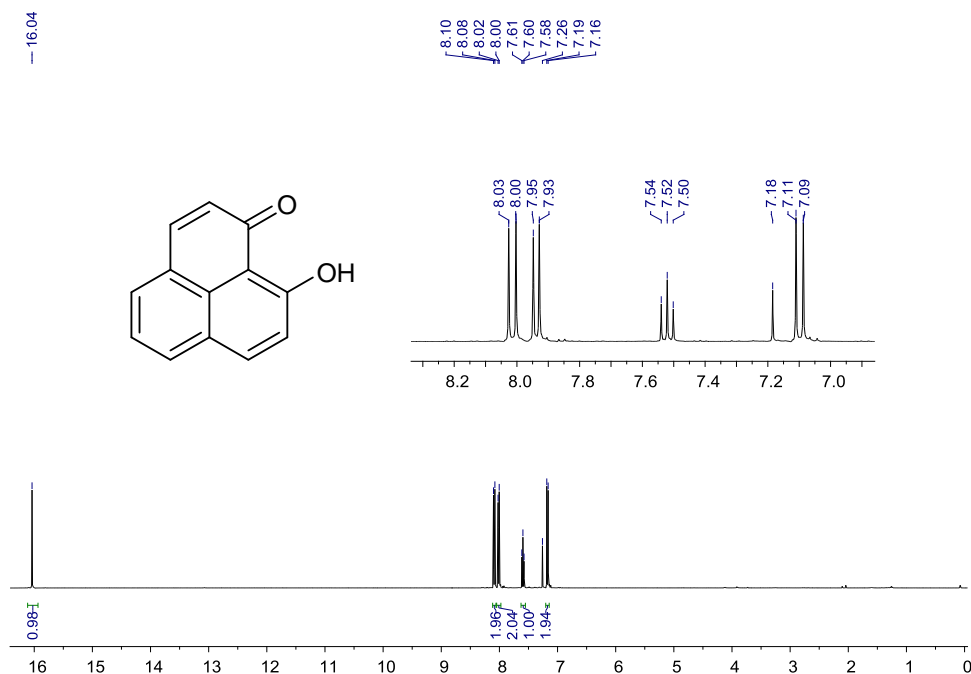


Appendix 35 ¹H-NMR spectrum (500 Hz; CDCl₃) of 9-(4-(bromomethyl)phenyl)-1*H*-phenalen-1-one.

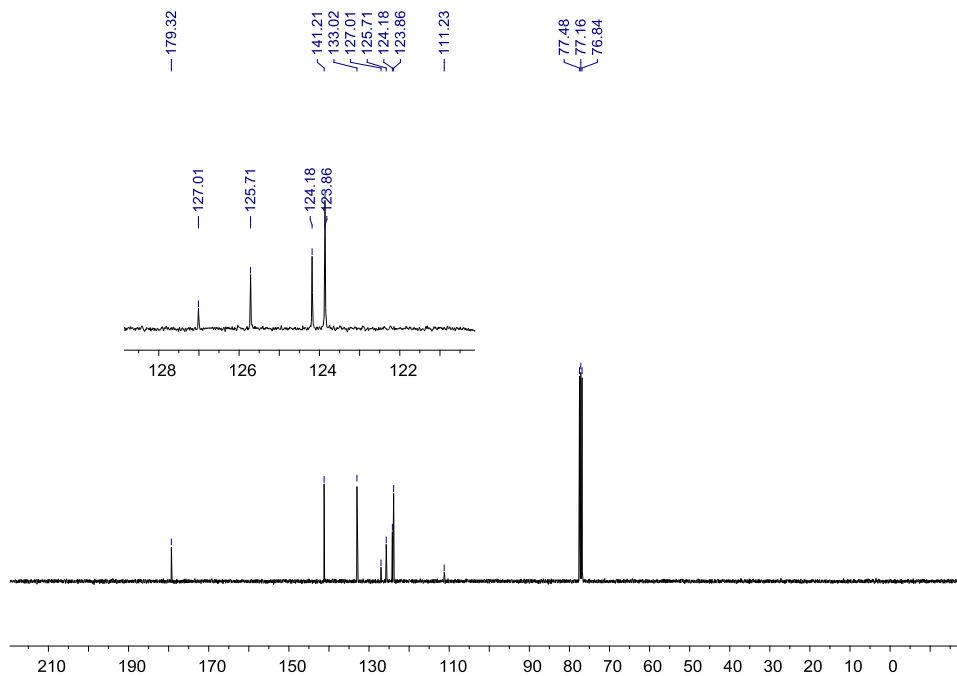


Appendix 36 ¹³C-NMR spectrum (125 MHz; CDCl₃) of 9-(4-(bromomethyl)phenyl)-1*H*-phenalen-1-one.

9-Hydroxy-1*H*-phenalen-1-one

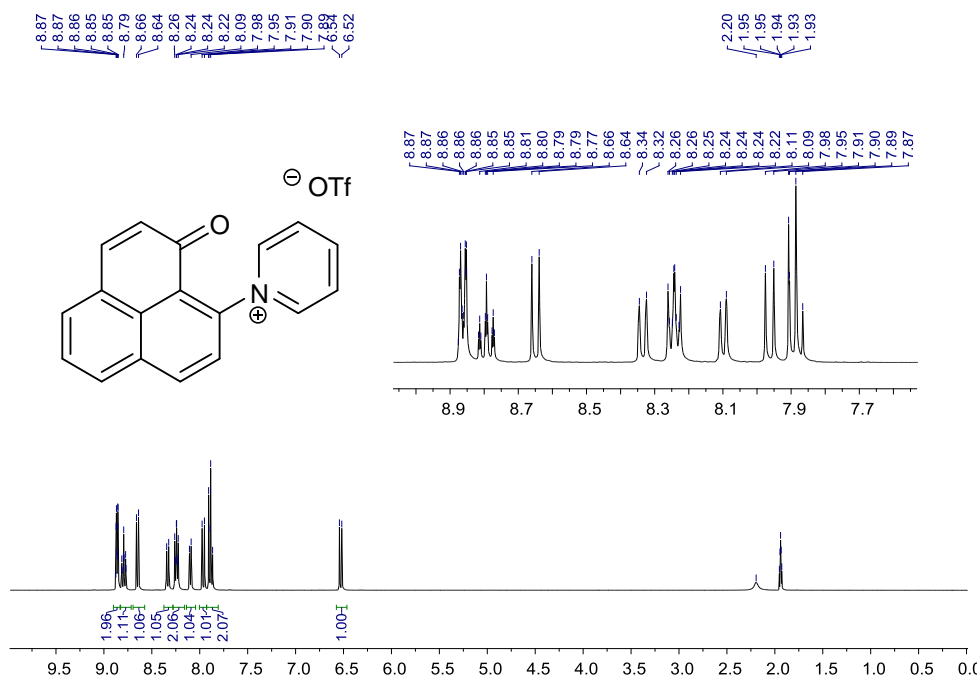


Appendix 39 ¹H-NMR spectrum (400 MHz; CDCl₃) of 9-hydroxy-1*H*-phenalen-1-one.

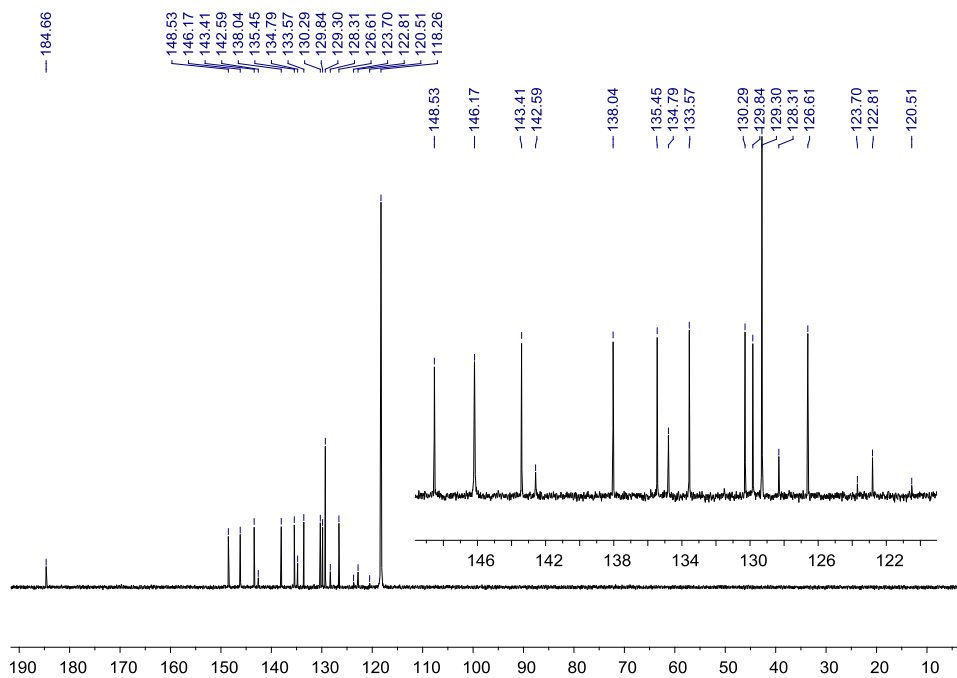


Appendix 40 ¹³C-NMR spectrum (100 MHz; CDCl₃) of 9-hydroxy-1*H*-phenalen-1-one.

1-(1-Oxo-1*H*-phenalen-9-yl)pyridinium triflate

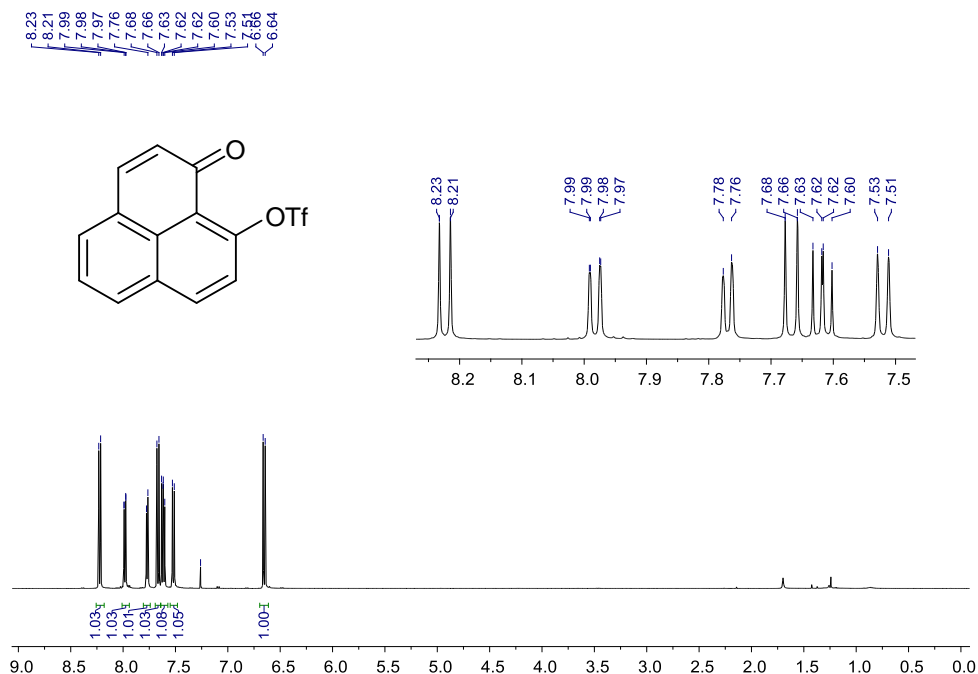


Appendix 41 ¹H-NMR spectrum (400 MHz; CD₃CN) of 1-(1-Oxo-1*H*-phenalen-9-yl)pyridinium triflate.

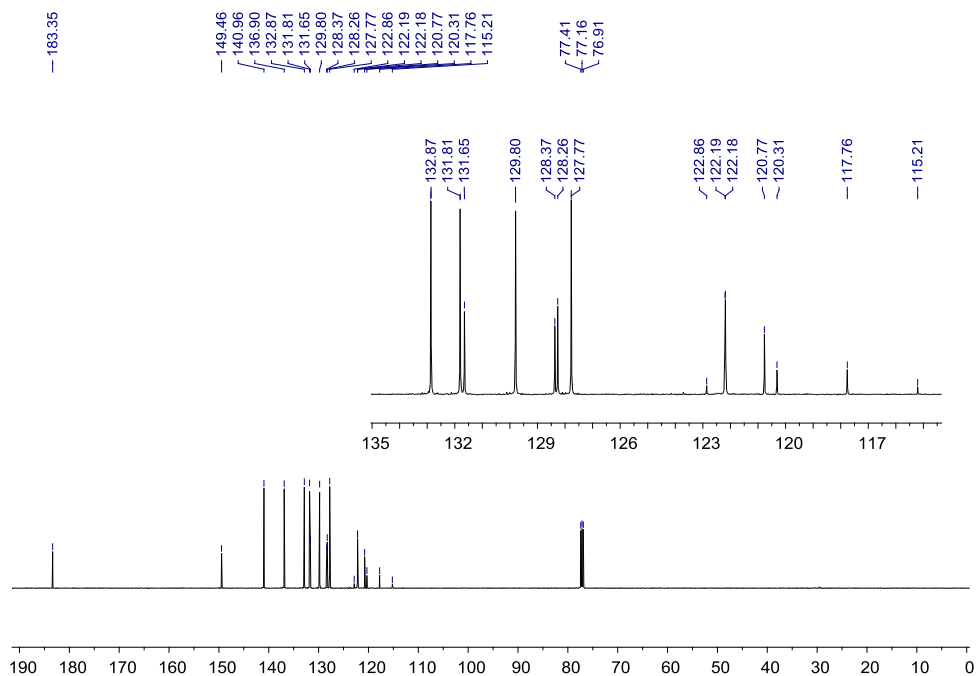


Appendix 42 ¹³C-NMR spectrum (100 MHz; CD₃CN) of 1-(1-Oxo-1*H*-phenalen-9-yl)pyridinium triflate.

1-Oxo-1*H*-phenalen-9-yl trifluoromethanesulfonate

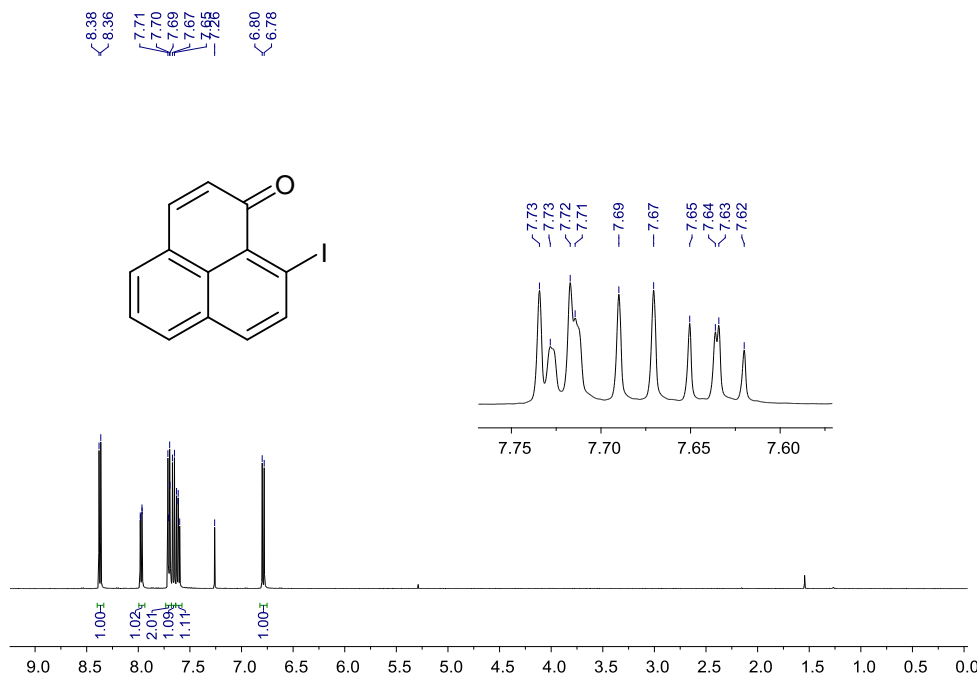


Appendix 43 ¹H-NMR spectrum (400 MHz; CDCl₃) of 1-Oxo-1*H*-phenalen-9-yl trifluoromethanesulfonate.

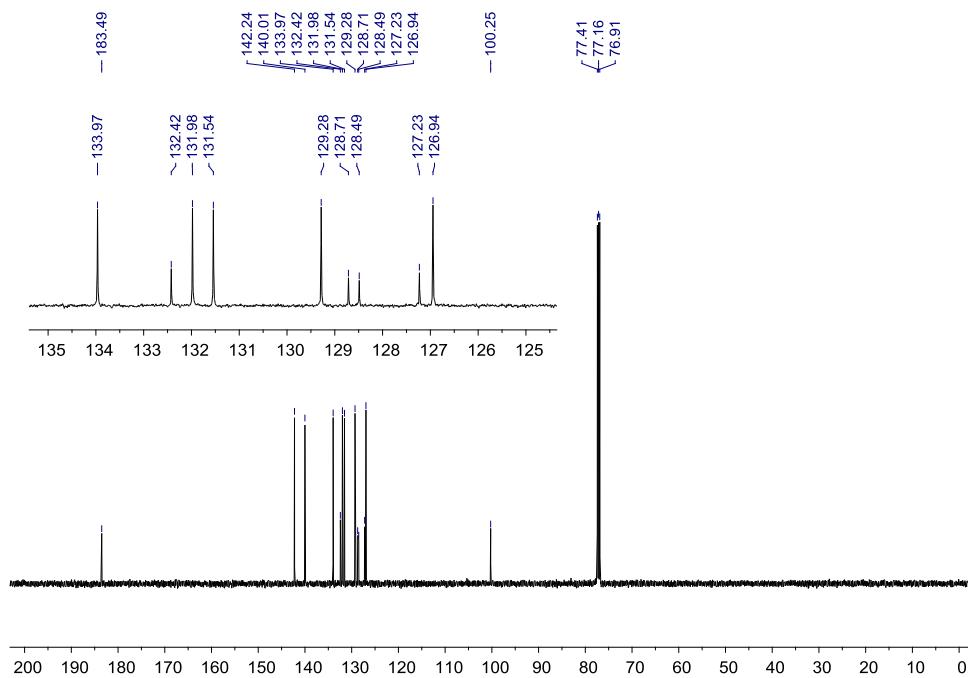


Appendix 44 ¹³C-NMR spectrum (100 MHz; CDCl₃) of 1-Oxo-1*H*-phenalen-9-yl trifluoromethanesulfonate.

9-Iodo-1*H*-phenalen-1-one

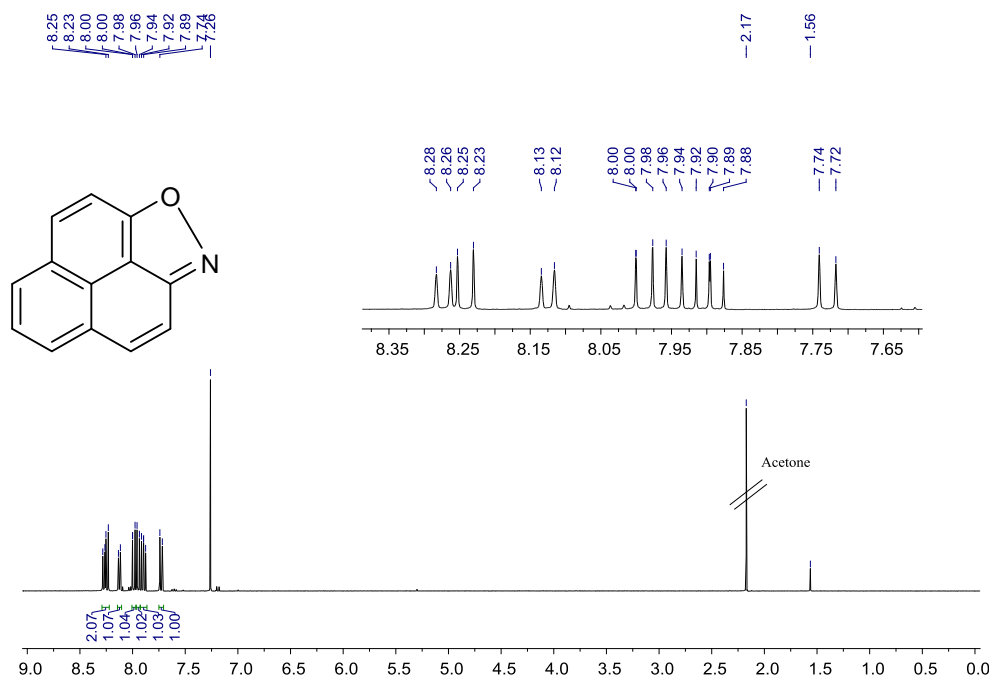


Appendix 45 ¹H-NMR spectrum (500 MHz; CDCl₃) of 9-iodo-1*H*-phenalen-1-one.

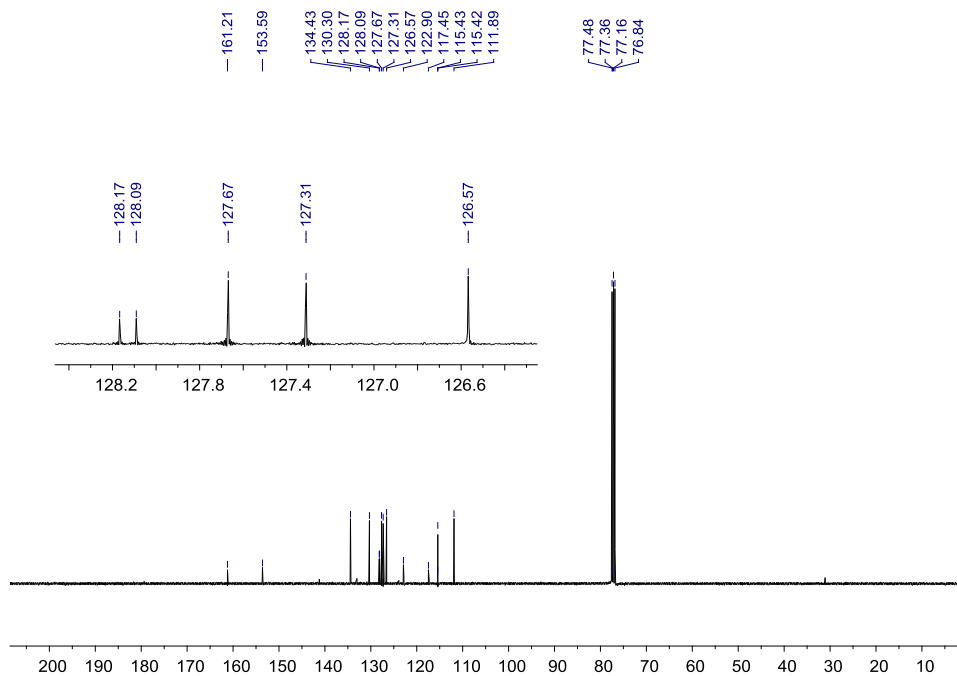


Appendix 46 ¹³C-NMR spectrum (125 MHz; CDCl₃) of 9-iodo-1*H*-phenalen-1-one.

Phenaleno[1,9-*cd*]isoxazole

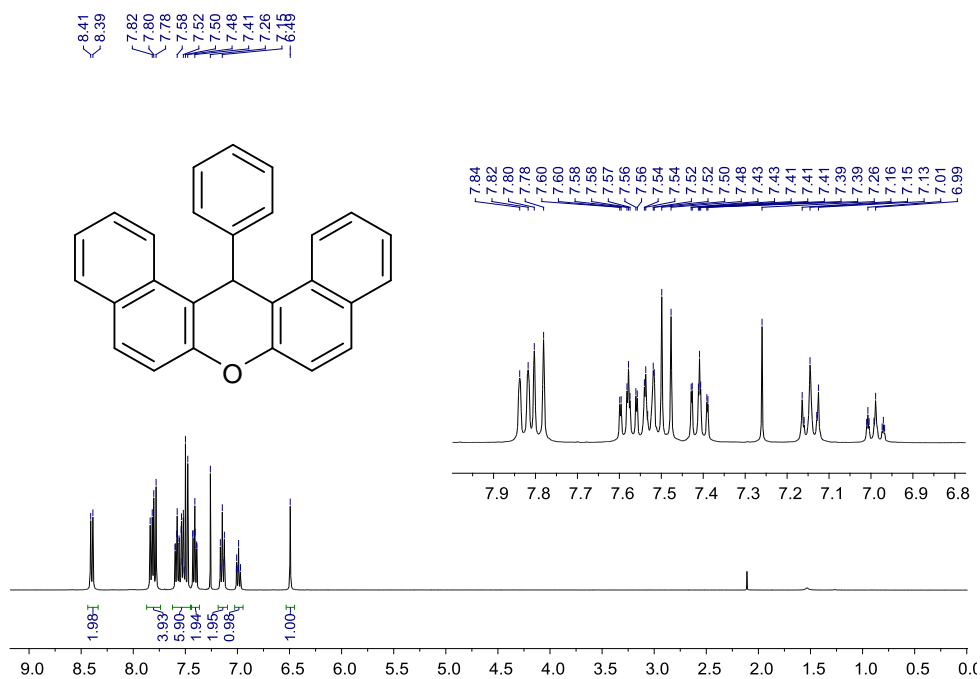


Appendix 47 ¹H-NMR spectrum (400 MHz; CDCl₃) of phenaleno[1,9-*cd*]isoxazole.

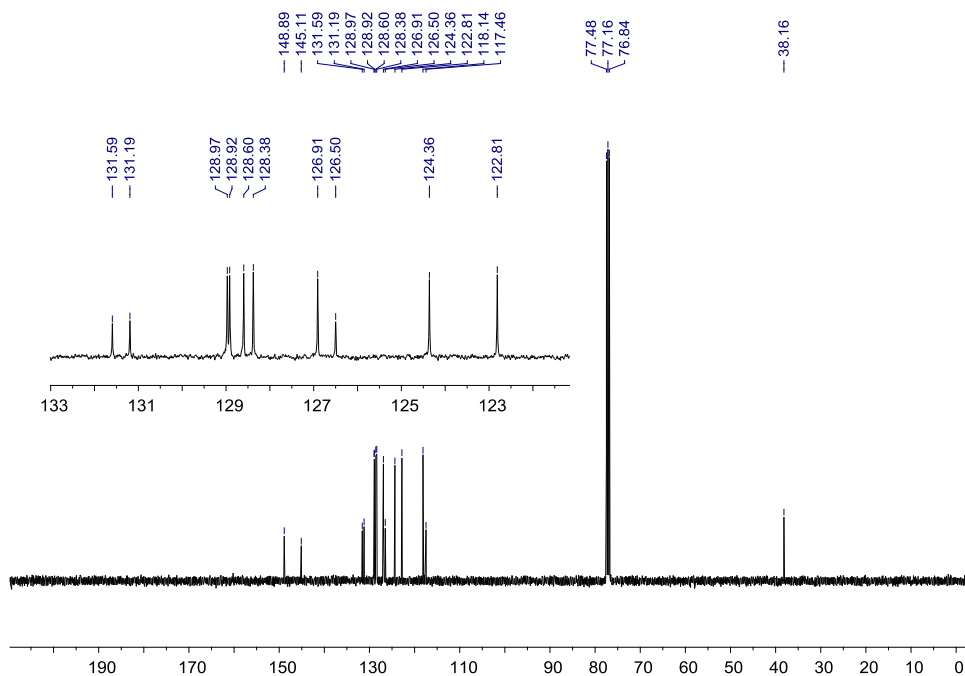


Appendix 48 ¹³C-NMR spectrum (100 MHz; CDCl₃) of phenaleno[1,9-*cd*]isoxazole.

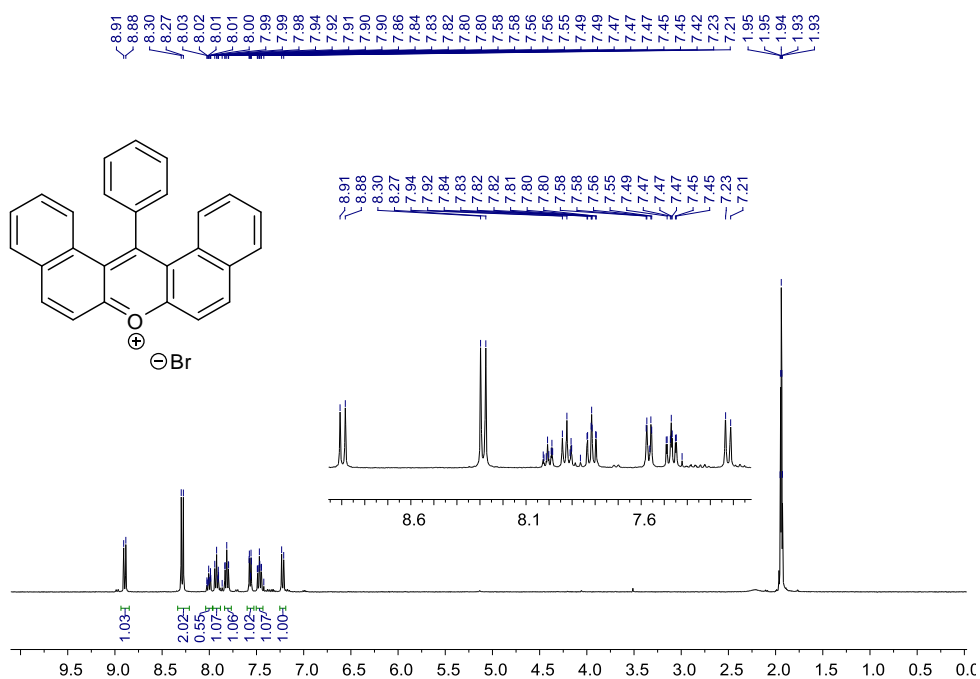
14-Phenyl-14*H*-dibenzo[*a,j*]xanthene



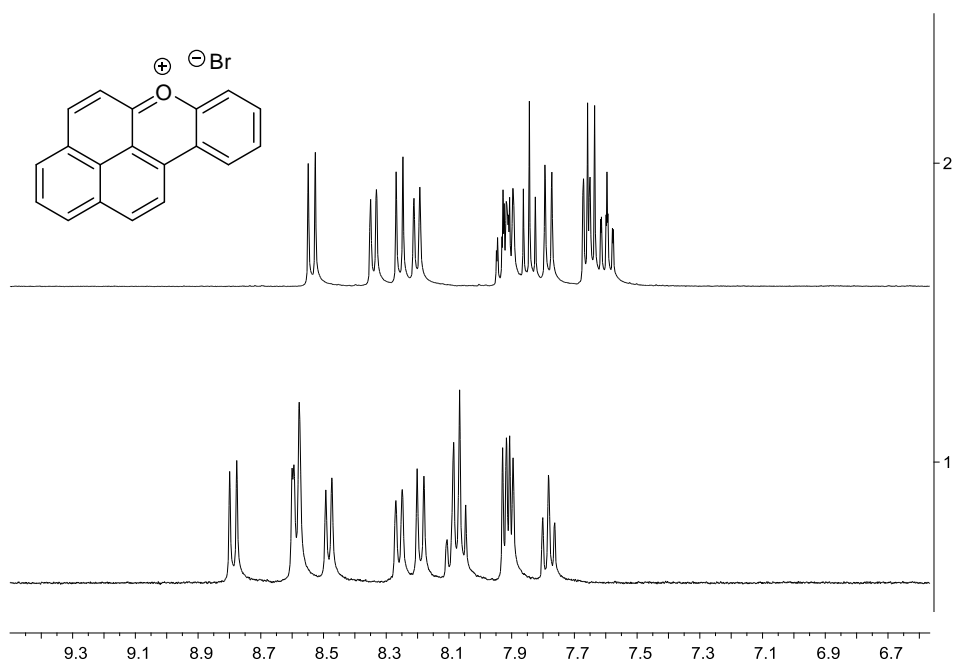
Appendix 49 ¹H-NMR spectrum (400 Hz; CDCl₃) of 14-phenyl-14*H*-dibenzo[*a,j*]xanthene.



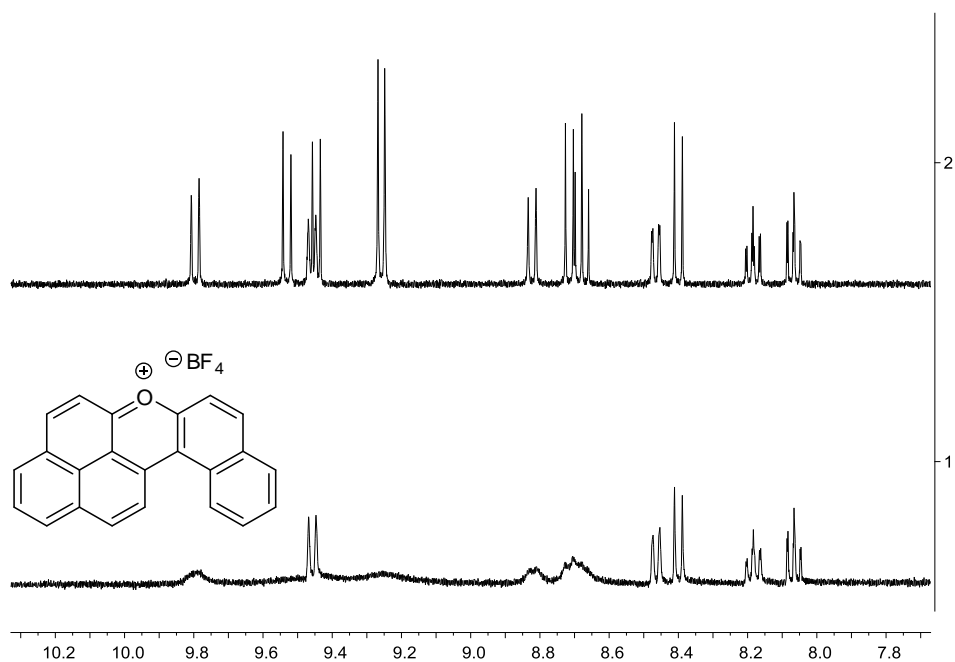
Appendix 50 ¹³C-NMR spectrum (100 Hz; CDCl₃) of 14-phenyl-14*H*-dibenzo[*a,j*]xanthene.



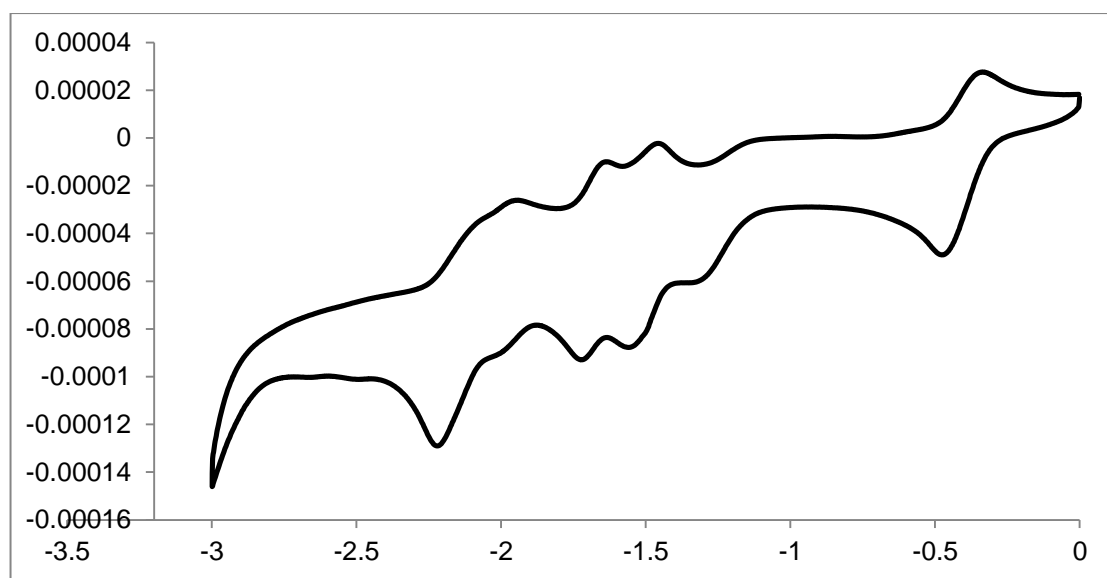
Appendix 51 ¹H-NMR spectrum (400 Hz; MeCN) of 14-phenyldibenzo[*a,j*]xanthenium bromide.



Appendix 52 Two stacked ¹H-NMR (400 MHz; D₂O) spectra of naphtho[2,1,8-*mna*]xanthenium bromide (NXBr) from different batches indicating alternations of chemical shifts based on π - π stack interactions. Due to difficulties to isolate NXBr in the solid state the quantity of concentration was not available.



Appendix 53 $^1\text{H-NMR}$ (400 MHz; CD_3CN) spectra of benzo[*a*]naphtho[8,1,2-*jkl*]xanthenium tetrafluoroborate. Spectrum 1 is a recorded spectrum after dissolution; spectrum 2 is recorded after 2 hours of UV-irradiation.

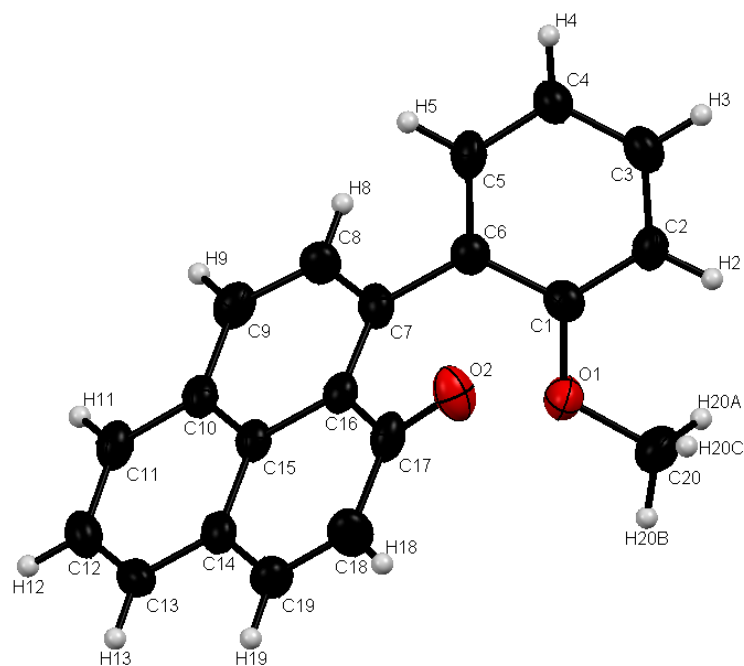


Appendix 54 Cyclic voltammogram of NXBF_4 at room temperature under air obtained at a scan rate of 100 mV s^{-1} on a glassy carbon working electrode of area 0.071 cm^2 . A Pt mesh counter electrode was used and the reference electrode was Ag/AgNO_3 . The electrolyte ($0.1 \text{ M NBU}_4\text{-BF}_4$ in CH_3CN) was not degassed before spectrum acquisition. Pseudo reference vs. Ag/AgNO_3 .

X-ray data

Crystal data and structure refinement for 9-(2-methoxyphenyl)-1H-phenalen-1-one .	
Empirical formula	C ₄₀ H ₂₈ O ₄
Formula weight	572.62
Temperature	293(2) K
Wavelength	0.71073 Å
Crystal system, space group	Triclinic, P-1
Unit cell dimensions	a = 8.9091(5) Å α = 83.432(7) deg. b = 11.0931(10) Å β = 89.807(5) deg. c = 14.5265(11) Å γ = 81.560(6) deg.
Volume	1410.65(18) Å ³
Z, Calculated density	2, 1.348 Mg/m ³
Absorption coefficient	0.086 mm ⁻¹
F(000)	600
Crystal size	0.28 x 0.12 x 0.09 mm
Theta range for data collection	2.72 to 25.09 deg.
Limiting indices	-10 ≤ h ≤ 10, -13 ≤ k ≤ 13, -17 ≤ l ≤ 17
Reflections collected / unique	21286 / 4993 [R(int) = 0.1285]
Completeness to theta = 25.09	99.2 %
Absorption correction	Analytical
Max. and min. Transmission	0.995 and 0.987
Refinement method	Full-matrix least-squares on F ²
Data / restraints / parameters	4993 / 0 / 400
Goodness-of-fit on F ²	1.025
Final R indices [I > 2σ(I)]	R1 = 0.0613, wR2 = 0.1148
R indices (all data)	R1 = 0.1696, wR2 = 0.1677
Extinction coefficient	0.0067(15)
Largest diff. peak and hole	0.23 and -0.23 e.Å ⁻³

Appendix 55



Bond lengths			Bond angles			
Atom 1	Atom 2	Length	Atom 1	Atom 2	Atom 3	Angle
C1	C2	1.389(6)	C2	C1	C6	120.2(4)
C1	C6	1.411(5)	C2	C1	O1	123.6(4)
C1	O1	1.373(5)	C6	C1	O1	116.1(3)
C2	H2	0.929(4)	C1	C2	H2	120.1(4)
C2	C3	1.390(6)	C1	C2	C3	119.8(4)
C3	H3	0.930(4)	H2	C2	C3	120.1(4)
C3	C4	1.378(5)	C2	C3	H3	119.7(4)
C4	H4	0.930(5)	C2	C3	C4	120.6(4)
C4	C5	1.375(6)	H3	C3	C4	119.7(4)
C5	H5	0.930(4)	C3	C4	H4	120.7(4)
C5	C6	1.377(6)	C3	C4	C5	118.7(4)
C6	C7	1.491(6)	H4	C4	C5	120.6(4)
C7	C8	1.405(6)	C4	C5	H5	118.4(4)
C7	C16	1.399(6)	C4	C5	C6	123.1(4)
C8	H8	0.929(4)	H5	C5	C6	118.4(4)
C8	C9	1.374(6)	C1	C6	C5	117.4(4)
C9	H9	0.930(4)	C1	C6	C7	122.2(4)
C9	C10	1.407(6)	C5	C6	C7	120.2(4)
C10	C11	1.419(5)	C6	C7	C8	116.2(4)
C10	C15	1.424(5)	C6	C7	C16	125.1(4)
C11	H11	0.929(4)	C8	C7	C16	118.7(4)
C11	C12	1.370(6)	C7	C8	H8	119.0(4)
C12	H12	0.930(4)	C7	C8	C9	122.1(4)
C12	C13	1.400(6)	H8	C8	C9	119.0(4)
C13	H13	0.930(5)	C8	C9	H9	119.6(4)
C13	C14	1.376(6)	C8	C9	C10	120.8(4)
C14	C15	1.423(6)	H9	C9	C10	119.6(4)
C14	C19	1.445(6)	C9	C10	C11	122.2(3)
C15	C16	1.432(4)	C9	C10	C15	118.3(3)
C16	C17	1.489(5)	C11	C10	C15	119.4(3)

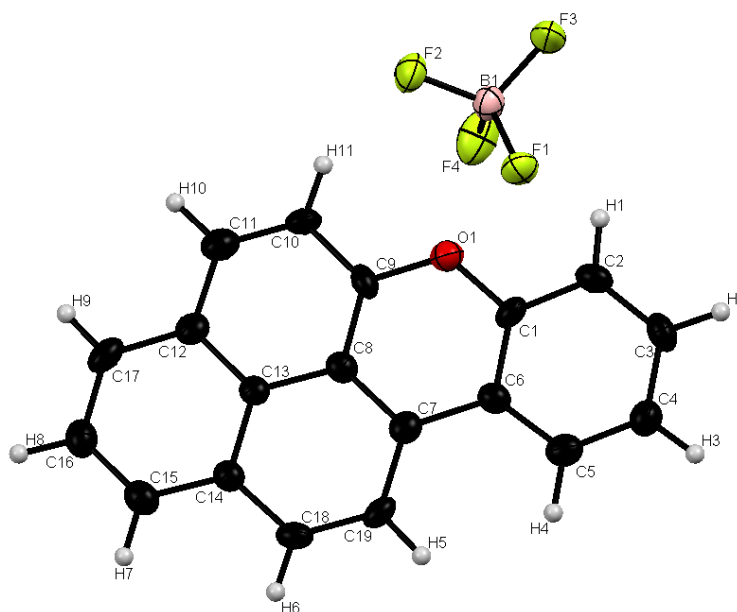
C17	C18	1.458(6)	C10	C11	H11	119.5(4)
C17	O2	1.244(5)	C10	C11	C12	120.9(4)
C18	H18	0.930(4)	H11	C11	C12	119.6(4)
C18	C19	1.342(6)	C11	C12	H12	120.2(4)
C19	H19	0.930(5)	C11	C12	C13	119.6(4)
C20	H20A	0.959(4)	H12	C12	C13	120.2(4)
C20	H20B	0.960(5)	C12	C13	H13	119.2(4)
C20	H20C	0.960(4)	C12	C13	C14	121.5(4)
C20	O1	1.433(4)	H13	C13	C14	119.2(4)
C21	C22	1.376(6)	C13	C14	C15	120.2(4)
C21	C26	1.399(5)	C13	C14	C19	121.2(4)
C21	O3	1.382(5)	C15	C14	C19	118.6(4)
C22	H22	0.930(4)	C10	C15	C14	118.3(3)
C22	C23	1.380(6)	C10	C15	C16	120.0(3)
C23	H23	0.930(4)	C14	C15	C16	121.7(3)
C23	C24	1.376(5)	C7	C16	C15	119.8(3)
C24	H24	0.930(4)	C7	C16	C17	122.3(3)
C24	C25	1.389(6)	C15	C16	C17	117.9(3)
C25	H25	0.930(4)	C16	C17	C18	117.3(3)
C25	C26	1.393(6)	C16	C17	O2	122.7(4)
C26	C27	1.499(6)	C18	C17	O2	119.9(4)
C27	C28	1.409(6)	C17	C18	H18	118.8(4)
C27	C36	1.398(5)	C17	C18	C19	122.3(4)
C28	H28	0.931(4)	H18	C18	C19	118.8(4)
C28	C29	1.367(6)	C14	C19	C18	121.8(4)
C29	H29	0.931(5)	C14	C19	H19	119.1(4)
C29	C30	1.417(6)	C18	C19	H19	119.1(4)
C30	C31	1.414(6)	H20A	C20	H20B	109.5(4)
C30	C35	1.425(6)	H20A	C20	H20C	109.5(4)
C31	H31	0.931(5)	H20A	C20	O1	109.5(4)
C31	C32	1.356(6)	H20B	C20	H20C	109.4(4)
C32	H32	0.930(5)	H20B	C20	O1	109.4(4)
C32	C33	1.399(6)	H20C	C20	O1	109.4(4)
C33	H33	0.931(4)	C1	O1	C20	117.2(3)
C33	C34	1.383(6)	C22	C21	C26	120.8(4)
C34	C35	1.427(5)	C22	C21	O3	124.7(4)
C34	C39	1.444(6)	C26	C21	O3	114.5(3)
C35	C36	1.423(4)	C21	C22	H22	119.9(4)
C36	C37	1.493(6)	C21	C22	C23	120.1(4)
C37	C38	1.458(6)	H22	C22	C23	120.0(4)
C37	O4	1.241(5)	C22	C23	H23	119.7(4)
C38	H38	0.930(5)	C22	C23	C24	120.6(4)
C38	C39	1.348(6)	H23	C23	C24	119.7(4)
C39	H39	0.930(4)	C23	C24	H24	120.4(4)
C40	H40A	0.960(4)	C23	C24	C25	119.2(4)
C40	H40B	0.960(4)	H24	C24	C25	120.4(4)
C40	H40C	0.960(5)	C24	C25	H25	119.3(4)
C40	O3	1.438(4)	C24	C25	C26	121.3(4)
			H25	C25	C26	119.4(4)
			C21	C26	C25	118.0(4)
			C21	C26	C27	121.7(4)
			C25	C26	C27	119.7(4)
			C26	C27	C28	115.0(3)
			C26	C27	C36	125.8(3)
			C28	C27	C36	119.2(3)
			C27	C28	H28	119.0(4)

C27	C28	C29	121.9(4)
H28	C28	C29	119.0(4)
C28	C29	H29	119.7(4)
C28	C29	C30	120.5(4)
H29	C29	C30	119.7(4)
C29	C30	C31	122.0(4)
C29	C30	C35	118.2(4)
C31	C30	C35	119.9(4)
C30	C31	H31	119.7(4)
C30	C31	C32	120.7(4)
H31	C31	C32	119.6(4)
C31	C32	H32	119.7(4)
C31	C32	C33	120.5(4)
H32	C32	C33	119.8(4)
C32	C33	H33	119.5(4)
C32	C33	C34	120.9(4)
H33	C33	C34	119.6(4)
C33	C34	C35	120.1(4)
C33	C34	C39	121.2(4)
C35	C34	C39	118.7(4)
C30	C35	C34	117.9(3)
C30	C35	C36	120.5(3)
C34	C35	C36	121.6(3)
C27	C36	C35	119.5(3)
C27	C36	C37	122.0(3)
C35	C36	C37	118.5(3)
C36	C37	C38	117.1(3)
C36	C37	O4	122.8(4)
C38	C37	O4	120.1(4)
C37	C38	H38	118.7(4)
C37	C38	C39	122.4(4)
H38	C38	C39	118.9(4)
C34	C39	C38	121.6(4)
C34	C39	H39	119.2(4)
C38	C39	H39	119.2(4)
H40A	C40	H40B	109.5(4)
H40A	C40	H40C	109.4(4)
H40A	C40	O3	109.5(4)
H40B	C40	H40C	109.4(4)
H40B	C40	O3	109.5(4)
H40C	C40	O3	109.5(4)
C21	O3	C40	117.3(3)

Appendix 56 Bond lengths and bond angles of 9-(2-methoxyphenyl)-1*H*-phenalen-1-one.

Crystal data and structure refinement for naphtho[2,1,8-<i>mna</i>]xanthenium tetrafluoroborate	
Empirical formula	C ₁₉ H ₁₁ BF ₄ O
Formula weight	342.09
Temperature	100(2) K
Wavelength	0.71073 Å
Crystal system, space group	Triclinic, P-1
Unit cell dimensions	a = 7.9775(2) Å α = 68.0280(10) deg. b = 9.9922(3) Å β = 86.5200(10) deg. c = 10.3742(3) Å γ = 70.1990(10) deg.
Volume	719.48(3) Å ³
Z, Calculated density	2, 1.579 Mg/m ³
Absorption coefficient	0.131 mm ⁻¹
F(000)	348
Crystal size	0.4 x 0.2 x 0.05 mm
Theta range for data collection	2.12 to 27.52 deg.
Limiting indices	-10 ≤ h ≤ 10, -12 ≤ k ≤ 12, -13 ≤ l ≤ 13
Reflections collected / unique	6359 / 3296 [R(int) = 0.0686]
Completeness to theta = 27.52	99.4 %
Absorption correction	Semi-empirical from equivalents
Max. and min. Transmission	Full-matrix least-squares on F ²
Refinement method	Full-matrix least-squares on F ²
Data / restraints / parameters	3296 / 0 / 270
Goodness-of-fit on F ²	0.912
Final R indices [I > 2σ(I)]	R1 = 0.0491, wR2 = 0.099
R indices (all data)	R1 = 0.1475, wR2 = 0.1039
Extinction coefficient	0.353 and -0.24 e.Å ⁻³
Largest diff. peak and hole	0.23 and -0.23 e.Å ⁻³

Appendix 57



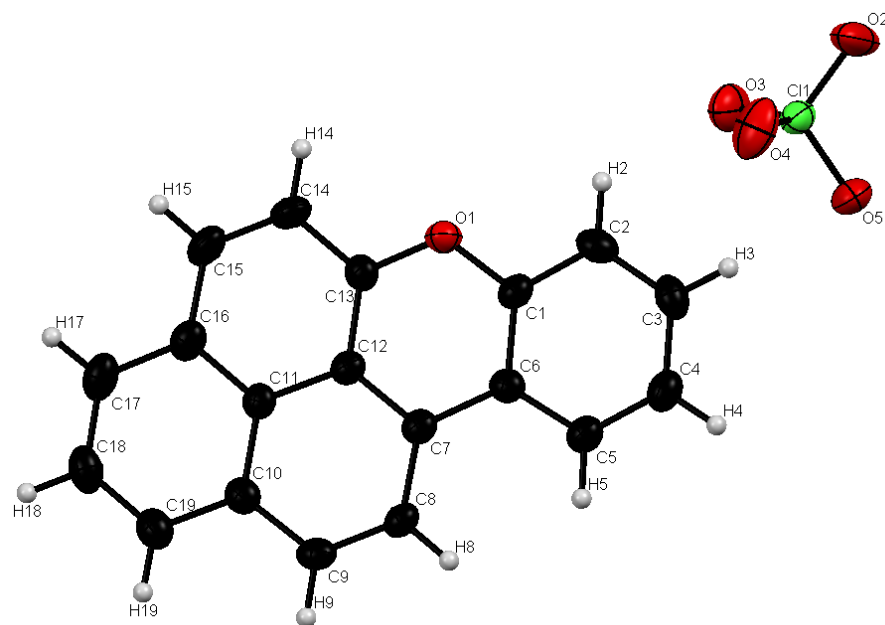
Bond lengths			Bond angles			
Atom 1	Atom 2	Length	Atom 1	Atom 2	Atom 3	Angle
F1	B1	1.389(3)	F1	B1	F2	110.1(2)
F2	B1	1.391(3)	F1	B1	F3	109.3(2)
F3	B1	1.378(3)	F1	B1	F4	107.9(2)
F4	B1	1.391(4)	F2	B1	F3	109.9(2)
O1	C1	1.375(3)	F2	B1	F4	109.5(2)
O1	C9	1.338(2)	F3	B1	F4	110.2(2)
C1	C6	1.396(3)	C1	O1	C9	120.9(2)
C1	C2	1.394(3)	O1	C1	C6	122.3(2)
C13	C8	1.408(3)	O1	C1	C2	115.4(2)
C13	C14	1.419(3)	C6	C1	C2	122.2(2)
C13	C12	1.420(3)	C8	C13	C14	119.5(2)
C8	C9	1.420(3)	C8	C13	C12	120.2(2)
C8	C7	1.408(3)	C14	C13	C12	120.3(2)
C6	C7	1.452(3)	C13	C8	C9	117.6(2)
C6	C5	1.397(3)	C13	C8	C7	121.7(2)
C14	C18	1.427(3)	C9	C8	C7	120.6(2)
C14	C15	1.400(3)	C1	C6	C7	118.0(2)
C12	C17	1.407(3)	C1	C6	C5	117.6(2)
C12	C11	1.420(3)	C7	C6	C5	124.4(2)
C9	C10	1.400(3)	C13	C14	C18	117.7(2)
C7	C19	1.408(3)	C13	C14	C15	118.7(2)
C5	C4	1.360(3)	C18	C14	C15	123.6(2)
C5	H4	1.02(2)	C13	C12	C17	118.0(2)
C2	C3	1.384(3)	C13	C12	C11	119.0(2)
C2	H1	0.96(2)	C17	C12	C11	122.9(2)
C19	C18	1.370(3)	O1	C9	C8	120.4(2)
C19	H5	0.96(2)	O1	C9	C10	117.6(2)
C18	H6	0.95(2)	C8	C9	C10	121.9(2)
C4	C3	1.394(4)	C8	C7	C6	117.8(2)
C4	H3	0.97(2)	C8	C7	C19	118.3(2)
C10	C11	1.344(3)	C6	C7	C19	123.9(2)
C10	H11	0.97(2)	C6	C5	C4	120.8(2)
C17	C16	1.388(4)	C6	C5	H4	119(1)

C17	H9	0.95(2)	C4	C5	H4	121(1)
C15	C16	1.366(3)	C1	C2	C3	118.3(2)
C15	H7	0.97(2)	C1	C2	H1	117(1)
C3	H2	0.97(2)	C3	C2	H1	125(1)
C16	H8	1.01(2)	C7	C19	C18	120.7(2)
C11	H10	1.02(2)	C7	C19	H5	121(1)
			C18	C19	H5	118(1)
			C14	C18	C19	122.1(2)
			C14	C18	H6	116(1)
			C19	C18	H6	122(1)
			C5	C4	C3	121.1(2)
			C5	C4	H3	122(1)
			C3	C4	H3	117(1)
			C9	C10	C11	119.7(2)
			C9	C10	H11	118(1)
			C11	C10	H11	122(1)
			C12	C17	C16	121.1(2)
			C12	C17	H9	116(1)
			C16	C17	H9	122(1)
			C14	C15	C16	121.3(2)
			C14	C15	H7	119(1)
			C16	C15	H7	119(1)
			C2	C3	C4	120.0(2)
			C2	C3	H2	121(1)
			C4	C3	H2	119(1)
			C17	C16	C15	120.5(2)
			C17	C16	H8	118(1)
			C15	C16	H8	122(1)
			C12	C11	C10	121.6(2)
			C12	C11	H10	118(1)
			C10	C11	H10	121(1)

Appendix 58 Bond lengths and bond angles of naphtho[2,1,8-*mna*]xanthenium tetrafluoroborate.

Crystal data and structure refinement for naphtho[2,1,8-<i>mna</i>]xanthenium perchlorate	
Empirical formula	C ₁₉ H ₁₁ ClO ₅
Formula weight	354.73
Temperature	150(2) K
Wavelength	0.71073 Å
Crystal system, space group	Triclinic, P-1
Unit cell dimensions	a = 7.9557(8) Å α = 67.889(5) deg. b = 10.0738(10) Å β = 86.904(5) deg. c = 10.5637(9) Å γ = 70.955(5) deg.
Volume	739.13(12) Å ³
Z, Calculated density	2, 1.594 Mg/m ³
Absorption coefficient	0.288 mm ⁻¹
F(000)	364
Crystal size	0.12 x 0.06 x 0.02 mm
Theta range for data collection	2.09 to 26.00 deg.
Limiting indices	-9 ≤ h ≤ 9, -12 ≤ k ≤ 12, -13 ≤ l ≤ 13
Reflections collected / unique	11443 / 2898 [R(int) = 0.0263]
Completeness to theta = 26.00	99.9 %
Absorption correction	Empirical
Max. and min. Transmission	0.9943 and 0.9662
Refinement method	Full-matrix least-squares on F ²
Data / restraints / parameters	2898 / 0 / 226
Goodness-of-fit on F ²	1.049
Final R indices [I > 2σ(I)]	R1 = 0.0414, wR2 = 0.1028
R indices (all data)	R1 = 0.0523, wR2 = 0.1105
Extinction coefficient	none
Largest diff. peak and hole	0.41 and -0.40 e.Å ⁻³

Appendix 59



Bond lengths			Bond angles			
Atom 1	Atom 2	Length	Atom 1	Atom 2	Atom 3	Angle
C1	C2	1.395(3)	C2	C1	C6	122.3(2)
C1	C6	1.398(3)	C2	C1	O1	115.4(2)
C1	O1	1.371(3)	C6	C1	O1	122.3(2)
C2	H2	0.950(2)	C1	C2	H2	121.0(2)
C2	C3	1.381(3)	C1	C2	C3	118.0(2)
C3	H3	0.950(2)	H2	C2	C3	121.0(2)
C3	C4	1.391(4)	C2	C3	H3	119.7(2)
C4	H4	0.950(2)	C2	C3	C4	120.7(2)
C4	C5	1.359(3)	H3	C3	C4	119.7(2)
C5	H5	0.950(2)	C3	C4	H4	119.7(2)
C5	C6	1.402(3)	C3	C4	C5	120.6(2)
C6	C7	1.448(3)	H4	C4	C5	119.7(2)
C7	C8	1.404(3)	C4	C5	H5	119.5(2)
C7	C12	1.409(3)	C4	C5	C6	121.0(2)
C8	H8	0.950(2)	H5	C5	C6	119.5(2)
C8	C9	1.369(3)	C1	C6	C5	117.4(2)
C9	H9	0.950(2)	C1	C6	C7	118.2(2)
C9	C10	1.431(3)	C5	C6	C7	124.4(2)
C10	C11	1.413(3)	C6	C7	C8	124.1(2)
C10	C19	1.405(3)	C6	C7	C12	117.1(2)
C11	C12	1.419(3)	C8	C7	C12	118.8(2)
C11	C16	1.411(3)	C7	C8	H8	119.7(2)
C12	C13	1.413(3)	C7	C8	C9	120.7(2)
C13	C14	1.399(3)	H8	C8	C9	119.6(2)
C13	O1	1.335(2)	C8	C9	H9	119.1(2)
C14	H14	0.950(2)	C8	C9	C10	121.7(2)
C14	C15	1.351(3)	H9	C9	C10	119.2(2)
C15	H15	0.949(2)	C9	C10	C11	118.4(2)
C15	C16	1.419(4)	C9	C10	C19	122.6(2)
C16	C17	1.412(3)	C11	C10	C19	119.1(2)
C17	H17	0.950(2)	C10	C11	C12	119.1(2)
C17	C18	1.382(4)	C10	C11	C16	120.7(2)

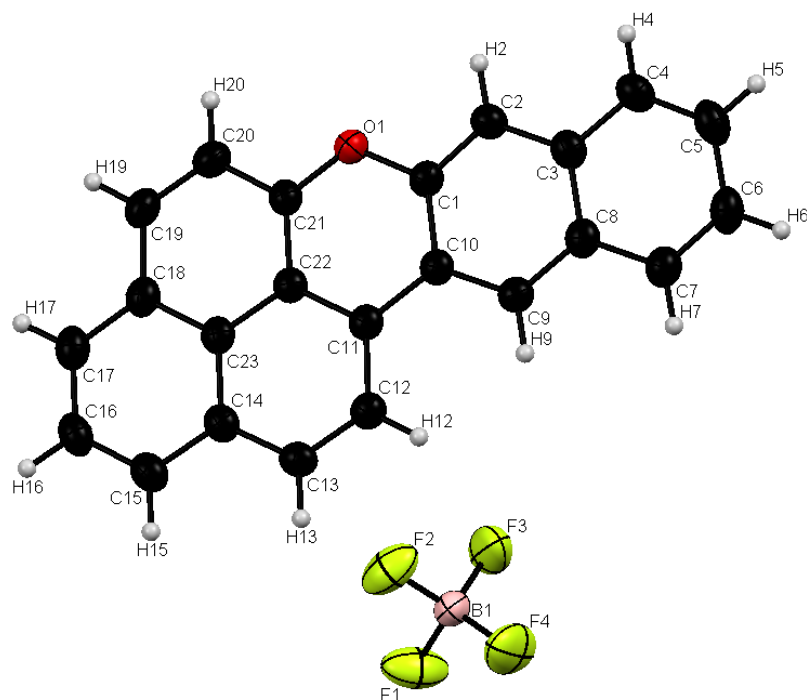
C18	H18	0.951(2)	C12	C11	C16	120.2(2)
C18	C19	1.376(3)	C7	C12	C11	121.3(2)
C19	H19	0.950(3)	C7	C12	C13	121.2(2)
O2	C11	1.423(2)	C11	C12	C13	117.5(2)
O3	C11	1.438(2)	C12	C13	C14	122.2(2)
O4	C11	1.436(3)	C12	C13	O1	120.3(2)
O5	C11	1.429(2)	C14	C13	O1	117.5(2)
			C13	C14	H14	120.3(2)
			C13	C14	C15	119.4(2)
			H14	C14	C15	120.3(2)
			C14	C15	H15	119.1(2)
			C14	C15	C16	121.7(2)
			H15	C15	C16	119.2(2)
			C11	C16	C15	119.0(2)
			C11	C16	C17	118.3(2)
			C15	C16	C17	122.7(2)
			C16	C17	H17	119.7(2)
			C16	C17	C18	120.5(2)
			H17	C17	C18	119.8(2)
			C17	C18	H18	119.3(2)
			C17	C18	C19	121.4(2)
			H18	C18	C19	119.3(2)
			C10	C19	C18	120.1(2)
			C10	C19	H19	119.9(2)
			C18	C19	H19	120.0(2)
			C1	O1	C13	120.8(2)
			O2	C11	O3	109.6(1)
			O2	C11	O4	110.0(1)
			O2	C11	O5	109.3(1)
			O3	C11	O4	110.0(1)
			O3	C11	O5	109.9(1)
			O4	C11	O5	108.0(1)

Appendix 60 Bond lengths and bond angles of NXClO₄.

Crystal data and structure refinement for **benzo[*i*]naphtho[2,1,8-*mna*]xanthenium perchlorate**

Empirical formula	C ₂₃ H ₁₃ BF ₄ O	
Formula weight	392.14	
Temperature	150(2) K	
Wavelength	1.54178 Å	
Crystal system, space group	Triclinic, P-1	
Unit cell dimensions	a = 8.0816(7) Å 10.1745(8) Å 11.9752(9) Å	α = 67.764(7) deg. b = β = 71.133(8) deg = γ = 71.903(8) deg.
Volume	842.32(12) Å ³	
Z, Calculated density	2, 1.546 Mg/m ³	
Absorption coefficient	1.048 mm ⁻¹	
F(000)	400	
Crystal size	0.38 x 0.20 x 0.04 mm	
Theta range for data collection	4.10 to 67.49 deg.	
Limiting indices	-9 ≤ h ≤ 9, -12 ≤ k ≤ 12, -14 ≤ l ≤ 14	
Reflections collected / unique	11968 / 3002 [R(int) = 0.0344]	
Completeness to theta = 67.49	99.1 %	
Absorption correction	Analytical	
Max. and min. Transmission	0.9593 and 0.6915	
Refinement method	Full-matrix least-squares on F ²	
Data / restraints / parameters	3002 / 64 / 283	
Goodness-of-fit on F ²	1.041	
Final R indices [I > 2σ(I)]	R1 = 0.0577, wR2 = 0.1591	
R indices (all data)	R1 = 0.0727, wR2 = 0.1768	
Extinction coefficient	none	
Largest diff. peak and hole	0.73 and -0.45 e.Å ⁻³	

Appendix 61



Bond lengths			Bond angles			
Atom 1	Atom 2	Length	Atom 1	Atom 2	Atom 3	Angle
C1	C2	1.366(3)	C2	C1	C10	122.8(2)
C1	C10	1.425(3)	C2	C1	O1	116.3(2)
C1	O1	1.381(2)	C10	C1	O1	120.9(2)
C2	H2	0.950(2)	C1	C2	H2	120.1(2)
C2	C3	1.407(3)	C1	C2	C3	119.8(2)
C3	C4	1.422(3)	H2	C2	C3	120.1(2)
C3	C8	1.432(3)	C2	C3	C4	122.2(2)
C4	H4	0.950(3)	C2	C3	C8	118.9(2)
C4	C5	1.359(3)	C4	C3	C8	118.8(2)
C5	H5	0.950(2)	C3	C4	H4	119.8(2)
C5	C6	1.418(4)	C3	C4	C5	120.4(2)
C6	H6	0.950(2)	H4	C4	C5	119.8(3)
C6	C7	1.367(3)	C4	C5	H5	119.4(3)
C7	H7	0.950(3)	C4	C5	C6	121.1(2)
C7	C8	1.421(3)	H5	C5	C6	119.5(3)
C8	C9	1.400(3)	C5	C6	H6	119.9(3)
C9	H9	0.951(2)	C5	C6	C7	120.2(2)
C9	C10	1.391(3)	H6	C6	C7	119.9(3)
C10	C11	1.443(3)	C6	C7	H7	119.8(3)
C11	C12	1.415(3)	C6	C7	C8	120.4(2)
C11	C22	1.414(3)	H7	C7	C8	119.8(2)
C12	H12	0.950(2)	C3	C8	C7	119.0(2)
C12	C13	1.373(3)	C3	C8	C9	119.5(2)
C13	H13	0.950(2)	C7	C8	C9	121.5(2)
C13	C14	1.424(3)	C8	C9	H9	119.2(2)
C14	C15	1.408(3)	C8	C9	C10	121.7(2)
C14	C23	1.412(3)	H9	C9	C10	119.1(2)
C15	H15	0.950(3)	C1	C10	C9	117.2(2)
C15	C16	1.383(3)	C1	C10	C11	118.8(2)
C16	H16	0.950(2)	C9	C10	C11	124.0(2)
C16	C17	1.390(4)	C10	C11	C12	123.9(2)

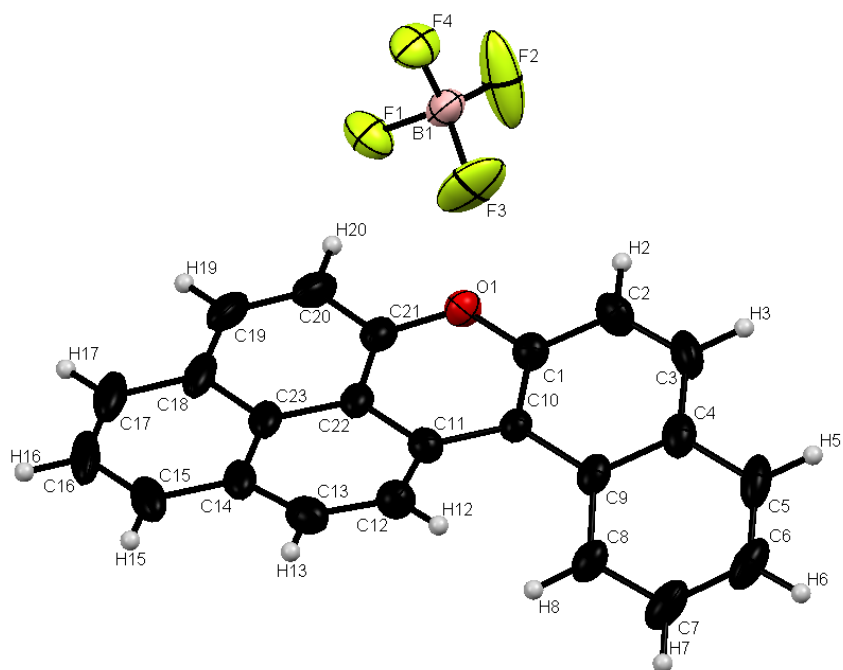
C17	H17	0.950(2)	C10	C11	C22	117.4(2)
C17	C18	1.401(3)	C12	C11	C22	118.7(2)
C18	C19	1.428(3)	C11	C12	H12	119.7(2)
C18	C23	1.419(3)	C11	C12	C13	120.6(2)
C19	H19	0.950(2)	H12	C12	C13	119.7(2)
C19	C20	1.362(3)	C12	C13	H13	119.2(2)
C20	H20	0.950(2)	C12	C13	C14	121.7(2)
C20	C21	1.404(3)	H13	C13	C14	119.2(2)
C21	C22	1.409(3)	C13	C14	C15	122.5(2)
C21	O1	1.337(2)	C13	C14	C23	118.7(2)
C22	C23	1.420(3)	C15	C14	C23	118.8(2)
B1	F1	1.371(6)	C14	C15	H15	119.7(2)
B1	F2	1.375(6)	C14	C15	C16	120.7(2)
B1	F3	1.385(4)	H15	C15	C16	119.7(3)
B1	F4	1.361(5)	C15	C16	H16	119.8(3)
			C15	C16	C17	120.5(2)
			H16	C16	C17	119.7(3)
			C16	C17	H17	119.6(3)
			C16	C17	C18	120.9(2)
			H17	C17	C18	119.5(2)
			C17	C18	C19	122.9(2)
			C17	C18	C23	118.6(2)
			C19	C18	C23	118.5(2)
			C18	C19	H19	119.1(2)
			C18	C19	C20	121.8(2)
			H19	C19	C20	119.1(3)
			C19	C20	H20	120.3(2)
			C19	C20	C21	119.5(2)
			H20	C20	C21	120.2(2)
			C20	C21	C22	121.6(2)
			C20	C21	O1	116.8(2)
			C22	C21	O1	121.6(2)
			C11	C22	C21	120.6(2)
			C11	C22	C23	120.9(2)
			C21	C22	C23	118.5(2)
			C14	C23	C18	120.5(2)
			C14	C23	C22	119.4(2)
			C18	C23	C22	120.1(2)
			C1	O1	C21	120.7(2)
			F1	B1	F2	108.3(3)
			F1	B1	F3	107.5(3)
			F1	B1	F4	107.7(3)
			F2	B1	F3	109.2(3)
			F2	B1	F4	112.8(3)
			F3	B1	F4	111.2(3)

Appendix 62 Bond lengths and bond angles of B[i]NXBF₄.

Crystal data and structure refinement for **benzo[*a*]naphtho[8,1,2-*jk*l]xanthenium tetrafluoroborate**

Empirical formula	C ₂₃ H ₁₃ BF ₄ O	
Formula weight	392.14	
Temperature	150(2) K	
Wavelength	0.71073 Å	
Crystal system, space group	Triclinic, P -1	
Unit cell dimensions	a = 7.1692(8) Å b = 8.6347(11) Å c = 13.9776(15) Å	α = 86.021(6) deg. β = 77.850(6) deg. γ = 86.143(6) deg.
Volume	842.616 Å ³	
Z, Calculated density	2, 1.546 Mg/m ³	
Absorption coefficient	0.123 mm ⁻¹	
F(000)	400	
Crystal size	0.3 x 0.2 x 0.1 mm	
Theta range for data collection	2.37 to 26.00 deg.	
Limiting indices	-8 ≤ h ≤ 8, -10 ≤ k ≤ 10, -17 ≤ l ≤ 16	
Reflections collected / unique	12126 / 3291 [R(int) = 0.0265]	
Completeness to theta = 26.00	99.3 %	
Absorption correction	Empirical	
Max. and min. Transmission	0.980 and 0.843	
Refinement method	Full-matrix least-squares on F ²	
Data / restraints / parameters	3291 / 31 / 296	
Goodness-of-fit on F ²	1.048	
Final R indices [I > 2σ(I)]	R1 = 0.0668, wR2 = 0.1666	
R indices (all data)	R1 = 0.0850, wR2 = 0.1816	
Extinction coefficient	none	
Largest diff. peak and hole	0.70 and -0.30 e.Å ⁻³	

Appendix 63



Bond lengths			Bond angles			
Atom 1	Atom 2	Length	Atom 1	Atom 2	Atom 3	Angle
C1	C2	1.401(4)	C2	C1	C10	123.7(3)
C1	C10	1.395(4)	C2	C1	O1	114.3(3)
C1	O1	1.359(4)	C10	C1	O1	122.0(3)
C2	H2	0.950(3)	C1	C2	H2	120.9(3)
C2	C3	1.358(4)	C1	C2	C3	118.3(3)
C3	H3	0.950(3)	H2	C2	C3	120.8(3)
C3	C4	1.415(5)	C2	C3	H3	119.2(3)
C4	C5	1.417(4)	C2	C3	C4	121.6(3)
C4	C9	1.418(4)	H3	C3	C4	119.2(3)
C5	H5	0.950(3)	C3	C4	C5	120.7(3)
C5	C6	1.366(6)	C3	C4	C9	120.1(3)
C6	H6	0.950(3)	C4	C5	H5	119.5(3)
C6	C7	1.386(5)	C4	C5	C6	121.0(3)
C7	H7	0.950(4)	H5	C5	C6	119.6(4)
C7	C8	1.385(5)	C5	C6	H6	119.9(4)
C8	H8	0.951(3)	C5	C6	C7	120.1(3)
C8	C9	1.411(5)	H6	C6	C7	119.9(4)
C9	C10	1.452(4)	C6	C7	H7	119.7(4)
C10	C11	1.430(4)	C6	C7	C8	120.6(3)
C11	C12	1.418(4)	H7	C7	C8	119.6(4)
C11	C22	1.423(4)	C7	C8	H8	119.7(3)
C12	H12	0.951(3)	C7	C8	C9	120.6(3)
C12	C13	1.367(4)	H8	C8	C9	119.6(3)
C13	H13	0.950(4)	C4	C9	C8	118.4(3)
C13	C14	1.401(4)	C4	C9	C10	118.4(3)
C14	C15	1.411(5)	C8	C9	C10	123.1(3)
C14	C23	1.405(5)	C1	C10	C9	116.7(3)
C15	H15	0.950(4)	C1	C10	C11	117.5(3)
C15	C16	1.395(6)	C9	C10	C11	125.8(3)
C16	H16	0.949(3)	C10	C11	C12	127.1(3)
C16	C17	1.381(7)				

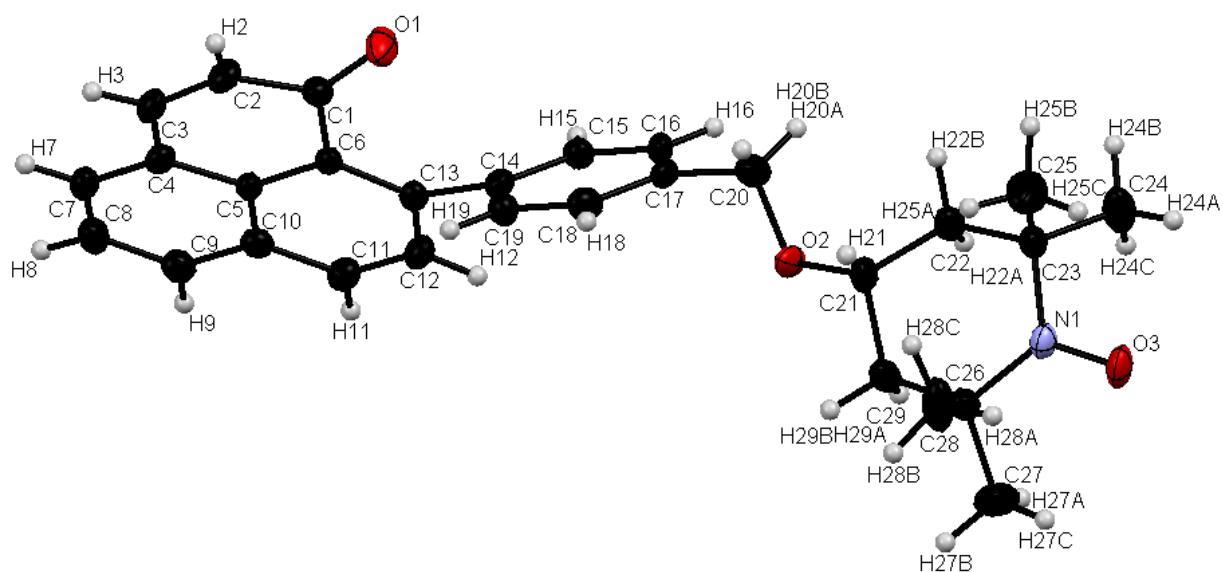
C17	H17	0.950(4)	C10	C11	C22	117.6(3)
C17	C18	1.398(4)	C12	C11	C22	115.0(3)
C18	C19	1.413(6)	C11	C12	H12	119.2(3)
C18	C23	1.431(5)	C11	C12	C13	121.5(3)
C19	H19	0.950(3)	H12	C12	C13	119.3(3)
C19	C20	1.352(4)	C12	C13	H13	118.4(3)
C20	H20	0.950(3)	C12	C13	C14	123.2(3)
C20	C21	1.412(4)	H13	C13	C14	118.3(3)
C21	C22	1.396(5)	C13	C14	C15	123.5(3)
C21	O1	1.332(3)	C13	C14	C23	117.4(3)
C22	C23	1.419(4)	C15	C14	C23	119.0(3)
B1	F1	1.450(5)	C14	C15	H15	120.1(4)
B1	F2	1.36(1)	C14	C15	C16	119.6(3)
B1	F3	1.343(7)	H15	C15	C16	120.2(4)
B1	F4	1.377(6)	C15	C16	H16	119.3(4)
			C15	C16	C17	121.4(4)
			H16	C16	C17	119.3(4)
			C16	C17	H17	119.6(4)
			C16	C17	C18	120.9(3)
			H17	C17	C18	119.5(4)
			C17	C18	C19	122.4(3)
			C17	C18	C23	118.1(3)
			C19	C18	C23	119.5(3)
			C18	C19	H19	119.5(3)
			C18	C19	C20	121.1(3)
			H19	C19	C20	119.5(3)
			C19	C20	H20	120.4(3)
			C19	C20	C21	119.3(3)
			H20	C20	C21	120.3(3)
			C20	C21	C22	123.0(3)
			C20	C21	O1	116.5(3)
			C22	C21	O1	120.5(3)
			C11	C22	C21	120.0(3)
			C11	C22	C23	122.7(3)
			C21	C22	C23	117.3(3)
			C14	C23	C18	120.9(3)
			C14	C23	C22	119.2(3)
			C18	C23	C22	119.9(3)
			C1	O1	C21	121.1(2)
			F1	B1	F2	101.6(5)
			F1	B1	F3	102.4(4)
			F1	B1	F4	106.4(4)
			F2	B1	F3	112.8(6)
			F2	B1	F4	117.6(5)
			F3	B1	F4	113.8(5)

Appendix 64 Bond lengths and bond angles of B[*a*]NXBF₄.

Crystal data and structure refinement for **9-(4-((TEMPO)methyl)phenyl)-1*H*-phenalen-1-one**

Empirical formula	C ₂₉ H ₃₁ NO ₃	
Formula weight	441.54	
Temperature	150(2) K	
Wavelength	0.71073 Å	
Crystal system, space group	Monoclinic, P2(1)/n	
Unit cell dimensions	a = 13.1251(7) Å b = 6.3804(4) Å c = 14.1854(7) Å	α = 90.00 deg. β = 96.464(3) deg. γ = 90.00 deg.
Volume	1180.38 Å ³	
Z, Calculated density	2, 1.239 Mg/m ³	
Absorption coefficient	0.080 mm ⁻¹	
F(000)	470	
Crystal size	0.20 x 0.16 x 0.10 mm	
Theta range for data collection	2.24 to 26.00 deg.	
Limiting indices	-16 ≤ h ≤ 14, -7 ≤ k ≤ 7, -16 ≤ l ≤ 17	
Reflections collected / unique	16910 / 4605 [R(int) = 0.0456]	
Completeness to theta = 26.00	99.8 %	
Absorption correction	Empirical	
Max. and min. Transmission	0.9921 and 0.9843	
Refinement method	Full-matrix least-squares on F ²	
Data / restraints / parameters	4605 / 1 / 303	
Goodness-of-fit on F ²	1.037	
Final R indices [I > 2σ(I)]	R1 = 0.0546, wR2 = 0.1440	
R indices (all data)	R1 = 0.0697, wR2 = 0.1548	
Absolute structure parameter	-0.2(17)	
Extinction coefficient	0.018(4)	
Largest diff. peak and hole	1.17 and -0.22 e.Å ⁻³	

Appendix 65



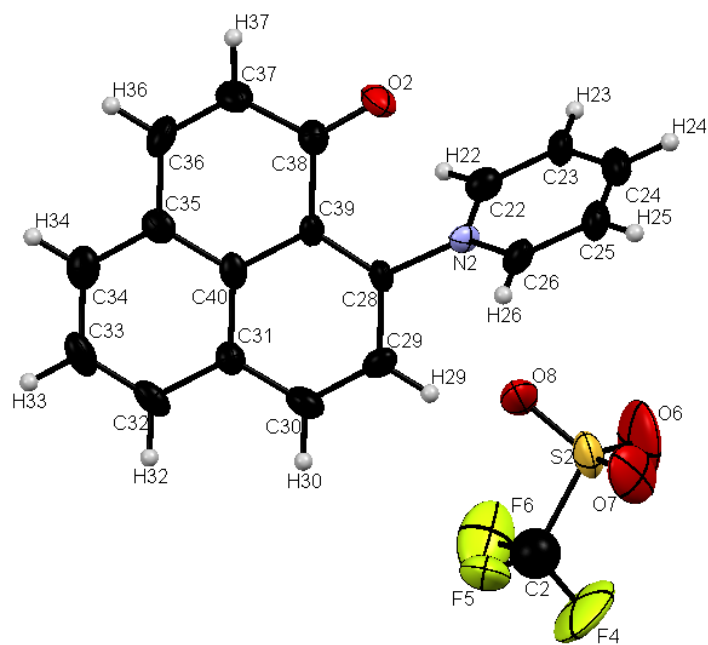
Bond lengths			Bond angles			
Atom 1	Atom 2	Length	Atom 1	Atom 2	Atom 3	Angle
C1	C2	1.469(4)	C2	C1	C10	123.7(3)
C1	C6	1.490(4)	C2	C1	O1	114.3(3)
C1	O1	1.230(3)	C10	C1	O1	122.0(3)
C2	H2	0.950(3)	C1	C2	H2	120.9(3)
C2	C3	1.326(4)	C1	C2	C3	118.3(3)
C3	H3	0.950(3)	H2	C2	C3	120.8(3)
C3	C4	1.443(4)	C2	C3	H3	119.2(3)
C4	C5	1.427(4)	C2	C3	C4	121.6(3)
C4	C7	1.391(4)	H3	C3	C4	119.2(3)
C5	C6	1.425(4)	C3	C4	C5	120.7(3)
C5	C10	1.423(4)	C3	C4	C9	120.1(3)
C6	C13	1.395(4)	C5	C4	C9	119.0(3)
C7	H7	0.950(3)	C4	C5	H5	119.5(3)
C7	C8	1.392(4)	C4	C5	C6	121.0(3)
C8	H8	0.950(3)	H5	C5	C6	119.6(4)
C8	C9	1.380(4)	C5	C6	H6	119.9(4)
C9	H9	0.951(3)	C5	C6	C7	120.1(3)
C9	C10	1.413(4)	H6	C6	C7	119.9(4)
C10	C11	1.401(4)	C6	C7	H7	119.7(4)
C11	H11	0.950(3)	C6	C7	C8	120.6(3)
C11	C12	1.371(4)	H7	C7	C8	119.6(4)
C12	H12	0.950(3)	C7	C8	H8	119.7(3)
C12	C13	1.412(4)	C7	C8	C9	120.6(3)
C13	C14	1.486(4)	H8	C8	C9	119.6(3)
C14	C15	1.381(4)	C4	C9	C8	118.4(3)
C14	C19	1.400(4)	C4	C9	C10	118.4(3)
C15	H15	0.950(3)	C8	C9	C10	123.1(3)
C15	C16	1.385(4)	C1	C10	C9	116.7(3)
C16	H16	0.950(3)	C1	C10	C11	117.5(3)
C16	C17	1.391(5)	C9	C10	C11	125.8(3)
C17	C18	1.395(4)	C10	C11	C12	127.1(3)
C17	C20	1.504(4)	C10	C11	C22	117.6(3)
C18	H18	0.950(4)	C12	C11	C22	115.0(3)

C18	C19	1.388(4)	C11	C12	H12	119.2(3)
C19	H19	0.950(3)	C11	C12	C13	121.5(3)
C20	H20A	0.990(3)	H12	C12	C13	119.3(3)
C20	H20B	0.990(4)	C12	C13	H13	118.4(3)
C20	O2	1.434(3)	C12	C13	C14	123.2(3)
C21	H21	1.000(4)	H13	C13	C14	118.3(3)
C21	C22	1.532(4)	C13	C14	C15	123.5(3)
C21	C29	1.515(4)	C13	C14	C23	117.4(3)
C21	O2	1.421(3)	C15	C14	C23	119.0(3)
C22	H22A	0.990(4)	C14	C15	H15	120.1(4)
C22	H22B	0.991(3)	C14	C15	C16	119.6(3)
C22	C23	1.528(4)	H15	C15	C16	120.2(4)
C23	C24	1.538(5)	C15	C16	H16	119.3(4)
C23	C25	1.524(6)	C15	C16	C17	121.4(4)
C23	N1	1.480(4)	H16	C16	C17	119.3(4)
C24	H24A	0.981(4)	C16	C17	H17	119.6(4)
C24	H24B	0.979(4)	C16	C17	C18	120.9(3)
C24	H24C	0.980(5)	H17	C17	C18	119.5(4)
C25	H25A	0.981(4)	C17	C18	C19	122.4(3)
C25	H25B	0.980(4)	C17	C18	C23	118.1(3)
C25	H25C	0.980(4)	C19	C18	C23	119.5(3)
C26	C27	1.521(4)	C18	C19	H19	119.5(3)
C26	C28	1.533(5)	C18	C19	C20	121.1(3)
C26	C29	1.528(4)	H19	C19	C20	119.5(3)
C26	N1	1.494(4)	C19	C20	H20	120.4(3)
C27	H27A	0.981(5)	C19	C20	C21	119.3(3)
C27	H27B	0.979(3)	H20	C20	C21	120.3(3)
C27	H27C	0.979(3)	C20	C21	C22	123.0(3)
C28	H28A	0.979(3)	C20	C21	O1	116.5(3)
C28	H28B	0.981(3)	C22	C21	O1	120.5(3)
C28	H28C	0.980(4)	C11	C22	C21	120.0(3)
C29	H29A	0.991(4)	C11	C22	C23	122.7(3)
C29	H29B	0.990(3)	C21	C22	C23	117.3(3)
N1	O3	1.286(3)	C14	C23	C18	120.9(3)
			C14	C23	C22	119.2(3)
			C18	C23	C22	119.9(3)
			C1	O1	C21	121.1(2)
			F1	B1	F2	101.6(5)
			F1	B1	F3	102.4(4)
			F1	B1	F4	106.4(4)
			F2	B1	F3	112.8(6)
			F2	B1	F4	117.6(5)
			F3	B1	F4	113.8(5)

Appendix 66 Bond lengths and bond angles of 9-(4-(TEMPO-methyl)phenyl)-1*H*-phenalen-1-one.

Crystal data and structure refinement for 1-(1-oxo-1<i>H</i>-phenalen-9-yl)pyridinium triflate	
Empirical formula	C _{20.50} H ₁₅ F ₃ NO _{4.50} S
Formula weight	436.4
Temperature	150(2) K
Wavelength	0.71073 Å
Crystal system, space group	Orthorhombic, P 2 ₁ 2 ₁ 2 ₁
Unit cell dimensions	a = 23.961(5) Å α = 90 deg. b = 23.211(5) Å β = 90 deg. c = 6.8908(16) Å γ = 90 deg.
Volume	3832.38 Å ³
Z, Calculated density	8, 1.513 Mg/m ³
Absorption coefficient	0.229 mm ⁻¹
F(000)	1792
Crystal size	0.13 x 0.10 x 0.06 mm
Theta range for data collection	1.95 to 25.43 deg.
Limiting indices	-23 ≤ h ≤ 28, -28 ≤ k ≤ 24, -8 ≤ l ≤ 7
Reflections collected / unique	23837 / 6873 [R(int) = 0.1786]
Completeness to theta = 25.43	99.5 %
Absorption correction	Empirical
Max. and min. Transmission	0.9864 and 0.9708
Refinement method	Full-matrix least-squares on F ²
Data / restraints / parameters	6873 / 0 / 540
Goodness-of-fit on F ²	0.997
Final R indices [I > 2σ(I)]	R1 = 0.0736, wR2 = 0.1198
R indices (all data)	R1 = 0.2125, wR2 = 0.1668
Absolute structure parameter	0.17(17)
Extinction coefficient	0.0019(3)
Largest diff. peak and hole	0.36 and -0.35 e.Å ⁻³

Appendix 67



Bond lengths			Bond angles			
Atom 1	Atom 2	Length	Atom 1	Atom 2	Atom 3	Angle
C2	F4	1.24(1)	F1	C1	F2	108.3(8)
C2	F5	1.34(1)	F1	C1	F3	106.4(7)
C2	F6	1.34(2)	F1	C1	S1	109.5(6)
C2	S2	1.85(1)	F2	C1	F3	108.9(8)
O6	S2	1.427(8)	F2	C1	S1	113.3(7)
O7	S2	1.424(7)	F3	C1	S1	110.3(6)
O8	S2	1.447(5)	C1	S1	O3	103.0(4)
C22	H22	0.950(8)	C1	S1	O4	102.3(4)
C22	C23	1.37(1)	C1	S1	O5	104.1(4)
C22	N2	1.36(1)	O3	S1	O4	114.2(3)
C23	H23	0.951(8)	O3	S1	O5	115.5(3)
C23	C24	1.37(1)	O4	S1	O5	115.2(3)
C24	H24	0.949(7)	F4	C2	F5	110.2(9)
C24	C25	1.36(1)	F4	C2	F6	111(1)
C25	H25	0.951(9)	F4	C2	S2	113.5(8)
C25	C26	1.38(1)	F5	C2	F6	105.8(9)
C26	H26	0.949(8)	F5	C2	S2	107.6(7)
C26	N2	1.33(1)	F6	C2	S2	108.8(8)
C28	C29	1.407(9)	C2	S2	O6	101.5(5)
C28	C39	1.35(1)	C2	S2	O7	103.5(5)
C28	N2	1.462(7)	C2	S2	O8	102.7(4)
C29	H29	0.951(7)	O6	S2	O7	115.1(4)
C29	C30	1.36(1)	O6	S2	O8	115.6(4)
C30	H30	0.950(7)	O7	S2	O8	115.5(4)
C30	C31	1.40(1)	H3	C3	C4	119.4(7)
C31	C32	1.42(1)	H3	C3	N1	119.4(7)
C31	C40	1.41(1)	C4	C3	N1	121.2(7)
C32	H32	0.951(7)	C3	C4	H4	120.2(8)
C32	C33	1.34(1)	C3	C4	C5	119.6(7)
C33	H33	0.950(7)	H4	C4	C5	120.2(8)
C33	C34	1.40(1)	C4	C5	H5	120.5(8)
C34	H34	0.950(7)	C4	C5	C6	118.8(7)

C34	C35	1.38(1)	H5	C5	C6	120.6(7)
C35	C36	1.46(1)	C5	C6	H6	120.3(7)
C35	C40	1.40(1)	C5	C6	C7	119.2(7)
C36	H36	0.949(7)	H6	C6	C7	120.5(7)
C36	C37	1.34(1)	C6	C7	H7	119.6(7)
C37	H37	0.950(7)	C6	C7	N1	120.6(7)
C37	C38	1.43(1)	H7	C7	N1	119.8(7)
C38	C39	1.52(1)	C10	C9	C20	123.7(7)
C38	O2	1.227(9)	C10	C9	N1	113.8(6)
C39	C40	1.42(1)	C20	C9	N1	122.4(7)
			C9	C10	H10	121.4(7)
			C9	C10	C11	117.2(7)
			H10	C10	C11	121.4(7)
			C10	C11	H11	118.7(7)
			C10	C11	C12	122.7(7)
			H11	C11	C12	118.6(7)
			C11	C12	C13	123.3(7)
			C11	C12	C21	118.1(7)
			C13	C12	C21	118.5(6)
			C12	C13	H13	119.3(7)
			C12	C13	C14	121.5(7)
			H13	C13	C14	119.3(7)
			C13	C14	H14	119.9(8)
			C13	C14	C15	120.4(7)
			H14	C14	C15	119.7(8)
			C14	C15	H15	119.5(7)
			C14	C15	C16	121.1(7)
			H15	C15	C16	119.4(7)
			C15	C16	C17	121.9(7)
			C15	C16	C21	119.7(7)
			C17	C16	C21	118.3(6)
			C16	C17	H17	119.2(7)
			C16	C17	C18	121.6(7)
			H17	C17	C18	119.2(7)
			C17	C18	H18	118.2(7)
			C17	C18	C19	123.6(7)
			H18	C18	C19	118.2(7)
			C18	C19	C20	115.1(6)
			C18	C19	O1	122.1(7)
			C20	C19	O1	122.7(7)
			C9	C20	C19	123.0(7)
			C9	C20	C21	118.4(7)
			C19	C20	C21	118.5(6)
			C12	C21	C16	118.7(6)
			C12	C21	C20	119.6(7)
			C16	C21	C20	121.6(7)
			C3	N1	C7	120.5(6)
			C3	N1	C9	119.5(6)
			C7	N1	C9	120.0(6)
			H22	C22	C23	120.0(8)
			H22	C22	N2	119.8(7)
			C23	C22	N2	120.1(7)
			C22	C23	H23	120.6(8)
			C22	C23	C24	118.7(7)
			H23	C23	C24	120.7(8)
			C23	C24	H24	119.5(8)

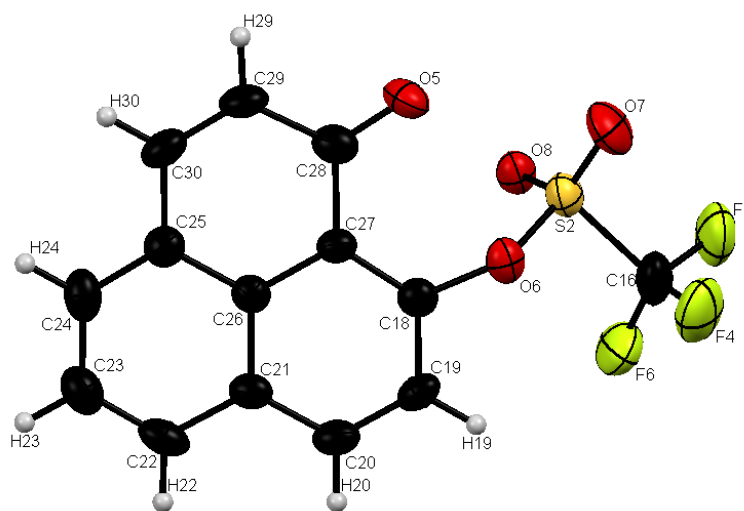
C23	C24	C25	120.9(8)
H24	C24	C25	119.6(8)
C24	C25	H25	120.4(8)
C24	C25	C26	118.9(7)
H25	C25	C26	120.7(8)
C25	C26	H26	119.9(8)
C25	C26	N2	120.2(7)
H26	C26	N2	119.9(7)
C29	C28	C39	122.7(6)
C29	C28	N2	115.0(6)
C39	C28	N2	122.3(6)
C28	C29	H29	120.8(7)
C28	C29	C30	118.6(7)
H29	C29	C30	120.5(7)
C29	C30	H30	119.4(7)
C29	C30	C31	121.4(7)
H30	C30	C31	119.2(7)
C30	C31	C32	122.2(7)
C30	C31	C40	119.1(7)
C32	C31	C40	118.7(7)
C31	C32	H32	119.5(7)
C31	C32	C33	120.9(7)
H32	C32	C33	119.5(8)
C32	C33	H33	119.7(8)
C32	C33	C34	120.7(7)
H33	C33	C34	119.6(8)
C33	C34	H34	120.0(7)
C33	C34	C35	120.2(7)
H34	C34	C35	119.9(7)
C34	C35	C36	120.5(7)
C34	C35	C40	120.2(7)
C36	C35	C40	119.2(7)
C35	C36	H36	119.7(7)
C35	C36	C37	120.9(7)
H36	C36	C37	119.4(7)
C36	C37	H37	118.4(7)
C36	C37	C38	123.5(7)
H37	C37	C38	118.2(7)
C37	C38	C39	116.2(6)
C37	C38	O2	121.9(7)
C39	C38	O2	121.7(7)
C28	C39	C38	122.9(6)
C28	C39	C40	118.8(7)
C38	C39	C40	118.3(6)
C31	C40	C35	119.2(7)
C31	C40	C39	119.3(7)
C35	C40	C39	121.5(7)
C22	N2	C26	121.2(6)
C22	N2	C28	118.8(6)
C26	N2	C28	119.9(6)
H41A	C41	H41B	109.5(8)
H41A	C41	H41C	109.4(8)
H41A	C41	C42	109.5(8)
H41B	C41	H41C	109.5(8)
H41B	C41	C42	109.5(8)
H41C	C41	C42	109.5(8)

C41	C42	C43	117.2(7)
C41	C42	O9	121.3(8)
C43	C42	O9	121.5(8)
C42	C43	H43A	109.4(8)
C42	C43	H43B	109.5(8)
C42	C43	H43C	109.4(8)
H43A	C43	H43B	109.4(8)
H43A	C43	H43C	109.5(8)
H43B	C43	H43C	109.5(8)

Appendix 68 Bond lengths and bond angles of 1-(1-oxo-1*H*-phenalen-9-yl)pyridinium triflate.

Crystal data and structure refinement for 1-oxo-1<i>H</i>-phenalen-9-yl trifluoromethanesulfonate	
Empirical formula	C ₁₄ H ₇ F ₃ O ₄ S
Formula weight	328.26
Temperature	150(2) K
Wavelength	0.71073 Å
Crystal system, space group	Monoclinic, Cc
Unit cell dimensions	a = 13.4040(4) Å α = 90.00 deg. b = 25.1954(6) Å β = 101.642(3) deg. c = 12.1027(4) Å γ = 90.00 deg.
Volume	4003.23 Å ³
Z, Calculated density	12, 1.634 Mg/m ³
Absorption coefficient	0.294 mm ⁻¹
F(000)	1992
Crystal size	0.30 x 0.09 x 0.07 mm
Theta range for data collection	2.88 to 25.70 deg.
Limiting indices	-15 ≤ h ≤ 16, -30 ≤ k ≤ 30, -14 ≤ l ≤ 14
Reflections collected / unique	16213 / 6944 [R(int) = 0.0392]
Completeness to theta = 25.70	99.6 %
Absorption correction	Analytical
Max. and min. Transmission	0.9797 and 0.9169
Refinement method	Full-matrix least-squares on F ²
Data / restraints / parameters	6944 / 2 / 596
Goodness-of-fit on F ²	1.058
Final R indices [I > 2σ(I)]	R1 = 0.0417, wR2 = 0.0780
R indices (all data)	R1 = 0.0596, wR2 = 0.0876
Absolute structure parameter	-0.05(6)
Extinction coefficient	0.00033(8)
Largest diff. peak and hole	0.24 and -0.24 e.Å ⁻³

Appendix 69



Bond Lengths			Bond angles			
Atom 1	Atom 2	Length	Atom 1	Atom 2	Atom 3	Angle
C16	F4	1.314(6)	F1	C1	F2	109.0(4)
C16	F5	1.335(5)	F1	C1	F3	110.6(4)
C16	F6	1.316(5)	F1	C1	S1	109.9(3)
C16	S2	1.828(4)	F2	C1	F3	109.1(4)
C18	C19	1.400(4)	F2	C1	S1	107.8(3)
C18	C27	1.382(4)	F3	C1	S1	110.4(3)
C18	O6	1.421(4)	C4	C3	C12	123.2(3)
C19	H19	0.951(3)	C4	C3	O2	115.7(3)
C19	C20	1.367(5)	C12	C3	O2	120.9(3)
C20	H20	0.951(3)	C3	C4	H4	120.5(3)
C20	C21	1.401(4)	C3	C4	C5	119.2(3)
C21	C22	1.418(5)	H4	C4	C5	120.3(3)
C21	C26	1.433(4)	C4	C5	H5	119.5(3)
C22	H22	0.951(3)	C4	C5	C6	121.1(3)
C22	C23	1.364(5)	H5	C5	C6	119.4(3)
C23	H23	0.951(4)	C5	C6	C7	121.6(3)
C23	C24	1.394(5)	C5	C6	C11	119.0(3)
C24	H24	0.951(3)	C7	C6	C11	119.3(3)
C24	C25	1.372(4)	C6	C7	H7	119.7(3)
C25	C26	1.424(4)	C6	C7	C8	120.7(3)
C25	C30	1.447(4)	H7	C7	C8	119.6(4)
C26	C27	1.424(4)	C7	C8	H8	120.0(4)
C27	C28	1.495(4)	C7	C8	C9	120.1(3)
C28	C29	1.455(5)	H8	C8	C9	119.9(4)
C28	O5	1.222(4)	C8	C9	H9	119.0(4)
C29	H29	0.950(3)	C8	C9	C10	121.8(3)
C29	C30	1.342(5)	H9	C9	C10	119.2(3)
C30	H30	0.949(3)	C9	C10	C11	119.0(3)
O6	S2	1.568(2)	C9	C10	C15	122.1(3)
O7	S2	1.409(2)	C11	C10	C15	118.9(3)
O8	S2	1.412(3)	C6	C11	C10	119.1(3)
			C6	C11	C12	120.4(3)
			C10	C11	C12	120.5(3)
			C3	C12	C11	117.0(3)
			C3	C12	C13	123.5(3)
			C11	C12	C13	119.5(3)

C12	C13	C14	116.4(3)
C12	C13	O1	121.9(3)
C14	C13	O1	121.7(3)
C13	C14	H14	118.5(3)
C13	C14	C15	123.0(3)
H14	C14	C15	118.5(3)
C10	C15	C14	121.5(3)
C10	C15	H15	119.2(3)
C14	C15	H15	119.3(3)
C3	O2	S1	122.6(2)
C1	S1	O2	98.6(2)
C1	S1	O3	106.5(2)
C1	S1	O4	104.7(2)
O2	S1	O3	111.3(1)
O2	S1	O4	108.5(2)
O3	S1	O4	124.0(2)
F4	C16	F5	108.1(3)
F4	C16	F6	109.6(3)
F4	C16	S2	111.3(3)
F5	C16	F6	108.4(3)
F5	C16	S2	107.7(3)
F6	C16	S2	111.6(3)
C19	C18	C27	123.0(3)
C19	C18	O6	114.8(3)
C27	C18	O6	121.9(3)
C18	C19	H19	120.3(3)
C18	C19	C20	119.4(3)
H19	C19	C20	120.4(3)
C19	C20	H20	119.4(3)
C19	C20	C21	121.3(3)
H20	C20	C21	119.3(3)
C20	C21	C22	122.6(3)
C20	C21	C26	118.6(3)
C22	C21	C26	118.7(3)
C21	C22	H22	119.5(3)
C21	C22	C23	121.0(3)
H22	C22	C23	119.5(4)
C22	C23	H23	119.9(4)
C22	C23	C24	120.2(3)
H23	C23	C24	119.9(4)
C23	C24	H24	119.1(4)
C23	C24	C25	121.7(3)
H24	C24	C25	119.2(3)
C24	C25	C26	119.7(3)
C24	C25	C30	121.2(3)
C26	C25	C30	119.1(3)
C21	C26	C25	118.8(3)
C21	C26	C27	120.4(3)
C25	C26	C27	120.9(3)
C18	C27	C26	117.2(3)
C18	C27	C28	123.5(3)
C26	C27	C28	119.3(3)
C27	C28	C29	116.4(3)
C27	C28	O5	122.3(3)
C29	C28	O5	121.2(3)
C28	C29	H29	118.6(3)

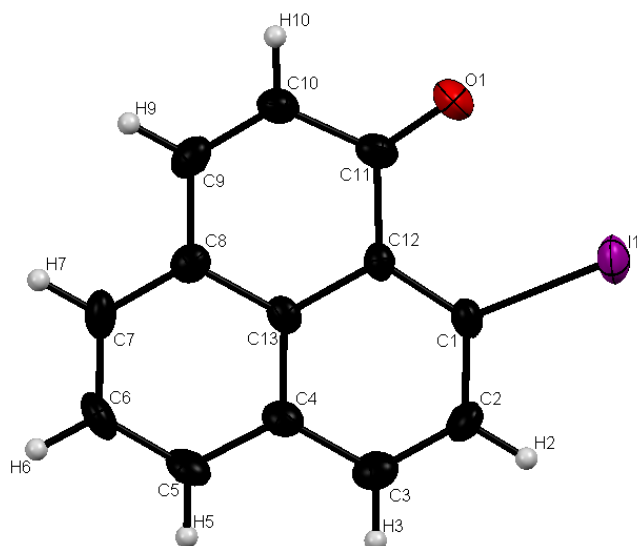
C28	C29	C30	123.0(3)
H29	C29	C30	118.5(4)
C25	C30	C29	121.4(3)
C25	C30	H30	119.3(3)
C29	C30	H30	119.3(3)
C18	O6	S2	123.3(2)
C16	S2	O6	98.1(2)
C16	S2	O7	105.7(2)
C16	S2	O8	106.1(2)
O6	S2	O7	108.8(1)
O6	S2	O8	111.4(1)
O7	S2	O8	123.4(1)
F7	C31	F8	108.9(4)
F7	C31	F9	109.7(4)
F7	C31	S3	110.1(3)
F8	C31	F9	109.5(4)
F8	C31	S3	108.0(3)
F9	C31	S3	110.6(3)
C34	C33	C42	123.8(3)
C34	C33	O10	114.8(3)
C42	C33	O10	121.1(3)
C33	C34	H34	120.6(3)
C33	C34	C35	118.9(3)
H34	C34	C35	120.5(3)
C34	C35	H35	119.6(3)
C34	C35	C36	120.9(3)
H35	C35	C36	119.5(3)
C35	C36	C37	121.6(3)
C35	C36	C41	119.3(3)
C37	C36	C41	119.1(3)
C36	C37	H37	119.7(3)
C36	C37	C38	120.7(3)
H37	C37	C38	119.7(3)
C37	C38	H38	119.8(3)
C37	C38	C39	120.4(3)
H38	C38	C39	119.8(3)
C38	C39	H39	119.5(3)
C38	C39	C40	120.9(3)
H39	C39	C40	119.6(3)
C39	C40	C41	119.7(3)
C39	C40	C45	121.5(3)
C41	C40	C45	118.7(3)
C36	C41	C40	119.2(3)
C36	C41	C42	119.9(3)
C40	C41	C42	120.9(3)
C33	C42	C41	117.3(3)
C33	C42	C43	123.6(3)
C41	C42	C43	119.0(3)
C42	C43	C44	116.4(3)
C42	C43	O9	121.9(3)
C44	C43	O9	121.7(3)
C43	C44	H44	118.9(3)
C43	C44	C45	122.4(3)
H44	C44	C45	118.8(4)
C40	C45	C44	122.5(3)
C40	C45	H45	118.8(3)

C44	C45	H45	118.7(4)
C33	O10	S3	122.1(2)
C31	S3	O10	98.4(2)
C31	S3	O11	106.6(2)
C31	S3	O12	105.0(2)
O10	S3	O11	111.7(1)
O10	S3	O12	108.5(1)
O11	S3	O12	123.5(2)

Appendix 70 Bond lengths and bond angles of 1-oxo-1*H*-phenalen-9-yl trifluoromethanesulfonate.

Crystal data and structure refinement for 9-iodo-1<i>H</i>-phenalen-1-one	
Empirical formula	C ₁₃ H ₇ IO
Formula weight	306.09
Temperature	150(2) K
Wavelength	0.71073 Å
Crystal system, space group	Monoclinic, C2/c
Unit cell dimensions	a = 12.8997(18) Å α = 90 deg. b = 12.184(2) Å β = 101.649(10)deg. c = 13.1411(13) Å γ = 90 deg.
Volume	2022.9(5) Å ³
Z, Calculated density	8, 2.010 Mg/m ³
Absorption coefficient	3.131 mm ⁻¹
F(000)	1168
Crystal size	0.18 x 0.10 x 0.08 mm
Theta range for data collection	2.99 to 25.47 deg.
Limiting indices	-15 ≤ h ≤ 15, -14 ≤ k ≤ 14, -15 ≤ l ≤ 15
Reflections collected / unique	8018 / 1872 [R(int) = 0.0399]
Completeness to theta = 25.47	99.4 %
Absorption correction	Analytical
Max. and min. Transmission	0.7878 and 0.6026
Refinement method	Full-matrix least-squares on F ²
Data / restraints / parameters	1872 / 0 / 136
Goodness-of-fit on F ²	1.122
Final R indices [I > 2σ(I)]	R1 = 0.0338, wR2 = 0.0652
R indices (all data)	R1 = 0.0464, wR2 = 0.0712
Extinction coefficient	none
Largest diff. peak and hole	0.53 and -0.56 e.Å ⁻³

Appendix 71



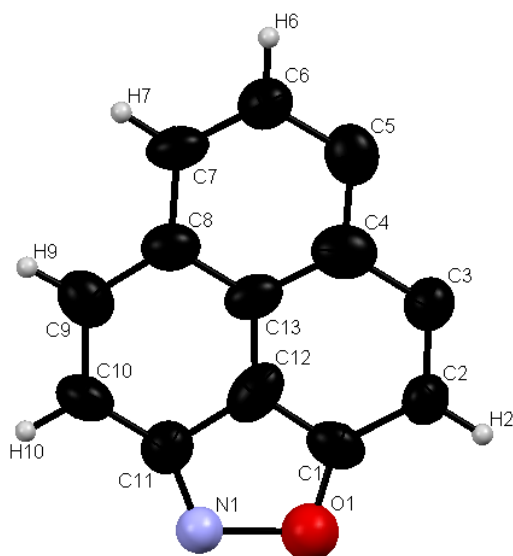
Bond lengths			Bond angles			
Atom 1	Atom 2	Length	Atom1	Atom2	Atom3	Angle
C1	C2	1.395(7)	C2	C1	C12	121.8(4)
C1	C12	1.387(6)	C2	C1	I1	114.3(3)
C1	I1	2.111(4)	C12	C1	I1	123.8(3)
C2	H2	0.950(5)	C1	C2	H2	119.4(4)
C2	C3	1.365(7)	C1	C2	C3	121.1(4)
C3	H3	0.949(5)	H2	C2	C3	119.5(5)
C3	C4	1.410(7)	C2	C3	H3	119.7(5)
C4	C5	1.419(7)	C2	C3	C4	120.6(4)
C4	C13	1.410(7)	H3	C3	C4	119.7(5)
C5	H5	0.950(5)	C3	C4	C5	122.2(4)
C5	C6	1.372(7)	C3	C4	C13	118.9(4)
C6	H6	0.949(5)	C5	C4	C13	118.9(4)
C6	C7	1.391(8)	C4	C5	H5	119.4(5)
C7	H7	0.951(4)	C4	C5	C6	121.2(5)
C7	C8	1.381(6)	H5	C5	C6	119.4(5)
C8	C9	1.456(7)	C5	C6	H6	120.2(5)
C8	C13	1.425(6)	C5	C6	C7	119.8(5)
C9	H9	0.951(5)	H6	C6	C7	120.1(5)
C9	C10	1.340(7)	C6	C7	H7	119.4(5)
C10	H10	0.951(5)	C6	C7	C8	121.1(4)
C10	C11	1.453(7)	H7	C7	C8	119.4(4)
C11	C12	1.492(7)	C7	C8	C9	120.6(4)
C11	O1	1.221(7)	C7	C8	C13	120.0(4)
C12	C13	1.455(6)	C9	C8	C13	119.4(4)
			C8	C9	H9	119.5(5)
			C8	C9	C10	121.0(4)
			H9	C9	C10	119.5(5)
			C9	C10	H10	118.4(5)
			C9	C10	C11	123.4(4)
			H10	C10	C11	118.2(4)
			C10	C11	C12	117.0(4)
			C10	C11	O1	120.9(4)
			C12	C11	O1	122.1(4)
			C1	C12	C11	124.5(4)
			C1	C12	C13	117.1(4)

C11	C12	C13	118.4(4)
C4	C13	C8	119.0(4)
C4	C13	C12	120.5(4)
C8	C13	C12	120.5(4)

Appendix 72 Bond lengths and bond angles of 9-iodo-1*H*-phenalen-1-one.

Crystal data and structure refinement for Phenalenol[1,9-<i>cd</i>]isoxazole	
Empirical formula	C ₁₃ H ₇ N O
Formula weight	193.20
Temperature	150(2) K
Wavelength	0.71073 Å
Crystal system, space group	Triclinic, P-1
Unit cell dimensions	a = 7.5727(9) Å α = 100.949(10) deg. b = 8.2341(9) Å β = 96.440(10) deg. c = 14.4327(19) Å γ = 94.028(9) deg.
Volume	874.11(18) Å ³
Z, Calculated density	4, 1.468 Mg/m ³
Absorption coefficient	0.094 mm ⁻¹
F(000)	400
Crystal size	0.28 x 0.23 x 0.21 mm
Theta range for data collection	2.72 to 24.47 deg.
Limiting indices	-8 ≤ h ≤ 8, -9 ≤ k ≤ 9, -16 ≤ l ≤ 16
Reflections collected / unique	8715 / 4372 [R(int) = 0.105]
Completeness to theta = 24.47	99.3 %
Absorption correction	Empirical
Max. and min. Transmission	1.000 and 0.757
Refinement method	Full-matrix least-squares on F ²
Data / restraints / parameters	4372 / 16 / 270
Goodness-of-fit on F ²	1.078
Final R indices [I > 2σ(I)]	R1 = 0.0976, wR2 = 0.2800
R indices (all data)	R1 = 0.1768, wR2 = 0.3178
Extinction coefficient	none
Largest diff. peak and hole	0.75 and -0.22 e.Å ⁻³

Appendix 73



Bond lengths			Bond angles			
Atom 1	Atom 2	Length	Atom 1	Atom 2	Atom 3	Angle
C1	C2	1.407(9)	C2	C1	C12	119.0(6)
C1	C12	1.368(9)	C2	C1	O1	133.0(7)
C1	O1	1.28(1)	C12	C1	O1	108.0(6)
C2	H2	0.950(6)	C1	C2	H2	120.6(6)
C2	C3	1.364(9)	C1	C2	C3	118.7(6)
C3	C4	1.421(9)	H2	C2	C3	120.7(6)
C4	C5	1.400(9)	C2	C3	C4	120.7(6)
C4	C13	1.413(9)	C3	C4	C5	118.7(6)
C5	C6	1.427(9)	C3	C4	C13	121.2(6)
C6	H6	0.950(7)	C5	C4	C13	120.1(6)
C6	C7	1.373(9)	C4	C5	C6	117.6(6)
C7	H7	0.949(6)	C5	C6	H6	119.0(6)
C7	C8	1.418(8)	C5	C6	C7	121.9(6)
C8	C9	1.393(9)	H6	C6	C7	119.1(6)
C8	C13	1.380(9)	C6	C7	H7	120.0(6)
C9	H9	0.950(7)	C6	C7	C8	120.0(6)
C9	C10	1.419(9)	H7	C7	C8	120.0(6)
C10	H10	0.950(6)	C7	C8	C9	124.5(6)
C10	C11	1.373(9)	C7	C8	C13	118.8(6)
C11	C12	1.451(9)	C9	C8	C13	116.7(6)
C11	N1	1.26(1)	C8	C9	H9	119.4(6)
C12	C13	1.368(9)	C8	C9	C10	121.2(6)
N1	O1	1.55(1)	H9	C9	C10	119.4(6)
			C9	C10	H10	119.0(6)
			C9	C10	C11	122.1(6)
			H10	C10	C11	119.0(6)
			C10	C11	C12	115.9(6)
			C10	C11	N1	143.0(7)
			C12	C11	N1	100.8(6)
			C1	C12	C11	113.9(6)
			C1	C12	C13	125.6(6)
			C11	C12	C13	120.5(6)
			C4	C13	C8	121.5(6)
			C4	C13	C12	114.9(6)
			C8	C13	C12	123.6(6)

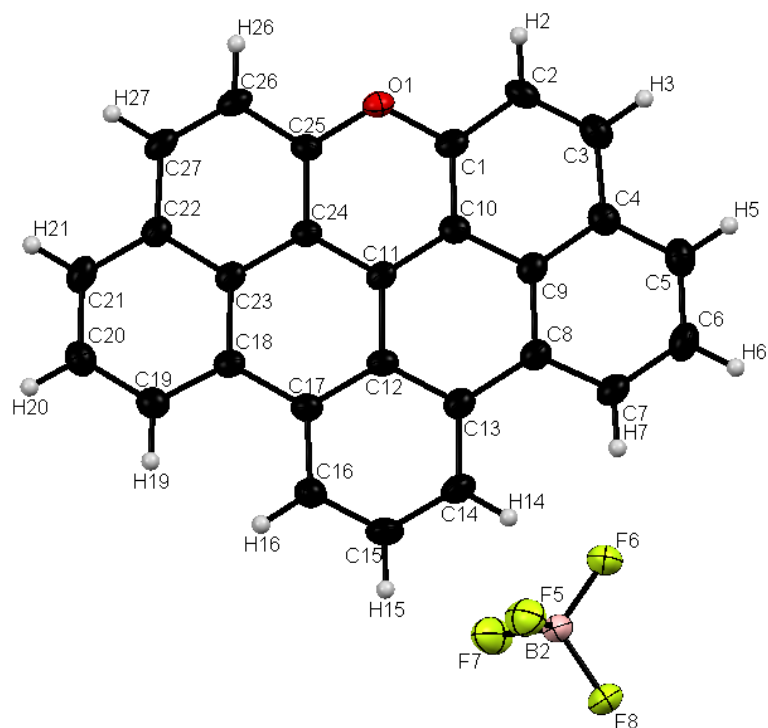
C11	N1	O1	113.1(8)
C1	O1	N1	104.2(7)
C15	C14	C25	119.3(7)
C15	C14	O2	135.8(8)
C25	C14	O2	104.8(7)
C14	C15	H15	120.7(7)
C14	C15	C16	118.5(7)
H15	C15	C16	120.7(7)
C15	C16	C17	123.5(7)
C16	C17	C18	121.6(8)
C16	C17	C26	118.5(8)
C18	C17	C26	119.9(8)
C17	C18	C19	117.9(7)
C18	C19	H19	119.3(8)
C18	C19	C20	121.2(7)
H19	C19	C20	119.5(7)
C19	C20	H20	118.7(7)
C19	C20	C21	122.6(7)
H20	C20	C21	118.7(8)
C20	C21	C22	125.8(7)
C20	C21	C26	117.0(7)
C22	C21	C26	117.2(6)
C21	C22	H22	120.2(7)
C21	C22	C23	119.6(7)
H22	C22	C23	120.2(7)
C22	C23	H23	118.7(9)
C22	C23	C24	122.7(8)
H23	C23	C24	118.7(9)
C23	C24	C25	113.0(8)
C23	C24	N2	136.8(9)
C25	C24	N2	110.2(9)
C14	C25	C24	110.9(7)
C14	C25	C26	116.9(7)
C24	C25	C26	132.1(8)
C17	C26	C21	121.5(7)
C17	C26	C25	123.1(7)
C21	C26	C25	115.4(6)
C24	N2	O2	105.7(8)
C14	O2	N2	108.3(8)

Appendix 74 Bond lengths and bond angles of phenaleno[1,9-*cd*]isoxazole.

Crystal data and structure refinement for **Benzo[5,6]naphthaceno[1,12,11,10-*ijklmna*]xanthylum tetrafluoroborate**

Empirical formula	C ₂₇ H ₁₃ BF ₄ O	
Formula weight	440.18	
Temperature	150(2) K	
Wavelength	0.71073 Å	
Crystal system, space group	Triclinic, P -1	
Unit cell dimensions	a = 7.0623(5) Å b = 10.8007(9) Å c = 24.0268(18) Å	α = 89.162(4) deg. β = 83.187(4) deg. γ = 89.936(4) deg.
Volume	1819.57 Å ³	
Z, Calculated density	4, 1.607 Mg/m ³	
Absorption coefficient	0.124 mm ⁻¹	
F(000)	896	
Crystal size	0.11 x 0.06 x 0.03 mm	
Theta range for data collection	1.89 to 25.75 deg.	
Limiting indices	-8 ≤ h ≤ 8, -13 ≤ k ≤ 13, -29 ≤ l ≤ 29	
Reflections collected / unique	24852 / 6922 [R(int) = 0.0360]	
Completeness to theta = 25.75	99.3 %	
Absorption correction	Empirical	
Max. and min. Transmission	0.9963 and 0.9865	
Refinement method	Full-matrix least-squares on F ²	
Data / restraints / parameters	6922 / 42 / 612	
Goodness-of-fit on F ²	1.022	
Final R indices [I > 2σ(I)]	R1 = 0.0466, wR2 = 0.1015	
R indices (all data)	R1 = 0.0969, wR2 = 0.1248	
Extinction coefficient	none	
Largest diff. peak and hole	0.30 and -0.26 e.Å ⁻³	

Appendix 75

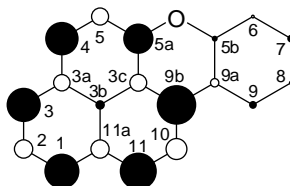


Bond lengths			Bond angles			
Atom 1	Atom 2	Length	Atom 1	Atom 2	Atom 3	Angle
C1	C2	1.401(4)	C2	C1	C12	121.8(4)
C1	C10	1.395(4)	C2	C1	H1	114.3(3)
C1	O1	1.359(4)	C12	C1	H1	123.8(3)
C2	H2	0.950(3)	C1	C2	H2	119.4(4)
C2	C3	1.358(4)	C1	C2	C3	121.1(4)
C3	H3	0.950(3)	H2	C2	C3	119.5(5)
C3	C4	1.415(5)	C2	C3	H3	119.7(5)
C4	C5	1.417(4)	C2	C3	C4	120.6(4)
C4	C9	1.418(4)	H3	C3	C4	119.7(5)
C5	H5	0.950(3)	C3	C4	C5	122.2(4)
C5	C6	1.366(6)	C3	C4	C13	118.9(4)
C6	H6	0.950(3)	C5	C4	C13	118.9(4)
C6	C7	1.386(5)	C4	C5	H5	119.4(5)
C7	H7	0.950(4)	C4	C5	C6	121.2(5)
C7	C8	1.385(5)	H5	C5	C6	119.4(5)
C8	H8	0.951(3)	C5	C6	H6	120.2(5)
C8	C9	1.411(5)	C5	C6	C7	119.8(5)
C9	C10	1.452(4)	H6	C6	C7	120.1(5)
C10	C11	1.430(4)	C6	C7	H7	119.4(5)
C11	C12	1.418(4)	C6	C7	C8	121.1(4)
C11	C22	1.423(4)	H7	C7	C8	119.4(4)
C12	H12	0.951(3)	C7	C8	C9	120.6(4)
C12	C13	1.367(4)	C7	C8	C13	120.0(4)
C13	H13	0.950(4)	C9	C8	C13	119.4(4)
C13	C14	1.401(4)	C8	C9	H9	119.5(5)
C14	C15	1.411(5)	C8	C9	C10	121.0(4)
C14	C23	1.405(5)	H9	C9	C10	119.5(5)
C15	H15	0.950(4)	C9	C10	H10	118.4(5)
C15	C16	1.395(6)	C9	C10	C11	123.4(4)

C16	H16	0.949(3)	H10	C10	C11	118.2(4)
C16	C17	1.381(7)	C10	C11	C12	117.0(4)
C17	H17	0.950(4)	C10	C11	O1	120.9(4)
C17	C18	1.398(4)	C12	C11	O1	122.1(4)
C18	C19	1.413(6)	C1	C12	C11	124.5(4)
C18	C23	1.431(5)	C1	C12	C13	117.1(4)
C19	H19	0.950(3)	C11	C12	C13	118.4(4)
C19	C20	1.352(4)	C4	C13	C8	119.0(4)
C20	H20	0.950(3)	C4	C13	C12	120.5(4)
C20	C21	1.412(4)	C8	C13	C12	120.5(4)
C21	C22	1.396(5)				
C21	O1	1.332(3)				
C22	C23	1.419(4)				
B1	F1	1.450(5)				
B1	F2	1.36(1)				
B1	F3	1.343(7)				
B1	F4	1.377(6)				

Appendix 76 Bond lengths and bond angles of Benzo[5,6]naphthaceno[1,12,11,10-jklmna]xanthylum tetrafluoroborate

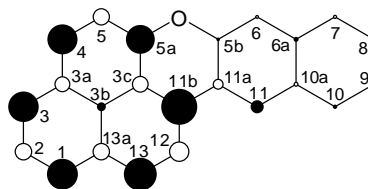
Calculated *Mulliken* spin densities of NX, B[*i*]NX and B[*a*]NX using Gaussian 09 using the basis set M05-2X/6-31G** (calculated by *G. Bucher*)



Carbon	Mull. Spin Dens.	Proton	Mull. Spin. Dens.
C1	0.2885	H1	-0.0122
C2	-0.1507	H2	0.0050
C3	0.2812	H3	-0.0119
C3a	-0.1345	#	#
C3b	0.0777	#	#
C3c	-0.1390	#	#
C4	0.2747	H4	-0.0116
C5	-0.1404	H5	0.0046
C5a	0.2492	#	#
C5b	0.0476	#	#
C6	-0.0216	H6	0.0005
C7	0.0634	H7	-0.0028
C8	-0.0261	H8	0.0007

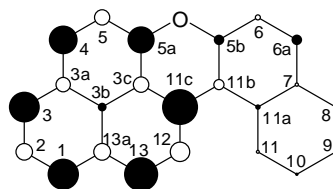
C9	0.0634	H9	-0.0028
C9a	-0.0687	#	#
C9b	0.3244	#	#
C10	-0.1718	H10	0.0057
C11	0.3050	H11	-0.0127
C11a	-0.1500	#	#

Appendix 77 Mulliken spin densities of NX (Spin density at oxygen is 0.0651).



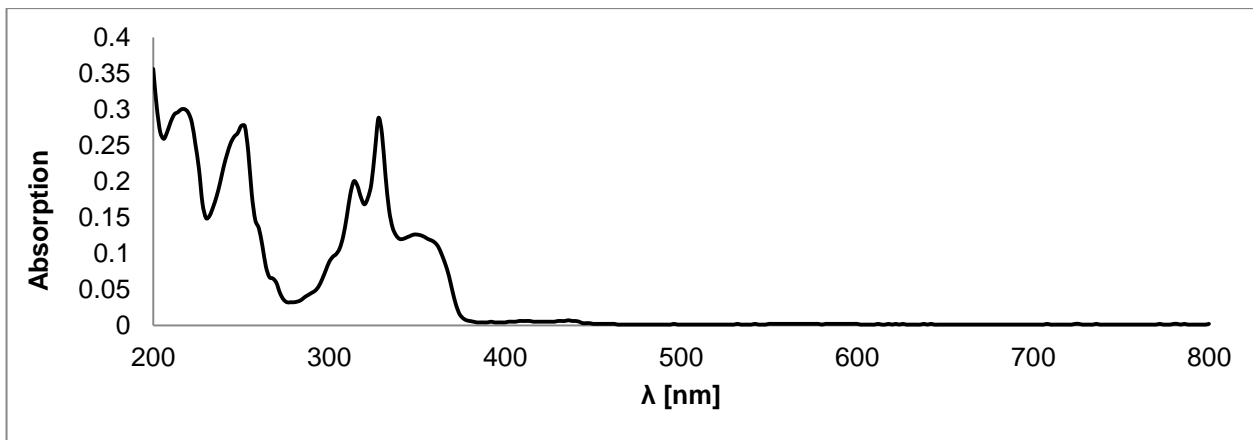
Carbon	Mull. Spin Dens.	Proton	Mull. Spin. Dens.
C1	0.281396	H1	-0.011531
C2	-0.14994	H2	0.004959
C3	0.277682	H3	-0.011415
C3a	-0.13522	#	
C3b	0.080042	#	
C3c	-0.14307	#	
C4	0.273096	H4	-0.011158
C5	-0.14729	H5	0.004782
C5a	0.262173	#	
C5b	0.033918	#	
C6	-0.02487	H6	0.000827
C6a	0.044855	#	
C7	-0.02791	H7	0.000999
C8	0.04388	H8	-0.001894
C9	-0.02298	H9	0.000779
C10	0.038967	H10	-0.001599
C10a	-0.03457	#	
C11	0.118484	H11	-0.004929
C11a	-0.08869	#	
C11b	0.328069	#	
C12	-0.17611	H12	0.005930
C13	0.299087	H13	-0.012075
C13a	-0.14931	#	

Appendix 78 Mulliken spin densities of B[i]NX. (Spin density at oxygen is 0.054628).

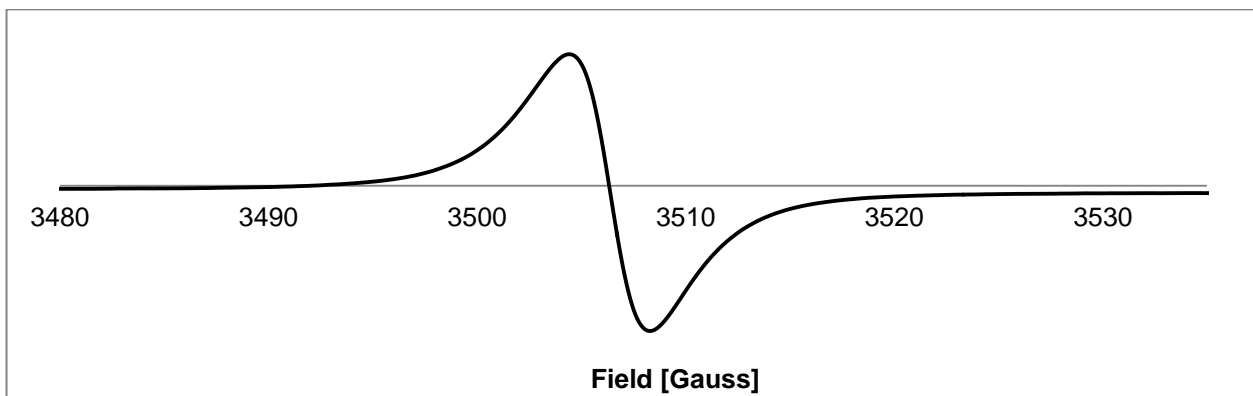


Carbon	Mull. Spin. Dens.	Protons	Mull. Spin. Dens.
C1	0.279437	H1	-0.011497
C2	-0.147881	H2	0.004891
C3	0.275120	H3	-0.011379
C3a	-0.128704	#	
C3b	0.077799	#	
C3c	-0.137662	#	
C4	0.256547	H4	-0.010555
C5	-0.136024	H5	0.004476
C5a	0.241949	#	
C5b	0.092985	#	
C6	-0.044777	H6	0.001356
C7	0.093666	H7	-0.003944
C7a	-0.028882	#	
C8	0.024878	H8	-0.001055
C9	-0.019014	H9	0.000681
C10	0.030139	H10	-0.001284
C11	-0.025556	H11	0.001280
C11a	0.045098	#	
C11b	-0.090897	#	
C11c	0.321035	#	
C12	-0.173935	H12	0.005788
C13	0.304573	H13	-0.012428
C13a	-0.149861	#	

Appendix 79 Mulliken spin densities of B[a]NX. (Spin density at oxygen is 0.073637).



Appendix 80 UV/Vis spectrum of phenaleno[1,9-*cd*]isoxazole **65** between 200-800 nm.



Appendix 81 CW-ESR spectrum (1st derivative) of DPPH with a g-factor of 2.0070 used as a reference for the calibration of the g-factors of the compounds **54** and NXTEMPO (applying $g_{\text{sample}} = 2.0036 * B_{\text{DPPH}}/B_{\text{sample}}$).

13. References

- ¹ F.C. Whitmore *J. Am. Chem. Soc.* **1932**, 54, 3274; *Annua. Rep. Prog. Chem.* **1933**, 177; *Chem. Eng. News* **1948**,
- ² D. Bethell, V. Gold *Carbonium Ions*, Academic Press, London, **1967**.
- ³ G.A. Olah *Angew. Chem.* **1973**, 85, 183; *Science* **1970**, 168, 1798.
- ⁴ A. Werner *Chem. Ber.* **1901**, 34, 3300.
- ⁵ A. Baeyer *Chem. Ber.* **1905**, 38, 569.
- ⁶ R.N. Cavalcanti, D.T. Santos, M.A.A. Meirees *Food Res. Int.* **2011**, 44, 499.
- ⁷ J.M. Edwards *Phytochem.* **1974**, 13, 1597.
- ⁸ H.D. VanEtten, J.W. Mansfield, J.A. Bailey, E.E. Farmer *The Plant Cell* **1994**, 6(9), 1191.
- ⁹ C. Flors, S. Nonell *Acc. Chem. Res.* **2006**, 39(5), 293.
- ¹⁰ A.L. Lavoisier *Traité élémentaire de chimie*, Paris: Chez Cuchet, **1789**.
- ¹¹ J.F. Liebig, F. Wöhler *Ann. Pharm.* Band III, Leipzig, **1832**.
- ¹² P. Walden *Chemie der freien Radikale*, Band II, Leipzig Hirzel, **1924**
- ¹³ J.J. Berzelius *Liebigs Ann. Chem.* **1833**, 6, 173.
- ¹⁴ A. Kekule *Liebigs Ann. Chem.* **1858**, 104, 143; **1853**, 106, 146.
- ¹⁵ M.J. Gomberg, *J. Am. Chem. Soc.* **1900**, 22(11), 757.
- ¹⁶ P.H. Rieger *Electron Spin Resonance Analysis and Interpretation*, Cromwell Press: Cambridge, **2007**.
- ¹⁷ A. Rajca *Chem. Eur. J.* **2002**, 8(21), 4834.
- ¹⁸ S.K. Pal, M.E. Itkis, F.S. Tham, R.W. Reed, R.T. Oakley, R.C. Haddon *Science* **2005**, 309, 281.
- ¹⁹ M.E. Itkis, X. Chi, A.W. Cordes, R.C. Haddon *Science* **2002**, 296, 1443.
- ²⁰ D. Wu, W. Pisula, M.C. Haberecht, X. Feng, K. Müllen *Org. Lett.* **2009**, 11(24), 5686.
- ²¹ A. Mukherjee, T.K. Sen, S.K. Mandal, D. Kratzert, D. Stalke, A. Döring, C. Schulzke *J. Chem. Soc.* **2011**, 123(2), 139.
- ²² N. Ngo, K.R. Larson, G.D. Mendenhall *J. Org. Chem.* **1986**, 51, 5390.
- ²³ R. Biswas, H. Kühne, G.W. Brudvig, V. Gopalan *Science Progress* **2001**, 84(1), 45.
- ²⁴ K. Hamachi, K. Matsuda, T. Itoh, H. Iwamura *Bull. Chem. Soc. Jpn.* **1998**, 71, 2937.
- ²⁵ J. Tamuliene, A. Tamulis, J. Kulys *Nonlinear Anal. Model. Control* **2004**, 9(2), 185.
- ²⁶ K. Sato, S. Nakazawa, R. Rahimi, T. Ise, S. Nishida, T. Yoshino, N. Mori, K. Toyota, D. Shiomi, Y. Yakiyama, Y. Morita, M. Kitagawa, K. Nakasuji, M. Nakahara, H. Hara, P. Carl, P. Höfer, T. Takui *J. Mat. Sci.* **2009**, 19, 3739.
- ²⁷ D.M. Murphy, R.D. Farley *Chem. Soc. Rev.* **2006**, 35, 249.
- ²⁸ M. Kasha *Discuss. Faraday Soc.* **1950**, 9, 5.
- ²⁹ K.S. Novoselov, A.K. Geim, S.V. Morozov, D. Jiang, Y. Zhang, S.V. Dubonos, I.V. Grigorieva, A.A. Firsov *Science* **2004**, 306, 666.
- ³⁰ L.D. Landau *Phys. Z. Sowjetunion* **1937**, 11, 26.
- ³¹ A. Kekulé *Ann. d. Chem. u. Pharm.* **1866**, 137(2), 129.
- ³² E. Hückel *Z. Physik* **1931**, 70, 204.
- ³³ E. Clar *Polycyclic Hydrocarbons* Academic Press: New York, **1964**.
- ³⁴ X. Feng, W. Pisula, K. Müllen *Pure Appl. Chem.* **2009**, 81(12), 2203.
- ³⁵ J.C. Fetzer *The Chemistry and Analysis of the Large Polycyclic Aromatic Hydrocarbons*, Wiley: New York **2000**, 27 (2), 143.
- ³⁶ K.F. Lang, J. Kalowy, H. Buffleb *Chem. Ber. Recl.* **1964**, 97, 494.
- ³⁷ C.D. Simpson, J.D. Brand, A.J. Berresheim, L. Przybilla, H.H. Rader, K. Müllen *Chem. Eur. J.* **2002**, 8, 1424.
- ³⁸ X. Yang, X. Dou, A. Rouhanipour, L. Zhi, S. De Feyter, K. Müllen *J. Am. Chem. Soc.* **2008**, 130, 4216.
- ³⁹ E. Clar *Z. Chem.* **1962**, 2(2), 35.
- ⁴⁰ T.W. Armit, R. Robinson *J. Chem. Soc.* **1925**, 1604.
- ⁴¹ B. Boggiano, E. Clar *J. Chem. Soc.* **1957**, 2681.
- ⁴² S.S. Zade, M. Bendikov *Angew. Chem.* **2010**, 49(24), 4012.
- ⁴³ M. Ramart-Lucas, M.J. Matti, T. Guilmar *Bull. Soc. Chim. Fr.* **1948**, 15, 1215.
- ⁴⁴ J. Ferguson, L.W. Reeves, W.G. Schneider *Can. J. Chem.* **1957**, 35, 1117.
- ⁴⁵ P.R. Schleyer *Chem. Rev.* **2001**, 101(5), 1117.
- ⁴⁶ N.C. Baird *J. Chem. Educ.* **1971**, 48(8), 509.
- ⁴⁷ J.M. Robertson *Acta Cryst.* **1948**, 1, 101.
- ⁴⁸ R. Kiralj, M.M.C. Ferreira *J. Chem. Inf. Comput. Sci.* **2002**, 42, 508.
- ⁴⁹ J. Kruszewski, T.M. Krygowski *Tetrahedron Lett.* **1972**, 13(36), 3839.

- ⁵⁰ R.I.T. Cromartie, J.N. Murrell *J. Chem. Soc.* **1961**, 2063.
- ⁵¹ H.J. Dauben Jr, J.D. Wilson, J.L. Laity *J. Am. Chem. Soc.* **1968**, 90(3), 811.
- ⁵² P.R. Schleyer, C. Maerker, A. Dransfeld, H. Jiao, N.J.R. van Eikema Hommes *J. Am. Chem. Soc.* **1996**, 118, 6317.
- ⁵³ A.T. Balaban, D. Oniciu, A.R. Katritzky *Chem. Rev.* **2004**, 104, 2777.
- ⁵⁴ A.T. Balaban *Tetrahedron* **1962**, 18(3), 315.
- ⁵⁵ J.C. Slater *Phys. Rev.* **1930**, 36, 57.
- ⁵⁶ V.I. Minkin, M.N. Glukhovtsev, B. Simkin, B. Ya *Aromaticity and Antiaromaticity. Electronic and Structural Aspects*, Wiley-Interscience: New York, **1994**.
- ⁵⁷ A.T. Balaban, C.D. Nenitzescu *Bull. Acad. Sci. (USSR)* **1960**, 9(11), 1918-1919.
- ⁵⁸ F. Pina, M.J. Melo, M. Maestri, P. Passanti, N. Camaioni, V. Balzani *Eur. J. Org. Chem.* **1999**, 3199.
- ⁵⁹ W. Bonthrone, D.H. Reid *J. Chem. Soc.* **1959**, 2773.
- ⁶⁰ C.R. Martinez, B.L. Iverson *Chem. Sci.* **2012**, 3, 2191.
- ⁶¹ C.H. Hunter, J.K.M. Sanders *J. Am. Chem. Soc.* **1990**, 112, 5525.
- ⁶² M.O. Sinnokrot and C.D. Sherrill *J. Phys. Chem. A* **2006**, 110, 10656.
- ⁶³ S. Grimme *Angew. Chem. Int. Ed.* **2008**, 47, 3430.
- ⁶⁴ G.B. McGaughy, M. Gagnes, A.K. Rappé *J. Biol. Chem.* **1998**, 273(25), 15458.
- ⁶⁵ Y. Morita, S. Suzuki, K. Satu, T. Takui *Nature Chemistry* **2011**, 3, 197.
- ⁶⁶ R.C. Haddon *Nature* **1975**, 256, 394.
- ⁶⁷ J.B. Woell, P. Boudjouk *J. Organomet. Chem.* **1979**, 172, C43
- ⁶⁸ S. Lin, P. Boudjouk *J. Organomet. Chem.* **1980**, 187, C11.
- ⁶⁹ R.M. Pagni, M.N. Burnett, H.M. Hassaneen *Tetrahedron* **1982**, 38 (6), 843.
- ⁷⁰ J.M. Zoellner, R.W. Zoellner *J. Mol. Struct.* **2008**, 863, 50.
- ⁷¹ J.F. Muller, D. Muller, H.J. Dewey, J. Michl *J. Am. Chem. Soc.* **1978**, 100, 1629.
- ⁷² J.A. Marshall, P.G. Wuts *J. Am. Chem. Soc.* **1978**, 100(5) 1629.
- ⁷³ J.J. Fisher, J.H. Penn, D. Döhnert, J. Michl *J. Am. Chem. Soc.* **1986**, 108, 1715.
- ⁷⁴ J.J. Fisher, J. Michl *J. Am. Chem. Soc.* **1987**, 109, 583.
- ⁷⁵ W.R. Roth, C. Unger, T. Wasser *Liebigs Ann.* **1996**, 2155.
- ⁷⁶ G. Lock, G. Gergely Ber. *Deutsch. Chem. Ges.* **1944**, 77B, 461.
- ⁷⁷ V. Boekelheide, C.E. Larrabee *J. Am. Chem. Soc.* **1950**, 72, 1245.
- ⁷⁸ M. Gerst, C. Rüchardt *Chem. Ber.* **1993**, 126, 1039.
- ⁷⁹ A. Streitweiser Jr., J.M. Word, F. Guilbé, J.S. Wright *J. Org. Chem.* **1981**, 46, 2588.
- ⁸⁰ D.H. Reid *Q. Rev. Chem. Soc.* **1965**, 19, 274.
- ⁸¹ D.H. Reid *Tetrahedron* **1958**, 3, 339.
- ⁸² K. Goto, T. Kubo, K. Yamamoto, K. Nakasuji, K. Sato, D. Shiomi, T. Takui, M. Kubota, T. Kobayashi, K. Yakusi, J. Ouyang *J. Am. Chem. Soc.* **1999**, 121, 1619.
- ⁸³ H. Sitzmann, H. Bock, R. Boese, T. Dezember, Z. Havlas, W. Kaim, M. Moscherosch *J. Am. Chem. Soc.* **1993**, 115, 12003.
- ⁸⁴ S. Suzuki, Y. Morita, K. Fukui, K. Sato, D. Shiomi, T. Takui, K. Nakasuji *J. Am. Chem. Soc.* **2006**, 128, 2530.
- ⁸⁵ K. Nakasuji, M. Yamaguchi, I. Murata, K. Yamaguchi, T. Fueno, H. Ohya-Nishiguchi, T. Sugano, M. Kinoshita *J. Am. Chem. Soc.* **1989**, 111, 9265.
- ⁸⁶ F. Gerson, E. Heilbronner, H.A. Reddoch, D.H. Paskovich, N.C. Das *Helv. Chim. Acta.* **1967**, 50, 813.
- ⁸⁷ R.C. Haddon, F. Wudl, M.L. Kaplan, J.H. Marshall, R.E. Cais, F.B. Bramwell *J. Am. Chem. Soc.* **1978**, 100(24), 7629.
- ⁸⁸ K. Bechgaard, V.D. Parker, C.T. Peterson *J. Am. Chem. Soc.* **1973**, 95(13), 4373.
- ⁸⁹ L. Beer, S.K. Mandal, R.W. Reed, R.T. Oakley, F.S. Tham, B. Donnadieu, R.C. Haddon *Crystal Growth & Design* **2007**, 7(4), 802.
- ⁹⁰ Y. Hou, H. Wang, Z. Li, Y. Liu, X. Wan, X. Xue, Y. Chen, A. Yu *Tetrahedron Lett.* **2011**, 52, 3670.
- ⁹¹ Y. Morita, S. Nishida, J. Kawai, K. Fukui, S. Nakazawa, K. Sato, D. Shiomi, T. Takui, K. Nakasuji *Org. Lett.* **2002**, 4 (12), 1985.
- ⁹² Y. Morita, J. Kawai, S. Nishida, K. Fukui, S. Nakazawa, K. Sato, D. Shiomi, T. Takui, K. Nakasuji *Polyhedron* **2003**, 22, 2205.
- ⁹³ Y. Morita, T. Okafuji, M. Satoh *Molecular crystalline secondary batteries*, JP 2007227186 A, Jpn. Kokai Tokyo Koho **2007**.
- ⁹⁴ Y. Morita, S. Nishida, T. Murata, M. Moriguchi, A. Ueda, M. Satoh, K. Arifuku, K. Sato, T. Takui *Nature Mat. Lett.* **2011**, 10, 947.

- ⁹⁵ Y. Morita, T. Ohba, N. Haneda, S. Maki, J. Kawai, K. Hatanaka, K. Sato, D. Shiomi, T. Takui, K. Nakasuji *J. Am. Chem. Soc.* **2000**, 122, 4825.
- ⁹⁶ C. Darwin *The Origin of Species*, Encyclopedia Britannica: Chicago, IL, 11, **1952**.
- ⁹⁷ J.M. Kornfeld, J.M. Edwards *Biochim. et Biophys. Acta* **1972**, 286, 88.
- ⁹⁸ F. Echeverri, F. Torres, W. Quiñones, G. Escobar, R. Archbold *Phytochem. Rev.* **2012**, 11(1), 1.
- ⁹⁹ J.G. Luis, W.Q. Fletcher, F. Echeverri, T. Abad, M.P. Kichi, A. Perales *Nat. Prod. Lett.* **1995**, 6, 23.
- ¹⁰⁰ N.Hirai, H. Ishida, K. Koshimizu *Phytochem.* **1994**, 37, 383.
- ¹⁰¹ J.G. Luis, F. Echeverri, W. Quinones, I. Brito, M. Lopez, F. Torres, G. Cardona, Z. Aguiar, C. Pelaez, M. Rojas *J. Org. Chem.* **1993**, 58, 4306.
- ¹⁰² R.H. Binks, J.R. Greenham, J.G. Luis, S.R. Gowen *Phytochem.* **1997**, 45, 47.
- ¹⁰³ D. Hölscher, B. Schneider *Nat. Prod. Lett.* **1995**, 7, 177.
- ¹⁰⁴ D. Hölscher, B. Schneider *J. Chem. Soc. Chem. Comm.* **1995**, 525.
- ¹⁰⁵ R. Schmidt, C. Tanielian, R. Dunsbach, C. Wolff *J. Photochem. Photobiol. A: Chem.* **1994**, 79, 11.
- ¹⁰⁶ T. Okutsu, S. Noda, S. Tanaka, A. Kawai, K. Obi, H. Hiratsuka *J. Photochem. Photobiol. A*, **2000**, 132, 37.
- ¹⁰⁷ S.K. Lower, M.A. El-Sayed *Chem. Rev.* **1966**, 66, 199.
- ¹⁰⁸ M.C. Daza, M. Doerr, S. Salzmann, C.M. Marian *Phys. Chem. Chem.* **2009**, 11, 1688.
- ¹⁰⁹ C. Flors, S. Nonell *J. Photochem. Photobiol. A: Chem.* **2004**, 163, 9.
- ¹¹⁰ E. Oliveros, P. Suardi-Murasecco, T. Aminian-Saghafi, H.J. Hansen, A. M. Braun *Helv. Chim. Acta* **1991**, 74, 79.
- ¹¹¹ E. Oliveros, S.H. Bossmann, S. Nonell, C. Martí, G. Heit, G. Tröscher, A. Neuner, C. Martínez, A.M. Braun *New. J. Chem.* **1999**, 85.
- ¹¹² C. Flors, P.R. Ogilby, J. G. Luis, T.A. Grillo, L.R. Izquierdo, P.L. Gentili, L. Bussotti, S. Nonell *Photochem. Photobiol.* **2006**, 82, 95.
- ¹¹³ J.C. Netto-Ferreira, W.J. Leigh, J.C. Scaiano *J. Am. Chem. Soc.* **1985**, 107, 2617.
- ¹¹⁴ J.N. Moothy, S.L. Monahan, R.B. Sunoj, J. Chandrasekhar, C. Bohne *J. Am. Chem. Soc.* **1999**, 121, 3093.
- ¹¹⁵ J.W. Leigh, J.A. Banish, M.S. Workentin *Chem. Comm.* **1993**, 988.
- ¹¹⁶ J.C. Scaiano, M.J. Perkins, J.W. Sheppard, M.S. Platz, R.L. Barcus *J. Photochem.* **1983**, 21, 137.
- ¹¹⁷ G. Bucher *J. Phys. Chem. A* **2008**, 112(24), 5411.
- ¹¹⁸ Unpublished results by G. Bucher, C. Flors, J.G. Luis, T.A. Grillo, S. Nonell.
- ¹¹⁹ R.G. Cooke, I.J. Dagley *Aust. J. Chem.* **1979**, 32, 1841.
- ¹²⁰ W. Quinoñes, G. Escobar, F. Echeverri, F. Torres, Y. Rosero, V. Arango, G. Cardona, A. Gallego *Molecules* **2000**, 5, 974.
- ¹²¹ F. Otálvaro, W. Quinoñes, F. Echeverri, B. Schneider *J. Label. Compd. Radiopharm.* **2004**, 47, 147.
- ¹²² C.F. Koelsch, J.A. Anthes *J. Org. Chem.* **1941**, 6, 558.
- ¹²³ G.I. Feutrill, M. L. Whitelaw *Aust. J. Chem.* **1981**, 34, 1423.
- ¹²⁴ R.G. Cooke, I.J. Dagley *Tetrahedron Lett.* **1978**, 7, 637.
- ¹²⁵ R.G. Cooke, B.K. Merrett, G.J. O'Loughlin, G.A. Pietersz *Aust. J. Chem.* **1980**, 33, 2317.
- ¹²⁶ J.L. Carey, R.H. Thomson, P.J. Cox *J. Chem. Soc. Perkin Trans. I.* **1983**, 1267.
- ¹²⁷ R.G. Cooke; R.L. Thomas *Aust. J. Chem.* **1975**, 28, 1053.
- ¹²⁸ R. Hicks *Org. Biomol. Chem.* **2007**, 5, 1321.
- ¹²⁹ I. Ratera, J. Veciana *Chem. Soc. Rev.* **2012**, 41, 303.
- ¹³⁰ Z. Sun; J. Wu *J. Mat. Chem.* **2012**, 22, 4151.
- ¹³¹ J. Huang, M. Kertesz *J. Am. Chem.* **2007**, 129, 1634.
- ¹³² V. Zaitsev, S.V. Rosokha, M. Head-Gordon, J.K. Kochi *J. Org. Chem.* **2006**, 71, 520.
- ¹³³ A. Ueda, K. Yoshida, S. Suzuki; K. Fukui, K. Nakasuji, Y. Morita *J. Phys. Org. Chem.* **2011**, 24, 952.
- ¹³⁴ Y. Morita, T. Aoki, K. Fukui, S. Nakazawa, K. Tamaki, S. Suzuki, A. Fuyuhiko, K. Yamamoto; K. Sato, D. Shiomi, A. Naito, T. Takui, K. Nakasuji *Angew. Chem. Int. Ed.* **2002**, 41, 1793.
- ¹³⁵ T. Kubo, M. Sakamoto, M. Akabane, Y. Fujiwara, K. Yamamoto, M. Akita, K. Inoue, T. Takui, K. Nakasuji *Angew. Chem. Int. Ed.* **2004**, 43, 6474.
- ¹³⁶ T. Kubo, K. Yamamoto, K. Nakasuji, T. Takui *Tetrahedron Lett.* **2001**, 42, 7997.
- ¹³⁷ K. Nakasuji, K. Yoshida, I. Murata *J. Am. Chem. Soc.* **1983**, 105, 5136.
- ¹³⁸ T. Kubo, A. Shimizu, M. Uruichi, K. Yakushi, M. Nakano, D. Shiomi, K. Sato, T. Takui, Y. Morita, K. Nakasuji *Org. Lett.* **2007**, 9(1), 81.
- ¹³⁹ S. Lin; P. Boudjouk *J. Organomet. Chem.* **1980**, 187, C11.
- ¹⁴⁰ J. B. Woell, P. Boudjouk *J. Organomet. Chem.* **1979**, 172, C43.
- ¹⁴¹ K.D. Franz, G.M. McLaughlin, R.L. Martin, G.B. Robertson *Acta Cryst.* **1982**, B38, 2476.

- ¹⁴² Y. Morita, S. Suzuki, K. Fukui, S. Nakazawa, H. Kitagawa, H. Kishida, H. Okamoto, A. Naito, A. Sekine, Y. Ohashi, M. Shiro, K. Sasaki, D. Shiomi, K. Sato, T. Takui, K. Nakasuji *Nature Materials* **2008**, *7*, 49.
- ¹⁴³ P. Bag, M.E. Itkis; S.K. Pal, E. Bekyarova, B. Donnadiou, R.C. Haddon *J. Phys. Org. Chem.* **2012**, *25*, 566.
- ¹⁴⁴ X. Chi, M.E. Itkis, B.O. Patrick, T.M. Barclay, R.W. Reed, R.T. Oakley, A.W. Cordes, R.C. Haddon *J. Am. Chem. Soc.* **1999**, *121*, 10395.
- ¹⁴⁵ P. Liao; M.E. Itkis, R.T. Oakley, F.S. Tham, R.C. Haddon *J. Am. Chem. Soc.* **2004**, *126*, 14297.
- ¹⁴⁶ S. Nishida, Y. Morita, K. Fukui, K. Sato, D. Shiomi, T. Takui, K. Nakasuji *Angew. Chem. Int. Ed.* **2005**, *44*, 7277.
- ¹⁴⁷ M.E. Itkis, X. Chi, A.W. Cordes, R.C. Haddon *Science* **2002**, *296*(5572), 1443.
- ¹⁴⁸ K. Goto, T. Kubo, K. Yamamoto, K. Nakasuji, K. Sato, D. Shiomi, T. Takui, M. Kubota, T. Kobayashi, K. Yakusi; J. Ouyang *J. Am. Chem. Soc.* **1999**, *121*, 1619.
- ¹⁴⁹ R.C. Haddon, S.V. Chichester, S.M. Stein, J.H. Marshall, A.M. Muijsce *J. Am. Chem. Soc.* **1987**, *52*(4), 711.
- ¹⁵⁰ R.C. Haddon, A.M. Hirani, N.J. Kroloff, J.M. Marshall *J. Org. Chem.* **1983**, *48*, 2115.
- ¹⁵¹ L. Beer, R.W. Reed, C.M. Robertson, R.T. Oakley, F.S. Tham, R.C. Haddon *Org. Lett.* **2008**, *11*(14), 3121.
- ¹⁵² J.C. Martin, R.G. Smith *J. Am. Chem. Soc.* **1964**, *86*(11), 2252.
- ¹⁵³ F.C. Krebs, B.W. Laursen, I. Johannsen, A. Faldt, K. Bechgaard, C.S. Jacobsen, N. Thorup, K. Boubekeur *Acta Cryst.* **1999**, *B55*, 410.
- ¹⁵⁴ B.W. Laursen, F.C. Krebs, M.F. Nielsen, K. Bechgaard, J.B. Christensen, N. Harrit *J. Am. Chem. Soc.* **1998**, *120*, 12255.
- ¹⁵⁵ A. Faldt, F.C. Krebs, N. Thorup *J. Chem. Soc. Perkin Trans. 2* **1997**, *11*, 2219.
- ¹⁵⁶ B.W. Laursen, J. Reynisson, K.V. Mikkelsen, K. Bechgaard, N. Harrit *Photochem. Photobiol. Sci.* **2005**, *4*, 568.
- ¹⁵⁷ T. Sørensen, B.W. Laursen *J. Org. Chem.* **2010**, *75*, 6182.
- ¹⁵⁸ A. Pothukuchy, C.L. Mazzitelli, M.L. Rodriguez, B. Tuesuwan, M. Salazar, J.S. Brodbelt, S.M. Kerwin *Biochemistry* **2005**, *44*, 2163.
- ¹⁵⁹ J. Reynisson, G.B. Schuster, S.B. Howerton, L.D. Williams, R.N. Barnett, L. Cleveland, U. Landman, N. Harrit, J.B. Chaires *J. Am. Chem. Soc.* **2003**, *125*, 2072.
- ¹⁶⁰ W.T. Bowie, M.R. Feldman *J. Am. Chem. Soc.* **1977**, *99*(14), 4721.
- ¹⁶¹ M.J. Sabacky, C.S. Johnson, R.G. Smith, H.S. Gutowsky, J.C. Martin *J. Am. Chem. Soc.* **1967**, *89*(9), 2054.
- ¹⁶² K. Fukuhura, N. Miyata, S. Kamiya *Tetrahedron Lett.* **1990**, *31*(26), 3743.
- ¹⁶³ A.K. Katz, H.I. Carrell, J.P. Glusker *Carcinogenesis* **1998**, *19*(9), 1641.
- ¹⁶⁴ M.K. Lakshman, P.L. Kole, S. Chaturvedi, J.H. Saugier, H.J.C. Yeh, J.P. Glusker, H.L. Carrell, A.K. Katz, C.E. Afshar, W.-M. Dashwood, G. Kenniston, W.M. Baird *J. Am. Chem. Soc.* **2000**, *122*, 12629.
- ¹⁶⁵ E. Campaigne, W.L. Archer *Org. Syn. Coll.* **1953**, *33*, 27; **1963**, *4*, 331.
- ¹⁶⁶ J.L. Luche *J. Am. Chem. Soc.* **1978**, *100*(7), 2226.
- ¹⁶⁷ L. Claisen, A. Claparède *Ber.* **1881**, *14*(2), 2460.
- ¹⁶⁸ G. Majetich, R. Hicks, S. Reister *J. Org. Chem.* **1997**, *62*, 4321.
- ¹⁶⁹ R.S. Laufer, G.I. Dmitrienko *J. Am. Chem. Soc.* **2002**, *124*(9), 1854.
- ¹⁷⁰ F. Otálvaro, J. Nanclares, L.E. Vásquez, W. Quiñones, F. Echeverri, R. Arango, B. Schneider *J. Nat. Prod.* **2007**, *70*, 887.
- ¹⁷¹ P. Ramart-Lucas *Bull. Soc. Chim. Fr.* **1950**, *17*, 259.
- ¹⁷² A. Lazzaro, M. Corominas, C. Martí, C. Flors, L.R. Izquierdo, T.A. Grillo, J.G. Luis, S. Nonell *Photochem. Photobiol. Sci.* **2004**, *3*, 706.
- ¹⁷³ J.F.W. McOmie, M.L. Watts, D.E. West *Tetrahedron* **1968**, *24*, 2289.
- ¹⁷⁴ A. Mitra, P.J. Seaton, R.A. Assarpour, T. Williamson *Tetrahedron* **1998**, *54*, 15489.
- ¹⁷⁵ K. Nakasuji, T. Kubo *Bull. Chem. Soc. Jpn.*, **2004**, *77*, 1791.
- ¹⁷⁶ R. Hicks *Stable Radicals: Fundamentals and Applied Aspects of Odd-Electron Compound*, Wiley: West Sussex, UK, **2010**.
- ¹⁷⁷ Y. Sugihara, H. Kawanaka, I. Murata *Angew. Chem.* **1989**, *101*(9), 1258.
- ¹⁷⁸ D.H. Reid, W. Bonthron *J. Chem. Soc.* **1965**, 5920.
- ¹⁷⁹ P. Boudjouk, P.D. Johnson *J. Org. Chem.* **1978**, *43*(20), 3979.
- ¹⁸⁰ R.G. Cooke, B.K. Merrett, G.J. O'Loughlin, G.A. Pietersz *Aust. J. Chem.* **1980**, *33*, 2317.
- ¹⁸¹ A.L. Chaffee, R.G. Cooke, I.J. Dagley, P. Perlmutter, R.L. Thomas *Aust. J. Chem.* **1981**, *34*, 587.
- ¹⁸² P. Linda, A. Lucarelli, G. Marino, G. Savelli *J. Chem. Soc. Perkin II*, **1974**, 1610.
- ¹⁸³ A. Schönberg, A. Sina *J. Am. Chem. Soc.* **1959**, *72*(8), 3396.
- ¹⁸⁴ R.S. Becker, S. Chakravorti, C.A. Gartner, M.G. Miguel *J. Chem. Soc.* **1993**, *Faraday Trans.* *89*(7), 1007.
- ¹⁸⁵ J. Borbély, V. Szabó *Tetrahedron Lett.* **1984**, *25*(50), 5813.

- ¹⁸⁶ L.F. Fieser, M.D. Gates *J. Am. Chem. Soc.* **1940**, 62(9), 2335.
- ¹⁸⁷ J.W. Cook, C.L. Hewett *J. Chem. Soc.* **1934**, 365.
- ¹⁸⁸ L.F. Fieser, E.B. Hershberg *J. Am. Chem. Soc.* **1938**, 60 (7), 1658.
- ¹⁸⁹ H.J. Williams, R.G. Schotter *Aust. J. Chem.* **1974**, 27, 685.
- ¹⁹⁰ I.K. Lewis, R.D. Topsom *Aust. J. Chem.* **1965**, 18 (6), 923.
- ¹⁹¹ G.S. Silverman, P.H. Rakita *Handbook of Grignard reagents*; Marcel Dekker Inc.: New York **1996**.
- ¹⁹² F. Bickelhaupt *Angew. Chem.* **1987**, 99, 1020.
- ¹⁹³ F. Otálvaro, J. Nanclares, L.E. Vásquez, W. Quiñones, F. Echeverri, R. Arango, B. Schneider *J. Nat. Prod.* **2007**, 70, 887.
- ¹⁹⁴ J.D. Roberts, D.Y. Curtin *J. Am. Chem. Soc.* **1946**, 68(8), 1658.
- ¹⁹⁵ I. Chambrier, M.J. Cook, D.A. Mayes, D.A. Mayes, C. MacDonald *J. Porphyrins Phthalocyanines* **2003**, 7, 426.
- ¹⁹⁶ A.T. Balaban, A. Dinculescu, G.N. Dorofeenko, G.W. Fischer, A.V. Koblik, V.V. Mezheritskii, W. Schroth *Pyrylium salts, Syntheses, Reactions, and Physical Properties*, Academic Press: New York, **1982**.
- ¹⁹⁷ H.I. Schlesinger, H.C. Brown, D.L. Mayfield, J.R. Gilbreath *J. Am. Chem. Soc.* **1953**, 75(1), 213.
- ¹⁹⁸ M.G. Freire, C.M.S.S. Neves, I.M. Marucho, J.A.P. Coutinho, A.M. Fernandes *J. Phys. Chem. A* **2010**, 114, 3744.
- ¹⁹⁹ W.C. Wolsey *J. Chem. Educ.* **1973**, 50(6), 335.
- ²⁰⁰ J. Guin, C. Besnard, J. Lacour *Org. Lett.* **2010**, 12(8), 1748.
- ²⁰¹ J. Reynisson, R. Wilbrandt, V. Brinck, B.W. Laursen, K. Nørgaard, N. Harrit, A.M. Brouwer *Photochem. Photobiol. Sci.* **2002**, 1, 763.
- ²⁰² D. Conreux, N. Mehanna, C. Herse, J. Lacour *J. Org. Chem.* **2011**, 76, 2716.
- ²⁰³ A. Pothukuchy, S. Ellapan, K.R. Gopidas, M. Salazar *Bioorg. Med. Chem. Lett.* **2003**, 13, 1491.
- ²⁰⁴ *Spin densities and hyperfine coupling constants were calculated by G. Bucher.*
- ²⁰⁵ T. Asari, N. Kobayashi, T. Naito, T. Inabe *Bull. Chem. Soc. Jpn.* **2001**, 74, 53.
- ²⁰⁶ H.J. Keller, D. Nöthe, H. Pritzkow, D. Wehe, M. Werner, P. Koch, D. Schweitzer *Mol. Cryst. Liq.* **1980**, 62, 181.
- ²⁰⁷ M.T. Duarte, M.F.M. Piedade, M.P. Robalo, C. Jacob, M.H. Garcia *Cryst. Struct. Comm.* **2006**, 62(11), 531.
- ²⁰⁸ Y. Shen, C.-F. Chen *Chem. Rev.* **2012**, 112(3), 1463.
- ²⁰⁹ L.E. Lyons *Aust. J. Chem.* **1980**, 33, 1717.
- ²¹⁰ Y.-H. Tian, G. Park, M. Kertesz *Chem. Mater.* **2008**, 20, 3266.
- ²¹¹ P.R. Schleyer, H. Jiao *Pure & Appl. Chem.* **1996**, 68(2), 209.
- ²¹² R. Kiralj, M.C. Ferreira *J. Chem. Inf. Comput. Sci.* **2002**, 42, 508.
- ²¹³ W.C. Herndon, C. Párkányi *J. Chem. Edu.* **1976**, 53(11), 689.
- ²¹⁴ A. Julg, P. François *Theor. Chim. Acta* **1967**, 8(3), 249.
- ²¹⁵ T.M. Krygowski *J. Chem. Inf. Comp. Sci.* **1993**, 33, 70.
- ²¹⁶ A.R. Katritzky, K. Jug, D.C. Oniciu *Chem. Rev.* **2001**, 101, 1421.
- ²¹⁷ P.R. Schleyer, C. Maerker, A. Dransfeld, H.Jiao, N.J.R.van.E. Hommes *J. Am. Chem. Soc.* **1996**, 118, 6317.
- ²¹⁸ J. Poater, X. Fradera, M. Duran, M. Sola *Chem. Eur. J.* **2003**, 9, 400.
- ²¹⁹ J. Kruszewski, T.M. Krygowski *Tetrahedron Lett.* **1972**, 36, 3839.
- ²²⁰ R.S. Mulliken *J. Chem. Phys.* **1955**, 23(10), 1833.
- ²²¹ R.L.T. Parreira, S.E. Galembeck *J. Mol. Struct. Theochem* **2006**, 760, 59.
- ²²² A.K. Phukan, R.P. Kalagi, S.R. Gadre, E.D. Jemmis *Inorg. Chem.* **2004**, 43(19).
- ²²³ B.T. Stepień, T.M. Krygowski, M.K. Cyrański, J. Mlochowski, P. Orioli, F. Abbate *ARKIVOC* **2004**, 3, 185.
- ²²⁴ J.W. Levell, A. Ruseckas, J.B. Henry, Y. Wang, A.D. Stretton, A.R. Mount, T.H. Galow, I.D.W. Samuel *J. Phys. Chem.* **2010**, 114, 13291.
- ²²⁵ T.J. Stone, T. Buckman, P.L. Nordio, H.M. McConnell *PNAS* **1965**, 54(4), 1010.
- ²²⁶ F. Troiani, M. Affronte *Chem. Soc. Rev.* **2011**, 40, 3119.
- ²²⁷ K.J. Oh, C. Altenbach, R.J. Collier, W.L. Hubbell *Meth. Mol. Biol.* **2000**, 145, 147.
- ²²⁸ R. Biswas, H. Kühne, G.W. Brudvig, V. Gopalan *Science Progress* **2001**, 84(1), 45.
- ²²⁹ E.V. Bobst, R.S. Keyes, Y.Y. Cao, A.M. Bobst *Biochem.* **1996**, 35(29), 9309.
- ²³⁰ L.J. Berliner, H.M. McConnell *PNAS* **1966**, 55(4), 708.
- ²³¹ I.C.P. Smith, T. Yamane *PNAS* **1967**, 58(3), 884.
- ²³² E.J. Hustedt, A.H. Beth *Annu. Rev. Biophys. Struct.* **1999**, 28, 129.
- ²³³ C. Galli, J.B. Innes, D.J. Hirsch, G.W. Brudwig *J. Mag. Res.* **1996**, Series B 110, 284.
- ²³⁴ E.J. Hustedt, A.I. Smirnov, C.F. Laub, C.E. Cobb, A.H. Beth *Biophys. J.* **1997**, 74, 1861.
- ²³⁵ J.C. Macosko, M.S. Pio, I. Tincoco JR., Y.-K. Shin *RNA* **1999**, 5, 1158.

- ²³⁶ G. Bucher *J. Phys. Chem. A* **2008**, 112, 5411-5417.
- ²³⁷ S. Nakazawa, S. Nishida, T. Ise, T. Yoshino, N. Mori, R.D. Rahimi, K. Sato, Y. Morita, K. Toyota, D. Shiomi, M. Kitagawa, H. Hara, P. Carl, P. Höfer, T. Takui *Angew. Chem. Int. Ed.* **2012**, 51, 9860.
- ²³⁸ F.L. Greenwood, M.D. Kellert, J. Sedlak *Org. Syntheses* **1963**, Vol 3, 108.
- ²³⁹ K. Matsumoto, T. Iwata, M. Suenaga, M. Okudomi, M. Nogawa, M. Nakano, A. Sugahara, Y. Bannai, K. Baba *Heterocycles* **2010**, 81(11), 2539.
- ²⁴⁰ Patent: WO2006/134489 A1, CTG Pharma S.R.L. **2006**,
- ²⁴¹ L.I. Rosquete, M.G. Cabrera-Serra, J.E. Piñero, P. Martín-Rodríguez, L. Fernández-Pérez, J.G. Luis, G. McNaughton-Smith, T. Abad-Grillo *Bioorg. Med. Chem.* **2010**, 18, 4530.
- ²⁴² R.C. Haddon, S.V. Chichester, S.L. Mayo *Synthesis* **1985**, 6(7), 639.
- ²⁴³ R.C. Haddon, A. Sarkar, S.K. Pal, X. Chi, M.E. Itkis, F.S. Tham *J. Am. Chem. Soc.* **2008**, 130, 13683.
- ²⁴⁴ K.D. Franz, R.L. Martin *Tetrahedron* **1978**, 34, 2147.
- ²⁴⁵ S.L. Solodar', L.M. Vinogradov *J. Org. Chem. USSR (Eng. Trans.)* **1980**, 16(10), 1805.
- ²⁴⁶ R.C. Haddon *Aust. J. Chem.* **1984**, 37, 2145.
- ²⁴⁷ G.A. Molander, C.-S. Yun *Tetrahedron* **2002**, 58, 1465.
- ²⁴⁸ J.H. Kirchhoff, M.R. Netherton, I.D. Hills, G.C. Fu *J. Am. Chem. Soc.* **2002**, 124, 13662.
- ²⁴⁹ E.-I. Negishi, T. Takahashi, A.O. King *Organic Syntheses* **1993**, 8, 430.
- ²⁵⁰ A. Kovács, V. Izvekov, K. Zauer, K. Ohta *J. Phys. Chem. A* **2001**, 105, 5000.
- ²⁵¹ D.E. Frantz, D.G. Weaver, J.P. Carey, M.H. Kressm U.H. Dolling *Org. Lett.* **2002**, 4(26), 4714.
- ²⁵² W. Stadlbauer, M. Fischer *J. Heterocyclic Chem.* **1998**, 35, 943.
- ²⁵³ R.S. Rowland, R. Taylor *J. Phys. Chem.* **1996**, 100, 7384.
- ²⁵⁴ A.T. Dlamini, H.J. Williams *Tetrahedron* **1973**, 29, 1327.
- ²⁵⁵ A.M. Echavarren, J.K. Stille *J. Am. Chem. Soc.* **1987**, 109, 5478.
- ²⁵⁶ T. Kamikawa, T. Hayashi *Tetrahedron Lett.* **1997**, 38(40), 7087.
- ²⁵⁷ D. Wu, L. Zhi, G.J. Bodwell, G. Cui, N. Tsao, K. Müllen *Angew. Chem. Int. Ed.* **2007**, 46, 5417.
- ²⁵⁸ F.J.M. Hoeben, P. Jonkheijm, E.W. Meijer, A.P.H.J. Schenning *Chem. Rev.* **2005**, 105, 1491.
- ²⁵⁹ S.V. Draper, D.J. Gregg, R. Madathil *J. Am. Chem. Soc.* **2002**, 124, 3486-3487.
- ²⁶⁰ W. Dilthey, F. Quint *Chem. Ber.* **1936**, 69, 1575.
- ²⁶¹ K. Venkataraman, *The chemistry of synthetic dyes*, Vol.4, p.204, Academic Press: New York and London, **1971**
- ²⁶² D. Wu, X. Feng, M. Takase, M.C. Haberecht, K. Müllen *Tetrahedron* **2008**, 64, 11379.
- ²⁶³ C.E. Loader, C.J. Timmons *J. Chem. Soc.* **1966**, 12, 1078.
- ²⁶⁴ C. Bazzini, S. Bovelli, T. Caronna, C. Gambarotti, M. Giannone, P. Macchi, F. Meinardi, A. Mele, W. Panezeri, F. Recupero, A. Sironi, A. Sironi, R. Tubino *Eur. Jour. Org. Chem.* **2005**, 7, 1247.
- ²⁶⁵ M.F. Budyka, N.I. Potashova, T.N. Gavrishova, V.M. Lee *High Energy Chem.* **2010**, 44(5), 404.
- ²⁶⁶ D. Wu *Heteroatom Containing Polycyclic Aromatic Hydrocarbons with Positive Charge – Synthesis and Characterization*, Dissertation, Mainz **2008**.
- ²⁶⁷ C. Schiele, G. Arnold, H.O. Kallinowski, D. Hendriks *Tetrahedron* **1968**, 24(5), 2293.
- ²⁶⁸ R.S. Becker, S. Chakravorti, C.A. Gartner, M.G. Miguel *J. Chem. Soc.* **1993**, Faraday Trans. 89(7), 1007.
- ²⁶⁹ R.R. Soni, K.N. Trivedi *Indian J. Chem., Sect B* **1988**, 27(1-12), 811.
- ²⁷⁰ L.S. Almeida, P.M. Esteves, M.C.S. Mattos *Synthesis* **2006**, 2, 221.
- ²⁷¹ L. Rintoul, A.S. Micallef, S.E. Bottle *Spectrochim. Acta Part A: Mol. and Biomol. Spec.* **2008**, 70(4), 713.
- ²⁷² H. Ghasemnejad-Bosra, M. Forouzani *Hetero. Comm.* **2011**, Vol. 17 (1-2), 83.

Acknowledgements

I would like to acknowledge my supervisor Dr *Götz Bucher* for giving me the opportunity to carry out this interesting project. Particularly, I would like to thank to former members of the *Bucher* group Dr *Stuart Caldwell*, Dr. *Margeret Smith* for their permanent support with regards to the chemistry and also for the funny conversations cheering up my mood when the chemistry became annoyingly unpredictable and weird. Also I am happy to have met our former Honours and Master students *Craig Smith*, *Gaius Alexander Rew* and *Lisa Eggebrecht*.

I am also happy that I was involved in a magnificiently super-duper teamwork with Dr *Mark D. Symes*, Dr *Christoph Busche* and Dr *Deliang Long*, from the *Cronin* group. Their personal commitment to support this project with regards to cyclic voltammetry, ESR spectroscopy and X-ray structure analysis was essential to obtain a great series of promising results. Moreover it was personally a great pleasure to meet them and to spare my time with them to talk about chemistry and non-chemistry stuff. This also includes their supervisor Prof *Lee Cronin* for his generous support.

Acknowledgements also go to Dr *Lynn Thomas* who carried out the X-ray structure analysis of my first target molecule and Dr *Brian Fitzpatrick* for his support regarding the UV/Vis and fluorescence spectroscopy. Also I would like to appreciate the great support by Prof *Graeme Cooke* and Dr *Joelle Prunet* for helping my project. Also, and finally, a big thank you to all the members of the Chemistry department who helped, cooperated with, or supported me. This, in particular, includes my former Soddy-colleague Dr *Ondrej Kysilka* with whom I enjoyed to share the laboratory as a duo for a half year.